Conference papers

Conference Proceeding (including doi) will be published at www.silos15.com

TABLE OF CONTENTS

15th International Conference on
Shock & Impact Loads on Structures
12-13 June 2025, Gothenburg, Sweden

RE-IMPLEMENTATION AND CHARACTERIZATION OF SJÖBO DRY SAND IN OPENRADIOSS: IMPROVING GROUND SHOCK PREDICTIONS THROUGH TRI-AXIAL AND WAVE VELOCITY TESTING

Leo Laine[a] and Ola Pramm Larsen[b]

[a]LL Engineering AB, Sjupundsgatan 41, 414 84 Göteborg, Sweden,
e-mail: leo.laine@telia.com, webpage: http://www.l2e.se,

[b]CAEWIZ Consulting A/S, Grinda 2B, 0861 OSLO, Norway,
email: ola.pramm.larsen@caewiz.no

Keywords: Ground shock, Dry Sand, Mechanical Properties of Dry Sand, Compaction Equation of State, Shear Strength Model, Shock Waves in Sand, OpenRadioss

Abstract

This paper presents the re-implementation of a well-established compaction and shear strength model, originally available in AUTODYN and widely cited in the literature, into OpenRadioss, an open-source explicit solver for broad range of applications, including shock and impact simulations. The objective is to enhance ground shock predictions by accurately capturing the compaction behavior and shear strength of dry sand. The study focuses on Sjöbo sand, a well-characterized quartz sand, with mechanical properties determined through triaxial compression tests under isotropic consolidation. A porous equation of state (EOS) was developed based on volumetric compression data, while shear wave and longitudinal wave velocity measurements provided estimates of bulk sound speed and shear modulus over a range of pressures. The in situ dry density of the sand was approximately 1574 kg/m³, with an average water content of 6.57%. The re-implementation ensures consistency with previous AUTODYN models while leveraging OpenRadioss' open-source capabilities for broader accessibility and further development. An improved approach for interpolating the unloading behavior from compaction curves was incorporated, ensuring accurate energy dissipation in high-pressure release scenarios. The implementation is validated through single-element tests and particle velocity impact simulations, providing a benchmark for further studies on granular materials under dynamic loading. As a successor to previous research efforts, this work aims to support the OpenRadioss community by providing a validated dry sand material model, enhancing the simulation of granular materials and facilitating further development in open-source computational mechanics.

1 INTRODUCTION

Accurate prediction of ground shock wave propagation and attenuation is critical in many engineering applications, including the design of protective structures, assessment of conventional weapon effects, and evaluation of buried explosions. The mechanical properties of granular materials, such as sand, strongly influence shock behavior. In 2001, Laine and Sandvik introduced the Sjöbo sand model [1], which provided an experimentally validated framework for characterizing sand behavior under dynamic loading. Its subsequent implementation in AUTODYN became a widely adopted approach in the field.

Since its initial publication of the material properties for dry sand [1], the Sjöbo sand model continues to be referenced, in recent studies (2023–2025), for example in [2] applied FEM tools to implement dynamic replacement of soft soils, while in [3] evaluated damage in fiberboard boxes during vertical impact tests. In [4] developed a state equation model incorporating pressure wave propagation speed during high-speed projectile impacts in sand, and [5] validated numerical models of explosive ground shock propagation in dry sand with digital image correlation. Further studies by [6]-[12] have extended the model's applicability and enriched our understanding of granular material behavior under dynamic loading conditions.

This paper presents the re-implementation of the Sjöbo sand model within OpenRadioss, an open-source explicit solver for shock and impact simulations [18]. By transitioning this well-established model to an open-source platform, we aim to provide a robust and accessible tool for the shock and blast community. The current study focuses on validating the re-implementation through single-element tests and particle velocity impact experiments, ensuring that the model accurately captures the compaction behavior and shear strength of dry sand.

The paper is organized as follows: Section 2 reviews the original mechanical properties derived for dry sand (2001) [1]. Section 3 discusses the re-implementation of the compaction EOS for the dry sand model within OpenRadioss and explains how the compaction EOS and unloading phase can be modified to reduce energy dissipation. Section 4 describes the re-implementation of the shear strength model. Section 5 presents simple validation tests using single 3D solid element simulations. Section 6 discusses the challenges of modeling ground shock in both near-field and far-field conditions. Finally, Section 7 provides conclusions and outlines future research directions for improving ground shock predictions using the Sjöbo sand model.

2 ORIGINAL MECHANICAL PROPERTIES DERIVED FOR DRY SAND (2001)

2.1 Original tri-axial tests

The Norwegian Geotechnical Institute (NGI) have both characterized the soil and performed triaxial tests on the sand from Sjöbo, Sweden [14]. Different isotropic and deviatoric stress loading conditions were conducted, during the different tri-axial stress states longitudinal- and shear waves were measured in the sand with piezoelectric sensors, which characterized the bulk sound speed for different densities.

2.2 Characterization of soil

The grain size distribution in the sand was medium to coarse, with grain size number C60/C10 approximately equal to 2. The content of organic compounds was less than one percent. The in situ dry density was approximately 1574 [kg/m^3]; the average water content was approximately 6.57 percent. Finally, the average specific weight of the grains was 2641 [kg/m^3] [13]. It is important to note that the material model data is valid for dry sand conditions, with the in situ dry density and average water content expressed in this section.

2.3 Original Mechanical Properties derived in 2001 paper

Following mechanical properties were derived from the NGI experiments in the original paper, see Fig. 1. Top left subplot shows compaction Equation of State (EOS), with linear unloading bulk modulus, which is calculated by the bulk sound speed c_i, $K_u = \rho_i \cdot c_i^2$, see top right plot in Fig. 1. Bottom left plot in Fig 1. shows the shear strength model as a function of pressure, which uses the shear modulus defined in bottom right corner in Fig 1.

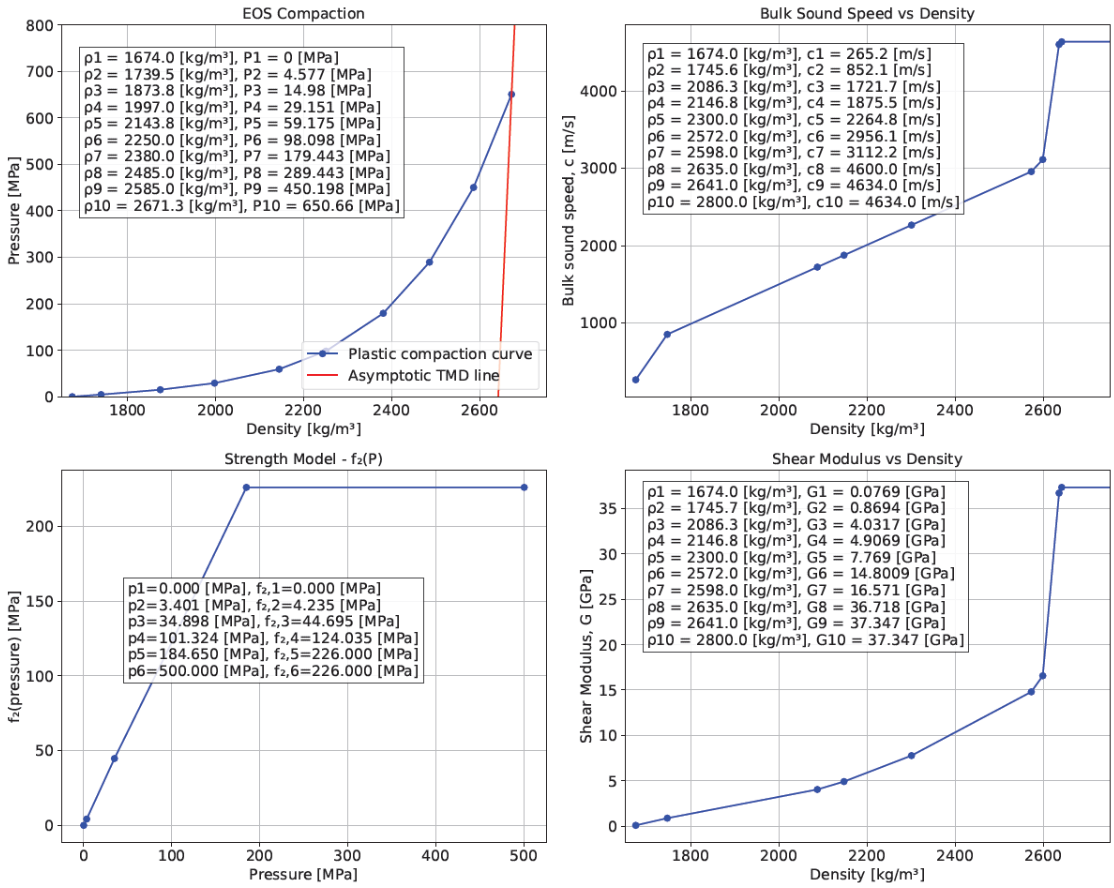

Figure 1. Original Mechanical Properties derived for Dry Sand from Sjöbo Sweden [1]. Yield surface is defined as $f_2(P)$.

3 RE-IMPLEMENTATION OF COMPACTION EOS

3.1 Compaction EOS with density dependent unloading bulk modulus

The plastic compaction curve is given as a 10 point piecewise linear curve, namely pressure as function of density $P_i(\rho_i)$, where the points below 60 MPa pressure was derived from the tri-axial tests [13]. The plastic compaction curve for pressures above 60 [MPa] was predicted by using a polynomial best fit of fifth order, see Fig 1 top left plot. The Theoretical Maximum Density (TMD) was set equal to the average specific weight of the grains in the sand, $\rho_{TMD} = 2641$ [kg/m³]. The solid "asymptotic TMD line" to this curve is linear:

$$P(\rho = \rho_{TMD}) = 0 \quad (1)$$

$$P = c_s^2 \rho_{TMD} \cdot \mu \qquad \text{with } \mu = \rho/\rho_0 - 1 \text{ and } \quad \rho \geq \rho_{TMD} \quad (2)$$

where ρ_{TMD} is the TMD density where no porosity is left, and c_s is the bulk sound speed of fully compacted solid material. The mineral content in the sand is similar what would be found in granite, thus the bulk sound speed of fully compacted material was derived from Shock Hugoniot Data for Westerly Granite [16]. The $c_s = 4636$ [m/s] value was given by the two states ($\rho_0 = 2627$ [kg/m^3], $P_0 = 0$) and ($\rho_1 = 3530$ [kg/m^3], $P_0 = 19.394$ [GPa]).

In the original model, the elastic unloading wave velocity c_i was based upon Pressure(P)-wave v_p and Shear(S)-wave v_s velocity measurements [1] and [13]. The bulk sound speed can be calculated by

$$c = \sqrt{(v_p^2 - \frac{4}{3} v_s^2)} \tag{3}$$

In Fig. 6 the measured P-wave and S-wave velocities for the dry sand are shown together with the calculated bulk sound speed c_i.

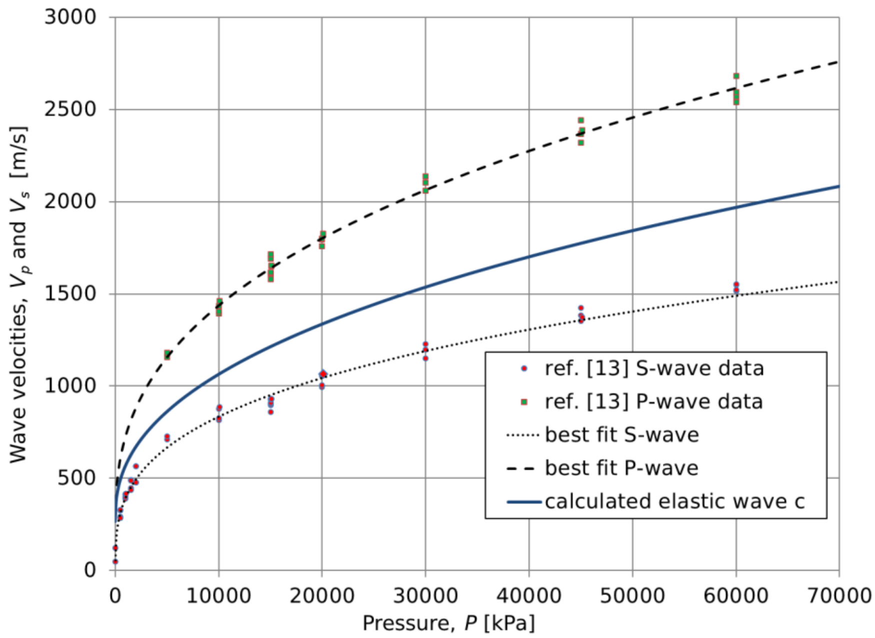

Figure 2. Measured pressure and shear wave velocities as a function of pressure for dry sand (Sjöbo). The blue line corresponds to calculated bulk sound speed c_i, from [1] and [13].

The longitudinal and shear wave velocities above the density 2150 [kg/m^3] were predicted by using linear approximation. The elastic unloading/re-loading compaction curve is given by the density dependent unloading bulk modulus $K_u = c_i^2(\rho_i) \cdot \rho_i$. In the material input the bulk sound speed is given as function of density as piecewise linear 10 points, $c_i(\rho_i)$, see Fig 1 top right plot.

A new feature has been introduced in the compaction EOS, allowing for different reloading response when the sand material expands back to its original volume. The model provides two reloading options: (0) the material follows the zero-pressure line until it reaches the most recent elastic unloading slope used, or (1) plastic compaction pressure reoccurs, treating the expanded material as virgin sand. This functionality is controlled by the Plastic Compaction Re-loading ON (PLACOREON) option in the input file, where PLACOREON = 0 disables plastic reloading and PLACOREON = 1 enables it.

3.2 Energy dissipation during shock propagation in dry sand during unloading

One of the most important effects when studying buried detonation of explosives and the ground shock propagation in far-field, i.e. scaled distances higher than D > 1 [m/kg$^{1/3}$] for TNT, is the fact that soils such as dry sand is compacted by the shock wave propagated in the surrounding media. If the compaction effect is too large during the unloading phase, the shock wave energy from the explosive is dissipated too fast which give a false low loading on buried structures. Therefore it is proposed that the unloading phase in EOS is given more modelling focus and that the unloading bulk sound speed is made not only density dependent $c_i(\rho_i)$ as top right plot in Fig. 1, but also make the bulk sound speed unloading pressure dependent, $c_i(\rho_{i,}P_u)$. This is in fact supported by just studying the mechanical isotropic loading and unloading during the tri-axial isotropic pressure loading and unloading conducted by NGI, see Fig. 3. For example, if the unloading curves from pressure 15 MPa, is followed towards pressures close to zero pressure, it is evident that the unloading bulk modulus is not only dependent on density but also the unloading pressure.

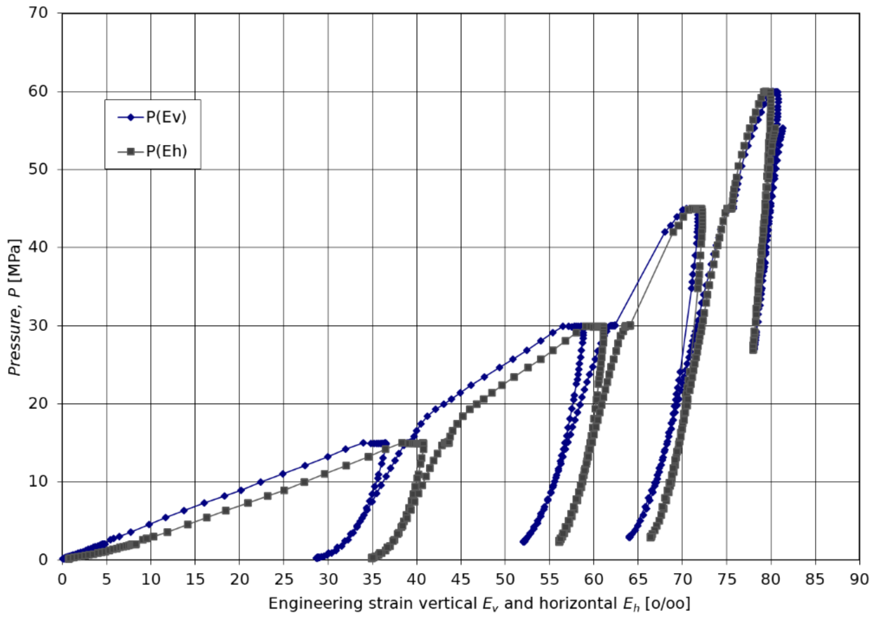

Figure 3. Pressure as a function of vertical and horizontal engineering strain, [14].

In year 2012, authors showed a proposal of how the EOS unloading phase could be modified and include the behavior seen in Fig. 3 for low unloading pressures and conducted implementation into user subroutine in AUTODYN [14], more details can be found in [15] which also includes an appendix with code.

The implemented compaction EOS in OpenRadioss is aimed to have two versions of unloading, the original version 2001, which matches with the Autodyn implementation, see section 2.3 which is in default given with derived mechanical properties of the dry sand, see Fig 1. The second unloading is the improved version from year 2012 with density and pressure dependent unloading bulk sound speed $c_i(\rho_{i,}P_u)$, see [14],[15].

3.3 Compaction EOS with density and pressure dependent unloading bulk modulus

As originally proposed in [14], the main input to the modified EOS uses three piece wise linear curves. The first one is the plastic compaction curve $P_c(\rho)$, see Fig. 5. The second piecewise linear input is the initial wave velocity $c_b(\lambda)$, where $\lambda = \rho(P = 0)$. The third piece wise linear input is how curved the unloading is along the density axis when the pressure is equal to zero $\gamma(\lambda)$, here named curve factor.

The unloading is described with following two equations

$$c_b(\lambda)^2 = \frac{P_c(\lambda+\rho_L(\lambda))}{\rho_L(\lambda)} \tag{4}$$

and

$$P_{\mathrm{UL}}(\rho) = \frac{P_{\mathrm{c}}(\lambda+\rho_{\mathrm{L}}(\lambda))}{\mathrm{e}^{\gamma(\lambda)}-1}\left(\mathrm{e}^{\frac{\gamma(\lambda)}{\rho_{\mathrm{L}}(\lambda)}(\rho-\lambda)} - 1\right) \tag{5}$$

where λ is the density in the $\rho - P$ space along the $P = 0$ line, $\rho_L(\lambda)$ is in ρ space and is defining the horizontal distance for an unloading or re-loading curve, according to Fig. 4. The equations (4) and (5) describes the relationship between the ρ space and the wave velocity c_b. Some of the main properties for the $P_{UL}(\rho)$ equation (5) is that when the density is on its initial or final values it becomes

$$P_{\mathrm{UL}}(\rho = \lambda) = 0 \tag{6}$$

and

$$P_{\mathrm{UL}}\big(\rho = \lambda + \rho_{\mathrm{L}}(\lambda)\big) = P_c. \tag{7}$$

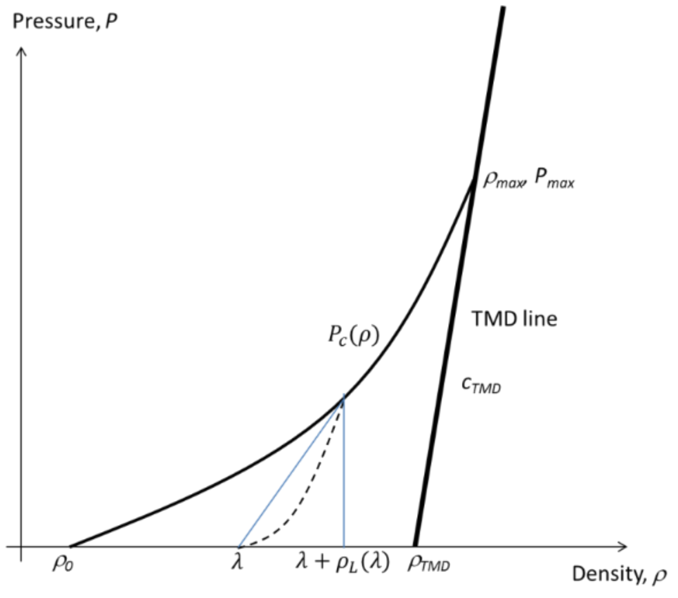

Figure 4. Shows the plastic compaction curve $P_c(\rho)$, Theoretical Maximum Density (TMD) line, the intersection of arbitrary unloading curve with the $P = 0$ line λ, and the density span of unloading curve $\rho_L(\lambda)$.

Fig. 4. Shows the plastic compaction curve $P_c(\rho)$, Theoretical Maximum Density (TMD) line, the intersection of arbitrary unloading curve with the $P = 0$ line λ, and the density span of

unloading curve $\rho_L(\lambda)$.

Another main property is how the curving of the unloading is treated in between the initial and end value. First when the curve factor goes towards zero:

$$\lim_{\gamma(\lambda)\to 0} P_{UL}(\rho) = \frac{P_c(\lambda+\rho_L(\lambda))}{\rho_L(\lambda)}(\rho-\lambda) = c_b(\lambda)^2(\rho-\lambda) \qquad (8)$$

This means that the unloading becomes the same as in the original model with density dependent elastic unloading. Secondly when the curve factor goes to infinity:

$$\lim_{\gamma(\lambda)\to\infty} P_{UL}(\rho) = \begin{cases} 0 \text{ if } \lambda \le \rho < \lambda+\rho_L(\lambda) \\ P_c\big(\lambda+\rho_L(\lambda)\big) \text{ if } \rho = \lambda+\rho_L(\lambda) \end{cases} \qquad (9)$$

This will give a flip turned L-shape like unloading curve. This means that equations (4) and (5) are relatively simple but powerful relationship formulation which gives the possibility to define the unloading for the whole $\rho - P$ space by using three independent piece wise linear input data curves $P_c(\rho)$, $c_b(\lambda)$, and $\gamma(\lambda)$.

To illustrate the relationship and how the curve factor $\gamma(\lambda)$ influence the unloading, the unloading shape is shown for $\gamma(\lambda) = 0,\ 5,\ \text{and}\ 100$, see Fig. 5.

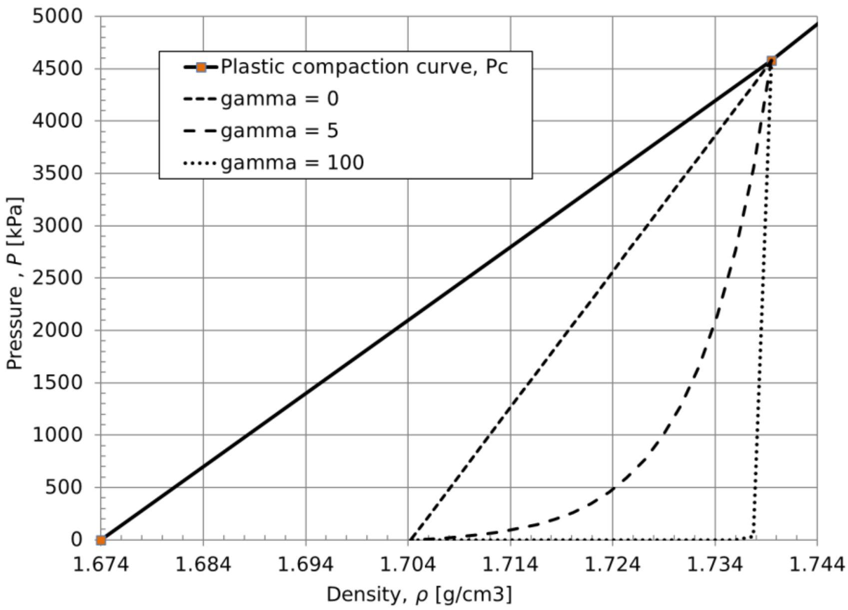

Figure 5. Three different unloading curves depending on the setting of the curve factor $\rho_L(\lambda)$ = 0, 5, and 100, respectively.

3.3 Derived input data for Dry Sand for improved modelling of unloading curves

The derived input data for dry sand is based on fitting the experimental tests from [1] and [13]. The first input is the plastic compaction curve $P_c(\rho)$, which is unchanged input from [1], see Fig. 6. The unloading shape derived from experiments are shown for three different pressure levels, see Fig. 6. The plastic compaction curve is given until it reaches the theoretical maximum density line, see also Fig. 4.

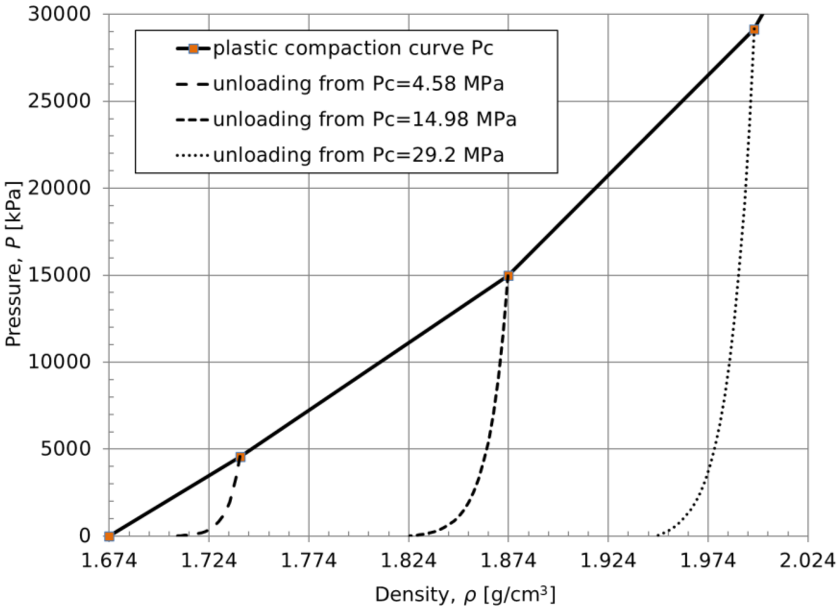

Figure 6. Plastic compaction curve until reaching theoretical maximum density line and unloading curves for three different pressure levels.

In the original model, the elastic unloading wave velocity $c_b(\lambda)$ was based upon wave speed measurements [1] and [13]. In Fig. 3 the measured pressure wave and shear wave for the dry sand is shown. From the measurements the calculated $c_b(\lambda)$ is also shown in Fig. 3. The input data of $c_b(\lambda)$ was modified and instead of using the measured waves the slope of the mechanical unloading curves was used to calculate the initial unloading wave, see Fig. 3.

In Fig. 7 the initial unloading wave $c_b(\lambda)$ is shown for the original model and the modified input. It can be seen that the black curve for the modified input is quite lower for the most part compared with the original model input [1].

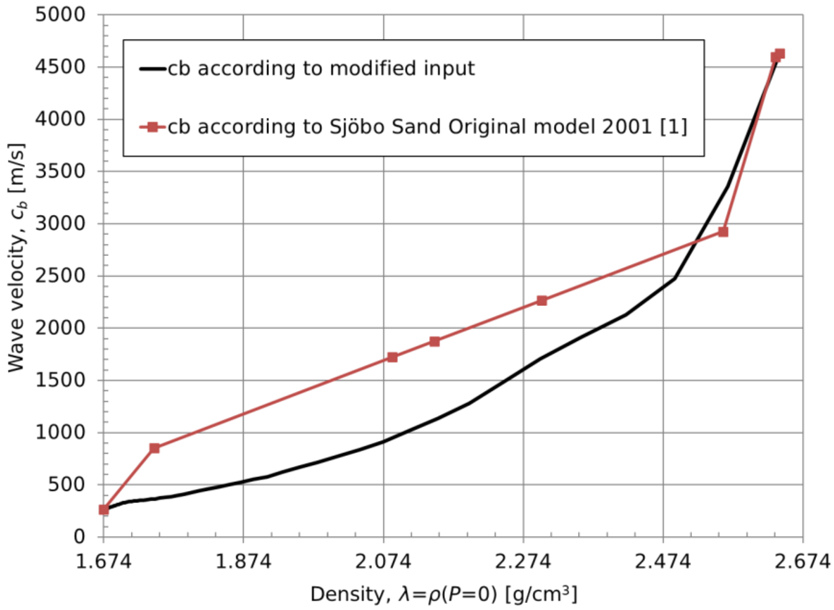

Figure 7. Initial unloading wave velocity $c_b(\lambda)$ as a function of density λ (along $P = 0$ line).

The third input is the curve factor $\gamma(\lambda)$ which defines the shape of the unloading curve. In Fig.

8 the curve factor is given for the modified input and it starts with about 5 to 6 and then decay down to 0 when the theoretical maximum density line is reached. The curve factor has been determined by fitting the experimental results to the model. At the theoretical maximum density line the unloading curve is linear with constant maximum unloading wave velocity.

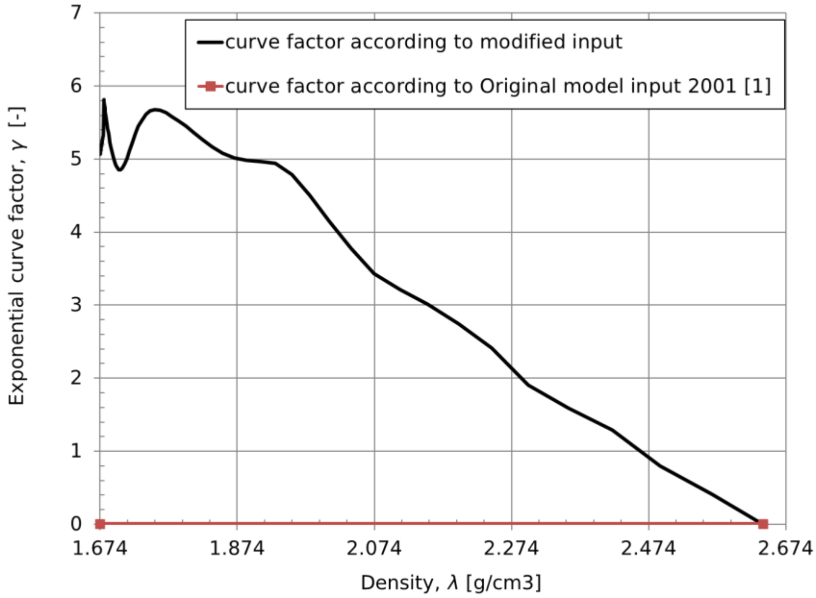

Figure 8. Curve factor $\gamma(\lambda)$ as a function of density λ (along $P = 0$ line).

The unloading curves represent an overall fit with several isotropic compression measurements performed on the dry sand [13]. The input data shown here is just one example of how the EOS model can be used. The implemented EOS model is a powerful way of numerically describe the loading and unloading for numerous soils with different properties of initial density, moisture content, and granularity.

4 RE-IMPLEMENTATION OF SHEAR STRENGTH MODEL

4.1 Density dependent shear modulus

By use of the measured values of the shear wave velocities v_s, see Fig 2, the shear modulus was calculated from

$$G_i = v_s^2 \rho_i \tag{10}$$

Input data for the density dependent shear modulus, G(ρ), is shown in Fig. 1 bottom right plot. The shear modulus curve is given as 10 point piecewise linear curve, namely shear modulus as function of density $G_i(\rho_i)$.

4.2 Pressure dependent yield surface

The yield surface is defined as pressure dependent and pressure hardening of von Mises type function:

$$Y_i = f_2(P_i) \tag{11}$$

The maximum stress difference from the tri-axial shear tests in [13] were utilized for determination of the maximum yield surface. For pressures above 102 [MPa], a linear approximation was utilized up to a maximum cut off value, which was set equal to the unconfined strength for Peaks Pike Granite [17.]. The yield surface is given by piecewise linear pairs $Y_i(P_i)$. The original data for the yield surface is shown in Fig 1 bottom left plot.

5 USER SUBROUTINE VALIDATION

5.1 Single 3D solid element tests

Single 3D solid element tests were conducted on a 1x1x1 m cube using SI units, with right hand side coordinate system. The first test involved an isotropic compression series to validate the EOS compaction (see Section 5.1). The nodes were constrained in such a way that, as the cube's volume decreased, its shape remained cubic. The second test introduced both shear and compression by applying a vertical velocity to two of the top Z-nodes until the displacement approached the full height of the cube (see Section 5.2). In this second test, all nodes were constrained to prevent horizontal movement, while the other two top Z-nodes were also restricted from vertical displacement. In both test cases, a simulation time of 2 seconds was used. A sandbox containing Python scripts for pre-processing, post-processing, and compiling user subroutines can be found in [19].

5.2 Repeated isotropic compressive displacement and release

The isotropic compressive displacement of the outer top Z-node is shown in Fig. 9 (top left). This figure illustrates multiple loading and unloading cycles, with the cube expanding beyond its original volume at 1.8 s. The top right plot in Fig. 9 depicts the piecewise linear plastic compaction of the EOS, with elastic unloading following a density-dependent slope, as expected. The internal energy levels in Fig. 9 (bottom left) show spikes corresponding to elastic unloading events. Finally, Fig. 9 (bottom right) confirms that no von Mises stresses were introduced during the test.

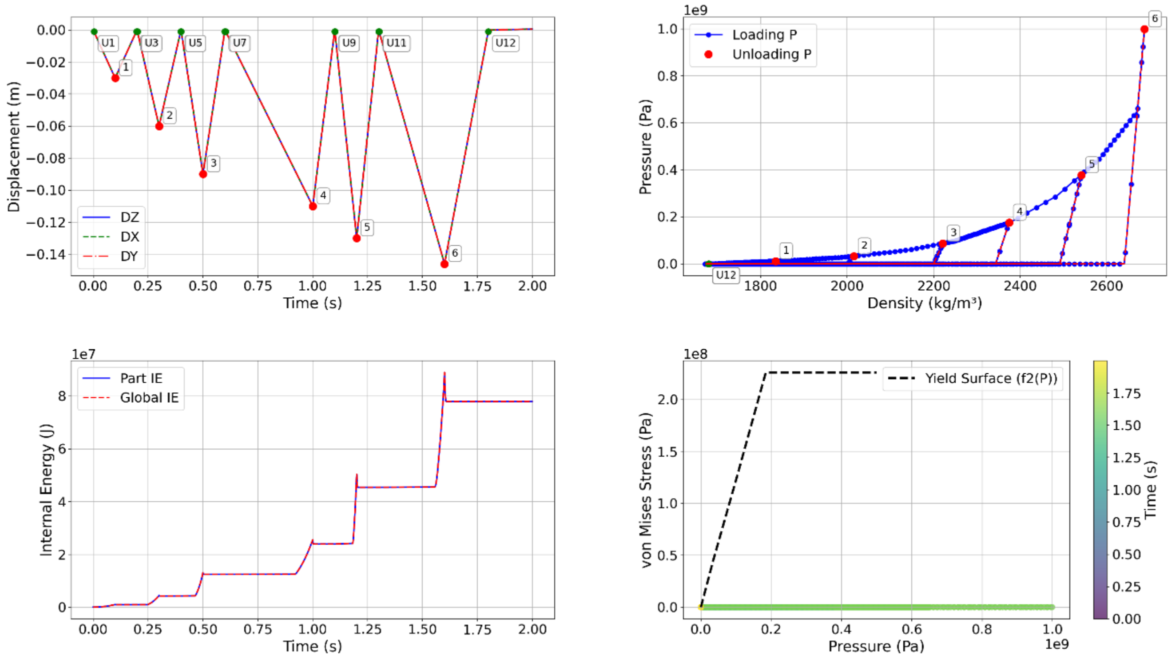

Figure 9. Tri-axial isotropic compression and expansion of single 3D solid element for material model version 2001.

5.3 Constant vertical compressive velocity of two top Z-nodes

The compressive displacement of the 3D solid element under a constant vertical velocity applied to the top two Z-nodes is shown in Fig. 10 (top left). Throughout the simulation, the element undergoes progressive compaction with no unloading phase. The top right plot in Fig. 10 shows the pressure–density response, following the plastic compaction curve of the material model for dry sand. The internal energy (Fig. 10, bottom left) rises steadily as the element absorbs energy during compaction. Meanwhile, the von Mises stress plot (Fig. 10, bottom right) confirms that the test generates both pressure and deviatoric stresses along the yield surface of the dry sand, as expected under a uniaxial compressive loading condition.

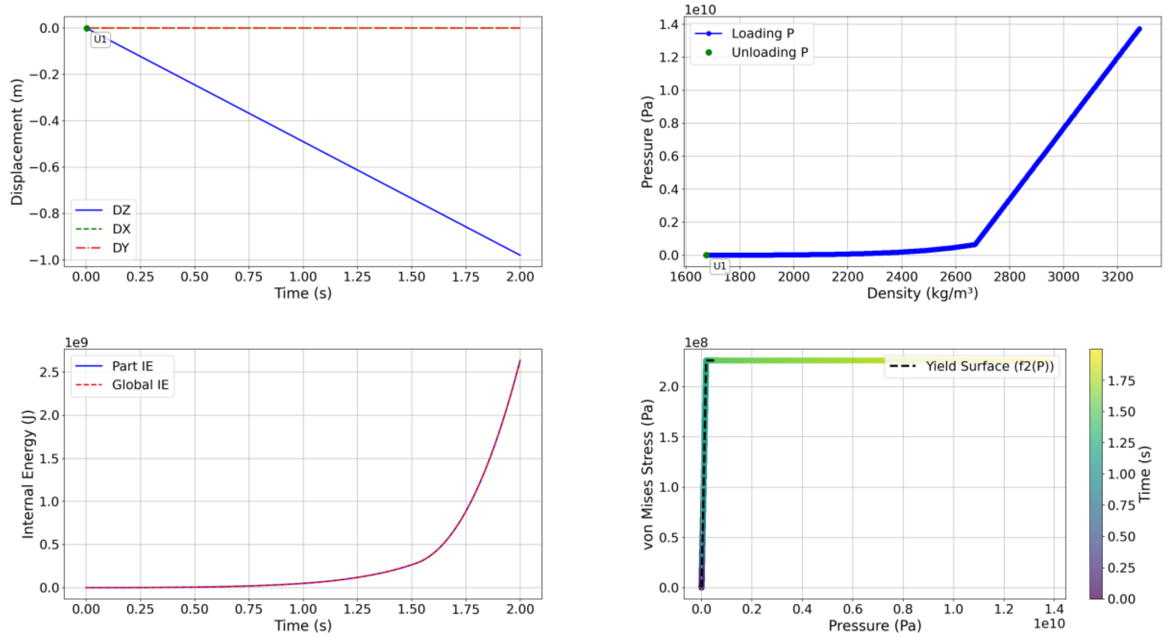

Figure 10. Vertical compressive velocity and expansion of single 3D solid element for material model version 2001.

6 DISCUSSIONS

The experiments in [5] validated numerical modeling of explosive ground shock propagation in dry sand with digital image correlation experiments related to Explosions from Buried Charges. Experiments were thoroughly set up with proper in-situ density and moisture content according to the material properties for dry sand given in [1]. Original dry sand material data from [1] was used and a AUTODYN comparable LS-DYNA model with EOS as EOS_TABULATED_COMPACTION with the possibility to include density dependent unloading bulk modulus $K(\rho)$ and shear strength model MAT_PSEUDO_TENSOR were parameterized. The scenario is having the full complexity of confined buried structure, where the Scaled Stand Off Distance (SSOD) varied from 0.22. 1.09 to 2.17 m/kg$^{1/3}$ TNT, where at least the SSOD< 1 m/kg$^{1/3}$ results in that the explosive gas expansion and cratering highly effects the buried structural response, which was modelled with ALE techniques in [5]. In [5] it was concluded that the near field case the original model dry sand model captured the midpoint deformation of the buried structure quite well. However, in [5] it was also concluded that far-field prediction of structural response needs further work. This aligns with section 3.1 and that the original model with only density dependent unloading bulk modulus $K(\rho)$ has too high energy dissipation for accurate far-field prediction of structural response, see further [15].

In [9] where experimental and numerical characterization of granular material until shock loading, the original dry sand model in AUTODYN was evaluated with following conclusion "The more sophisticated Model2 (original model) brings in additional physical phenomena of material deformation, such as a density-dependent shear modulus and yield stress. These dissipation phenomena notably improve the replication of the dynamic stress–strain curves". This strengthen the case that shear modulus $G(\rho)$ and bulk modulus $K(\rho)$ needs to be density dependent which is now also available in OpenRadioss as the 2001 model version in AUTODYN.

7 CONCLUSIONS AND FUTURE WORK

7.1 Conclusions

The original sand model from 2001 with compaction EOS and shear strength model, with dry sand input parameters, has been successfully implemented as a user subroutine in OpenRadioss. Both the bulk unloading modulus, $K(\rho)$, and the shear modulus, $G(\rho)$, are density-dependent. The default material data found in [1] adequately represents dry sand, provided that the in-situ density and moisture content remain consistent between experiments and simulations. The original model used 10 point pair data input, which still are used for original model data from 2001, however the OpenRadioss allows flexible number of inputs when defined as functions.

In addition, a new feature has been introduced, enabling the dry sand to undergo plastic compaction reloading when it expands back to a larger volume during simulation. This functionality is controlled by the PLACOREON option within the compaction EOS. This means that if the sand returns to its original volume, it will re-compact along the plastic compaction curve. This capability is particularly critical for buried structures that must withstand multiple loading scenarios, such as repeated buried explosions occurring in sequence, accompanied by cratering phenomena near the structure.

7.2 Future work

The next step is to implement the 2012 version of the EOS unloading formulation, incorporating an unloading bulk modulus, that depends on both density and pressure. This modification is crucial for minimizing excessive energy dissipation during ground shock propagation in dry sand, particularly for far-field applications (SSOD > 1 m/kg$^{1/3}$) [15].

Additionally, there may be a need to model shear strength using a shear modulus, $G(\rho, P)$, that is also dependent on both density and pressure. However, further analysis is required to confirm its necessity. This can be achieved through comparisons with elastic longitudinal and shear wave measurements, as conducted in the original experiments [13], and by evaluating its potential benefits in real shock experiments, such as those reported in [9].

ACKNOWLEDGEMENTS

The authors acknowledges the support given by Swedish Civil Contingencies Agency (MSB) and especially Lars Gråbergs, Senior Lecturer Dr. Joosef Leppänen, Adj. Prof. Dr. Morgan Johansson who all are members of the West Coast Sweden Shock Wave Group (WCSSWG) are highly acknowledged for their input. The authors acknowledge the excellent technical support from the Altair team, Thierry Schwoertzig, Marian Bulla, and Eric Lequiniou, about OpenRadioss and inclusion into the open source community.

REFERENCES

[1] Laine L. and Sandvik A.(2001), "Derivation of mechanical properties for sand", 4 th Asian-Pacific conference on Shock and Impact Loads on Structures, CI-Premier PTE LTD, vol. 4, pp 353-360, Singapore, https://www.msb.se/siteassets/dokument/amnesomraden/krisberedskap-ochciviltforsvar/befolkningsskydd/skyddsrum/vetenskapliga-artiklar/derivation-of-mechanical-properties-for-sand.pdf.

[2] Elsiwi, W., Gunaratne, M., and Mullins, G. (2023), "Application of FEM tools in efficient field implementation of dynamic replacement of soft soils", *International Journal of Geomechanics, 23(10)*, DOI: 10.1080/19386362.2023.2264052.

[3] Lengas, N., Johann, S., Kadoke, D., Müller, K., and Steuernagel, L. (2023), "Damage

assessment of complete, filled fiberboard boxes in regulative vertical impact tests by dropping", *Materials Today: Proceedings, Volume 93, Part 4, 2023, Pages 669-679,* DOI: https://doi.org/10.1016/j.matpr.2023.04.679.

[4] Zhang, K., Kinchi, M., & Watanabe, K. (2023), "Development of an Equation of State Model Considering Pressure Wave Propagation Velocity in High-Speed Projectile Impact and Penetration into Sand". *M&M2023 Materials Mechanics Conference, Japan Society of Mechanical Engineers (JSME) (in Japanese).* DOI: https://doi.org/10.1299/jsmemm.2023.CL0227.

[5] Waddoups, R., Clarke, S., Curry, R., Tyas, A., and Farrimond, D. (2024), "Validation of numerical modelling of explosive ground shock propagation in dry sand with digital image correlation experiments", *19th International Symposium on Interaction of the Effects of Munitions with Structures (IEMSs19) Bonn, Germany,* https://eprints.whiterose.ac.uk/220880/.

[6] Denefeld, V., and Aurich, H. (2024), "Experimental and numerical investigation on alternatives to sandy gravel", *Defence Technology Vol. 31, Pages 130-141.* DOI: https://doi.org/10.1016/j.dt.2023.06.016.

[7] Liu, Z., Li, X., Zhou, D., Wang, X., and Lu, F. (2024), "Influence of Water Cover on the Blast Resistance of Circular Plates", *Journal of Pressure Vessel Technology, 146(4),* DOI: https://doi.org/10.1115/1.4066807.

[8] Ba, B. P., & Vu, P. V. (2024), "Research on simulation of a bullet skimming the ground by the finite element method", *Journal of Military Science and Technology, vol. 100, no. 100*, DOI: https://doi.org/10.54939/1859-1043.j.mst.100.2024.139-145.

[9] Ruiz-Ripoll, M. L., Riedel, W., Stocchi, A., Bagusat, F., and Mayrhofer, K. U. (2024), " Experimental and Numerical Characterization of Granular Material Under Shock Loading", *Journal of Dynamic Behavior of Materials*, DOI: https://doi.org/10.1007 /s40870-024-00428-8

[10] Shi, B., Xu, X., Li, J., Li, G., Li, W., Xu, T., Guo, W., Xing, H., and Zhou, J. (2024). Experimental and numerical study on explosion cratering and coupled ground shock in clay. International Journal of Rock Mechanics and Mining Sciences, 173, 105579.

[11] Zhao, Z., Gao, W., Ren, J., Lan, Z., Zhang, Z., Gao, H., He, C., and Zhang, Q. (2025)," Surface-covering water significantly amplifies the explosion impulse of shallow buried explosives", *Defence Technology, In Press, Journal Pre-proof,* DOI: https:doi.org/ 10.1016/j.dt.2025.01.007

[12] Qin, F., Gao, C., Kong, X., and Yang, Y. (2025), "A new composite protective structure based on the controllability of blast load on the structure layer (Ⅱ): influence factors and design concept", Explosion and Shock Waves, Vol. 45, page 1-12, DOI: 10.11883/bzycj-2023-0463.

[13] Heyerdahl H., Madshus C.(2000), *EOS-data for sand, Triaxial tests on sand from Sjöbo*, Norwegian Geotechnical Institute, NGI, report nr: 20001157-1, 2000.

[14] Laine L. and Larsen O.P. (2012), "Implementation of Equation of State for Dry Sand in Autodyn", *Proceedings of 83rd Shock and Vibration Symposium, New Orleans, USA*, https://www.msb.se/siteassets/dokument/amnesomraden/krisberedskap-och-civilt-forsvar/befolkningsskydd/skyddsrum/vetenskapliga-artiklar/implementation-of-equation-of-state-for-dry-sand-in-autodyn.pdf.

[15] Laine L. (2012), Ground shock, *Markstötvåg*, (in Swedish), Report nr MSB344, 2020-09-28 revision 2, Myndigheten för Samhällsskydd och beredskap, 308p, Karlstad, Sweden, https://www.msb.se/siteassets/dokument/amnesomraden/krisberedskap-och-civilt-forsvar/befolkningsskydd/skyddsrum/referenslitteratur/markstotvag.pdf.

[16] Marsh S. P.(1980), LASL shock Hugoniot data, University of California Press, https://sgp.fas.org/othergov/doe/lanl/docs1/shd.pdf.

[17] Goodman R. E.(1989), Introduction to Rock Mechanics, 2. Ed., New York, Wiley.

[18] OpenRadioss (2025), website: https://github.com/OpenRadioss/OpenRadioss

[19] Laine L. (2025), SANDBOX – for material modelling of Dry Sand with OpenRadioss and python, DOI: https://doi.org/10.5281/zenodo.15001304

15th International Conference on
Shock & Impact Loads on Structures
12-13 June 2025, Gothenburg, Sweden

BLAST WAVE INJURY RISK ASSESSMENT IN COMPLEX SCENARIOS USING NUMERICAL SIMULATION

María Chiquito[a], **Andrew Nicholson**[b], Lina M. López[a], Ricardo Castedo[a], Anastasio P. Santos[a], Peter McDonald[b], Chris Stirling[b], Claudia Rastrojo[a] and Jose I. Yenes[c]

[a]Universidad Politécnica de Madrid, Spain, email: maria.chiquito@upm.es, [b]Viper Applied Science, United Kingdom, [c]Escuela Politécnica Superior del Ejército, Spain

Keywords: explosive, numerical modelling, primary injuries, adjusted severity injury index

Abstract

In recent decades, the rise of terrorist actions as a new threat has led to the need to increase safety levels in urban environments. These environments represent a complex scenario for the expansion of the blast wave, which entails an added difficulty when carrying out survivability analyses. Therefore, further research is necessary to better understand the risks of casualties from blast overpressure, particularly from improvised explosive devices (IEDs) and person-borne explosive devices (PBIEDs) detonated inside buildings. To develop a quick blast wave injury risk assessment, numerical simulation appears as a common tool. However, the complexity of the problem means that the level of uncertainty is usually quite high. For this reason, validation of the numerical results by means of experimental tests is of vital importance, but the number of full-scale experiments is very limited. In this research, three tests have been carried out with different IED configurations simulating a PBIED inside a building using vest bombs. The building consisted of a small concrete structure of 6.80 x 5.80 m with a corridor and an inner room. This work focuses on the injury risk assessment inside the building. For this purpose, the Viper Blast CFD solver is employed to accurately model the blast wave propagation and its interaction with the building's facade and structural elements. The assessment is made using Axelsson SP model by means of ASII (Adjusted Severity of Injury Index) together with tertiary blast injury due to whole body translation and impact. The combination of primary and tertiary blast injury results in an overall risk of fatality. The results are validated by comparing the pressure-time histories recorded during the testing with those obtained from numerical simulations at the same locations, demonstrating that such numerical tools can be used with some degree of confidence to perform predictive injury modelling.

1 INTRODUCTION

With the increasing frequency of conflicts shifting to urban areas, terrorist attacks, and industrial accidents like the 2020 Beirut blast, explosions are occurring more often in densely populated locations. In recent times, the most casualties of terrorism in the West have been caused by shooting, vehicle impact or PBIED attacks [1]. Most of the IED attacks over the past 15 years involved small bombs of less than 5 kg [2] or a person-borne improvised explosive device (PBIED) usually containing less than 10 kg of explosives [3], [4]. In these scenarios, structural damage or collapse is not likely to be an issue but human injury still persists. These events can cause devastating injuries, particularly from exposure to blast wave overpressure. There is a research gap related to primary and tertiary blast injuries, even though they are the main source of fatalities. Primary blast injuries are caused by the blast pressure wave and generally affect gas-containing organs, usually the eardrums and lungs.

The tertiary blast injuries result from strong blast winds and pressure that can accelerate and cause whole body translation and impact [5], [6]. Therefore, further research is necessary to better understand the risks of casualties from blast overpressure. Development of injury criteria has been ongoing for many years, but with the main focus on free field conditions [7]. With the rise of terrorist threats, explosions in urban areas have garnered increased attention. Blast injuries, resulting from exposure to overpressure caused by blast waves, can be estimated using injury criteria [8], [9]. However, many of these criteria are based on idealized scenarios that may not accurately represent real-world conditions. Urban environments, with their varied geometries and layouts, can significantly affect the impact of explosions and the resulting injuries. In such environments, blast wave interactions lead to phenomena like reflection, shielding, and channelling. In confined spaces, blast waves can reflect and combine, amplifying their effects. Some of these physical mechanisms, such as shielding, can offer protection, while others, like blast wave reflections from rigid surfaces, can exacerbate the overpressure. At present, it is not well understood how and to what extent the interaction between blast and structure influences injury risk, nor the appropriateness of injury criteria that assume an idealized loading. It is well known that urban environments can modify blast loading. However, the consequences of altering blast loading characteristics for potential blast injuries at different locations within the urban environment remain poorly understood. Additionally, the ability to model injury risk in urban blast scenarios, particularly the applicability of injury criteria based on idealized assumptions, has yet to be thoroughly examined [10]. This gap in knowledge is becoming more significant as researchers who model urban blast scenarios with high sophistication often overlook the validity and relevance of injury criteria in predicting the spatial extent of blast injuries.

Numerical simulation is commonly used to develop a quick blast wave injury risk assessment. There are different tools available on the market that are able to predict blast wave propagation and with the introduction of the injury criteria, vulnerability analysis can be carried out. However, when working in urban or complex scenarios, the lack of experimental data and the dispersion of existing data in the literature make the uncertainty factors introduced in the numerical models excessively high. Therefore, the validation of numerical results by means of experimental data are essential to reduce these uncertainty factors.

In this research, the Viper Blast CFD solver is used to simulate the detonation of a PBIED inside a building using vest bombs. With the numerical modelling, human injury metrics based on primary and tertiary blast injuries are studied and an overall risk of fatality is obtained. The validation of the numerical modelling is made by comparison of experimental data obtained in three full-scale tests. These trials were conducted inside a concrete structure using pressure sensors to record pressure-time histories.

2 EXPERIMENTAL TESTS

Experimental tests, using different types of explosives were conducted at full-scale. However, this research focuses on the first three tests performed as the recorded pressure data inside the room are used to validate the numerical simulations. The first detonation consisted of a test run to check that all the installed instrumentation was working perfectly. For this purpose, a 0.1 kg charge of PG2 (explosive equivalent in composition to C4) was placed on the floor in the centre of the room. The next two tests were conducted using black powder with a composition of potassium nitrate (75%), sulphur (10%) and carbon (15%). In these cases, the black powder was confined inside four steel tubes that were mounted on a vest and detonated on a dummy simulating a person wearing a suicide vest. The black powder was boosted by means of 0.7 m of 15 g/m detonating cord (PETN) inside each steel tube. The main characteristics of the PBIEDs used are summarized in Table 1.

Test	Explosive type	Charge (kg)	PETN (g)	Confinement
0	PG2	0.1		-
1	Black Powder	3.37	42	Steel tubes
2	Black Powder	3.27	42	Steel tubes

Table 1. Main characteristics of the detonated charges.

For the experimental trials, a small concrete building was constructed. The structure was made of reinforced concrete and consisted of a perimeter corridor and an inner room in which the PBIEDs were detonated. The external dimensions of the structure were 6.80 x 5.80 m with a clearance height of 3 m. The outer walls were built with a thickness of 0.4 m while the inner walls were 0.3 m thick, and the roof slab 0.25 m. Figure 1 shows a picture of the concrete building and a sketch with the most relevant dimensions of the building. More details about the structure and its mechanical properties can be found in Santos et al., 2022 [11].

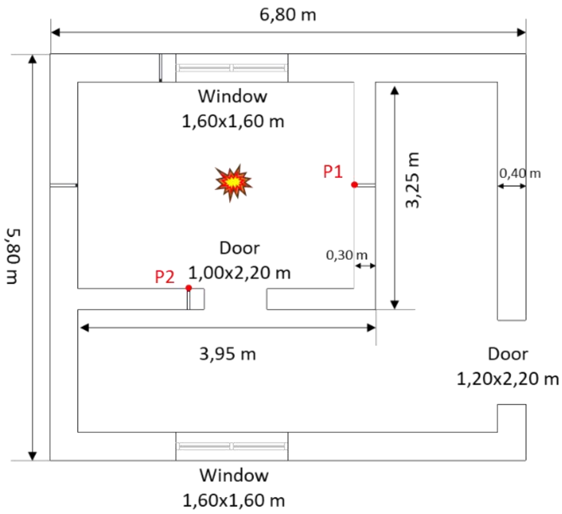

Figure 1. Photo and relevant measurements of the concrete building.

The tests were monitored with pressure gauges and accelerometers. As can be seen in Figure 1, pressure sensors P1 and P2 were located inside the inner room, where the charges were detonated. These sensors registered the reflected pressure as they were located directly on the concrete walls of the room. In addition, a high-speed camera was used to record the trials. As an example, an image sequence of one of the black powder tests is shown in Figure 2.

Figure 2. Image sequence of test T1.

3 NUMERICAL MODEL

The numerical model was built using Viper::Blast. Viper::Blast is a finite volume computational fluid dynamics code for the simulation of blast effects. The numerical scheme is based on the AUSMDV method, and it has further been extended to allow for the simulation of blast physics on GPU's. This leads to a significant increase in performance and scalability for problem types such as those described in this paper, typically by at least a 100 times over other commercially available blast solvers. Viper::Blast offers different approaches to solve the problem. The first step is to find the most accurate methodology to reproduce the problem that is faced here. Since the objective is to validate the software as a numerical tool to make survivability analysis, a comparison between different approaches will be made. Regarding the PG2 test, it is possible to reproduce the detonation by using the JWL equation of state of C4 as well as its equivalence in TNT. However, in case of black powder, this is not possible since black powder is not a HE explosive and therefore it cannot be properly described by a JWL equation of state. On the other hand, the PG2 test consisted of a small sphere of explosive detonated directly on the floor, while in case of black powder suicide vests were used. In these cases, approaches involving different shapes of the charge were tested.
Within the Viper::blast software there are two injury types that are calculated on a cross sectional basis. These are lung injury and tertiary injury, by being picked up and thrown by the blast. The lung injury model utilises the Axelsson Single Point (SP) method for calculation of the compression on the lung whilst the tertiary injury is based upon a median mass and presented area for a drag calculation, to derive a velocity of an individual being thrown. Both these methods are calculated dynamically on the cell-based values as the simulation evolves the Axelsson SP model acting like a SDOF model with a spring mass damper characteristic.
The advantage of these two models is that instead of the Bowen injury criteria they can both deal with the transient and multi reflection environment inherent from an internal blast event.
The metrics are compared to ASII injury scoring metric and head injury criteria for lung and tertiary injury respectively. The Risk criteria in the cross-sectional output is a combination of the lung and tertiary injury metrics into a combined risk of injury with an above 50% chance of injury being the high value. Figure 3 shows the numerical model created where the location of the pressure sensors can be observed. The yellow cross marks the position of the explosive charge.

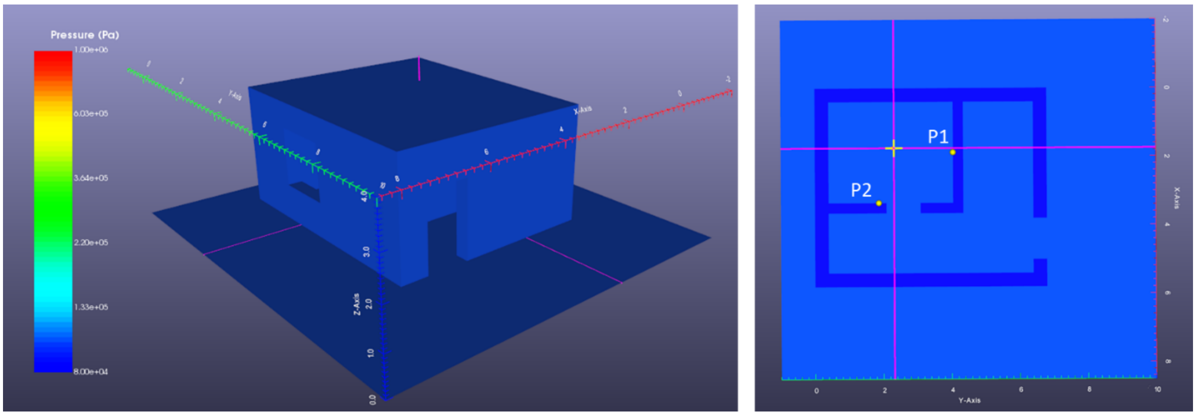

Figure 3. Numerical model of the concrete building and pressure sensor's location.

Since results of numerical modelling are highly dependent on the mesh size, a mesh sensitivity test was performed to select the most appropriate cell size. For this purpose, three different mesh sizes were tested for the first trial: 50 mm, 25 mm and 12.5 mm. After comparing the pressure results with the experimental data, it was concluded that a cell size of 25 mm was the most optimal for carrying out the simulations.

4 RESULTS AND DISCUSSION

As mentioned above, different approaches were considered in the tests regarding the type of explosive as well as the explosive shape. Therefore, results are presented separately for the PG2 and the Black Powder tests.

4.1 Test T0

In this test, 0.1 kg of PG2 were detonated directly on the floor of the inner room. The explosive shape was spherical, and it was initiated by a detonator inserted in the centre from the top of the charge. P1 and P2 were located at 1.51 and 1.55 m of height respectively.
Six different numerical simulations were conducted for this test. Three simulations were performed with 0.1 kg of C4 and the other three simulations with the equivalent charge of TNT, which was 0.14 kg of TNT. For each explosive, the approaches consisted of:

- Modelling from 1D to 3D using an Ideal-Gas (IG) EOS
- Modelling from 1D to 3D using a JWL+AB (JWL) EOS
- Modelling from 3D to 3D simulation detonating a sphere with the size of the test charge

To check the accuracy of the simulations, data of reflected pressure are compared with those obtained in the experimental trial. Prior to the comparison, experimental signals were filtered and adjusted according to the modified Friedlander equation. Therefore, values showed in Table 2 correspond to the adjusted reflected pressure.

P_r (kPa)	**P1**	**Dif. (%)**	**P2**	**Dif. (%)**	**Average dif. (%)**
Experimental	*88.72*		*129.80*		
TNT – IG	106.59	20.14	129.68	-0.09	10.12
C4 – IG	99.47	12.12	120.32	-7.30	9.71
TNT – JWL	118.52	33.59	143.56	10.60	22.09
C4 – JWL	98.05	10.52	118.16	-8.97	9.74
TNT – STL - JWL	125.72	41.70	146.80	13.10	27.40
C4 – STL - JWL	108.16	21.91	127.73	-1.59	11.75

Table 2. Reflected pressure data, experimental and simulated.

As can be seen in Table 2, the simulated values are in reasonable agreement with the experimental ones, with percentage differences depending on the case ranging from 0 to 40%. Comparing by sensor, the P1 sensor offers larger differences in peak pressure compared to the experimental one, although these differences are always positive, which means that the simulation overestimates the pressure and therefore, it would be on the safe side. To compare the data as a whole, an average difference value has been obtained for the data measured by both sensors. Looking at the mean differences, it can be seen that systematically the simulations performed with C4 obtain better results, around 10% difference with the experimental value.
Besides comparing the peak pressure of the first wave, a comparison of the full recorded pressure-time history of the experimental signal with the signal provided by the simulation has been carried out. This assessment serves to check that the numerical modelling is able to reproduce the shock wave reflections on the different walls. Figure 4 shows the comparison between the experimental and simulated signal for the for the simulation performed with C4 and ideal gases EOS. It can be seen how the simulation is not only able to reproduce the first peak of the pressure signal, but for 40 milliseconds, the wave pattern is quite similar.

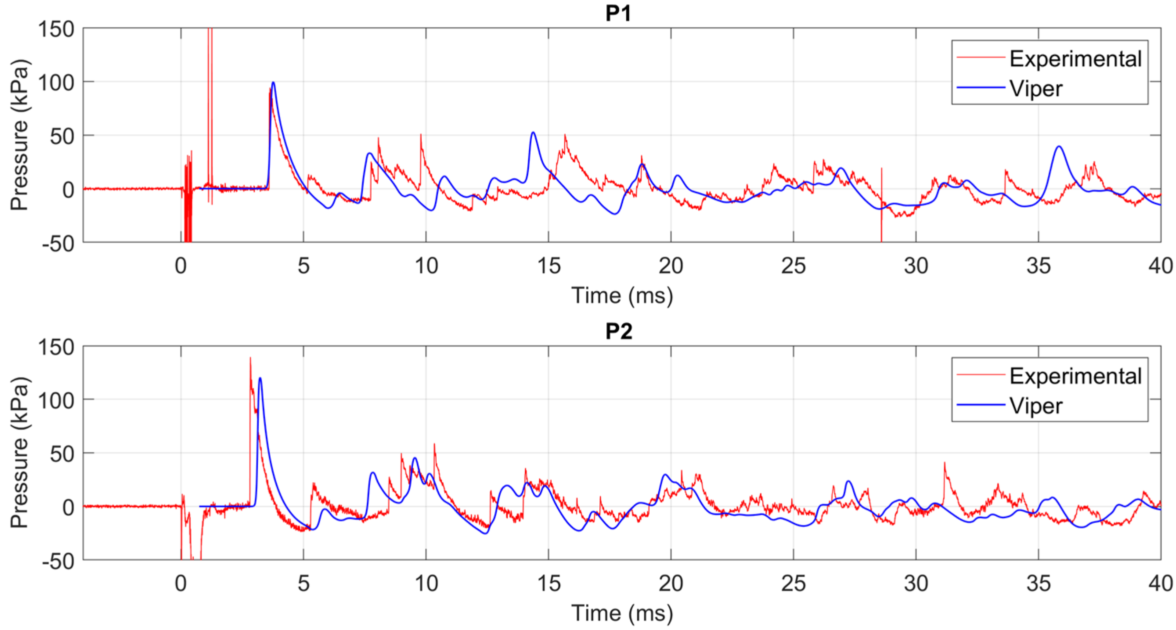

Figure 4. Pressure-time history of experimental and simulated signal.

4.2 Tests T1 and T2

As mentioned above, tests T1 and T2 were conducted using black powder with the addition of detonating cord as a booster to the main charge. The charge was confined inside four steel pipes to simulate a suicide vest. Since the vest was mounted on a dummy, the height of the charge was 1.1 m above the ground in both tests. For the numerical modelling, the TNT equivalent charge of the device was used, being 0.473 kg for test T1 and 0.467 kg for test T2. Due to the small difference in equivalent load between the two tests, an average value of 0.47 kg was adopted for the simulation. For this scenario, four different approaches regarding the charge shape were performed:

- Modelling from 1D to 3D using a sphere
- Modelling from 2D to 3D using a cylinder
- Modelling from 3D to 3D detonating four cylinders with the size of the test charge
- Modelling from 3D to 3D detonating a cuboid with the size of the test charge

For comparison with the experimental results, the mean values of pressure, impulse and time of arrival recorded during the tests were used. Table 3 lists the experimental values of both tests.

	T1 – P1	**T2 – P1**	**Mean P1**	**T1 – P2**	**T2 – P2**	**Mean P2**
P_r (kPa)	195.38	193.11	**194.25**	372.27	382.36	**377.32**
I_r (kPa.ms)	145.08	161.57	**153.33**	174.94	142.86	**158.90**
t_a (ms)	3.048	3.174	**3.111**	2.158	2.183	**2.171**

Table 3. Experimental data of tests T1 and T2.

In contrast to the T0 test, in the black powder tests it can be seen that the experimental pressure data recorded by the P2 sensor is approximately twice that recorded by the P1 sensor, and this is largely due to the shape of the charge. Table 4 shows the numerical results obtained by the different approaches performed.

	P1	Dif. (%)	P2	Dif. (%)	Average dif. (%)
P_r (kPa)					
Experimental	*194.25*		*377.32*		
Sphere	287.69	48.10	318.73	-15.53	31.82
1 Cylinder	338.15	74.09	377.84	0.14	37.11
4 Cylinders	204.44	5.25	562.74	49.14	27.19
Cuboid	200.88	3.42	542.40	43.75	23.59
I_r (kPa.ms)					
Experimental	*153.33*		*158.90*		
Sphere	149.30	-2.62	136.94	-13.82	8.22
1 Cylinder	151.18	-1.40	136.45	-14.13	7.76
4 Cylinders	136.25	-11.14	159.67	0.49	5.81
Cuboid	137.68	-10.20	157.27	-1.03	5.62
t_a (ms)					
Experimental	*3.111*		*2.171*		
Sphere	2.069	-33.49	1.931	-11.03	22.26
1 Cylinder	1.789	-42.49	1.681	-22.55	32.52
4 Cylinders	2.373	-23.72	1.437	-33.79	28.76
Cuboid	2.223	-28.54	1.421	-34.53	31.54

Table 4. Reflected pressure, impulse and arrival time data, experimental and simulated.

Looking at the pressure data it can be observed that the average differences range between 23 and 37%. These larger differences than in the T0 test can be attributed to the calculation of the TNT equivalence of the device charge, as black powder has a large variability in terms of TNT equivalent as well as having to consider factors such as confinement and the use of two types of explosives in the device. As the sensors are placed on two perpendicular walls, the shape of the load directly affects the results. The more the shape of the charge resembles the artefact, the better the results (4 cylinders and cuboid). As for the arrival time, in all cases the time is shorter than that recorded experimentally, which can again be attributed to the calculation of the TNT equivalence.

However, looking at the impulse data, it can be said that the simulation is quite accurate with a difference of less than 10% in all cases, again with the 4-cylinder and cuboid simulation being the best choices. This is very important as risk analysis models are mostly based on peak pressure and positive phase duration (i.e. impulse).

Again, the recorded signal is compared to the simulated one. The comparison is made with the simulation using four cylinders. Figure 5 shows the pressure-time history of both signals. It can be appreciated that, regardless of the arrival time lag, the wave pattern is similar, and as shown in Table 4, the impulses are quite close.

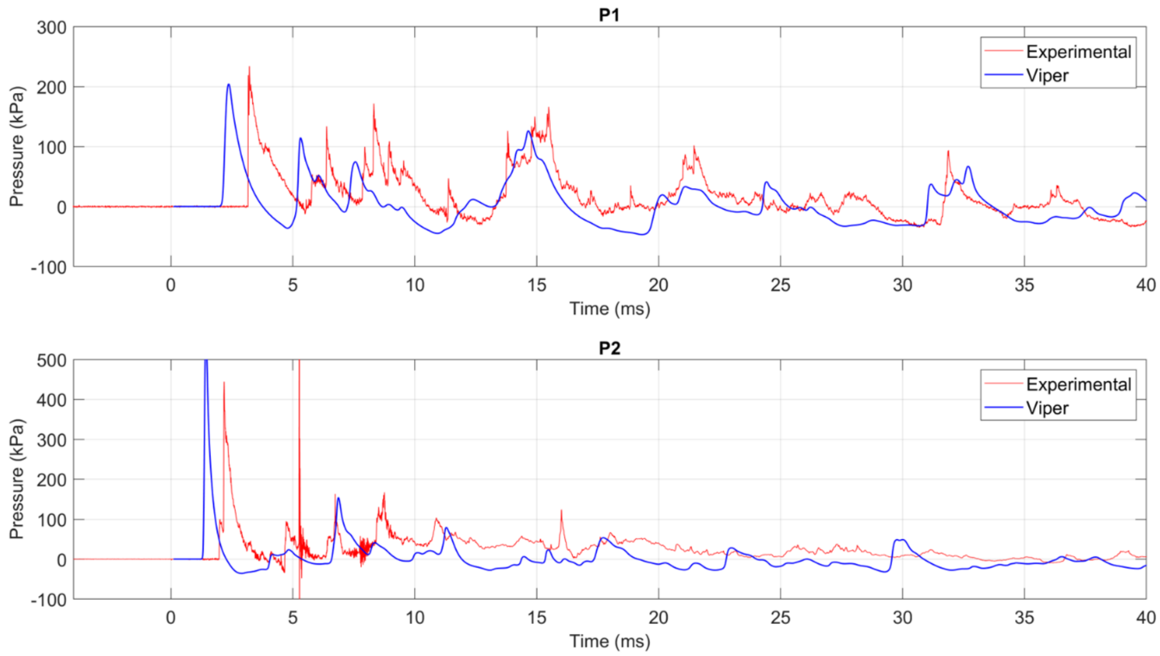

Figure 5. Pressure-time history of experimental signal and 4-cylinder simulation.

4.3 Injury models

Once the pressure data inside the building have been verified, thus validating the numerical models, the injury risk assessment is developed in order to evaluate the primary and tertiary injuries that would occur inside the building and to calculate the overall risk. For this purpose, the numerical models that gave the best results compared to the experimental data were used, which are the simulation with C4 and ideal gases EOS for the T0 test and the 4 cylinders for the T1-T2 test. In case of the PG2 test (T0), Figure 6 shows the results of lung and tertiary injury metrics as well as the overall risk of fatality. The section in the figure corresponds to the height of the charge, which was at ground level.

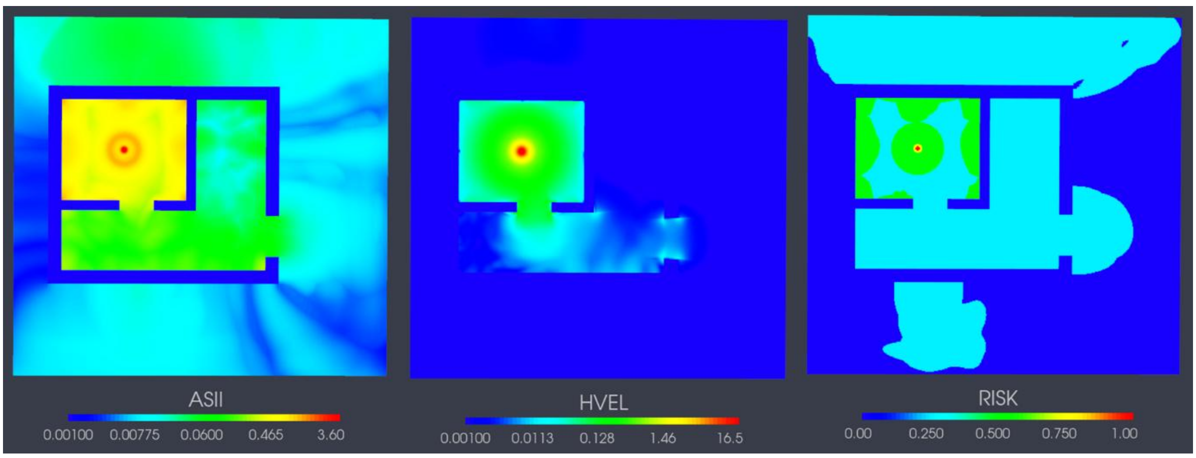

Figure 6. Simulation of lung and tertiary injury and the overall risk of fatality for PG2 test.

In this case, and due to the small charge detonated (0.1 kg PG2), the results show a ‘moderate to extensive’ probability for the risk of primary injury within the inner room (where the charge was detonated) based on the assigned Adjusted Severity of Injury Index (ASII). On the other

hand, the risk of primary injury decreases to ‘slight to moderate’ in the corridor and just in front of the window of the inner room. In terms of tertiary injury risk, there is a low probability of whole-body impact due to the velocities reached inside the building. As for the overall risk of fatality, a value of 1.00 means a 50% of risk. Therefore, there is a moderate risk of fatality in this scenario.
Figure 7 shows the simulated human injury metrics for the black powder tests (T1 and T2). In this case, the section in the figure is 1.1 m above the ground, which corresponds to the height of the charge.

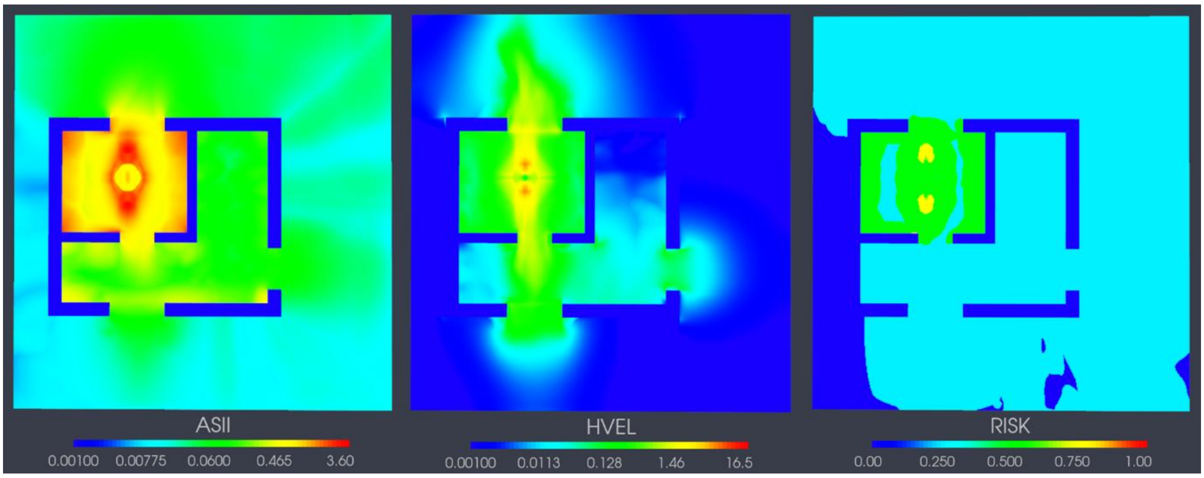

Figure 7. Simulation of lung and tertiary injury and the overall risk of fatality for black powder tests.

Looking at Figure 7, it can be seen that the risk of primary injury is ‘moderate to extensive’ inside the inner room, with above 50% of fatality (3.60 ASII) in the centre and corners of the room. As for the tertiary injury risk, it can be considered mostly ‘safe’ (velocities below 3 m/s) in most of the building except in the centre of the room. Regarding the overall risk of fatality, the worst area would be considered to be within the room. But even if the risk of fatality does not reach a value of 50%, due to the type of device used in the trial (a pipe bomb), the greatest risk of injury would be from secondary injuries caused by fragmentation of the device. This means that the chances of survival inside the room would be very low.

5 CONCLUSIONS

This research has been conducted to evaluate blast wave injury risk in complex scenarios using numerical simulation. For this purpose, the Viper Blast CFD solver is used to simulate the detonation of a PBIED inside a building using vest bombs. Pressure-time histories recorded in three experimental full-scale tests have been used to validate the numerical models created. After the validation, human injury metrics based on primary and tertiary blast injuries are studied and an overall risk of fatality is obtained. After examining the results, the following conclusions can be drawn:

- Overall, the generated numerical models show a good correlation with the experimental data in all the approaches considered.
- For the T0 test, numerical modelling was performed considering the detonated C4 charge and its TNT equivalent. The results showed that C4 is closer to the pressure values recorded in the test.
- For tests T1 and T2, the numerical models were based on the shape of the load. The results show that a better approximation of the charge shape gives better results (in this case 4 cylinders and cuboid). Furthermore, the differences in the impulse values are below 10% with respect to experimental values.

- Looking at the pressure-time histories, it can be seen that the simulation is able to capture the pressure wave properly as the wave patterns are quite similar in all tests.
- In terms of injury risk assessment, there is an increased probability of primary injury risk in both trials while tertiary injuries are considered moderate. Finally, the combined risk of fatality would be moderate except inside the room.

ACKNOWLEDGEMENTS

The authors of this work would like to thank the different institutions involved (BKA, C-IED COE, DIGENIN, GRUMA, TEAR) for their good work in the development of the experimental trials that support this research.

REFERENCES

[1] M. G. Stewart and J. Mueller, "Terrorism risks, chasing ghosts and infrastructure resilience," *Sustain Resilient Infrastruct*, vol. 5, no. 1–2, pp. 78–89, 2020, doi: 10.1080/23789689.2018.1448664.
[2] D. S. Williams, "Enhancing the Applicability of Blast Modelling and Advice," *International Journal of Protective Structures*, vol. 6, no. 4, pp. 701–710, 2015, doi: 10.1260/2041-4196.6.4.701.
[3] M. A. Price, V. Nguyen, O. Hassan, and K. Morgan, "An approach to modeling blast and fragment risks from improvised explosive devices," *Appl Math Model*, vol. 50, pp. 715–731, 2017, doi: 10.1016/j.apm.2017.06.015.
[4] P. W. Sielicki, M. G. Stewart, T. Gajewski, P. Peksa, H. Al-rifaie, and R. Studzi, "Field test and probabilistic analysis of irregular steel debris casualty risks from a person-borne improvised explosive device," *Defence Technology*, vol. 17, pp. 1852–1863, 2021, doi: 10.1016/j.dt.2020.10.009.
[5] D. Dante and Y. William, "Primary Blast Injuries — An Updated Concise Review," *World J Surg*, vol. 36, no. March, pp. 966–972, 2012, doi: 10.1007/s00268-012-1500-9.
[6] Z. R. Mathews and A. Koyfman, "Blast injuries," *Journal of Emergency Medicine*, vol. 49, no. 4, pp. 573–587, 2015, doi: 10.1016/j.jemermed.2015.03.013.
[7] I. Bowen, "Estimate of man's tolerance to the direct effects of air blast. Technical Progress Report.," 1968.
[8] H. Axelsson and J. T. Yelverton, "Chest Wall Velocity as a Predictor of Nonauditory Blast Injury in a Complex Wave Environment," *The Journal of Trauma: Injury, Infection, and Critical Care*, vol. 40, no. 3S, pp. 31S-37S, 1996.
[9] J. A. Teland and J. C. A. M. Van Doormaal, "Blast wave injury prediction models for complex scenarios."
[10] J. Denny, G. Langdon, S. Rigby, A. Dickinson, and J. Batchelor, "A numerical investigation of blast-structure interaction effects on primary blast injury risk and the suitability of existing injury prediction methods," *International Journal of Protective Structures*, vol. 15, no. 1, pp. 3–22, Mar. 2024, doi: 10.1177/20414196221136157.
[11] A. P. Santos *et al.*, "Reinforced Concrete Building with IED Detonation: Test and Simulation," *Applied Sciences (Switzerland)*, vol. 12, no. 15, Aug. 2022, doi: 10.3390/app12157803.

RESPONSE OF SIMPLY SUPPORTED LAMINATED GLASS PANELS TO SEMTEX 1A EXPLOSIONS

DYNAMIC PERFORMANCE AND RESIDUAL STRENGTH ASSESSMENT

Petr Hála[a], Paolo Del Linz[b], Petr Konrád[a], Přemysl Kheml[a], Alžběta Měrková[a]

[a]Experimental Centre, Faculty of Civil Engineering, Czech Technical University in Prague, Thákurova 7, 166 29 Prague 6, Czech Republic, email: petr.hala@fsv.cvut.cz,
[b]Cluster of Engineering, Singapore Institute of Technology, 10 Dover Road, Singapore 138683, Singapore

Keywords: multi-layer panels, sacrificial ply design, laminated glass, bending strength, blast

Abstract

Laminated glass is commonly used in structures requiring blast resistance due to its ability to dissipate energy and limit fragmentation. This study examines the performance of two configurations of multi-layer laminated glass panels subjected to Semtex 1A explosions. The panels were designed with a sacrificial ply concept, where one glass layer absorbs energy through fracture, while the remaining layers sustain residual loads. Simply supported panels were tested to simplify boundary conditions and enable numerical and analytical reproduction. The explosive tests measured mid-span deflections, with Semtex 1A chosen for its low soot generation and mass adaptability. Quasi-static three-point bending tests assessed the residual bending strength of blast-damaged panels and compared the bending strength under quasi-static and dynamic conditions for undamaged panels. The findings enhance understanding of the dynamic response and residual strength of laminated glass, contributing to improved designs for blast-resistant structures.

1 INTRODUCTION

Glass is extensively used in structural applications due to its aesthetics, sustainability, and transparency. Traditionally serving as a decorative or non-load-bearing material, its role has expanded in modern architecture to include load-bearing elements [1]. While theoretically possessing high tensile strength, its practical performance is dictated by microscopic surface flaws introduced during manufacturing and handling, which may evolve over time [2]. These flaws exhibit stochastic characteristics, making glass strength variable rather than a constant material property [3]. Under stress, cracks propagate subcritically until a critical threshold is reached, leading to sudden and unpredictable failure [4].

Due to its brittle nature and lack of residual load-bearing capacity [5], traditional float glass is unsuitable for applications demanding resilience and safety. Laminated glass offers an alternative, combining the advantages of float glass with improved safety. It consists of multiple glass layers bonded by a polymer interlayer, typically a highly flexible material capable of sustaining high strain without significant residual deformation. The interlayer absorbs impact energy and dampens vibrations due to its viscosity [6,7]. While glass layers may fracture under extreme loading, the interlayer binds the fragments together, providing post-break resistance [8]. This feature is particularly crucial in architectural applications for sensitive structures like government buildings and embassies, where protection against accidental explosions or deliberate attacks is essential.

To enhance safety and durability, the standard two-layer laminated glass can be extended to a multi-layer configuration and designed according to the sacrificial-glass-ply concept [9–13]. This approach allows the outermost ply to fracture upon impact, dissipating energy while preserving the remaining layers for structural support. As a result, the sacrificial ply is excluded from load-bearing calculations in design [11]. Studies show that even when some layers crack, laminated glass can still carry significant loads [8,12,14,15], reducing the need for immediate replacement while ensuring continued functionality. Aligning with the sacrificial ply concept, this study investigates two types of multi-layer laminated glass samples. Alongside the commonly studied three-layer composite [12], this research includes four-layer laminated glass specimens. While previous studies have largely examined the behaviour of multi-layer laminated glass under quasi-static and low-velocity impact loading [9–15], this work explores their response to blast loading.

Numerous field tests have investigated the effects of blast waves on two-layer laminated glass. For example, the far-field blast tests on laminated glass panels embedded in a support frame conducted in [16] have been replicated and expanded upon through computational and analytical studies, significantly advancing knowledge of laminated glass response to blast loads. In detail, Del Linz et al. analysed reaction forces along panel edges in [17], calculated pre-crack deflections and stresses in glass panels subjected to blast waves in [18], and examined post-crack deformations in [19]. Zhang et al. in [20,21] used the experimental data to validate the Johnson-Holmquist material model modified to predict laminated glass response to air blast loading. They also highlighted that the boundary conditions play a critical role in the behaviour of laminated glass under blast loading. The accuracy of window frame modelling can introduce uncertainties, complicating fracture simulations.

To minimize support influences, some researchers have conducted impact tests using freely suspended glass specimens. Pyttel et al. tested in [22] laminated glass suspended by cables under low-velocity soft-body impact, while Zemanová et al. employed in [7,23] a similar method for hard-body pendulum impact. Konrád et al. suspended in [8] rectangular multi-layer laminated glass specimens to study their response to 9mm bullet impacts. Kohoutová et al. tested in [24] the suspended laminated glass response to the near-field explosion.

In case of the localised impact or the near-filed explosion the inertia of the specimen edges acts as supports, thereby allowing the specimen to bend and fracture under explosive load. However, when the explosion occurs far from the target, the blast wave arrives uniformly, resulting in evenly distributed pressure loading on the target face. Therefore this study proposed alternative test setup with laminated glass specimen freely placed on supports. To the best of our knowledge, the experimental study on simply supported glass specimens exposed to blast conditions have not been published in scholarly journals. Consequently, this paper represents a novel endeavour in this realm.

2 MATERIALS AND METHODS

2.1 Laminated Glass Panels

Consistent with our previous research [23,24], two distinct laminate configurations were utilized. The 5-layer laminate (5LG) comprises three glass layers bonded with two polymer interlayers, whereas the 7-layer laminate (7LG) consists of four glass plies and three interlayers. The 7LG is about 1.5 times more expensive than the 5LG. Detailed information regarding the layer arrangements is provided in Figure 1.

The glass layers were manufactured using standard float soda–lime–silica glass, while the polymer interlayers were composed of polyvinyl butyral (PVB), specifically the TROSIFOL BG R20 type. Aligning with the sacrificial-glass-ply design concept [9] and the critical role of the middle glass layer [12], the external glass layers were intentionally made thinner than the inner layers. This configuration supports the post-fracture performance of the laminated samples by protecting the thicker inner glass layers with a polymer interlayer and an additional outer glass layer [23]. Consequently, the inner glass surfaces are less likely to incur micro-defects during transportation and handling before impact testing, which is expected to result in higher tensile strength compared to the outer surfaces [25].

Furthermore, using thinner outer glass plies minimizes the likelihood of extensive interlayer debonding [26], which can be undesirable. As in our prior research [8], the laminated glass panels selected for the experimental campaign had nominal dimensions of 1100 mm × 360 mm.

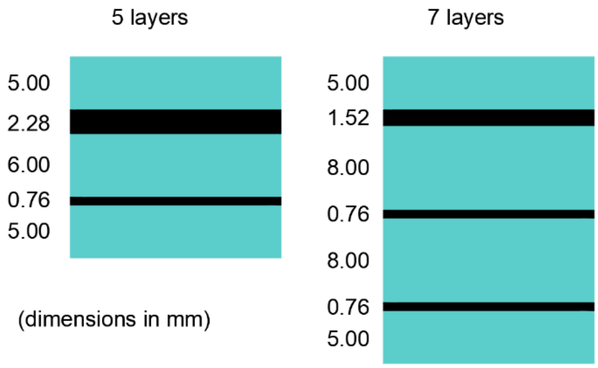

Figure 1. Glass and polymer interlayer configurations. Nominal thicknesses.

2.2 Experimental Analysis

This chapter outlines the procedures employed to evaluate the performance of laminated glass panels under both quasi-static and dynamic loading conditions. The quasi-static tests involved three-point bending experiments on undamaged and blast-damaged specimens to assess their residual bending strength, using displacement-controlled loading and precise measurement instrumentation. The blast tests examined the dynamic response of the panels using Semtex 1A plastic explosive, with varying charge weights and standoff distances, to determine the thresholds of damage. Key experimental details, including support setups, instrumentation, and loading configurations, are described to provide a comprehensive understanding of the methodologies employed.

2.2.1 Quasi-Static Tests

Quasi-static three-point bending experiments were conducted on an undamaged 5LG1 specimen and a 7LG1 specimen in which the bottom layer was cracked during the blast tests. Steel half-cylinders were used as supports and load-distributing elements, with a span of 1000 mm between the supports. The experimental setup, as illustrated in Figure 2, included linear variable differential transformer (LVDT) displacement sensors and strain gauges, which were carefully adhered to the specimens for precise measurements. The test was displacement-controlled, with a loading rate of 1 mm/min.

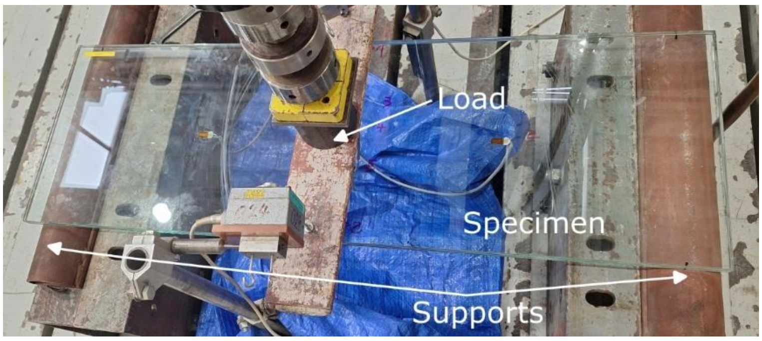

Figure 2. Setup of the three-point bending experiment.

2.2.2 Blast Tests

The blast test setup, as illustrated in Figure 3, featured two steel support structures spaced 1000 mm apart, with the tested sample positioned horizontally on top. An accelerometer (PCB Model 350B04) with a maximum capacity of 50,000 m/s² was affixed to the centre of the bottom layer to capture dynamic response data.

Data acquisition was performed using a portable PC oscilloscope (OWON Technology Model VDS6074A). A metal detonator loaded with Semtex 1A plastic explosive was suspended above the centre of the panel. For specimens 5LG3, 7LG3, and 5LG2, a constant charge weight of 100 g was used, with an initial standoff distance of 100 cm. This distance was reduced in 10 cm increments for subsequent tests until the specimen sustained damage.

For specimens 7LG1 and 7LG2, the standoff distance was maintained at 50 cm, while the charge weight was gradually increased from an initial 100 g until the specimen was damaged. Additionally, rubber pads were placed between the supports and the 7LG2 specimen to mitigate localized stress concentrations.

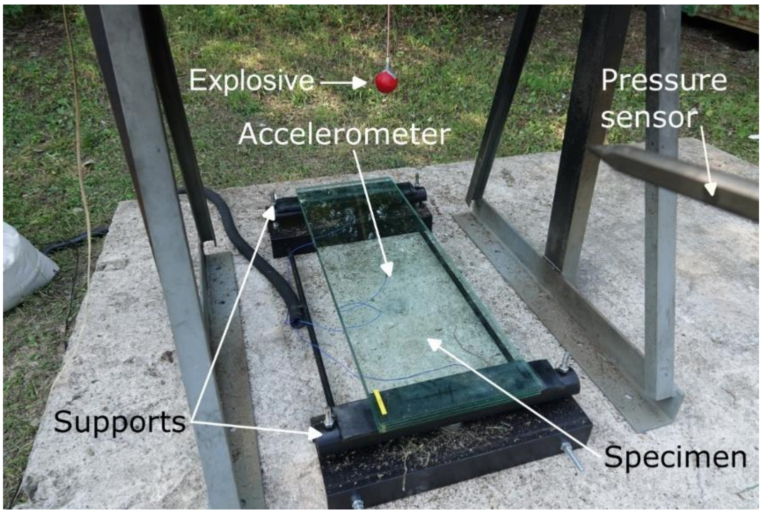

Figure 3. Setup of the blast test.

2.3 Computational Analysis

Building upon the experimental investigations, this chapter presents the analytical and numerical approaches used to evaluate the structural response of laminated glass. The quasi-static response was assessed using the Enhanced Effective Thickness (EET) method, which provides an efficient means of estimating displacement and strain under bending loads. For blast response, high-fidelity numerical simulations were conducted in LS-DYNA to capture the complex, dynamic behaviour of the material under extreme loading. These methods complement the experimental findings, offering additional insight into the performance of laminated glass under different conditions.

2.3.1 Quasi-Static Response

The Enhanced Effective Thickness (EET) analytical method was utilized to determine displacement and strain values. This approach, detailed in [27], has been applied to evaluate the deflection of multi-layer laminated glass under quasi-static bending, as demonstrated in [8]. The authors of [27] concluded that the EET method yields more precise results than other simplified analytical techniques. It was selected for this study due to its practicality in laminated glass design—offering a straightforward implementation while still providing a relatively accurate prediction of the structural response.

The deflection effective thickness for the displacement calculations can be determined using the following equation:

$$\hat{h}_w = \sqrt[3]{1/\left(\frac{\eta}{\sum h_i^3 + 12\sum h_i d_i^2} + \frac{1-\eta}{\sum h_i^3}\right)} \tag{1}$$

where h_i is the thickness of the *i*th glass layer and d_i is the distance of its centre to the centre of the whole composition. The reducing coefficient η can be determined using the following equation:

$$\eta = 1\Bigg/\left(1 + \frac{E\psi \sum I_i \sum A_i d_i^2}{G w I_{tot}\left(\sum \frac{H_j^2}{t_j}\right)}\right) \tag{2}$$

where E is the modulus of elasticity of glass, G is the shear modulus of the interlayer (taken from [8]), w is the width of the specimen, I_{tot} is the moment of inertia as if the specimen was monolithic, I_i is the moment of inertia of the *i*th glass layer, A_i is the cross-sectional area of the *i*th glass layer, H_j is the distance between centres of glass layers adjacent to the *j*th interlayer, and t_j is the thickness of the *j*th interlayer. The coefficient ψ can be calculated using the following equation [27]:

$$\psi = \frac{10}{l^2} \tag{3}$$

where l is the span of the panel.

Using the aforementioned parameters, the stress effective thickness for the stress and strain calculations can be determined as follows:

$$\hat{h}_\sigma = \sqrt{1/\left(\frac{2\eta d_\sigma}{\sum h_i^3 + 12\sum h_i d_i^2} + \frac{h_\sigma}{\hat{h}_w^3}\right)} \tag{4}$$

where h_σ is the thickness of the glass layer where the extreme stress is evaluated and d_σ is the distance of its centre to the centre of the whole composition.

2.3.2 Blast Response

This research examines the behaviour of laminated glass under blast loading using numerical simulations conducted in LS-DYNA (version R13.1.1). LS-DYNA is a general-purpose finite element analysis software widely recognized for its ability to model intricate real-world scenarios, especially nonlinear dynamic events. The solver employs explicit time integration techniques, making it particularly effective for blast loading.

To improve computational efficiency and streamline the model, only one-quarter of the laminated glass plate was meshed, taking advantage of symmetry within the problem. This strategy helped reduce computational costs and simplify the model structure. Contact surfaces between adjacent layers were defined using shared nodes, minimizing the number of unknowns and eliminating the need for explicit contact condition definitions. The support structure was represented as a half-cylinder, with displacement and rotation constraints imposed on the bottom nodes. A mesh with 10 mm element side lengths was used, which was confirmed as sufficient for obtaining reliable results through a mesh sensitivity study and in accordance with established best practices.

Both the support and individual layers were discretized using a default element type—constant stress solid elements. Standard settings were applied for hourglass control, including a viscous formulation with Flanagan-Belytschko integration and a coefficient of 0.1. Additional simulations were carried out using fully integrated brick elements, which produced comparable results but significantly increased computational time.

The simulation assumed an elastic material model for both the glass and the steel support, with no consideration of material damage. To accurately capture the time- and temperature-dependent behaviour of the polymer interlayer, a viscoelastic generalized

Maxwell model incorporating Williams-Landel-Ferry shift parameters was used. The parameters for these material models were sourced from a previous study [23].

To simulate the effects of the explosion, a multi-material arbitrary Lagrangian-Eulerian (MMALE) approach was utilized. The ALE method integrates Lagrangian and Eulerian computation techniques by dividing the simulation cycle into a Lagrangian phase and a possible advection phase. Depending on the formulation, the mesh can either remain unchanged (pure Lagrangian), return to its original shape (pure Eulerian), or adjust to a more suitable configuration. In this case, the MMALE formulation was used, allowing materials to flow through a fixed mesh, with each element potentially containing multiple ALE materials.

The surrounding air and the explosive material (Semtex 1A) were modelled as described in [28] and [29], respectively. The input parameters of Semtex 1A were further refined based on the information provided by the manufacturer. Interaction between the air and the laminated glass panel was handled through a penalty-based method, which preserves the total energy of the system and applies explicit nodal forces by tracking the relative motion of each point. If a fluid particle intrudes into a Lagrangian element, a penalty force proportional to the penetration depth is applied to both the fluid and the Lagrangian node to prevent further penetration

3 RESULTS AND DISCUSSION

Figure 4 presents the displacements of the 7LG sample under the impact of a 100 g Semtex 1A explosion at a distance of 40 cm, as determined through experimental and numerical methods. The results exhibit good agreement across both approaches, effectively validating one another.

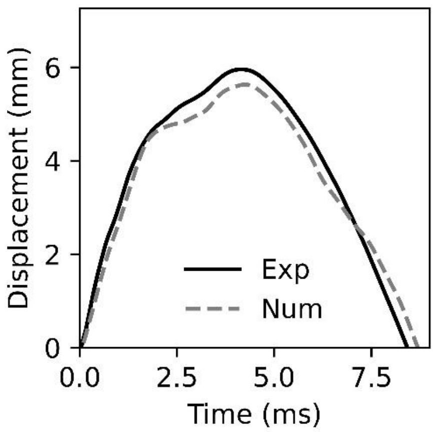

Figure 4. The time evolution of the displacement of the 7LG sample when subjected to the explosion of 100 g of Semtex 1A from a distance of 40 cm.

Figure 5 shows that the maximum central displacements of the laminated glass panels increase as the distance of the explosive from the panel decreases. As expected, the displacements of the thicker, and therefore stiffer, seven-layer composition were consistently lower than those of the five-layer composition. The measured maximum central displacements of the 5LG samples were approximately twice those of the 7LG samples.

The 5LG2 and 5LG3 samples failed when the explosion distance of 100 g of Semtex 1A was reduced to 50 cm and 40 cm, respectively. The 7LG3 sample sustained damage when the distance was further reduced to 30 cm. At a 50 cm distance with 100 g of Semtex 1A, all glass layers in the 5LG2 sample cracked, whereas the glass layers in all 7LG samples remained intact. The bottom layer of the 7LG1 sample cracked only when the explosive weight was increased to 200 g, while all glass layers of the 7LG2 sample were damaged when the explosive weight was raised to 275 g.

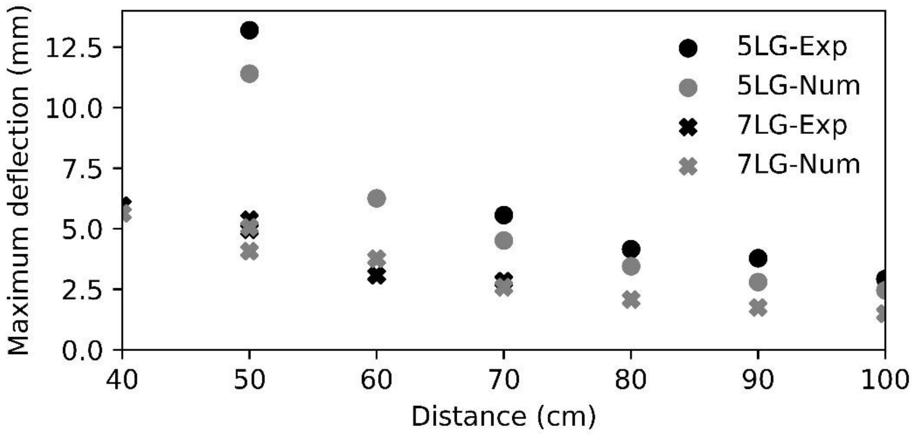

Figure 5. Dependence of the maximum displacement of the laminated glass panel on its distance from a 100 g of Semtex 1A explosive.

In some cases, cracks formed near the supports when subjected to explosions with lower explosive masses, see Figure 6. As the explosive mass increased, these cracks continued to widen. However, they never extended towards the centre of the panel and therefore did not affect its overall resistance. By placing rubber pads between the laminated glass panel and the steel supports, cracks near the supports could be prevented. However, this modification led to an approximately 15% increase in the maximum central displacement, see Figure 7.

Figure 6. Cracks in the vicinity of the steel supports.

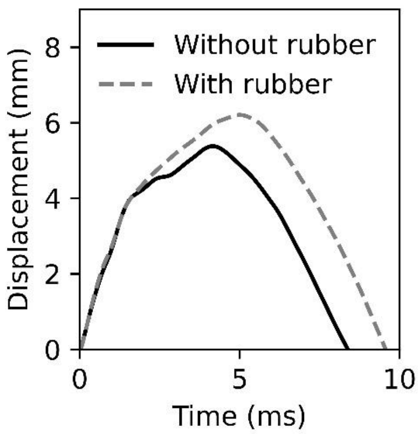

Figure 7. The influence of the rubber pads placed between the steel supports and the 7LG sample on the time evolution of the sample displacement when subjected to the explosion of 100 g of Semtex 1A from a distance of 50 cm.

Figure 8 presents the force-displacement curves recorded during the quasi-static bending tests. It can be observed that the 7LG sample, despite having its bottom glass layer cracked by the explosion, still exhibits nearly twice the bending strength of the undamaged 5LG sample.

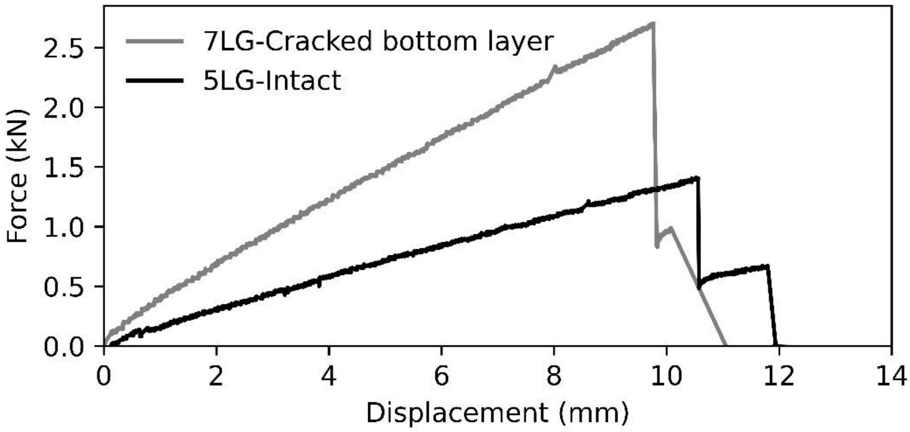

Figure 8. The force-displacement curves of the 5LG sample with no pre-test damage and the 7LG sample with the bottom glass layer cracked by explosion.

The hand calculations predicted a greater displacement at the maximum bending strength, estimating 13.02 mm compared to the measured 10.53 mm. The calculated microstrain at a quarter of the span was 239, which was slightly higher than the measured value of 220. Future studies will focus on refining the methods to minimize these discrepancies.

4 CONCLUSION

This study examined the performance of two configurations of simply supported multi-layer laminated glass panels subjected to Semtex 1A explosions. The following conclusions emerge from this study:

- The blast results exhibit good agreement across experimental and numerical methods, effectively validating one another.
- The seven-layer laminated glass showed lower displacements and higher blast resistance compared to the five-layer composition. The displacements were approximately half and the panel was able to withstand an explosion of more than twice the weight of the charge.
- The seven-layer laminated glass, despite having its bottom glass layer cracked by the explosion, still exhibited nearly twice the bending strength of the undamaged five-layer sample.
- By inserting rubber pads between the laminated glass panel and the steel supports, cracks in the vicinity of the support could be prevented, but the maximum central displacement increased by approximately 15%.
- The hand calculations predicted a slightly greater displacement at the maximum bending strength and a slightly higher microstrain at a quarter of the span compared to the measured values.

ACKNOWLEDGEMENTS

The publication was supported by the Czech Science Foundation grant No. 25-16071S.

REFERENCES

[1] K. Osnes, O.S. Hopperstad, T. Børvik, Rate dependent fracture of monolithic and laminated glass: Experiments and simulations, *Eng Struct* 212 (2020) 110516.

https://doi.org/10.1016/j.engstruct.2020.110516.
[2] M. Overend, K. Zammit, A computer algorithm for determining the tensile strength of float glass, *Eng Struct* 45 (2012) 68–77. https://doi.org/10.1016/j.engstruct.2012.05.039.
[3] M.J. Meyland, J.H. Nielsen, C. Kocer, Tensile behaviour of soda-lime-silica glass and the significance of load duration – A literature review, *Journal of Building Engineering* 44 (2021) 102966. https://doi.org/10.1016/j.jobe.2021.102966.
[4] J.P. Guin, S.M. Wiederhorn, Crack growth threshold in soda lime silicate glass: role of hold-time, *J Non Cryst Solids* 316 (2003) 12–20. https://doi.org/10.1016/S0022-3093(02)01932-4.
[5] A. Pauli, G. Siebert, Simplified approach for modeling standard PVB at large deformations and long-term loading, *Glass Structures & Engineering* 9 (n.d.). https://doi.org/10.1007/s40940-023-00236-x.
[6] P. Hála, A. Zemanová, T. Plachý, P. Konrád, R. Sovják, Experimental modal analysis of glass and laminated glass large panels with EVA or PVB interlayer at room temperature, *Mater Today Proc* 62 (2022) 2421–2428. https://doi.org/10.1016/j.matpr.2022.02.578.
[7] A. Zemanová, P. Hála, P. Konrád, T. Janda, R. Hlůžek, The influence of interlayer properties on the response of laminated glass to low-velocity hard-object impact, *Int J Impact Eng* 159 (2022) 104036. https://doi.org/10.1016/j.ijimpeng.2021.104036.
[8] P. Konrád, P. Hála, J. Schmidt, A. Zemanová, Laminated Glass Plates Subjected to High-Velocity Projectile Impact and Their Residual Post-Impact Performance, *Materials* 15 (2022) 8342. https://doi.org/10.3390/ma15238342.
[9] D.N. Kaiser, A.R. Behr, E.J. Minor, R.L. Dharani, F. Ji, A.P. Kremer, Impact Resistance of Laminated Glass Using “Sacrificial Ply” Design Concept, *Journal of Architectural Engineering* 6 (2000) 24–34. https://doi.org/10.1061/(ASCE)1076-0431(2000)6:1(24).
[10] J.T. Saxe, A.R. Behr, E.J. Minor, A.P. Kremer, R.L. Dharani, Effects of Missile Size and Glass Type on Impact Resistance of “Sacrificial Ply” Laminated Glass, *Journal of Architectural Engineering* 8 (2002) 24–39. https://doi.org/10.1061/(ASCE)1076-0431(2002)8:1(24).
[11] P. Foraboschi, Hybrid laminated-glass plate: Design and assessment, *Compos Struct* 106 (2013) 250–263. https://doi.org/10.1016/j.compstruct.2013.05.041.
[12] X. er Wang, J. Yang, W.T.A. Chong, P. Qiao, S. Peng, X. Huang, Post-fracture performance of laminated glass panels under consecutive hard body impacts, *Compos Struct 254* (2020) 112777. https://doi.org/10.1016/j.compstruct.2020.112777.
[13] X. er Wang, Y. Meng, J. Yang, X. Huang, F. Wang, H. Xu, Optimal kernel extreme learning machine model for predicting the fracture state and impact response of laminated glass panels, *Thin-Walled Structures* 162 (2021) 107541. https://doi.org/10.1016/j.tws.2021.107541.
[14] X. er Wang, J. Yang, Q. Liu, C. Zhao, Experimental investigations into SGP laminated glass under low velocity impact, *Int J Impact Eng* 122 (2018) 91–108. https://doi.org/10.1016/J.IJIMPENG.2018.06.010.
[15] C. Zhao, J. Yang, X. er Wang, I. Azim, Experimental investigation into the post-breakage performance of pre-cracked laminated glass plates, *Constr Build Mater* 224 (2019) 996–1006. https://doi.org/10.1016/j.conbuildmat.2019.07.286.
[16] P.A. Hooper, R.A.M. Sukhram, B.R.K. Blackman, J.P. Dear, On the blast resistance of laminated glass, *Int J Solids Struct* 49 (2012) 899–918. https://doi.org/10.1016/j.ijsolstr.2011.12.008.
[17] P. Del Linz, P.A. Hooper, H. Arora, D. Smith, L. Pascoe, D. Cormie, B.R.K.K. Blackman, J.P. Dear, Reaction forces of laminated glass windows subject to blast loads, *Compos Struct* 131 (2015) 193–206. https://doi.org/10.1016/j.compstruct.2015.04.050.

[18] P. Del Linz, Y. Wang, P.A. Hooper, H. Arora, D. Smith, L. Pascoe, D. Cormie, B.R.K. Blackman, J.P. Dear, Determining Material Response for Polyvinyl Butyral (PVB) in Blast Loading Situations, *Exp Mech* 56 (2016) 1501–1517. https://doi.org/10.1007/s11340-016-0179-5.
[19] P. Del Linz, X. Liang, P.A. Hooper, H. Arora, L. Pascoe, D. Smith, D. Cormie, J.P. Dear, A numerical method for predicting the deformation of crazed laminated windows under blast loading, *Eng Struct* 172 (2018) 29–40. https://doi.org/10.1016/j.engstruct.2018.05.030.
[20] X. Zhang, H. Hao, Z. Wang, Experimental study of laminated glass window responses under impulsive and blast loading, *Int J Impact Eng* 78 (2015) 1–19. https://doi.org/10.1016/j.ijimpeng.2014.11.020.
[21] X. Zhang, H. Hao, G. Ma, Dynamic material model of annealed soda-lime glass, *Int J Impact Eng* 77 (2015) 108–119. https://doi.org/10.1016/j.ijimpeng.2014.11.016.
[22] T. Pyttel, H. Liebertz, J. Cai, Failure criterion for laminated glass under impact loading and its application in finite element simulation, *Int J Impact Eng* 38 (2011) 252–263. https://doi.org/10.1016/j.ijimpeng.2010.10.035.
[23] A. Zemanová, P. Hála, P. Konrád, R. Sovják, M. Šejnoha, Gradual fracture of layers in laminated glass plates under low-velocity impact, *Comput Struct* 283 (2023). https://doi.org/10.1016/j.compstruc.2023.107053.
[24] A. Kohoutová, P. Del Linz, P. Kheml, P. Konrád, P. Hála, Freely hanging multi-layer laminated glass subjected to near-field blast, *Glass Structures & Engineering* 9 (2024) 499–523. https://doi.org/10.1007/s40940-024-00275-y.
[25] C. Alter, S. Kolling, J. Schneider, An enhanced non–local failure criterion for laminated glass under low velocity impact, *Int J Impact Eng* 109 (2017) 342–353. https://doi.org/10.1016/j.ijimpeng.2017.07.014.
[26] F.W. Flocker, R.L. Dharani, Low Velocity Impact Resistance of Laminated Architectural Glass, *Journal of Architectural Engineering* 4 (1998) 12–17. https://doi.org/10.1061/(ASCE)1076-0431(1998)4:1(12).
[27] L. Galuppi, G. Royer-Carfagni, Enhanced Effective Thickness of multi-layered laminated glass, *Compos B Eng* 64 (2014) 202–213. https://doi.org/10.1016/J.COMPOSITESB.2014.04.018.
[28] H.B. Rebelo, C. Cismasiu, A Comparison between three air blast simulation techniques in LS-DYNA, *11th European LS-DYNA Conference*, Salzburg, DYNAmore. https://www.dynalook.com/Conferences/11th-European-Ls-Dyna-Conference/Air-Blast-2/a-Comparison-between-Three-Air-Blast-Simulation-Techniques-in-Ls-Dyna/View (2017).
[29] R. Panowicz, M. Trypolin, M. Konarzewski, Numerical comparison of blast waves generated by cylindrical explosive charges with varying shapes and materials, *Computer Assisted Methods in Engineering and Science* 23 (2016) 205–212.

ENGINEERING OF A FOAM-FILLED AUXETIC ABSORBER FOR LOCALIZED IMPACT

Sebastiano Di Mauro[a], Alessandro Airoldi[a], Paolo Astori[a], Nejc Novak[b],
Serena Graziosi[c], Raffaele Pugliese[d] and Alessandro Gadola[c]

[a]Department of Aerospace Science and Technology, Politecnico di Milano, Milan, Italy,
email: sebastiano.dimauro@polimi.it,
[b]Faculty of Mechanical Engineering, University of Maribor, Maribor, Slovenia,
[c]Department of Mechanical Engineering, Politecnico di Milano, Milan, Italy,
[d]Nemo Lab, ASST Grande Ospedale Metropolitano Niguarda, Milan, Italy

Keywords: Cellular materials, hexachiral structure, localized impact, drop-weight impact, 3D-printing, thermoplastic polyurethane, numerical modelling, experimental testing, metamodel, optimisation technique

Abstract

In this work the design of an impact energy absorber, based on an auxetic hexachiral frame filled with foam, was developed and was focused on the identification of the geometrical parameters for the fulfilment of the requirements in a pre-defined application scenario. Some of the outcomes of two research in the literature were the starting point of the present work: specifically, the importance of the combination of materials used to build the auxetic structure and the beneficial effects of the interaction between an auxetic frame and foam, which leads to substantial increments of absorbed energy per unit volume and mass. Using materials with high elongation at break, such as an elastomeric material, deserved investigation since it could guarantee the preservation of the auxetic property for the whole duration of the localized impact, as the early breakage of chiral ligaments or chiral nodes, which induce the loss of the auxetic property, could be avoided. All these aspects were considered in the engineering of an absorber concept in a specific crash scenario, represented by the impact between a Vulnerable Road User and the bumper of a vehicle. The regulation EEVC/WG17 EURO Phase2 was taken as a reference in order to perform a realistic study of the energy absorber. Moreover, among different polymeric materials, a thermoplastic polyurethane with micronized waste-tire-rubber was used to build the auxetic frame. It exhibits a large strain at failure and can be 3D-printed to obtain auxetic topologies, and involves the use of recycled material. Dynamic drop-weight impacts were conducted on sample structures and compared with the numerical model. Initial numerical-experimental correlation showed that the FE model had some differences with the experimental results, and this was probably due to the preliminary numerical material model developed and used for the hexachiral frame, but the use of elastomeric material was promising. Despite the differences in its calibration, the FE model was used to build a database and to train two metamodels. Finally, an optimization procedure based on a genetic algorithm was presented. Two optimal solutions of foam-filled hexachiral structure were found, considering the penetration and level of force as targets, and using the geometrical parameters of the auxetic frame as design variables. Results indicated that the optimized auxetic structures were able to absorb the impact energy by mitigating the force on the simplified VRU below the desired level, with a limited penetration.

1. INTRODUCTION

In the recent years the quest for developing lighter, stronger, and more efficient energy absorbers is a driving force behind industrial and academic research, leading to innovative configurations with unique properties. Among these, auxetic structures, having the ability to exhibit negative Poisson's ratio (NPR), have attracted significant interest due to their exceptional characteristics, such as shear resistance, and enhanced energy absorption capability [1], [2], [3]. Many research focused on studying auxetic energy absorbers under uniform compression and impact loads, but there is also a great interest in studying the same type of structures under localized impacts. For example, in [4] a comparison between an auxetic-cored sandwich panel and a traditional aluminium foam-cored panels under a ballistic impact was described, whereas [5], [6] proposed an innovative concept based on an auxetic hexachiral frame filled with foam to absorb energy in an impact scenario.
The outcomes of the latter two research were the starting point of the present work, in which a new material combination of the foam-filled hexachiral structure was investigated aiming at engineering the energy absorber for a specific crash scenario. One of the findings of the previous studies was that it is important to guarantee the preservation of the auxetic property throughout the duration of the localized impact, as the early buckling or breakage of chiral ligaments and nodes induce the loss of the auxetic property, and, consequently, the loss of energy absorbing efficiency. For such a reason, in this work a thermoplastic polyurethane (TPU) with micronized waste-tire-rubber (WTR) was used to build the auxetic frame [7]. It exhibits a large strain at failure and can be 3D-printed to obtain auxetic topologies, and involves the use of recycled material. These aspects were considered in the design of the energy absorber concept in a specific crash scenario, represented by the impact between a Vulnerable Road User (VRU) and the bumper of a vehicle. In fact, many studies in the literature investigated the design of vehicle bumpers for mitigating the injury of pedestrian lower extremities: for example, the studies conducted in [8], [9] proposed the design of vehicle bumpers based on numerical simulations and meeting the requirements imposed by the EEVC/WG17 EURO Phase2 regulation. Other research investigated the performance of innovative absorbers by exploiting the numerical technique of surrogate models, which allows the reduction in computational effort and leads to the identification of optimal designs [10], [11], [12]. This design methodology was used in the present work to engineer the foam-filled hexachiral structure, enhancing the understanding of this innovative type of auxetic structure in a real crash scenario.

2. FINITE ELEMENT MODELING

2.1. Description of the numerical model

The finite element (FE) model of the foam-filled hexachiral structure, also referred to as energy absorber in this work, was developed using an updated version of the MATLAB script described in [6] and solved through the Simulia/Abaqus Explicit code. The MATLAB script was based on the parameterisation of the hexachiral frame, and permitted to generate the mesh of the model, and all the input files required for the Abaqus simulation. The foam cylinders and triangular foam prisms were modelled using hexahedral elements type C3D8, and the auxetic frame using shell elements type S4, as shown in Figure 1(a). The interaction between the foam and the frame was a simple contact, and it was modelled through the general contact algorithm available in the solver code. Concerning the material of the foam, the CF-45M is considered: it is one of the commercially available versions of Confor open-celled urethane foams, currently applied in automotive and aerospace fields. It is numerically modelled through the **Low Density Foam* material card, and its characteristics were well described in [5]. Regarding the hexachiral frame, the TPU-WTR was considered. This material was characterised in [7], and for the present work a preliminary numerical model was calibrated to fit the experimental static and dynamic data. Specifically, a hyper-viscoelastic material model was chosen to describe this material, given its hyperelastic behaviour, typical of elastomers, and its sensitivity to strain rate. Material cards *Hyperelastic* and *Viscoelastic* were used together to define the TPU-WTR.

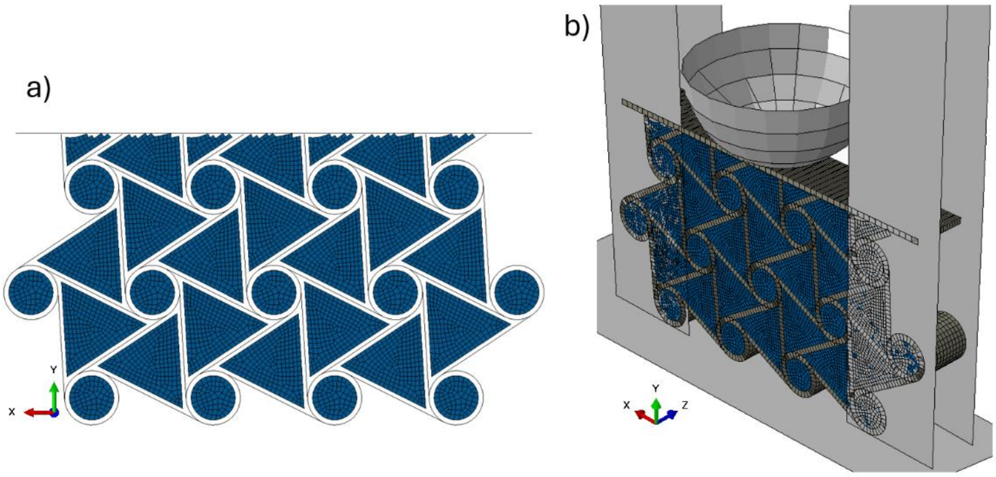

Figure 1. FE model: (a) frontal view of the energy absorber only, (b) isometric view with the hemispherical impactor, lateral guides and shell thickness rendering.

2.2. Setup of the experimental test

The FE model of the hexachiral structure has already been validated in the previous study [6], but given the different material combination adopted in this work, a new numerical-experimental correlation was performed. The hexachiral frame consisted of 2 cells in X-axis and 2 cells in Y-axis, of which the top two were partially cut by a flat surface called skin in this work, and could be considered as a rectangle with dimensions 200 x 120 x 30 mm^3. The thicknesses of chiral ligaments, chiral nodes and skin were 3.26, 3.66 and 3.06 mm respectively. The characteristic ratio L/r was set equal to 4.0. The energy absorber was subjected to drop-weight impacts. A hemispherical stainless steel impactor with a mass of 5.457 kg and a diameter of 100 mm impacted the structure at two different impact speeds, namely 3 m/s and 5 m/s. The energy absorber was placed on a thick steel plate, and kept in position by four plexiglass guides to prevent lateral displacement during the collapse. The impactor, the steel plate and the lateral guides were modelled as rigid analytical surfaces, as visible in Figure 1(b).
In order to better calibrate the FE numerical model, besides the hexachiral structure filled with foam, the simple hexachiral structure without foam was also considered. Figure 2 (a)-(b) show the deformation at the impactor maximum penetration for both the impact speeds of the energy absorber with foam, whereas Figure 2 (c)-(d) show the deformation at the impactor maximum penetration for both the impact speeds of the energy absorber without foam. The beneficial effects [6] of the foam was clearly evident: contributing to absorb the energy and, thanks to the interaction between the auxetic frame and the foam, delaying ligaments buckling, ensuring that auxeticity was maintained throughout the duration of the impact, and leading to substantial increments of absorbed energy per unit volume and mass.
These experimental tests were adopted to calibrate the numerical FE model and also to better calibrate the material model of the TPU-WTR. The initial numerical-experimental correlation revealed some differences between numerical and experimental results. Nevertheless, the FE model was used in the design of the energy absorber in a specific crash scenario.

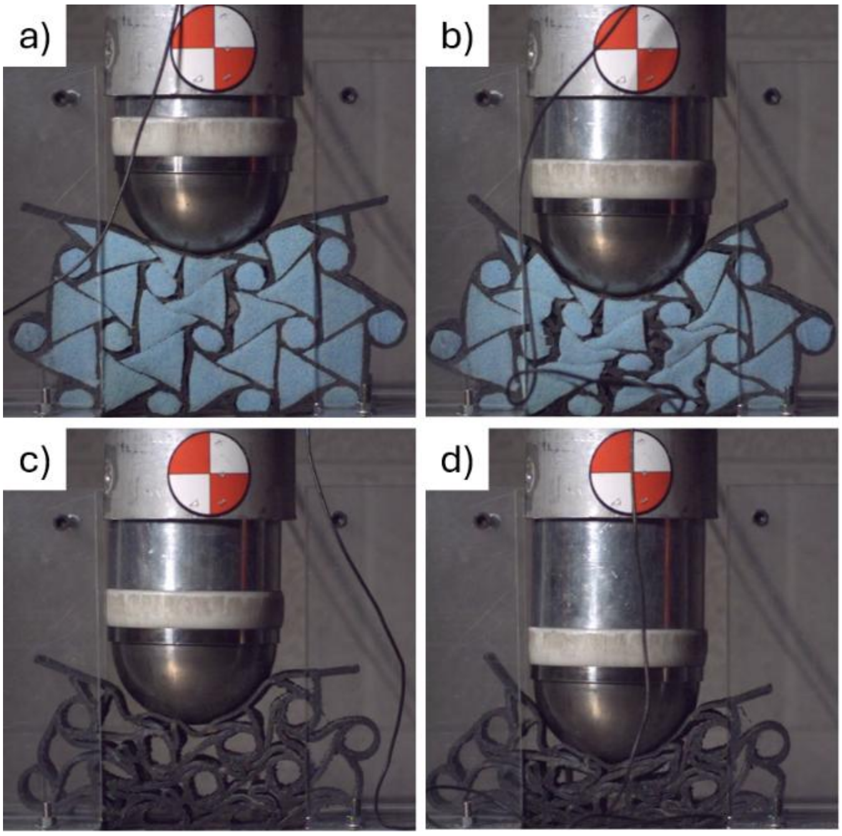

Figure 2. Deformation at the impactor maximum penetration: (a) absorber with foam impacted at 3 m/s, (b) absorber with foam impacted at 5 m/s, (c) absorber without foam impacted at 3 m/s, (d) absorber without foam impacted at 5 m/s.

3. APPLICATION CASE: CRASH SCENARIO

3.1. Description of the problem

As explained in the introduction, the present work aimed at investigating the use of the foam-filled hexachiral structure described previously as a bumper. Specifically, the crash scenario was represented by the impact between the lower leg of a pedestrian, a typical VRU, and the front bumper of a vehicle. The impact event investigated was greatly simplified, but the requirements and load conditions prescribed by the EEVC/WG17 EURO Phase2 regulation were taken as a reference in order to perform a realistic study of the energy absorber.

The lower leg was modelled as a rigid cylindrical impactor with a mass of 12 kg, a diameter of 100 mm and impacted the energy absorber at a speed of 9 m/s (32.4 km/h). The injury criterion considered was the one associated with the maximum acceleration measured at the upper end of the tibia, that must not exceed 150 g in compliance with the standards. In this work, the limit was considered in terms of force and was set at 10 kN, i.e. 85 g. The energy absorber had global dimensions of 300 x 150 x 100 mm^3 (Figure 3(a)). The thicknesses of chiral ligaments, chiral nodes and skin, as well as the number of cells in X-axis and the ratio L/r were the geometrical parameters considered in the investigation. It is worth noting that the characteristic dimensions of the simplified lower leg and of the hexachiral structure were similar to the realistic ones [8], [10].

The main objective of the design was to identify the geometrical parameters of the hexachiral frame limiting the load applied on the impactor and minimising the penetration of the impactor in the absorber. To do this, many numerical simulations would have been required, and the current FE model was very time-consuming. For this reason, the following assumption was made: since the load was applied uniformly across the width (i.e. in Z-axis), then only a 1-mm-slice of the FE model was considered, as visible in Figure 3(b). With this assumption, the numerical impactor was 1 mm wide and had a mass of 0.12 kg, i.e. the actual mass divided by the actual width of the energy absorber (i.e. 100 mm). Moreover, the 1-mm-slice energy absorber, that was actually 1-finite-element-wide, had the nodes of one side constrained with a Z-symmetry condition, while the nodes of the other side were free to move. This assumption was verified performing simulations on both the whole and sliced structure. Figure 4 shows the impactor responses, and it should be noted that in Figure 4(d) the force of the impactor in the sliced mode was multiplied by the actual width. Therefore, it was inferred that the assumption could be considered valid.

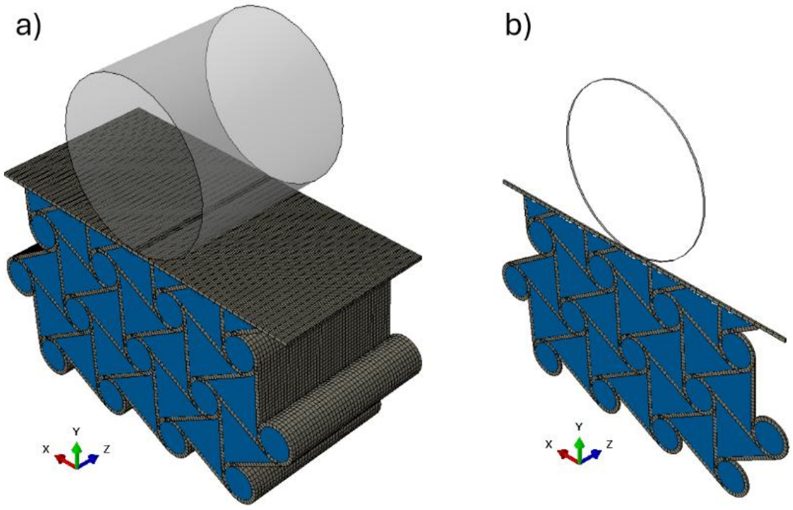

Figure 3. FE mode: (a) whole energy absorber, (b) 1-mm-slice energy absorber.

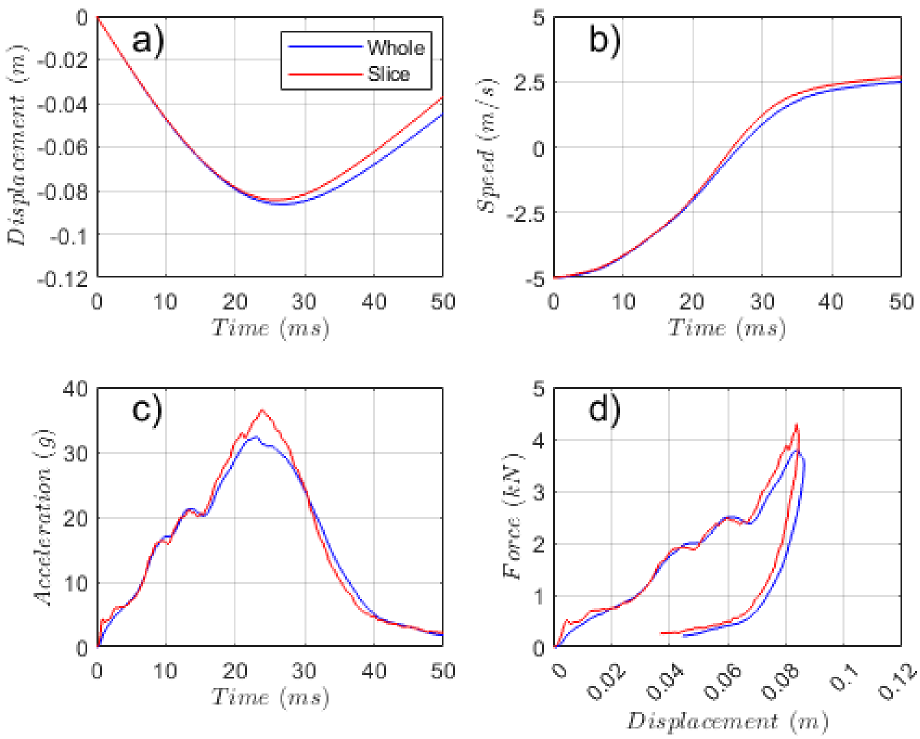

Figure 4. Comparison of the impactor responses between whole and sliced model: (a) displacement vs time, (b) speed vs time, (c) acceleration vs time, (d) force vs displacement.

3.2. Database definition and metamodel training

The simplified sliced FE model described in the previous paragraph was used to build a database and two surrogates models, or metamodels, were trained from it. A total of 175 simulations were done. The parameterisation of the FE model considered five design variables: the thickness of chiral ligaments (t_L), the thickness of chiral nodes (t_N), the thickness of the skin (t_S), the number of cells in X-axis (N_X) and the ratio L/r (Lr). The Latin hypercube statistical technique was used to define the combinations of the design variables, given the lower and upper bounds shown in Table 1. From each FE simulation the maximum force and the maximum displacement of the impactor were stored and then added to the database.

	t_L (mm)	t_N (mm)	t_S (mm)	N_X (-)	Lr (-)
Lower bound	0.8	0.8	0.8	2	2
Upper bound	3	3	3	8	10
Accuracy	0.0001	0.0001	0.0001	1	0.001

Table 1. Lower and upper bounds of the design variables.

The MATLAB app Regression Learner was used to choose, train and validate the metamodels. Among those available, the Matern 5/2 Gaussian Process Regression and the Exponential Gaussian Process Regression were chosen as the most reliable. Specifically, the former was used to predict the impactor maximum displacement by giving the five geometrical parameters as predictors, whereas the latter was used to predict the impactor maximum force by giving the five geometrical parameters and the maximum displacement as predictors. For the latter case, it was observed that adding the displacement as a predictor resulted in a more reliable metamodel.
The two specific metamodels were chosen from the others after having validated them by considering 10 % of the 175 experiments. Subsequently, all the 175 experiments were used to train the metamodels. Training results are reported in Table 2. It is worth noting that the Normalised Root Mean Square Error (NRMSE), was calculated as the Root Mean Square Error (RMSE) divided by the difference between actual maximum and minimum values, as reported in Equation 1.

$$NRMSE = \frac{RMSE}{y_{max} - y_{min}} \tag{1}$$

The values of NRMSE presented in Table 2, as well as the correlation between predicted and actual data visible in Figure 5, allowed the metamodels to be considered of reasonable accuracy [12].

	Metamodel type	Number of predictors	RMSE	NRMSE	R^2
Impactor displacement	Matern 5/2 Gaussian Process Regression	5	2.0989 (mm)	4.21 (%)	0.95
Impactor force	Exponential Gaussian Process Regression	6	12.5 (N)	8.6 (%)	0.85

Table 2. Training results of the two metamodels.

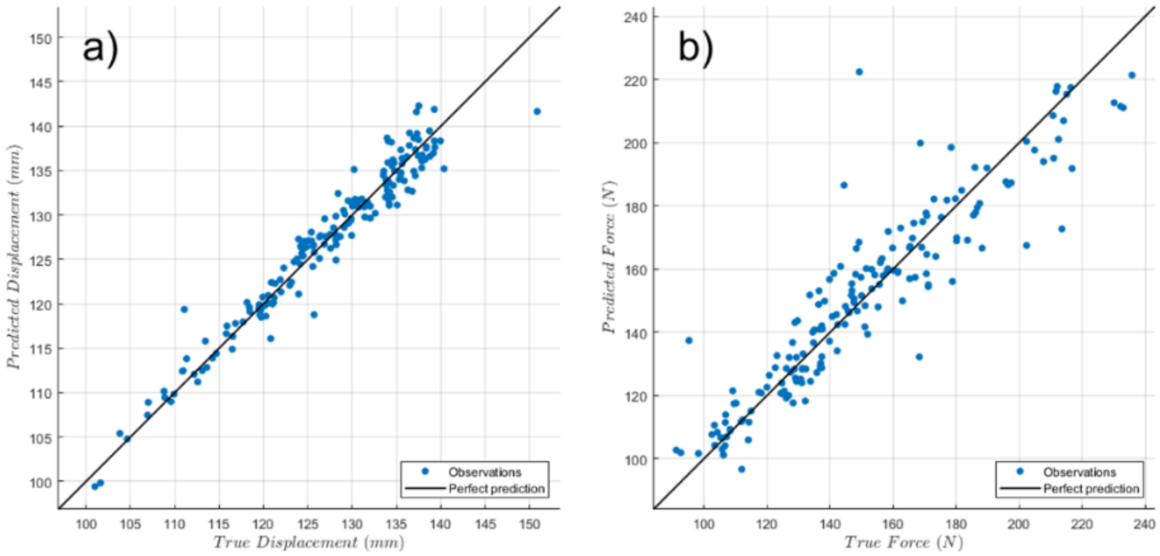

Figure 5. Predicted vs actual data: (a) impactor maximum displacement, (b) impactor maximum force.

3.3. Optimisation

The optimisation of the foam-filled hexachiral structure was performed having the objective of minimising the penetration of the impactor while simultaneously limiting the maximum load applied on the impactor. Regarding the force limit, given the requirements and the model simplifications explained in paragraph 3.1, the maximum load limit is set at 0.1 kN, i.e. 100 N.

The optimal combination of the five geometrical parameters were obtained using a function available in the Global Optimisation Toolbox of MATLAB. In details, a genetic algorithm was used to find the optimal solution. The two trained metamodels were used to estimate the maximum displacement and maximum force. In addition, a linear constraint and a non-linear constraint were imposed on the geometrical parameters. Regarding the latter, a constraint on the minimum radius R of the hexachiral nodes was imposed due to technological reasons.

Two optimal combinations were found that differed in the minimum value of R imposed. The first solution considered the non-linear constraint R ≥ 10 mm, whereas the second solution considered R ≥ 5 mm. Table 3 reported the optimal combination of the five geometrical parameters of the two cases considered. The energy absorber of case R≥10 had a total mass of 2938 g (270 g foam + 2668 g hexachiral frame), while the energy absorber of case R≥5 had a total mass of 4301 g (195 g foam + 4106 g hexachiral frame).

	t_L (mm)	t_N (mm)	t_S (mm)	N_X (-)	Lr (-)
Case R≥10	2.9999	2.9945	1.8052	5	2.236
Case R≥5	3.0000	3.0000	1.6006	8	3.082

Table 3. Optimal combination for the two cases considered.

It should be noted that the combination of geometrical parameters of the case R≥10 was almost identical to that of experiment number 60 in the database, while the combination of the case R≥5 did not match any of the combinations of the experiments used to train the metamodels.
To verify these optimal combinations, two FE simulations of the simplified model (Figure 6) were performed. As visible in Figure 7, the two optimal energy absorbers found by the genetic algorithm using the two trained metamodels almost met the requirement imposed on the maximum force (the force values in the graph were multiplied by the actual width).

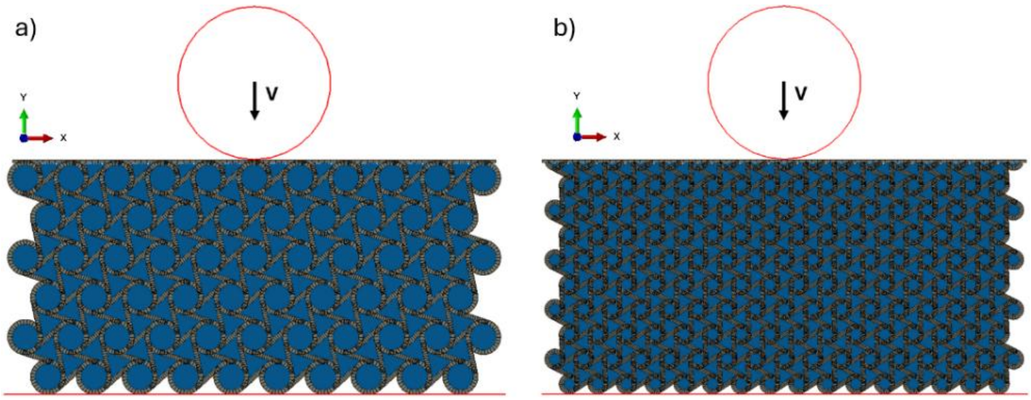

Figure 6. FE models of the optimal combinations: (a) case R≥10, (b) case R≥5

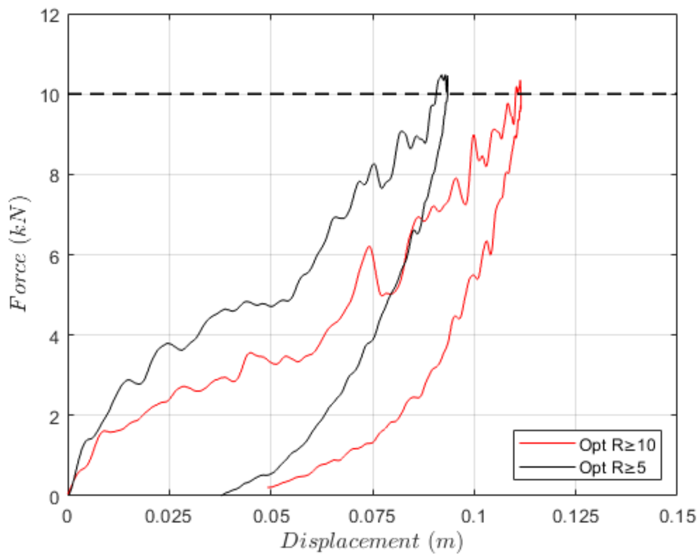

Figure 7. Force vs displacement curves of the two optimal combinations.

	Simplified FE Model		Metamodel		ΔDisp (%)	ΔForce (%)
	Max displacement (mm)	Max force (N)	Max displacement (mm)	Max force (N)		
Case R≥10	111.53	103.47	113.22	106.70	+1.51	+3.12
Case R≥5	93.47	104.83	95.19	99.99	+1.84	-4.62

Table 4. Comparison of simplified FE model results and metamodel predictions.

To quantify better the reliability of the optimal combinations found, the results of the simplified FE model and the values predicted by the two metamodels are reported in Table 4 for both the two cases analysed. The percentage errors reported in the last two columns represented the difference of the metamodels with respect to the simplified FE model.
As a final step, to further verify these optimal results, a FE simulation was performed considering the whole energy absorber of only case R≥10, and a comparison between the whole and sliced FE models could be done. The analyses was very time-consuming, and numerical problems arose, as evidenced by the interrupted blue line in Figure 8. Anyway, the impactor maximum displacement and impactor maximum force could be found. The results of the whole FE model and the values predicted by the two metamodels are reported in Table 5. The percentage errors reported in the last two columns represented the difference of the metamodels with respect to the whole FE model.

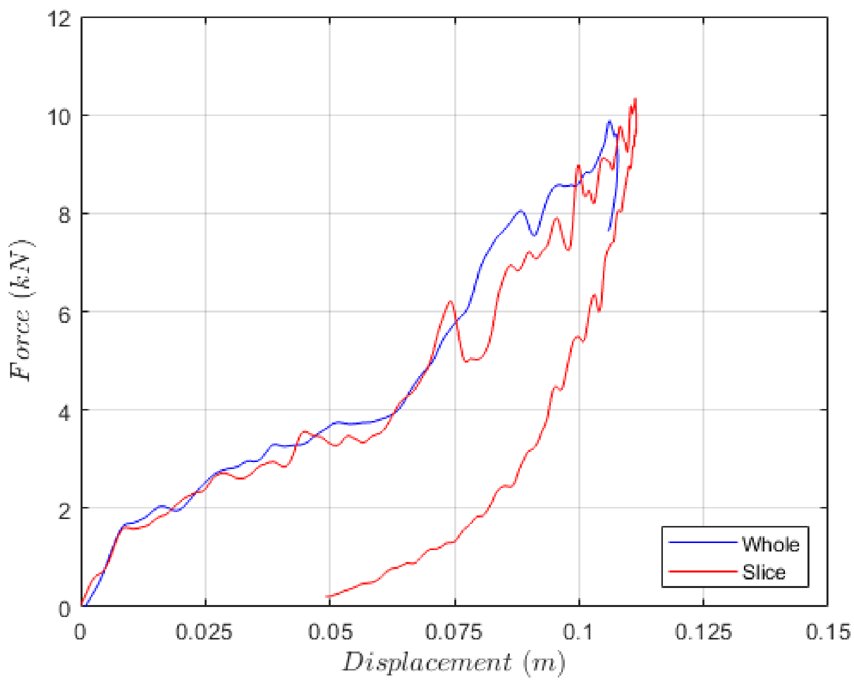

Figure 8. Force vs displacement curves of case R≥10: comparison between whole FE model and simplified sliced FE model.

	Whole FE Model		Metamodel		ΔDisp (%)	ΔForce (%)
	Max displacement (mm)	Max force (N)	Max displacement (mm)	Max force (N)		
Case R≥10	107.82	98.75	113.22	106.70	+5.00	+8.05

Table 5. Comparison of whole FE model results and metamodel predictions (the force value of the whole FE model was divided by the actual width).

4. CONCLUSION

The present work described the engineering of a novel concept of energy absorber based on an auxetic hexachiral structure filled with foam by exploiting the numerical techniques of surrogate models and genetic optimisation.
The combination of CF-45M and TPU-WTR materials, new compared with those described in the literature, was considered for foam and hexachiral frame, respectively. Experimental tests, represented by drop-weight impacts, were conducted both on the energy absorber filled with foam and on the energy absorber without the foam in order to validate the FE model of the energy absorber. From the initial numerical-experimental correlation, it was observed that the FE model had some differences with the experimental results: this was probably due to the preliminary numerical model of the TPU-WTR, given the good correlations of the other combination materials well described in the previous work in the literature. As a consequence, the FE model will have to be improved a lot, but this elastomeric material combination investigated made it clear that it could be a potential solution to guarantee the auxeticity throughout the duration of the impact, since it avoided the breakage of hexachiral frame.
Even though not well correlated, the FE numerical model was used to engineer the energy absorber concept for a specific crash scenario, represented by the impact between the lower leg of a pedestrian, i.e. a typical VRU, and the front bumper of a vehicle. The impact event, as well as the FE model of the energy absorber, were greatly simplified, but requirements of the EEVC/WG17 EURO Phase2 regulation and some research in the literature were taken as a reference in order to perform a realistic study of the energy absorber. A database of 175 FE simulation results was built, from which two surrogate models were trained to predict the maximum displacement and maximum force of the simplified lower leg, i.e. a rigid cylindrical impactor. The NRMSE values of displacement and force, 4.21 % and 8.6 % respectively, allowed the metamodels to be considered of reasonable accuracy. Finally, these two trained metamodels were used in the genetic optimisation that had the objective of minimising the penetration of the impactor while simultaneously limiting the maximum load applied on the impactor. Two optimal combinations of the hexachiral geometrical parameters were found, differing in the minimum imposed value of the radius of the hexachiral nodes. The optimal results were verified performing FE analyses: the percentage differences in displacement and force evaluated by the metamodels compared with the FE models were +1.51 % and +3.12 % for case R≥10 and +1.84 % and -4.62 % for case R≥5. These differences could be considered acceptable.
This design methodology had proven very promising in the investigation of this type of auxetic structure and its engineering in a real crash scenario. Further improvements of the FE numerical model and expansion of the database could enable more reliable results and new optimal solutions.

ACKNOWLEDGEMENTS

This study was carried out within the MOST - Sustainable Mobility National Research Center and received funding from the European Union Next-Generation EU (Piano Nazionale di Ripresa e Resilienza (PNRR) - Missione 4. Componente 2, Investimento 1.4 - D.D. 1033 17/06/2022, CN00000023). This manuscript reflects only the authors' views and opinions, neither the European Union nor the European Commission can be considered responsible for them.

REFERENCES

[1] X. Ren *et al.*, 'Mechanical properties of foam-filled auxetic circular tubes: Experimental and numerical study', *Thin-Walled Structures*, vol. 170, p. 108584, Jan. 2022, doi: 10.1016/j.tws.2021.108584.

[2] H. C. Luo *et al.*, 'Mechanical properties of foam-filled hexagonal and re-entrant honeycombs under uniaxial compression', *Composite Structures*, vol. 280, p. 114922, Jan. 2022, doi: 10.1016/j.compstruct.2021.114922.

[3] N. Novak *et al.*, 'Quasi-static and impact behaviour of foam-filled graded auxetic panel', *International Journal of Impact Engineering*, vol. 178, p. 104606, Aug. 2023, doi: 10.1016/j.ijimpeng.2023.104606.

[4] S. Yang, C. Qi, D. Wang, R. Gao, H. Hu, and J. Shu, 'A Comparative Study of Ballistic Resistance of Sandwich Panels with Aluminum Foam and Auxetic Honeycomb Cores', *Advances in Mechanical Engineering*, vol. 2013, Jan. 2015, doi: 10.1155/2013/589216.

[5] A. Airoldi, N. Novak, F. Sgobba, A. Gilardelli, and M. Borovinšek, 'Foam-filled energy absorbers with auxetic behaviour for localized impacts', *Materials Science and Engineering: A*, vol. 788, p. 139500, Jun. 2020, doi: 10.1016/j.msea.2020.139500.

[6] C. Chen, A. Airoldi, A. M. Caporale, G. Sala, and X. Yin, 'Impact response of composite energy absorbers based on foam-filled metallic and polymeric auxetic frames', *Composite Structures*, vol. 331, p. 117916, Mar. 2024, doi: 10.1016/j.compstruct.2024.117916.

[7] S. Badini, S. Graziosi, M. Carboni, S. Regondi, and R. Pugliese, 'Sustainable 3D printing with recycled tire rubber-based filaments: an investigation of process parameters and mechanical behaviour', *RPJ*, vol. 30, no. 3, pp. 571–587, Feb. 2024, doi: 10.1108/RPJ-08-2023-0309.

[8] T.-L. Teng, V.-L. Ngo, and T.-H. Nguyen, 'Design of pedestrian friendly vehicle bumper', *J Mech Sci Technol*, vol. 24, no. 10, pp. 2067–2073, Oct. 2010, doi: 10.1007/s12206-010-0612-0.

[9] H. Samaka, H. Al-Bugharbee, and M. Al-Azawy, 'Redesign the Front Shape of the Sedan Car for Pedestrian Safety and Mitigating Leg Injuries at Accidents', *International Journal of Safety and Security Engineering*, vol. 10, pp. 747–752, Dec. 2020, doi: 10.18280/ijsse.100604.

[10] S. Yang, Y. Sun, and C. Qi, 'Performance assessment and optimal design of hybrid material bumper for pedestrian lower extremity protection', *International Journal of Mechanical Sciences*, vol. 165, p. 105210, Jan. 2020, doi: 10.1016/j.ijmecsci.2019.105210.

[11] H. Tan *et al.*, 'Crashworthiness design and multi-objective optimization of a novel auxetic hierarchical honeycomb crash box', *Struct Multidisc Optim*, vol. 64, no. 4, pp. 2009–2024, Oct. 2021, doi: 10.1007/s00158-021-02961-9.

[12] R. P. Bohara, S. Linforth, H.-T. Thai, T. Nguyen, A. Ghazlan, and T. Ngo, 'Multi-objective bulk scale optimisation of an auxetic structure to enhance protection performance', *Engineering Structures*, vol. 280, p. 115729, Apr. 2023, doi: 10.1016/j.engstruct.2023.115729.

15th International Conference on
Shock & Impact Loads on Structures
12-13 June 2025, Gothenburg, Sweden

STRUT AND TIE MODELS FOR IMPULSE-LOADED REINFORCED CONCRETE BEAMS

Viktor Peterson[a], Mikael Hallgren[a,b], Anders Ansell[a],

[a]KTH Royal Institute of Technology, Sweden, email: vpeterso@kth.se,
[b]Tyréns AB, Sweden

Keywords: Strut and tie model, impact-loaded, blast-loaded, reinforced concrete, shear failure

Abstract

Impact loads may arise due to collisions, falling masses, ballistics, or fragments. Such scenarios result in concentrated dynamic forces with durations generally much shorter than the structure's natural period. Explosions may be accidental or antagonistic and result from, e.g. ignition of combustible clouds or explosive charges. The resulting dynamic load is distributed over the structure and is generally relatively short in duration. Both load types fall under the category of impulse-loads. Flexural failure modes are generally desirable for impulse-loaded reinforced concrete elements to safely absorb the work done by the external force. Flexural failures are characterized by wide cracks with significant plastic strain in the reinforcement, resulting in large energy absorption capacities. Shear-type failures are avoided, as these generally are characterized by one significant crack with minor plastic strain in the reinforcement, showing decreased energy absorption capabilities. Thus, models that can predict shear-type failures are needed, such that the beam can be reinforced against them. An agreed-on rational model for shear-type failures for beams without stirrups has yet to be found for static loading cases. Impulse loads add to the complexity of shear-type failures, as inertia- and strain rate effects should also be considered. A simple strut and tie model (STM) was used to predict the dynamic capacity of impulse-loaded beams simulated in the general-purpose finite element package Abaqus FEA. The study utilized material properties validated against previous drop-weight testing in the lab. Concentrated dynamic forces were first applied at an increasing rate on beams with varying shear span-to-depth ratios (moment-to-shear ratios) and compared against the results from the STM. The calculation model and simulation agreed well for the load rates and shear span-to-depth ratios larger than one. Distributed forces were then translated to equivalent concentrated forces using the expression found in the literature for static loads. This expression overestimated the length of the shear span, and a modification for the translation of distributed loads to equivalent concentrated loads based on the load rate is presented

1 INTRODUCTION

Despite more than a century of research, a unified model for shear in reinforced concrete beams has not been determined. Ritter [1] developed an early model in 1899 based on 45-degree compressive struts carrying shear forces by its vertical component. Using the lower-bound plasticity theorem, Drucker [2] in 1961 developed Strut and Tie Models (STMs) with diagonal concrete struts balanced by steel ties. Since then, many sectional models have been used in the design provisions based on empirical and mechanical models. Examples of such mechanical models are, for instance, models based on the Modified Compression Field Theory (MCFT) [3] and the Critical Shear Crack Theory (CSCT) [4]. These models account for important parameters such as size effects, strain effects and the moment-to-shear ratio, corresponding to the shear span-to-depth ratio for concentrated forces. Figure 1 shows testing conducted by Leonhardt and Walter [5] in 1962 on beams with varying shear span-to-depth ratios for concentrated and distributed forces. The results indicate that the shear strength decreased with increasing shear span-to-depth ratio.

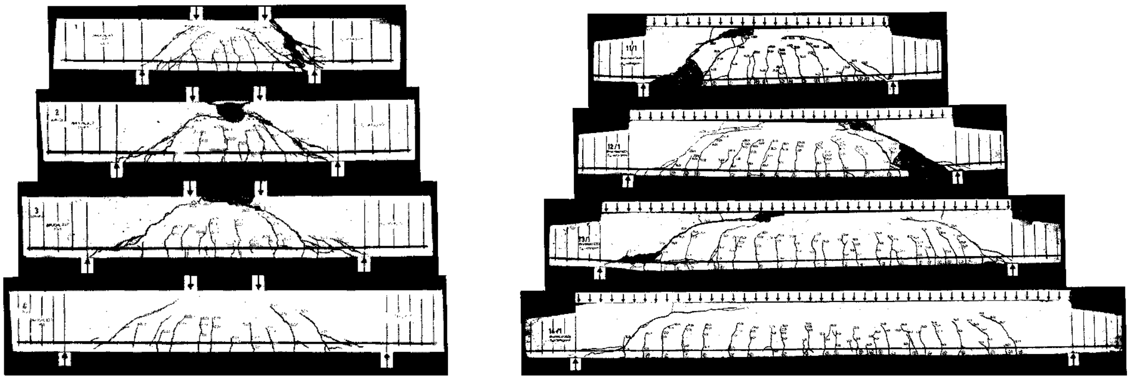

(a) (b)

Figure 1. Tests by Leonhardt and Walter [5] investigating the effect of the shear span-to-depth ratio for concentrated and distributed loads.

Kani [6] performed further testing and developed "Kanis Valley", shown in Figure 2 (a). The maximum applied external load V_u in experiments were compared to the results V_{pl} determined using the STM shown in Figure 2 (b) with varying shear span-to-depth ratios a/d. The STM generally converges with experiments for deep beams with shear span-to-depth ratios less than one. For larger ratios, the experimental capacity first decreases as cracks penetrate the direct strut before the capacity increases again as beam action governs the shear transfer. To consider the effect of cracks penetrating the compressive strut, a strength reduction factor, as shown in Figure 2 (c), is used in the European design provisions [7].

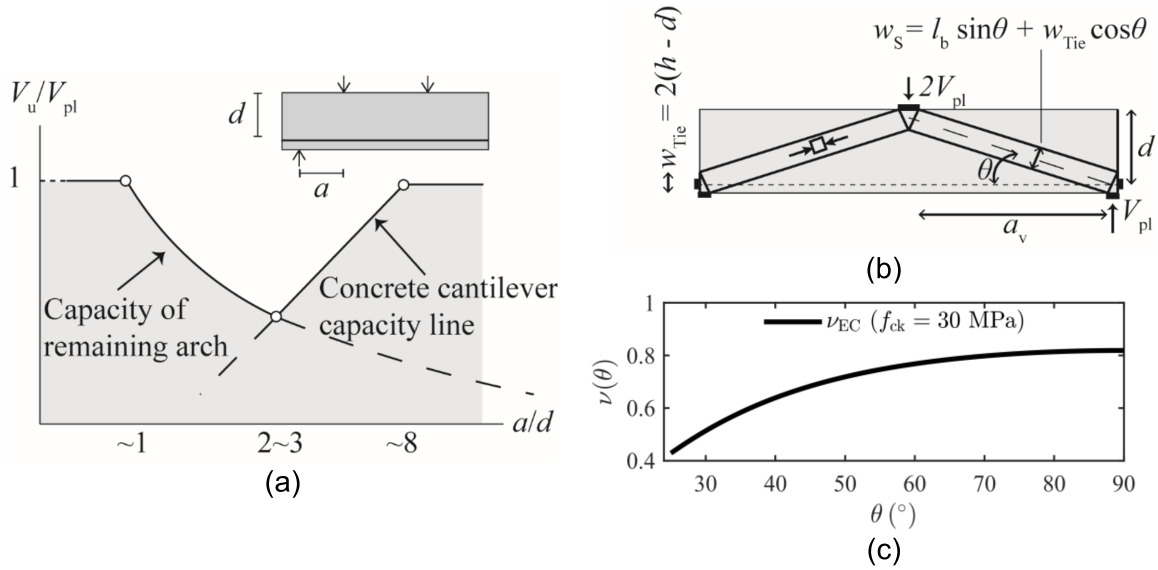

Figure 2. (a) The "Kanis valley" (redrawn from [4]) (b) STM for the plastic solution V_{pl} and (c) strength reduction factor $\nu(\theta)$ as function of the strut inclination in the second generation of the European design provisions [8].

Sagaseta and Vollum [9] presented an STM for short beams (shear span-to-depth ratio spanning 1.0 - 2.0) with and without stirrups subjected to concentrated loads. The load is in the model carried by the vertical component of the direct strut to the support. The force F_s in the direct strut may be determined as

$$F_{\mathrm{s}} = f_{\mathrm{csb}} b(l_{\mathrm{b}} \sin\theta + 2c \cos\theta) \tag{1}$$

where f_{csb} is the strut capacity, b the cross section width, l_{b} the support plate width, θ the direct strut inclination and c the distance from the bottom face to the centroid of the reinforcement. The vertical component V_{u} of the direct strut is then the maximum force that may be carried by the strut, i.e.

$$V_{\mathrm{u}} = \sin(\theta) F_{\mathrm{s}} \tag{2}$$

To determine the unknown strut inclination, equilibrium at the top node under the load plate may be used and must be solved simultaneously as

$$V_{\mathrm{u}} = 2\tan(d - (a_{\mathrm{v}} - l_{\mathrm{t}}(2 - n_{1\mathrm{p}})/4\,)\tan\theta) b\, f_{\mathrm{cd}} \tag{3}$$

where a_{v} is the clear shear span, l_{t} the load plate width, $n_{1\mathrm{p}}$ the number of load plates and f_{cd} the design compressive strength. The strength of the direct strut may be determined using the strength reduction factor as

$$f_{\mathrm{csb}}(\theta) = f_{\mathrm{cd}} \nu(\theta) \tag{4}$$

The strength reduction then depends on the major principal strain in the strut $\varepsilon_1(\theta)$ (see [8])

$$\nu(\theta) = 1/(1 + 110\varepsilon_1(\theta)) \tag{5}$$

A model was first calibrated by Ceberg and Holm [10] against previous drop-weight experimental testing shown in Figure 3 (a). This model was then used to simulate a similar series as that by Leonhardt and Walter [5], i.e. concentrated and distributed loads were applied to beams with increasing moment-to-shear ratio. The simulations were conducted using the general-purpose finite element package Abaqus FEA [11]. The loads used are dynamic loads with a load rate spanning 100 - 100 000 kN/s. The results are then compared to those using the STM described by Sagaseta and Vollum [9] with the strength reduction factor presented in Figure 2 (c).

2 NUMERICAL MODELS

2.1 Calibration against experiments

A model was first calibrated by Ceberg and Holm [10] against experiments shown in Figure 3 (a). This was a 2D model of the concrete beam, constructed of triangular plane stress element with a 5.0 - 7.5 mm side length. The Concrete Damage Plasticity model (CDPM) was used with a bi-linear softening law by Grassl [12], regularized using fracture energy for tension. Linear unloading was considered in compression, regularized using a crushing displacement following Červenka [13]. The reinforcement was modelled using beam elements with a perfect bond to the concrete and an elastic-plastic material model with a stress-strain curve from testing.

The results in Figure 3 (b) show good agreement between the crack pattern in the experiment and fully damaged elements in the simulation. The critical inclined crack in the long shear span to the right of the impact zone is captured. The diagonal cracks adjacent to the impact zone on each side are also captured. The main discrepancy is the larger amount of flexural cracks in the simulations, which is an effect of the assumption of a perfect bond. The reaction forces in Figure 3 (c) indicated good agreement for the left reaction force. The maximum amplitude of the right support reaction slightly shifts in time in the simulation, but the results generally converge.

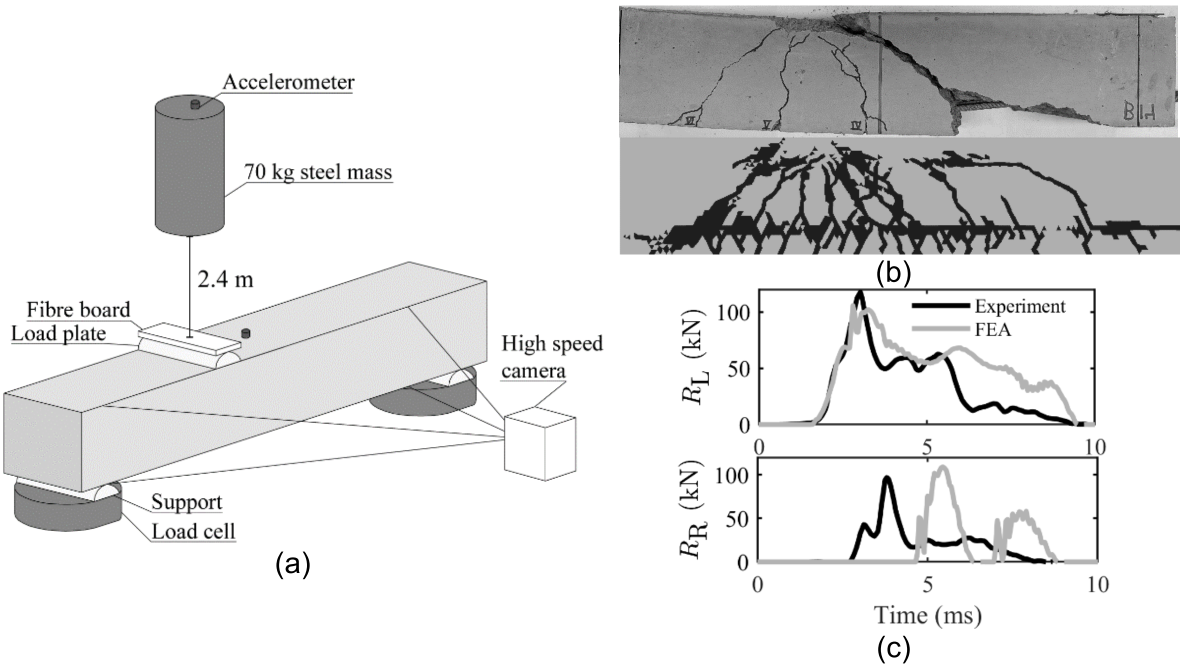

Figure 3. (a) Previous drop-weight testing (redrawn from [10]), (b) fully damaged elements ($d_t > 0.99$) in the model compared against damage in the experiment and (c) comparison of left R_L and right R_R support reactions.

2.2 Simulations with varying moment-to-shear ratios and load rates

Simulations were conducted to study the influence of moment-to-shear ratio for concentrated and distributed loads at various load rates. Beams with concentrated loads were tested with moment-to-shear ratios (shear span-to-depth ratios) spanning 0.6 to 3.0, as shown in Figure 4 (a). The symmetry plane at mid-span was utilized to model half the beam, the support plate was free to rotate, resulting in simply-supported boundary conditions, and the load plate and the support plate were 50 mm wide. The beams with distributed loads are shown in Figure 4 (b). These beams had moment-to-shear ratios (determined as $L/(4d)$) spanning 0.8 to 3.0. To study dynamic effects, the concentrated load and resultant of the distributed load were applied at rates 100 – 100 000 kN/s, as shown in Figure 4 (c). The material models did not consider strain rate effects, meaning only dynamic inertia effects were studied.

3 RESULTS AND DISCUSSION

3.1 Concentrated loading

Results for beams with concentrated loads with the various load rates are first presented. Figure 5 shows the stress field during maximum support reaction, generally occurring right before strut failure. Black colours indicate elements with minor compressive stresses larger than the plastic stress used for the strut in the STM limit analysis. This stress was determined as the product of the mean compressive strength and the strength reduction factor. Figure 5 shows that the stress fields generally converge for the high load rate in (a) with the much lower load rate in (b). For both cases, clear direct struts develop between the support plate and the

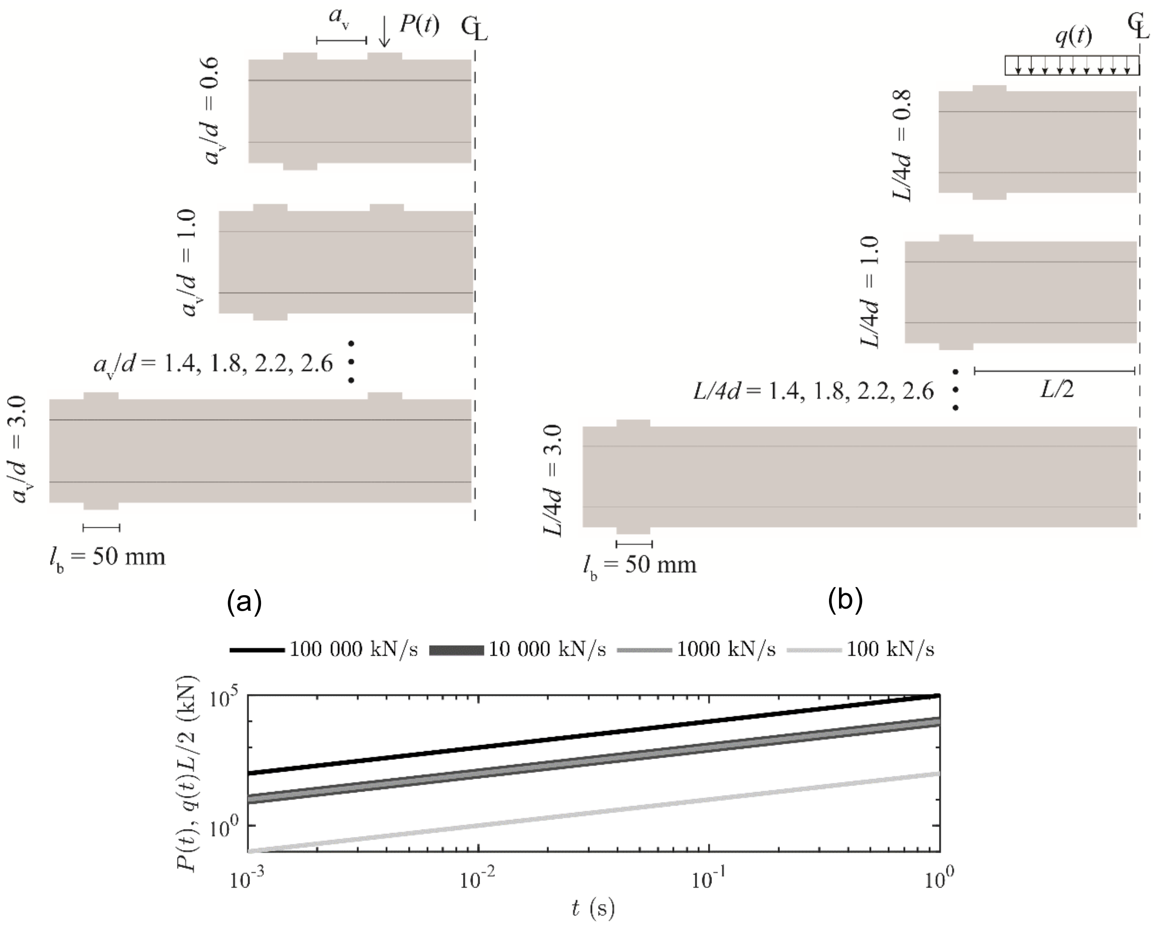

(c)

Figure 4. Beams loaded by: (a) concentrated dynamic loads $P(t)$ with clear shear span a_v and (b) distributed dynamic loads $q(t)$ with loaded length L. (c) Variation of the concentrated load and the resultant for the distributed load over time in log-log scale.

load plate on top. The strut is straighter for the small shear span-to-depth ratio, while a bottle-neck shape with a larger width at the mid-point of the strut is observed for the larger shear span-to-depth ratio. The direct strut is shown to be heavily disturbed by damage, as shown by the loss of compressive stress in its width direction, for shear span-to-depth ratios 1.4, 2.2 and 3.0. This is not the case to the same extent for the shear span-to-depth ratio of 0.6.

Figure 6 shows fully damaged elements in tension during maximum support reaction. The damage is similar for both load rates and a shear span-to-depth ratio of 0.6, with an undamaged volume spanning the support and load. For shear span-to-depth ratios larger than 0.6, cracks span the support plate to the load plate inside the shear span, penetrating the direct strut. For these cases, a strength reduction factor is needed to consider the tensile strain in the strut. Without such a factor, the solution cannot be deemed lower bound.

The maximum support reaction, or vertical component of the direct strut, is plotted for all shear span-to-depth ratios tested with all load rates in Figure 7 (a). Simulations with 100 – 10 000 kN/s in general converges for the shear span-to-depth ratios tested. The highest load rate, 100 000 kN/s, results in a higher maximum support reaction for the smallest shear span-to-depth ratio, after which the curve converges with the others. The result of applying the STM with and without the strength reduction factor is also shown. The simulations converges with the plastic solution without the reduction factor for the lowest shear span-to-depth ratio. This is because cracks were shown not to penetrate the strut. At a shear span-to-depth ratio of 1.0 and higher, the simulations instead converge with the STM solution considering the strength reduction factor. Generally, the STM with a strength reduction provides a lower-bound solution for all cases.

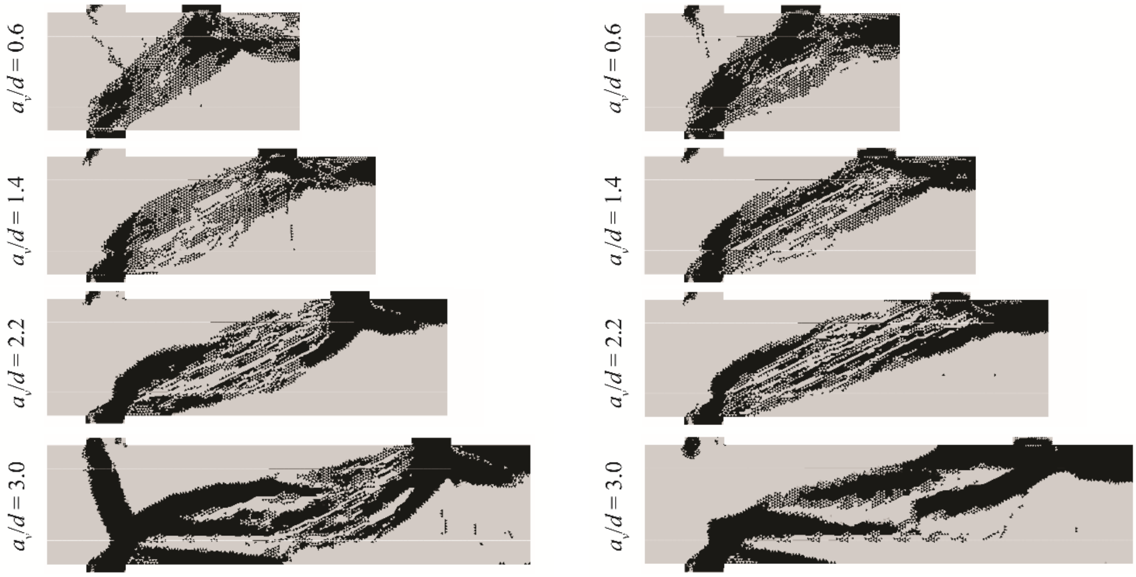

(a) 100 000 kN/s (b) 100 kN/s

Figure 5. Minor principal stresses larger than f_{csb} at the time of maximum reaction force.

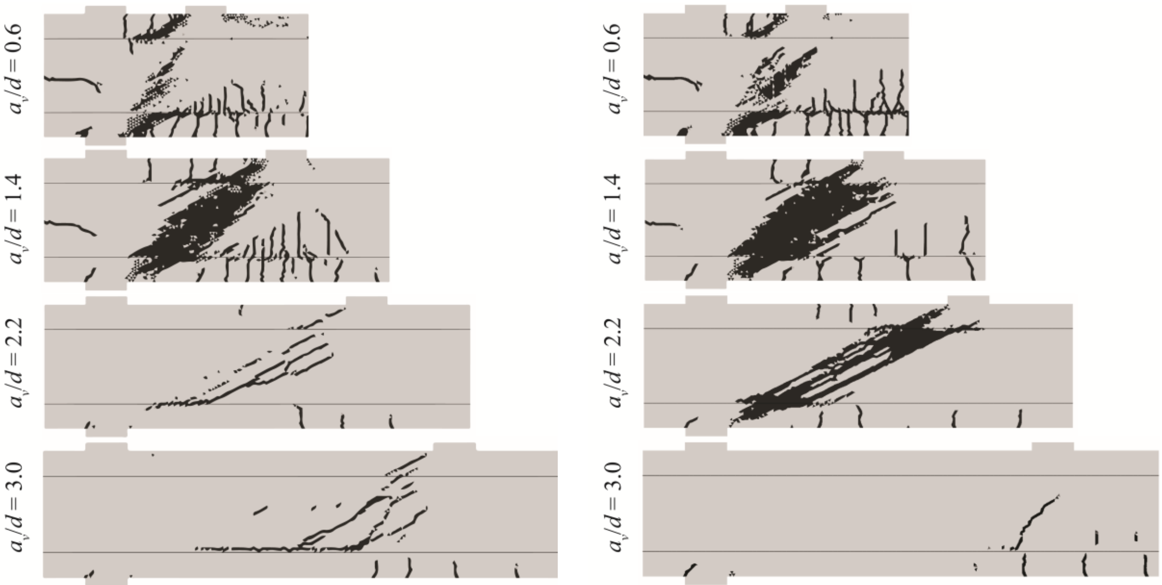

(a) 100 000 kN/s (b) 100 kN/s

Figure 6. Fully damaged elements ($d_t > 0.99$) at the time of maximum reaction force.

"Kanis Valley" was reconstructed in Figure 7 (b) by finding the ratio of the maximum support reaction to the plastic limit STM solution. Here, the simulations with the highest load rate again diverge from the others, indicating a significant effect of inertia. This discrepancy could be even larger if strain rates are considered, but this is outside the scope of this paper. Generally, the curves follow the limits previously seen, i.e. the ratio between the maximum support reaction and the plastic solution is around 1.0 at a shear span-to-depth ratio of around 0.6-1.0. The ratio then decreases as the shear span-to-depth ratio increases from 1.0 to around 2.5, after which it increases again due to cantilever action governing the shear transfer capacity. The strength reduction factor is used to consider this effect of decreasing capacity with increasing shear span-to-depth ratio due to transverse tensile strain in the strut.

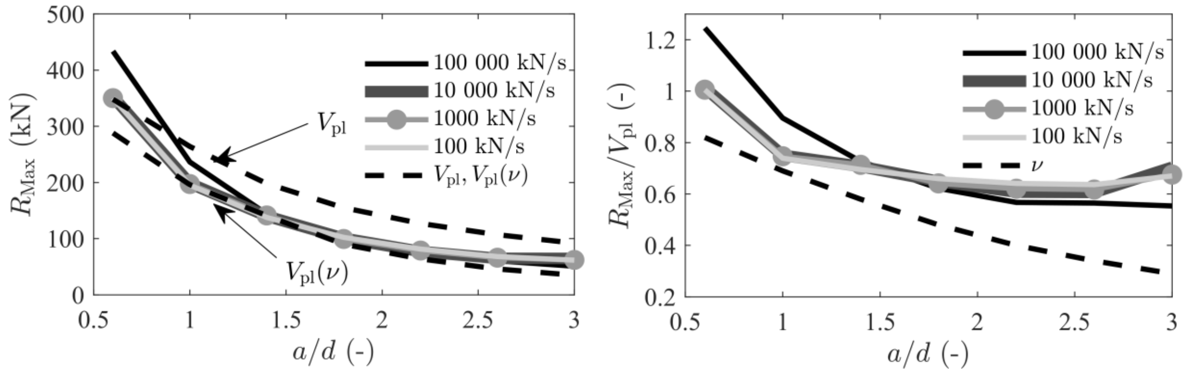

(a) (b)

Figure 7. (a) Maximum reaction force as the shear span-to-depth ratio varies and (b) Kani's valley for the different load rates.

3.2 Distributed loading

Beams with a similar moment-to-shear ratio were simulated using distributed loading. The resulting compressive stress fields are shown in Figure 8, with force vectors at the top face indicating the position for the resultant of the distributed loading at the quarter-span. For the lower load rate in Figure 8 (b), the inclination of the strut agrees well with the position of the resultant at quarter-span for the low length-to-depth ratios. However, the discrepancy increases slightly for the higher ratios. Figure 8 (a) shows the compressive struts for the highest load rate. Here, the strut inclination stops coinciding with the position of the resultant for length-to-depth ratios larger than 1.4. For higher ratios, the strut inclination is independent of the beam length. This did not occur for the concentrated load and indicates a larger influence of load rate and inertia effects for the distributed load compared to the concentrated load.

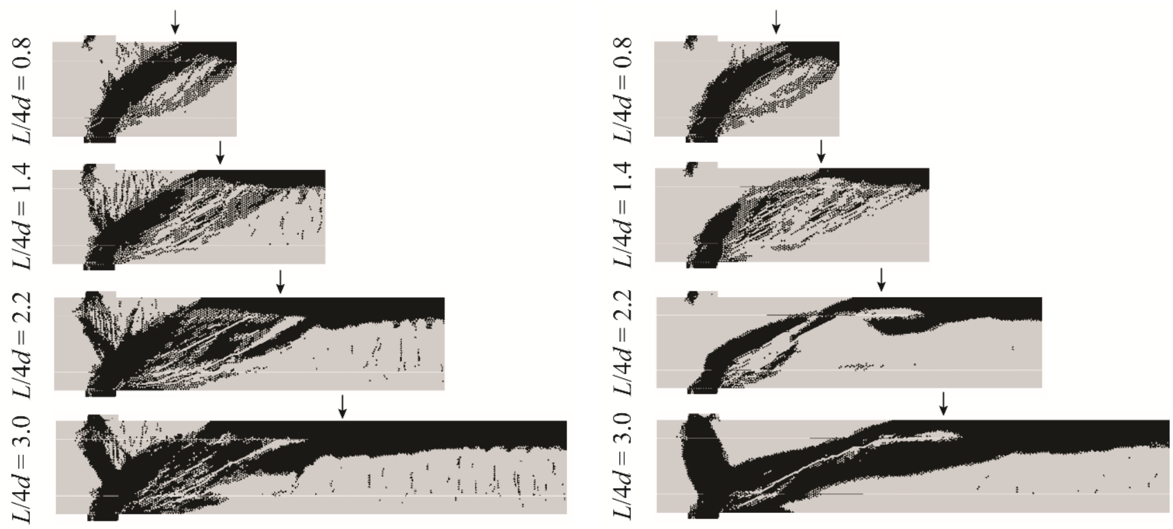

(a) 100 000 kN/s (b) 100 kN/s

Figure 8. Minor principal stresses larger than f_{csb} at the time of maximum reaction force for beams with distributed loading (resultant vectors at the quarter-length are shown).

The damage to the beams with concentrated loads is shown in Figure 9. Inclined cracks adjacent to the support disturbs the stress fields for all length-to-depth ratios. Beams with concentrated loading instead showed damage mainly around the concentrated load for the high shear span-to-depth ratios.

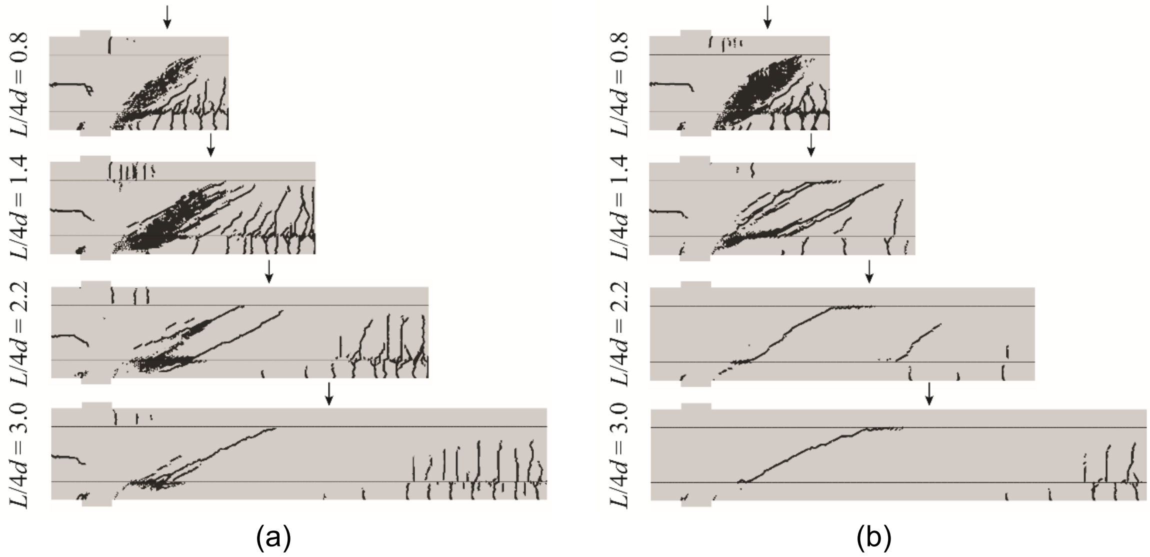

Figure 9. Fully damaged elements (d_t > 0.99) at the time of maximum reaction force (resultant force vectors at the quarter-length of the free span is also shown).

The maximum support reaction was plotted for the length-to-depth ratios and load rates in Figure 10 (a). The curves generally agree, with a load rate of 100 000 kN/s having the largest discrepancy. It is shown that that for a load rate of 100 000 kN/s, the capacity is not decreased with increasing moment-to-shear ratios larger than 1.4. This is an effect of the strut inclination not changing, as shown in Figure 8 (a). Figures 10 (a) and (b) show that the simulations almost converge with the plastic solution. However, the damage plots in Figure 9 indicated that cracks penetrate the direct strut for the length-to-depth ratios larger than 0.8, and the ratio between the maximum reaction and STM solution should, therefore, be less than one in Figure 10 (b).

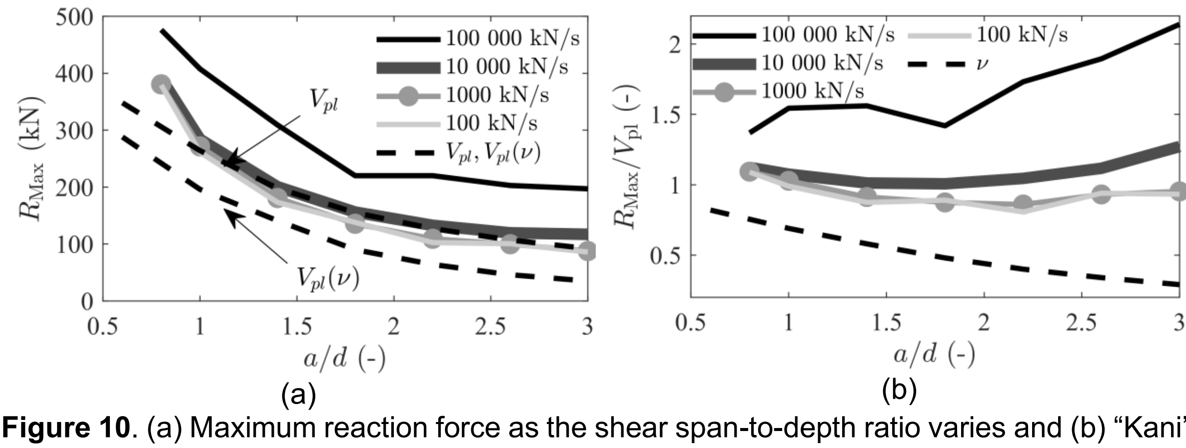

Figure 10. (a) Maximum reaction force as the shear span-to-depth ratio varies and (b) “Kani’s valley” for the different load rates.

3.3 Comparison distributed and concentrated loads

The stress fields for beams with a moment-to-shear ratio of 1.4 and 3.0 are compared for both loads types with a rate of 100 000 kN/s in Figure 11. Figure 11 (a) shows that the strut inclination for the beam under distributed loading is slightly steeper than for the beam with concentrated loading. This results in a smaller equivalent shear span of the distributed load $a_{\mathrm{v,q}}$ compared to the shear span $a_{\mathrm{v,P}}$ of the beam with a concentrated load and the same moment-to-shear ratio. This discrepancy is much larger for the beams with a moment-to-shear ratio of 3.0, as shown in Figure 11 (b). Here, the equivalent shear span of the distributed load is about half of the shear span of the concentrated load. The results indicate an insufficient relation between moment-to-shear and length-to-depth ratios for this load rate.

This is further shown for all cases in Figure 12. In Figure 12 (a), all results for beams with distributed loads are slightly shifted to higher moment-to-shear ratios, indicating that the relation between the moment-to-shear and length-to-depth ratio is overestimated. The results of this is shown in Figure 12 (b). The relation between the maximum support reaction for the simulation of the concentrated load $R_{\mathrm{Max,P}}$ and distributed load $R_{\mathrm{Max,q}}$ at each moment-to-shear ratio is a maximum of 0.8 for load rates 100 and 1000 kN/s, 0.7 for 10 000 kN/s and 0.6 for 100 000 kN/s.

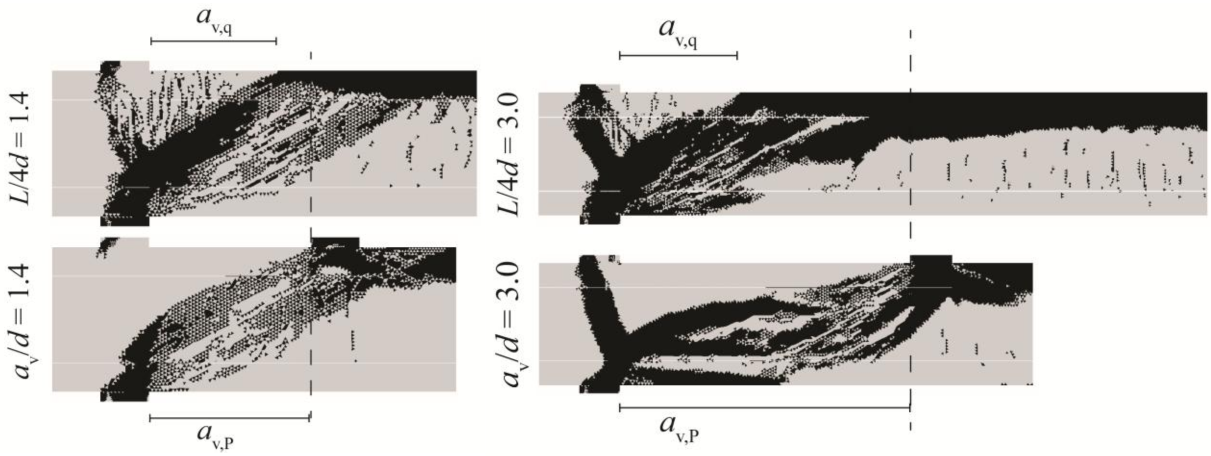

(a) 100 000 kN/s (b) 100 000 kN/s

Figure 11. Stress fields and shear spans for beams loaded with distributed and concentrated forces at a load rate of 100 000 kN/s and: (a) a moment-to-shear ratio of 1.4 and (b) 3.0.

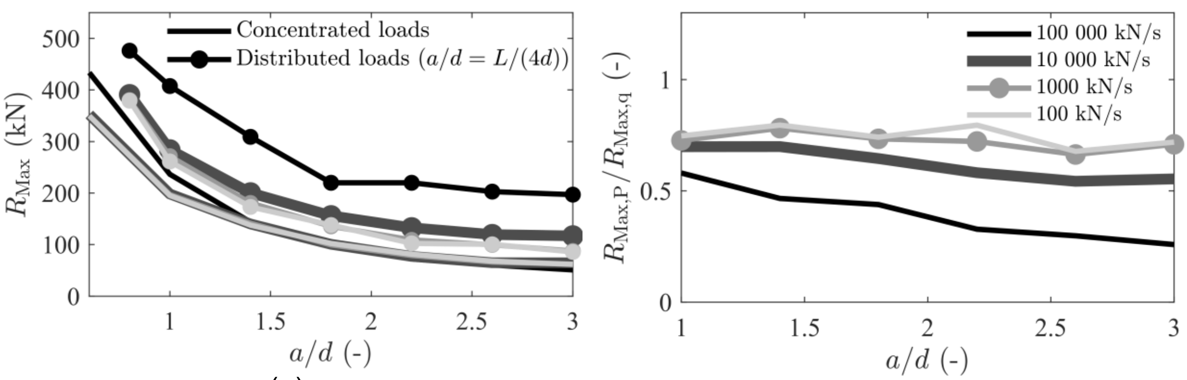

(a) (b)

Figure 12. (a) Maximum reaction force as the shear span-to-depth ratio varies and (b) ratio between the maximum reaction force for beams with concentrated and distributed loads.

The relation between moment-to-shear ratios and length-to-depth ratios was modified in Figure 13 for the distributed loads to better account for the observed equivalent shear-spans shorter than the quarter-length. Simulations using $L/6.9d$, $L/5.8d$ and $L/5.1d$ for load rates spanning 100 – 100 000 kN/s were shown to better represent the beams simulated in this paper. The results are compared to the beams with concentrated loads in Figure 13 (a), indicating good convergence except for the highest load rate of 100 000 kN/s, where the effective shear-span for the distributed load did not increase with length after a certain level. The results in Figure 13 (b) indicate that the results for both load cases match well, and the STM model based on concentrated loads, which converged with simulation results, may also be used for distributed loads. This is if the moment-to-shear ratio is corrected. The corrected moment-to-shear ratio may be described by

$$a/d = L/(\alpha 4d\,) \tag{6}$$

where α is a correction factor dependent on the load rate $\dot{P}$ (kN/s), which may by power-fitting be determined as

$$\alpha(\dot{P}) = 1.2 + 1/133\,\dot{P}^{1/e} \tag{7}$$

consisting of a constant term of 1.2, indicating a discrepancy of 20% also for static loading when the load rate is small, and a load rate dependent term which accounts for inertia effects. This function is only fit to data spanning 100 – 100 000 kN/s, and the effect of smaller or larger load rates is not considered. Also, the effect of other variables such as material or geometrical properties of the beam is not considered.

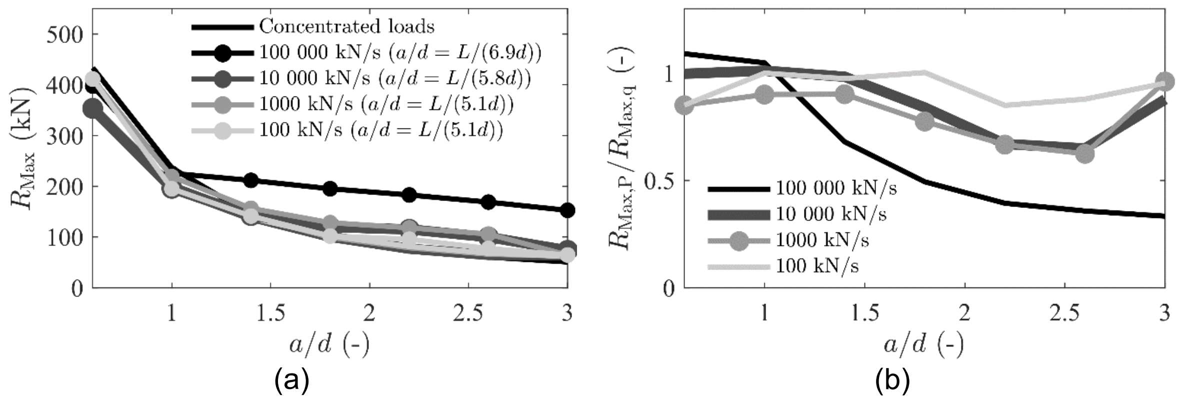

Figure 13. (a) Maximum reaction force as the shear span-to-depth ratio varies (with correction to the shear slenderness for distributed loads) and (b) the resulting ratio between the maximum reaction forces.

4 CONCLUSIONS

The results indicate that simple strut and tie models with strength reduction factors following static design provisions are sufficient for a conservative prediction of the shear capacity for a wide range of load rates and shear span-to-depth ratios. For instance, this model may be used to determine the maximum capacity of impact-loaded beams. Similar calculations for beams with distributed loads and with moment-to-shear ratios determined as $L/4d$ were over-conservative, and a correction factor dependent on the load rate was proposed. This correction factor does, however, not consider the observed effect for high load rates where the moment-to-shear ratio did not change with increasing loaded length.

ACKNOWLEDGEMENTS

Funding for the project was provided by the Swedish Transport Administration, the Swedish Fortifications Agency and the Civil Contingencies Agency (MSB).

REFERENCES

[1] W. Ritter, “Die bauweise hennebique. III. Schluss”, *Schweizerische Bauzeitung*, vol. 33, pp. 59-61, 1899.

[2] D.C. Drucker, “On structural concrete and the theorems of limit analysis”, *IABSE Publication*, vol. 21, pp. 49-59, 1961.

[3] M.P. Collins, D. Mitchell. Biggs, *Prestressed concrete structures*. Prentice-Hall, New Jersey, USA, 1991.

[4] M. Ruiz, A. Muttoni and J. Sagaseta, “Shear strength of concrete members without transverse reinforcement: A mechanical approach to consistently account for size and strain effects”, *Engineering Structures*, vol. 99, pp. 360-372, May 2015.

[5] W. Leonhardt and R. Walter, “Schubversuche an einfeldrigen stahlbeton balken mit und ohne schubbewehrung”, Deutscher Ausschuss Für Stahlbeton, vol. 151, 1962.

[6] G.N.J. Kani, “The Riddle of Shear Failure and Its Solution”, Journal of the American Concrete Institute, vol. 61, pp. 441-468, April 1962.

[7] CEN, Eurocode 2: Design of Concrete Structures – Part 1-1: General Rules and Rules for Buildings, European Comittee for Standardization, Belgium, 2005.

[8] M.F. Ruiz, L.C. Hoang and A. Muttoni, “Stress Fields and Strut-and-Tie Models as a Basic Tool for Design and Verification in Second Generation of Eurocode 2”, *Hormigón y Acero*, vol. 74, pp. 79-90, 2023.

[9] J. Sagaseta and R.L Vollum, “Shear design of short-span beams”, *Magazine of Concrete Research*, vol. 62, pp. 267-282, April 2010.

[10] E. Kolmodin and K. Kubiak, Effects of Impulse Intensity and Boundary Conditions for Blast-Loaded Reinforced Concrete Beams. MSc Thesis, KTH Royal Institute of Technology, Div. Concrete Structures, Stockholm, Sweden, 2024, pp. 130.

[11] Dassault Systémes, ABAQUS/Standard User’s Manual, Version 6.14, Dassault Systémes Simulia Corp, USA, 2014.

[12] P. Grassl, “Modelling the dynamic response of concrete with the Damage plasticity model CDPM”, 10th International Conference on Fracture Mechanics of Concrete and Concrete Structures, March 2023, France.

[13] V. Červenka, L. Jendele and J. Červenka, ATENA Program Documentation – Part 1 Theory, Cervenka Consulting, Prague, Czech, 2011.

15th International Conference on
Shock & Impact Loads on Structures
12-13 June 2025, Gothenburg, Sweden

DROP-WEIGHT IMPACT TEST ON REINFORCED CONCRETE BEAMS

John Abdalnour[a], Johan Magnusson[a], and Viktor Peterson [b]

[a]Fortifications Agency, Sweden, email: John,abdalnour@fortifikationsverket.se, [b] KTH Royal Institute of Technology, Sweden

Keywords: Reinforced concrete beams, dynamic loading, shear failure, shear reinforcement configuration, load position, strain rate effect, impact.

Abstract

Reinforced concrete (RC) is commonly used in defence and protective structures such as shelters and barriers. Such protective structures may be subjected to dynamic loads from explosions from conventional weapons. Protective structures are designed for a ductile response, thereby preventing shear-type failures. The results of this paper are based on experiments conducted on 27 reinforced concrete beams, where 18 were tested dynamically and 9 were tested statically at KTH Royal Institute of Technology. A mass was dropped onto the beams in the dynamic tests, while an MTS machine was used to perform the static tests. The load position was varied at different distances from one of the supports. The beams were designed with both compression and tensile reinforcement and three different configurations of shear reinforcement: no stirrups and stirrups with 90 mm and 45 mm spacing, respectively. The tests were instrumented with load cells and accelerometers. The recorded data were analyzed, focusing on three main factors: the effect of load position, shear reinforcement configuration, and dynamic versus static loading effects. The results indicated that compression strut failures occurred when the load was positioned closest to the support, while the failure mode transitioned to flexural shear with the load further from the support. Beams without shear reinforcement exhibited inclined cracks, with a significant shear influence and less contribution from bending. In contrast, beams with higher shear reinforcement content predominantly developed bending cracks with a diminished influence from shear.

1 INTRODUCTION

Reinforced concrete (RC) structural elements are widely used in society and for defence purposes. Flexural and shear strength capacities determine the load capacity of concrete structures. Shear failure modes are brittle, sudden and occur without showing any warning signs before failure. In contrast, the flexural failure mode is desirable due to its ductility, showing early warnings before failure, such as wide cracks. Furthermore, ductile failure modes are also desirable under impulsive loads due to their larger energy absorption capacity, see Peterson et al. [1] and Peterson [2].

Magnusson [3] describes different shear failure mechanisms such as direct shear failure, failure caused by crushing or splitting of the compressive strut compressive strut, shear failure by shear compression and flexural shear failure. The occurrence of shear failure types is strongly dependent on loading conditions and shear slenderness, i.e. *a/d* where *a* is the length of the shear span and *d* is the effective depth of the beam. In a blast loading scenario with a distributed load across a concrete beam, the shear slenderness is, however, not well-defined. The shear slenderness varies throughout the response from a very small slenderness and continuously increasing over time. Thus, it is of interest to investigate the shear response of beams for different values of shear slenderness.

This paper aims to present selected results of an experimental study investigating different types of shear failures of beams subjected to both dynamic and static loading conditions. The investigation focused on point loads at different positions from one of the supports. The basis of this paper is a report by Abdalnour and Saliba [4]

2 EXPERIMENTAL PROCEDURES

2.1 Overview

The experimental study included 27 concrete beams subjected to dynamic and static loads. The beams were designed with three different shear reinforcement configurations and only one longitudinal reinforcement configuration. In the investigation, 18 beams were subjected to drop weight tests and 9 beams were tested statically using an MTS machine. This paper focuses on a selected number of tests, i.e. 9 drop-weight tests and 3 static tests, see Table 1. The geometry of the tested beams is $150 \times 150 \times 800$ mm with 3Ø8 tensile reinforcing bars, and 2Ø8 compression reinforcing bars of grade K500C-T. Further, the stirrups were of Ø6 of the same grade. Figure 1 illustrates the geometry of the beam designed with different shear reinforcement configurations.

The concrete compressive strength was determined on 150 mm cubes, which resulted in a mean compressive strength of 43.7 MPa. Tensile tests on the rebars were conducted to determine the yield and ultimate strengths. The mean yield strength of Ø6 and Ø8 bars were 547 MPa and 517 MPa, respectively, and the ultimate strengths were 515 MPa and 622 MPa for the corresponding bars.

Table 1. Static and dynamic load capacity obtained from tests of beams with shear reinforcement S90.

Beam number	Load position	Stirrup spacing [mm]
B2-D	04*d*	45
B4-D	1*d*	45
B6-D	2*d*	45
B11-D	04*d*	NoS
B13-D	1*d*	NoS
B14-D	2*d*	NoS
B19-D	04*d*	90
B21-D	1*d*	90
B24-D	2*d*	90
B25-S	04*d*	90
B26-S	1*d*	90
B27-S	2*d*	90
D: Dynamic test; S: Static test. NoS: No stirrups.		

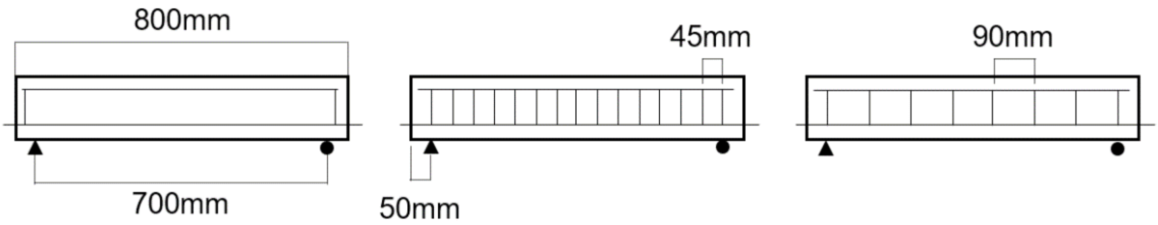

Figure 1. Schematic representation of the beams with different shear reinforcement configurations.

2.2 Static tests

The beams were tested statically by using an MTS machine, which enabled deformation-controlled tests with a rate of 0.5 mm/min, see Figure 2. The concrete beams were supported by two roller supports on each side, and the loading point varied in the same way as in the dynamic tests, i.e., at distances of 0.4*d*, 1*d*, and 2*d* from one of the supports. The static tests were conducted at an age of around 60 days after casting.

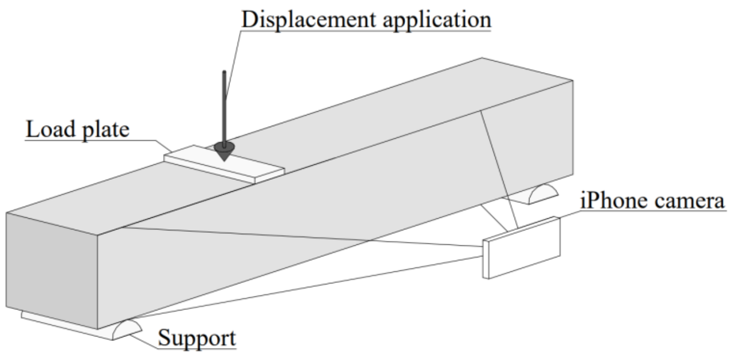

Figure 2. Set-up of the static tests [5].

2.3 Dynamic tests

The dynamic tests were conducted by dropping a cylindrical steel mass of 70 kg from a height of 2.4 m onto the beams where the beam supports consisted of steel half-cylinders. A plastic tube was used to guide the mass during the tests. Two accelerometers were installed, one on top of the drop weight and the other on top of the beam at mid-span. The support reaction forces were registered with load cells beneath each support. Furthermore, a piece of fiberboard placed on the half of cylinder was used to soften the impact, see Figure 3. The tests were conducted after approximately 40-60 days of casting.

The impact force was determined from the deceleration of the striker at impact. The acceleration measured on top of the striker was filtered using a low-pass filter with a cut-off frequency of about 2 kHz. This resulted in mainly rigid-body deceleration. The impact force was then approximated as the product of the rigid body deceleration and the total mass of the striker.

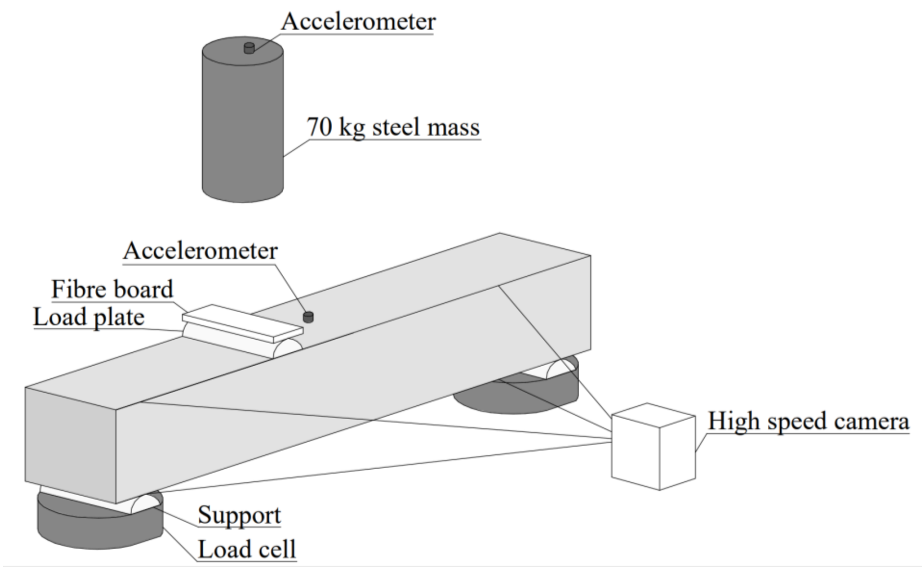

Figure 3. Set-up of the dynamic tests [5].

3 RESULTS

3.1 Variation of load position

This section includes the results of the dynamically loaded beams with emphasis on the differences caused by different load positions for the same shear reinforcement configuration.

3.1.1 Beams without shear reinforcement

As the load position moved from 0.4*d* to 2*d*, the acceleration, velocity, and displacement increased. B11 exhibited lower acceleration, velocity, and displacement compared to B13 and B14, indicating that B11 had a stiffer response compared to the latter, according to Abdalnour and Saliba [4].

According to the recorded data, shown in Figure 4, the reaction forces decreased as the impact point was further from the support, i.e., the reaction forces for beams tested with load position 2*d* are smaller than the reaction forces for beams tested at load positions 0.4*d* and 1*d*. This indicates a lower shear capacity for the beam with a load positioned 2*d* from the support.

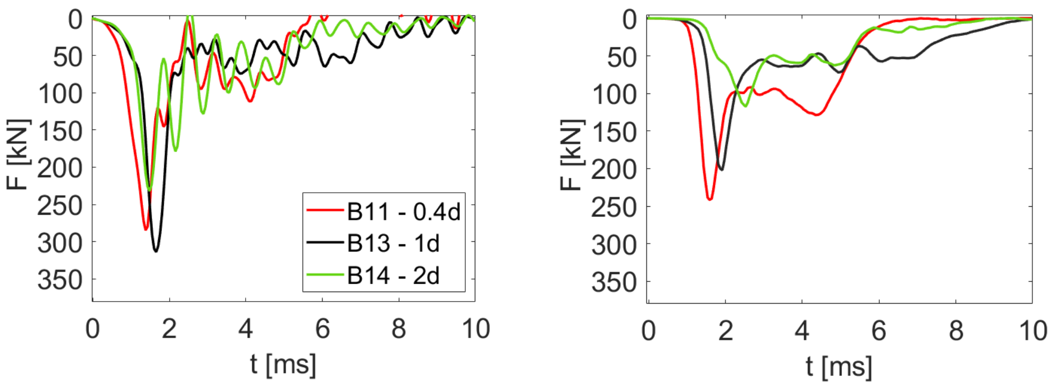

Figure 4. Impact force (left) and reaction forces LC (right) for beams B11, B13 and B14.

Cracks caused by impact load at different positions are shown in Figure 5. The number of cracks formed increased as the distance between the loading position and the support increased. Additionally, B11 and B13 failed primarily in shear failure caused by a crushed compressive strut, when cracks initiated at the support and propagated towards the impact load. Furthermore, the failure mode shifted to flexural shear failure at a loading position 2*d*, where shear cracks propagated from flexural cracks and upward.

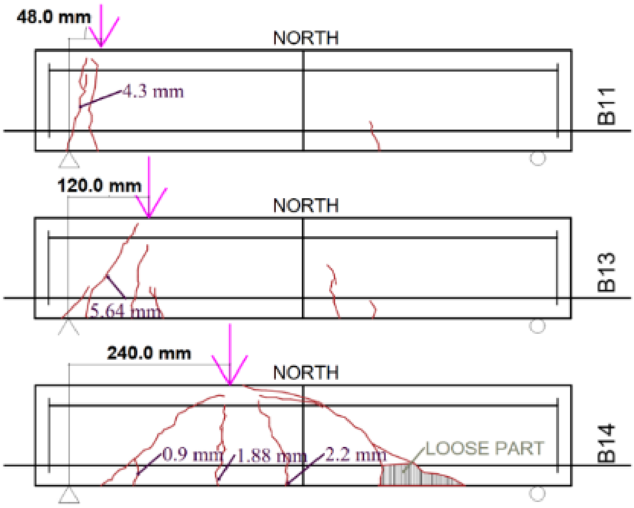

Figure 5. Cracks from dynamic loading of beams without shear reinforcement.

3.1.2 Beams with S90 configuration

The impact forces for B19, B21, and B24 are presented in Figure 6. The reaction force for the closest support decreased as the loading position moves from 0.4*d* to 2*d*. As shown in Figure 7, B19 and B21 failed by shear mode of the crushed compressive strut, which followed the same failure mechanisms for B11 and B13, beams without shear reinforcement. On the other hand, B24 exhibited a flexural mode.

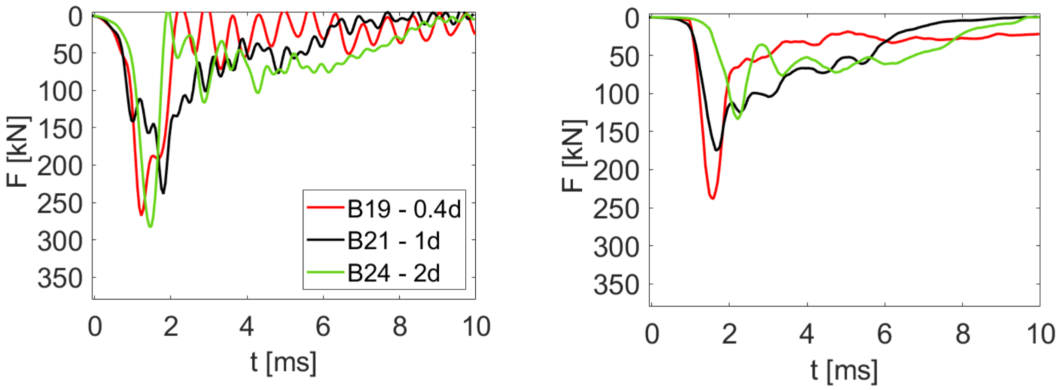

Figure 6. Impact force (left) and reaction forces LC (right) for beams B19, B21, and B24.

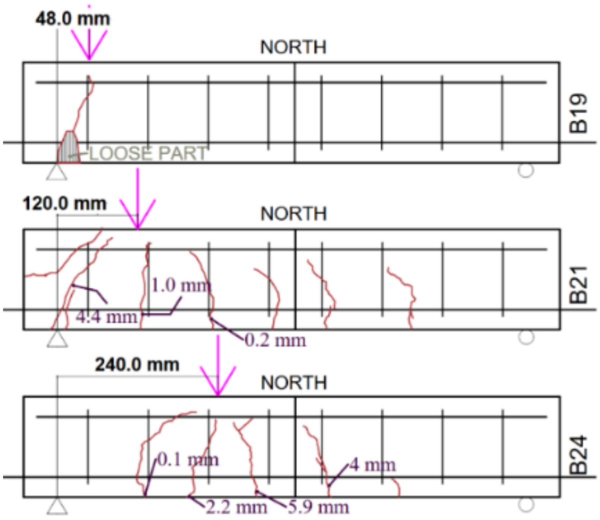

Figure 7. Cracks from dynamic loading of beams with shear reinforcement S90.

3.1.3 Beams with S45 configuration

In general, beams with shear reinforcement configurations S90 and S45 exhibited similar behaviour in terms of crack formation, and contact and reaction forces. Figure 8 shows that the reaction forces, measured at the closest support to impact point, tend to be smaller as the loading position moves from 0.4*d* to 2*d*. The impact force is largest for B4 and smaller for B6 and B2. From crack drawings in Figure 9, B2 and B4 failed in the shear mode caused by a crushed compressive strut. This can be seen in the diagonal crack towards the impact position. B6 showed mainly vertical cracks indicating a flexural mode.

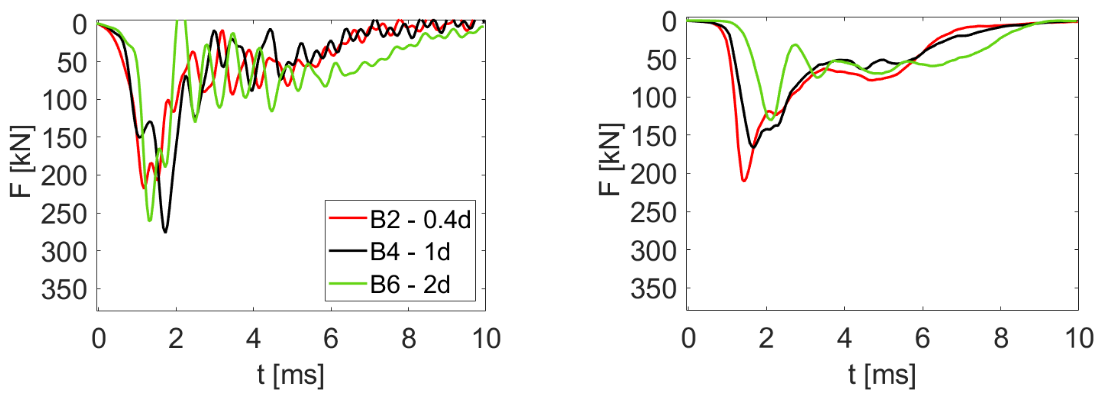

Figure 8. Impact force (left) and reaction forces LC (right) for beams B2, B4, and B6.

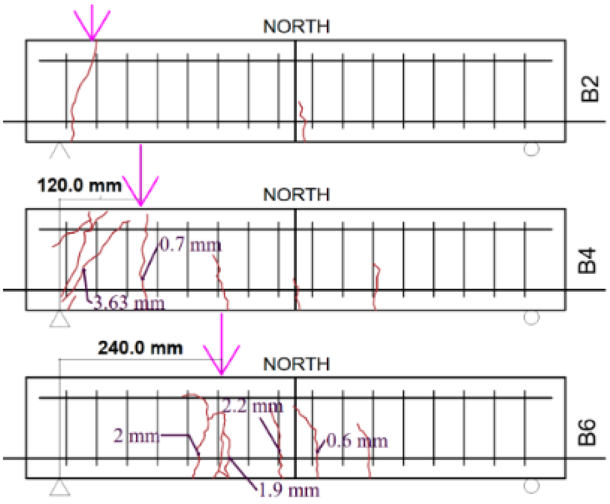

Figure 9. Cracks in beams with shear reinforcement S45.

3.2 Shear reinforcement configuration

This section includes the results of the dynamically loaded beams, emphasising the differences caused by varied shear reinforcement configurations at fixed load positions.

3.2.1 Load at position 0.4d

The reaction forces for beams B11 and B19, with configuration NoS and S90, were found to be almost the same value, as shown in Figure 10. Meanwhile, the reaction force of beam B2, with S45 reinforcement configuration, is significantly smaller. Maximum contact force was obtained by beam B11, beam without shear reinforcement. Figure 11 shows the cracks, and it is clear that all beams failed in shear failure by a crushed compressive strut. The cracks in all beams initiated at the support and propagated toward the impact point.

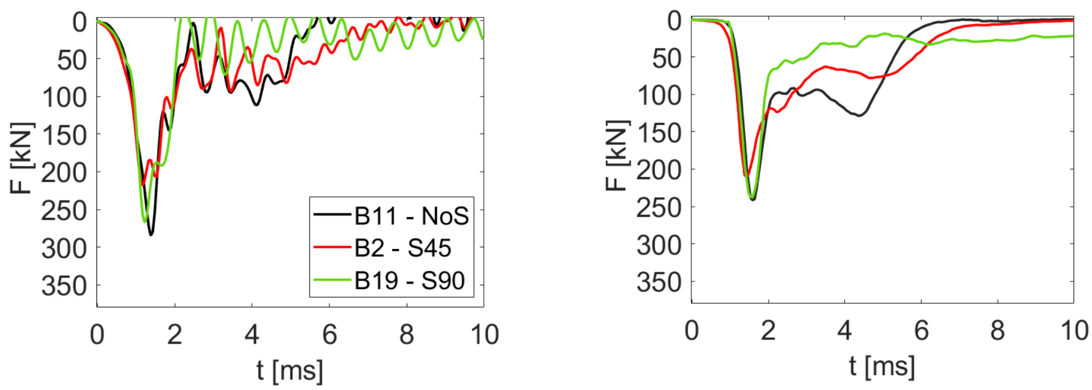

Figure 10. Impact force (left) and reaction forces LC (right) for beams B11, B2, and B19.

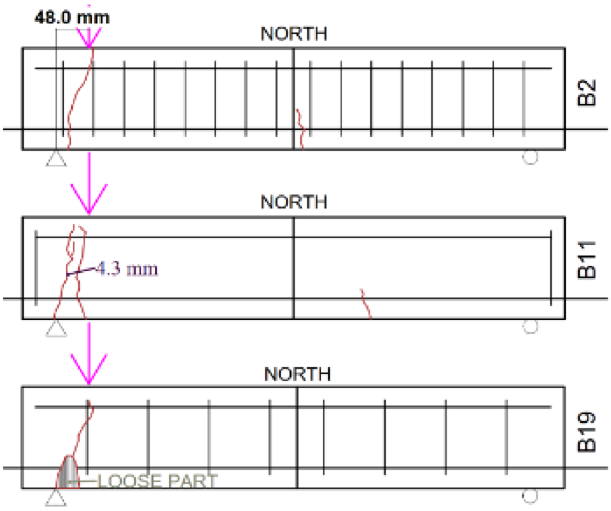

Figure 11. Cracks from dynamic loading of beams, loaded at the 0.4*d* position.

3.2.2 Load at position 1*d*

The beam without shear reinforcement exhibited significantly larger acceleration, velocity, and displacement compared to the beam designed with shear reinforcement configurations S90 and S45, which exhibited approximately the same values. In addition, an effect of missing shear reinforcement when the acceleration for beam B13 decreased slowly, according to Abdalnour and Saliba [2].

In Figure 12, Beams without shear reinforcement got hold of the maximum contact force which decreased as the shear reinforcement content increased. The reaction forces for beam without shear reinforcement, B13, were slightly larger than the reaction forces for beams with shear reinforcement B4 and B21, which were found to be almost of the same magnitude.

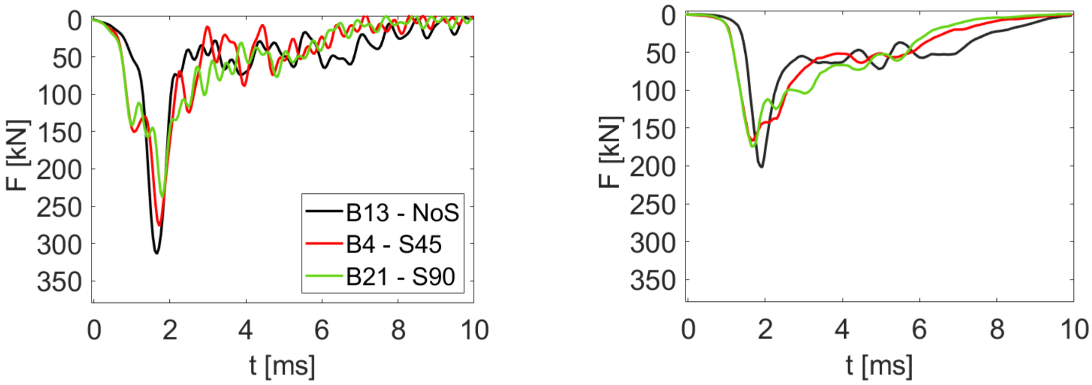

Figure 12. Impact force (left) and reaction forces LC (right) for beams B13, B4, and B21.

The shear reinforcement content has an influence on the number of observable cracks, see Figure 13. The beam without shear reinforcement (B13) exhibits the lowest number of cracks, while the number of the cracks for beams B21 and B4 with shear reinforcement configurations S90 and S45 are similar.

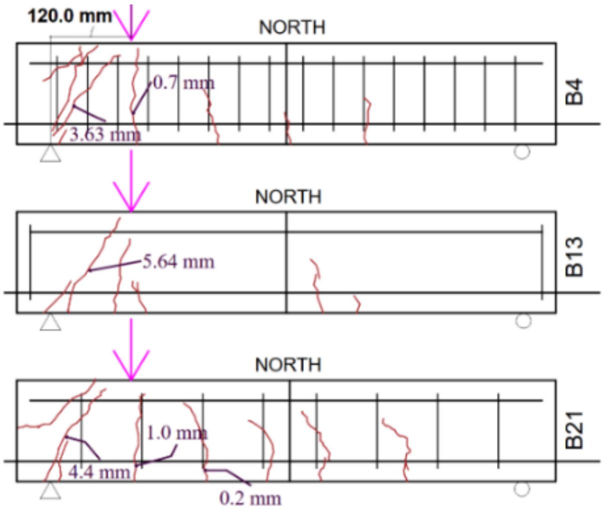

Figure 13. Cracks from dynamic loading of beams, loaded at the 1*d* position.

3.2.3 Load at position 2*d*

Figure 14 shows that B24 obtained the largest maximum contact force, and a smaller minimum force is obtained by B14. The reaction forces are almost equal amongst the beams B6 and B24, and slightly smaller for the beam B14.

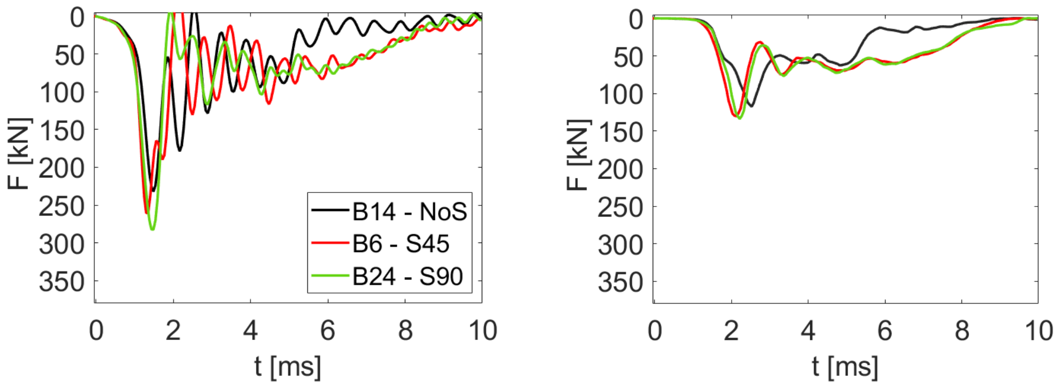

Figure 14. Impact force (left) and reaction forces LC (right) for beams B14, B6, and B24.

In Figure 15, shear reinforcement content has a clear effect on failure mode, where beams reinforced with configuration S90 and S45 responded in a flexural mode, while beam without shear reinforcement exhibited a flexural shear failure mechanism which is indicated by the large inclination of the cracks.

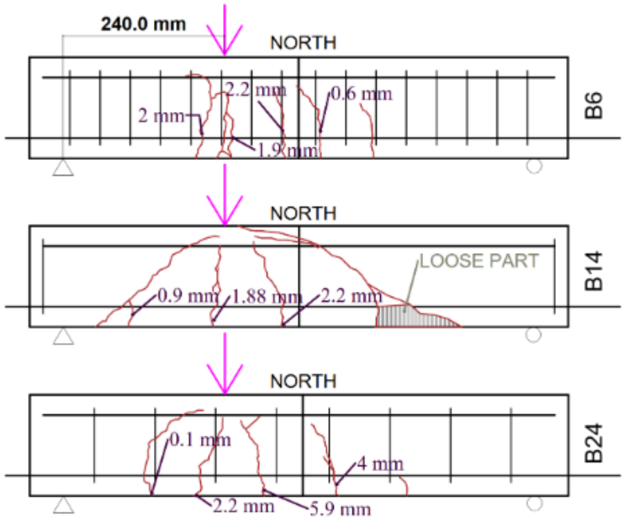

Figure 15. Cracks from dynamic loading of beams, loaded at the 2*d* position.

3.3 Effect of loading condition

The response of reinforced concrete structures differs depending on whether they are subjected to dynamic or static loading conditions. This section presents results for beams designed with the same amount and reinforcement arrangement, tested both dynamically and statically. The results presented in this section correspond to beams with shear reinforcement configuration S90.

In the results obtained from the static load tests, an initial displacement of 4 mm was observed, which could be attributed to the compression of the rig that contained the MTS machine before the deformation of the beams was initiated. The figures also display minor peaks due to the loading process, as the load was stopped every 10 kN to study the damage progression. The contact force registered during the dynamic tests will be used to observe the dynamic load capacity.

3.3.1 Load at position 0.4*d*

B19 failed at a load of 130 kN and displacement of 10 mm in the static test, shown in Table . In contrast, a similar beam, B25, with the same load position under dynamic conditions failed at approximately 250 kN as obtained from the reaction force.

3.3.2 Load at position 1*d*

The static load capacity for B26, was up to 134 kN as shown in Table , further, the displacement was up to around 10.5 mm. Meanwhile, the dynamic load capacity of a similar beam, B21, was approximately 180 kN with a displacement of 12 mm.

3.3.3 Load at position 2*d*

B27, when statically loaded, showed a similar trend as the cases with load positions 0.4*d* and 1*d*, where the static load capacity is significantly lower than the dynamic load capacity. The static load capacity for B27, according to Table , is found to be 96 kN, while the reaction force for a similar beam tested dynamically, B24, was found to be approximately 140 kN. The displacement under static loading was greater than that under dynamic loading, with values of 18.4 mm and 13.9 mm, respectively.

Table 2. Static and dynamic load capacity obtained from tests of beams with shear reinforcement S90.

Load position	**0.4*d***	***1d***	***2d***
Static load capacity [kN]	130	134	96
Dynamic load capacity [kN]	250	180	140

The cracks, shown in Figure 16 (a) and (b), indicate that beams tested at load positions of 0.4*d* and 1*d* tested statically and dynamically failed in a shear by a crushed compressive strut. Furthermore, at load position 2*d*, the failure mode is flexural shear, which occurs in both static and dynamic tests, as shown in Figure 16 (c).

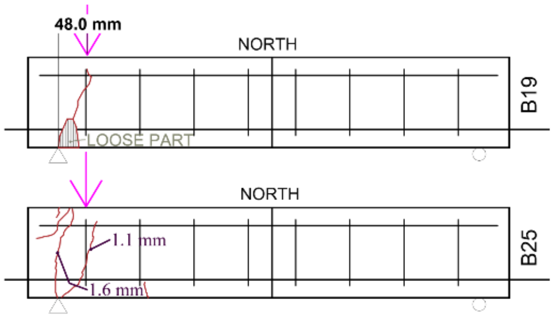

(a): B19-S & B25-D at position 0.4*d*.

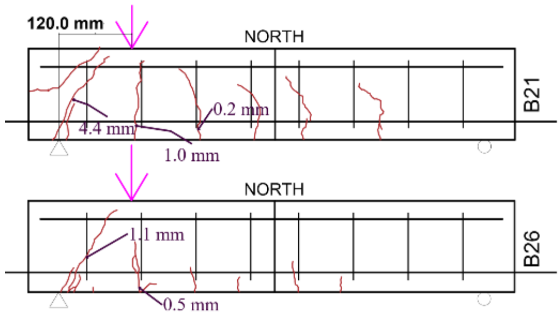

(b): B21-D & B26-S at position 1*d*.

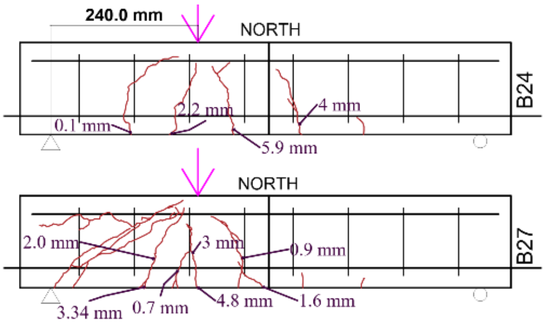

(c): B24-D & B27-S at position 2*d*.

Figure 16. cracks for beams tested statically and dynamically.

4 DISCUSSION

4.1 Influence of load position

It was observed that that the acceleration of the beam increased as the load position shifted from 0.4*d* to 1*d* and 2*d*. This behaviour is because when the load strikes close to the support, a relatively large portion of the impact force is transferred through the compressive strut directly to the support. As a result, the beam accelerations are limited. However, as the load moves away from the support, the transferred forces through the compressive strut become smaller and the remaining load is transferred by bending of the beam. Thus, the failure mechanism shifts from shear failure, characterized by crushed compressive struts into a flexural shear failure. An interesting example of flexural shear failure can be seen in B14, which had a loosen part in the unloaded side of the beam. An explanation for the loosening part is possibly the activation of the dowel action of the flexural reinforcement.

4.2 Influence of shear reinforcement

Beams tested at load position 0.4d showed similar responses and almost the same crack patterns. At load positions 1*d* and 2*d*, beams without shear reinforcement exhibited cracks, which were strongly influenced by shear but also bending cracks. In contrast, the cracks in the beams with shear reinforcement configurations S45 and S90 exhibited more flexural cracks, indicating a stronger influence of a bending behaviour and a reduced influence from shear. This was specifically the case for the test with load position 2*d* where the flexural shear failure of the beam without shear reinforcement was prevented in beams with reinforcement configurations S45 and S90. This observation is a clear indication that the beams exhibited greater shear capacity with shear reinforcement S45 and S90 compared to beams without shear reinforcement.

4.3 Influence of load condition

From the obtained results, the beams exhibited greater dynamic load capacity than the static load capacity. It was also found that the beams tested (S90) at load position 2*d*, exhibited different behaviours depending on type of the loading. The beam dynamically tested exhibited a flexural mode, while the statically loaded beam failed in flexural shear. This indicates that the flexural shear capacity during dynamic loading is larger than that during static loading.

5 CONCLUSIONS

- The load position has a clear influence on the failure mode mechanism, shifting from shear failure to flexural shear failure as the load moved away from the support.
- The load capacity of the beams differs depending on the loading condition and whether the load is applied statically or dynamically.
- The tests indicate that the flexural shear capacity during dynamic loading is larger than the capacity during static loading.

Understanding behaviour of reinforced concrete structure subjected to blast and impact load can be complex. For future research, it is of interest to analyze the failure mechanism and beam response using the finite element method. Another interesting factors to investigate are the influence of the beam depth and boundary conditions.

ACKNOWLEDGEMENT

This paper is part of an ongoing research on dynamically loaded reinforced concrete structures at KTH Royal Institute of Technology and Chalmers University, with financial support from the Swedish Fortifications Agency, the Swedish Civil Contingencies Agency (MSB) and Swedish Transport Administration (Trafikverket). Their support is greatfully acknowledged.

REFERENCES

[1] V. Peterson, A. Ansell, & M. Hallgren. “On the Residual Static and Impact Capacity of Shear-Reinforced Concrete Beams Subjected to an Initial Impact”*, Applied Science*, vol. 12, pp. 1-19 November 2022.
[2] V. Peterson, *Assessment of shear- and energy-absorption capacity o reinforced concrete elements under impulsive loads*, Lic. Thesis. KTH Royal Institute of Technology, Stockholm, Sweden, 2023.
[3] J. Magnusson, *Shear in Concrete Structural Elements Subjected to Dynamic Loads*, PhD Thesis. KTH Royal Institute of Technology. Stockholm, Sweden, 2019.
[4] J. Abdalnour, and M. Saliba, *Drop-weight impact tests on reinforced concrete beams*, M.Sc. Thesis. KTH Royal Institute of Technology, Stockholm, Sweden, 2023.
[5] E. Ceberg, and E. Holm, *Numerical Simulations of Impact-Loaded Reinforced Concrete Beams*, M.Sc. Thesis. KTH Royal Institute of Technology, Stockholm, Sweden, 2024.

STUDY ON FLOW VELOCITY OF BOULDERLY DEBRIS FLOW ON IMPACT LOAD ON FLEXIBLE BARRIERS

Yuta Miyahara[a], Toshiyuki Horiguchi[a]

[a]National Defense Academy, Japan email: ed24010@nda.ac.jp,

Keywords: debris flow, flow velocity, impact load, flexible barrier, buffering effect

Abstract
Debris flow disasters cause severe damage and pose a significant threat to human life in Japan. In particular, the frequency of such disasters caused in small-scale streams has been increasing. Consequently, the need for effective mitigation measures in these environments has become urgent. However, implementing such measures is challenging because small-scale streams are often located near residential areas, leaving limited space for construction. Flexible barriers have been widely adopted as protective structures due to their relatively light weight, ease of installation, and suitability for narrow construction sites. Despite their widespread use, their structural performance under debris flow impact remains unclear. Therefore, this study focuses on debris flow patterns and examines how these patterns influence the impact on flexible barriers. A series of flume experiments was conducted to investigate different debris flow patterns impacting a flexible barrier model. The debris flow models have different debris flow in velocities and depths. Two types of flexible barrier models were tested -one made of steel wires and the other of nylon nets- to evaluate the effect of barrier material stiffness. Additionally, a rigid barrier model was inclined as a reference to quantify the relative buffering capacity of flexible systems. The experimental results indicate that the maximum tensile force in the lower rope of a flexible barrier occurs when the debris flow pressure reaches the middle height of the barrier, while the maximum tensile force in the upper rope occurs when the debris flow reaches the top of the barrier. The tensile force in the rope of steel wire model was larger than that of the nylon net model. In contrast, the impact load acting on both types of flexible barriers showed little difference. Furthermore, the tests demonstrate that flexible barriers can reduce peak impact loads by up to approximately 50% compared to rigid barriers, thereby enhancing energy dissipation under debris flow events. Nonetheless, in some scenarios, the peak impact loads on flexible and rigid barriers were nearly identical. These findings reveal that debris flow velocity significantly affects the impact buffering capability of flexible barriers. As debris flow velocity increases, the effectiveness of flexible barriers to reduce impact loads diminishes, making their performance converge with that of rigid barriers. These insights contribute to a more comprehensive understanding of debris flow protective structure and provide guidance for the design, placement, and implementation of flexible barriers in small-scale streams.

1 INTRODUCTION

Debris flow is a natural phenomenon in which a mixture of water, boulders, gravel, and other sediments rapidly flows down a mountain stream, and is typically triggered by heavy rainfall or similar events. Once a debris flow occurs, it can severely damage human life and property. Countermeasures constructed from rigid materials, such as concrete and steel, are commonly employed to mitigate the impact of debris flows. In recent years, numerous structures of this type have been constructed [1, 2]. Extensive research has been conducted on rigid structures, including closed concrete and open steel dams, and their design methodologies are well-established in Japan [3]. However, rigid dams made of concrete and similar materials often require large-scale construction, which makes them unsuitable for small-scale streams. In recent years, the frequency of debris-flow damage originating from small-scale streams has increased, highlighting the need for effective preventative measures [4].

As illustrated in **Figure 1**, flexible barriers are constructed from materials such as steel nets and cables, making them relatively lightweight and easy to install. Because of these advantages, they are considered promising countermeasures for small-scale streams and numerous construction examples have been reported in various countries [5, 6]. However, despite several proposed design methodologies for flexible barriers [7-10], the interaction between deforming flexible barriers and debris flows is highly complex. Huo et al. [11] performed flume experiments using a 3D-printed flexible barrier model and demonstrated that the static load acting on the barrier can be estimated using a hydrostatic pressure-based model that accounts for the piled sediment height. Xiao et al. [12] examined the response of flexible barriers to three types of debris flows through experimental studies and a discrete element method (DEM). Their findings revealed that sediment segregation and the average gravel diameter within the debris flow significantly influenced the load exerted on the flexible barrier, leading to the proposal of a design framework tailored to the anticipated properties of the debris flow. Kong et al. [13] explored the relationship between barrier deformation and load by employing a coupled simulation approach that integrated computational fluid dynamics (CFD) and DEM.

Wendeler et al. [14] highlighted the buffering effect resulting from net deformation as a structurally advantageous feature of flexible barriers. Numerous studies have focused on the buffering effect. For instance, Ashwood et al. [15] demonstrated that the buffering effect becomes significant when the deformation of a flexible barrier exceeds 25% of the debris flow depth, with further enhancement observed when the deformation reaches a comparable level. Song et al. [16] conducted an experiment involving various types of debris and sediment flows with different bulk densities and revealed that the load exerted on flexible barriers was generally lower than that on rigid barriers. In addition, when the debris flow conditions were held constant and the cable stiffness was varied [17], a buffering effect was observed; however, the acting load remained constant regardless of the net deformation. This finding contradicted the results reported by Ashwood et al. [14]. Although these studies investigated the influence of cable stiffness, the net stiffness, which serves as the trapping surface, was not examined. Furthermore, it has been suggested that the viscosity of test materials may influence the buffering effect. By contrast, flume experiments conducted by Berger et al. [18] and Wendeler et al. [19] indicated that the load acting on a flexible barrier can be greater than that acting on rigid barriers, diverging from previous findings. This discrepancy may be attributed to the fact that the gravel impacting a rigid barrier is often deflected above the dam, converting its kinetic energy into potential energy. In contrast, gravel striking a flexible barrier was captured within the trapping surface, potentially resulting in higher energy absorption by the flexible barrier. Consequently, there is no consensus regarding the buffering effects of flexible barriers.

Figure 1. Photograph of flexible barrier trapping boulders (Magawa-river, Toyama, Japan)

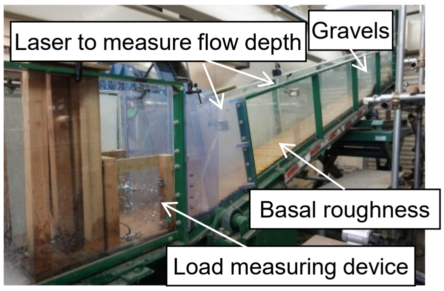

Figure 2. Overview of experimental device

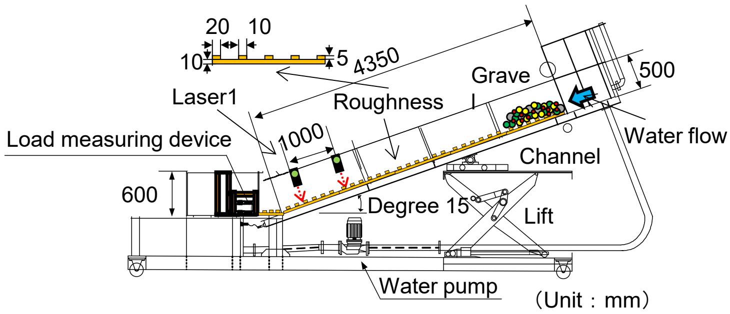

Figure 3. Schematic of experimental channel

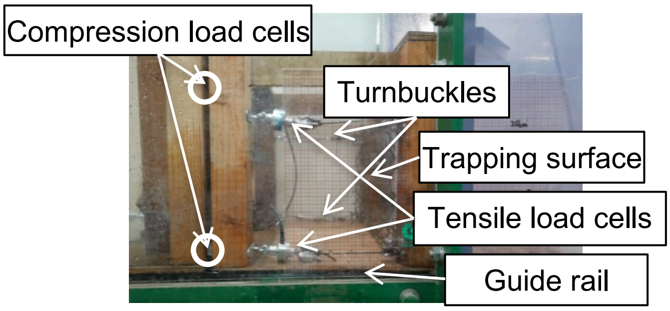

Figure 4. Photograph of Load measuring device

Studies examining the buffering effects of rubber and other materials known to exhibit similar impact mitigation properties have demonstrated that the buffering effect diminishes as the impact velocity increases [20-22]. This suggests that the velocity of the debris flows may influence the buffering effect of flexible barriers.

This study aims to identify the factors affecting the buffering effect of flexible barriers, with a particular focus on the velocity of debris flows. To achieve this, four types of debris flow with varying flow velocities were generated and their buffering effects were systematically compared. Additionally, the influence of the net stiffness was investigated by comparing two distinct levels of stiffness.

2 EXPERIMENTAL METHODS

2.1 Overview of experimental device

The experimental setup is shown in **Figure 2**. In this study, a load measurement device was installed downstream of the experimental channel to measure the load exerted by the debris flows. Gravel mixed with water was introduced from the upstream end of the channel to simulate debris flow. The experimental channel measured 4,350 mm, 300 mm, and 500 mm in length, width, and depth, respectively, as shown in **Figure 3**. The bed inclination of the channel was adjustable within a range of θ = 0 ° to 20 ° and was set to θ = 15 °, based on precedents for the installation of a flexible barrier as a debris flow countermeasure [23, 24]. To promote debris flow segregation, bed roughness elements with 20 mm spacing, 5 mm height, and 10 mm width were installed upstream of the load measurement device [25]. In addition, two laser displacement gauges (LB-300, KEYENCE) were positioned 1.0 m apart upstream of the load measurement device to measure the flow depth and calculate the velocity of the debris flow. The experimental scale was set to 1/20, based on Froude's similarity law.

2.2 Load measurement device

Figure 4 illustrates the load measurement device. The main body of the device was mounted on a guide rail, enabling horizontal movement in both upstream and downstream directions. A trapping surface was attached to the main body, and compression load cells (LMB-500-N, KYOWA, Japan) were installed downstream of the main body. These

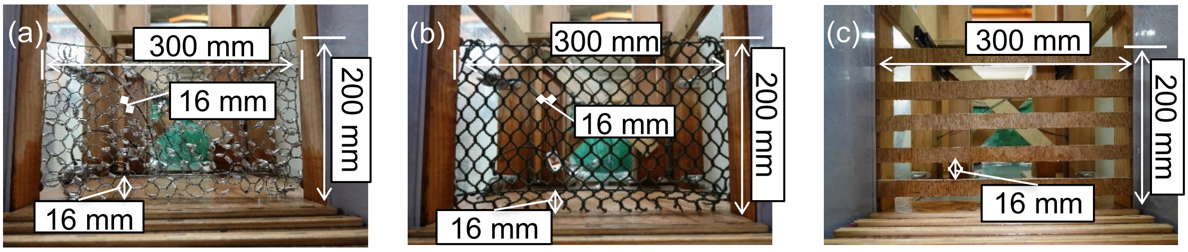

Figure 5. Three types of trapping surface model (a) ring-net; (b) nylon-net; (c) wooden plate

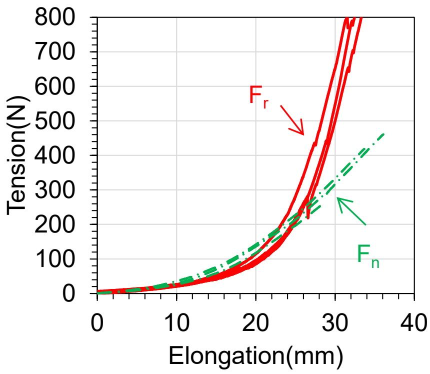

Figure 6. Tension-elongation behavior of flexible net material

Table 1. List of trapping surface specifications

Trapping surface	Material	Mesh spacing
F_r	Steel wire	16 mm
F_n	Nylon	18 mm
R_o	Wooden plate	16 mm

compression load cells engaged when the trapping surface captured the debris flow, allowing the load acting on the trapping surface to be measured. The sum of the loads measured by the compression load cells was referred to as the total load.

Three types of trapping surface models were installed on the main body: ring-shaped nets (flexible: F_s), tortoiseshell-shaped nets (flexible: F_n), and wooden plates with a transparent structure (rigid: R_o), as depicted in **Figure 5**. Each model had a dam height of 200 mm and an effective width of 300 mm. corresponding to an actual scale dam height of 4.0 m and width of 6.0 m. The lower rope was positioned 16 mm above the channel bed because of its connection to the tension load cell. The mesh spacing of each model ranged from 16 mm to 18 mm. The flexible-net models were supported by cables threaded through meshes on the top, bottom, left, and right sides. The eyelets are attached to the ends of the top and bottom cables on both the left and right sides. The left shore-side end was connected to a tension load cell (LUR-A-200NSA1, KYOWA) via a pulley to measure the tension generated during the debris flow capture. The right shore-side end was connected to a turnbuckle and an initial tension of 1.0 N was applied to ensure uniform experimental conditions. A wooden plate is fixed directly to the main body. In this study, the tensions in the top and bottom cables are referred to as the top and bottom tensions, respectively. The measurements were performed using an energy-dispersive X-ray spectrometer (EDX-100A, KYOWA) with a sampling frequency of 100 Hz [26].

The stiffnesses of the flexible surfaces were also compared to investigate the effect of stiffness on the load. Uniaxial tensile tests were conducted on the flexible surfaces to determine their stiffness. In the tests, a net specimen with a side length of 80 mm was used to allow movement in the horizontal tensile direction. **Figure 6** presents a comparison of the uniaxial tensile test results for the two types of flexible trapping-surface models, F_s and F_n. The results confirmed that F_s, which was constructed from steel wire, exhibited higher stiffness than F_n, which was made of nylon. The cables supporting the net models were made of the same material as the trapping surfaces, with F_s using a steel wire and F_n using a nylon cable. **Table 1** summarizes the specifications of the trapping-surface models used in the experiments.

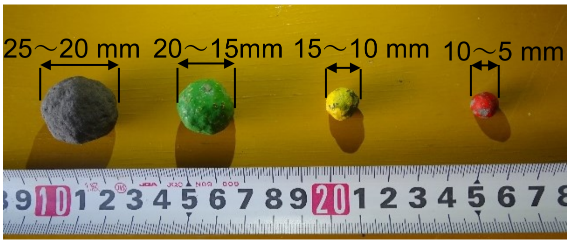

Figure 7. Composition of debris flow model

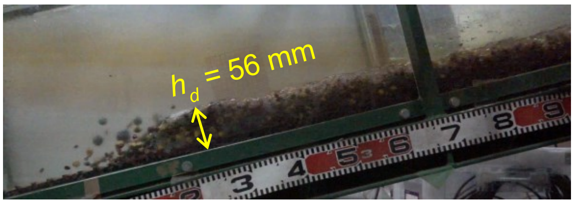

Figure 9. Example of flow form (h_s = 150 mm, Q = 6.8 L/s)

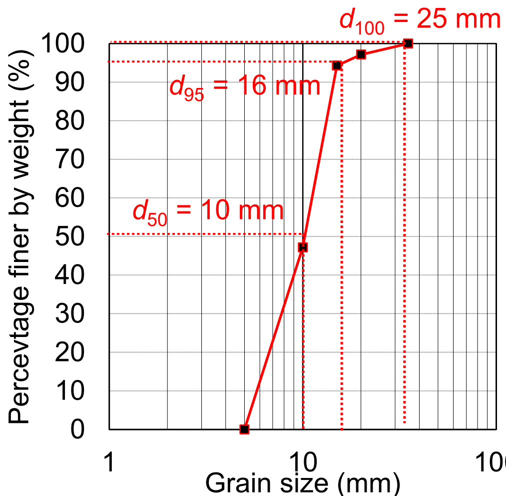

Figure 8. Grain size distribution of test material

Table 2. List of debris flow specification

Material volume V_t [L]	Unit weight γ_d [N/L]	Initial setting height h_i [mm]	Flow rate Q [L/s]	Velocity U [m/s]	Depth h_d [mm]
20	15.4	50	4.0	0.73	57
			6.8	1.4	49
		150	4.0	1.1	56
			6.8	1.5	51

2.3 Debris flow model

Four types of gravel (specific gravity: 1.9) with particle sizes of 25-20 mm, 20-15 mm, 15-10 mm, and 10-5 mm were used as materials for the debris flow, as shown in **Figure 7**. These gravels were colored gray, green, yellow, and red, respectively. The total amount of gravel used was 20 L. **Figure 8** shows the particle size distribution of the mixed material, which indicates a maximum gravel diameter of d_{95} = 16 mm and an average gravel diameter of d_{50} = 10 mm. The mesh size of the trapping surface models used in this experiment corresponds to approximately 1.0 times the maximum gravel diameter d_{95} of the debris flow model. Gravel was piled in a trapezoidal shape approximately 4.0 m upstream of the load measurement device, and the debris flow model was generated by steadily supplying water at a constant flow rate from behind the gravel piles. Four types of debris flow models were generated using two initial setting heights (50 mm, and150 mm) and two types of flow rates (4.0 L/s, 6.8 L/s). The initial setting height refers to the vertical distance from the bottom of the channel to the top of the trapezoidal-piled gravel.

Figure 9 illustrates an example of a debris flow pattern. Relatively large amounts of gray, green, and yellow gravel were concentrated near the front of the debris flow, confirming the occurrence of a sorting phenomenon. **Table 2** summarizes the specifications of each debris flow model derived from the measurements. The flow depths represent the average values, and the flow velocities are calculated based on the time difference between the recordings from the two laser displacement gauges. Four distinct flow velocities were examined in this experiment.

2.4 Experimental cases

Table 3 lists the experimental results. A total of 12 tests were conducted, in which debris flows with four different flow velocities collided with three different types of trapping

Table 3. Experimental case

Test*	Trapping surface	Debris flow parameters	
		Initial setting height	Flow rate
F_r-5-S	Ring-net	50 mm	4.0 L/s
F_r-5-L			6.8 L/s
F_r-15-S		150 mm	4.0 L/s
F_r-15-L			6.8 L/s
F_n-5-S	Nylon-net	50 mm	4.0 L/s
F_n-5-L			6.8 L/s
F_n-15-S		150 mm	4.0 L/s
F_n-15-L			6.8 L/s
R_o-5-S	Wooden plate (open type)	50 mm	4.0 L/s
R_o-5-L			6.8 L/s
R_o-15-S		150 mm	4.0 L/s
R_o-15-L			5.2 L/s

*test no. -trapping surface, -initial setting height, -flow rate

surfaces: F_s, F_n, and R_o. The total loads of the flexible and rigid trapping surfaces were compared to examine the load-buffering effect of the flexible trapping surface. The results were compared for each difference in flow velocity, and their influence was considered. The stiffness of the flexible trapping surface was also examined.

3 EXPERIMENTAL RESULTS AND DISCUSSION

3.1 After trapping each model and net deflection

The condition of each trapping-surface model after debris-flow trapping is presented. **Figure 10** shows the appearance of each model for a flow rate of Q = 4.0 L/s, and an initial setting height of h_s = 5 mm, which corresponds to the lowest velocity test. Most of the gravel in contact with the trapped surface was gray, green, or yellow and consisted of relatively large particles, indicating a bouldery debris flow model. It was also confirmed that the height of the deposited gravel did not reach the dam height in any case. The flexible trapping surface deformed upon impact, with net deflections of 70 mm in the case of F_r, and 95 mm in the case of F_n. This result confirms that a surface with a lower stiffness result in a greater net deflection. **Figure 11** illustrates the state of each model after debris flow trapping at a flow rate of Q = 6.8 L/s, and an initial setting height of h_s = 15 mm, which represents the highest velocity test. In this case, the height of the deposited gravel reached the dam height in all models. The deformations of the flexible trapping surface were 95 mm for F_r and 130 mm for $F_{n,}$ both of which were greater than those observed in the low-flow velocity test. The net deformation reached approximately half of the height of the dam. Furthermore, it was clarified that the stiffness of the trapping surface affected the amount of deformation after debris flow trapping. The gradient of the gravel deposited at R_o, where the trapping surface did not deform, was steeper than those observed at the flexible trapping surfaces F_r and F_n.

3.2 Comparison of load time history

This section compares the time history of the measured load between the rigid and flexible trapping surfaces and examines the effect of the stiffness of the flexible trapping surface.

Figure 10. Photograph of after trap for low flow velocity (a) Test F_r -5-S; (b) Test F_n -5-S; (c) Test R_o-5-S

Figure 11. Photograph of after trap for high flow velocity (a) Test F_r-15-L; (b) Test F_n-15-L; (c) Test R_o-15-L

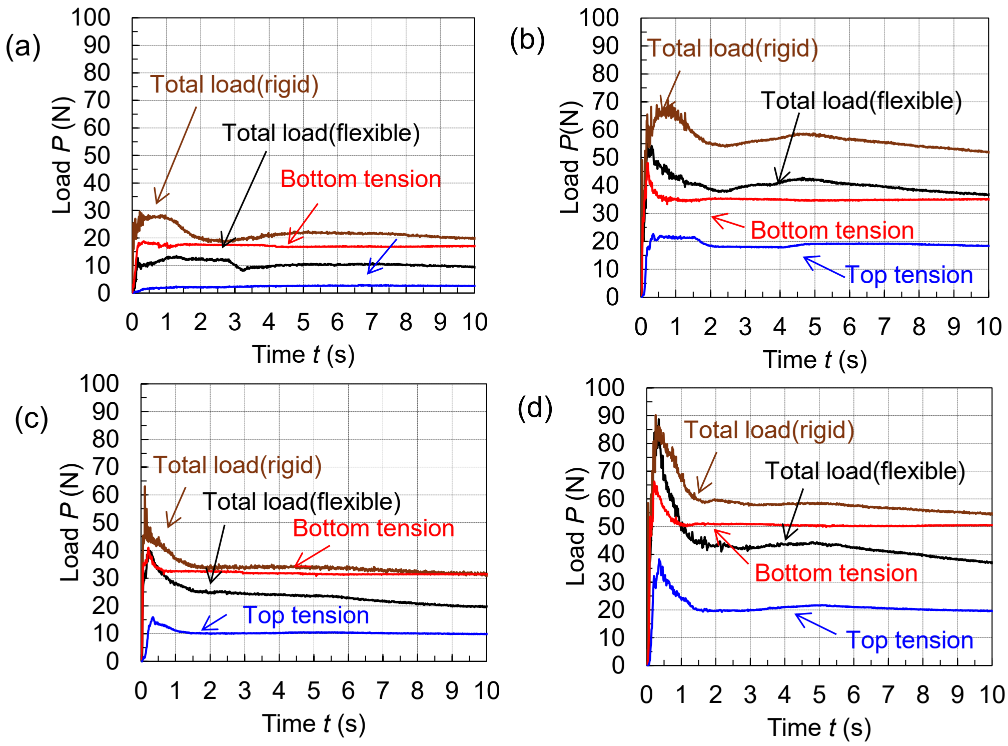

Figure 12. Comparison of force time history for flexible and rigid barrier test (a) F_r-5-S vs R_o-5-S; (b) F_r-5-L vs R_o-5-L; (c) F_r-15-S vs R_o-15-S; (d) F_r-15-L vs R_o-15-L

3.2.1 Comparison between rigid and flexible barrier

First, the measurement results for the rigid and flexible trapping surfaces were compared. **Figure 12** presents a graph comparing the load-time histories of the rigid and flexible trapping surfaces. This comparison focused on the results of F_r and R_o. **Figure 12(a)** compares the cases with the lowest flow velocities. It is evident that the total load was significantly smaller for F_r than for R_o. Additionally, although a distinct peak was observed in the total load for R_o,

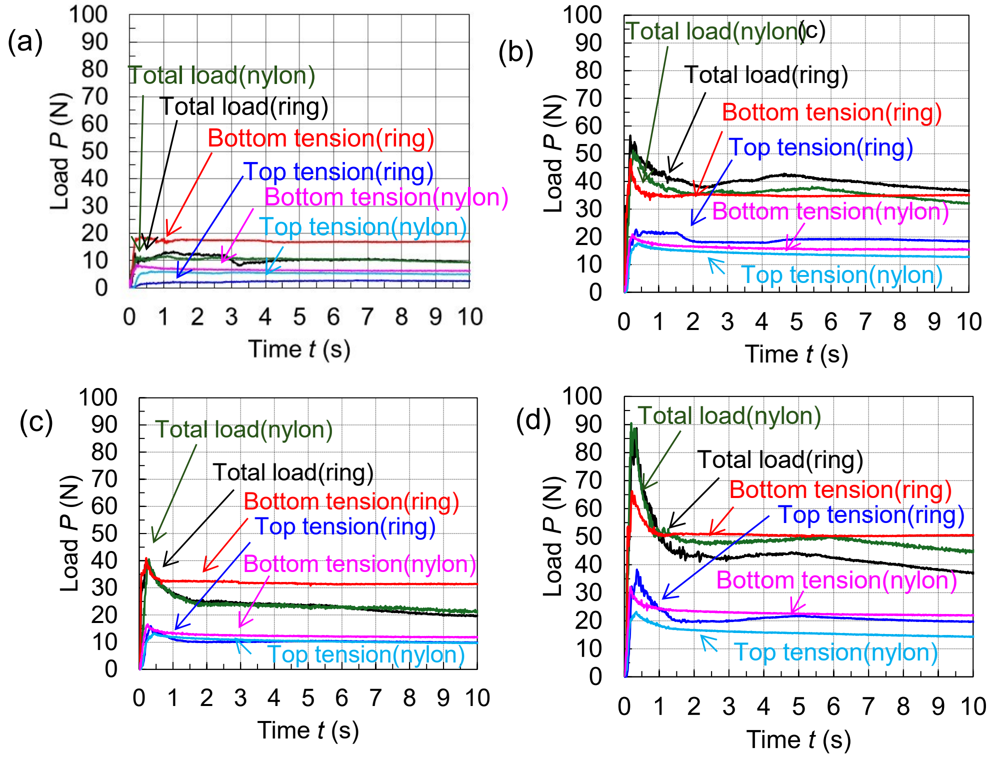

Figure 13. Comparison of measured force in both flexible barriers (a) F_r-5-S vs F_n-5-S; (b) F_r-5-L vs F_n-5-L; (c) F_r-15-S vs F_n-15-S; (d) F_r-15-L vs F_n-15-L

no clear peak was present for F_r, confirming the buffering effect of the flexible trapping surface. The cable tension was greater in the lower cable than in the upper cable, and there was almost no tension in the upper cable. This occurs at low velocities, as shown in **Figure 10**, and the debris flows before reaching the top of the dam. Therefore, the upper cable experiences tension only when it is pulled by the trapping surface. **Figure 12(b)** and **(c)** compare F_r-5-L with R_o-5-L and F_r-15-S vs. R_o-15-S. In these cases, peaks occurred in the total load for both F_r and R_o, and the peak values were more than twice as large as those observed for the lowest flow velocity case. Moreover, peaks were observed for both the upper and lower cable tensions. Furthermore, in both cases, the total load on the flexible trapping surface is smaller, demonstrating a buffering effect. However, for the highest flow velocity, as shown in **Figure 12(d)**, the maximum total loads on the flexible and rigid trapping surfaces were approximately the same, indicating that the expected buffering effect of the flexible structure could not be confirmed. This suggests that the effectiveness of flexible structures in buffering impact loads may be influenced by the flow velocity.

3.2.2 Comparison of barrier stiffness

Figure 13 shows a comparison of the time history of the load based on the stiffness of the flexible trapping surface. The results indicated that the total load was not affected by the stiffness of the flexible trapping surface, showing similar waveforms and values across all cases. This trend aligns with the findings of Song et al. [17], who investigated the effect of cable stiffness alone. Next, the tension generated in each cable was smaller for F_n, which had a lower stiffness than F_r. This result is consistent with previous studies [17]. Thus, in addition to the previously known effect of the cable stiffness, the stiffness of the trapping surface itself does not appear to influence the total load. On the other hand, Song et al. [17] found that cable stiffness significantly affects the applied load when a single boulder impacts the structure, with lower stiffness resulting in a smaller applied load. The difference in the results between the impact of a large number of boulders in a collective state and that of a single boulder is important for understanding the buffering mechanism of flexible structures.

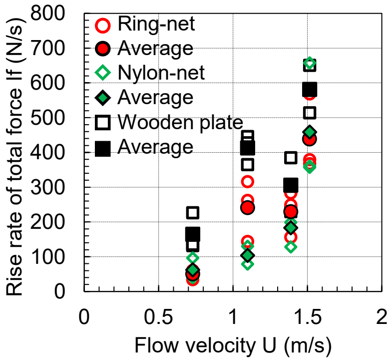

Figure 14. Relationship between raise rate of total force and velocity

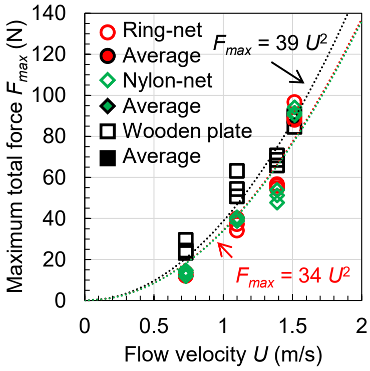

Figure 15. Relationship between maximum load and velocity

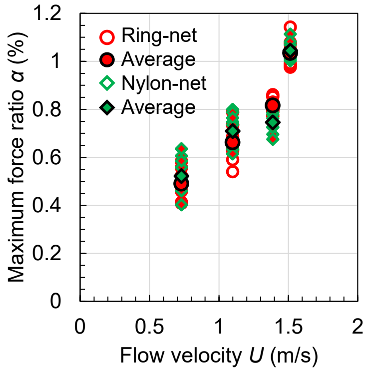

Figure 16. Relationship between maximum force ratio and flow velocity

However, this experiment did not fully clarify the mechanism, and further research will be conducted to address this issue.

3.3 Effect of debris flow velocity

Thus, the results suggest that the buffering effect of flexible structures is significantly influenced by the velocity of the debris flow, which is a parameter of the acting load, rather than by the stiffness of the trapping surface, which is a parameter of the structure. Therefore, this section examines the effect of debris flow velocity on the various results.

3.3.1 Rise rate of total load

Figure 14 shows the relationship between the increased rate of the total load and the flow velocity. The red circles represent the results for F_r, green diamonds represent F_n, black squares represent R_o, and the filled markers indicate the average values for each case. Here, the rise rate refers to the rate of increase in the total load and is defined as the load 0.1 s after the initial load rises, divided by 0.1 s. Thus, a larger increase rate indicates a faster increase in the load, implying a more significant impact. The results showed that the rise rate generally increased with increasing flow velocity, suggesting that higher debris-flow velocities lead to greater impact forces. In addition, the rate of increase was generally lower for a flexible trapping surface than for a rigid surface. This indicates that, upon impact, the deformation of the flexible trapping surface exerts a buffering effect, reducing the impact force.

3.3.2 Maximum total load

Figure 15 shows the relationship between the maximum total load and flow velocity. The results confirm that the maximum total load increases with flow velocity, regardless of whether the trapping surface is flexible or rigid. For flow velocities between 0.75 m/s and 1.4 m/s, the total load on the flexible trapping surface is lower than that on the rigid surface. However, at 1.5 m/s, the total loads on both surfaces were approximately identical. The dotted lines show the results of the nonlinear regression using the square of the flow velocity for all results of F_r, F_n, and R_o. The reason for using the square of the flow velocity is that the fluid force of debris flows in Japan is defined as the square of the flow velocity, as expressed in Eq.(1).

$$F_d = K_h \cdot \frac{\gamma_d}{g} \cdot D_d \cdot U^2 \tag{1}$$

where F_d is the fluid force of the debris flow per unit width, U is the flow velocity of the debris flow, D_d is the depth of the debris flow, g is the acceleration of gravity, K_h is a coefficient (=1.0), and γ_d is the unit weight of the debris flow. The regression curves obtained were Eq.(2) for the rigid trapping surface and Eq.(3) for both F_r and F_n for the flexible surface, and showed a relatively high correlation with the coefficient of determination R^2 = 0.85.

$$F_{max} = 39U^2 \tag{2}$$

$$F_{max} = 34U^2 \tag{3}$$

The regression coefficients for the rigid and flexible surfaces were 39 and 34, respectively, indicating that the load acting on the flexible trapping surface was smaller. This suggests that, under certain conditions, the flexible trapping surface reduces the impact load.

3.3.3 Buffering effect

Figure 16 illustrates the relationship between the buffering effect and the flow velocity based on **Figure 15**. In this experiment, the buffering effect refers to the ratio of the maximum total load acting on the rigid and flexible trapping surfaces and was calculated using Eq.(4).

$$\alpha = \frac{F_{max\text{-}R}}{F_{max\text{-}F}} \tag{4}$$

Where, α is the maximum load ratio, $F_{max\text{-}R}$ is the maximum load acting on the rigid trapping surface, and $F_{max\text{-}F}$ is the maximum load acting on the flexible trapping surface.

Thus, the smaller the maximum load ratio α, the higher the buffering effect. The maximum load ratio was 50% at a flow velocity of 0.75 m/s, which is approximately half that of the rigid trapping surface. However, it increased as the flow velocity increased. and At a flow velocity of 1.5 m/s, the load ratio was approximately 100%, meaning there is no buffering effect.

This suggests that as the debris-flow velocity increases, the buffering effect of the flexible structure diminishes beyond a certain threshold. In this experiment, the threshold was found to be 1.5 m/s, whereas the actual debris-flow velocity in natural settings can reach 6.7 m/s. Such velocities are common in mountain streams, highlighting the need for further discussions on the design of flexible structures that rely on the buffering effect.

4 CONCLUSIONS

This study focused on the influence of debris flow velocity and stiffness of flexible trapping surfaces by investigating the load-buffering effect of flexible structures. Laboratory experiments were conducted using two types of flexible trapping surfaces and a rigid trapping surface with debris flows at four different velocities. In addition, experiments were conducted using debris flows at four different flow velocities. The main findings are summarized as follows:

1. The load acting on the flexible trapping surface is generally lower than that acting on the rigid trapping surface. However, once a certain velocity is reached, the load on the flexible trapping surface becomes approximately equal to that on the rigid trapping surface.
2. A comparison of the two flexible trapping surfaces with different stiffnesses showed that the stiffness had little effect on the acting load. However, a higher stiffness results in greater tensile force.
3. The results indicated that a higher debris-flow velocity led to a greater increase in the total load. Additionally, the increase rate of the total load for the flexible trapping surface was lower than that for the rigid trapping surface, suggesting that the flexible trapping surface mitigated the impact of the debris flow regardless of the initial collision velocity.
4. The magnitudes of the tensile force and applied load increased with flow velocity. Notably, the maximum total load exhibited a relatively strong correlation with the square

of the flow velocity, and the regression coefficient was lower for the flexible trapping surface than for the rigid trapping surface.

5. The buffering effect of flexible structures as a debris flow countermeasure was found to be significantly influenced by debris flow velocity. Under these experimental conditions, a buffering effect was observed at flow velocities of 1.4 m/s or lower. In particular, at the lowest tested velocity, the maximum load on the flexible trapping surface was approximately half that on the rigid trapping surface. However, at a velocity of 1.5 m/s, the loads on the rigid and flexible trapping surfaces are nearly identical, indicating that the buffering effect is no longer present. This suggests the existence of a threshold flow velocity beyond which the flexible structures do not provide a buffering effect.

Notably, in this experiment, the mechanical similarity law for the trapping surface model was not fully satisfied. Therefore, the load values and other quantitative results obtained in this study cannot be directly applied under actual conditions. However, the insights gained from the comparative analysis of the experiments contribute to a better understanding of flexible debris-flow countermeasures and are expected to serve as valuable guidelines for their design, placement, and implementation in small streams.

REFERENCES

[1] G. Piton, S. Carladous, A. Recking, J.M. Tacnet, F. Lièbault, D. Kuss, Y. Queffèlèan and O. Marco, Why do we build check dams in Alpin streams? An historical perspective from the French experience, *Earth Surface Process and Landforms*, vol.42, pp.91-108, June 2016, doi: 10.1002/esp.3967.

[2] Y.Shimoda, Transition of erosion control technology, *Journal of Japan Society of Erosion Control Engineering*, vol.60, no.3, pp.1-2, September 2007, doi: 10.11475/sabo1973.60.3_1. (In Japanese)

[3] National Institute for Land and Infrastructure Management & Ministry of Land, Infrast ructure, Transport and Tourism, Japan, Manual of Technical Standard for designing Sabo facilities against debris flow and driftwood, https://www.nilim.go.jp/lab/bcg/siry ou/tnn/tnn0905pdf/ks0905.pdf.

[4] T. Ueno, H.Tsunakawa, T. Arisawa, M. Ogawa, N. Akita, Y. Koishi, T. Sato and T. Yano, Proposal of a new sabo dam construction method in a narrow area, *Journal of Japan Society of Erosion Control Engineering*, vol.72, no.5, pp.67-73, January 2020.

[5] C. Wendeler, B.W. McAredell, A. Volkwein, M. Denk and E. Gröner, Debris flow mitigation with flexible ring net barriers-field tests and case studies, *WIT Transactions on Engineering Sciences*, vol.60, pp.23-31, June 2008.

[6] K. Momma, M. Watari and K. Imai, Study on mechanism of capturing debris flow into wire net works, *Journal of Japan Society of Erosion Control Engineering*, vol.58, no.5, pp.3-12, January 2006.

[7] A. Volkwein, C. Wendeler and G. Guasti, Design of flexible debris flow barriers, *Italian Journal of Engineering Geology and Environment*, pp.1093-1100, November 2011, doi: 10.4408/IJEGE.2011-03.B-118.

[8] A. Volkwein, C. Wendeler, L. Stieglitz, G. Lauber, New approach for flexible debris flow barriers, *IABSE conference*, September 2015, Switzerland.

[9] G. Yung and A. Ng, Design suggestions on flexible debris-resisting barriers, *The HKIE Geotechnical Division 37th Annual Seminar*, May 2017, China.

[10] M. Marchelli and C. Deangeli, A time-independent reliability based design approach for debris flow flexible barriers, *8th International Conference on Debris Flow Hazard Mitigation*, June 2023, Italy.

[11] M. Huo, S. Lambert, F. Fontaine and G. Piton, Capture of near-critical debris flows by flexible barriers: an experimental investigation, *EGU sphere [preprint]*, https://doi.org/10.5194/egusphere-2024-3575, December 2024.

[12] S. Xiao, X. Xu, H. Wang, D. Li, Z. Wei and T. Zhang, Effects of flow regimes on the interaction between granular flow and flexible barrier, PLOS One, vol.18, no.8, e0285559, August 2023, doi: 10.1371/journal.pone.0285559.

[13] Y. Kong, X. Li, J. Zhao and M. Guan, Load–deflection of flexible ring-net barrier in resisting debris flows, Gèotechnique, vol. 74, no.5, pp.486-489, May 2024, doi: 10.1680/jgeot.22.00135.
[14] C. Wendeler, A. Volkwein, A. Roth, M. Denk and S. Wartmann, Field measurement and numerical modeling of flexible debris flow barriers, *4th International Conference on Debris Flow Hazard Mitigation*, September 2007, China.
[15] W. Ashwood and O. Hungr, Estimating total resisting force in flexible barrier impacted by a granular avalanche using physical and numerical modeling, *Canadian Geotechnical Journal*, Vol.53, pp.1700-1717, June 2016, doi: 10.1139/cgj-2015-0481.
[16] D. Song, C.E. Choi, C.W.W. Ng, G. G. D. Zhou, Geophysical flows impacting a flexible barrier: effects of solid-fluid interaction, *Landslides*, vol.15, pp.99-110, January 2018, doi: https://doi.org/10.1007/s10346-017-0856-1.
[17] D. Song, G.G.D. Zhou, C.E. Choi and Y. Zheng, Debris flow impact on flexible barrier: effects of debris-barrier stiffness and flow aspect ratio, *Journal of Mountain Science*, vol.16, pp.1629-1645, July 2019, doi: 10.1007/s11629-018-5314-6.
[18] S.M. Berger, R. Hofmann and A. Preh, Impacts on Embankments, Rigid and flexible barriers against rockslides: model experiments vs. DEM Simulations, *Rock Mechanism and Rock Mechanism*, vol. 57, pp.793-2808, April 2024, doi: 10.1007/s00603-023-03721-5.
[19] C. Wendeler, A. Volkwein, B.W. McArdell and P. Bartelt, Load model for designing flexible steel barriers for debris flow mitigation, *Canadian Geotechnical Journal*, vol. 99, pp.1-39, August 2018, doi: 10.1139/cgj-2016-0157.
[20] Y. Yoichi, H. Tamai, M. Uno, Y. Sonoda and T. Kasugai, Fundamental experiment of shape and confining effect on rubber pieces' cushioning characteristics, *Journal of Structural Engineering*, vol.61A, March 2015.
[21] Y. Yoichi, H. Tamai, H. Ishii, Y. Sonoda, T. Kasugai, Estimation of maximum load on bridge restrainers by weight-drop tests with large size weight, *Journal of Structural Engineering*, vol.61A, March 2016.
[22] T. Mizuyama, K. Matsumura, T. Yamamoto, Tests of shock absorbers for debris-flow control structures, *Journal of Japan Society of Erosion Control Engineering*, vol.41, no.3, pp.17-22, January 1988.
[23] T. Motoyama, On-site works for the sediment-related disaster due to heavy rainfall in Hiroshima, August 2024, *Journal of the Japan Society of Erosion Control Engineering*, vol.69, no.6, pp.92-96, March 2017.
[24] Landslide Research Department National Institute for Land and Infrastructure Manag ement, Yagi 3-chome (stream number I-1-9-303) on-site survey report, https://www.n ilim.go.jp/lab/bbg/saigai/h26/140821hiroshima_yagi.pdf. (In Japanese)
[25] H. Shibuya, S. Katsuki, H. Kokuryo, H. Ohsumi and N. Ishikawa, Experimental study of load for steel frame check dam caused by debris flow with woody debris, *Journal of the Japan Society of Erosion Control Engineering*, vol.65, no.1, pp.54-61, May 2012.
[26] T. Horiguchi, Measurement method of debris flow load acting on Sabo structures, *Journal of the Japan Society of Erosion Control Engineering*, vol.75, no.3, pp. 23-28, July 2022, doi: 10.11475/sabo.75.2_23. (In Japanese)

IMPACT EXPERIMENTS ON REINFORCED CONCRETE SPECIMENS

INVESTIGATION OF REPEATABILITY AND SCALING

Thomas Schubert[a], Petr Máca[b], Marcus Hering[c], Georg Fiedler[c] and Birgit Beckmann[d]

[a]TUD Dresden University of Technology, Germany, email: thomas.schubert2@tu-dresden.de, [b,d]TUD Dresden University of Technology, Germany, [c]Bundesanstalt für Materialforschung und –prüfung (BAM), Germany

Keywords: reinforced concrete, drop-weight impact, scaling, repeatability, digital image correlation

Abstract

Nowadays, the impact resistance of concrete structures has become a prominent concern for critical infrastructure operators, particularly amidst escalating geopolitical tensions. Regulators and design engineers know that reinforced concrete structures can only be developed with high efficiency by considering nonlinear structural and highly nonlinear material behavior. Therefore, specific guidelines on impact design provide instructions for design and analysis of structures required to resist impact loading. These instructions are usually based on published results and evaluated data of impact experiments carried out in laboratories. To widen the knowledge and increase the scientific data the Institute of Concrete Structures (IMB) at TUD Dresden University of Technology (TUD) has carried out many impact experiments on reinforced concrete specimens in recent years. A specially designed drop tower is available for this purpose on the premises of the Otto Mohr Laboratory, TUD.

In the framework of the past research at TUD some important issues, such as influence of rebar arrangement, structural thickness, scalability of specimen and repeatability, with regard to experimental impact testing were investigated. This article presents the drop tower facility and research results of impact experiments on reinforced concrete slabs. First, the scalability of impact experiments will be discussed in conjunction with already known theoretical scaling parameters provided by researchers in the past, e.g. Rüdiger et al. [1]. Scalability of experimental data is of huge importance since protective structures made of reinforced concrete differ usually in size in comparison to experimental specimens. The second important research focus is on repeatably of impact experiments. Since impact experiments are usually time consuming and expensive, a certain impact scenario is mostly carried out only once. It is intended to show the range of deviation of impact tests on some already carried out experiments on reinforced concrete slabs. A possible standard deviation is estimated for the applied test setup.

1 INTRODUCTION

Structural elements made of reinforced concrete (RC), such as slabs and beams used in buildings of critical infrastructure, may be subjected to low-velocity impact loads during their service life. These impact loads are caused by events such as falling objects, vehicle collisions, or debris strikes [2], [3]. Unlike static loads, low-velocity impacts generate short-duration forces of high intensity, leading to complex structural responses that include localized damage, spalling, and punching shear failure.

Understanding the behavior of RC structures under such load conditions is vital for ensuring the safety and resilience of infrastructure. For that reason, RC structures exposed to impact loads are typically designed and evaluated based on advanced experimental research conducted at specialized facilities such as Meppen or VTT, and reported in studies by Rüdiger et al. [1] and Saarenheimo et al. [4] respectively. While significant progress has been made in understanding the impact response of RC elements, ongoing research and testing are crucial to addressing unresolved questions related to impact loading.

Experimental studies on scaled specimens are often conducted due to limitations in testing full-scale structures. However, transferring results from small-scale tests to real-size structures requires careful consideration of scaling laws and potential size effects [5]. The scaling problem was addressed for instance by, Weber [6], Sugano et al. [7] and Horschel [8]. While Weber [6] dealt with the issues of similarity physics across disciplines, the core topic of impact was taken up much more by Sugano et al. [7]. The focus of the Sugano group was more on the scalability of an engine and scaled representation of impact experiments. The use of scaling laws enables the extrapolation of results from scaled models to full-sized structures, but this process introduces complexities. Scaling effects—such as differences in material behavior, strain rates, and energy dissipation mechanisms—can lead to discrepancies between model predictions and actual structural responses. For instance, traditional scaling laws based solely on geometric similarity (see Tab. 1) may not fully account for nonlinear material properties or dynamic effects under impact. The behavior of an impact loaded scaled target structure is discussed in the work of Horschel [8].

Parameter	Dimension	Reference model	Scaled model
Length	L	d	$\varphi \cdot d$
Mass	M	m	$\varphi^3 \cdot m$
Time	T	t	$\varphi \cdot t$
Velocity	LT^{-1}	v	v
Acceleration	LT^{-1}	a	$\varphi^{-1} a$
Force	MLT^{-2}	f	$\varphi^2 \cdot f$

Table 1. Parameter scaling for impact experiments. Dimensional scaling relationships for a reference model and a scaled model (scaling factor φ), following Sugano et al. [7].

Repeatability is another critical aspect of experimental research on RC slabs. Impact tests are inherently variable due to factors such as material heterogeneity, test setup inconsistencies, and accuracy of used sensors. Ensuring repeatable results is essential for validating experimental findings and developing reliable design guidelines. Yet, achieving high repeatability remains challenging, particularly in dynamic impact tests where even minor variations can significantly affect the outcomes. Our investigations have shown that repeated drop-weight impact tests often exhibit large scatter in results, with measured values typically falling within a range of the mean of ± 2 standard deviations (*s*) [11]. Quantifying this variability is crucial for improving the reliability of experimental data and establishing confidence in design recommendations.

1.1 Research Significance

This study aims to address two fundamental challenges in impact testing of RC slabs: **scaling** and **repeatability**. By analyzing experimental data of scaled tests, we seek to refine our understanding of how scaling laws influence the dynamic response of RC slabs under low-velocity impacts. Additionally, the study evaluates the repeatability of impact experiments by quantifying variations across multiple tests conducted under nearly identical conditions. This includes estimating standard deviations and identifying key factors contributing to variability.

By addressing these critical issues, this study provides a foundation for bridging the gap between laboratory-scale experiments and real-world applications in structural engineering. The findings of our research can help to develop more accurate prediction methods. Especially with regards to scaling effects. This knowledge will ultimately lead to safer and more resilient structural designs of critical infrastructure capable of withstanding potential impact scenarios.

2 TESTING FACILITIES AND MEASURING CONCEPT

The scaled impact tests and repeatability tests were performed at the drop tower facility at Otto Mohr Laboratory (OML) at TU Dresden University of Technology. The tests with a scaling factor of 2.0 were performed at the Test Site for Technical Safety (Testgelände Technische Sicherheit - TTS) at Federal Institute for Materials Research and Testing (Bundesanstalt für Materialforschung und -prüfung - BAM). A brief description of the testing facilities follows:

The **drop tower facility of OML, TUD** has two modes of applying impact loads: free-fall mode, and accelerated mode which was used in this study. The accelerated mode allows varying the impactors' velocities in a wide range from 10 m/s to 160 m/s. The impactor mass is also variable from 5 kg to 60 kg, making the accelerated configuration ideal for performing scaling tests. The maximal diameter of the impactor is limited by the 100 mm inner diameter of the steel pipe that accelerates the impactor with compressed air of up to 16 bar. The detailed description of the drop tower is provided in [9] and [10].

The **drop system at the TTS, BAM** is a purely gravity-driven test facility, utilizing a cable winch to drop weights of up to 50 t. The maximum achievable speed is approximately 16.6 m/s, corresponding to the maximum lifting height of 18 m. The facility features a 21 cm thick steel slab at its base, designed to support reinforced concrete slabs during testing. The RC slabs are supported at four points near the corners, allowing for precise measurement of test parameters according to the test plan. To facilitate this setup, a steel framework constructed from HEM100 profiles was developed. This framework can be securely friction-fitted to the drop tower's steel slab via welding points, ensuring a stable and controlled testing environment.

For all experimental investigations, the placement of sensors was consistent to ensure reliable and comparable data collection. Figure 2 illustrates the measuring plan of the four-point-supported RC slab. The slab support force was measured using load cells labeled LC1 to LC4. The load cells have a circular contact surface with a diameter of 200 mm. Deflections were measured using a combination of laser displacement sensors L1 and L2 as well as Laser Doppler Vibrometer LDV.

Laser L1 measured the midpoint deflection on the rear side of the slab. Sensor L2, positioned at 42 % of the slab's side length L from the center, also measured rear-side deflection, offering additional insights into deformation patterns away from the midpoint. The LDV was used to measure displacement on the front surface of the slab at a location 15 % of side L from the center. The utilization of contactless sensors ensured that the data is not influenced by the inertia of the movable core of standard LVDTs. The sampling rate was 200 kHz for all sensors.

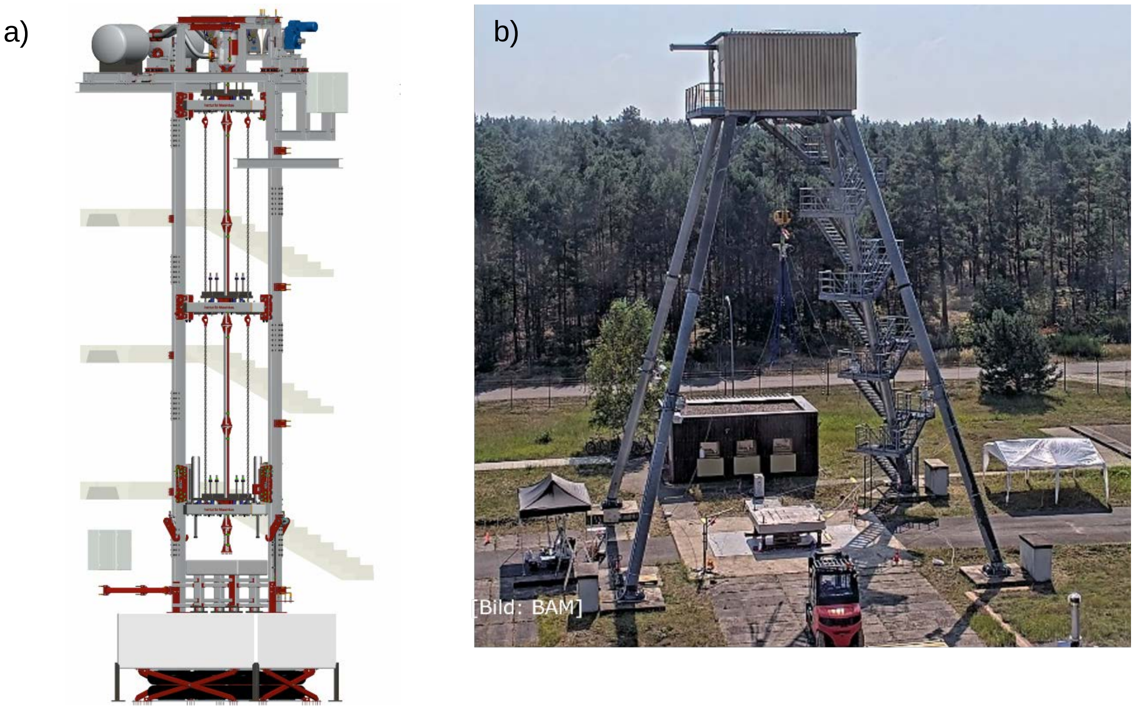

Figure 1. Drop tower facility at a) OML, TUD (drawing: Tino Kühn); b) TTS, BAM (photo: BAM)

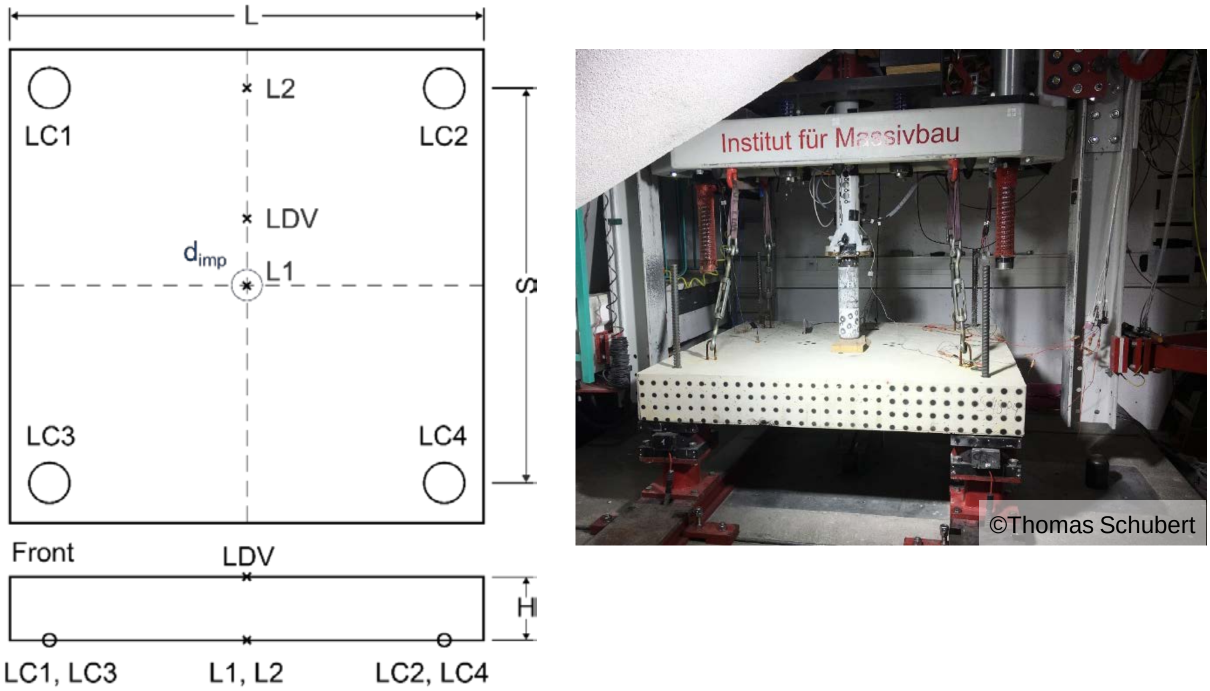

Figure 2. Left: parametric slab design and position of laser sensors L1 and L2, Laser Doppler Vibrometer LDV and load cells LC1-LC4. Right: slab in the drop tower of OML, TUD.

3 INVESTIGATIONS OF EXPERIMENT REPEATABILITY

3.1 Specimen and Material

To evaluate the repeatability of impact experiments and the variability in results, a reinforced concrete slab with a side length of L = 1500 mm and height of H = 200 mm was selected. The slabs for the repeatability tests were made of concrete C35/45 with a maximal grain size of 8 mm. Two layers of B500B reinforcement, with a diameter of 8 mm, were placed crosswise at the bottom and top of the slab. The reinforcement spacing was 100 mm.

Identical slabs were tested under nearly the same conditions to ensure consistency in the experimental setup. The impact velocity was maintained at around 44 m/s to replicate impact scenarios without slab perforation. After each test, the slabs were visually inspected for damage and photographed to assess and compare the extent of cracking, spalling, and other failure mechanisms. This approach allowed for a systematic evaluation of the repeatability of the results and provided insights into the variability inherent in dynamic impact testing.

3.2 Evaluation of Repeatability

The repeatability of impact experiments has not been extensively studied due to the high costs and significant effort involved. Despite these challenges, understanding deviations and scatter in experimental results is crucial for developing reliable planning and assessment methodologies, particularly for structures and materials exhibiting nonlinear behavior under dynamic loading conditions. Nonlinearities, such as strain rate sensitivity and energy dissipation mechanisms, can amplify variability in impact responses, making repeatability a vital factor in validating experimental findings. Addressing repeatability in impact testing helps bridge the gap between laboratory-scale experiments and real-world applications, ensuring critical infrastructure can be assessed and designed with greater confidence.

In previous work [11] we conducted an experimental study on the repeatability of impact tests, focusing on a small yet well-defined set of experiments. These tests were conducted under identical load levels and structural conditions, ensuring comparability and allowing for an adequate estimation of scatter ranges. The impact velocity of the considered tests varied less than 0.5 %.

In [11] we demonstrated that when reinforced concrete structures exhibit nonlinear material and structural behavior, the results of impact tests show significant scatter. This variability is particularly pronounced due to factors such as strain rate sensitivity, energy dissipation mechanisms, and localized damage patterns under dynamic loading conditions. Two times the standard deviation from the mean value ($\pm 2s$) is used as a determining limit for measured support forces, providing a statistically robust range within which most results are expected to fall (see Figure 3).

In this study, a new equivalent test with RC slab called PL274 aligns well within this scatter range, as the calculated sum of the support forces fits within the established boundaries. At the beginning of the force-time curve, the sum of forces approaches the upper limit of $+2s$, indicating a tendency toward higher force values during this phase. Conversely, in the later stages of the experiment (between 6 ms and 10 ms), after the shear failure of the concrete structure, the force trends toward the lower limit of $-2s$, reflecting reduced structural resistance or lower impact force. The max peak value is 710 kN. It is less than the max values stated in [11] and occurs also on a different point of time, but it lies in the 12 % scattering range noted. If the test results for force behavior from PL274 were included into the statistical evaluation of our prior study [11], the existing scatter range of $-2s$ to $+2s$ would likely increase.

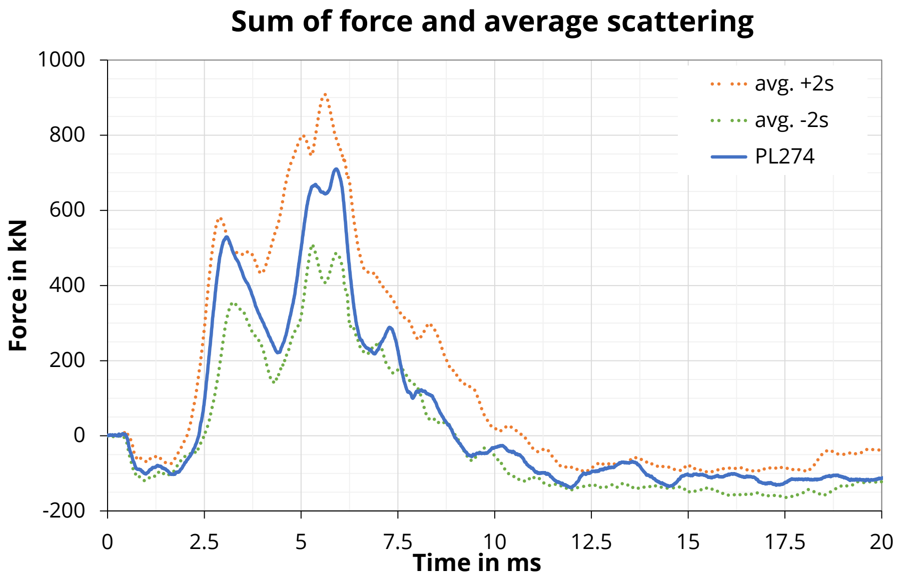

Figure 3. Average force-time diagram with ±2*s* bands for the total support forces (LC1+LC2+LC3+LC4) extracted from [11] with the new result PL274.

The relatively high force measurements and resistance observed before fracture are further corroborated by deflection data obtained from the LDV, which was positioned on the top surface of the test specimen to provide precise displacement measurements during the impact event. At the beginning of the displacement-time curve, up to approximately 10 ms, the test specimen exhibits a more rigid response, with displacement lower than the mean value determined in [11], see Figure 4. Consequently, the dynamic reverse bending at its maximum (around 14 ms) is also lower. The max displacement of 5.7 mm is within the pronounced scattering range of 13 % of the given mean maximum value of 6.1 mm [11]. Here too, the new displacement measurement would slightly reduce the limits and mean value of the displacement data established in [11].

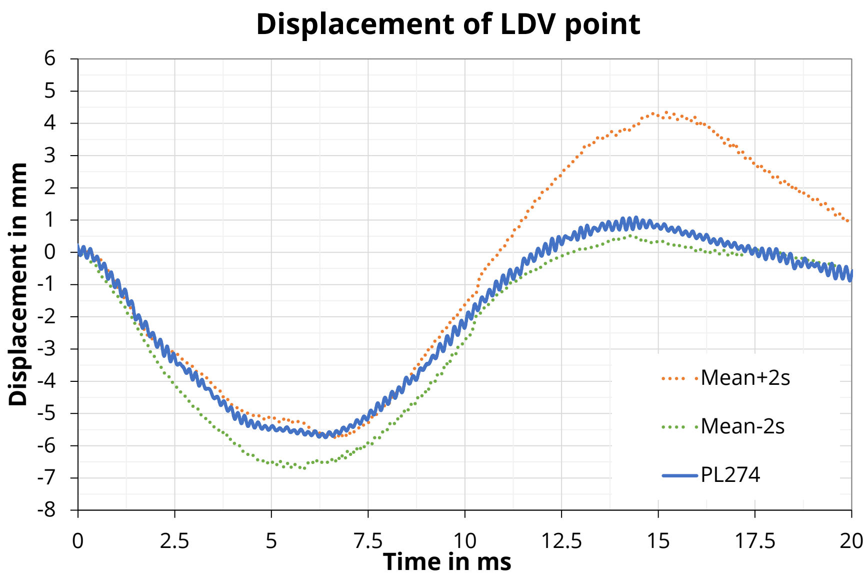

Figure 4. Displacement-time diagram with ±2*s* bands for the point near the center of the slab extracted from [11] with the new result PL274.

During the repeatability tests, concrete crushed directly under the impactor nose due to localized high energy input. This localized damage corresponds to the initial phase of high force measurements and lower displacement, indicating that the specimen resisted deformation before experiencing material failure. However, no spalling was observed near the impact location on the top surface. Based on visual inspection, the concrete around the impact site exhibited a few minor cracks, but no significant cracking was visible on the top surface of the slabs. The concrete scabbing was 20.15 kg for the slab PL274 as compared to the average scabbing of 18.13 kg and standard deviation of 4 % as reported in the previous study [11]. This means that the scabbing of PL274 lies slightly above the upper scattering band of 19.59 kg (avg.+2*s*), suggesting a higher tendency for material loss in this test.

4 INVESTIGATIONS OF SCALING

Scaling effects in impact experiments on RC structures have been a subject of ongoing investigation. Previous studies, conducted using small- to medium-scale specimens within the drop tower facility at OML, TUD [12], [13], [14] have provided valuable insights into the behavior of scaled models. However, these initial investigations revealed limitations in the sensitivity of low scaling factors of around 1.5 to capture the most influential factors governing impact response. Similar findings were reported by other research institutes [15], which were also employing scaling factors of approximately 1.5. These observations highlighted that the low scaling factors of about 1.5 might not be sensitive enough to most influencing factors. To address these limitations, a present study expands the scope of investigation by incorporating experiments with a larger scaling factor of 2.0 in free-fall impact tests.

4.1 Specimen, Material and Scaling Factors

The experimental investigations to evaluate the scaling effects were performed in two stages. The concrete C35/45 and the steel reinforcement B500B was the same for both stages. In the first step only the drop tower facility at OML, TUD was utilized (see Sec. 2) and the maximal slab edge was 1800 mm. The scaling factors are shown in Table 2.

Building on the findings from the first stage, the second stage of the research employed the drop tower at TTS, BAM (see Sec. 2), allowing for tests with a larger maximum slab edge of 3000 mm. The corresponding scaling factors can be found in Table 3. The scaling parameters employed in the experimental study are presented in Table 2 and 3, outlining key dimensions and properties of both the impactor and the slab for four different scale factors φ: 0.8, 1.0, 1.2, and 2.0. The parameters were varied proportionally according to the chosen scaling factor, allowing a systematic analysis of the influence of scale on the impact response of the slabs. In Table 2 and 3 $\boldsymbol{d_{imp}}$ is the impactor diameter, $\boldsymbol{L_{imp}}$ is the impactor length, $\boldsymbol{m_{imp}}$ is the impactor mass. $\boldsymbol{L}$ represents the side length of the square slab, $\boldsymbol{S}$ is the span between the center of supports, $\boldsymbol{H}$ is slab height (thickness), $\boldsymbol{d_{re}}$ is the reinforcement diameter and $\boldsymbol{s_{rc}}$ is the rebar spacing. The scaling approach ensures that both internal (e.g., reinforcement configuration) and external (e.g., impactor geometry and mass) parameters are consistently adjusted to maintain geometric similarity across all scales.

Whereas during the first phase the aggregate diameter $\boldsymbol{d_{agg}}$ was not scaled, in the second phase it was scaled from 8 mm to 16 mm. Also, the concrete cover ($\boldsymbol{c_{cover}}$) was only scaled in the second stage and it increased from 25 mm to 50 mm for the scaling factors of 1.0 and 2.0, respectively. These modifications aimed to ensure geometric consistency and capture the effects of material composition on impact response. The impactor velocity was maintained at about 13.6 m/s for phase two, enabling a direct comparison of structural behavior across different scaling conditions.

Scaling factor	Impactor			Slab						Miscellaneous	
	d_{imp}	L_{imp}	m_{imp}	L	S	H	d_{re}	s_{rc}	**label**	d_{agg}	c_{cover}
	mm	mm	kg	mm	mm	mm	mm	mm		mm	mm
0.8	66.7	200	5.44	1200	1000	160	8	80	PL238	8	20
1.0	83.3	250	10.62	1500	1250	200	10	100	PL239	8	20
1.2	100	300	18.40	1800	1500	240	12	120	PL245	8	20

Table 2. Scaling parameters according to the similarity principle used during the **first phase** of the experimental work at OML, TUD for impactor velocity 47 m/s to 48 m/s.

Scaling factor	Impactor			Slab					Miscellaneous	
	d_{imp}	L_{imp}	m_{imp}	L	S	H	d_{re}	s_{rc}	d_{agg}	c_{cover}
	mm	mm	kg	mm	mm	mm	mm	mm	mm	mm
1.0	100	1055	59	1500	1250	200	8	100	8	25
2.0	200	2330	472	3000	2500	400	16	200	16	50

Table 3. Scaling parameters according to the similarity principle used during the **second phase** of the experimental work at TTS, BAM for impactor velocity of 13.6 m/s.

4.2 Scaling Experiments Results

A detailed description of the TUD scaling tests from the first phase is provided in [13]. In this work we focus on the results of the slabs impacted by an impactor traveling at velocities between 47 m/s and 48 m/s. The following presents key experimental results, including force-time (Figure 5) and displacement-time (Figure 6) unscaled curves as recorded by respective sensors. The force-time curve represents the sum of the support forces measured by LC1 to LC4, while the displacement-time curves capture the deflection of the test specimen at the center of the rear side of the slab, as measured by L1 and near to the edge on the rear side of the slab as measured by L2 (see Figure 2).

Figure 5 also compares the force-time history after applying the corresponding scaling factors listed in Table 2. The scaled experiments do not follow the same path exactly, as load transfer is heavily influenced by the shear failure behavior of the concrete structure. This shear failure behavior is further affected by the heterogeneity of the concrete, the strength of the aggregates and the formation of microcracks in the drying, setting and aging phase of the concrete. While the heterogeneity and microcracking are only minimally affected by the specimen size, the shear cone formation does not strictly follow the scaling factors, which explains why the force-time histories do not align perfectly. However, all results would still lie safely within the scattering range if PL238 would be the mean, confirming that the scaling factors remain valid within this scaling range.

The displacement-time curves for both unscaled and scaled specimens are presented in Figure 6, with corresponding scaling factors and dimensions detailed in Table 2. The displacement progression over time, as measured by the laser sensors, follows a similar pattern, indicating similar structural behavior. A detailed analysis of the time differences between the maximum deflection peaks reveals a clear correlation with the applied scaling factors. However, L1 of specimen PL238, which has an applied scaling factor of 0.8, records lower displacement than expected. This trend becomes even more pronounced in the right diagram of Figure 6, where the application of the appropriate scaling factor further highlights the deviation. These findings suggest that while most displacement trends align with scaling expectations, variations may arise due to localized material effects and experimental uncertainties.

Support conditions, particularly for smaller specimens, may play a significant role in these deviations. The load cells, which remain constant in size (200 mm), are relatively closer to the impact point for smaller slabs, influencing the structural response more significantly due to the localized nature of impact loading. As the absolute size of the specimen increases, the relative influence of the support dimensions diminishes, as their proportion to the slab side length decreases. Furthermore, the specimens are restrained at the support points against lift up by a force of approximately 25 kN. However, this still does not fully account for the lower-than-expected deflections. A possible explanation is that the microcracking and shear cone failure mechanisms do not strictly adhere to the expected scaling factors, leading to deviations in the measured response. These deviations, combined with material property variations, support condition scaling discrepancies, and strain rate effects, contribute to the observed reduction in displacement.

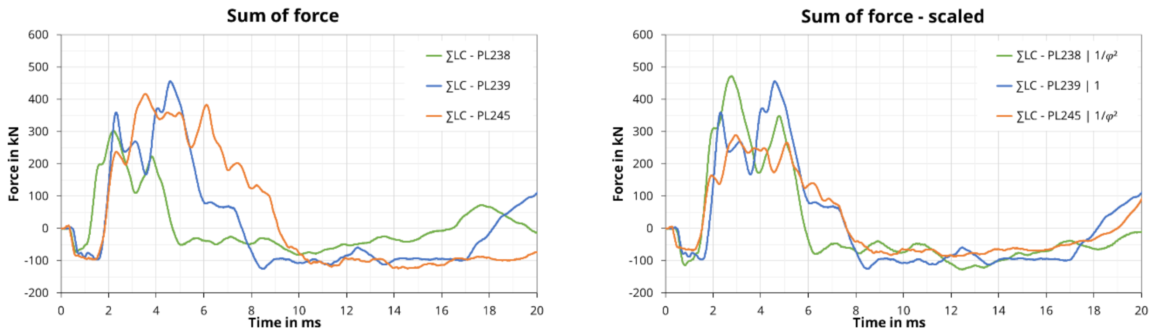

Figure 5. Support force-time diagram from [13]. Left: unscaled support forces, right: scaled support forces according to the similarity principle.

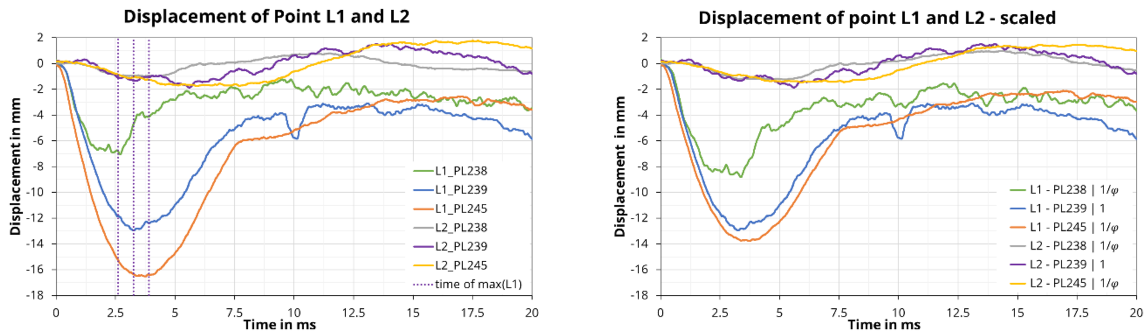

Figure 6. Displacement-time diagram for laser sensors L1 and L2. Left: unscaled displacements, right: scaled displacements.

In the following, new experimental results of the **second phase** are presented, addressing issues such as aggregate size, nonlinear behavior, and the influence of load cell size by using larger slabs with a scaling factor of φ = 2.0. The reduction in impact velocity and the increase in absolute slab size still led to specimen cracking due to shear failure; however, the damage on the outer surface of the slabs was noticeably less pronounced. Currently the first test set up of second phase is under intense review and more test are planned.

The midpoint deflection of the rear side of the RC slab as measured by sensor L1 in the new test series is presented in Figure 7. The dimensions of the specimen and impactor used in these tests are detailed in Table 3, and all the tests were conducted at an impactor velocity of 13.6 m/s. The overall behavior of the displacement curves for both specimens is consistent, indicating a similar structural response under impact loading. However, during the measurements on the larger specimen some measurement errors occurred due to dust or small debris affecting the laser sensor. These erroneous data were removed from the signal to ensure accuracy. Despite these issues, the maximum deflection was accurately captured and recorded. The scaled displacement curves, shown in the right graph of Figure 7, demonstrate a similar progression over time, falling well within the established scatter boundaries discussed in Section 3. This consistency supports the validity of the scaling approach used in these experiments.

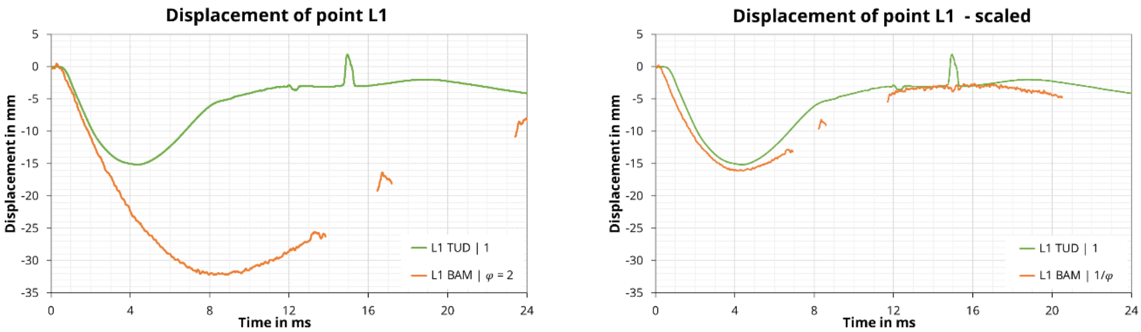

Figure 7. Displacement-time diagram for laser sensors L1 from the **second phase**. Left: unscaled displacements, right: scaled displacements.

5 CONCLUSIONS

This paper examines two critical aspects of impact engineering: repeatability and scaling. Based on previous analyses of similar impact tests on RC slabs, it has been shown that repeated tests fall within an identified scattering band of ±2*s* (*s* = standard deviation). Variations due to factors such as strain rate effects, concrete heterogeneity, and microcracks result in a wider scatter range in comparison with quasi-static tests.

The evaluation of scaling effects is based on two different approaches. The first involves scaling tests with small factors from 0.8 to 1.2, while the second presents preliminary findings from an ongoing investigation using a larger scaling factor of 2.0. The results indicate that scaling based on scientific principles (similarity law for impact tests) generally provides consistent structural behavior and impact responses. However, experimental scaling tests are significantly influenced by deviations in the test setup, non-scalable factors, and limitations associated with low scaling factors.

To conclude, this study aims to assist researchers and engineers in the field of impact engineering by emphasizing the importance of carefully accounting for repeatability and scaling effects in the design and assessment of RC structures subjected to impact loading.

ACKNOWLEDGEMENTS

The project on which this report is based was funded by the Federal Ministry for the Environment, Nature Conservation, Nuclear Safety and Consumer Protection (BMUV) on the basis of a resolution of the German Bundestag under the funding codes 1501541, 1501542, 1501647 and 1501648.

Supported by:

Federal Ministry
for the Environment, Nature Conservation,
Nuclear Safety and Consumer Protection

based on a decision of
the German Bundestag

Special thanks are due to the staff of the OML and BAM and BAM-TTS. Without their support, the investigations presented here would not have been possible.

REFERENCES

[1] E. Rüdiger, E. Renz, and H. Riech, “Experimentelle und theoretische Untersuchungen zum Aufprall kompakter Projektile auf Stahlbetonplatten”, Frankfurt am Main, RN 18052412, 1982.

[2] J. Li, R. Zhang, L. Jin, D. Lan, and X. Du, “Scaling laws of low-velocity impact response for RC beams: Impact force and reaction force”, *Int. J. Impact Eng.*, vol. 186, p. 104887, Apr. 2024, doi: 10.1016/J.IJIMPENG.2024.104887

[3] H. Abbas, N. K. Gupta, and M. Alam, “Nonlinear response of concrete beams and plates under impact loading”, *Int. J. Impact Eng.*, vol. 30, no. 8–9, pp. 1039–1053, Sep. 2004, doi: 10.1016/j.ijimpeng.2004.06.011

[4] A. Saarenheimo, K. Calonius, and M. Tuomala, “Bending and punching studies on impact loaded plate,” in *Transactions of the 23rd Conference of Structural Mechanics in Reactor Technology (SMiRT 23)*, Machester, United Kingdom: International Association for Structural Mechanics in Reactor Technology (IASMiRT), Aug. 2015.

[5] W. S. Abdulsahib, M. S. Abduljabbar, and B. S. Almuhsin, “Low Velocity Impact Response of Reinforced Concrete Flat Slabs”, *Open Civ. Eng. J.*, vol. 17, no. 1, pp. 1–11, 2023, doi: 10.2174/18741495-v17-e230113-2022-75

[6] M. Weber, “Das Allgemeine Ähnlichkeitsprinzip der Physik und sein Zusammenhang mit der Dimensionslehre und der Modellwissenschaft”, in *Jahrbuch der Schiffbautechnischen Gesellschaft*, Berlin, Heidelberg: Springer Berlin Heidelberg, 1930, pp. 274–354. doi: 10.1007/978-3-642-92021-9_14

[7] T. Sugano *et al.*, “Local damage to reinforced concrete structures caused by impact of aircraft engine missiles Part 1. Test program, method and results”, *Nucl. Eng. Des.*, vol. 140, no. 3, pp. 387–405, Jun. 1993, doi: 10.1016/0029-5493(93)90120-X

[8] D. S. Horschel, “Construction of a 1/6-Scale Concrete Containment Model,” *Nucl. Eng. Des.*, vol. 104, pp. 341–347, 1986, doi: 10.1016/0029-5493(87)90212-3

[9] M. Just, M. Curbach, T. Kühn, and M. Hering, “Bauteilverhalten unter stoßartiger Beanspruchung durch aufprallende Behälter (Flugzeugtanks); Phase 1A: Maßstabseffekte bei stoßartiger Beanspruchung”, TU Dresden, Institut für Massivbau, Abschlussbericht zum Reaktorsicherheitsforschungs-Vorhaben Nr. 1501438, 2016. doi: 10.2314/GBV:868615218

[10] B. Batarlar, M. Hering, F. Bracklow, T. Kühn, B. Beckmann, and M. Curbach, “Experimental investigation on reinforced concrete slabs strengthened with carbon textiles under repeated impact loads”, *Struct. Concr.*, vol. 22, no. 1, pp. 120–131, 2021, doi: 10.1002/suco.201900319

[11] T. Schubert, F. Bracklow, N. Unger, M. Hering, and B. Beckmann, “Impact tests on reinforced concrete slabs - variation in results and residual load bearing capacity due to hard impact”, in *Transactions of the SMiRT 27*, Yokohama: International Association for Structural Mechanics in Reactor Technology (IASMiRT), 2024.

[12] F. Bracklow, A. Babiker, M. Hering, T. Kühn, M. Curbach, and U. Häußler-Combe, “Bauteilverhalten unter stoßartiger Beanspruchung durch aufprallende Behälter (Flugzeugtanks) - Phase 1C: Experimentelle und numerische Untersuchungen zu Maßstabseffekten, Versagensmechanismen und Bauteilschädigung.”, TU Dresden, Institut für Massivbau, Abschlussbericht zum Reaktorsicherheitsforschungs-Vorhaben Nr. 1501541, 2021. doi: 10.2314/KXP:1789564956

[13] M. Hering, F. Bracklow, and M. Curbach, “Impact experiments on scaled reinforced concrete plates,” in *Transactions of the SMiRT 26*, Berlin/Potsdam: International Association for Structural Mechanics in Reactor Technology (IASMiRT), 2022, p. 10.

[14] M. Hering, T. Kühn, and M. Curbach, “Bauteilverhalten unter stoßartiger Beanspruchung durch aufprallende Behälter (Flugzeugtanks) Phase 1B: Quantifizierung der Schädigungen des Betongefüges, Teilprojekt: Fallturmversuche”, TU Dresden, Institut für Massivbau, Abschlussbericht zum Reaktorsicherheitsforschungs-Vorhaben Nr. 1501479, 2017. doi: https://doi.org/10.2314/GBV:100128142X

[15] A. Vepsä, A. Fedoroff, S. G. Khasraghy, C. Heckötter, S. Sawada, and F. Tarallo, “Effect of impact location on the punching shear resistance of a concrete wall: near edge impact test”, in *Transactions of the SMiRT 27*, Yokohama, Japan: International Association for Structural Mechanics in Reactor Technology (IASMiRT), Mar. 2024, p. 10.

ESTIMATION METHOD OF DEBRIS FLOW LOAD USING CHANNEL FLUME WITH MOVABLE BED IN DEM

Toshiyuki Horiguchi[a] and Kazuki Saito[b]

[a]National Defense Academy of Civil Engineering, Japan; email: htoshi@nda.ac.jp
[b]National Defense Academy of Civil Engineering, Japan

Keywords: *Bouldery debris flow*, impact load, distinct element method, channel flume, movable bed

Abstract

In Japan, the frequency of debris flow disasters has been increasing each year, with large-scale events often triggered by localized torrential rainfall and typhoons. Generally, debris flows can be classified into two categories: bouldery debris flow and mudflow. Bouldery debris flow that is characterized by the concentration of boulders at the front part imparts extremely high impact forces and can cause severe damage to residential areas and other communities. Consequently, the development and implementation of effective measures against these hazards has become an urgent priority. Among the various mitigation measures, steel pipe open Sabo dams that are protective structure for controlling sediment have been constructed. In current design practice, the fluid forces of debris flows acting on the upstream side of the dam are combined with sediment pressure loads extending from the downstream side toward the upstream one. However, recent cases of damage to members and failures at joint sections of steel pipe open Sabo dam have been reported. An analysis of these damaged Sabo dams revealed that the loads acting on the dams can vary locally, influenced by the riverbed morphology and the sediment already trapped. These findings emphasize the need for a more detailed analysis of debris flow loads. Consequently, it is necessary to investigate and clarify the mechanisms underlying load evaluations under conditions resembling a movable bed, where gravel is present from the outset. The study conducted load experiments under a movable bed condition, focusing on the temporal evolution of the load to clarify its characteristics. Furthermore, it performed the distinct element method to reproduce debris flow loads under a condition where a movable bed and pre-deposited gravel were present. The results revealed that pre-deposited gravel significantly influences the maximum load acting on the dam. Large loads occur where the debris flow front collides with each step height of the dam. In addition, the results investigated the underlying mechanisms of impact forces in debris flow loading under detailed experimental data.

1 INTRODUCTION

The occurrence of debris flow disasters in Japan is increasing annually, with large-scale debris flow triggered by localized heavy rainfall and typhoons [1]. Bouldery debris flows, in which large boulders are concentrated at the front, exert significant impact forces and cause severe damage to residential areas [2]. Steel pipe open Sabo dams *(referred to as open Sabo dams)* have been constructed to mitigate such disaster as shown to **Figure 1**. Steel pipe open Sabo dams control debris flow and sediment. Current design approaches combine debris flow fluid forces and sediment pressure loads [3,4]. However, recent cases of damage to steel components and joint failures have been reported [5,6]. This suggests that the actual loads exceed design assumptions [7]. Therefore, it is necessary to conduct failure verification of

Figure 1. Destructive event of open Sabo dam (Nigata prefecture, Nechi river)

concrete-type closed Sabo dams [8] and structural analyses incorporating the ultimate limit states to establish a quantitative evaluation method [9,10]. It is essential to assess debris flow loads while considering the riverbed morphology and deposition conditions of the trapped debris flow. Various studies have been conducted to evaluate the debris flow loads (ex. [11, 12]). Iketani et al. [13] examined debris flow loads by dividing them into water fluid force loads based on fluid theory and debris flow loads based on solid mechanics. Mizuyama et al. [14] investigated the impact force estimation methods for a closed Sabo dam classified according to these load types. Daido [15] proposed a method to estimate impact forces by treating debris flows as either incompressible or compressible fluids. Furthermore, as an analytical approach to solid-fluid interactions, Fukuda et al. [16] analyzed the movement mechanism of tsunami boulders using the APM numerical model of the IRS, which couples solid and fluid motions. Tsuji et al. [17] combined the ISPH method with DEM to conduct a seepage failure analysis of the rubble mound of a caisson-type breakwater and successfully reproduced the qualitative motion of caisson blocks. Kato et al. [18] conducted three-dimensional numerical experiments using a resolved CFD-DEM model that allowed for the direct evaluation of fluid forces acting on particles from the surrounding flow field by employing a computational fluid mesh smaller than the particle scale. Their study focused on sediment transport phenomena involving stony particles and investigated riverbed and riverbank erosion mechanisms. We propose a coupled analysis method that models gravel using the DEM while incorporating a velocity distribution model [19,20]. However, previous studies have not sufficiently examined the reproducibility of local impact loads at different heights or considered the conditions under which the riverbed behaves as a movable bed. This study investigated debris flow loads using the DEM by configuring a movable bed in a straight channel and placing pre-deposited gravel in front of the dam.

2 EXPERIMENTAL GUIDELINES

2.1 Experiment device

Figure 2 illustrates the specifications of the channel used in the experiment. The channel is a two-step slope with a length of 4.5 m, width of 300 mm, and height of 500 mm. The experimental slope was set to θ = 15 °. The channel bed was designed as a movable bed covered with gravel at a deposition height of 5 cm. The dam model had a height of 315 mm and width of 300 mm (**Figure 3**). It was constructed using a combination of wood and steel to prevent deformation under debris flow loads. The measurement device is shown in **Figure 3(a)** and consists of a pressure plate combined with a steel component in front of each load cell. The device was designed to measure the loads applied at different heights at the front of the dam. As shown in **Figure 3(b)**, a 500 N load cell (LMB-A-500 N) was placed on the left and right sides behind the pressure plate. The measurement heights of each stage were set at 3.1 cm, 7.3 cm, 11.4 cm, 15.6 cm, 19.8 cm, 24.2 cm, and 28.4 cm, with a total of 14 measurement points. The dam model was fixed at a position 4.0 m downstream from the

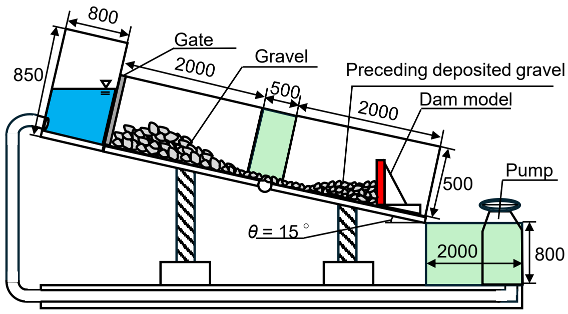

Figure 2. Outline of experimental flume

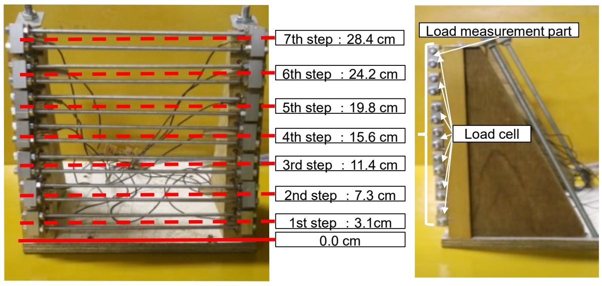

(a) Front view **(b)** Side view

Figure 3. Dam model

Table 1. Debris flow model

Pre-deposited gravel	Gravel diameter	Total weight	Debris flow model	Pre-deposited gravels and gravel volume of movable bed
0 %	40-60	35.7	25.5	10.2
	25-40	44.1	31.5	12.6
	15-25	25.2	18.0	7.2
50 %	40-60	35.7	15.3	15.3
	25-40	44.1	18.9	18.9
	15-25	25.2	10.8	10.8

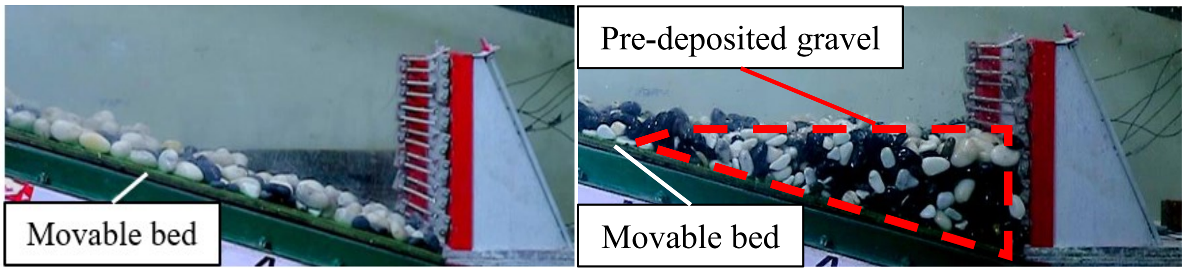

(a) 0 % (PDG_0) **(b)** 50 % (PDG _50)

Figure 4. Location of pre-deposited gravels

upstream gate of the channel.

2.2 Debris flow model

The debris flow model consisted of a mixture of three types of gravel with different particle sizes and a specific gravity of 2.6. **Table 1** presents the mass distribution of each particle size. For the movable bed, 30 kg of gravel was used to create a 5 cm thick deposition layer in the upstream section of the channel. Additionally, 15 kg of pre-deposited gravel was placed in front of the dam model, accumulating up to half the dam height. In the experiment, gravel was evenly spread across a width of approximately 50 cm in the uppermost section of the channel. Next, flow was generated using the dam-break method, releasing 75 L of water upstream from the deposited gravel. The debris flow was recorded using a high-speed camera at a frame rate of 150 fps and shutter speed of 1/3,000 to analyze the flow velocity and gravel movement patterns.

2.3 Case of experiment

Figure 4 illustrates the gravel arrangement in front of the dam under different experimental conditions. To analyze the effect of pre-deposited gravel on the applied load, two experimental cases were considered: one without pre-deposited gravel (PDG_0) as shown to **Figure 4(a)**, and other where gravel was deposited up to half the dam height (PDG_50) as shown to **Figure 4(b)**. Each test was conducted five times, and the relationship between the load and time was analyzed.

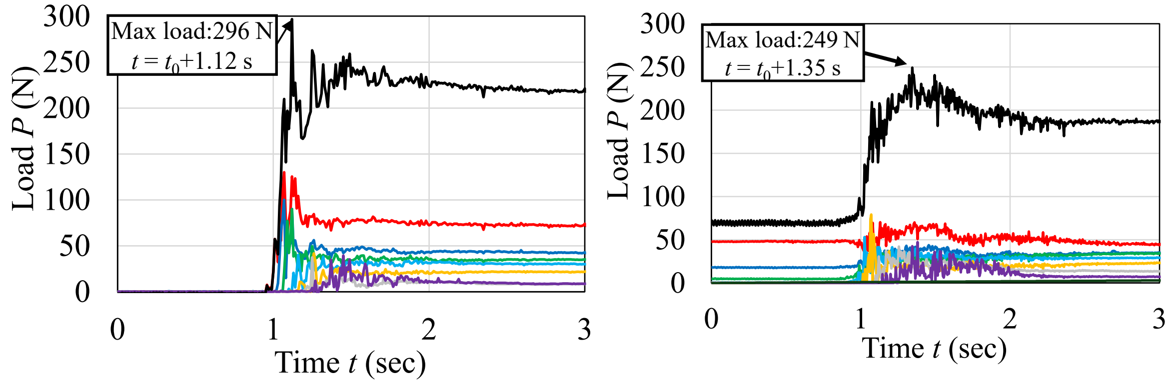

(a) 0 % (PDG_0) **(b)** 50 % (PDG_0)

Figure 5. Load and total load at each stage-time relationship

3 OUTLINE OF EXPERIMENT RESULTS

Figure 5 shows the time history of the load at each measurement height and the total load for cases without pre-deposited gravel (hereafter, PDG_0) and with pre-deposited gravel at 50 % of the dam height (hereafter, PDG_50). The total load is the sum of the loads measured at each stage; for comparison, only one representative experimental result is shown for each case. In the PDG_0 case (**Figure 5(a)**), the load in the first stage begins to increase at $t = t_0$+1.00 s, reaching the maximum load of P_{max} = 296 N at $t = t_0$ + 1.12 s. The load gradually decreased over time and eventually stabilized as the static pressure load from the deposited gravel increased. The load at each stage peaked with a time lag as height increased, and the total load reached its maximum when the load in the third stage peaked. On the other hand, in the PDG_50 case (**Figure 5(b)**), the load in the fourth stage starts to rise at $t = t_0$ + 1.00 s, and the maximum load of P_{max} = 249 N is recorded at $t = t_0$ + 1.35 s. Compared to PDG_0, PDG_50 exhibits a slightly lower maximum load and a delayed peak load timing. The overall response was approximately 40 N lower, suggesting that the pre-deposited gravel influenced the load initiation process.

4 ANALYSIS MODEL

4.1 Outline of water velocity fluid distribution

Analyzing the interaction between water and gravel and directly applying fluid forces to each element, as in the velocity distribution model, enables the experimental reproduction of gravel-dam interactions. Therefore, in this experiment, a velocity distribution model based on gravel flow was established. Here, the fluid force acting on a spherical element was calculated based on the relative velocity between the element and the flowing water. This force was applied as a fluid force acting on the centroid of the element. The fluid force $\mathbf{f}_{wi}$ acting on the centroid element is expressed as,

$$\mathbf{f}_{wi} = C_D A_i \rho_w |\mathrm{v}_i - \mathrm{v}_w|^2 + \rho_w g V \tag{1}$$

where g represents the gravitational acceleration, C_D is the drag coefficient, ρ_w is the density of the surrounding water, A_i is the projected area of the element in the flow direction, v_i is the velocity vector of the element, v_w is the velocity vector of the surrounding water flow, and V *is the volume of the element.*

4.2 Approaching domain

As shown in **Figure 6**, the upstream region of the dam was set as the approach domain, where

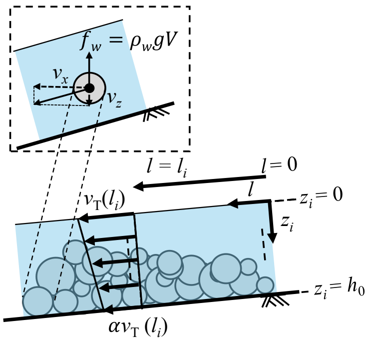

Figure 6. Approaching domain of water flow velocity distribution

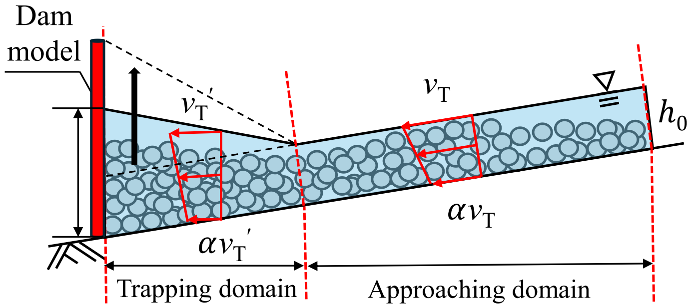

Figure 7. Water flow distribution model

a constant water depth and velocity were applied until the gravel was trapped by the dam. In this region, the channel bed slope and water surface were assumed to be equal, allowing water to flow while the gravel moved irregularly downstream. Although the velocity distribution in depth direction is inherently nonlinear, previous studies observed linear velocity distribution in bouldery debris flows. Therefore, a linear velocity distribution was adopted, as shown in **Figure 6**. The velocity acting on the gravel was reduced by applying a reduction coefficient *α* to the surface velocity, linearly decreasing from the water surface toward the channel bed. The references for the initial velocity vector v_0 and initial water depth h_0 were given, with the velocity at the channel bed set to 30 % of the surface velocity v_0, decreasing linearly in the depth direction. The reduction coefficient α was determined as α = 0.3, based on experimental observations where the velocity ratio between the water surface and the gravel at the channel bed ranged from 1/10 to 3/10, making it the most representative of the experimental flow conditions. The velocity vi at a given element integration point height z_i is expressed as follows:

$$\begin{cases} \mathbf{v}_i = \left(\frac{h_0 - \alpha z_i}{h_0}\right)\mathbf{v}_0 & (0 \le z_i \le h_0) \\ \mathbf{v}_i = 0 & (z_i > h_0) \end{cases} \tag{2}$$

The flow velocity was applied along the channel slope. When calculating the fluid force acting on each element, the velocity components were decomposed into vertical and horizontal components to determine the relative velocity.

4.2 Trapping domain

Figure 7 illustrates the velocity distribution in the approach and trapping domains. Before the gravel was trapped by the closed Sabo dam, the velocity was assigned to the approach domain. After the gravel was trapped, the trapping region was defined stepwise, covering the range from the front face of the dam to the upstream side, where the velocity was lower than the infiltration velocity. In addition, the water depth was adjusted to match the experimental flow conditions. **Figure 7** shows an increase in water depth in front of the dam. As the gravel accumulated at the front of the dam, the amount of water passing through the deposited gravel decreased, leading to an increase in water depth. This change can be expressed by the following equation:

$$\begin{cases} h' = H \cdot s & (0 \le s \le 1) \\ h' = H & (s > 1) \end{cases} \tag{3}$$

where h' is the water depth after the increase on the upstream side of the dam, *H* is the height of the dam model (31.5 cm), $h_0$is the initial water depth, and *s* is a coefficient that changes the water depth.
This coefficient *s* is the ratio of the total cross-sectional area *A*, including the permeable section, to the sum of the projected areas of the deposited gravel upstream of the dam This

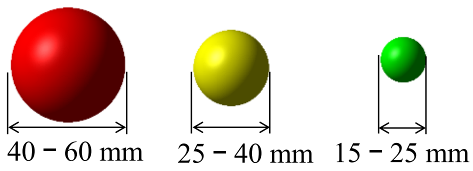

(a) Gravel model (spherical element)

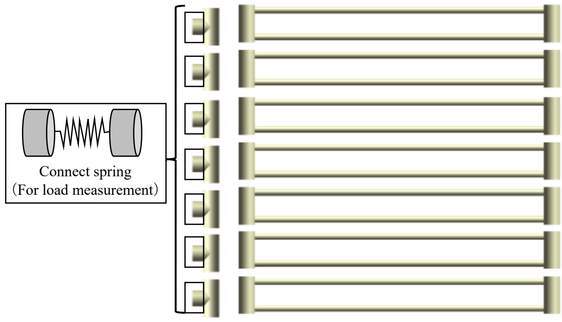

(b) Dam model

Figure 8. Analysis model

coefficient *s* is the ratio of the total cross-sectional area, including the permeable section, to the sum of the projected areas of the deposited gravel upstream of the dam, $\sum A_i$ and is expressed by the following equation:

$$s = \frac{\sum A_i}{A} \tag{4}$$

When the trapping amount exceeded a certain value, the water depth was set to the maximum value, which was the height of the dam. In the velocity distribution of the trapping domain, the average velocity from the leading edge to the trailing edge was set to balance the discharge of flowing water based on the continuity equation. The flow velocity equation for the water surface in the trapping domain is as follows:

$$v_{\mathrm{T}}{}' = \frac{h_0}{h'} v_0 \tag{5}$$

Similar to the approach domain, the velocity in the depth direction decreased according to the water depth in the trapping domain.

5 Analysis result

5.1 Analysis model

Figure 8 illustrates the gravel and dam models used in the analysis. **Figure 8(a)** shows the gravel model based on the grain size distribution of the gravel used in the experiment. Three types of grain sizes were randomly assigned to the model, ensuring that the grain size distribution matched both the experimental and analytical conditions. The total weight was adjusted to match the experimental conditions. **Figure 8(b)** illustrates the dam model. The dam model was set up similar to the experiment, with the ability to measure the load at heights of steps 1-7. Load measurement elements were arranged behind each segment with a 7 mm gap between segments to avoid contact. This model was used for load evaluation, and the dam model and a fixed cylindrical element placed behind it were used to evaluate the load in terms of the spring force. Springs were permanently installed between the elements, and the spring force was calculated based on the displacement from the initial position. The axial stiffness of the spring was set to EA = 1.0 × 10^5 N/m, which was confirmed to be the limit at which the solution stabilized. Increasing stiffness of DEM parameter did not affect load evaluation.

Figure 9 presents a description of the channel model. **Figure 9(a)** shows PDG_0, which is a channel model with PDG_0. **Figure 9(b)** PDG_50 is the channel model with PDG_50. The initial gravel placement in the channel model was performed using the dropping method, starting 2.4 m upstream of the dam front. For the movable bed gravel model, the gravel was initially placed in a flatbed using the dropping method to densely pack the gravel, after which

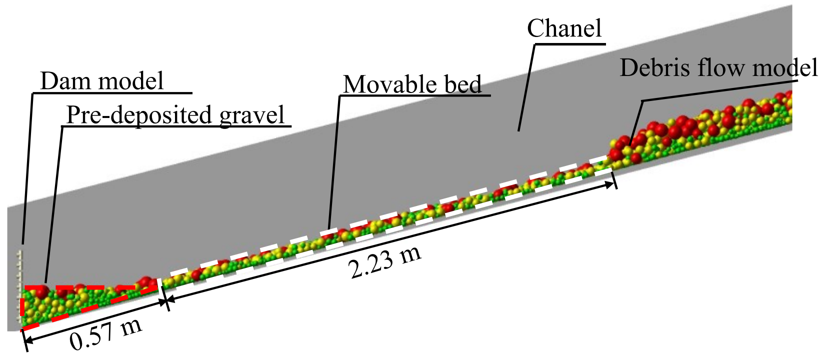

(a) 0 % (PDG_0)

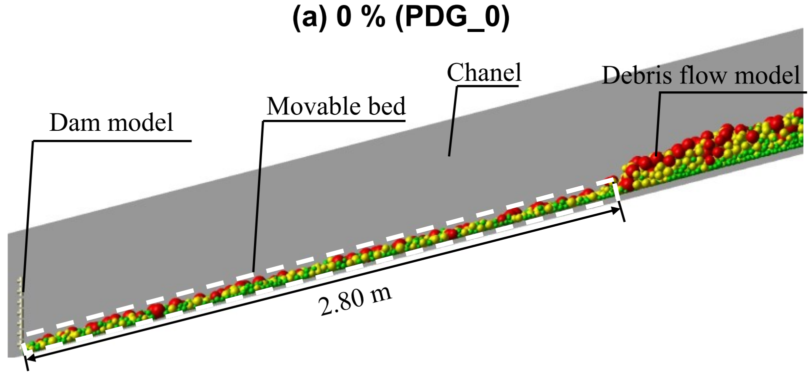

(b) 50 % (PDG_50)

Figure 9. Channel model

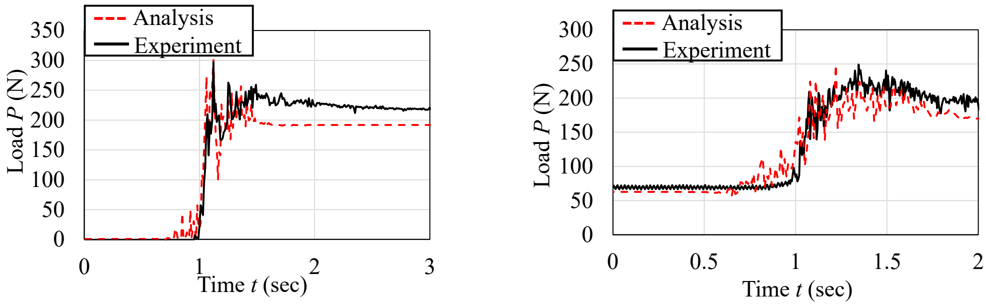

(a) 0 % (PDG_0)

(b) 50 % (PDG_50)

Figure 10. Total load versus time relationship in experiments and analysis

the flow velocity was applied under frictionless conditions. Gravel models with a height greater than 0.05 m were excluded, and the bed slope was set to 15°, placing the mobile bed 2.4 m upstream of the dam front. In PDG_0, gravel trapped after the flow of the debris-flow model was deposited up to 50 % of the dam height, as shown in PDG_50.

Figure 10 shows the total load-versus-time relationship in the experiments and analyses for PDG_0 and PDG_50. In PDG_0, the load increase in the analysis was organized similarly to that in the experiment, with the load increase starting at $t = t_0+1.00$ s. The maximum load in the analysis results shown in **Figure 10(a)** is 296 N, which approximately reproduces the maximum load observed in the experiment. As shown in **Figure 10(b)**, the load before $t = t_0+1.00$ s in the analysis occurred slightly earlier than that in the experiment. This is likely due to the pre-deposited gravel, modeled by spherical elements, being pushed by the debris flow. However, the load response and maximum load (249 N) were consistent with the experimental results.

Figure 11 shows the load-versus-time relationship for the 1st to 6th stages in PDG_0 (experiment vs. analysis). The load increase initiation at each stage was generally consistent. The loads for the 2nd and 4th stages were slightly overestimated. However, the other stages exhibited reasonable agreement. Overall, significant loads occurred in the 1st to 4th stages,

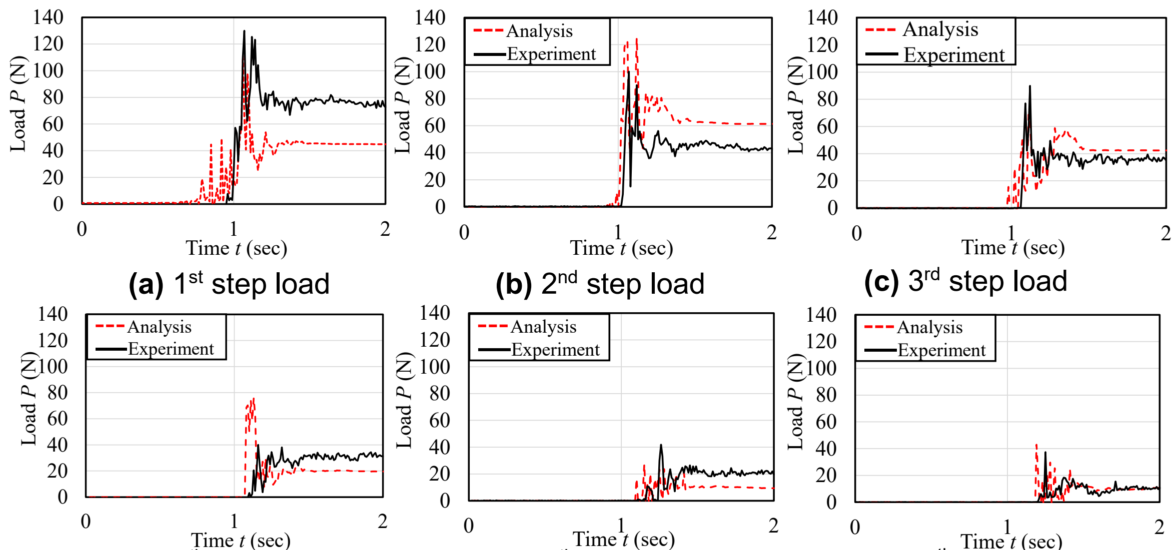

(a) 1^{st} step load **(b)** 2^{nd} step load **(c)** 3^{rd} step load

(d) 4^{th} step load **(e)** 5^{th} step load **(f)** 6^{th} step load

Figure 11. Load versus time relationship for the 1^{st} to 6^{th} stages in PDG_0 (experiment versus analysis)

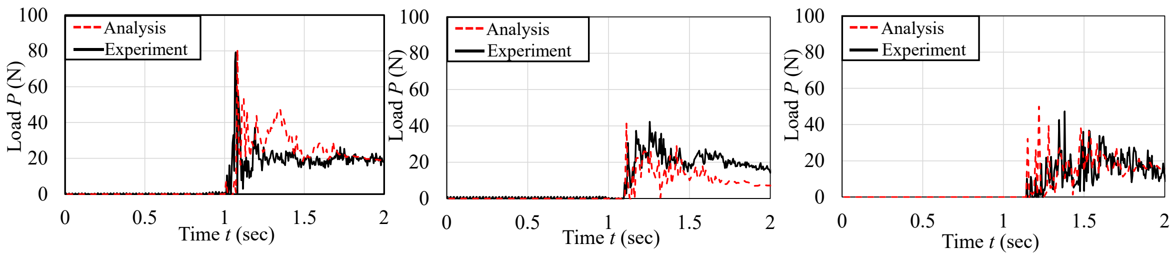

(a) 5^{th} step load **(b)** 6^{th} step load **(c)** 7^{th} step load

Figure 12. Load versus time relationship for 5^{th} to 7^{th} stages in PDG_50 (experiment versus analysis)

where the debris-flow head collided with the dam segments. The 7^{th} stage exhibited almost the same response as the 6^{th} stage, and because only the sediment pressure was observed for the other stages, it was omitted from the analysis.

Figure 12 shows the load–time relationship for the 5^{th} to 7^{th} stages in PDG_50 (experiment vs. analysis). For PDG_50, in stages 1-4, the load was transmitted through the pre-deposited gravel when the debris flow head entered the pre-deposited gravel section. Because the load from the pre-deposited gravel did not change significantly, it was omitted from the analysis. In the 5^{th} and 7^{th} stages, the load rise and maximum load are generally reproduced. Compared to the 5^{th} and 6^{th} stages of PDG_0, PDG_50 experienced larger loads. This is because of the localized loads occurring at the point of collision with the debris flow head. The 7^{th} stage reached the maximum load earlier than in the experiment, suggesting that the decrease in the velocity of the individual elements was smaller than that observed in the experiment.

Figure 13 shows the deposition process in PDG_0 (experimental versus analysis). **Figure 13(a)** shows the situation where $t = t_0 + 1.00$ s. In the experiment, the head of the debris flow indicated that water preceded part of the flow, and the gravel appeared to have a relatively low density. However, the gravel concentrated and flowed downstream immediately thereafter. As the movable bed passed through the debris flow head, the height of the debris flow body was greater than that in the experiment. This is because the spherical element model makes it easier for the gravel to overcome the flow, and the gravel at the leading edge, which has a reduced velocity due to the movable bed, is pushed upward by the following gravel. **Figure 13(b)** shows the situation where $t = t_0 + 1.12$ s. The maximum load is shown in both the experiment and the analysis. In the experiment, the gravel collided in the 1^{st} to 3^{rd} stages,

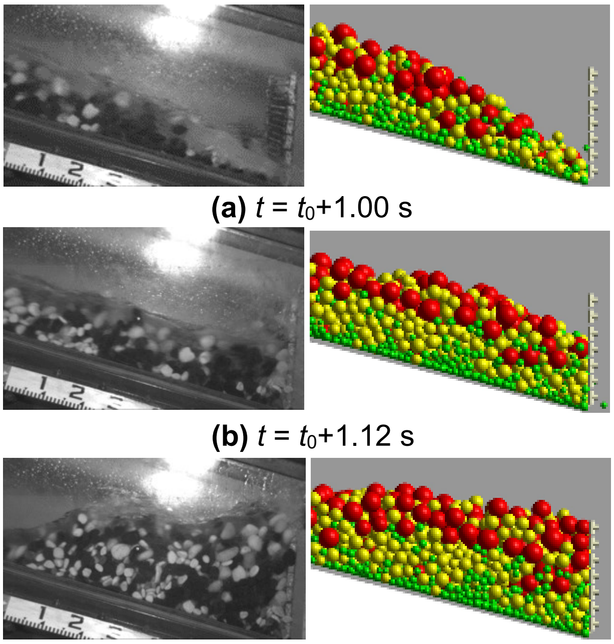

(a) $t = t_0$+1.00 s

(b) $t = t_0$+1.12 s

(c) $t = t_0$+2.00 s

Figure 13. Deposition process in PDG_0 (experiment versus analysis)

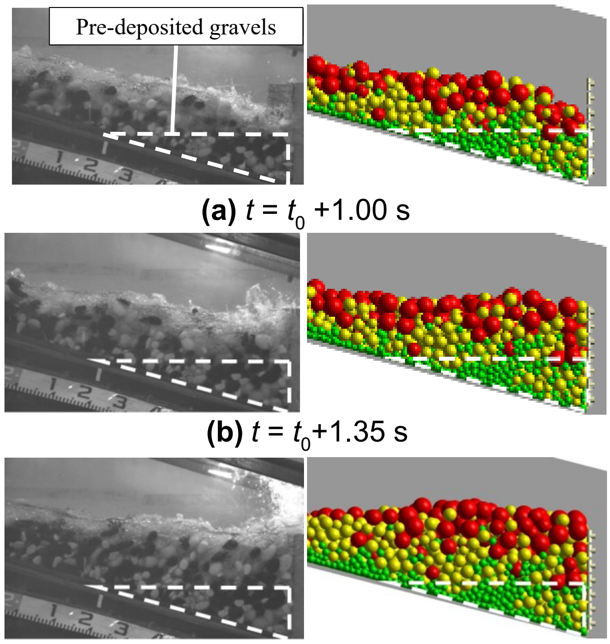

(a) $t = t_0$ +1.00 s

(b) $t = t_0$+1.35 s

(c) $t = t_0$+2.00 s

Figure 14. Deposition process in PDG_50 (experiment versus analysis)

whereas in the analysis, it collided in the 1st to 5th stages. This earlier deposition in the analysis was due to the gravel flowing in an elevated manner. **Figure 13(c)** shows the situation where $t = t_0 + 2.00$ s. The contact surface of the dam and deposition conditions were generally consistent between the experiment and analysis.

Figure 14 compares the deposition shapes of PDG_50 (experiment versus analysis). **Figure 14(a)** shows the situation of $t = t_0 + 1.00$ s. Comparing the experiment and analysis, the height of the debris-flow body before the collision was higher in the analysis. **Figure 14(b)** shows the situation where $t = t_0 + 1.35$ s**.** The maximum loads observed in both the experiment and analysis are shown. In the experiment, the gravel at the leading edge of the debris flow collided during the 5th and 6th stages, whereas in the analysis, it collided during the 5th to 7th stages, where the maximum load occurred. **Figure 14(c)** shows the situation where $t = t_0 +$ 2.00 s. The dam was fully filled with gravel in both the experiment and the analysis.

5.2 Considerations on load reduction effect

Figure 15 shows a schematic diagram of dead zone formation and load reduction by pre-deposited gravel in PDG_0 and PDG_50. In PDG_0, before the debris flow collided with the dam, it flowed rapidly while engulfing the movable bed. When the debris flow collided with the dam, the gravel at the leading edge was trapped by the dam. The stopped gravel then accumulated because of collisions with other gravel particles and the dam, forming a dead zone. Additionally, the gravel collides with the dead zone, causing a decrease in velocity. As the gravel rose, the dead zone expanded, causing a further decrease in the velocity of the subsequent gravel. This leads to a reduction in the load acting on the dam, particularly during the upper stages. Eventually, a contact surface is formed, and the subsequent gravel is trapped.

In PDG_50, the load reduction mechanism caused by the pre-deposited gravel is as follows: When the debris-flow head enters the pre-deposited gravel section, the gravel at the leading edge collides with the pre-deposited gravel, causing a decrease in velocity. The load decreases upon collision with the dam. After being trapped by the dam, a dead zone forms pre-deposited gravel. This zone expands and reduces the velocity of the following flow like the behavior in PDG_0. Eventually, a contact surface is formed, and the subsequent gravel is trapped.

PDG	I. Before collision	II. Front collision
0 %	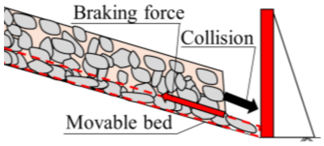	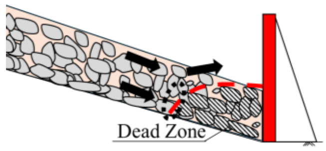
50 %	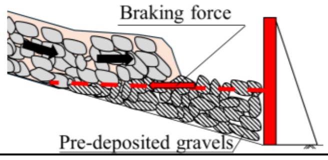	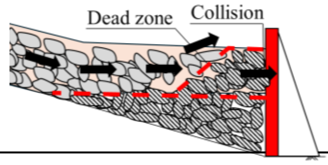
Considerations	Decrease in velocity due to pre-deposited gravels and riverbed gravels	Dead Zone Formation and Gravel Rise
PDG	III. After dead zone formation	IV. Contact surface formation
0 %	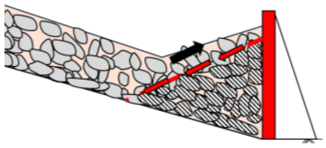	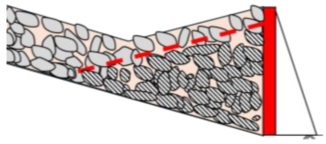
50 %	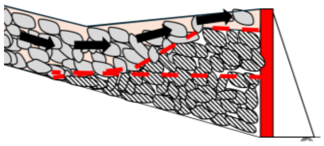	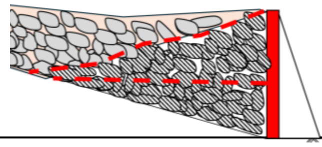
Considerations	Expansion of dead zone and decrease in velocity of gravel toward the upper section of the dam	Impact surface formation and subsequent gravel deposition

Figure 15. Mechanism of dead zone formation and load-reducing effect of pre-deposited gravels

6 CONCLUSIONS

This study investigated the applicability of debris flow load evaluation using a DEM under channel flume conditions with a movable bed and pre-deposited gravel.

1. Experiments were conducted using a movable bed and pre-deposited gravel, and the loads acting on the dam were measured at various heights. Regardless of the presence of pre-deposited gravel, the highest load was observed at the point of impact, where the debris flow front collided with the dam.
2. Although modeling the debris flow fluid force under experimental conditions is complex, the analysis confirmed a certain level of applicability in reproducing the load evaluation.
3. When the front part of debris flow was trapped by the dam, a gravel deposition zone formed upstream because of the halted particles, reducing the velocity of subsequent gravels and leading to an overall decrease in the load.

As a future challenge, further investigations will focus on constructing a dynamic debris-flow load model by estimating and analyzing the loads based on modeled case studies of actual disaster conditions.

REFERENCES

[1] National Institute for Land and Infrastructure, Occurrence of sediment-related disasters in

2022, https://www.mlit. go.jp/river/sabo/jirei/r4dosha/r4doshasaigai.pdf (In Japanese)
[2] National Institute for Land and Infrastructure, A debris flow disaster occurred in Yomi, Minami Kiso Town, *Kiso District Nagano Prefecture*, 2014. (In Japanese)
[3] National Institute for Land and Infrastructure Management, Sabo basic plan formulation guideline (debris flow/driftwood countermeasures) commentary, No.904, 2016. (In Japanese)
[4] SABO & LANDSLIDE TECHNICAL CENTER, New edition steel pipe Sabo dam design Handbook (2021), Steel Sabo dams Committee, *Nissei eblo*, 2021. (In Japanese)
[5] Hideki, T. Kouichi, N. Kaori, H. Akihiko, T. and Hiroshi, M., Status of debris flow capture by Nakajo Sabo Dam, *Summary of the 63rd JSECE conference paper*, P2-69,2014. (In Japanese)
[6] Niigata Prefecture Civil Engineering Department, Erosion Control Division, Nechi River No. 10 Erosion Control Dam Countermeasures Review Committee, 3rd Discussion Materials, 2018. (In Japanese)
[7] Sakaya, T. Nobutaka, I. and Moriyama, H., Disaster case of 5th Sabo dam in Obu river, *Sabo Steel Structure Damage Investigation Committee*, 2019. (In Japanese)
[8] Kazuki, S. Toshiyuki, H., Fundamental examination for the damage factors of a steel pipe Sabo dam due to overflow boulder, *Journal of the Japan Society of Erosion Control Engineering,* Vol. 76, No. 6, pp. 3-10, 2024. (In Japanese)
[9] Shima, J. Matsuzawa, R. Ishikawa, N. and Mizuyama, T., Safety verification of steel open type Sabo dams against large scale debris flow, *Journal of the Japan Society of Erosion Control Engineering*, Vol. 71, No. 1, pp. 15-21, 2018. (In Japanese)
[10] Hiroshi, K. Joji, S. Toshiyuki, H. Yoshimi, S. and Nobutaka, I., QUANTITIVE ASSESSMENT ON LOAD-CARRYING CAPACITY OF STEEL OPEN DAMS, *Japan Society Civil Engineering A1*, Vol. 78, No. 3, pp. 316-330, 2022. (In Japanese)
[11] Miyoshi, I. and Suzuki, M., Experimental Study on Impact Load on a Dam Due to Debris Flow, *Journal of the Japan Society of Erosion Control Engineering*, Vol. 43, No. 2, pp. 11-19, 1990. (In Japanese)
[12] Takahisa, M. Hisami, S. Hiroshi, N. and Kazuki, M., Experimental Study of the Impact Force of Debris Flow to a Sabo Dam Made of Steel Pipes, *Journal of the Japan Society of Erosion Control Engineering*, Vol. 37, No. 5(136), pp. 30-34, 1985. (In Japanese)
[13] Kouji, I., Classification of debris flow, *Journal of the Japan Society of Erosion Civil Engineering Journal*, 20(3), pp. 44-49, 1978. (In Japanese)
[14] Takahisa, M., Calculation of debris flow impact force on defense dams and its problems, *Journal of the Japan Society of Erosion Control Engineering*, Vol. 112, pp. 40-43, 1979. (In Japanese)
[15] Atuyuki, D. Masahito, Y. and Kenta, N., Impact Force of Mud-Debris Flows Acting on Structure, *Annual journal of hydraulic engineering,* Vol. 38, pp. 557-562, 1994. (In Japanese)
[16] Tomoo, F. Kouta, G. and Eizo, N., MOVEMENT MECHANISM OF TSUNAMI BOULDERS ANALYZED BY THREE-DIMENSIONAL NUMERICAL SIMULATIONS OF COUPLED FLUID-SOLID MOTIONS, *Journal of Japan Society Civil Engineering*, Vol.80, No.7, 23-00064, 2024. (In Japanese)
[17] Kumpei, T. Mituteru, A. and Kiyonobu, K., SEEPAGE FAILURE SIMULATION OF A CAISSON-TYPE BREAKWATER USING AN ISPH-DEM COUPLED METHOD, *Journal of Japan Society Civil Engineering A2,* Vol.77, No.2, I_105-I_116, 2021. (In Japanese)
[18] Hiroki, K. and Shoji, F., STUDY ON THE VALLEY BEDS AND BANKS EROSION BY DEBRIS FLOWS, *Journal of Japan Society Civil Engineering*, Vol.80, No.16, 23-16051, 2024. (In Japanese)
[19] Osamu, S. Horiguchi, T. Masuhiro, B. and Satoshi, K., Analysis on effect of compressed deformation at joints on destruction form of steel open sabo dam, *Journal of Steel Construction Engineering*, Vol. 29, No. 116, pp. 29-39, 2022. (In Japanese)
[20] Shimakawa, O. Komatsu, Y. Horiguchi, T. and Katsuki, S., Debris Flow Load Reduction Effect on Front Inclination Angle of Open Sabo Dam Possessed By DEM, *Journal of*

applied mechanics, *Japan Society Civil Engineering*, Vol. 75, No. 2, I_175 - I_185, 2019. (In Japanese)

ELASTO-PLASTIC IMPACT RESPONSE ANALYSIS OF CUSHION RUBBER SET RC BEAMS

Tomoki Kawarai[a], Masato Komuro[b], Norimitsu Kishi[b] and Yasuyoshi Nagai[b]

[a]Muroran Institute of Technology, Japan, email: kawarai@muroran-it.ac.jp, [b]Muroran Institute of Technology, Japan

Keywords: RC beam, cushion rubber, drop-weight impact, FEM, impact response analysis

Abstract

Recently, a cushion rubber was placed on the girder ends of the bridge to mitigate the impact force excited due to the girder colliding with the abutment at earthquake shaking. Even though the intensity of the impact force can be effectively decreased by placing the rubber, the dynamic response characteristics of the rubber placed structures might not have clearly been understood. In addition, since the experimental studies are very costly, it is essential to promote the numerical studies. In this paper, to establish an numerical analysis method to acurately predict the dynamic response characteristics of the rubber placed RC beams under impact loading, 3D elasto-plastic impact response analysis of the RC beams was conducted and the applicability of the method was investigated comparing with the drop-weight impact loading test results. In this study, the time histories of the impact force, the reaction force, and the midspan deflection and also the crack patterns of the side-surface of the beam after the experiment were compared. The results obtained from this study are as follows; 1) dynamic response behavior of the cushion rubber placed RC beams can be appropriately evaluated by using the proposed analysis model and 2) maximum reaction force, maximum and residual deflections may not be significantly decreased by placing the rubber on the impacted area.

1 INTRODUCTION

The impact force occurred due to rocks dropping on the roof of the rockfall protection galleries is decreased by placing an absorbing material and/or system on the roof such as three-layered absorption system composed of sand layer, RC core slab, and an Expanded Poly-Styrene (EPS) block[1]. These absorption performances were investigated both experimentally and numerically. However, a cushion rubber is also sometimes used as an absorption material

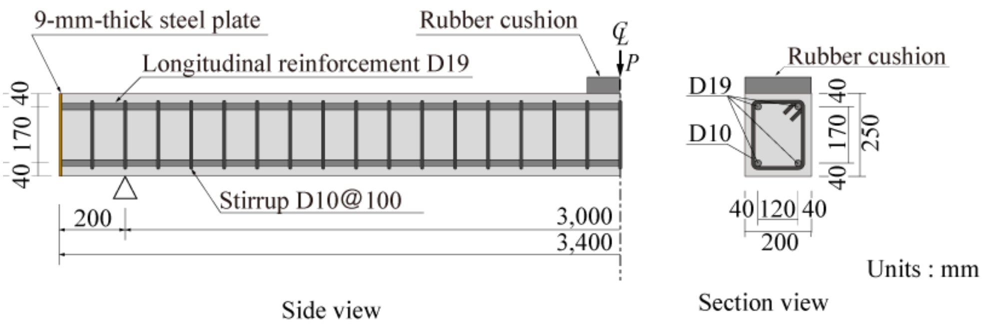

Figure 1. Configuration of specimen.

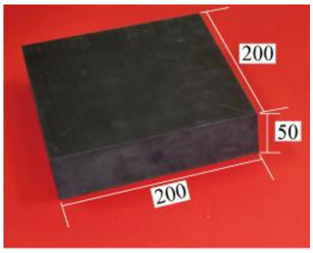

Unit : mm

Figure 2. Dimensions of cushion rubber.

applied to the fenders of ships, as the girder-end absorption device and/or the bridge fall prevention device to mitigate the damage occurred due to seismic loading.

Regarding impact loading tests of the structure with placing the rubber, Li et al. [2] investigated dynamic performance of the RC beam-column joints under impact loading with placing the rubber pad. Xiong et al. [3] conducted impact loading tests by using a blast simulator and numerical analyses for the RC slabs with placing the rubber. However, the impact loading tests of the RC structures with the rubber may be limited in the world. In Japan, even though the impact loading tests for the rubbers were conducted to decrease the primary impact force, the mitigation effect of the rubber on damage of the RC structures may not be investigated sufficiently [4, 5]. Since such experimental studies are very costly, it is also significantly important to establish a numerical analysis method to accurately evaluate the impact response behavior of the RC structures with placing the rubber under impact loading.

From this point of view, in order to establish a numerical analysis method for appropriately evaluating the impact-resistance behaviour of the cushion rubber placed RC structures under impact loading, 3D elasto-plastic impact response analysis of the RC beams was conducted changing constitutive model for the material of concrete: Karagozian & Case Concrete model (KCC) [6]; Continuous Surface Cap model (CSC) [7]; and a proposed model by using soil and foam failure model provided into the LS-DYNA code. The applicability of these models was investigated comparing with the experimental results. Here, the LS-DYNA code was used for these numerical analyses.

2 EXPERIMENTAL OVERVIEW

2.1 Overview of Specimen and Cushion Rubber

Figure 1 shows the dimensions and the rebar arrangement of the beams used in this study. The specimens have a rectangular cross-section of 200 × 250 × 3,000 mm (width × height × clear span length). Two axial rebars of D19 were placed at the upper and lower fibres and were welded to a 9 mm-thick steel plate at the ends to save the anchoring length of the rebars. Stirrups of D10 were placed at 100 mm intervals. The cushion rubber was placed on the loading point.

Figure 2 shows dimensions of the rubber. In this study, the natural rubber with hardness of 65 was used and its dimensions were 200 × 200 ×50 mm (width × length × depth) considering the width of the beam and the diameter of the cylindrical-shaped weight.

Table 1 listed the experimental conditions conducted in this study. The drop height of the weight was set as 1.0 m based on the previous study [5]. In this table, the measured velocity V' of the weight just before impacting, compressive strength f'_c of concrete, and yield strengthes f_y of the axial rebar and stirrup were also listed. The velocity V' was estimated using the equation of $V' = L/T$ in which T is the time of the laser sensor crossing the plate (L = 30 mm) attached to the side-surface of the drop weight just before impacting. The calculated bending strength P_{usc} was calculated using the multilayered method in accordance with the JSCE [1]. The ultimate compressive strain of the concrete was

Set drop height of the weight H (m)	Calculated impact velocity of the weight V (m/s)	Estimated impact velocity of the weight V' (m/s)	Compress-ive strength of concrete f'_c (MPa)	Yield stress of axial rebar f_{ya} (MPa)	Yield stress of stirrup f_{ys} (MPa)	Calculated bending strength P_{usc} (kN)	Calculated shear capacity V_{usc} (kN)
1.0	4.43	4.52	32.4	379	364	55	277

Table 1. Experimental conditions.

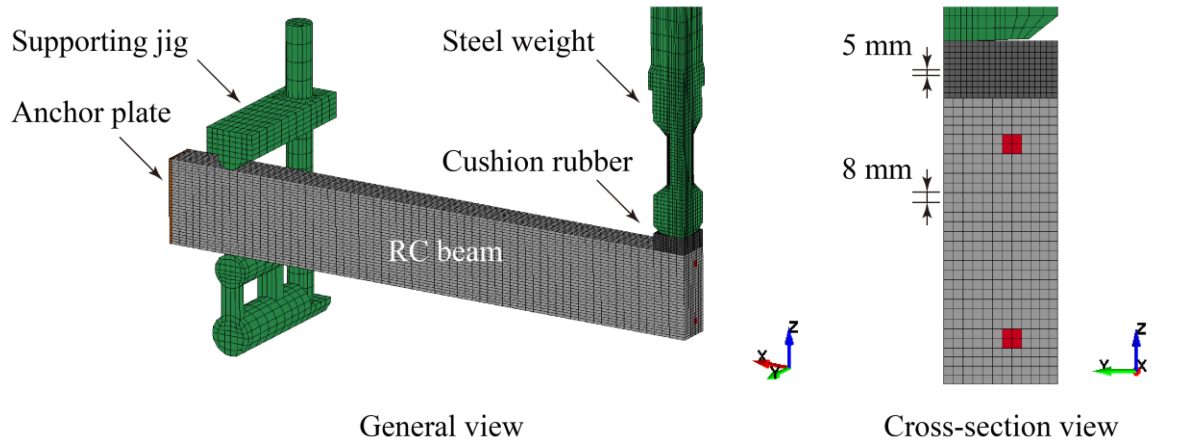

Figure 3. FE model.

assumed to be 0.35% following the Japan Concrete Standard [8]. The calculated shear capacity V_{usc} was also evaluated in accordance with the Standard [8].

2.2 Experimental Method

In this study, a 300 kg steel weight was used in which diameter of the cylindrical part is 200 mm and a nose part is squeezed to the diameter of 150 mm and is tapered spherically having 2 mm height. The weight was dropped on the midspan point from the predetermined height of H = 1.0 m.

The RC beams were placed on the supports equipped with load cells to measure the reaction forces, and they were clamped at the support points by using cross beams to prevent from lifting. The supports were able to freely rotate while restraining the horizontal movement of the beam. The measured items at the experiments are the impact force of the weight (referred to hereinafter as impact force), the total reaction force (referred to hereinafter as reaction force), and the midspan deflection of the beam (referred to hereinafter as the deflection). The impact force and reaction force were measured using load cells and the deflection, using a laser-type LVDT. In addition, a high-speed camera was used as a backup for the LVDT.

3 OVERVIEW OF NUMERICAL ANALYSIS

3.1 Numerical Model

Figure 3 shows the mesh geometry of the cushion rubber placed RC beam. One quarter of each RC beam was three-dimensionally modelled considering biaxial symmetry with respect to the midspan cross section and the central surface in the width direction of the beam. In this model, concrete, axial rebar, and the rubber were divided using eight node solid elements and stirrup was divided using beam elements. Axial rebars and stirrups were assumed to be perfectly bonded to concrete in this analysis. Element size of the concrete in the axial direction

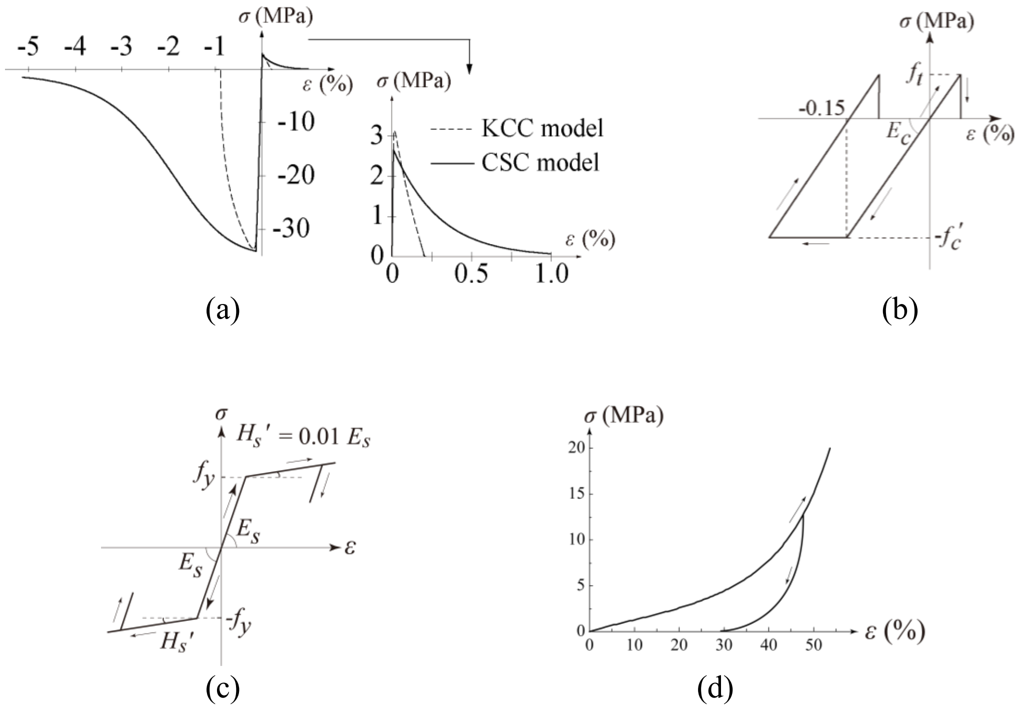

Figure 4. Constitutive models: (a) soil and foam failure model (mat 14); (b) KCC and CSC model (mat 72R3 and 159); (c) rebar; and (d) cushion rubber

was assumed to be 25 mm long basically. The rubber was divided into 5 mm cubes. The drop weight was also precisely divided using solid elements following the actual shape.

3.2 Constitutive Model

Figure 4 shows the constitutive models applied in this study. Many concrete models have been provided into the LS-DYNA code, for example, KCC model [6] and CSC model [7]. However, the applicability of these models to numerical analysis for the rubber placed RC beams under impact loading has not been sufficiently investigated yet. In this study, the applicability of each model: KCC (Mat 72R3), CSC (Mat 159), and a proposed model (Mat 14), was investigated comparing with the experimetnal results. These stress-strain relationships are shown in Fig. 4(a) and (b), respectively. Even though the functions for presenting behavior of the tension and compression softening are prepared in the KCC and CSC models, gradients of the softening are different between two models as shown in Fig. 4(a). the proposed model shown in Fig. 4(b) was assumed that, in the compression region: (1) yield stress was equal to the compressive strength f_c' ; (2) yield strain was set as 0.15% strains; and (3) yielding of concrete follows the Drucker-Prager's yield criterion; in the tension region, the tensile stress was cut off at reaching the tensile strength of the concrete. The tensile strength was evaluated using negative pressure. Compressive strength $f'c$ of concrete was 32.4 MPa, which is obtained from the material test at commencement of the experiment. Fig. 4(c) shows the constitutive model for the axial rebar and stirrups. The stress-strain relationship was defined using a bilinear isotropic hardening model. Here, the plastic hardening modulus (*H'*) was assumed to be 1 % of the elastic modulus (*E*s). Yielding was evaluated following the von Mises yield criterion. Fig. 4(d) shows the constitutive model for the rubber. The relationship was defined based on the experimental results and using simplified rubber model (Mat 181). In the large strain region, the relationship was extapolated by using the experimental results. The steel weight, supporting jigs, load-cells, and anchor plates for axial rebars were assumed to be elastic body according to the experimental

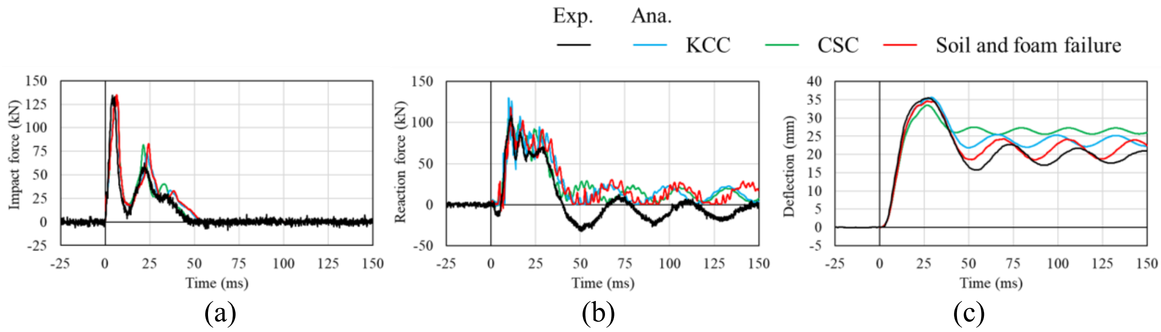

Figure 5. Comparisons of time histories of dynamic responses: (a) impact force; (b) reaction force; and (c) midspan deflection.

observations because no plastic deformation was observed in this study. Their material properties: Young's modulus E_s, Poisson's ratio v_s, and density ρ_s were assumed as E_s = 206 GPa, v_s = 0.3, and ρ_s = 7.85 g/cm^3, respectively.

4 COMPARISON OF NUMERICAL AND EXPERIMENTAL RESULTS

4.1 Time Histories of Dynamic Responses

Figure 5 shows comparisons of the time histories of the dynamic responses for the rubber placed RC beams between experimental results and numerical results obtained changing the constitutive model of the concrete mensioned above. Focusing on the impact force waveform shown in Fig. 5(a), the experimental results exhibit that a predominant impact force having amplitude of about 125 kN was excited at the beginning of impact and afterwards a second wave with a duration of about 35 ms was occurred. The numerical results obtained using three models indicate similar response characteristics to the experimentral ones.

From Fig. 5(b), it is observed that the reaction force time history obtained from the experimental result consists of a half-sine wave with a maximum reaction force of about 125 kN and a duration of about 40 ms and a damped free vibration wave after unloading. The main wave of reaction force obtained from three models considered in this study are approximately similar to the experimental results. However, the damped free vibration periods obtrained by using the CSC and KCC models are shorter than the experimetnal result and that obtained using the proposed model may be in better agreement with the experimental one.

Focusing on the deflection waveform shown in Fig. 5(c), the following can be observed: the maximum defelction obtained from the experiment is approximately 35 mm at passed time of about 25 ms from the beginning of impact and the experimental maximum and residual defelctions can be most accurately evaluated by using the proposed model among three models.

4.2 Crack Pattern

Figure 6 shows comparisons of the crack patterns on the side-surface of the rubber placed RC beam between experimental and numerical results. In these numerical analysis results, the elements that are evaluated to be under the crack opened completely, were colored in red. From Fig. 6(a), the experimental results exhibit that the bending cracks developed from the lower fiber at approximately equal intervls in the whole span of the beam. From Fig. 6(b), it is observed that the crack patterns obtained using both of the KCC and the proposed models may be in good agreement with the experimetnal results, however, the numercial results obtained by using the CSC model were evaluated for few crack to be distributed.

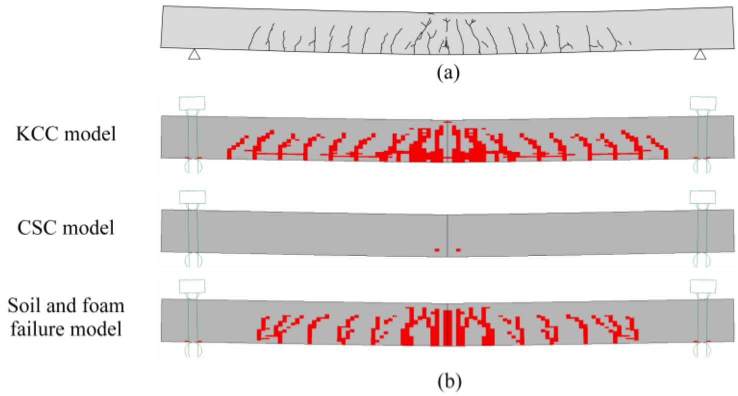

Figure 6. Crack patterns of side-surfaces of the beams: (a) experimental result; and (b) numerical results.

5 CONCLUSION

In this study, in order to establish an numerical analysis method to appropriately evaluate the impact-resistance behavior of the RC beams with placing the cushion rubber on the loading area, the impact response analyses were conducted changing the constitutive model for the material of concrete. The applicability of each constitutive model for the concrete was investigated comparing with the experimental results. As a result, it is seen that the proposed concrete model (Soil and foam failure model, Mat 14) can most appropriately evaluate the experimental results between the models considered in this study.

REFERENCES

[1] JSCE, Impact resistant design of rock-shed structures, Structural Engineering Series 8, Yotuya, Tokyo, Japan, 1998. (In Japanese)
[2] Li, H., Chen, W., Huang, Z., Hao, H., Ngo, T.T., Pham, T.M., "Influence of various impact scenarios on the dynamic performance of concrete beam-column joints", *International Journal of Impact Engineering*, Vol.167: 104284, 2022.
[3] Xiong, Z., Wang, W., Yu, G., Ma, J., Zhang, W., and Wu, L., "Experimental and numerical study of non-explosive simulated blast loading on reinforced concrete slabs", *Materials*, vol. 16(12): 4410, 2023.
[4] Kishi N., Ohno T., Mikami H. and Ando T., "Effects of boundary conditions on impact behaviors of reinforced concrete beams subjected to falling-weight impact loads", *Journal of JSCE*, vol. 731/I-63, pp. 299-316, 2003. (In Japanese)
[5] Kawarai T., Komuro M., Kishi N., Mikami H. and Suzuki K., "Drop-weight impact loading tests of cushion rubber set RC beams", *Journal of Structural Engineering*, vol. 67A, pp. 816-825, 2021. (In Japanese)
[6] Malvar, L. J., Crawford, J. E., Wesevich, J. W., Simons, D., "A plasticity concrete material model for DYNA3D", *International Journal of Impact Engineering*, Vol.19, No.19, pp. 847-873, 1997.
[7] Murray, Y. D., "Users manual for LS-DYNA concrete material model 159", Technical Report, 2007.
[8] JSCE, Standard specification for concrete structures-2007 design. Tokyo, Japan, 2007. (In Japanese)

15th International Conference on
Shock & Impact Loads on Structures
12-13 June 2025, Gothenburg, Sweden

MODELLING OF BOND-SLIP FOR IMPACT-LOADED REINFORCED CONCRETE BEAMS

Anders Ansell [a], Marek Pixa [a,b], Viktor Peterson [a], Mikael Hallgren [a,b]

[a] KTH Royal Institute of Technology, Sweden, email: ansell@kth.se
[b] Tyréns AB, Sweden

Keywords: Reinforced concrete, Drop-weight impact, Numerical modelling.

Abstract
Reinforced concrete is well-suited for resisting compressive stresses but relies on steel reinforcement to withstand tensile stresses, such as those caused by flexural deformations in beams or slabs. The interaction between concrete and steel, known as bond, facilitates stress transfer and relative displacement, known as bond slip. Concrete structural elements, including beams and slabs, may be subjected to static and dynamic loads. Static loads remain constant over the structure's lifespan, while dynamic loads, such as impacts or collisions, act briefly and intensively. This study investigates the bond-slip behaviour of reinforced concrete under static and dynamic loading through numerical simulations. A calibrated model for static pull-out tests of reinforcing bars was developed, incorporating two simulation approaches: the Cohesive and Connector methods. Both methods were assessed for accuracy, computational efficiency, and ability to capture important results, including deflection and plastic strain over time. Results indicate that both methods yield comparable outcomes but exhibit distinct differences. Compared to previous experimental data, the Cohesive method effectively captures reduced stiffness under static pull-out conditions. However, it underestimates the response once the nonlinear behaviour begins, where the Connector method provides a better match. The Connector method more accurately replicates experimentally observed failure modes for impact loading scenarios and is computationally more efficient. Meanwhile, the Cohesive method better represents deflection trends over time. Notably, lower bond strengths tend to result in bending failures, which are less brittle and offer greater energy absorption than shear failures. The results indicate important modelling considerations and the effect of the bond quality on the resulting failure mode.

1 BACKGROUND

In reinforced concrete structures, the bond that transfers tensile stresses between the reinforcing steel bars, rebars, and the surrounding concrete guarantees the load-carrying capacity. Bond influences the overall performance of structural concrete members, such as the number of cracks forming, their spacing, and the cross-section stiffness. Because of this stress transfer, the internal forces in steel and the surrounding concrete vary along the length of e.g. a beam. In a section where there is a difference in strain between concrete and steel, a relative displacement occurs, a phenomenon called bond-slip. Static loading most often leads to the formation of fine concrete cracks. However, partial or complete bond loss could lead to substantially wider cracks, which are not beneficial for structural stability. This does not necessarily have to be true for impact-loaded concrete structural elements.

Reviews of current research on bond-slip in reinforced concrete structures are presented by Zheng et al. [1] and Huang & Liu [2], focusing on ultra-high-performance concrete for the latter. An example of a recent investigation on the pull-out behaviour of steel bars in concrete is the work by Burdziński & Niedostatkiewicz [3]. Peterson & Ansell [4] describe a large test series on impact-loaded reinforced concrete beams. Relatively heavy impacting drop-weights were used to investigate the yielding of the reinforcing bars as the beams absorbed the kinetic energy from the load. Lozano Mendoza & Makdesi Aphram [5] and Syversen & Trinh [6] have also performed laboratory experiments with concrete beams loaded by drop-weights. The latter, carried out at Chalmers, provides the test results for comparison with the numerical analyses presented in this paper. Recently, Peterson et al. [7], Abdalnour & Saliba [8] and Ceberg & Holm [9] have also carried out projects with experimental testing on concrete beams followed by numerical analysis at KTH.

A recent project initiated at KTH [10] aim at investigating how the bond strength and the partial loss of the bond between reinforcement and surrounding concrete affects the structural performance and the cracking of structural elements. Based on results from previous laboratory tests [6], numerical simulations were carried out to investigate the importance of bond-slip in cases of impact loading. This paper summarizes part of this work, focusing on the relations between calculated element response and the choice of input parameters for the analysis. The aim was to study to what extent bond-slip models based on published research and guidelines describe the actual behaviour following impact loading.

2 CONCRETE-STEEL BOND

To achieve a composite structure, the forces from the steel must be transferred to the surrounding concrete. The bond allows anchorage of straight reinforcing bars, which are the major elements in reinforced concrete structural elements. The bond strength results from the interaction of three basic phenomena: adhesion, friction, and mechanical interlocking. Together, these mechanisms make transferring forces between reinforcement and concrete possible. However, a pull-out or splitting failure occurs along the reinforcing bars if these forces are too high.

2.1 Bond-slip behaviour

A consequence of the stress transfer is that the forces in the steel and surrounding concrete will vary along the length of a beam. In the section where the strain in concrete and steel differs, the relative displacement known as bond slip [10] follows the schematic behaviour shown in Figure 1. This is suggested in the Model Code [11] and is based on many pull-out tests. When the slip s is equal to or less than s_1, bond cracking and micro crushing of concrete is initiated and lead to a non-linear behaviour, following:

$$\tau = \tau_{\max} \left(\frac{s}{s_1}\right)^{\alpha} \tag{1}$$

where the coefficient α describes the increase in bond stress. Several possible forms of bond stress can be modelled depending on the coefficient selection.

For a bond with constant stress the coefficient is $\alpha = 0$, for a non-linear bond stress increase the coefficient is $0 < \alpha < 1$, and for a linear bond stress increase the coefficient is $\alpha = 1$, [11]. The maximum bond strength $\tau_{\max}$ is determined according to Eq. (2), which includes the bond coefficient β and the square root of the mean compressive value f_{cm}.

$$\tau_{\max} = \beta\sqrt{f_{\mathrm{cm}}} \tag{2}$$

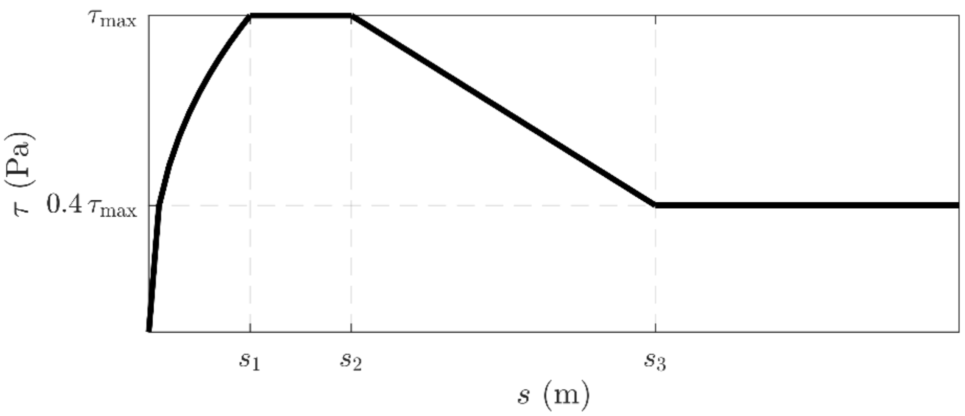

Figure 1. General bond stress-slip relation for reinforcement with various conditions and failure modes. According to [11].

In order to determine the coefficient β, the values of slip s for each stage, and the shear strength τ_f for the final stage, the Model Code [11] recommends using the values shown in Table 1. The bond strength τ_f can be calculated from a measured, applied tensile force F_a in a pullout experiment, see [10]. Based on EN 10080 [12], the following relation applies:

$$\tau_{\mathrm{f}} = \frac{1}{5\pi}\frac{F_a}{d^2}\frac{f_{\mathrm{cm,tar}}}{f_c} \tag{3}$$

Here, the diameter of the bar is d, the target value of the mean compressive strength $f_{\mathrm{cm,tar}}$ and the average concrete strength of the test specimens f_c. In Model Code [11] the following equation is suggested:

$$\tau_{\mathrm{f}} = \frac{F_a}{\pi\, d\, l_b} \tag{4}$$

that also accounts for the effective bond length l_b.

Table 1. Parameters defining bond strength and slip, from [11].

	Good bond	Other bond
β (–)	2.5	1.25
s_1 (mm)	1.0	1.8
s_2 (mm)	2.0	3.6
s_3 (mm)	c_{clear}*	c_{clear}*
α (–)	0.4	0.4
τ_f (MPa)	$0.4\,\tau_{\max}$	$0.4\,\tau_{\max}$

* c_{clear} is the spacing of the ribs.

2.2 Effect of bond strength

Many ways of determining the maximum bond strength are suggested in the literature. However, most versions follow the relation given by Eq. (2). In the Model Code [11], the suggested parameters for good bond conditions are those shown in Table 1. This value is a prediction, and it is therefore necessary to compare those with experimental results, as was done in [10]. By comparing the maximum experimental bond strength $\tau_{\exp}$ to the maximum calculated bond strength τ_{max}, characteristic ratios τ_{exp}/τ_{max} were obtained for combinations of different types of concrete strengths and steel diameters. Only pull-out tests following the specifications written in RC-6 [13] or EN 10080 [12] with a bonded zone length of five diameters were used. The results included originate from [3, 14-20]. In order to facilitate comparison, the results of each study were converted to bond strength τ_f. This was done using Eqs. (2-4). The resulting comparison is shown in Figure 2.

The conclusion from [10], shown in Figure 2, is that the Model Code [11] underestimates the bond strength. The calculated bond strength τ_{max} can be between 60% to 80% of the actual experimental value of τ_{exp}. On the other hand, the results of one paper [16] show that the Model Code [11] may sometimes also give an overestimation, with failure occurring earlier than expected.

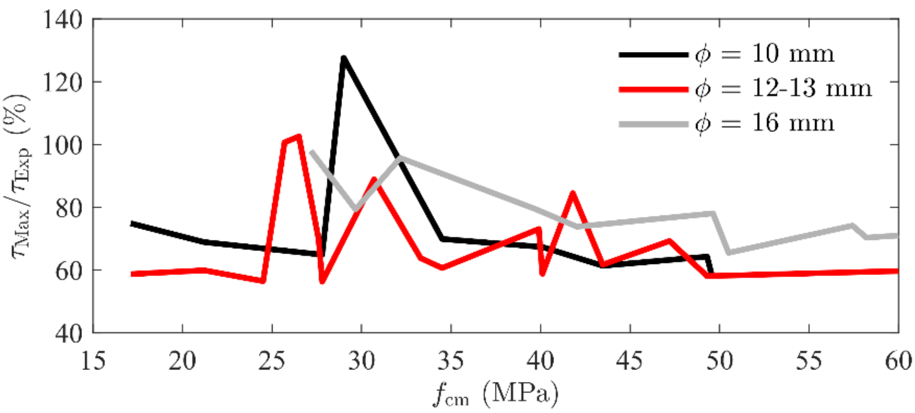

Figure 2. Comparison of calculated and experimental results of maximal bond strength based on concrete strength and bar diameter. From [10].

3 FINITE ELEMENT MODELS VS. EXPERIMENTS

The effect of bond-slip behaviour is in [10] studied through numerical simulations utilizing the general-purpose finite-element package Abaqus FEA [21]. Two types of models were created. The first study focuses on the static pull-out response of rebars, and the other studies the effect of repetitive impact loading on reinforced concrete structures. Experiments found in the literature were used to validate the models before investigating the bond-slip response.

3.1 Pull-out experiments

The effect of varying the bond coefficients and the methods for modelling the bond-slip response were studied [10]. For the Cohesive method of modelling bond, the interaction consisted of surface-to-surface contact between solid elements representing the concrete and reinforcement. This ensures that the steel and concrete interact. The linear elastic range of the bond stress relationship and the initiation and evolution of damage were then modelled using a traction-separation law following Eq. (1). On the other hand, the Connector method employs a model of the reinforcement as a beam or a truss, utilising connectors to establish a node-to-node bond. An intermediary part, directly connected to the concrete elements, is then created as a copy of steel reinforcement but with lower material stiffness. Both the Cohesive and Connector methods are described in detail by Mathern & Yang [22].

In Figure 3, the model based on the Cohesive method is shown to the left. Hexahedral solid elements with reduced integration and enhanced hourglass control are used with a mesh size of 10 mm on average for the concrete component and 2.5 mm for the reinforcement. The model includes both bonded and unbonded zones. The concrete block is clamped at the surface where the reinforcement is displacement controlled upwards. The restrictions apply to all displacement and rotations. The reinforcement is connected to the concrete by cohesive behaviour. Figure 3 also depicts a model of the Connector method, with an average mesh size of 5.0 mm for the concrete and 2.5 mm for the reinforcement. As the reinforcement is embedded in the concrete, only the bonded zone is modelled, as the unbonded zone cannot be represented. Translators connect the embedded intermediary part to the reinforcement. The boundary conditions are modelled identically to those employed in the Cohesive method. Hence, the concrete block is clamped at the surface where the reinforcement is loaded.

The experimental data and the curve determined using Model Code [11] are compared in Figure 4 to the left under the assumption of a pull-out failure with good bond conditions. The results are presented in terms of pull-out force and displacement. The curves show that Model Code [11] underestimates the experiment's results. This coincides with the conclusions from Section 2.2, which predicted underestimations of approximately 70%. In this comparison, it was discovered that the Model Code curve's maximum pull-out force is 61% of the experimental one. In order to reproduce the experimental results, the bond coefficient was modified. In Figure 4 to the right, two FE simulations and experiment results are compared. The results are presented in terms of force and displacement. The calibrated FE model, i.e. with a maximum bond coefficient of 4.1 compared to the recommendation of 2.5, agrees with the experimental results. The maximum pull-out force is comparable. The principal difference between the two methods is that the Connector method results in a larger initial stiffness than the Cohesive method. That is an interesting observation, because the Connector method aligns exactly with the Model Code curve, whereas this cannot be said about the Cohesive method. The Cohesive method better captures the earlier stiffness of the experiment until the non-linear behaviour is initiated. The difference between the two methods arises when slip initiates.

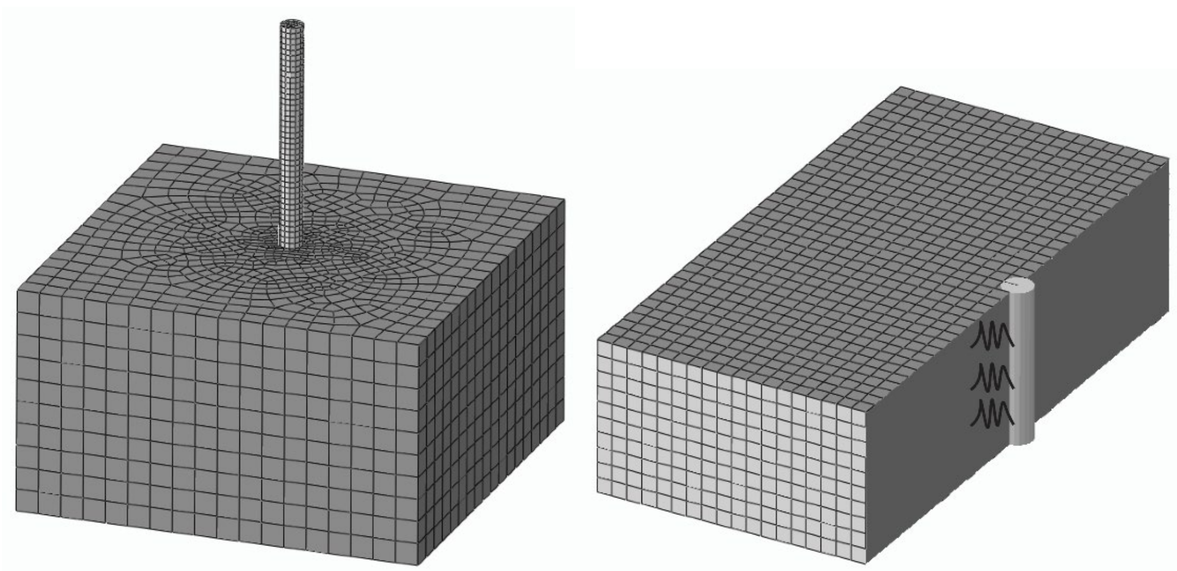

Figure 3. Models of the Cohesive method (L) and the Connector method (R), from [10].

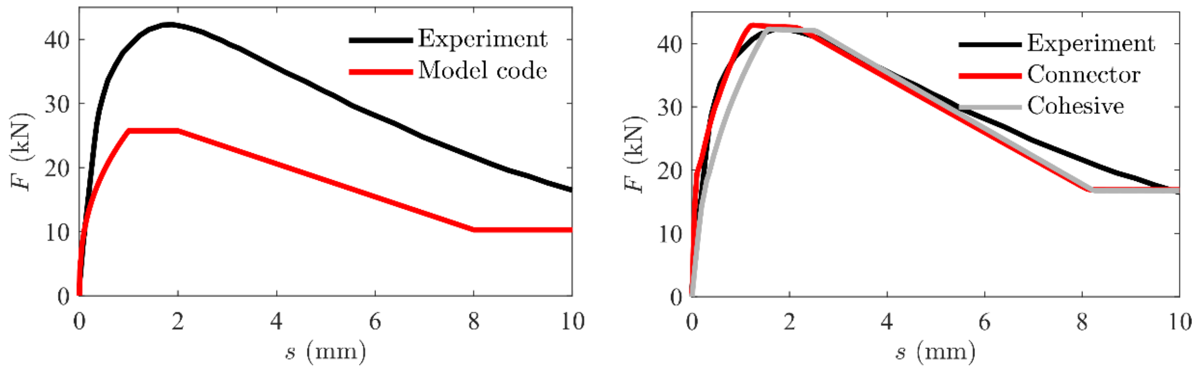

Figure 4. Comparison of experimental results with Model Code calculations (L) and between calibrated FE models and experiments (R), from [10].

3.2 Impact loading experiment

An experiment conducted at Chalmers [6] was used to study the effect of bond-slip parameters and modelling. The experiment consisted of concrete beams subjected to single and repeated loading from falling masses. The results for some of the beams show horizontal cracks in the concrete at the level of the reinforcement, which indicates significant bond-slip and is therefore appropriate for the study. A total of 18 beams were tested, with varying reinforcement of 6, 8, and 10 mm in diameter. The length of the beams was 2800 mm with a cross-section of 100×200 mm^2. Four longitudinal reinforcements were placed 40 mm from the top and bottom edge of the beam. Impact loading was created by dropping a weight from a height of 5 m. The drop-weight had the shape of a cylinder with a diameter of 120 mm. The beams were placed on roller supports, restricting the downward and upward movement. The supports were fixed to the concrete surface to ensure that all beams were in the same position when tested, as seen in Figure 5.

The concrete beam was modelled [10] utilizing mid-point symmetry to reduce the overall computational time. Two basic models were simulated, one for the Cohesive method and one for the Connector method. For the concrete beam, hexahedral solid elements with reduced integration and enhanced hourglass control were used with an average mesh size of 10 mm. A mesh size of 5 mm was employed for the reinforcement used in both models. The reinforcement was also represented as hexahedral solid elements with reduced integration for the model using the Cohesive method. For the single loading, the striker was modelled of hexahedral solid elements with reduced integration with a mesh size of 5 mm, also here using symmetry. The striker was dropped from 5 m onto the beam. In the model this drop is represented by the impacting velocity v_0 of the striker. In Figure 6, the complete model is shown.

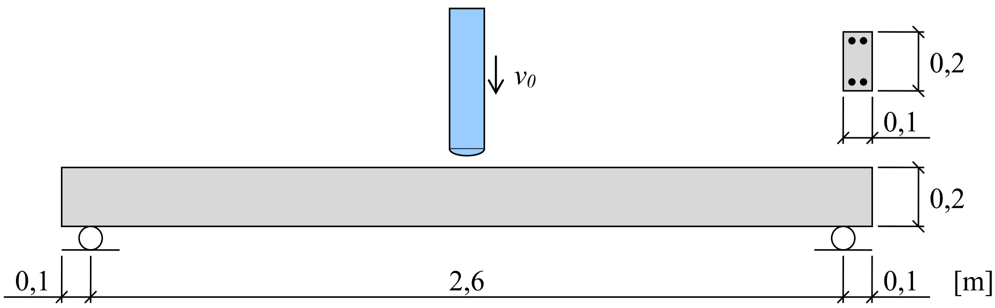

Figure 5. The drop-weight test setup used in [6].

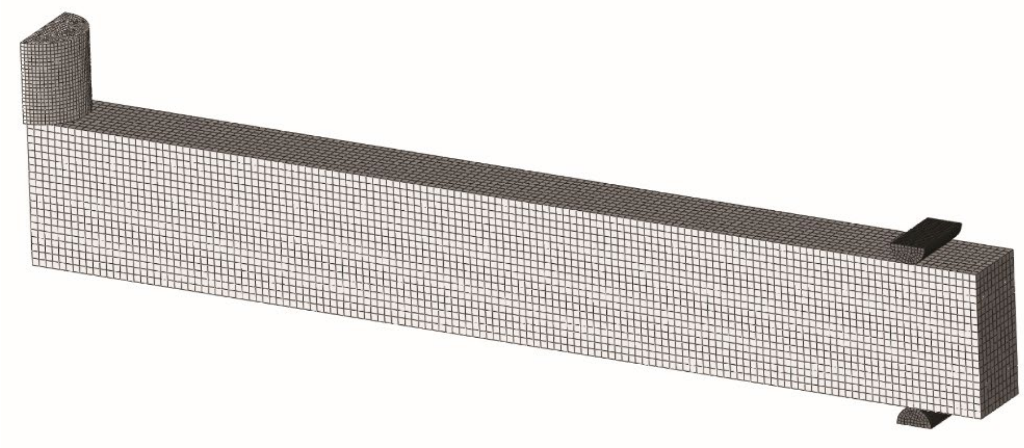

Figure 6. Meshed FE model of concrete beam, supports and drop-weight, from [10].

4 RESULTS

A contact force is developed at impact as the striker's momentum decreases. Figure 7 illustrates the contact force on the beam in time, determined from the contact stresses in simulation with the Connector method, assuming a perfect bond (PB) between the concrete and steel [10]. When the striker contacts the beam, a peak force of 450 kN develops. At approximately 0.15 ms, the two bodies separate for a short period. At approximately 0.25 ms, the striker hits the beam once again. This results in the beam being separated once more at approximately 1 ms. The third strike occurs around 1.7 ms. This marks the last separation, and then the two bodies are connected. This phenomenon precisely aligns with the theory of hard impacts.

Figure 8 shows examples of beam damage due to repeated loading by a drop weight. After the first drop, the beam displays a few flexural cracks at its bottom. Furthermore, damage around the reinforcement develops. After the second drop, much larger damage around reinforcement is visible. A few flexural cracks and a small crack at the top reinforcement can also be seen. After the third drop, a substantial horizontal crack appears, indicating the concrete's bond failure. Furthermore, the concrete is crushed where the striker hits the beam, and significant spalling takes place. A wide flexural crack under the impact zone is also visible.

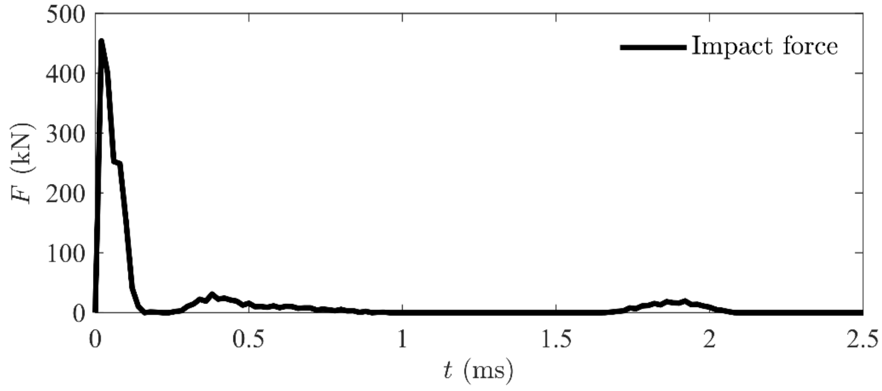

Figure 7. Load from striker impact, with Connector method under PB assumption, from [10].

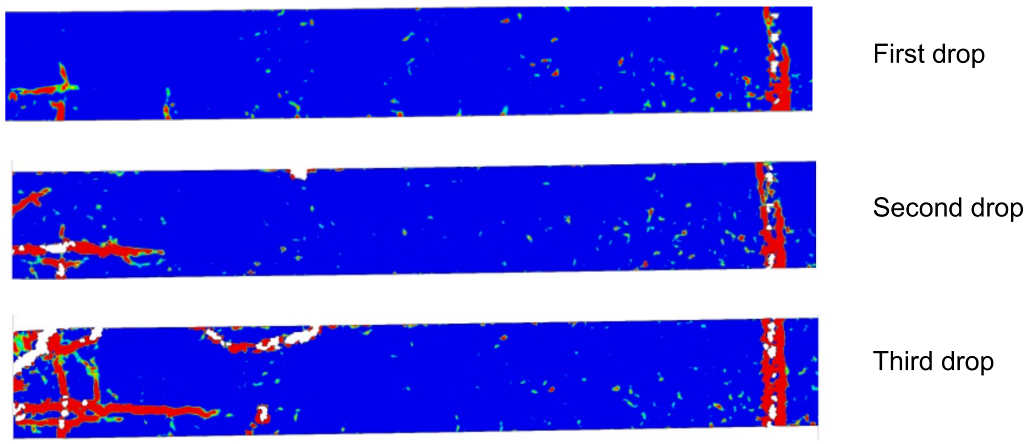

Figure 8. The strain fields of plastic deflection for repeated impact – first, second and third drop, from [6].

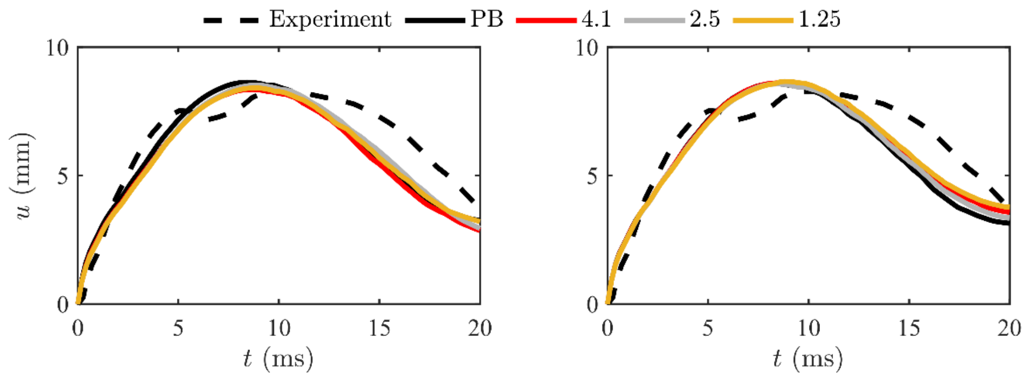

Figure 9. Effect of bond - Connector method (L) and Cohesive method (R). From [10].

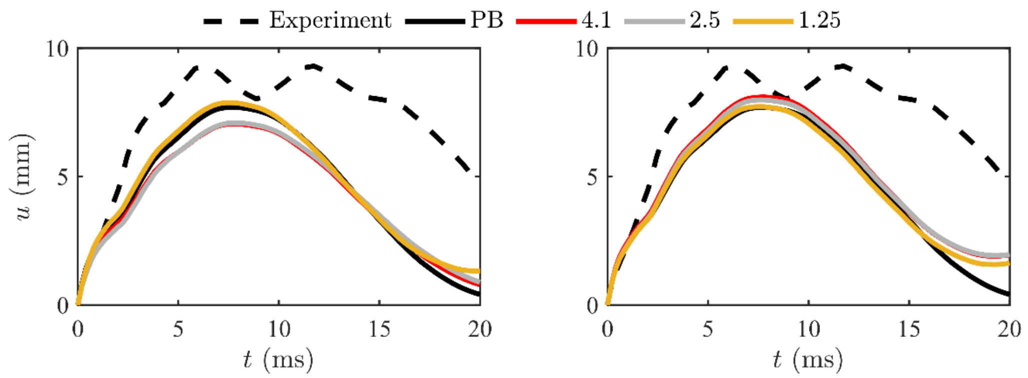

Figure 10. Comparison of FE simulation for different bond coefficients for the third drop - Connector method (L) and Cohesive method (R). From [10].

Figure 9 shows the results obtained with the Connector and Cohesive methods. In the experimental data shown, the displacement is derived using the reference displacement at the support (see [6] for this definition). However, the deflection for the FE simulations is obtained only using the midpoint vertical displacement. Therefore, the "shift" at around 5 ms is not visible in the FE results. Both methods capture the maximum deflection at the same time, indicating that both FE simulations replicate the experimental response. The simulations capture the initial stiffness of the experiment, as all of the curves are similar at that stage. The peaks of the FE simulations are slightly higher than for the experiment, but the results are similar. The discrepancies in the obtained peak values are between 0.7-4.0% for the Connector method and 3.8-4.5% for the Cohesive method.

Figure 10 shows the results for the third drop. The largest deflection occurred using a perfect bond (PB) for the previous drops. However, at the third drop, it was instead the model with a bond coefficient of 1.25. One possible explanation for this phenomenon is that the steel reinforcement exhibits a larger slip due to the lower bond capacity. The curves of the 2.5 and 4.1 bond coefficients are comparable, but the model with 4.1 shows a slightly smaller deflection, consistent with the results observed from the previous drops. The Cohesive method exhibits the opposite behaviour for the bond coefficients. The largest deflection occurs for the model with a bond coefficient of 4.1, followed by the model with 2.5. The curves are, however, generally similar. Apart from the deflection of the curve, the response in the models utilizing the two methods is comparable.

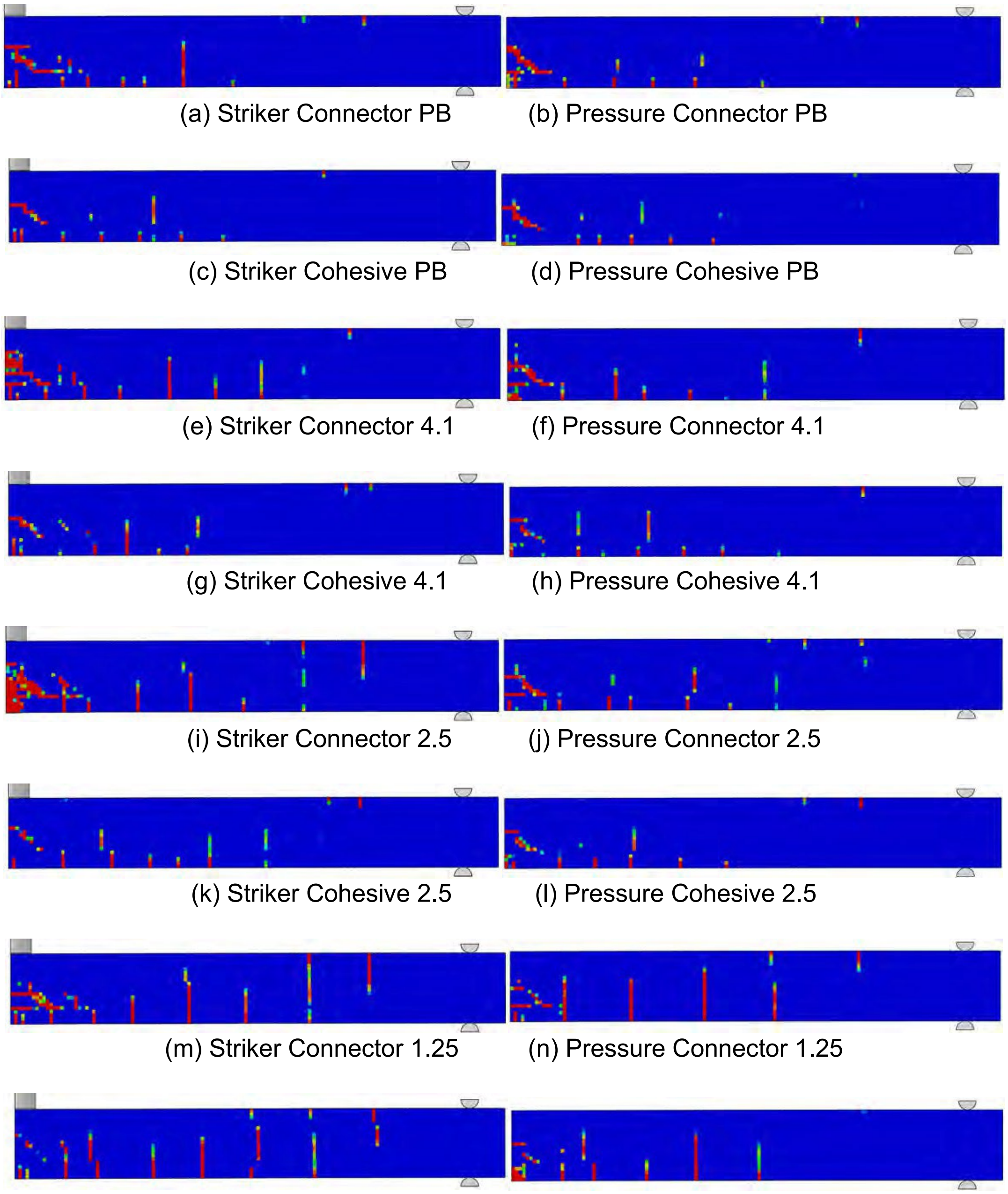

(a) Striker Connector PB (b) Pressure Connector PB

(c) Striker Cohesive PB (d) Pressure Cohesive PB

(e) Striker Connector 4.1 (f) Pressure Connector 4.1

(g) Striker Cohesive 4.1 (h) Pressure Cohesive 4.1

(i) Striker Connector 2.5 (j) Pressure Connector 2.5

(k) Striker Cohesive 2.5 (l) Pressure Cohesive 2.5

(m) Striker Connector 1.25 (n) Pressure Connector 1.25

(a) Striker Cohesive 1.25 (b) Pressure Cohesive 1.25

Figure 11. The damage in tension for striker impact and pressure load. Red indicates fully damaged elements. From [10].

Figure 11 illustrates 16 different beam configurations and compares two different load types - a striker hitting the beam and an impact load applied as a pressure, as described in Section 3.2. For further details, see [10]. The same bond coefficient modifications are presented next to each other, i.e. used for each row. The results of the striker and the pressure methods are generally comparable. The Cohesive method with assumed PB is a notable example, as the results appear similar and indicate the same type of behaviour. The least satisfactory results were obtained using the Connector method for bond coefficient 2.5, where the differences between the two methods are significant. There is less cracking for the pressure method, and the damage around reinforcement failures starts to show. However, the methods still display similar behaviour in terms of failure mode, which is important, and it can be stated that using pressure instead of a solid striker generally leads to good results.

Table 2 displays the computation time for each method and case and the average computation time for each method. The time required with the assumed PB is considerably less than that required with the Connector method. This is expected, given that the reinforcement is modelled as a beam in the Connector method compared to the Cohesive method, where it is a solid. The beam has a significantly smaller number of nodes, resulting in much shorter calculations.

Table 2. Computation time (sec.). From [10].

Type of simulation	Connector method	Cohesive method
Striker PB	00:15:37	00:34:42
Striker 4.1	00:52:00	00:52:00
Striker 2.5	00:52:05	00:43:42
Striker 1.25	00:51:18	00:42:02
Average Striker	00:42:45	00:43:07
Repeated load PB	00:27:26	01:15:19
Repeated load 4.1	01:50:17	02:18:48
Repeated load 2.5	01:51:38	01:55:28
Repeated load 1.25	01:47:53	01:37:16
Average Repeated load	01:29:19	01:46:43
Average Total time	01:06:02	01:14:55

5 CONCLUSIONS

The comparison between experimental testing and numerical modelling results indicates that the bond-slip behaviour in the Model Code [11] generally underestimates the bond strength. Therefore, a method for calibrating the bond strength between steel reinforcement and concrete was suggested and tested. A bond coefficient of 4.1 was found to be comparable to the experiments. This is for impact-problems important to consider, as a lower coefficient may in general design be conservative, but for impact loads this may wrongfully indicate a flexural failure mode which instead is non-conservative. Thus, a design based on the Model code would not be for the worst possible case. For conservative model results, a high bond coefficient or perfect bond should be used.

The comparison between the two methods tested for FE modelling, the Cohesive and Connector methods, reveals that both are generally comparable. However, slight differences in the results are evident, particularly in Figure 4, which illustrates the comparison between the calibrated FE model and experimental data. The Cohesive method closely matches the experimental stiffness initially, while the Connector method becomes more accurate as the analysis progresses. Since the only difference between the two methods is how the reinforcement is represented, this accounts for the observed variations. The way force transfer is influenced varies depending on the method used. The Connector method calculates nodal forces at the nearest nodes, which translators connect. In contrast, the Cohesive method directly transfers forces, leading to a smaller contact area when slip occurs, thus reducing the available area for force transfer. Theoretically, the Cohesive method should offer greater precision as it accurately represents stress transfer and reinforcement. However, this is not entirely the case, as the Connector method is more effective at capturing the failure mode. The Connector method is also more time-efficient, which could be crucial in complex analyses. When comparing deflection, the Cohesive method performs better in representing the peak displacement value. Based on these findings, the Connector method is advantageous for crack analysis and time efficiency. Conversely, the Cohesive method excels at simulating deflection, although it can be argued that the Connector method is sufficiently accurate.

The influence of varying bond conditions is substantial. In the static pull-out test, bond strength is significantly reduced when a smaller bond coefficient is applied, which aligns closely with the results predicted through hand calculations. These findings remain consistent under impact loading, where stress patterns follow the same principles. It can be concluded that a lower bond coefficient increases the likelihood of flexural failure in the beam as opposed to shear failure. Furthermore, with decreased bond strength, less concrete crushing is observed. This flexural-dominated behaviour is beneficial, as bending failure is less brittle and offers enhanced safety due to its higher energy absorption capacity. Experimental results also indicate these findings, demonstrating bond-slip behaviour and minimal flexural cracking without shear failure. For beams subjected to multiple impacts, results indicate that cracks will appear after the first drop, and the load response to subsequent impacts will differ somewhat. However, numerical results still show satisfactory outcomes.

The impact load was modelled both as a striker and as a pressure. In conclusion, the two modelling approaches yield similar results for deflection and crack patterns. This is an important finding, as using the pressure-modelled load reduces computational time, a critical factor in complex simulations.

ACKNOWLEDGEMENTS

Funding for the project was provided by the Swedish Transport Administration, the Swedish Fortifications Agency and the Civil Contingencies Agency (MSB), which is gratefully acknowledged. Many thanks also to Chalmers for providing test results as input for this study.

REFERENCES

[1] Y. Zheng, C. Fan, J. Ma, S. Wang. “Review of research on bond–slip of reinforced concrete structures”, *Construction and Building Materials*, 385:131437, 2023.

[2] Y. Huang, Y. Liu. “Review of bond-slip behavior between rebar and UHPC: Analysis of the proposed models”, *Buildings*, 13(5), 2023.

[3] M. Burdziński, M. Niedostatkiewicz. “Experimental-numerical analysis of the effect of bar diameter on bond in pull-out test”, *Buildings*, 12(9), 2022.

[4] V. Peterson, A. Ansell. “Static and dynamic four-point flexural tests of concrete beams with variation in concrete quality, reinforcement properties and impact velocity”, *Nordic Concrete Research*, 6, pp. 19-38, 2021

[5] F. Lozano Mendoza, J. Makdesi Aphram. *Concrete beams subjected to drop-weight impact and static load: Structural behavior and plastic rotational capacity from experiments and finite element analysis*. Master thesis, Chalmers University of Technology, Gothenburg, Sweden, 2017.

[6] S. Syversen, C. Trinh. *Reinforced concrete beams subjected to repeated drop-weight impact and static load*. Master thesis, Chalmers University of Technology, Gothenburg, Sweden, 2023.

[7] V. Peterson, A. Ansell, M. Hallgren. “On the residual static and impact capacity of shear reinforced concrete beams subjected to an initial impact”, *Applied Sciences*, 12, 11377, (2022).
[8] J. Abdalnour, M. Saliba. *Drop-weight impact tests on reinforced concrete beams*. Master thesis, KTH Royal Institute of Technology, Stockholm, Sweden, 2023.
[9] E. Ceberg, E. Holm. *Numerical simulations of impact-loaded reinforced concrete beams*. Master thesis, KTH Royal Institute of Technology, Stockholm, Sweden, 2024.
[10] M. Pixa. *Dynamic loaded reinforced concrete Influence of bond-slip behaviour.* Master thesis, KTH Royal Institute of Technology, Stockholm, Sweden, 2024.
[11] J. Cairns. *Model Code 2010 - First complete draft*. International Federation for Structural Concrete (fib), 2010.
[12] European Committee for Standardization. *Steel for the reinforcement of concrete – weldable reinforcing steel – general*. EN 10080:2005, 4 2005.
[13] M. Arezoumandi, A. R. Steele, J. S. Volz. “Evaluation of the bond strengths between concrete and reinforcement as a function of recycled concrete aggregate replacement level”, *Structures*, 16, pp. 73-81, 2018.
[14] M. Baena, L. Torres, A Turon, C. Barris. “Experimental study of bond behaviour between concrete and FRP bars using a pull-out test”, *Composites Part B: Engineering*, 40(8), pp. 784-797, 2009.
[15] E. P. Carvalho, E. Guariento Ferreira, J. Celso da Cunha, J. C. de Souza Rodrigues, M. Nilton da Silva. “Experimental investigation of steel-concrete bond for thin reinforcing bars”, *Latin American Journal of Solids and Structures*, 14(11), pp. 1932-1951, 2017.
[16] T. J. Looney, M. Arezoumandi, J. S. Volz, J. J. Myers. “An experimental study on bond strength of reinforcing steel in self-consolidating concrete”, *International Journal of Concrete Structures and Materials*, 6, pp. 187-197, 2012.
[17] N. Majain, A. B. Abd. Rahman, A. Adnan, R. Noor Mohamed. “Pullout behaviour of ribbed bars in self-compacting concrete with steel fibers”, *Materials Today: Sustainable Integrated Engineering International Conference*, 2021.
[18] RILEM TC. *RC 6 Bond test for reinforcement steel. 2. Pull-out test, 1983*. E & FN SPON, 1994.
[19] D. Shen, X. Shi, H. Zhang, X. Duan, G. Jiang. “Experimental study of early-age bond behavior between high strength concrete and steel bars using a pull-out test”, *Construction and Building Materials*, 113, pp. 653-663, 2016.
[20] B. V. Silva, M. P. Barbosa, L. C. P. Silva Filho, M. S. Lorrain. ”Experimental investigation on the use of steel-concrete bond tests for estimating axial compressive strength of concrete: Part 1”, *Bracon Structures and Materials Journal*, 6(5), pp. 715–736, 2013.
[21] Dassault Systemes. *ABAQUS/CAE 21.* 2021.
[22] A. Mathern,. J. Yang. ”A practical finite element modeling strategy to capture cracking and crushing behavior of reinforced concrete structures”, *Materials*, 14(3), pp. 1-24, 2020.

15th International Conference on
Shock & Impact Loads on Structures
12-13 June 2025, Gothenburg, Sweden

DYNAMIC RESPONSE BEHAVIOR OF SUBWAY STATION STRUCTURE INPUTTING FORCED DISPLACEMENT AT BEDROCK VARYING NUMBER OF CFT CENTRAL COLUMNS

Norimitsu Kishi[a], Masato Komuro[b] and Tomoki Kawarai[c]

[a]Muroran Institute of Technology, Japan, email: kishi@muroran-it.ac.jp, [b]Muroran Institute of Technology, Japan, [c]Muroran Institute of Technology, Japan

Keywords: Hanshin-Awaji earthquake, inland earthquake, subway station, impulse uplift, elasto-plastic response analysis

Abstract

The Daikai Station subway structure in Japan completely collapsed in the great Hanshin-Awaji earthquake that occurred 30 years ago, on January 17, 1995. Since it deformed in an approximately symmetrical manner with respect to the shortened central columns, it might have experienced its catastrophic collapse due to a vertical impulse motion. To investigate the dynamic response behaviour of the structure with the central columns composed of concrete-filled steel tubes (CFTs) that were used to increase the strength of the existing RC columns when the station was reconstructed, a 3D elastoplastic transient response analysis of the station structure was conducted by surcharging an isolated upward pulse-like displacement wave from the bedrock and varying the number of the CFTs for each central column. The results obtained from this study are as follows: on inputting a displacement wave of 5 ms duration and 4 m/s velocity, crushing of the central columns may be effectively prevented by replacing the RC structure with a CFT structure for the central columns; thus the reconstructed station structure, whose central column was strengthened by using three CFTs, should be in a structurally healthy condition when suffering a severe earthquake such as the Great Hanshin-Awaji earthquake.

1 INTRODUCTION

The Hyogoken-Nanbu (Hanshin-Awaji) earthquake occurred 30 years ago, on January 17, 1995, in southwestern Japan. More than 4,600 people's lives were lost and many bridges and infrastructures in the Kobe-Osaka area suffered severe damage. The registered magnitude of the earthquake was 7.2 on the Richter scale and the focal depth was 16 km below ground level. The Kobe Ocean Meteorological Observatory Station located approximately 20 km northeast of the epicenter recorded peak ground accelerations of 8.2 m/s^2, 6.2 m/s^2, and 3.3 m/s^2 in the N-S, E-W, and U-D directions, respectively, with a peak ground velocity of 1.05 m/s.

Almost all infrastructures were damaged due to the strong lateral vibration of the earthquake. However, it was found that the damage was due to the unlikely phenomenon of a strong lateral vibration of the earthquake; circumferential cracks occurred in the concrete bridge piers and the upper and/or lower parts of the bridge piers were crushed. The collapse of the Daikai Station subway structure [1] indicates that the failures could be caused by the observed vertical motion. In particular, the significant damage to the Daikai Station subway structure as shown in Figure 1 was the first severe failure worldwide to

Figure 1 and Figure 2 are added images. Their tags and the figure text are below.

Figure 1. Compression failure of the central columns of the Daikai Station subway structure [2].

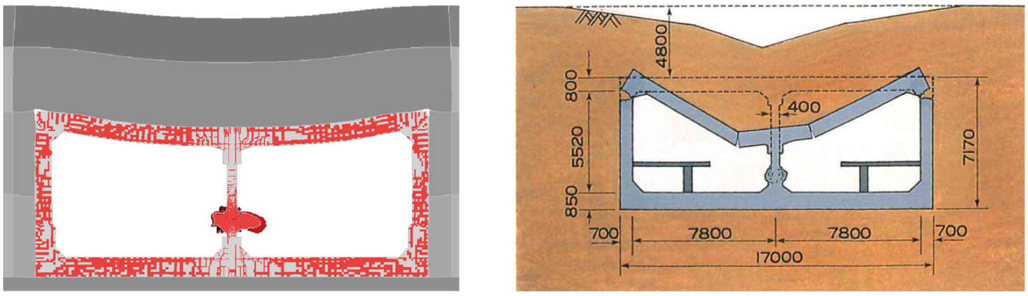

(a) (b)

Figure 2. Crack patterns and deformation of the station structure under a single uplift displacment: (a) numerical results [3]; and (b) actual damage [2].

correct the general perception of geotechnical engineers regarding underground structures having a higher seismic performance than surface structures. This is because (if there is no liquefaction) underground structures that do not cross an active fault follow the deformation of the surrounding ground during the earthquake and usually have a smaller unit weight than that of the subsoils. Since the structure was significantly deformed due to axial compression failure, while remaining approximately symmetrical with respect to the shortened central columns, it is not easy to maintain that the damage was caused by the strong lateral vibration of the earthquake.

The authors have tried to represent numerically the compression failure of the Daikai Station subway structure by including soil layers underneath the station and a single pulse-like uplift displacement at the base stratum [3]. The results indicated that the central column of the station collapsed in the compression failure mode and the ground surface subsided by more than 600 mm below the original ground level for a load duration of 5 ms and a velocity of 4 m/s as shown in Figure 2.

In this study, to investigate the dynamic response behaviour of the station structure with the central columns composed of concrete-filled steel tubes (hereinafter, CFTs) applied to additionally strengthen the existing RC columns when the station was reconstructed, 3D elastoplastic dynamic response analyses of the station structure were conducted, varying the number of CFTs for each central column. These numerical simulations were conducted using LS-DYNA code [4].

2 OUTLINE OF NUMERICAL ANALYSIS

2.1 Numerical model

Figure 3 shows the cross-sectional dimensions and an actual central column of the

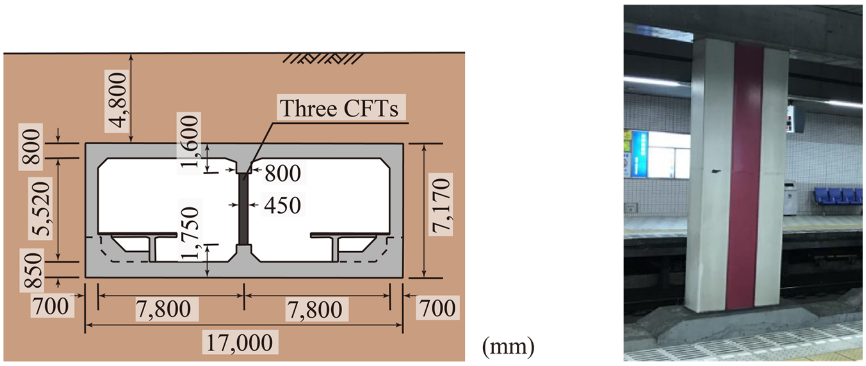

(a) (b)

Figure 3. Post-earthquake reconstructed subway station: (a) dimensions of cross-section; and (b) a view of the central column.

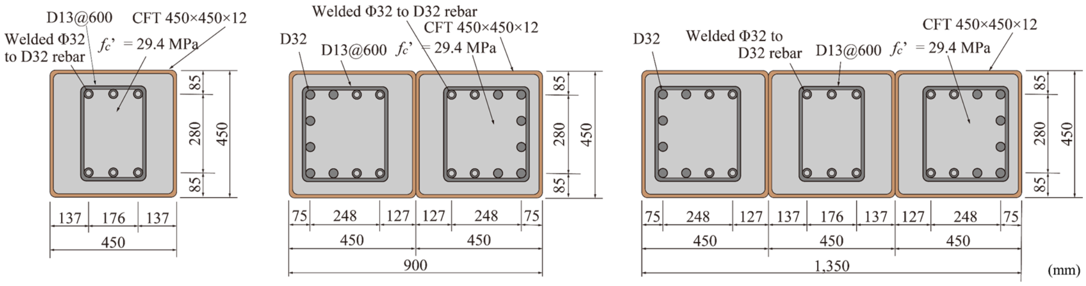

(a) (b) (c)

Figure 4. Cross-sectional dimensions and rebar arrangement of central columns: (a) Column 1-CFT; (b) Column 2-CFT; and (c) Column 3-CFT.

reconstructed Daikai Station subway structure. Figure 4 shows the cross-sectional dimensions and rebar arrangement for each central column considered, wherein these are designated as Columns 1-CFT, 2-CFT, and 3-CFT, respectively. In this study, the number of CFTs was varied from 1 to 3, with 3 CFTs is for the column investigated here. The numerical simulation was carried out for the structure subjected to an isolated upward displacement wave of short duration focusing on the main section, that suffered severe damage during the Hanshin-Awaji earthquake. Figure 5 shows the numerical analysis model, in which Figure 5(a) shows the discretization for the symmetrical cross section of the whole structure including the surrounding soils. The soil layers were discretized in the region from the base stratum to the ground surface and laterally more than twice the width of the main section of the station on both sides. The surrounding soils consist of 7 layers, in which diluvial deposits (Pleistocene clay, sand, and gravel) have been overlain by alluvial deposits (Holocene clay and sand) [5]. The decomposed granite soil was used as backfill material for the sidewalls.

A non-reflecting boundary condition was applied to the ends of the surrounding soil layers and the bottom surface of the base stratum. A contact algorithm with the ability to consider sliding without friction and separating actions was employed for the following two adjoining surface elements: between backfilled elements and the outer surface of the sidewall, between the bottom surface of the base slab and the upper surface of the soil layer in contact with the slab, and between the bottom surface of the overburden soil and the upper surface of the ceiling slab, respectively. Figure 5(b) shows the 3D discretization for the main section of the station without platforms for the numerical simulation. Since the station's central columns are arranged in a centre-to-centre spacing of 3.5 m, just a part of the station supported by a single column was taken into consideration in the longitudinal

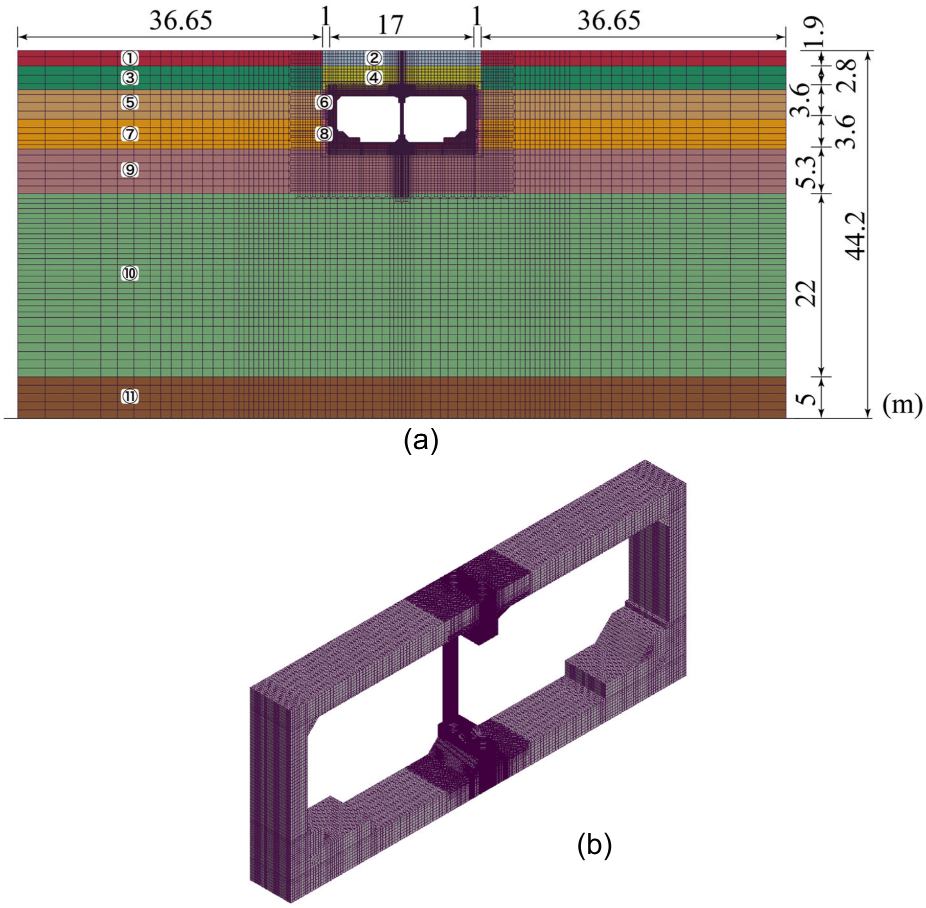

Figure 5. FE model of the Daikai Station subway structure: (a) discretization of the cross-section including surrounding soils; and (b) 3D discretization of main section of the station.

direction. The rebars were discretized by using beam elements and isolating from the concrete elements following the actual structure of the station before collapse. These were perfectly bonded with the concrete elements by coupling.

Regarding the boundary conditions, the nodal points in the symmetrical surface and the end surface in the longitudinal direction were restrained in the normal directions. The damping factor was ignored. Self-weight was also considered in the numerical analyses.

2.2 Constitutive model

Figure 6 shows the stress-strain relationship for each material used in this numerical analysis: concrete, rebars, overburden and backfilled soils. However, the surrounding soil layers excluding the remoulded soils described above were assumed to be elastic. The material properties for each layer were listed in Table 1 [5] [6]. In this table, layer numbers refer to those in Figure 5(a).

In this study, the Karagozian & Case concrete model (KCC model or MAT072R3 in LS-DYNA [4]) as shown in Figure 6(a) was employed for the concrete. This model can allow automatic generation for all the parameters by inputting only the compressive strength f'_c, Poisson's ratio v_c, density of concrete ρ_c, and element size [7]. The compressive strength of the concrete was set to f'_c = 37 MPa [6]. The Poisson's ratio and density were assumed as v_c = 1/6 and ρ_c = 2.3×10^3 kg/m^3, respectively. The tensile strength was estimated to be

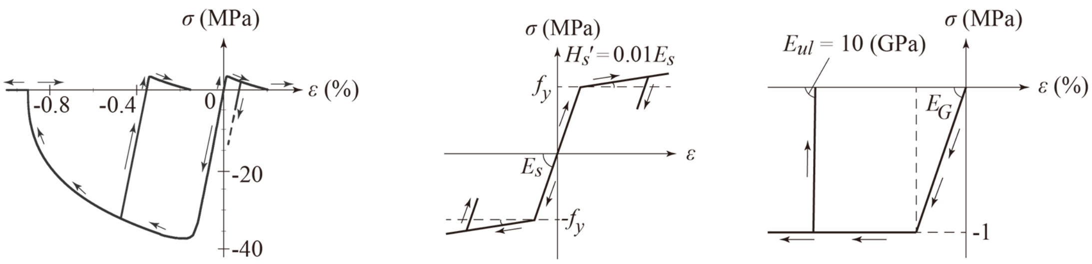

(a) (b) (c)

Figure 6. Constitutive models for materials: (a) concrete; (b) rebar and CFT; and (c) overburden soil.

Layer No.	Soil type	Density ρ_G (kg/m^3)	Young's modulus E_G (MPa)	Shear velocity C_G (m/s)	Comp. strength (MPa)	Yield strain	Poisson's ratio
1	Alluvium clay	1.9×10^3	99	140	1	0.01	0.33
2	Backfilled	1.9×10^3	54	100	1	0.018	0.43
3	Alluvium sand	1.9×10^3	111	140	1	0.009	0.49
4	Backfilled	1.9×10^3	96	130	1	0.01	0.49
5	Diluvium sand	1.9×10^3	164	170	-	-	0.49
6	Backfilled	1.9×10^3	145	160	1	0.007	0.49
7	Diluvium clay	1.9×10^3	205	190	-	-	0.49
8	Backfilled	1.9×10^3	146	160	1	0.007	0.49
9	Diluvium clay	1.9×10^3	326	240	-	-	0.49
10	Diluvium gravel	2×10^3	648	330	-	-	0.49
11	Diluvium clay	2.1×10^3	1,544	500	-	-	0.49

Table 1. List of material properties of soil layers.

approximately one-tenth of the compressive strength, and the compressive and tensile stresses were released at approximately -0.9 % and 0.2 % strain, respectively.

Figure 6(b) shows the stress-strain relationship for the axial and shear rebars used in this study, in which a bi-linear type of constitutive model was applied taking into account the plastic hardening effect after yielding. The yield strength of the rebar was set to f_y = 306 MPa. The density ρ_s, elastic modulus E_s, and Poisson's ratio v_s for the rebar were assumed using the nominal values: ρ_s = 7.85 × 10^3 kg/m^3, E_s = 206 GPa, and v_s = 0.3, respectively. It was assumed that yielding of the rebar followed the von Mises yield criterion and the plastic hardening coefficient H'_s was assumed to be 1 % of the Young's modulus E_s.

Figure 6(c) shows the stress-strain relationship for the overburden soils at the station constructed by means of the cut-and-cover method and backfill for the outer side of the walls. The model was assumed to be a perfectly elastoplastic body and the elastic modulus at unloading, E_{Gul} = 10 GPa for the stress to be perfectly released as soon as the soil unloaded and also not to resist the tensile force.

2.3 Model of input uplift displacement wave

Assuming a single pulse-like uplift motion with a period T_0 at the base stratum, the bottom surface of the stratum was forcibly and linearly moved up to the maximum displacement $d_{i,max}$ during the half time of the period T_0 and was then kept at this displacement. Figure 7 shows the schematic displacement d_i-time t and velocity of the displacement V_i-time t relationships. From this figure, it is seen that the velocity V_i of this movement is obtained as $V_i = 2\ d_{i,max} / T_0$ and after passing the time of T_0/2 the velocity V_i drops to zero.

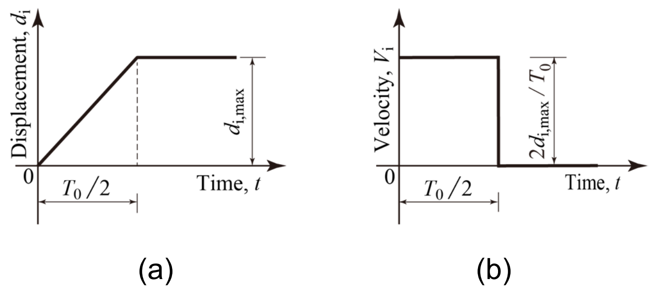

Figure 7. Schematic time histories of input wave: (a) displacement; and (b) velocity of displacement.

In this study, numerical simulations were conducted inputting the period T_0 = 10 ms and velocity of the movement V_i = 4 m/s, in which the maximum displacement $d_{i,max}$ was estimated as $d_{i,max}$ = 20 mm.

3 NUMERICAL RESULTS

3.1 Time history of displacement

Figure 8 shows comparisons of the time histories of the vertical displacements d and the velocities V in the station structure and soil layers in the cases of varying the number of CFTs of the central columns together with the RC column (hereinafter, referred to as Column RC) before it suffered damage from the earthquake. In this figure, to investigate the propagation

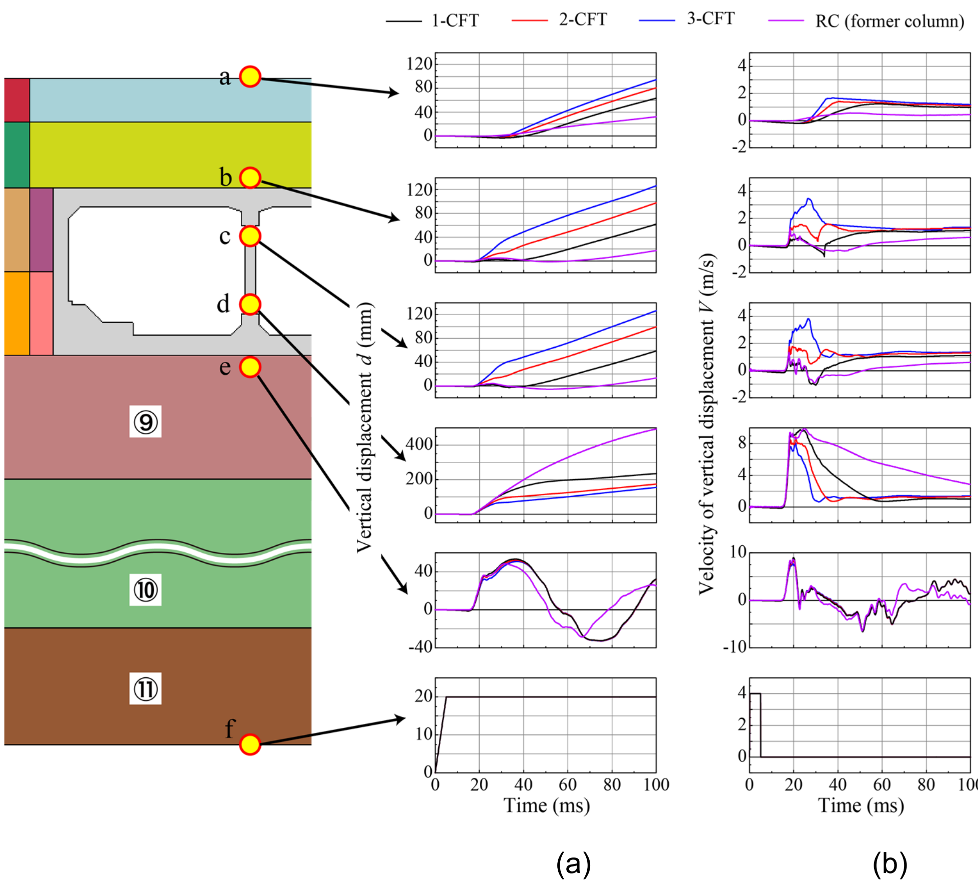

Figure 8. Comparisons of time histories of dynamic responses: (a) vertical displacement; and (b) velocity of vertical motion.

characteristics of the wave passing through the station structure from the base stratum, each time history is indicated for points along the axes of the central column up to the time t = 100 ms from the beginning of uplift loading (hereinafter, referred to as time t).

In Figure 8(a), the time histories are compared with the displacements between the lower point of the column and the upper surface point of the soil layer just below the base slab. Even though the time histories behave similarly up to the time t = 23 ms, afterwards, all time histories at the column increase monotonically but the time histories at the soil layer do not increase in magnitude in a similar way to them and the soil layer vibrates alternatively with a period of approximately 60 ms regardless of the number of CFTs. The amplitude of the time history at the column tends to increase corresponding to the decrease of the number of CFTs and that for Column RC is the largest among them. The displacement time histories at the upper point of the column increase monotonically and tend to increase corresponding to an increase of the number of CFTs; the amplitudes of the time histories for 1-CFT, 2-CFT, and 3-CFT columns at time t = 100 ms are approximately 60, 100, and 130 mm, respectively, and that for the Column RC is the smallest and is less than 20 mm. Therefore, it is seen that the relative displacement between the lower and upper points of the column tends to increase corresponding to the decrease of the axial stiffness of the column as mentioned below.

From the distributions of the time history of the displacement velocity at the upper surface point of the soil layer just below the base slab shown in Figure 8(b), it is seen that the distributions in a sinusoidal vibration state are similar to those of the displacement. The velocities of the motion at the lower point of the column for Columns 1-CFT and RC are the highest among all the columns considered and the velocity tends to increase corresponding to a decrease of the axial stiffness of the column. The decreasing ratio of the velocity after reaching the maximum velocity of the motion tends to increase with an increase of the axial stiffness of the column; the velocity for Column 3-CFT with the largest stiffness for all columns considered rapidly decreased and then is asymptotically close to velocity of 1 m/s. The region over the lower point of the column in the case of the central column with CFTs at around time t = 100 ms move up with velocity of approximately 1 m/s and that for the case of Column RC, more slowly than those of the column with the CFTs.

Figure 9 shows comparisons of the time histories of the relative displacement and the average strain between the lower and upper points of the central column composed of three columns with CFTs and with Column RC. From this figure, it is observed that the displacement (average strain) at time t = 100 ms tends to decrease with an increase of the number of the CFTs: the displacements (strains) for Columns 1-CFT, 2-CFT, and 3-CFT are 177 mm (4.7%), 75 mm (2%), and 30 mm (0.8%), respectively. Since the displacements (strains) for all cases except Column RC are constant after passing approximately the time t = 50 ms, the severe local buckling of the column may not occur for the station structure as in the compression failure state. On the other hand, in the case of Column RC, the station is certainly in a

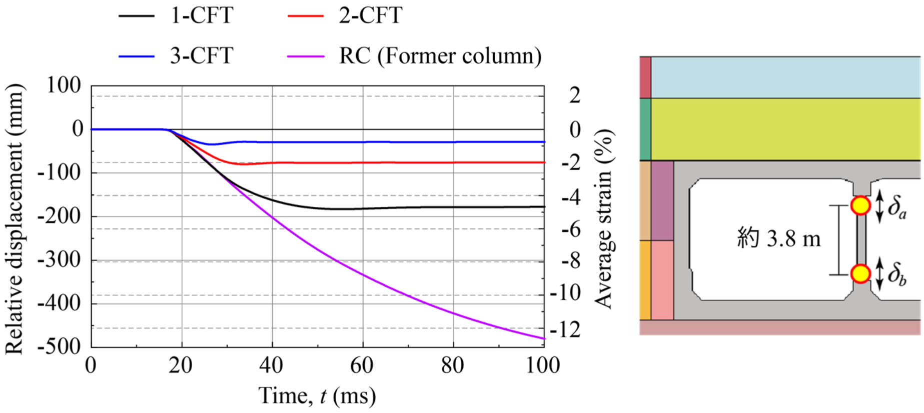

Figure 9. Comparisons of time histories of relative displacement between lower and upper points of central column for three CFT columns and the Column RC.

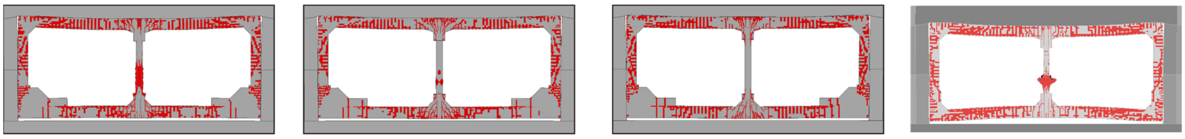

(a) (b) (c) (d)

Figure 10. Comparisons of damage patterns in the station structure at time *t* = 100 ms varying number of CFTs for the central column and Column RC: (a) Column 1-CFT; (b) Column 2-CFT; (c): Column 3-CFT; and (d) Column RC.

compression failure state, because the displacement (strain) monotonically increases at time *t* = 100 ms with values of 480 mm (10%).

Figure 10 shows comparisons of damage patterns to the station structure at time *t* = 100 ms varying the number of CFTs for the central column and Column RC. In this study, based on the concept of the constitutive model for the concrete shown in Figure 6(a), the element is colored in red as suffering damage; crack opening and/or crushing, for the damage index to be larger than 1.98 [4].

From this figure, it is observed that when using Column RC for the central column, the station structure collapses due to compression failure of the column. The vertical upward displacement of the RC slab below the column is larger than for those near the sidewalls. On the other hand, in the case of Column 1-CFT, the steel tube buckles locally in a sine-shaped curve mode in the lower part of the column. However, the station structure may not suffer a collapse because the relative displacement between the lower and upper points of the column is kept constant, as mentioned above, and the vertical upward displacement of the RC slab is approximately equal over its entirety. In the case of Column 2-CFT, a half sine-shaped curve local buckling occurs. However, the damage suffered may be smaller than that for Column 1-CFT, while the amplitude of the mode is significantly smaller. In the case of Column 3-CFT, the CFTs are not buckled and cracking is hardly found in the column. The vertical upward displacement of the RC slab below the column may be smaller than near the sidewalls, differing from the case of Column RC. Thus, it is seen that the station structure with the central columns composed of 3-CFTs may be mostly in a structural healthy state for three columns after the earthquake.

4 CONCLUSIONS

In this study, to investigate the dynamic behaviour of the Daikai Station subway structure with the central columns composed of concrete-filled steel tubes (CFTs), used to increase the strength compared to the RC columns that collapsed due to the great Hanshin-Awaji earthquake, a 3D elastoplastic transient response analysis was carried out, surcharging with an isolated pulse-like upward displacement (duration of 5 ms and velocity of 4 m/s) with a varying number of CFTs. The results obtained from this study were as follows:

1) the station structure having a central column with 1-CFT will probably not collapse, even though sine-shaped curve buckling occurs;

2) the damage level for the station tends to decrease when increasing the number of CFTs for the column whereby the axial stiffness is increased; and

3) the reconstructed station structure, whose central columns were strengthened by using three CFTs, should still be in a structurally healthy state when subjected to a severe earthquake like the Great Hanshin-Awaji earthquake.

REFERENCES

[1] Hanshin Expressway Public Corp., *Report on damage to the Hanshin Expressway during the Hyogoken-Nanbu earthquake*, Hanshin Expressway Public Corp., Osaka, Japan, 1995. (In Japanese.)

[2] Architectural Institute of Japan and Japan Society of Civil Engineers, *Records of the 1995 Great Hanshin-Awaji Earthquake disaster*, Maruzen, Tokyo, Japan, 1995.
[3] N. Kishi, K. Sonoda, M. Komuro, and T. Kawarai, “Numerical simulation of the Daikai Station subway structure collapse due to sudden uplift during earthquake”, *J. Eng. Mech.*, ASCE, 147(3), 2021, 04020152.
[4] ANSYS, Inc., *LS-DYNA user's manual Version R15*, Canonsburg, PA, 2024.
[5] H. Iida, T. Hirota, N. Yoshida, and M. Iwafuji, “Damage to Daikai subway station”, *Soils Found.*, Special Issue, 36, 283-300, 1996.
[6] Sato Kogyo, *Document on disaster recovery of the Daikai Station for the Tozai line of the Kobe Rapid Transit System,* Sato Kogyo, Tokyo, Japan, 1997, In Japanese.
[7] L. J. Malvar, J. E. Crawford, and K. B. Morill, *K&C concrete material model release III: automated generation of material model input*, TR-99-24.3. Karagozian & Case, Glendale, CA, 2000.

15th International Conference on
Shock & Impact Loads on Structures
12-13 June 2025, Gothenburg, Sweden

STRESS WAVE SCATTERING AND CUMULATIVE DAMAGE OF UNDERGROUND OPENING SUBJECTED TO DYNAMIC LOADING

Rui Zhao[a], Ming Tao[a], Linqi Huang[a], Tubing Yin[a], Jiangzhan Chen[a], Zilong Zhou[a], and Xibing Li[a]

[a]School of Resources and Safety Engineering, Central South University, 410083, Changsha, China, email: mingtao@csu.edu.cn

Abstract:

In underground mining and geotechnical construction, Excavation Damage Zone (EDZ) and external dynamic disturbances such as blasting, and fault activity are common and cause damage to rock mass. Therefore, understanding the cumulative damage and failure mechanisms of underground openings containing EDZ under dynamic loading, especially in great depth, is crucial. This study used the Continuous Surface Cap Model (CSCM) to model the damage development and failure of stressed rock masses induced by internal excavation unloading and external dynamic loading. This was implemented by combining the implicit-explicit algorithm and the restart technology in the LS-DYNA to account for cumulative damage. The simulation results indicated that the depth of the EDZ increased proportionally with the initial stress, and under external dynamic disturbances, the process zones around the EDZ would fail and form new process zones at the new stable boundary of the Dynamic Damaged Zone (DDZ), which widen the damage extent of the surrounding rock mass and potentially cause multiple dynamically triggered rockbursts.

1 INTRODUCTION

With the rapid depletion of shallow resources and space, there has been continuous exploration of the deep space within the Earth's crust. However, as excavation depth increases, rock destabilization hazards become frequent, which pose a great threat to the safe production of underground engineering. The initial stress increases proportionally with depth, and in rock engineering such as mining and tunneling, excavation inevitably disturbs the surrounding rock mass due to changes in the stress state. Excavation releases radial and shear stresses, leading to tangential stress elevation and generating EDZ [1-3], resulting in weakening and discontinuity of the rock properties. In addition, external dynamic disturbances such as blasting, fault activity, rock fall, etc., create additional stresses around the opening causing instability of rock mass and even triggering rockburst. To optimize the support system and mitigate destabilization hazards in rock engineering, there is an urgent need to clarify the failure characteristics and mechanism of the surrounding rock mass under excavation unloading and external dynamic loading. High initial stresses and redistributed stresses caused by excavation unloading are considered to be the prerequisite factors leading to EDZ [4]. Numerical simulations and field observations also have shown that rapid unloading is a critical factor in the formation of EDZs.

The EDZ significantly reduces the mechanical properties of the surrounding rock after tunnel excavation [5]. Additionally, external dynamic disturbances generated by adjacent construction and fault activity propagate as stress waves through the rock mass. When these waves encounter structural and material discontinuities caused by excavation, they scatter and produce dynamic stress concentrations [6]. In such a situation, the superposition of two disadvantageous factors is more likely to cause dynamic instability of the surrounding rock mass. With these and knowledge, it is possible to obtain the cumulative damage and failure characteristics of a stressed excavation-damaged underground opening subjected to external dynamic disturbances by a combination of explicit-implicit sequence solution and restart techniques. This facilitates understanding the dynamic damage evolution of rock masses after excavation and the triggering mechanism of rockburst, which has rarely been considered in an integrated context and studied by combining initial stresses, EDZ, and dynamic disturbances, in particular, a comprehensive study combining theoretical and numerical modeling.

2. EDZ FORMATION AND STRESSES INDUCED BY EXTERNAL DYNAMIC DISTURBANCE AROUND AN UNDERGROUND OPENING

In some projects, two or more tunnels are close to each other, e.g., Fig. 1a-b shows the arrangement of mining and water diversion tunnels in Jinping II hydropower station and Xiangxi Gold Mine, and they are all affected by blasting in the nearby region. These tunnels are in greater depth and higher initial stress state, and a certain range of EDZ has been formed around them during the excavation unloading, which, together with the external dynamic loading, further affects the stability of the tunnels as shown in Fig.1c.

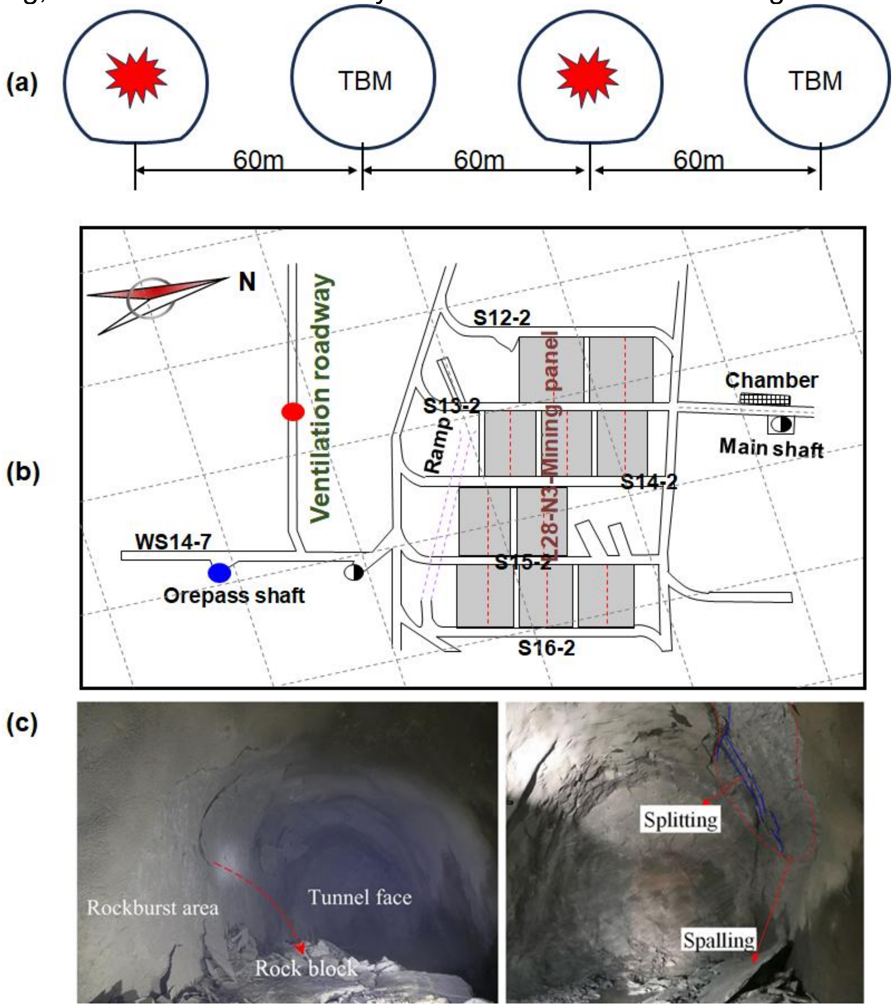

Figure 1. Tunnels subjected to a dynamic disturbance in (a) Jinping II diversion (b) a panel layout of Xiangxi Golden Mine and (c) Splitting, spalling, and rockburst caused by dynamic disturbance in the Bayu Tunnel, Shannan City [7].

The whole process from the onset of excavation to completion of underground openings is subjected to both internal unloading and external dynamic disturbances. To evaluate the stress evolution around the tunnel generated by excavation and external disturbances, both of which can be simplified as elasto-dynamics problems in a medium with density ρ, modulus of elasticity E, Poisson's ratio υ, Lame constants λ and shear modulus, G. Then the equilibrium equations are satisfied as:

$$\frac{\partial \sigma_r}{\partial r} + \frac{1}{r}\frac{\partial \sigma_{r\theta}}{\partial \theta} + \frac{1}{r}(\sigma_r - \sigma_\theta) = \rho \frac{\partial^2 u_r}{\partial t^2} \tag{1a}$$

$$\frac{\partial \sigma_{r\theta}}{\partial r} + \frac{1}{r}\frac{\partial \sigma_\theta}{\partial \theta} + \frac{2}{r}\sigma_{r\theta} = \rho \frac{\partial^2 u_\theta}{\partial t^2} \tag{1b}$$

Where σ_r, σ_θ, $\sigma_{r\theta}$ are the stress components in radial, tangential, and shear. u_r and u_θ are the displacements at r and θ directions in the polar coordinate system with the centre of the tunnel as the origin, and t is the time variable. By introducing a pair of displacement potential functions ψ and ϕ, Eq.1 can be written as:

$$\nabla^2 \phi = \frac{1}{c_p^2}\frac{\partial^2 \phi}{\partial t^2} \tag{2a}$$

$$\nabla^2 \psi = \frac{1}{c_s^2}\frac{\partial^2 \psi}{\partial t^2} \tag{2b}$$

Here ∇^2 is the Laplacian Operator, $c_{p,s}$ is the P- and S-wave velocity respectively, and Eq. 2 is the wave equation expressed in terms of the potential function. The solutions of Eq.2 are a series of linear superpositions of Cylindrical Functions with unknown coefficients:

$$\phi = \sum_{n=0}^{\infty} A_n Z_n(k_p r) \cos n\theta \tag{3a}$$

$$\psi = \sum_{n=0}^{\infty} B_n Z_n(k_s r) \sin n\theta \tag{3b}$$

Here $k_p = \frac{\omega}{c_p}$, $k_s = \frac{\omega}{c_s}$, ω is the circular frequency, $Z_n(\cdot)$ is the Cylindrical Functions of order n (n is an integer). A_n and B_n are the undetermined coefficients which will be solved according to the boundary conditions in the following sections.

Although both the excavation unloading of the tunnel and the external dynamic disturbances are governed by Eq. 2 and can be represented by a generalized solution in the form of Eq. 3, the two processes generally happen at different times and therefore the whole problem is decomposed into two sub-problems i.e.

(i) The tunnel under initial stress state subjected to excavation unloading and lead to stress redistribution and EDZ formation.

(ii) The tunnel is subjected to external dynamic disturbance after the excavation is completed, the stress wave scatters around the tunnel, and dynamic stress distribution is induced.

2.1. Mechanism of formation of Excavation Damage Zone

During tunnel excavation, initial stress unloading and redistribution of stresses are the primary causes of EDZ around the tunnel. To obtain the mechanism of EDZ formation and the effect of the stress state, the stress evolution around the tunnel during the unloading process will be calculated. In this study, the opening in a hydrostatic stress field of magnitude σ_0 is considered to quantitatively assess the effect of the initial stress magnitude, in such a case Eq. 2b and Eq.3b are eliminated.

As a constant unload rate path, the liner unload path has been widely used to study the unloading-related problem of tunnels [3, 8, 9]. Under the hydrostatic stress state, the unloading boundary condition of the excavation with a linear path can be expressed as follows：

$$\begin{cases} \sigma_{rr}|_{r=r_0} = -\frac{\sigma_0 t}{t_0} \\ \sigma_{\theta\theta} = 0 \\ \sigma_{r\theta} = 0 \end{cases} \tag{4}$$

Here, t_0 is the unloading period, and r_0 is the tunnel radius. It is difficult to solve such a problem directly in the time domain. Therefore, the Laplace transform is used to transform

Eq.3 and boundary condition Eq.4 into the Laplace *S*-domain, then the corresponding tangential stress in the Laplace domain is:

$$\tilde{\sigma}_{\theta\theta}(r,p) = \frac{\sigma_0(1-e^{-t_0 S})r_0\left[\lambda K_1^{'}\left(\frac{Sr}{cp}\right)+\frac{\lambda+2\mu}{r}K_1\left(\frac{Sr}{cp}\right)\right]}{S^2 t_0\left[(\lambda+2G)r_0 K_1^{'}\left(\frac{Sr_0}{cp}\right)+\lambda K_1\left(\frac{Sr_0}{cp}\right)\right]} \quad (5)$$

Eq.5 is Laplace inversed into the time domain by employing the numerical inverse method proposed by Valsa and Brančik [10]. The unloading time has a pronounced influence on the unloading stress redistribution. Excavation unloading is firstly calculated at the excavation boundary $r = r_0$ with different unloading times. The results of the tangential stress histories with unloading times of ~0ms, 2ms, 5ms, and 10ms are plotted in Fig.2. The amplitude of the redistributed stresses is different for various unloading times (unloading rates). Transient unloading, as the most rapid unloading method, is characterized by the highest unloading rate, and in this case, at the moment of unloading onset, a stress drop occurs, where the stress first decreases to 0.75 of the initial state, then rises to reach a magnitude of ~2.25, which is about 12.5% higher than the static stress level. As the unloading time increases, the magnitude of the tangential stress decreases, and when the unloading time is 10 ms, the peak of the tangential stress concentration decreases to ~2.04, which is very close to the static value of 2.0.

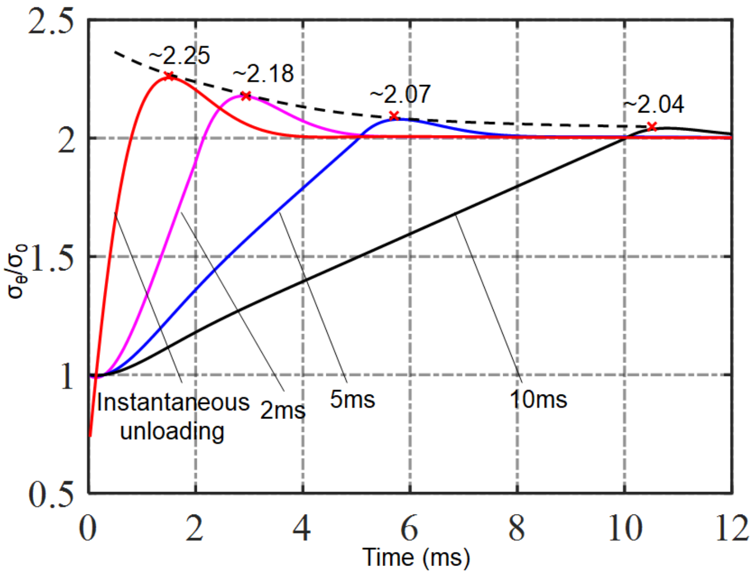

Figure 2. Stress histories at tunnel boundary under different unloading time

In the temporal aspect, faster unloading leads to higher stress concentrations. Here, Fig.3 plots the spatial distribution of the tangential stresses as a 2ms dynamic unloading and quasi-static unloading is employed. Because the deformation and damage of the rock mass are dependent on the stress state, it is assumed that there is a failure limitation of rock mass (see Fig.3), and as the stress state in the surrounding rock mass exceeds this limit, the EDZ will be generated. A conclusion is thus obtained that the range of EDZ around the tunnel increases with increasing initial stresses and unloading rates.

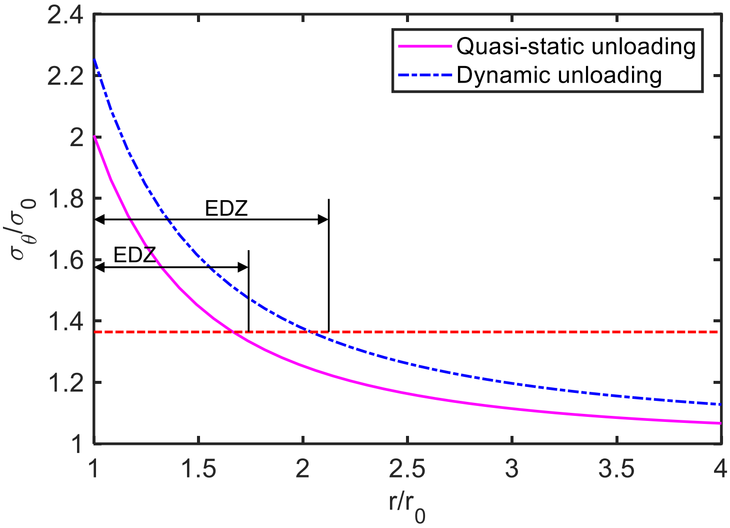

Figure 3. Maximum tangential stress variation with the distance to the tunnel boundary under 2-ms dynamic unloading and quasi-static unloading.

2.2. Dynamic stress concentration around a damaged opening

The second sub-problem deals with the stress distribution around a tunnel containing an EDZ after excavation subjected to external dynamic disturbance. The depth of the EDZ is varied under different stress states and unloading rates, assuming that the radius of the EDZ is r_1 (see Fig.4). The elastic parameters of the undisturbed surrounding rock mass are denoted by the subscript $_1$, and the elastic parameters of the EDZ are denoted by subscript $_2$, such as the elastic modulus $E_{1,2}$, Poisson's ratio $v_{1,2}$, etc.

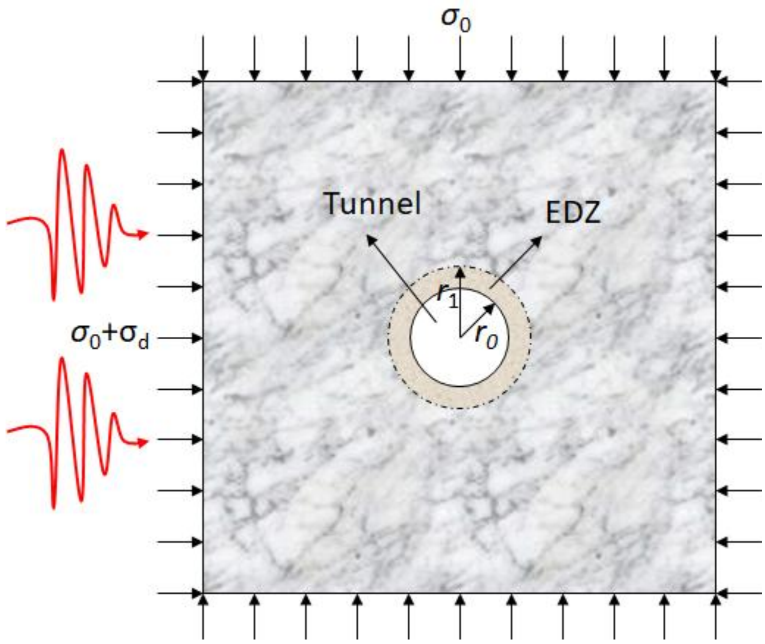

Figure 4. Sketch of a tunnel with EDZ subjected to dynamic disturbance

As for the problem laid out in Fig.4, supposing a P-wave is applied horizontally, a reflected P-wave and a scattered SV-wave are generated both at the inner surface of the tunnel and at the interface between the EDZ and the undisturbed surrounding rock mass (r=r_1). The incident reflected and scattered waves are expressed as a Fourier series of Cylindrical Functions in the form of Eq. 3, and the incident wave is [11]:

$$\phi^{(i)} = \sigma_d \sum_{n=0}^{\infty} \varepsilon_n i^n J_n(k_{p1} r) \cos n\,\theta e^{-i\omega t} \tag{6}$$

where $J_n(\cdot)$ is the Bessel function of the first kind of integer order n, σ_d is the peak of dynamic loading. Here $\varepsilon_n = 1$ for $n = 0$ and $\varepsilon_n = 2$ for $n > 0$. Due to the difference in properties between the EDZ and the undisturbed rock mass, the incident wave is reflected and scattered on their interface. The P- and SV wavefields in undisturbed rock mass are [11]：

$$\phi_1 = \sum_{n=0}^{\infty}[\underbrace{\varphi_0\varepsilon_n i^n J_n(k_{p1}r)}_{Incident\ P-wave} + \underbrace{A_n^1 H_n^{(1)}(k_{p1}r)}_{Reflected\ P-wave}\ ]\cos n\,\theta e^{-i\omega t} \tag{7a}$$

$$\psi_1 = \sum_{n=0}^{\infty}\ \underbrace{B_n^1 H_n^{(1)}(k_{s1}r)}_{Scattered\ SV-wave}\ \sin n\,\theta e^{-i\omega t} \tag{7b}$$

Similarly, the wavefields in EDZ are:

$$\phi_2 = \sum_{n=0}^{\infty}[\ \underbrace{A_n^2 H_n^{(2)}(k_{p2}r)}_{Incident\ P-wave\ in\ EDZ} + \underbrace{C_n^2 H_n^{(1)}(k_{p2}r)}_{Scattered\ P-wave\ in\ EDZ}\ ]\cos n\,\theta e^{-i\omega t} \tag{8a}$$

$$\psi_2 = \sum_{n=0}^{\infty}[\ \underbrace{B_{n\,n}^2 H_n^{(2)}(k_{s2}r)}_{Incident\ SV-wave\ in\ EDZ} + \underbrace{D_n^2 H_n^{(1)}(k_{s2}r)}_{Scattered\ \ SV-wave\ in\ EDZ}\ ]\sin n\,\theta e^{-i\omega t} \tag{8b}$$

Here, $H_n^{(1,2)}$ is the Hankel function of the first and second kind of integer order n. And $A_n^{1,2}$, $B_n^{1,2}$, $C_n^{1,2}$, $D_n^{1,2}$ are the coefficients to be determined based on the boundary conditions. There are two sets of boundaries to determine these parameters, one is the radial and shear stresses are zero at the inner surface of the tunnel as:

$$\left.\begin{aligned}\sigma_{rr2} = 0\\ \sigma_{r\theta 2} = 0\end{aligned}\right\} \tag{9}$$

The other set of boundary conditions is the displacement and stress relations at the interface, given that some discontinuities between the EDZ and the undisturbed rock mass arise due to excavation, the interface is therefore imperfect, denoted as [12]:

$$\sigma_{rr1} = \sigma_{rr2} = k_r(u_{r1} - u_{r2}) \quad \text{if } u_{r1} \geqslant u_{r2}, \tag{10a}$$

$$\sigma_{rr1} = \sigma_{rr2} \text{ and } \quad u_{r1} = u_{r2} \quad \text{otherwise.} \tag{10b}$$

$$\sigma_{r\theta 1} = \sigma_{r\theta 2} = k_\theta(u_{\theta 1} - u_{\theta 2}) \tag{10c}$$

Here, k_r and k_θ are the normal and transverse spring constants of the interface, respectively. By combining Eq.6-8 with the boundary conditions Eq.9-10, the undetermined coefficients and stress distributions are fully determined. It is clear from Eq.6-8 that the stress is highly affected by the elastic parameters of both EDZ and undisturbed rock mass. Moreover, the frequency of the stress wave decreases as propagation and the EDZ depth vary with the unloading rate and the initial stress as estimated in section 2.1. Thus, the response of the tunnel at different frequency ranges and EDZ depths is studied. In this study, c_{p1}/c_{p2}=0.5, and $k_r = k_\theta$ =0.5G/r_1 are specified to study the influences of EDZ depths and wave frequencies on the dynamic stress around the tunnel.

Fig.6 plots the stress response on the interface between ($r = r_1$) the EDZ and intact rock mass and the inner surface ($r = r_0$) of the tunnel in horizontal and vertical directions. In the figures, the frequency range is selected as ω= 0~2500Hz, which includes most frequency of the natural and artificial dynamic disturbances [13, 14].

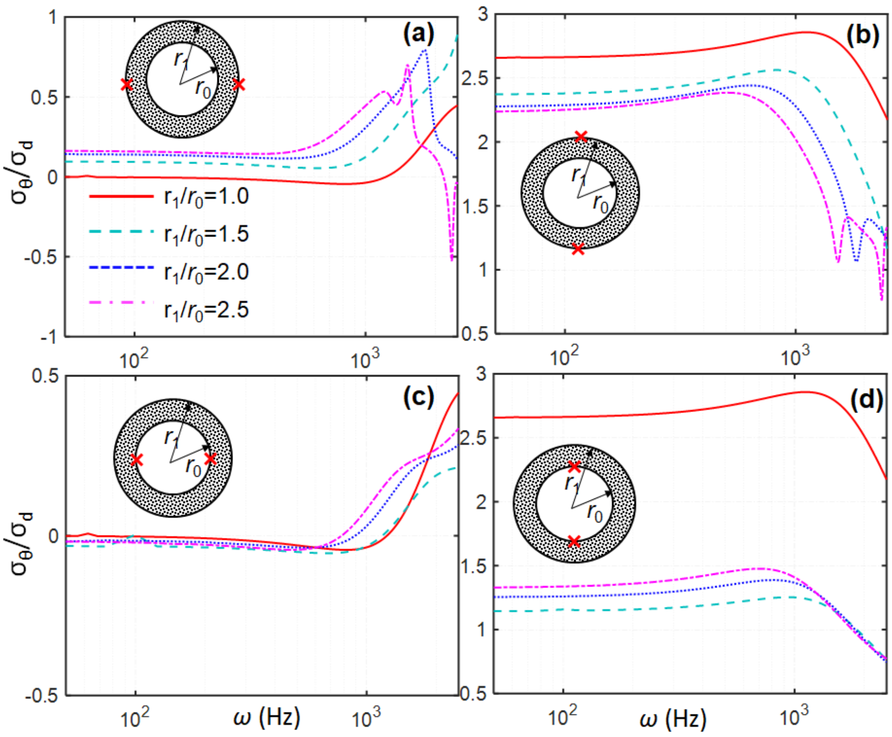

Figure 5. Frequency response curves of the tunnel with different EDZ depths at (a) $r = r_1$ in the horizontal direction, (b) $r = r_1$ in the vertical direction, (c) $r = r_0$ in the horizontal direction, and (d) $r = r_0$ in the vertical direction.

In the case without EDZ, i.e., an intact tunnel, a stress concentration of ~2.7 is generated in the vertical direction at $r = r_0$, and tensile stresses appear in the horizontal direction of the incidence. For the frequency of the incident wave up to ~1000 Hz, in the case with EDZ, the stresses in the tunnel surrounding rock mass gradually increase with the depth of the EDZ for all conditions, except for the vertical direction at $r = r_1$, which decreases with the depth of the EDZ. When the frequency exceeds ~1000 Hz, the stress response around the tunnel oscillates because with increasing frequency of the incident wave, more wave peaks and valleys are contained within the tunnel diameter range and resonance causing the response pattern to be more complicated, and multiple stress peaks may also occur around the tunnel. As most of the stress waves generated by blasting have a frequency within 1000 Hz, in this frequency band, the tunnel has an amplifying effect on the dynamic loads in the vertical direction, resulting in large compressive stresses, while tensile stresses may be generated in the incident directions.

In conjunction with the conclusions in Section 2.1, rapid unloading at high-stress conditions produces a deeper EDZ that reduces the quality of the surrounding rock mass and also increases the additional stresses when the tunnel is subjected to external dynamic disturbances which further lead to tunnel instability.

3. NUMERICAL MODELLING

3.1 Method and Numerical Model

In this section, LS-DYNA was used to carry out numerical simulations. An implicit-explicit sequence solution and iterative process are then employed to obtain the damage evolution and failure of the tunnel containing EDZ under dynamic disturbances after excavation at different initial stress states . A simplified calculation flowchart is illustrated in Fig.6, where *dynain,* and *d3dump* files are the system output of LS-DYNA [15]. These two files are used to store the stress and strain information of the elements and nodes of the model in the previous calculation and are inherited in the following calculation. The FEM model and the applied dynamic loading are shown in Fig.7.

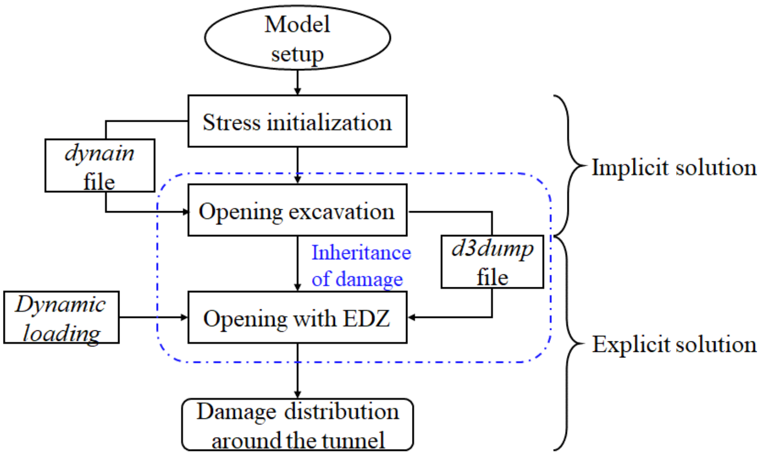

Figure 6. Flowchart for the implicit-explicit solution approach adopted in this study.

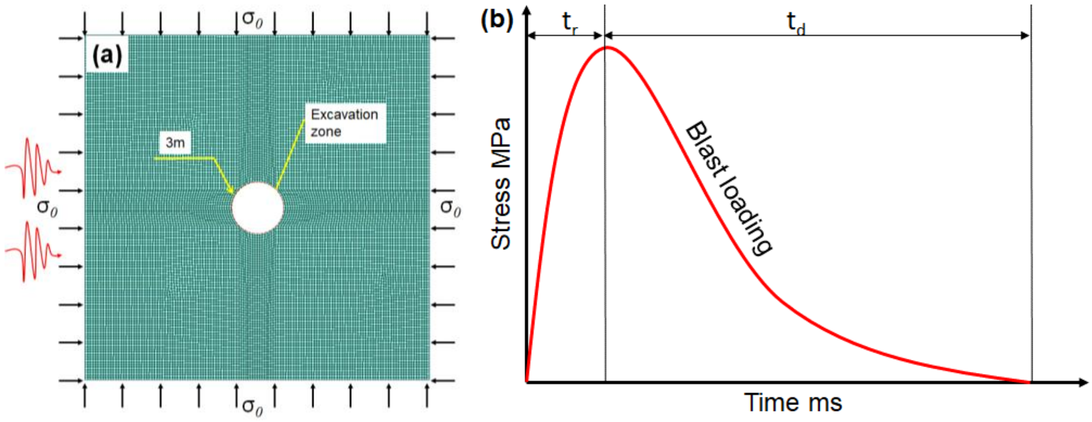

Figure 7. (a) FEM mesh and (b) applied dynamic loading.

In Fig. 7b, t_r and t_d are the raising and decay times of the dynamic loading. The applied dynamic loading is an equivalent blasting loading proposed by Tao et al . In this study, t_r and t_d are set as 0.25ms and 0.75ms, respectively, and unloading times of 1ms under different initial stress σ_0= 30MPa to 60MPa at intervals of 10MPa are investigated.

3.2 Material Model

Due to CSCM can realize the brittle and ductile damage of the rock mass and achieve the stress redistribution after excavation, whereas RHT and HJC are unable to obtain the redistributed stress after excavation accurately, in the study, the CSCM mater model was chosen for modelling the failure characteristic of rock mass. The yield surface is shown in Fig.8 and the yield function of CSCM is defined by:

$$Y(I_1, J_2, J_3, \kappa) = J_2 - \Re(J_3)^2 F_f^2(I_1) F_c(I_1, \kappa) \quad (11)$$

Here I_1 is the first invariant of the stress tensor, J_2, and J_3 are the second and third invariants of the deviatoric stress tensor. F_f (I_1) is the shear failure surface, which is written as Eq.12, and α_f, β_f, θ_f, and λ_f are the failure surface control parameters [16].

$$F_f(I_1) = \alpha_f + \theta_f I_1 - \lambda_f e^{-\beta_f I_1} \quad (12)$$

F_c (I_1, κ) is the hardening cap and κ is the cap hardening parameter. $\Re(J_3)$ is the Rubin three-invariant reduction factor. And the hardening cap F_c (I_1, κ) is expressed as:

$$F_c(I_1,\kappa)=\begin{cases}1-\frac{[I_1-L(\kappa)]^2}{[X(\kappa)-L(\kappa)]^2} & I_1\geqslant L(\kappa)\\ 1 & I_1\leqslant L(\kappa)\end{cases} \tag{13}$$

here:

$$L(\kappa)=\begin{cases}\kappa & \kappa\geqslant\kappa_0\\ \kappa_0 & \kappa\leqslant\kappa_0\end{cases} \tag{14}$$

In Eq.14, κ_0 is the value of I_1 at the initial intersection of the cap and shear surfaces before hardening is engaged, and more details on CSCM were reported by Murray[16] .

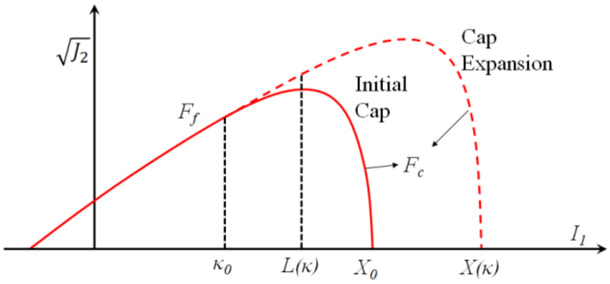

Figure 8. General shape of CSCM yield surface in two dimensions.

The intact rock specimens are collected from a gold mine in China, with a depth of over 1000m. Field survey results show GSI = 80, some parameters of the selected intact rock are σ_{ci}=148MPa, σ_{ti}=6.0MPa, Poisson's ratio 0.21, and elastic modules E_i =48GPa.

4. NUMERICAL RESULTS AND ANALYSIS

The effect of the magnitude of the initial stress, and the dynamic loading on the damage to the surrounding rock mass of the tunnel will be simulated and analyzed in the following subsections.

4.1. Simulated Damage around the Tunnel

Fig.9 shows the EDZ caused by the initial stress unloading under different stress states.

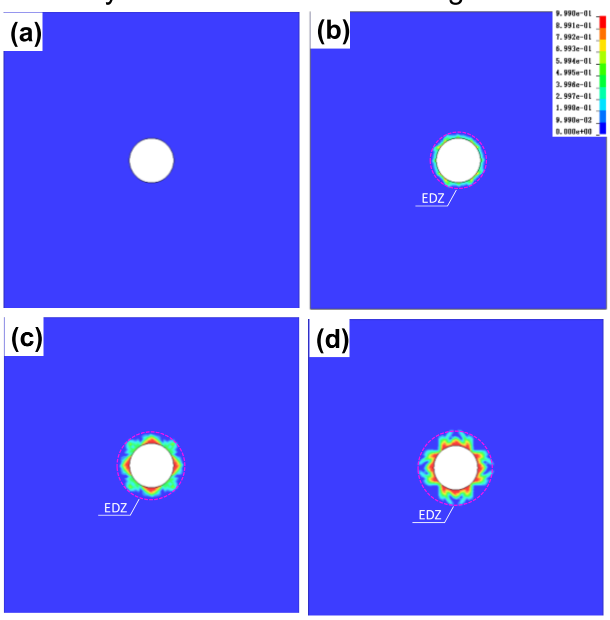

Figure 9. EDZs around the tunnel under different stress states of (a) σ_0=30MPa, (b) σ_0=40MPa, (c) σ_0=50MPa, and (d) σ_0=60MPa.

The EDZ depth around the tunnel increases with the increase in σ_0, as σ_0 increases from

30MPa to 60MPa, the EDZ depths around the tunnel are 0, 0.36, 0.72, and 1.08m, respectively. After the excavation of the opening, a dynamic loading with a peak load of 40MPa is applied on the left side of the model.

4.2. Influence of Peak Dynamic Loading on Damage of Rock Mass around Tunnels

While the initial static stresses influence the extent and degree of EDZ, the dynamic loading amplitude has an equally strong influence on the development of DDZ, due to the dynamic loading generating stress concentrations around the tunnel. The distributions of DDZ in the surrounding rock mass under different dynamic loading amplitudes are given in Fig.10.

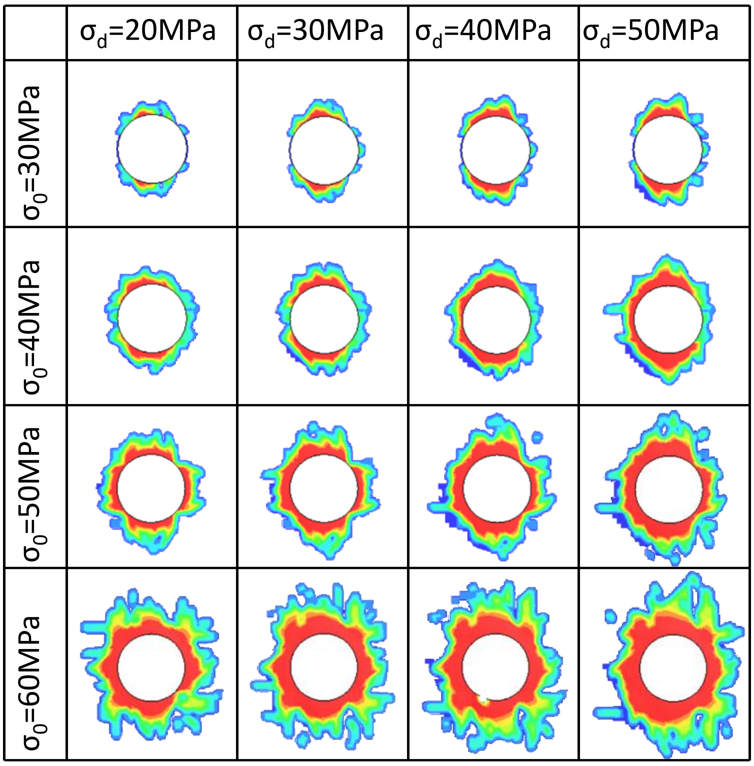

Figure 10. DDZs around the tunnels under different initial and dynamic stress load conditions (Only damaged zones are shown in figures).

It is observed in Fig.10 that the DDZ range shows a proportional increase with the increase of σ_0 and σ_d. Fig.11 plots the variation of the maximum DDZ depth R_d increasing σ_0 and σ_d, in which a liner relationship between the DDZ depths and σ_0 and σ_d is observed. Under the dynamic loading with various amplitudes from 20 to 50 MPa, the R_d and σ_0 satisfy the following relationship:

$$0.0443\sigma_0 - 0.332 > \ R_d/r_0 > 0.0443\sigma_0 - 1.218 \tag{15}$$

For different σ_0, the linear relationship between σ_d the and DDZ depth, are:

$$R_d/r_0 = 0.85\sigma_d + \begin{cases} 16.00; \ \sigma_0 = 30MPa \\ 29.75; \ \sigma_0 = 40MPa \\ 61.75; \ \sigma_0 = 50MPa \\ 89.50; \ \sigma_0 = 60MPa \end{cases} \tag{16}$$

In Eq.16, as the initial stress increases, the intercept of the fitted line increases. To further determine their interrelationships, a three-dimensional least squares linear regression is also carried out and plotted in Fig. 8c, where the following interrelationship is satisfied:

$$R_d/r_0 = 0.0125\sigma_0 + 0.0292\sigma_d - 0.6792; R^2 = 0.95 \tag{17}$$

The R_d is positively correlated with initial stress and dynamic loading, and the effect of dynamic loading amplitude is greater than that of initial stress.

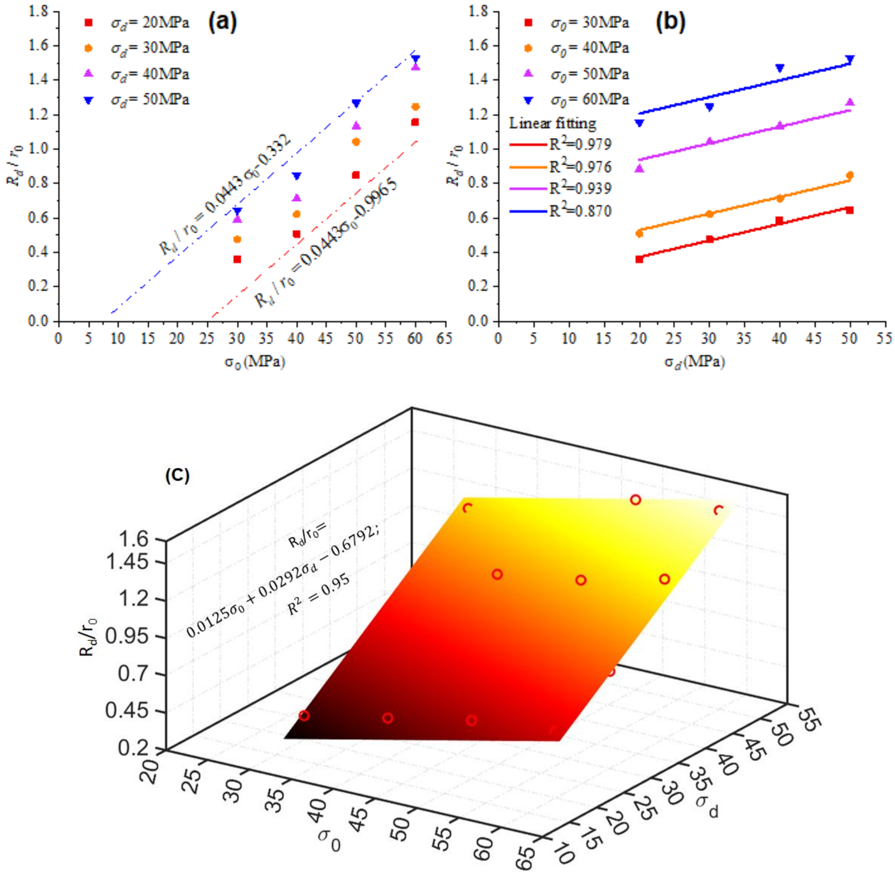

Figure 11. Relationship between the maximum damaged depth around the tunnel under dynamic loading vs. (a) σ_0, (b) σ_d, and (c) their interrelationship.

Under a higher stress state, the surrounding rock mass is directly damaged after excavation, and even a rockburst occurs. Whereas, when the initial stress is lower, the surrounding rock mass does not destroy directly, but it is also disturbed by the excavation unloading. In this situation, the introduction of dynamic disturbances increases the stress and energy in the surrounding rock mass, which leads to the failure of the surrounding rock mass. The external dynamic input energy required for the damage of the surrounding rock mass is different for various initial stress states [17]. For a higher initial stress state, a single small-amplitude far-field dynamic disturbance is likely to result in a rockburst, since the rock has long been at the criticality of damage. For a lower initial stress state, a single high amplitude dynamic loading or multiple dynamic loadings of small amplitude would also induce rockburst.

5. CONCLUSIONS

This study analysed the formation of EDZ and its influence on the dynamic stability of the surrounding rock mass. Numerical simulations were carried out to assess the damage evolution and its extension around the tunnel under excavation unloading and subjected to external dynamic loading for different initial stress states. The effects of the initial stress state and the peak of the dynamic loading were also investigated. It was found that excavation under high stress state results in EDZ which causes scattering and stress concentration of external dynamic loading in the surrounding rock mass, further exacerbating the damage to the surrounding rock mass. External dynamic disturbances break the EDZ down and form a new process zone, which elevates local stresses in the surrounding rock mass. Under high stress state, this leads to multiple triggered rockbursts, and under low stress state, this is the cause of cumulative damage and rockburst occurring in surrounding rock mass after multiple dynamic disturbances. We defined a linear relationship between the maximum DDZ depth and the initial stress and peak external dynamic loading, with dynamic loading having a more pronounced effect on the maximum DDZ depth for the same magnitude. Based on the obtained results it is recommend that explicit and implicit solution and restart technique should be used to accurately calculate cumulative damage of rock masses under dynamic loading.

REFERENCES

[1] T. Siren, P. Kantia, M. Rinne, Considerations and observations of stress-induced and construction-induced excavation damage zone in crystalline rock, International Journal of Rock Mechanics and Mining Sciences, 73 (2015) 165-174.

[2] J.B. Martino, N. Chandler, Excavation-induced damage studies at the Underground Research Laboratory, International Journal of Rock Mechanics and Mining Sciences, 41 (2004) 1413-1426.

[3] J.P. Carter, J.R. Booker, Sudden excavation of a long circular tunnel in elastic ground, International Journal of Rock Mechanics and Mining Sciences & Geomechanics Abstracts, 27 (1990) 129-132.

[4] C.D. Martin, R. Christiansson, Estimating the potential for spalling around a deep nuclear waste repository in crystalline rock, International Journal of Rock Mechanics and Mining Sciences, 46 (2009) 219-228.

[5] S. Emsley, O. Olsson, L. Stenberg, H.J. Alheid, S.D. Falls, ZEDEX - a study of damage and disturbance from tunnel excavation by blasting and tunnel boring, in, 1997.

[6] Z. Huatao, M. Tao, X. Li, Theoretical analysis of dynamic stress distribution around a circular damaged roadway under transient disturbance, International Journal for Numerical and Analytical Methods in Geomechanics, 47 (2023).

[7] J. Jiang, X.-T. Feng, C. Yang, G. Su, Experimental Study on the Failure Characteristics of Granite Subjected to Weak Dynamic Disturbance Under Different σ3 Conditions, Rock Mechanics and Rock Engineering, 54 (2021) 5577-5590.

[8] W. Cao, X. Li, M. Tao, Z. Zhou, Vibrations induced by high initial stress release during underground excavations, Tunnelling and Underground Space Technology, 53 (2016) 78-95.

[9] J.H. Yang, Q.H. Jiang, Q.B. Zhang, J. Zhao, Dynamic stress adjustment and rock damage during blasting excavation in a deep-buried circular tunnel, Tunnelling and Underground Space Technology, 71 (2018) 591-604.

[10] J. Valsa, L. Brančik, Approximate formulae for numerical inversion of Laplace transforms, International Journal of Numerical Modelling: Electronic Networks, Devices and Fields, 11 (1998) 153-166.

[11] Y.H. Pao, C.C. Mow, J.D. Achenbach, The Diffraction of Elastic Waves and Dynamic Stress Concentration, Journal of Applied Mechanics, 40 (1973) págs. 213-219.

[12] J. Achenbach, H. Zhu, Effect of interfacial zone on mechanical behavior and failure of fiber-reinforced composites, Journal of the Mechanics and Physics of Solids, 37 (1989) 381-393.

[13] J.H. Yang, W.B. Lu, Q.H. Jiang, C. Yao, C.B. Zhou, Frequency comparison of blast-induced vibration per delay for the full-face millisecond delay blasting in underground opening excavation, Tunnelling and Underground Space Technology, 51 (2016) 189-201.

[14] X. Zhang, P. Yan, W. Lu, Y. Cheng, C. Sun, J. Zhu, W. Guo, X. Cheng, Frequency spectrum characteristics of blast-induced vibration with electronic detonators in ground blasting, Journal of Building Engineering, 74 (2023) 106892.

[15] LSTC, Ls-Dyna keyword user’s manual vol. I, II, III. Version R10.0. Livermore Software Technology Corporation, Livermore, California., California., 2018.

[16] Y.D. Murray, Users Manual for LS-DYNA Concrete Material Model 159, 2007.

[17] C. Li, A new energy-absorbing bolt for rock support in high stress rock masses, International Journal of Rock Mechanics and Mining Sciences, 47 (2010) 396-404.

15th International Conference on
Shock & Impact Loads on Structures
12-13 June 2025, Gothenburg, Sweden

IMPACT OF SOIL-STRUCTURE INTERACTION ON UNDERGROUND SHELTERS WITH PILE FOUNDATIONS AND PERIPHERY WALLS UNDER BLAST LOADING

Arunkumar G[a], Arumugam D[b], and Dhanasekaran B[C]

[a]Larsen & Toubro Construction, India. email: arun.kumar10@lntecc.com, [b]Larsen & Toubro Construction, India, [c]Larsen & Toubro Construction, India,

Keywords: Blast Impact, Dynamic Analysis, Nonlinear Springs, Piles, Periphery Walls, Underground Buildings, Shelters

Abstract

The rising global threat of war has emphasized the need for underground shelters as vital protection. These shelters have become essential for safeguarding lives in the face of escalating security risks worldwide. In the event of a blast, underground shelters with piles first experience the load on their peripheral walls, supported by the surrounding soil, which then transfers the load to the piles. The optimized pile design can be done by considering the interaction behaviour between the soil and the periphery wall. Dynamic response of the underground building with pile foundation and periphery wall during blast loading condition using the finite element analysis done in ABAQUS CAE software was investigated. The structure is modelled using shell elements, wherein the effects of soil-structure interaction are incorporated by modelling the soil using frequency independent spring dashpot mass model. This study focusses on the effect of soil structure interaction for the above-mentioned building by giving soil conditions with higher and lower stiffness and with blast load of varying duration. The results indicate that, during static conditions the force transfer to the piles is lesser when soil stiffness condition is higher as the periphery wall attracts more force than piles and vice versa. During dynamic conditions, the same behaviour follows with the increased reaction with lesser blast duration and then arrives the static equivalent reaction as the blast duration increases. The findings of the study can be used to optimize the design of pile foundation system along with periphery wall for underground buildings by taking advantage of the surrounding soil.

1 INTRODUCTION

The frequency of war and terrorist attacks is increasing worldwide, posing significant challenges for governments in ensuring the safety of their citizens. Well-developed countries can provide dedicated emergency shelters, with underground structures being the preferred choice due to their enhanced protection against blast-related impacts. Extensive research on real-world scenarios and numerical studies has provided insights into the effects of air blasts, blast waves, and shock wave transmission. The propagation of surface blasts through soil varies depending on soil type and the number of layers between the blast location and the shelter. The impact of blast loads on semi-buried structures varies depending on the depth of burial and the number of blast scenarios considered. Analysis of multiple blast scenarios indicates that as the depth of the structure increases, the stress induced by the blast event decreases. This reduction in stress occurs because the surrounding soil absorbs and dissipates a significant portion of the blast wave energy, thereby minimizing the direct impact on the structure. (Mukesh Kumar, 2014) The deeper the structure is buried, the more effectively the soil acts as a protective barrier, reducing the transmission of shock waves and blast-induced pressures. These findings highlight the importance of burial depth as a key design parameter for blast-resistant underground structures, ensuring enhanced structural resilience and occupant safety in extreme conditions.

Underground shelters are typically constructed with reinforced concrete (RCC) periphery walls to safeguard occupants. In blast scenarios, lateral loads become predominant. In regions with poor soil conditions, pile foundations become essential. (L.B.Jayasinghe, 2013). Piles must be designed to withstand both vertical and lateral loads induced by blast events. Generally, piles exhibit lower lateral load-bearing capacity compared to vertical capacity. During a blast event, underground shelters with pile foundations first experience loading on their peripheral walls, which is transmitted through the surrounding soil and subsequently transferred to the piles. Optimizing pile design requires a comprehensive understanding of the interaction between soil and the periphery wall.

This study focuses on the effects of soil-structure interaction in underground shelters by considering soil conditions with varying stiffness and blast loads of different durations. The dynamic response of the periphery wall and piles under blast loading is analysed using finite element modelling in ABAQUS CAE. The findings of this study contribute to the optimization of underground shelter design, enhancing structural resilience against blast-induced forces.

2 MODELLING, MATERIALS AND METHODS

2.1 Numerical Modelling

The numerical modelling was done using a 2D planar model representing a deformable underground shelter with dimensions of 15 m × 7 m. The structure consists of a periphery wall, roof, and raft with thicknesses of 1 m, 1 m, and 2 m, respectively. A pile foundation with a length of 8 m was considered. The section properties were defined as Shell/Continuum Shell, homogeneous type, with a thickness of 1 m. Both the shelter and pile were assigned concrete material properties, with a density of 2400 kg/m³, Young's modulus of 25,000 MPa, and Poisson's ratio of 0.17. The structural components were assembled as shown in the Figure 1, incorporating six piles arranged at a centre-to-centre distance of 3 m. A tie constraint was applied to the pile-to-shelter joints to ensure connectivity. Meshing was performed with a seed value of 0.25 m, ensuring four elements per meter width for adequate resolution. The soil properties were modelled as uniform, with simplified stiffness support on either side of the periphery wall. Nonlinear compression-only springs were utilized to simulate soil-structure interaction, with two stiffness cases:

Case 1: Lower stiffness value of 6000 N/mm.

Case 2: Higher stiffness value of 18,000 N/mm.

Reference points were created at least 1 meter away from the mesh nodes using the Springs/Dashpots option. Fixed boundary conditions were applied to the springs, and the displacements U1, U2, and U3, along with the rotational degree of freedom (ROTY), were constrained at the pile ends.

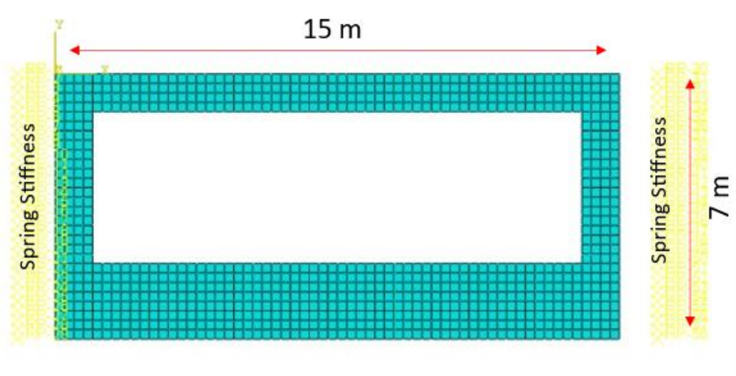

Figure 1 Underground Shelter Model

2.2 Static Analysis

To analyse the combined behaviour of wall stiffness and pile response, a static load of 100 N/mm was applied as a SHELL EDGE load along the left-side edge of the wall in both Case 1 and Case 2 models, incorporating the respective nonlinear spring stiffness values.

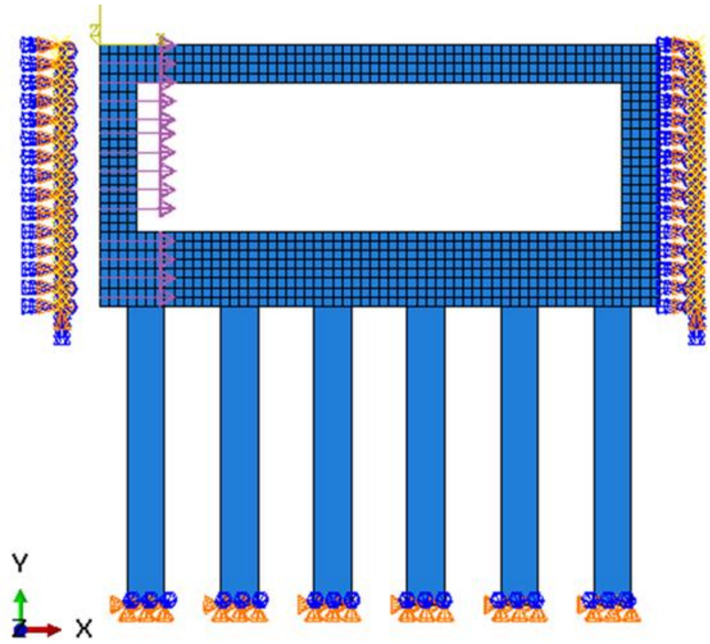

Figure 2 Model Static Analysis

Table 1 Results Static Analysis

Description		Case 1	Case 2
Stiffness	=	6000 N/mm	18000 N/mm
Total Force	=	700000 N	700000 N
Reaction Force on Right Side Wall	=	174000 N	500000 N
Reaction Force on Left Side Wall	=	Nil	Nil
Reaction Force on Piles	=	525977 N	200000 N
% Wall	=	24.8 %	71.4 %
% Pile	=	75.1%	28.5%

Soil with higher stiffness absorbs a greater portion of the lateral load, resulting in reduced load transfer to the pile. In contrast, soil with lower stiffness transfers a larger proportion of the load to the pile, leading to higher reaction forces at the pile-soil interface.

2.3 Blast Load Consideration

The propagation of a blast load follows a pattern where the shock wave originates from the detonation point and reaches the structure, generating an incident pressure. This results in an initial positive pressure phase (Pso^{+}), which gradually decreases and is followed by a suction effect, creating a negative pressure phase (Pso^{-}). The time interval during which the positive pressure acts on the structure is termed the positive duration, while the subsequent negative pressure phase is referred to as the negative duration. The total duration (T) of the blast load on the structure is the sum of these two phases. Similarly, the structure, depending on its stiffness, possesses a natural time-period (T_n). The interaction between the blast duration (T) and the natural time-period (T_n) influences the structural response, potentially amplifying or reducing the effects of the blast load. Additionally, the ductility of the structure plays a crucial role in mitigating the impact. In this study, a static load of 100 N/mm is considered, with varying blast durations, referenced against the natural time-period of the structure, determined through modal analysis.

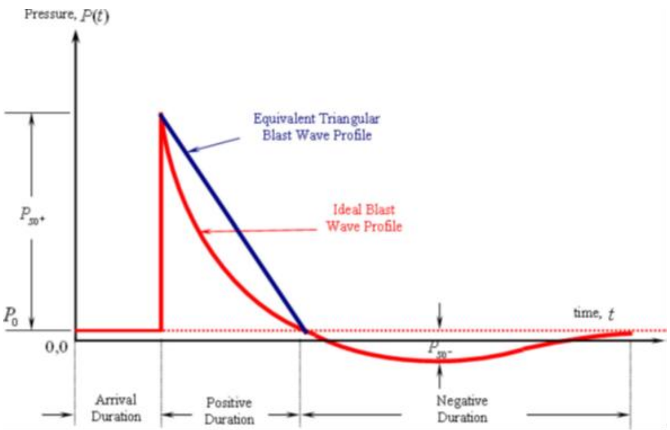

Figure 3 Ideal Blast Wave Profile

2.3.1 Modal Analysis

Modal analysis can be performed on a separate model with the same initial conditions, but without applying any external load. The Field Output Request is configured to extract frequency data using the Linear Perturbation procedure. The resulting output provides the natural time-period of the entire structure, including the shelter building and pile system.

Table 2 Results Modal Analysis

Mode	1	2	3	4	5	6	7	8	9	10
Time, ms	-	-	-	454	394	279	250	237	236	162

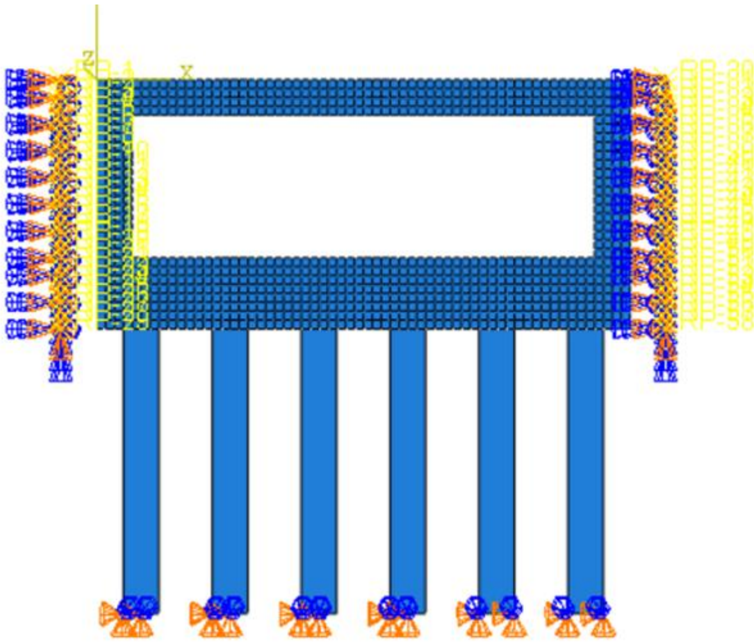

Figure 4 Model – Modal Analysis

2.4 Dynamic Analysis

For dynamic analysis, a Dynamic, Implicit step is used with Nonlinear Geometry (NLGEOM) enabled. The blast duration is determined based on the modal values presented in Table 2 (Results – Modal Analysis), ranging from 1 ms to 1000 ms. The blast duration is applied using a Time vs. Amplitude table, where the peak pressure is set at 0.1 times the total blast duration, ensuring the load follows an equivalent triangular wave, as illustrated in Figure 3. A representative Time vs. Amplitude table for a 100 ms blast duration is provided in Table 3

Table 3 Time vs Amplitude – 100ms

Time	Amplitude
0	0
0.01	1
0.1	0
0	0

The dynamic analysis is conducted multiple times by systematically varying the blast duration. The duration is initially set to 1 ms and 5 ms, followed by increments in multiples of 10, ranging from 1 ms to 1000 ms. This approach ensures a comprehensive evaluation of the structure's response to different blast durations. The typical displacement of the structure is shown in Figure 5.

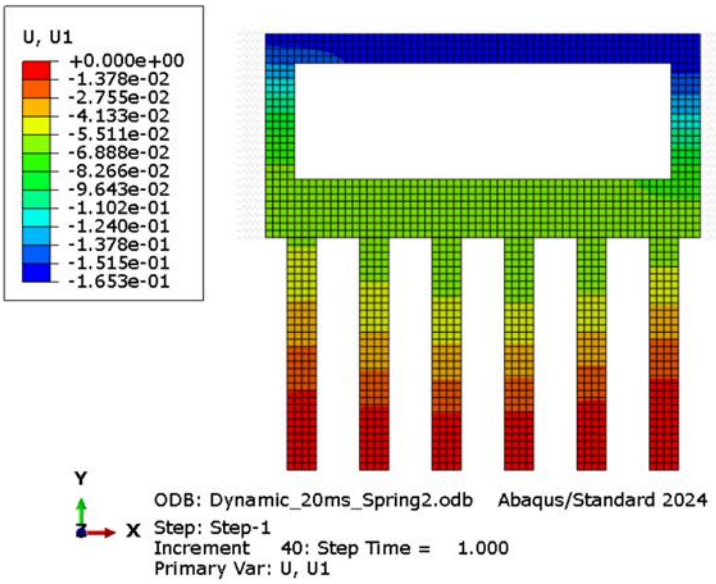

Figure 5 Typical Displacement along U1 Direction

3 RESULTS AND DISCUSSION

A force of 100 N/mm is applied to the left side of the shelter building with varying time periods. The wall-side stiffness springs, positioned on both sides of the wall, along with the pile bottom nodes, provide reaction forces during both loading and rebound. The reaction force (RF1) is extracted separately from all models for the left-side wall springs, right-side wall springs, and pile bottom nodes to analyse the structural response. For shorter blast durations, the reaction force is significantly lower due to the influence of the structure's natural time-period on the load-reaction behaviour. The results of Static and Dynamic analysis is shown in Figure 6, Figure 7, Figure 8 and Figure 9.

The relationship between the applied force and the reaction generated varies depending on the soil stiffness.

Case 1: Soil with Lower Stiffness
For Case 1, where the soil has lower stiffness, the reaction force generated is initially very low when subjected to shorter blast durations. However, as the blast duration increases and approaches the natural time-period (T_n) of the structure, the reaction force gradually increases. At this stage, the reaction reaches approximately 1.5 times the applied force.

A detailed breakdown, as shown in Figure 8, indicates that the right-side wall springs and the pile nodes contribute significantly to the reaction force, following the same pattern described above.

Case 2: Soil with Higher Stiffness
For Case 2, where the soil has higher stiffness, a similar trend is observed. Initially, for shorter blast durations, the reaction force remains low. However, as the blast duration increases, the reaction force grows substantially, reaching approximately 5 times the applied force.

In this scenario, the left-side wall springs contribute the most to the reaction force. This is because, during structural oscillations, the rebound effect causes the structure to take additional support from the left-side wall, leading to an increase in reaction force from that side. Meanwhile, the pile nodes and right-side wall springs generate reaction forces comparable to those observed in Case 1.

These findings highlight the significant influence of soil stiffness on the load-reaction behaviour of underground structures subjected to blast loads

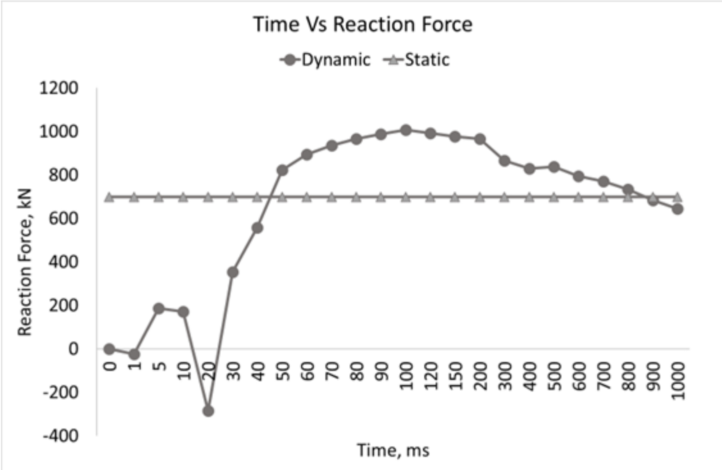

Figure 6 Time vs Total Reaction Force – Static & Dynamic Case1

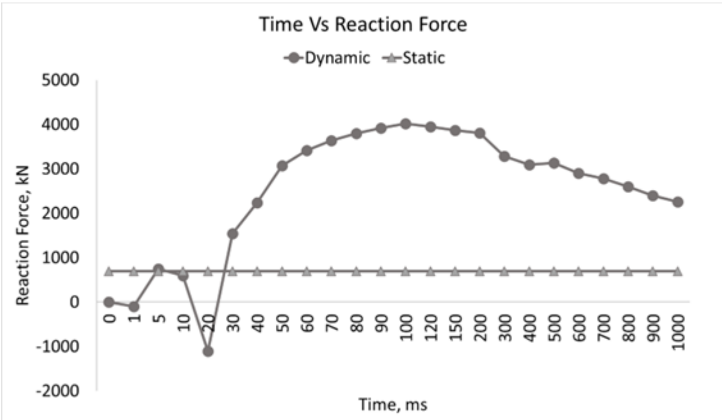

Figure 7 Time vs Reaction Force – Static & Dynamic Case 2

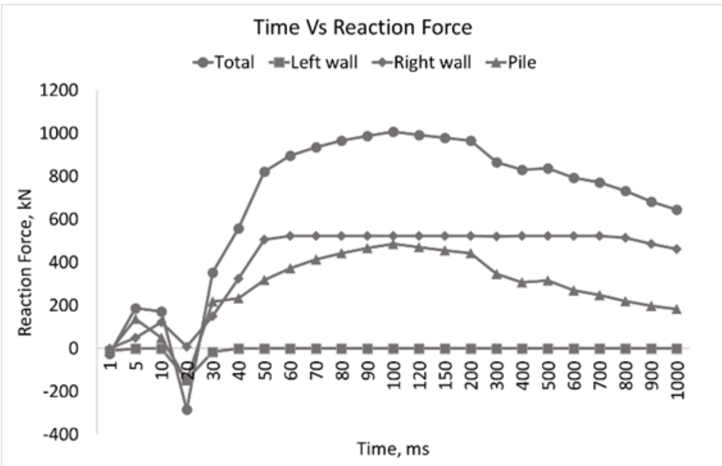

Figure 8 Time vs Reaction – Dynamic Analysis Case 1

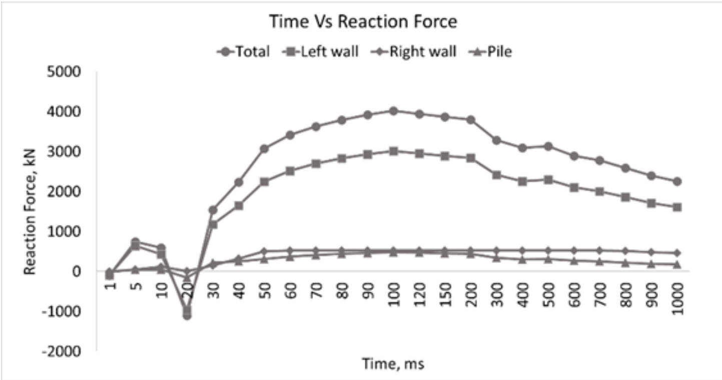

Figure 9 Time vs Reaction – Dynamic Analysis Case 2

4 CONCLUSIONS

Blast threats generate significant lateral pressure, which can be challenging for pile foundations, especially since piles typically have lower lateral load-bearing capacity. To compensate for this limitation, an increase in the number of piles is often required to distribute the load effectively.

However, by incorporating structural periphery walls, the stiffness of the surrounding soil plays a crucial role in counteracting lateral pressure. The soil and the piles work together as a combined system, thereby enhancing the overall structural resistance against blast-induced forces.

The dynamic effect of blast pressure on the structure varies with blast duration. When the blast duration is short, the reaction forces generated within the structure remain relatively low. However, as the blast duration increases, the impact of lateral pressure intensifies, leading to a significant rise in reaction forces. In some cases, the reaction force can reach up to twice the applied pressure, demonstrating the strong correlation between blast duration and structural response.

These findings emphasize the importance of considering both soil-structure interaction and blast duration effects when designing underground shelters to withstand extreme loading conditions.

ACKNOWLEDGEMENTS

I sincerely acknowledge Madala Vikkas Reddy from the National Institute of Technology Karnataka for his valuable contributions in initiating this research work during his tenure as a student intern at Larsen & Toubro. His dedication, analytical approach, and commitment during the internship period played a significant role in shaping the foundation of this study.

I extend my gratitude to Larsen & Toubro for providing the opportunity and resources that facilitated this research initiative.

REFERENCES

L.B.Jayasinghe, D. N. (2013). Computer simulation of underground blast response of pile in saturated soil. *Computers and Structures*, 86-95.

Mukesh Kumar, M. D. (2014). Response of Semi Buried Structures Subjected to Multiple Blast Loading Considering Soil-Structure Interaction. *Indian Geotec Journal*.

15th International Conference on
Shock & Impact Loads on Structures
12-13 June 2025, Gothenburg, Sweden

OPTIMISATION OF BLAST DOOR STRUCTURES

Sherlene Ng*, Paolo Del Linz*, Le Shen* and Yiaw Heong Ng+

*Cluster of Engineering, Singapore Institute of Technology, 138683, Singapore

+ TTJ Design & Engineering Pte. Ltd. , Singapore

Emails: Sherlene.Ng@singaporetech.edu.sg; Paolo.DelLinz@singaporetech.edu.sg

Keywords: OpenRadioss; blast protection; door optimisation; ironmongery

Abstract. *Blast protection of structures is an increasing concern worldwide. This issue is particularly relevant in Singapore, where specific legislation mandates that certain structures incorporate built-in protective measures. Blast doors are often critical components of such security strategies, as they must ensure an adequate level of protection while maintaining accessibility to facilities. The objective of this project is to optimize the performance of blast door systems subjected to blast loads from bare charges. These doors typically consist of two metal plate skins connected by steel spacers, often in the form of C-sections or I-beams. However, this design could be improved by incorporating honeycomb cores, which may be fabricated using conventional methods or, in the future, advanced 3D printing techniques. In this study, a finite element analysis (FEA) model was developed using OpenRadioss and validated to evaluate various core designs. Validation was achieved using data from existing literature tests on panels constructed with traditional I-beam spacers, with the model replicating peak deflections. Subsequently, several innovative core configurations were modelled and compared, including square, hexagonal, and re-entrant honeycomb structures. Parametric studies were conducted to assess the influence of honeycomb cell size and wall thickness, while maintaining a consistent panel mass across all designs. The results demonstrated that honeycomb panels outperformed traditional panels with C-section spacers under blast loading, achieving reduced peak and permanent deflections for equivalent panel weights.*

1 INTRODUCTION

Enhancing the resistance of structures to blasts, whether originating from malicious attacks or from accidental explosions, is a design requirement in many situations. This is especially the case in Singapore, where local legislation, in the form of the Infostructure Protection Act [1], require designated buildings to offer a minimum level of protection from attacks. Openings in the building envelope, such as glazing and doors, represent weaker points which are especially susceptible to damage during such events. Their destruction can cause direct injuries due to the fragments generated and to the ingress of the blast waves into the buildings. Additionally, such elements can be specifically targeted as their destruction can provide a mean to access the building.

Blast doors represent a design solution to protect doorways. These elements need to be able to resist the threats being considered, which leads them to be constructed with heavy structural sections. At the same time they are still required to perform as normal doorways. Therefore, limiting their weight without compromising the level of protection is an important parameter, which can both improve their performance in every day use and potentially reduce their costs.

Panels of this type were studied by authors in the past, for example by Rana [2], who conducted an experimental study with cased charges on steel blast door panels. Some of these studies also included the performance of ironmongery, which could be included in simulations to different levels of precision to assess the performance of the whole door system [3], [4], [5].

Standard door designs usually employ sandwich steel structures, where two steel plates are spaced by either C or I beam sections. These are often fillet welded to one of the plates, whilst spot welds are employed on the other side for the second plate. The resulting structures are strong and can resist the applied blast pressures adequately. Such panels can be optimized through the use of higher-grade materials and different configurations of standard spacers sections and plates [6], however this is limited in scope. An alternative approach is to use different structural forms for the core component. One of these is honeycomb steel sheets, which can be fabricated with thin steel plates and can efficiently space the front and back plates. Such elements can provide a more constant support through the door surface, avoiding damage to the plates and distributing the loading more efficiently. Through these characteristics, their performance can represent a substantial improvement from traditional structural forms and lead to weight savings for the doors.

Such panels have been considered by some authors in the past [7], [8], [9]. These studies often concentrated on smaller scale panels to be used for vehicles and employing materials such as fibre reinforced composites and aluminium. They generally showed that the honeycomb structures were efficient at reducing deformations and overall panel damage, absorbing energy efficiently through plastic deformations of the honeycomb structure.

In this paper, the performance of full size steel door panels employing such cores has been studied and compared with a traditional construction option. The honeycombs selected could be constructed relatively easily with traditional fabrication techniques, allowing such potential designs to be quickly adopted by industry players. The study was performed using high fidelity FEA models. A hydrocode was used to create these, as it could represent both the loading and the material behaviour accurately. For this work, OpenRadioss was employed as it can simulate all aspects of the test. An initial model was created of a literature blast door experiment, as presented previously [6]. This was used to validate the proposed simulation techniques, including the method to simulate the blast loading and the choice of mesh, material and other modelling options.

Following this, a realistic door panel was modelled using C sections as spacers. The ironmongery was included to assess its effect on the door behaviour. The door core was then replaced with several honeycomb structures, using different cell geometries. The mass and the depth of the doors were kept approximately constant to offer a fair comparison. The doors behaviour during a blast was then compared, considering especially central deflections and plastic deformations, as these would be indicative of the door behaviour during an attack.

2 METHOD

2.1 Validation models

The panels were simulated using high fidelity FEA models built in OpenRadioss. The validation, reported in [6], was based on a literature experiment [2]. In this, panels were subjected to combined blast and fragment loading. As part of the research presented in the literature, the tests were simulated with LS-Dyna, through which it was shown that simulating the blast as a bare charge also produced accurate results for the samples employed. Therefore, the same test was simulated in OpenRadioss to validate the modelling choices.

The geometry of the validation panel is provided in figure 1. The sample consisted of two steel plate, 12 mm and 5 mm thick, spaced with UB sections welded side by side along the entirety of the flanges. Full penetration butt welds were used for this. The front and back plates were then spot welded to the beams. The sample was held in a fully enclosed cubicle, which prevented pressures from wrapping around the panel and affecting its rear face. The overall dimensions where 4 m x 1.2 m. The UB sections employed grade S300 Plus steel, with a yield stress of 332 MPa, whilst the plates where fabricated with grade 250 steel having a yield strength of 300 to 330 MPa. The free field pressures and the central deflections were recorded to assess the panel behaviour and for comparison with simulations. A 15 kg cased charge at a stand-off distance of 2.57 m was used to load the sample.

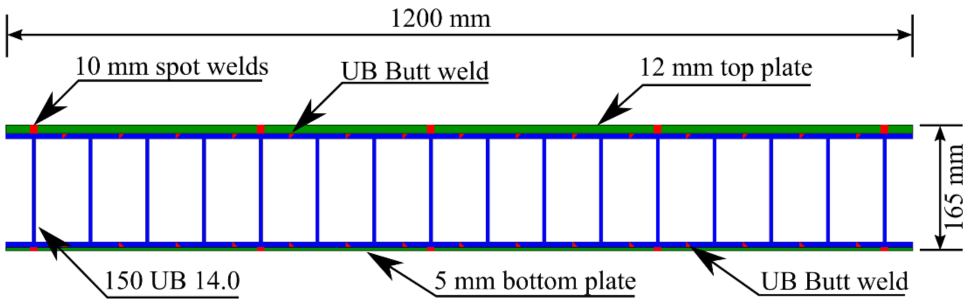

Figure 1. Steel panel geometry [xx]

The validation model was created to simulate the panel as closely as possible. Therefore all the dimensions were kept as in the experiment. Approximately 10 mm solid elements were used throughout. Reduced integration elements were used as these were considered appropriate for the blast highly dynamic simulation. A viscous hourglass control was employed to avoid unrealistic energy losses due to this. Three elements were used through the steel plate thickness to ensure that eventual bending stresses could be accounted for.

The steel material was represented with the Johnson Cook material model. This was chosen as it can simulate the high strain rate behaviour of the material, as well as its plastic deformation and eventual failure. The values were obtained from literature [10] and are shown in table 1, with the value of *A* adjusted to match the estimated yield strength of the material.

Table 1. Johnson Cook material parameters

ρ (kg/m^3)	E (MPa)	υ	A (MPa)	B (MPa)	n	C	m	$\dot{\varepsilon}_0$	T_{melt} °C	T_{room} °C
7800	210000	0.3	350	234	0.643	0.076	1.03	1	1370	20

The panel was supported at the top and bottom edges as in the test. The nodes in the appropriate location were pinned to achieve this.

The loading was applied using the PBLAST load function in OpenRadioss. This employs the CONWEP equations to simulate the blast loading, including different arrival times along the plate. The loading was set as in the experiment. The central deflection was extracted to be compared with the experimental results.

2.2 Parametric study models

Different models were then created to verify the effect of different core shapes on the panel behaviour. These models were based on common existing blast door designs. The original door consisted of two steel plates spaced by C sections, as shown in figure 2. The model was created using the same method used in the validation case. In this case though, the C sections were assumed to be welded throughout their length on both side of the flange to one of the steel plate. The other steel plate instead was spot welded to the opposite flanges, at approximately 200 mm centre to centre along the C sections length. The ironmongery details were also included, with simplified locking mechanisms modelled at the top and bottom of the door panel. The door was supported through a boundary condition set in the ironmongery detail. The front and back plates were assumed to be fabricated with S690 steel, whilst internal hot rolled sections used S355 steel.

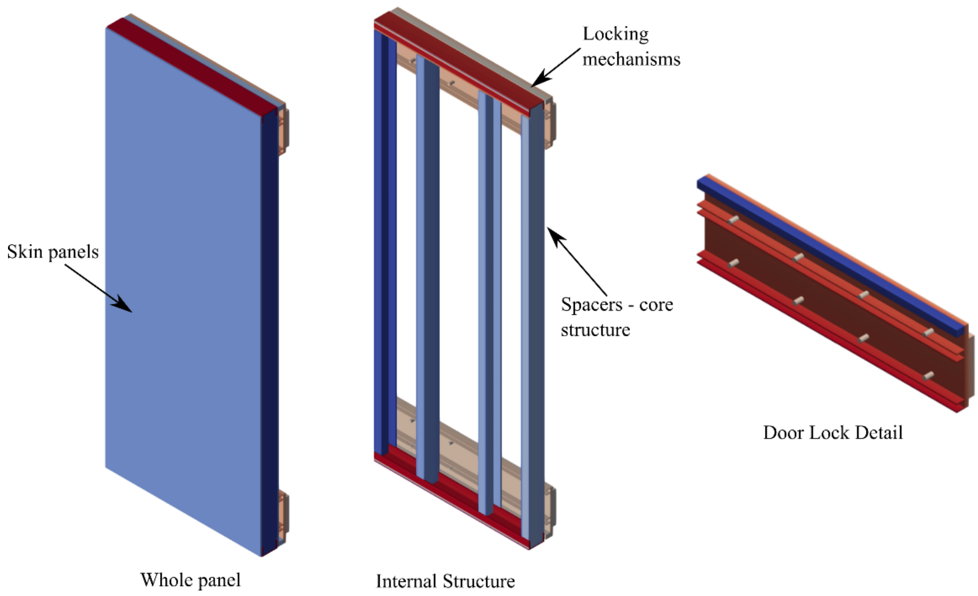

Figure 2. Deflection angle

The load was applied as a pressure with a linear decay on the front face of the panel. This time, a more significant threat was simulated to observe the behaviour of the panels nearer their failure limit. The maximum pressure simulated was p_{max} = 2.0 MPa, with a load duration t_0 = 3 ms.

Additional panel configurations were then created using different types of honeycomb cores. Three main honeycomb shapes were considered, as shown in figure 3. These were hexagonal honeycombs, honeycombs with re-entrant corners and square honeycombs. The properties of these is shown in table 2, including their total mass, the characteristic length of the cells and the thickness of the cells walls.

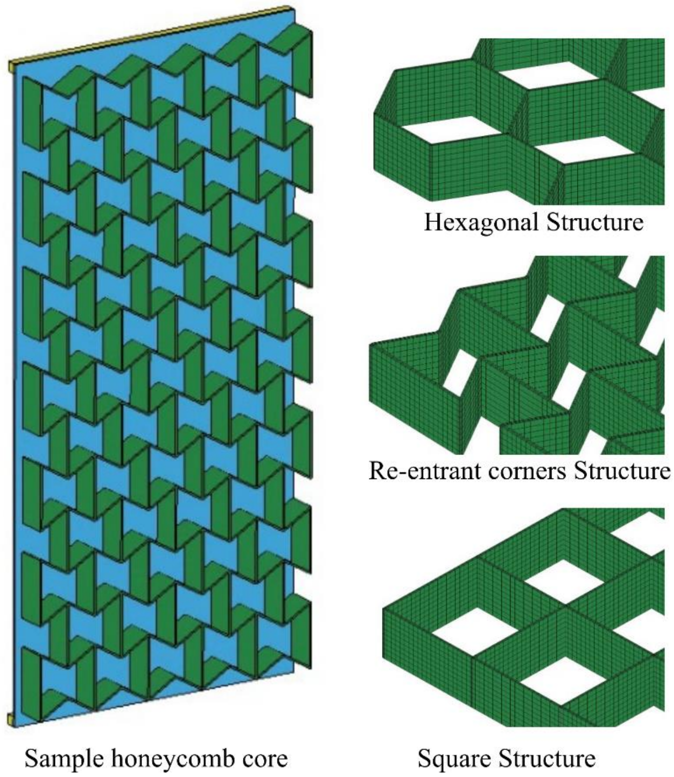

Figure 3. Honeycomb structures

Table 2. Honeycomb panels properties

Model	C sections	Hexagonal Honeycomb	Re-entrant Honeycomb	Square Honeycomb
Mass (kg)	475	421	400	564
Characteristic length *l* (mm)	n.a.	200	100	200
Cell wall thickness *t* (mm)	n.a.	5.0	4.4	6.5

The panels performance were compared through their peak and estimated residual deflection. Additionally, the plastic damage of the steel cores was also compared.

3 RESULTS & DISCUSSION

The validation case was ran first, as was presented in [6]. Figure 4 shows the deflections recorded during the experiment and in the simulation. The peak experimental deflection was 27 mm, whilst the FEA peak deflection was 23 mm. The model could therefore represent the deformation reasonably accurately, validating the methods used in the models.

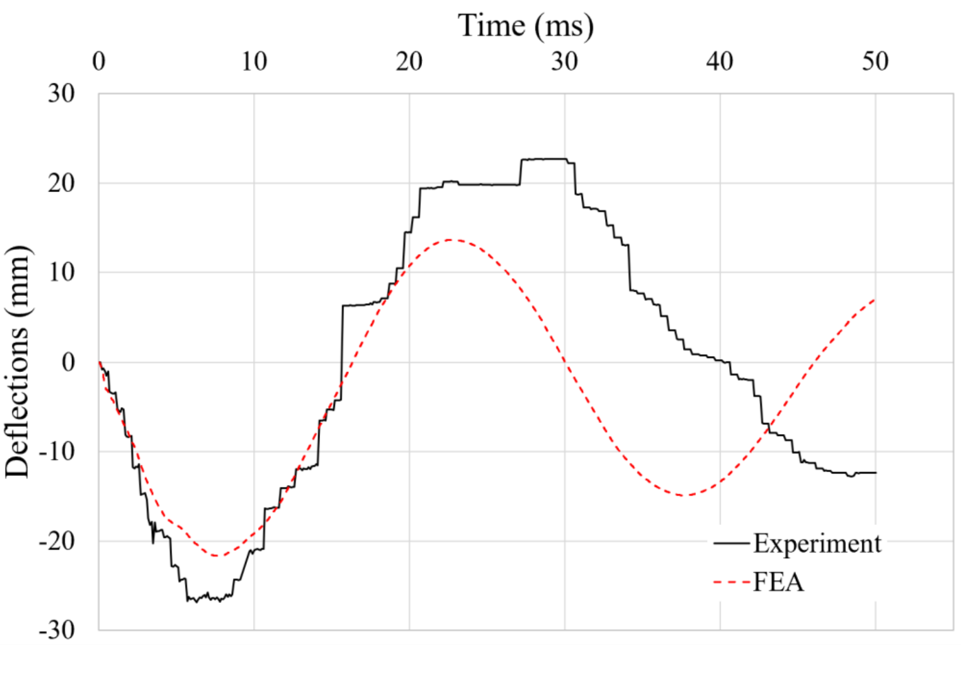

Figure 4. Validation case central deflection time history [xxx]

The honeycomb models were then run. The central deflections are shown in figure 5. The graph indicates that the base model had the highest deflections, with a peak of 51 mm. The residual deflection was approximately 10 mm. All the honeycomb panels displayed a lower maximum deflection. The most efficient one was the re-entrant corner panel, with a peak deflection of 11 mm and a residual deflection of less than 1 mm. Its mass though was greater than the other options. All the results are summarized in table 3.

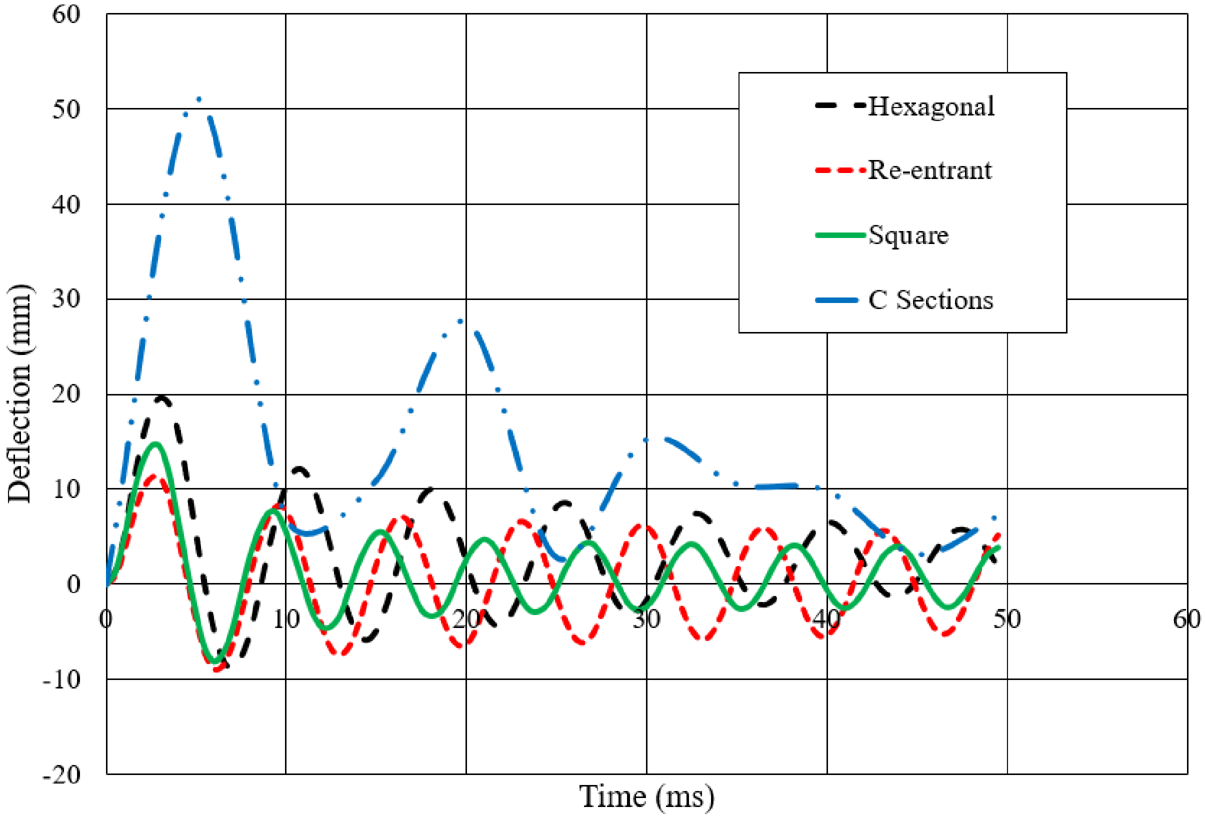

Figure 5. Central deflections of the panels

Table 3. Model results

Model	C sections	Hexagonal Honeycomb	Re-entrant Honeycomb	Square Honeycomb
Maximum deflection (mm)	51	19.5	11.1	14.5
Approximate central Deflection (mm)	10	3	0	1

The plastic strain results show that the honeycomb panels were less damaged overall, with no significant plastic deformation in the honeycomb structure, as shown in figure 6, which represents a typical result. This was most likely due to the denser network of supporting plates, which avoided the stress concentrations which would characterize the traditional C section elements. This was likely the main aspect which caused the improved performance of these types of structures and will be investigated further varying the density and thickness of the core cells.

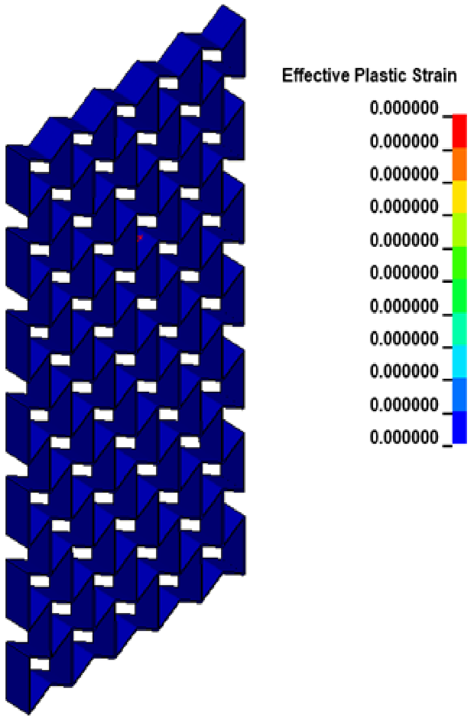

Figure 6. Plastic strain of a honeycomb panel

4 CONCLUSION

As part of this project, a blast door model was created and validated using the Hydrocode OpenRadioss. In the work presented here, the validated technique was employed to verify the performance of alternative core structures to be used in blast door panels. A traditional panel built using C sections as spacers was compared with alternative honeycomb-type cores. These employed different geometries, with either hexagonal, square or re-entrant corners cells. The panels were all of the same overall height and had comparable mass.

The results showed that the honeycomb panels reduced the deflections significantly, with a reduction in the peak deflections of up to 80% and a complete avoidance of permanent deformations. The most effective honeycomb shape was re-entrant corner cells, however all the options considered showed an improvement when compared to C section spacers. The steel plastic deformations were also reduced, as also evidenced by the reduced permanent deflections. Whilst several of the honeycomb options had a higher mass, the improvement in performance seems greater than could be justified by this factor alone, suggesting that the structural form is significantly more efficient. A possible factor leading to this is the more distributed support for the face plates, which would have allowed the loads to be spread more uniformly. This improvement in the efficiency could lead to a potential reduction in mass and thickness of the doors.

Some of the panels proposed here will be tested experimentally in the future to confirm and further validate the simulation results. Further work should then explore the relationship between honeycombs plate thickness and the cell size to optimize the performance of the system. These studies should also include the effect of different fabrication techniques, such as the quantity of welds and the methods to assemble the honeycombs themselves, as these could affect the door performances. Additionally, the effect of different holding mechanisms should also be explored, as the honeycombs render the doors effectively double spanning, compared to the single spanning traditional designs. The effect of alternative geometries, such as the use of crushable cores, to improve the resistance to closer in blasts could also be studied.

It is hoped that these studies will further the understanding of the detailed behaviour of these panels, considering especially the fabrication techniques employed for their manufacture. This will allow contractors to design lighter, more easily fabricated panels, reducing costs and allowing more structure to be protected in the future.

ACKNOWLEDGEMENT

This work is supported by Construction Technology Innovation Laboratory (CTIL) in SIT, Woh Hup Pte. Ltd., TTJ DE Pte. Ltd, National Research Foundation, Singapore, and Building and Construction Authority (BCA) under its Built Environment Technology Alliance (BETA) Catalyst Funding Grant (Award No: BETA-20230224004).

DISCLAIMER

This work is partly funded by National Research Foundation, Singapore and Building and Construction Authority (BCA) Singapore under its Built Environment Technology Alliance (BETA) Catalyst Funding Grant (Award No: BETA-20230224004). Any opinions, findings and conclusions or recommendations expressed in this material are those of the authors and do not reflect the views of the National Research Foundation, Singapore and the Building and Construction Authority (BCA) Singapore.

REFERENCES

[1] Singapore Governament, *Infrastructure Protection Act 2017*. Singapore: Singapore Parliament, 2017.

[2] M. M. Rana, A. Khan, P. Del Linz, C. K. Lee, and T. C. Fung, “Effect of cased charges on plain steel and steel-concrete sandwich targets,” *Thin-Walled Structures*, vol. 136, pp. 302–314, Mar. 2019, doi: 10.1016/J.TWS.2018.12.022.

[3] V. A. Salomoni, G. Mazzucco, G. Xotta, R. Fincato, C. E. Majorana, and M. Schiavon, “Nonlinear modelling, design, and test of steel blast-resistant doors,” *Advances in Mechanical Engineering*, vol. 2013, 2013, doi: 10.1155/2013/908373.

[4] K. Ganorkar, M. D. Goel, and T. Chakraborty, “Numerical Analysis of Double-Leaf Composite Stiffened Door Subjected to Blast Loading,” *Journal of Performance of Constructed Facilities*, vol. 37, no. 1, Feb. 2023, doi: 10.1061/(asce)cf.1943-5509.0001783.

[5] L. Xinzheng and J. Jianjing, “Dynamic FEA and Simulation for A Series of Blast-Resist-door,” Science Press, 2002.

[6] P. Del Linz and Y. H. Ng, “Optimisation Of Steel Blast Door System,” in *Protect 24*, Singapore, 2024.

[7] G. Tiwari and N. Khaire, "Ballistic performance and energy dissipation characteristics of cylindrical honeycomb sandwich structure," *Int J Impact Eng*, vol. 160, Feb. 2022, doi: 10.1016/j.ijimpeng.2021.104065.

[8] M. Patel and S. Patel, "Blast mitigation analysis of novel designed sandwich structures using novel approaches," *Mechanics of Advanced Materials and Structures*, 2023, doi: 10.1080/15376494.2023.2243614.

[9] R. Li, T. Fu, C. Yang, and M. Zhao, "Blast resistance analysis of butterfly-like reentrant circular honeycomb sandwich structure," *Mechanics of Advanced Materials and Structures*, 2024, doi: 10.1080/15376494.2024.2426777.

[10] A. Shrot and M. Bäker, "Determination of Johnson–Cook parameters from machining simulations," *Comput Mater Sci*, vol. 52, no. 1, pp. 298–304, Feb. 2012, doi: 10.1016/j.commatsci.2011.07.035.

15th International Conference on
Shock & Impact Loads on Structures
12-13 June 2025, Gothenburg, Sweden

NUMERICAL SIMULATION ON THE CHARACTERISTICS OF BLAST PRESSURE ACTING ON A STRUCTURE

Masuhiro Beppu[a], Chien Trinh Minh[b], Ryo Matsuzawa[c] and Hiroyoshi Ichino[b]

[a]National Defense Academy, Japan, email: beppu@nda.ac.jp,

[b]National Defense Academy, Japan

[c] ITOCHU Techno-Solutions Corporation, Japan

Keywords: blast pressure, numerical simulation, blast resistant design

Abstract

This study investigated the blast pressure characteristics acting on a structure by conducting explosion tests and numerical simulations. Prior to the explosion tests, a method for evaluating the blast pressure characteristics proposed by the Unified Facilities Criteria was described and its unpublished concept was discussed. Then, scaled explosion tests for investigating the blast pressure acting on a box-type structure were conducted by using composition C-4 high explosive. Blast pressure characteristics at a front wall, a top roof, and side and rear walls were discussed comparing those estimated by the facility criteria. Numerical simulation was carried out to further investigate the blast pressure characteristics. Numerical results showed good agreement with the test results.

1 INTRODUCTION

To design a structure subjected to blast pressure, evaluating the blast loads acting on the structure is necessary [1]-[3]. According to previous studies, based on the geometrical similarities and experimental results, the scaled distance Z ($=R/W^{1/3}$), which is defined as the distance R between a structure and an explosive (stand-off distance) divided by the cubic root of the explosive mass W (charge weight), has been proposed and used as an index for calculating blast pressure parameters [1]-[5]. Using the scaled distance, the peak incident pressure, peak reflected pressure, blast duration, and blast impulse can be calculated using the figures in the U.S. Protective Facilities Standards (TM 5-855-1 [1], UFC 3-340-02 [2]) and the approximation formulae in the Canadian Design Guidelines [5]. As a typical time history of incident pressure is illustrated in **Figure 1(a)**, the incident pressure increases instantaneously to the peak pressure and then declines, resulting in a negative pressure below the ambient pressure. Pressure above ambient pressure is called positive pressure and pressure under ambient pressure is called negative pressure. In blast resistant design of structures, a triangular pressure history as shown in **Figure 1(b)** representing the positive pressure has been used [1]-[5]. This method has been referred to worldwide, and validations of blast pressures that the incident pressure is perpendicular or oblique to the structure were conducted by the authors [6]-[7].

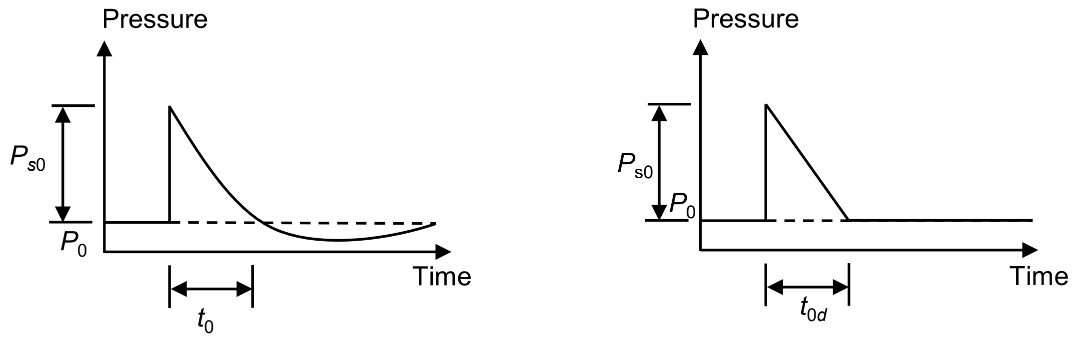

(a) Incident pressure history (b) Pressure history for design

Figure 1. Idealization of pressure history for blast resistant design

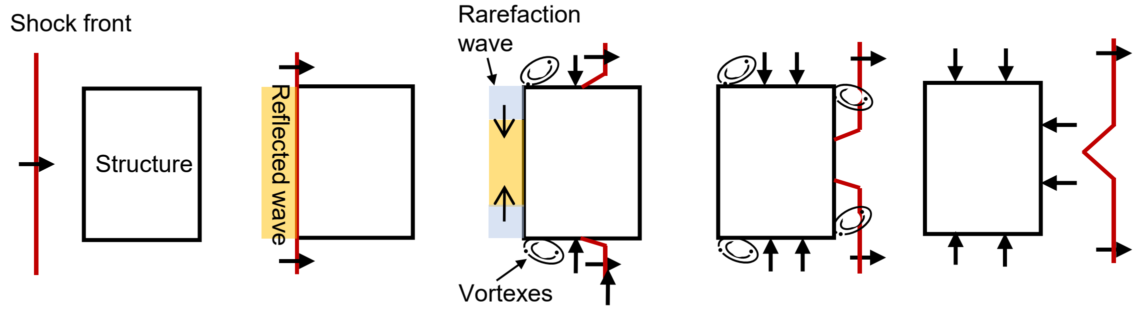

(a) Ground plan

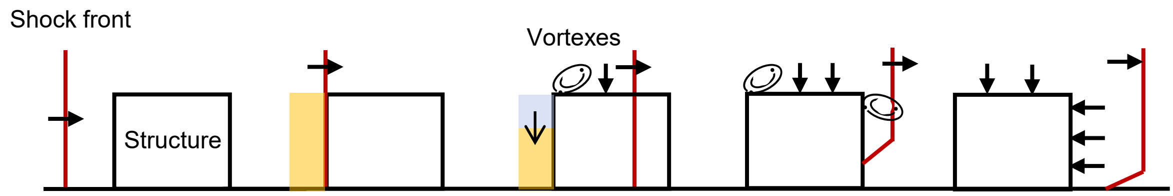

(b) Side view

Figure 2. Blast phenomena surrounding a structure subjected to blast wave

Although the abovementioned methods can be applied for the evaluation of blast pressure acting on members such as beams and columns, they would not be applied to structures composed of facade members such as buildings. **Figure 2** shows a schematic diagram of blast pressure acting on a box-type structure [2], [8]. When a blast wave acts on the structure, the reflected pressure is generated on the front wall. At the same time, vortexes and clearing waves are generated at the edges of the front wall and then reduce the reflected pressure. When the blast wave continues to travel through the structure, blast pressure acts on the top roof and side walls. Furthermore, vortexes are generated when the blast pressure passes through the roof and side walls, diffracting and exerting pressure on the rear wall. Although these phenomena are very complex, the Protective Facilities Standards [1], [2] propose a design method by calculating uniform distributed pressure history on the front wall, top and side walls, and rear wall respectively. However, there are no technical documents or design guidelines that explain the concept of the method, and the safety of the structure designed using the method can not be estimated.

This study aims to investigate blast pressure characteristics on a box-type structure by conducting explosive tests and numerical simulations. First, explosion tests were conducted to investigate the pressure characteristics acting on the structure. Then, numerical simulation of the experiment was performed to reproduce the test results, and future issues are discussed.

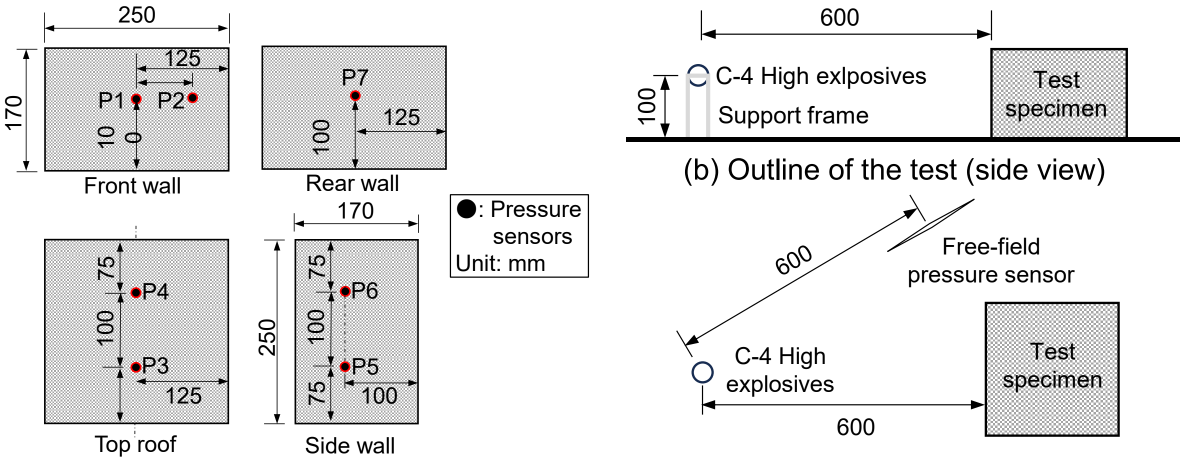

(a) Dimensions of the test specimen (b) Outline of the test (side view) (c) Outline of the test (ground plan)

Figure 3. Outline of the test specimen and the explosion test

2 OVERVIEW OF EXPLOSIVE TESTS ON BLAST PRESSURE CHARACTERISTICS AROUND BOX-TYPE STRUCTURE

Figure 3 (a) illustrates an overview of the box-type structural model (test specimen) used in the tests. The test specimen is made of Steel Plate Cold Commercial material with a thickness of 3.2mm and dimensions of 250mm×250mm×170mm. Two holes were provided in the front wall, the top roof, and one side wall of the test specimen to allow for the installation of pressure sensors. Only one hole was provided in the rear wall. The measurement capacity of pressure sensors at the front wall was 690MPa because high reflected pressure was expected to be generated. For the top roof and side wall, sensors with the measurement capacity of 69MPa were deployed, and a pressure sensor with the measurement capacity of 6.9MPa was used for the rear wall. The height of the pressure sensors was the same as the detonation height of the explosive, which will be described later.

Composition C-4 high explosives (explosive) with a density of 1.4 g/cm^3 and the mass of 31g was formed into a spherical shape and detonated by a No.6 electrical detonator installed in the center of the explosive. Strain gauges were installed on the explosive to detect the detonation time. A plywood board (base) was fixed on sandy ground with steel piles, and the test specimen was set up on the base. The explosive was detonated at 600 mm away from the structure and a height of 100 mm from the base, as shown in **Figure 4(b)**. To measure the incident pressure acting on the structure, an ambient pressure sensor (free-field pressure sensor) was used at the same stand-off distance as the front wall, as shown in **Figure 4(b)**. The experiment was conducted seven times, and scattering was also examined.

3 NUMERICAL SIMULATION AND DISCUSSION OF BLAST PRESSURE CHARACTERISTICS SURROUNDING STRUCTURES

3.1 Overview of numerical simulation

Figure 5 illustrates an overview of numerical model constructed with the hydrocode ANSYS AUTODYN [10]. As the computational cost of a 3D detonation simulation is high, a detailed one-dimensional detonation simulation was conducted in advance, and the results were mapped into a 3D model to simulate blast propagation.

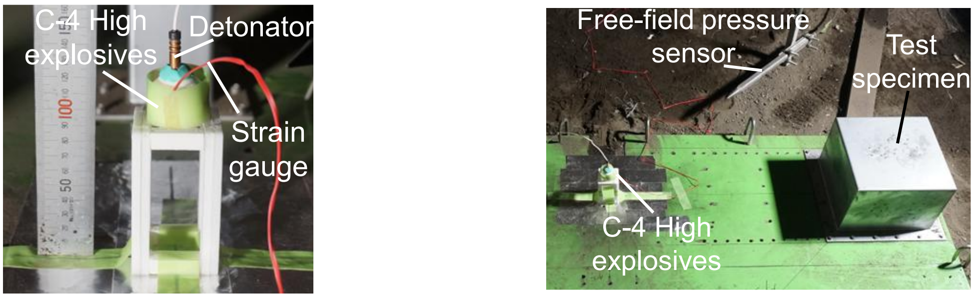

(a) C-4 high explosives (b) Test setups

Figure 4. Overview of the explosion tests

(a) 1D explosion simulation model (b) 1D simulation result

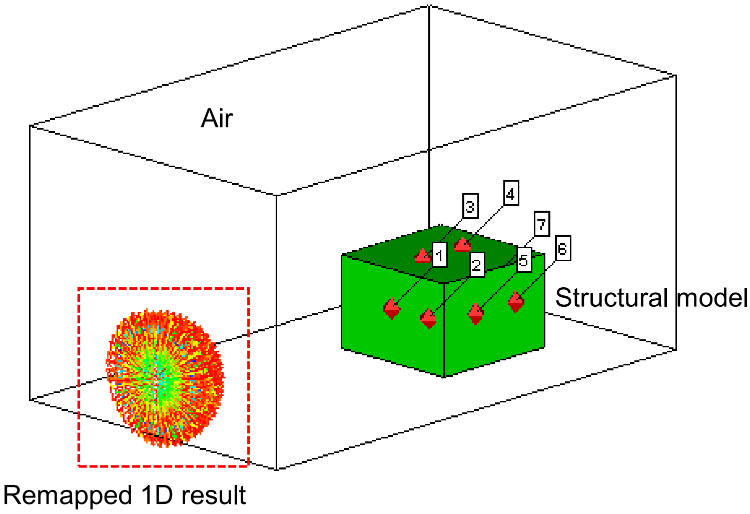

(c) 3D Simulation model

Figure 5. Overview of the simulation model

As shown in **Figure 5 (a)**, C-4 explosive of the same radius as in the experiment were filled in the one-dimensional Eulerian space, and air was set up outside the C-4 explosive. The mesh size for 1D simulation was 2 mm. The boundary condition for the air farthest from the detonation point was set as the flow-out condition, and the Jones-Wilkins-Lee (JWL) equation of state was used for the explosive.

$$P = A_1\left(1-\frac{\omega\eta}{R_1}\right)e^{\frac{-R_1}{\eta}} + A_2\left(1-\frac{\omega\eta}{R_2}\right)e^{\frac{-R_2}{\eta}} + \omega\eta\rho_0\varepsilon \qquad (1)$$

Where P is pressure, A_1, A_2, R_1, R_2, and ω are material constants, ε is specific internal energy, $\eta=\rho/\rho_0$, where ρ is density and ρ_0 is initial density. For C-4 explosive with a reference density of 1.4 g /cm^3 used in the experiments, AUTODYN set values [10] shown in **Table 1** were applied.

The following equation of state for ideal gas was applied for air.

Table 1. JWL equation of state constants used in the simulation

Density (g/mm^3)	A_1 (MPa)	A_2 (MPa)	R_1	R_2	ω	Detonation velocity (m/s)
1.4×10^{-3}	6.1×10^5	1.3×10^4	4.5	1.4	0.25	8.2×10^3

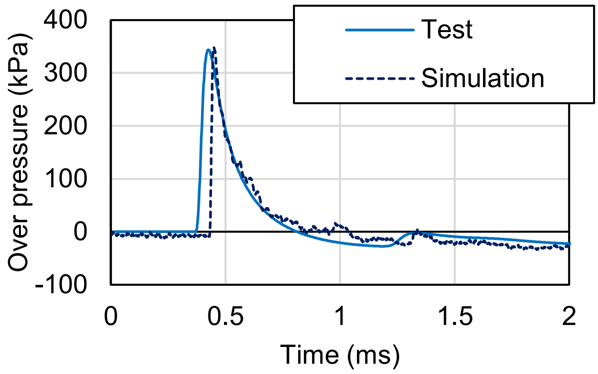

Figure 6. Incident overpressure at 600mm

$$P = \rho(\gamma - 1)\varepsilon \tag{2}$$

Where P is pressure, ρ is density, and γ is the specific heat ratio. Generally, γ is set to 1.4. For the initial values of air, the initial pressure is 101.3kPa (1atm) and the initial density is 1.225kg/m^3.

As shown in **Figure 5 (b)**, 1D simulation was conducted until 0.02 ms after detonation, and the results was saved. Next, the ideal gas equation of state shown in Equation. (2) was applied to the air in the 3D model. The structure model was assumed to be a rigid body, and the pressure was mapped to the same position as in the experiment. A preliminary simulation was conducted to determine the space discretization, and the mesh size was set to 10 mm. Flow-out conditions were applied to all sides of the 3D space except the XY plane.

3.2 Numerical Results and discussion

Figure 6 exhibits the comparison of the incident overpressure at 600mm between the numerical and test results. **Figure 6** demonstrates that the arrival time of the blast wave in the numerical simulation was approximately 0.07ms earlier than the test result, but the peak overpressure for the numerical simulation and test result was both approximately 350 kPa. The loading duration in the numerical simulation was nearly equal to that in the experiment, indicating that the simulation reproduced the experimental results well.

Figure 7 compares the simulated overpressures acting on the structural model with the experimental results. **Figure 8** compares the peak overpressure and impulse in the experiment and simulation. As shown in **Figure 7(a)** and **Figure 8**, the simulated blast pressure at the front wall arrived slightly earlier than the experimental one, and the simulated peak overpressure was approximately 60% that of the experiment. The reason for the smaller simulated peak overpressure may be due to the inclusion of high-frequency components in the experimental result and the smoothening of the shock front in the numerical simulation. On the other hand, the simulated impulse was 85% of the experimental result and the reproduction of the blast duration and impulse was relatively high. For the top roof and side walls as shown in **Figure 7 (b), (c)**, and **Figure 8**, the simulated blast arrived slightly earlier than the tests, and the peak overpressure is 20 to 40% smaller than in the tests. However, as with the front wall, the impulse is 85 to 95% of the experimental value, indicating that the reproduction of the impulse was high. A comparison of the top roof and side wall shows that, as in the experiment, the peak overpressure at the side walls is higher than at the top roof.

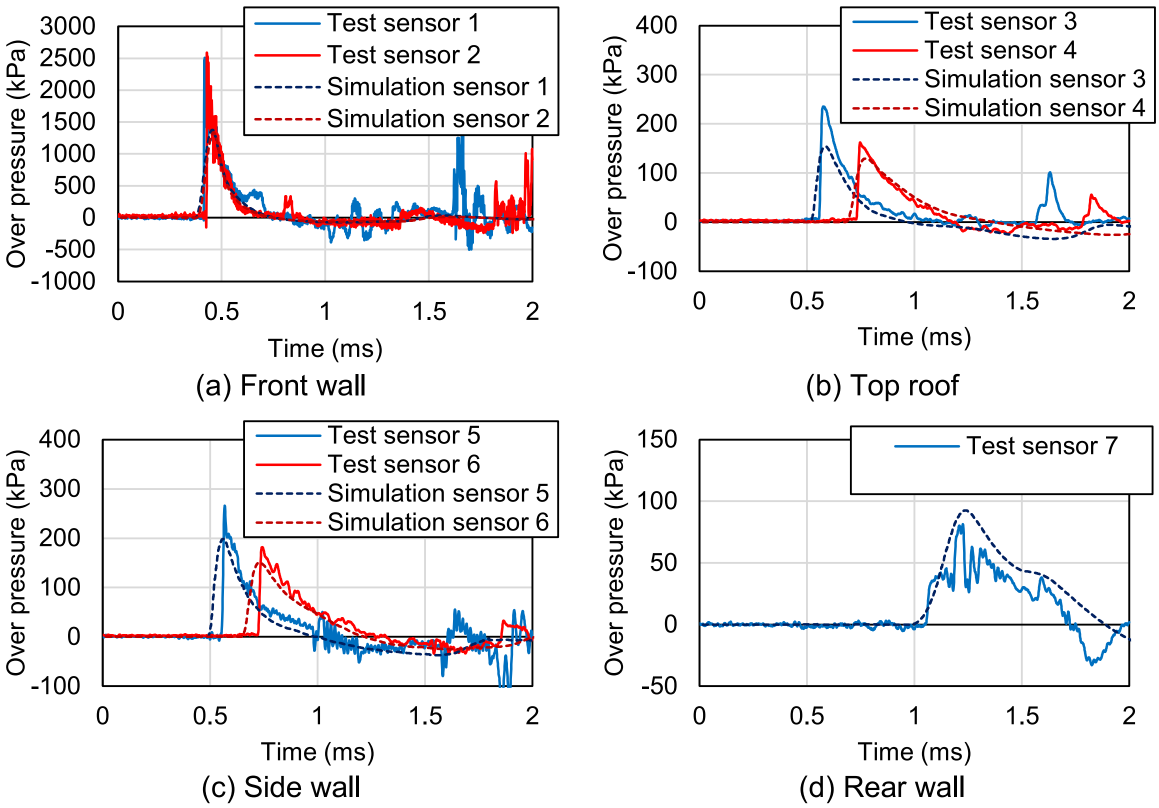

Figure 7. Comparison of simulation and test result for pressure acting on the structural model

Moreover, the arrival time at the side wall is earlier than that at the top roof. These results indicate that the pressure characteristics slightly varied between points at the same stand-off distance from the explosive even though the pressure discrepancies were minor. Thus, the effects of structure dimensions should be taken into consideration. For the rear wall as shown in **Figure 7(d)** and **Figure 8**, the simulated results generally reproduce the characteristics of the experimental waveform. The arrival time, the peak pressure, and the blast duration of the simulated pressure showed similar trends with the test results.

Figure 9 depicts the propagation of the blast and pressure distribution from 0.1ms to 1.2ms after the detonation. The contour in the figures demonstrates absolute pressure including air pressure. **Figure 9(a)** indicates that the pressure propagates in a spherical shape from the detonation point at 0.2ms after detonation. Particularly, a triple point is formed by the overlap of the incident wave and the reflected wave from the base. At 0.5ms after detonation, the blast wave arrives at the front wall forming a high-pressure area, as shown in **Figure 9(b)**. It can be seen that the pressure diffracts at the edges of the front wall. These phenomena correspond to the schematic diagram as shown in **Figure 2**. Numerical simulation allowed a detailed view of the clearing and diffraction behavior of the blast waves. Note that negative pressure did not occur until 0.5ms after detonation. At 0.8ms and 1.2ms after detonation, the blast wave diffracting from the front wall to the top roof and rear wall can be observed as shown in **Figure 9(c)** and **(d)**. As shown in the legend, negative pressure was generated at the edge between the front wall and the top roof. **Figure 10** illustrates the velocity vector of the elements in the simulation along with pressure contours. The figure shows that vortex-like turbulence occurs at the edges of the structural model, and the negative pressure may have been generated by such turbulence. However, this simulation used only the equation of state for calculating blast pressure and did not consider the turbulence model or parameters to reproduce the effect of the vortex. Hence, conducting validation and collecting more experimental data are necessities to improve the accuracy of the simulations in the future.

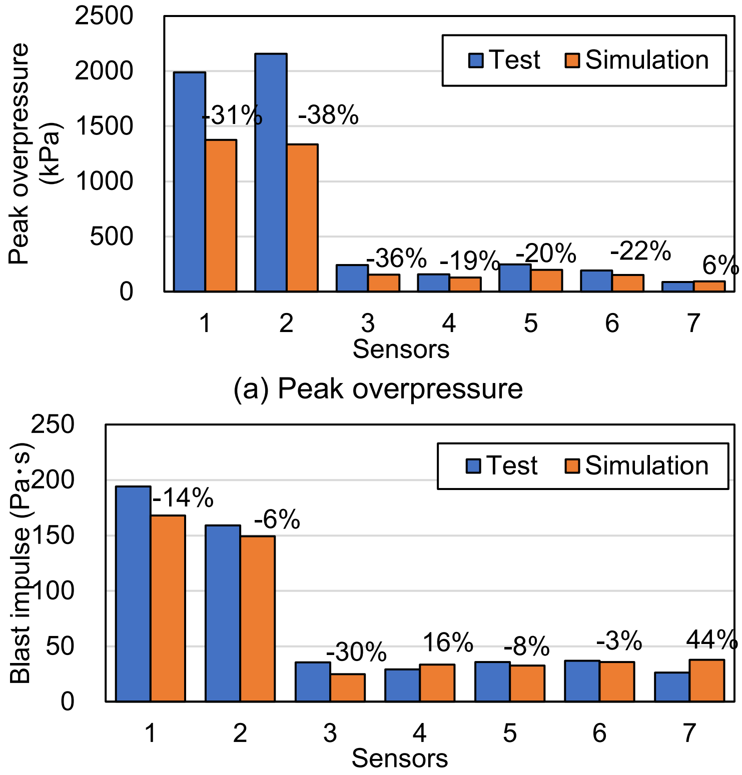

(a) Peak overpressure

(b) Blast impulse

Figure 8. Comparison of simulation and test results for peak overpressure and blast impulse

4 CONCLUSION

This study investigated the characteristics of blast pressure acting on a box-type structure by conducting fundamental explosive tests and numerical simulations. The results are summarized below.

(1) Explosion experiments were conducted to investigate the pressure characteristics acting on a box-type structure. The variation of the pressures acting on the structure was great as compared to the incident pressure.

(2) Numerical simulation for the experiments was performed to examine the reproducibility. Numerical model used in this study generally reproduced the experimental pressure characteristics, and the reproducibility of the impulse was higher than that of the peak pressure.

ACKNOWLEDGEMENTS

This research was partially supported by Grant-in-Aid for Scientific Research (24K01141). The authors would like to thank Koki Mori and Takuma Terazawa, Graduate Course of Science and Engineering, National Defense Academy of Japan, for their great cooperation in conducting this research. We would like to express our gratitude to them.

REFERENCES

[1] Headquarters, Departments of the Army: Fundamentals of protective design for conventional weapons, TM5-855-1, 1986.
[2] Department of Defense: Unified Facilities Criteria (UFC) UFC 3-340-02: Structures to resist the effects of accidental explosions, 2014.

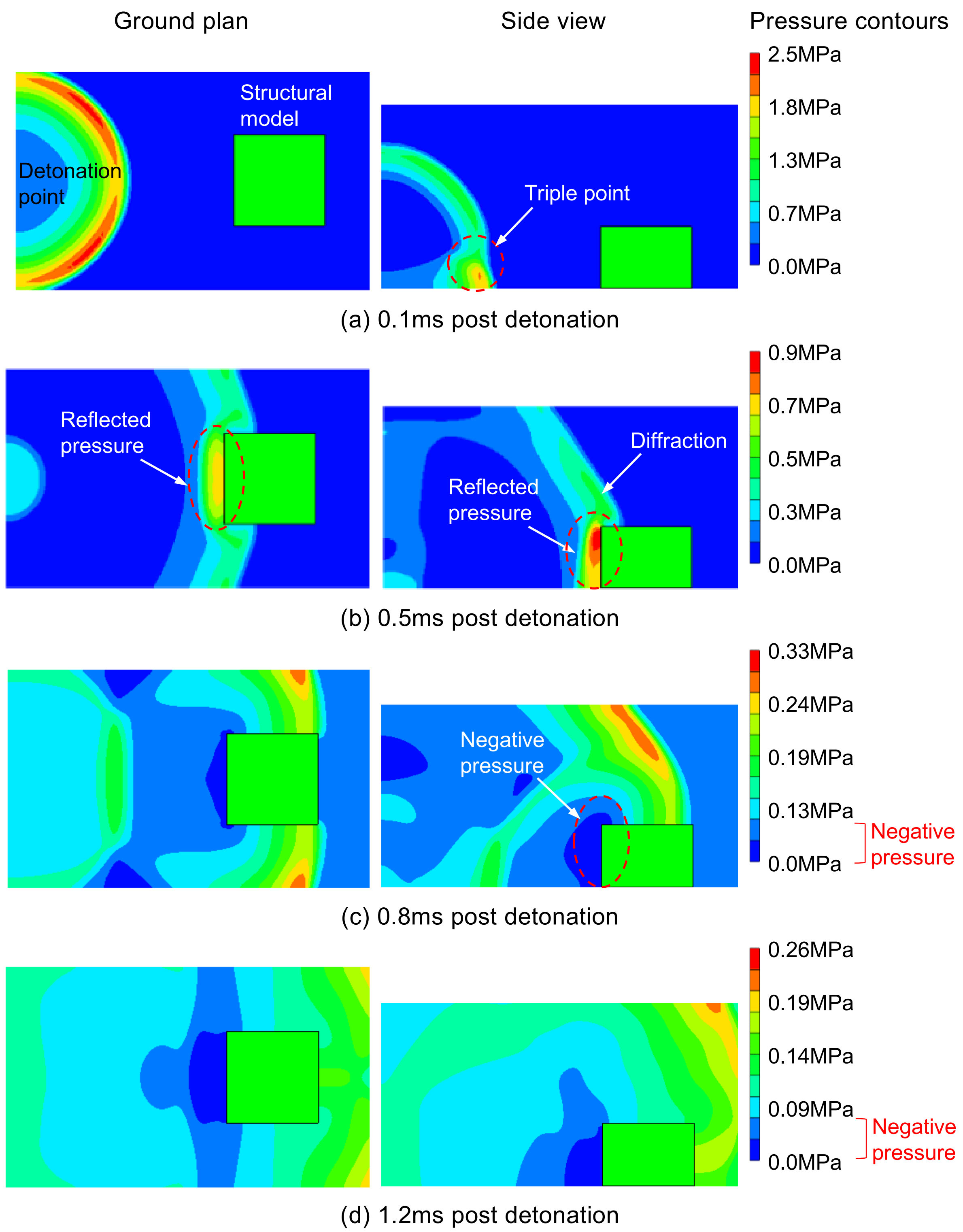

Figure 9. Propagation of blast pressure in the simulation

[3] Krauthammer, T.: Modern protective structures, CRC Press, 2008.
[4] Japan Defense Facilities Association: Safety Evaluation of Concrete Structures Subjected to Explosive Action - Evaluation Methods and Countermeasure Techniques -, Japan Defense Facilities Association, 2018.
[5] Canadian Standards Association: Design and assessment of buildings subjected to blast loads, 2012.
[6] Makoto Nagata, Masuhiro Beppu, and Hiroyoshi Ichino: Proposal of Evaluation Method for Bending Response of RC Beams Subjected to Distributed Loading by

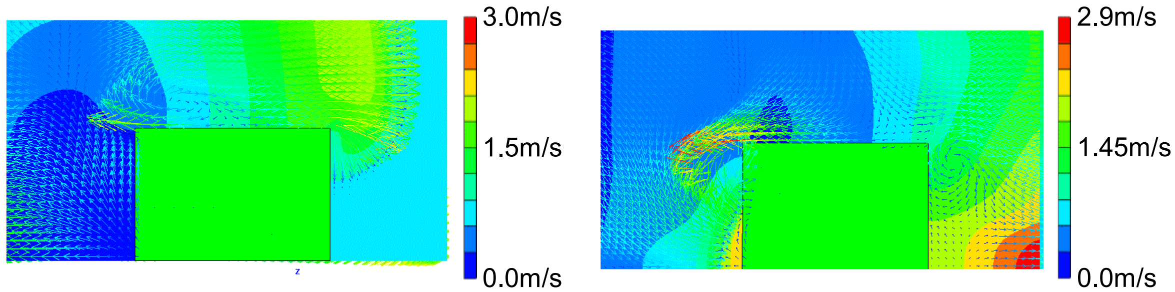

(a) 1.0ms post detonation (a) 1.5ms post detonation

Figure 10. Formation of vortexes in the simulation (Velocity vector fields)

Nearby Explosion, Journal of JSCE, A1 (Structural and Earthquake Engineering), Vol. 74, No. 3, pp. 399-416, 2018.

[7] Nagata, M., Beppu, M., Ichino, H., Takahashi, J.: Method for evaluating the displacement response of RC beams subjected to close-in explosion using modified SDOD model, Engineering Structures, Vol. 157, pp. 105-118, 2018.

[8] Japan Society of Civil Engineering: Safety Evaluation of Civil Engineering Structures Subjected to Explosion and Impact Action - Preparing for Rare Events, 2017.

[9] Yoshio Nakayama: The Power of Explosive Terrorism, Safety Engineering, Vol. 55, No. 6, pp. 427-434, 2016.

[10] ANSYS AUTODYN User's Manual, 2019.

EVALUATION OF INTERNAL FORCES DISTRIBUTION IN RC BEAMS SUBJECTED TO IMPACT LOADS

Gonzalo S.D. de Ulzurrun[a] and Carlos Zanuy[a]

[a] Department of Continuum Mechanics and Structures, ETS Ingenieros de Caminos, Canales y Puertos, Universidad Politécnica de Madrid, Spain
g.ulzurrun@upm.es

Keywords: reinforced concrete, drop-weight, digital image correlation, impact, shear-span to depth ratio, numerical model

Abstract

The behavior of civil and buildings structures under accidental impulsive loads (impacts or blast) remains a significant research challenge. Impulsive loading leads to resistance and failure modes that differ substantially from those observed under quasi-static loads. Reinforced concrete (RC) structures are very sensible to develop a brittle failure when subjected to impulsive loads. This might be explained by the particularities of the dynamic behavior of structures. In the dynamic range, effects such as the development of inertia forces or the sensibility of failure mechanisms to the strain rate must be considered. In addition, in highly dynamic events, adiabatic conditions are in general prevalent. In the case of the impacts, the load imparted during the shock depends on various factors, such as the kinetic energy of the collision and the interaction between the impacting bodies. This interaction is determined by their stiffness, mass, materials mechanical properties and the non-linear behavior of the contact.

Therefore, evaluating the failure mode of a RC structure under these dynamic conditions might be challenging. One critical aspect of the structural verification under impulsive loads is that the internal forces distribution (shear and bending) is uncertain. In previous contributions, the authors have employed an experimental methodology to assess the time-varying distribution of these forces. This methodology is based on the combined use of digital image correlation (DIC) and a high-speed (HS) camera.

The present study analyzes the time-varying internal forces distribution of RC beams subjected to low-velocity impact loads. The study has an experimental basis and discusses the results with a numerical elastoplastic model. The experimental campaign consists of 12 RC beams with a longitudinal reinforcement ratio of ρ = 1.0%, different quantities of shear reinforcement (ρ_w = 0 and 0.3%) and three shear span-to-depth ratios (a/d), between 2 and 5.3. The aim of the study is to discuss experimental observations with numerical results, focusing on the failure mode and in the sectional forces distribution during the impact event for the different spans of the beams.

1 INTRODUCTION

Contemporary society is aware of the importance of ensuring structural safety when constructions are subjected to extreme loading conditions. These events – be they of natural or anthropogenic origin – attract significant media and public attention due to their sudden, catastrophic, and unpredictable nature. Among extreme loads, impulsive actions such as impacts or blast can be particularly damaging. Ideally, structures should absorb the imparted energy by the dynamic loads by elastic and, especially, ductile deformation. However, under impulsive loads some structural systems are likely to develop low energy absorbing failure modes. That is the case of reinforced concrete (RC) structures, which subjected to impulsive loads show a high tendency to develop brittle failure, due to shear (beams) or punching (slabs). This has been observed even in structures prone to bending failure under static conditions [1,2].

The different behavior between static and dynamic might be explained by dynamic effects at the material and structural level. Experimentally it has been observed that material properties are affected by the loading rate. Commonly, this sensitivity is characterized by the ratio of the dynamic to the static value of a property, known as dynamic increase factor (DIF), for a given strain rate. In the case of concrete and steel strength their DIF has been characterized experimentally [3,4] for strain rates up to 225 s^{-1}. In addition, in highly dynamic events, such as high-velocity impacts or blasts, adiabatic conditions are prevalent, thus, temperature effects on the material properties might also be significant.

These effects at the material level alter the strength of the governing failure modes at the structural level. However, the dynamic strength assessment of RC structures, especially in shear and punching, is still a challenge. There have been various studies that have proposed various reinforcement alternatives to avoid shear failure under impulsive loads [5-7]. For instance, the authors of the present paper have proposed two possible alternatives to avoid the development of shear failures under impact loads [8,9], the use steel fibers in RC (SFRC) or the reinforcement of tensile face of RC structures with thin layer of ultra-high-performance fiber RC (RC+UHPFRC). Other studies have focused on formulations to evaluate the dynamic strength of local and global shear-related failure modes [10-14]. However, there is no broadly accepted formulation applicable to any generic impulsive loading case.

In order to understand the dynamic shear and punching strength of RC it is essential to understand the internal forces distribution caused by impulsive loads. One of the key obstacles determining the internal forces is the assessment of the load-time history of impulsive actions. In the case of impacts, the load-time history ($F_{imp}(t)$) is the result of the transfer of linear momentum between the colliding bodies through the contact point. In RC structures the behavior of the contact is non-linear due to cracking and local plastifications [15]. Furthermore, structural accelerations caused by the impulsive load modify significantly the structure's dynamic response compared to its static behavior. In the first stages, the impulsive load is balanced by the inertia forces, thus, its effects are contained near the application area, known as effective span. Afterwards, dynamic load effects propagate toward the supports increasing the effective span length. The first effects of the impulsive loads propagate as a shear wave, with a constant velocity ($v_G = \sqrt{G_c/\rho_c}$) [16]. Experimentally, it has been observed that the shear wave induces only minor effects, while the beam's dominant response propagates subsequently as a flexural wave, which has variable velocity due to its dispersive nature [17,18]. As a result, the time-history distribution internal forces differs significantly from that produced by static loads. The dynamic distribution of shear forces and bending moment is not well characterized in the literature, and there is no widely accepted analytical or numerical method for its evaluation.

This paper focuses on the determination of dynamic sectional forces of RC beams with variable shear-span to depth ratios (*a*/*d*) subjected to impact loads. Sectional forces have been evaluated experimentally, post-processing HSV recordings with DIC and sensors measurements, and numerically, with non-linear beams models. The results have allowed to analyze the development of shear failures with dynamic shear-bending interaction curves.

2 EXPERIMENTAL METHODOLOGY

2.1 Specimen definition

The experimental campaign included impact tests on RC prismatic beams. Tested specimens were grouped into six series, defined by the presence of transversal reinforcement (L: without stirrups, LT: with stirrups) and span length (L = 0.6, 1.1 and 1.6 m). Each series consisted of two beams that were tested under impact loading.

The specimens were 2.0 m long with a rectangular cross-section of 0.15 m width and 0.20 m depth, see Figure 1. The longitudinal reinforcement was identical in all beams: 2 bars of 12 mm diameter ($\rho = A_s/b{\cdot}d$ = 1.0%) in each face of the beam, top and bottom, with a concrete cover of 43 mm. The transversal reinforcement, included in LT series, was formed by 8 mm diameter closed loop stirrups spaced at s_w = 200 mm ($\rho_w = A_w/b{\cdot}s_w$ = 0.3%).

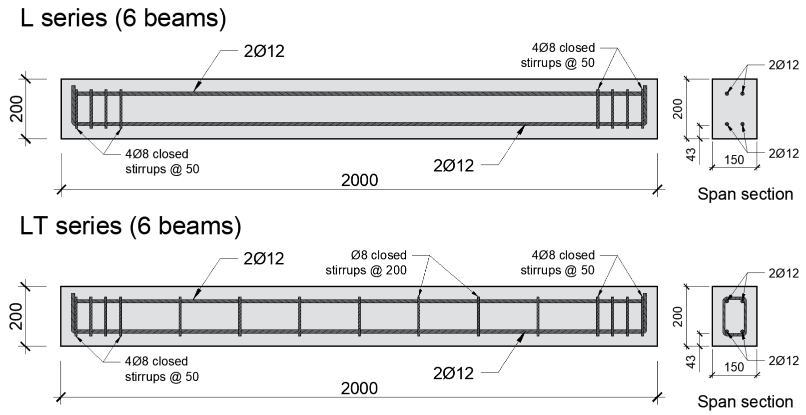

Figure 1. Dimensions and reinforcement of tested beams (dimensions in mm).

Beams with the same properties of those presented in this study have been tested in quasi-static conditions in a three point bending configuration [19]. The series with stirrups (LT-1.6, LT-1.1 and LT-0.6) and the 1.6 m span series without stirrups (L-1.6) achieved the yielding of the longitudinal reinforcement. These series, except LT-1.6 series, developed a shear failure during the post-peak ductility staged with a span (L) to midspan (δ) deflection ratio between L/δ = 90-135. The other series without stirrups (L -1.1 and L-0.6), which were designed with a similar bending and shear static strength, failed by shear just before the yielding of the reinforcement.

2.2 Materials

The prismatic beams tested were made of conventional reinforced, consisting of 331 kg/m^3 of cement type CEM II/A-L 42.5 R, a water/cement ratio of 0.46 and siliceous aggregates of 12 mm maximum size. The concrete strength was obtained at 28 days on cylinder specimens of 150 mm diameter and 300 mm height according to European testing standards [20,21]. The average compressive strength was 26.61 MPa (2.1 MPa standard deviation) and the average indirect (splitting) tensile strength was a 2.5 MPa (0.1 MPa standard deviation). The reinforcing steel was B500 SD (characteristic yield and ultimate strength of 500 and 575 MPa, respectively [22,23]).

2.3 Testing configuration

Beams were tested in a three-point bending conditions, with different span lengths, 0.6, 1.1 and 1.6 m. Impact tests were carried out with an instrumented drop-weight testing machine of the Structural Engineering Group at UPM with a 3.9 kJ impact capacity. The machine drops a guided free falling steel mass (between 100 and 200 kg) from heights up to 2 m onto the tested specimens. Supports and striking end of the drop weight were formed by steel cylinders with a radius of 29 mm and a width of 160 mm, which were in direct contact with RC beams, without any intermediate plates. At the supports, the uplift of the beam was prevented with steel yokes, in contact with the beam upper face through a thin layer of soft material. For further details of the machine please refer to [18].

Impact test configuration presented in this paper is show in Figure 2. Beams were impacted at midspan by 100 kg mass dropped from a height of 1.80 m (5.9 m/s), with an impact energy of 1.8 kJ. Dynamic measurements were obtained with integrated sensors at a sampling rate of 40 kHz. Impact and reaction forces were recorded with three built-in dynamic load cells, one at the free-falling weight sticking end (700 kN) and others in each of the supports (170 kN). Accelerations of representative points, beam's midspan and free-falling weight, were taken with attached piezo-electric accelerometers (±1000g).

The lateral face of the beam was recorded with a high-speed video (HSV) camera, Photron FASTCAM NOVA S9 with a lens Nikon AF-S 20 MM f/1.8G ED. The HSV camera recorded with a resolution of 1024 x 288 pixels (px), at a rate of 22500 frames per second. The recorded part of the beam covers the region between supports, Figure 2(a), with an area of 1680 × 472.5 mm. The spatial scale of the recording is 1 px = 1.64 mm. The recoded face of the specimen was painted with black speckles of 18-25 mm (10-15 px) on a white background, forming a random pattern to analyze in the post-processing the recordings with Digital Image Correlation (DIC), employing the software GOM Correlate [24].

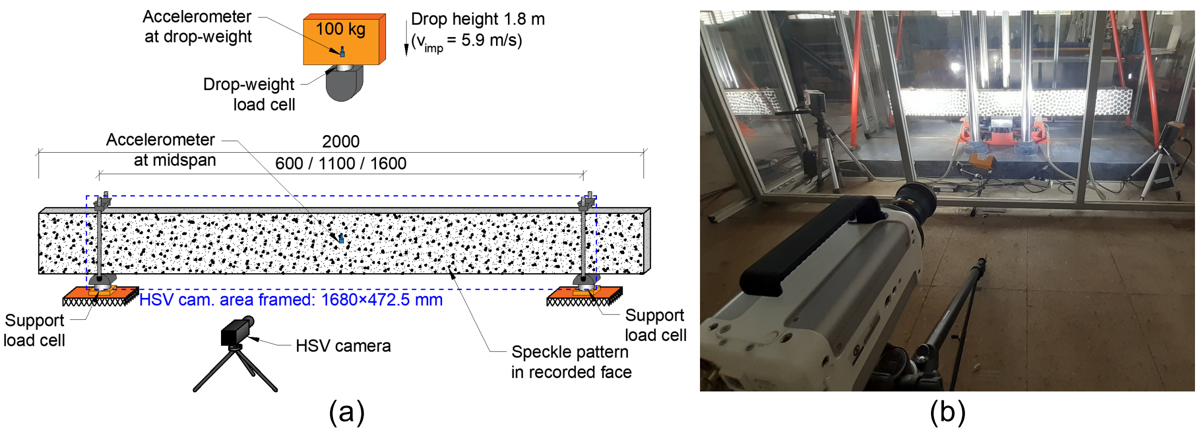

Figure 2. Impact tests: (a) geometric configuration (dimensions in mm); (b) photograph the experimental setup.

2.4 Experimental derivation of sectional forces

Using DIC combined with HSV allows obtaining the full-field response of the tested beams. The specimen's displacements field within the framed area was measured using a 3×25 grid of 40 px facet points centered with the beam axis. The longitudinal and vertical spacing of the grid were 50 mm and 65 mm, respectively. In the areas where the columns of the testing facility and the steel yokes at the supports hid the specimen surface, Figure 2(b), the longitudinal spacing of the grid was adjusted. Measurements in areas not recorded by HSV camera, such as hidden surfaces and part of the cantilevers at beams ends, were obtained by data extrapolation.

The displacement field measured allowed the derivation of the beam's accelerations distribution (*a*) along its axis (*x*) at each instant (*t*). Noise due to the measurements derivation was mitigated using time and spatial filters. Accelerations derived were averaged within each beam section taking into account tests symmetry and the results of the three measurement points per vertical section of the grid. In addition, accelerations were smoothed over time using a five-step centered moving-average filter. Considering the mass of each section of the beam (m) and the acceleration distribution ($a(x,t)$) inertia forces developed during the impact have been evaluated as shown in equation (1).

$$i(x,t) = -m(x) \cdot a(x,t) \tag{1}$$

Sectional forces distribution (shear force $V(x,t)$ and bending moment $M(x,t)$) have been determined at each instant (t) imposing the equilibrium of forces in each segment of the beam, considering the effect of the inertia forces ($i(x,t)$) and external actions, the impact force ($F(t)$) and reactions ($R_1(t)$ and $R_2(t)$), Figure 3. Further methodological details are available in [9,19].

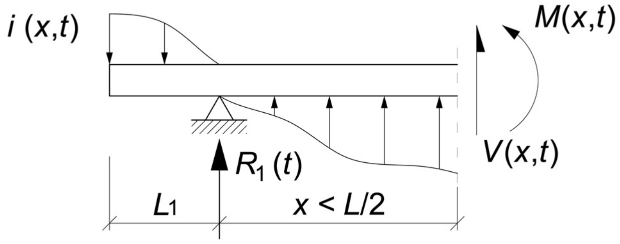

Figure 3. Experimental derivation of dynamic sectional forces from DIC derived measurements and force equilibrium.

3 NUMERICAL MODEL

The impact response of tested specimens has been analyzed using a numerical model, which included a free falling mass, the beam and springs that represent the contact conditions, Figure 4(a). This model has also the capability to assess the internal forces along the beam due to the impact load. The model was formulated and solved with the commercial software ANSYS [25].

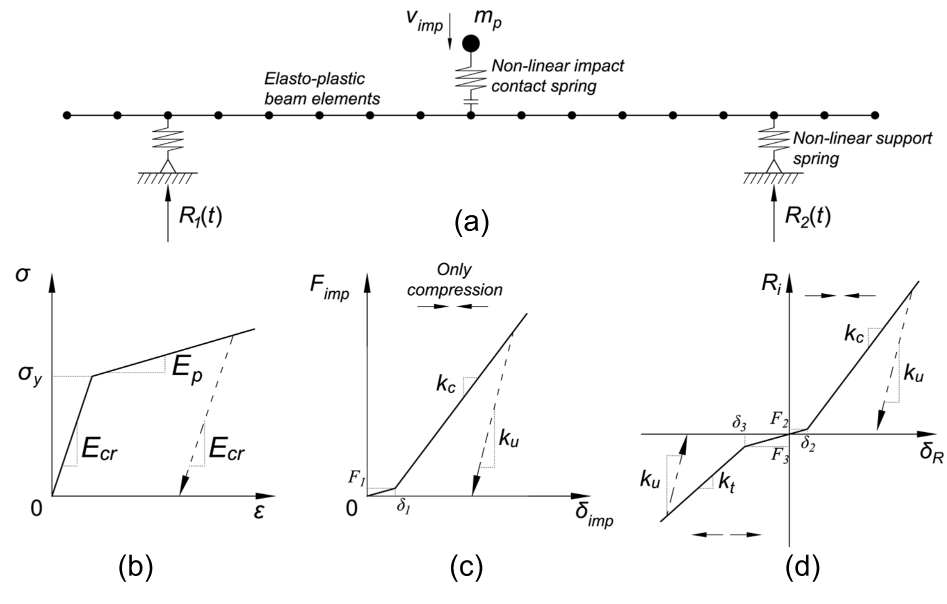

Figure 4. Definition of the numerical: (a) model scheme; (b) beam elements material properties; (c) non-linear spring at the impact point; (d) non-linear spring at the supports.

The dynamic bending behavior of the structure was simulated with 200 elastic-plastic 2-node Timoshenko beams (BEAM23). The bending behavior of RC beam has been simulated using the gross concrete sectional properties with an equivalent material. This material has the same density as RC (ρ_c = 2.5 ton/m^3) and a constitutive law defined as isotropic elastic-plastic bilinear with hardening (BISO), with a yield stress of σ_y = 14.6 MPa, a Young modulus of E_{cr} = 6.55 GPa and a strain hardening modulus of E_p = 15 MPa, Figure 4(b). The mechanical properties of the equivalent material were calibrated to replicate the bending behavior of the tested RC beams subjected to impact, considering a curvature rate of 200 $(s\cdot m)^{-1}$ during the loading, according to previous studies [19]. The bending moment-curvature response of the beam has been computed with a multi-layer cross-sectional model [5,18]. The analysis assumed plane deformation of the cross section, a perfect rebar-concrete bond, a concrete constituent model defined by [26] (disregarding its tensile strength) and a bilinear stress-strain curve with hardening for the reinforcement steel. Strain rate effects defined by [4,27] were included on the materials constituent laws.

The free falling mass has been modelled as a 100 kg concentrated nodal mass (m_p, MASS21) above the beam midspan with an initial velocity of v_{imp} = 5.9 m/s. The contact conditions at the impact point and supports have been defined as a non-linear springs (COMBIN39). The behavior of these non-linear elements is shown in Figure 4(c) and (d), respectively, where the defining parameters are k_c = 200 kN/mm, k_t = 25 kN/mm, k_u = 500 kN/mm, δ_1 = 0.5 mm, F_1 = 10 kN, δ_2 = 0.1 mm, F_2 = 2 kN, δ_3 = -2.5 mm, F_3 = -10 kN. In the case of the support contact element, it has been defined differently from the impact point contact in order to include the effect the steel yokes and shelf-weight preload. Damping has been included in the system by Rayleigh alpha and beta factors.

The numerical solution has been performed with full-time integration, using the Newmark implicit integration method with ANSYS default parameters (γ = 0.005, α = 0.2525, δ = 0.5050). A variable time step has been employed, with a normal, minimum, and maximum value of $2\cdot10^{-5}$, $5\cdot10^{-7}$ and $4\cdot10^{-3}$ ms. The time in which the dynamic response of the impacted beam was analyzed has been 7.5, 15 and 20 ms for 0.6, 1.1 and 1.6 m span beams. The average computational time for each case was 5 minutes.

4 DISCUSSION OF NUMERICAL RESULTS BASED ON EXPERIMENTAL DATA

Crack patterns of tested beams are show in Figure 5. The impact load induced in all specimens the development of both vertical and diagonal cracks along the beams length. Flexural cracks were especially relevant in midspan bottom face. In addition, bending cracks in the beam top face were observed between the loading point and beam ends. The development of these cracks has been related to propagation effects [16], which has been experimentally confirmed with DIC [28,19].

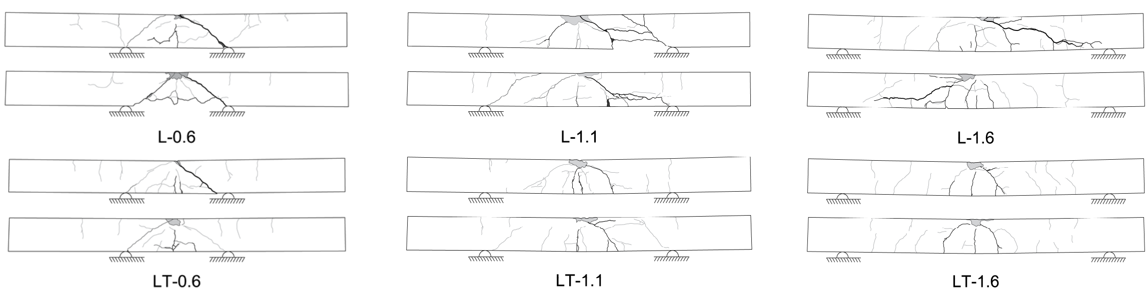

Figure 5. Crack pattern of tested beams: without (L) and with stirrups (LT).

Diagonal cracks observed in tested beams have been classified according to the types defined by [29]: (I) shear-plug cracks at the loading point, with an inclination of approximately 45º; (II) shear-bending cracks with a smaller inclination developed between the impact point and the supports. All tested beams showed type I cracks, while signs of shear-bending interaction (type II cracks) only were observed in beams with a shear-span to depth ratio $a/d \geq 3.6$ (L-1.1, LT-1.1, L-1.6 and LT-1.6 series). HSV combined with DIC has allowed to determine that shear plug cracks (type I) formed during the first stages of the impact, whereas shear-bending crack developed once the reaction forces developed [19,28].

Failure due to the development of a critical shear plug (type I crack) was prevalent in 0.6 m span beams (*a*/*d* = 2), except in one of the two tested beams with stirrups (LT-0.6 series), in which these cracks were rather narrow. Beams with longer spans developed (1.1 and 1.6 m, *a*/*d* = 3.6 and 5.3) non-critical type I cracks. However, beams without shear reinforcement (L-1.1 and L-1.6) developed critical shear-bending interaction cracks (type II). These developed form the shear plug towards the support. In the case of beams with stirrups (LT-1.1 and LT-1.6), these showed narrow inclined cracks in the shear span.

Experimental measurements with the sensors and DIC-derived parameters are presented in Figure 6 and Figure 7. These Figures also include the comparison with the results of the numerical models, described in Section 3. Due to the damaging nature of the impact load, in certain tests some sensors could not record data, especially those located in the most impulsive position, such as the load cell at the impact point. Consequently, their results, and derived parameters, were omitted from the Figures in this section.

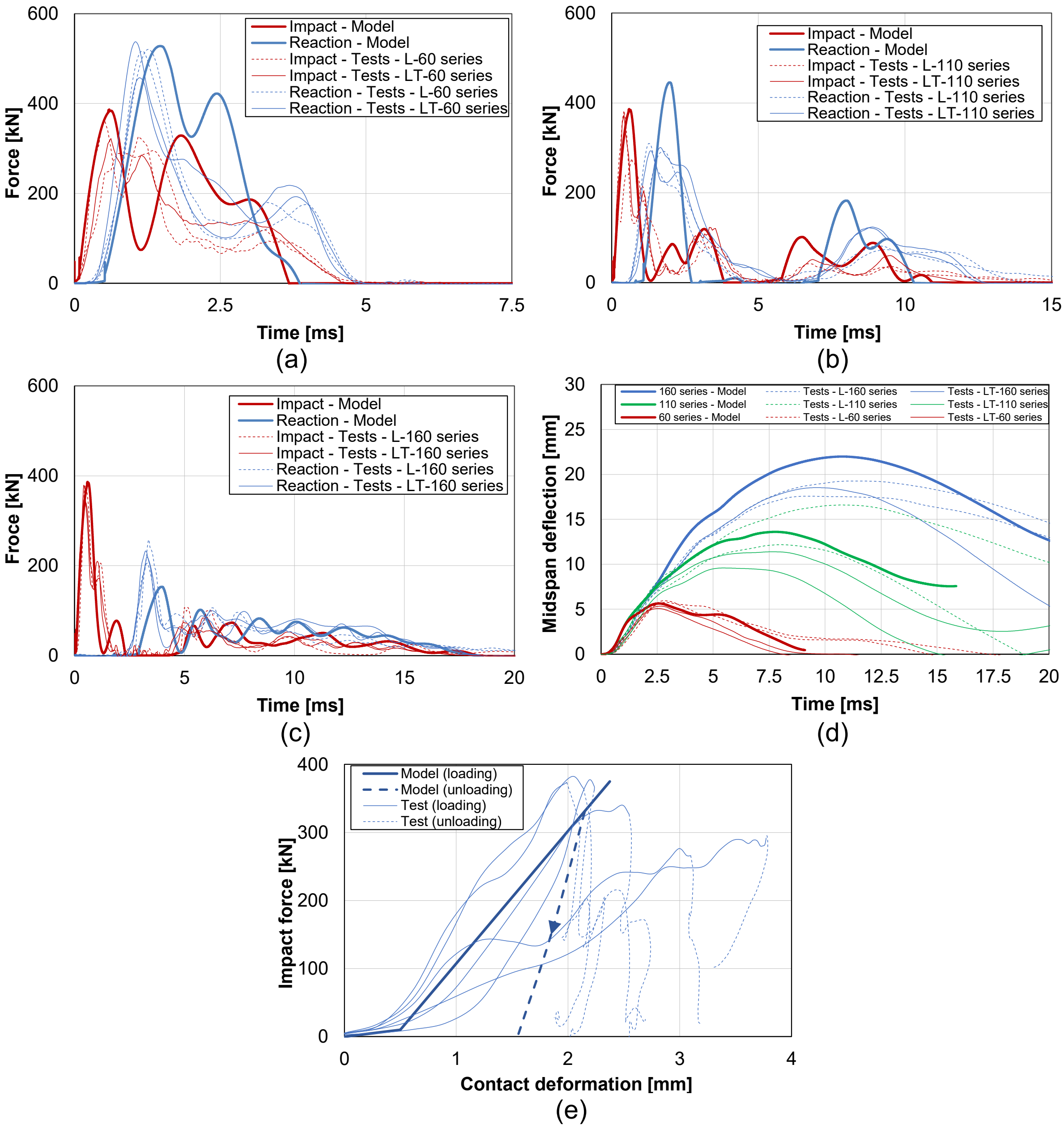

Figure 6. Comparison test and numerical results: (a) forces L = 0.60 m series; (b) forces L = 1.10 m series; (c) forces L = 1.60 m series; (d) midspan deflection; (e) contact behavior.

Experimental results show the impulsive behavior of the impact load, Figure 6(a)-(c). The impact load time-histories exhibited identical behavior up to the peak load, regardless of the span length. Subsequently, the post-peak impact load decreased at faster rate for longer spans. On the contrary, the total reaction forces ($R_1 + R_2$) became more impulsive for shorter spans. The time gap between the rise of the impact and reaction forces has been on average 0.3, 0.6 and 2.4 ms for span lengths of 0.6, 1.1 and 1.6 m, respectively, being the propagation velocity between 330 and 1000 m/s. Shear reinforcement had little influence on the impact force measured. In the case of the reaction forces, L series tend to display slightly lower force values than the LT series in the post-peak stage. Previous studies have related this to the development of the shear failure [28]. Figure 6(d) shows the experimental midspan displacement, obtained through double integration of the measurements of the accelerometer located at the beam midspan. Midspan deflection increased with the beam span length and it was similar regardless of the shear reinforcement up to development of the shear failure. Following the failure, L series showed higher deflection than the beams with stirrups (LT series).

Regarding the numerical results, these exhibit a good agreement with the experimental measurements. In terms of the impact force, Figure 6(a)-(c), the numerical model shows its high accuracy, especially in beams with 1.1 and 1.6 m span. The impact force in the 0.6 m span beam showed a strong agreement in the first peak. In the post-peak behavior it showed some acceptable divergences. These differences coincide with the formation of the shear plug observed experimentally. This suggest that model has locally a stiffer response in that stage, likely because the shear plug formation was not included in the model routine. Total reaction force showed a higher variance than the impact force. This is probably due to the complex the contact of the beam with the support, as the experimental setup includes a steel yoke and interface layer of soft material on the upper surface of the beam to prevent uplift. In addition, model reactions have slightly higher lag time with the impact force. This suggests that tested beams had a stiffer response globally than the model. This is probably due to the disregard of the tensile contribution of the concrete in the model (see Section 3). Lastly, contact behavior used in the definition of the model has been compared with the experimental results, Figure 6(e). The experimental contact deformation was derived from the accelerometers located at the beam midspan and the drop-weight, Figure 2(a). The numerical model simulates the complex contact response with a simplified bilinear curve with a stiff unloading path, consistent with most experimental observations presented in Figure 6(e). In the calibration of the spring, it was observed that its behavior had a high influence on the impact and reactions time-history derived from the model. Thus, its definition is crucial for the model accuracy.

Sectional forces at the representative sections are shown and compared in Figure 7 for all series. The sections considered are midspan and over the supports. For the shear force, the sections are at a distance of $h/2$ from the midspan and d from the supports, except for 0.6 m span series, where these distances were reduced 50% to avoid superposition between sections. Tests results were coherent regardless of the shear reinforcement. In addition, they present high frequency components or noise, especially for the bending moment. It is probable that such high-frequency components are an amplification of the measurement noise in the post-processing of the measured data.

Experimental shear forces presented two primary peaks: the first, occurring near the impact point, had a fast rise-time and displayed a consistent magnitude across all spans, while the second developed near the supports. The second peak value increased as the span decreases, whereas its rise-time and lag from first peak time increased with the span length. For both peaks, bending moment rise-time was longer than that of the shear force. The bending moment also presented two peak values: one positive at the impact point and secondary negative over the supports. Midspan bending moment exhibiting a plateau-like peak, corresponding to the beam sectional behavior flexural behavior (see its definition in

Section 3). The duration of this peak increase with the span length. Conversely, section over the support developed negative bending moments (hogging), with a rise-time shorter than the shear force peak at that locations. The peak value at this location increased with inversely to span length, probably due to the increase of the end cantilevers. For 0.6 m span series, the negative moment even reached the flexural capacity of the cross-section. This explains the extensive cracking observed in Figure 5 at the top face of these beams over supports.

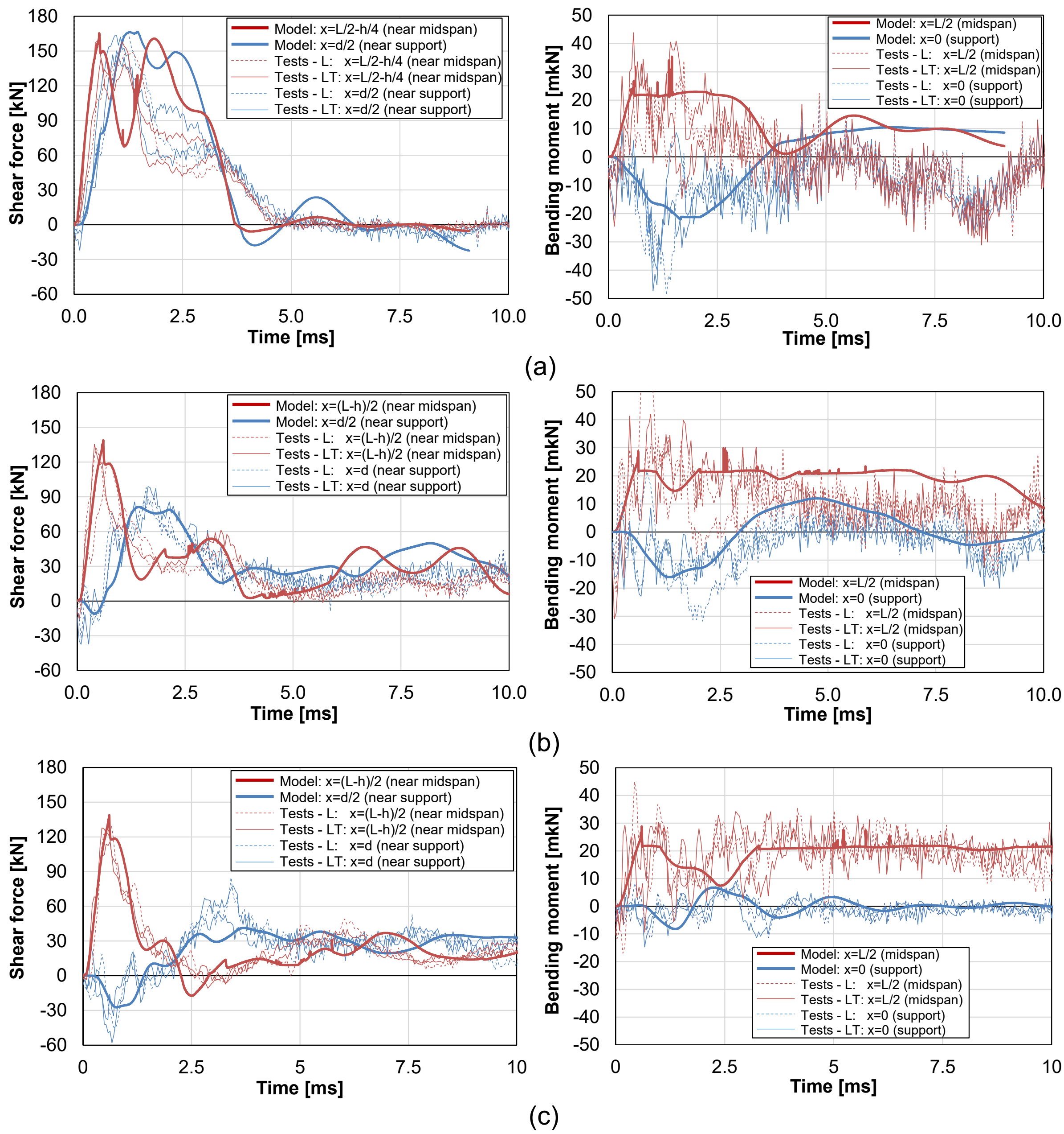

Figure 7. Comparison test and numerical internal forces (V and M): (a) L = 0.60 m series; (b) L = 1.10 m series; (c) L = 1.60 m series.

Sectional forces obtained from the numerical model correlate with those derived from the test results, Figure 7. Correlation increased significantly in the beams with longer span length. Shear forces are generally identical, with only punctual discrepancies, especially in the 0.6 span beam. Regarding the bending moment, the model accurately simulated dominant trend, even though the model did not include the high frequency components, or noise. The precision of the model for the 0.6 and 1.1 m beams was particularly high in the initial 3 ms of the impact, whereas for 1.6 m series, accuracy remained high throughout the simulation duration.

5 STRENGTH EVALUATION OF TESTED BEAMS

This section analyzes the development of shear cracks by comparing the sectional forces obtained with the model with the shear-bending (*M-V*) interaction curves. In the literature there are proposals of formulations that define the dynamic interaction for certain types of structures [12,18]. Generally accepted models for *M-V* interaction have been defined for quasi-static conditions. That is the case of Bentz's simplified version of the Modified Compression Field Theory (SMCFT) [30], which has used in the present study the dynamic *M-V* interaction for RC beams. Dynamic effects have been introduced by modifying the strength of failure mechanisms according to their sensitivity to strain rate. However, the strain rate during an impact event is variable in time and location, thus, uniform values of strain rate have been considered, as a simplification. Strain rate ($\dot{\varepsilon}$) effects defined by [4] were considered for steel yield and ultimate strength and for the concrete strength in compression and tension formulations proposed by [27] and [31] were employed, respectively.

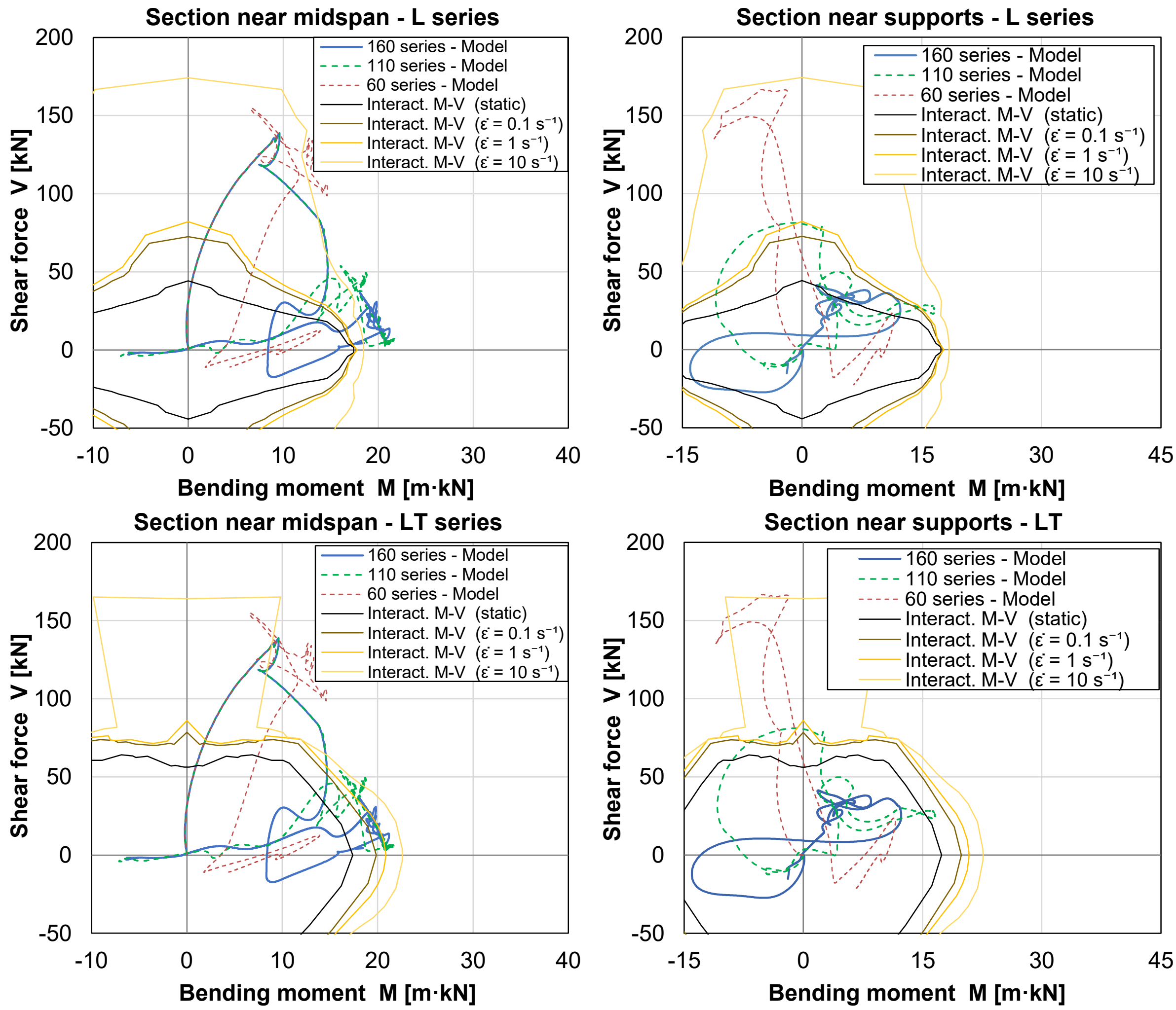

Figure 8. Interaction shear-bending moment in critical sections.

The shear-bending interaction of the tested beams is analyzed in Figure 8 in the two critical sections, near midspan (at *h*/2, and *h*/4 for 0.6 m span beams) and supports near midspan (at *d*, and *d*/2 for 0.6 m span beams), similarly to Figure 7. Various interaction curves have been included in that Figure 8, corresponding to the dynamic *M-V* interaction for strain-rates ranging from 0.1 to 10 s^{-1}, with the static case included as a reference.

In the section near the midspan all beams exceeded *M-V* interaction curves, regardless of the shear reinforcement, specially short beams (L-0.6 and LT-0.6). High shear forces observed in this location developed especially in the first stages of the impact load, as it can be observed in Figure 7. This explains the development of the shear-plug in this stage. In the case of LT-1.1 and LT-1.6 series, shear reinforcement avoided the further progress of these cracks. In the section near the supports, the *M-V* interaction curves explain the different failure modes observed in L-1.6 and LT-1.6 series, which the former failed by shear-bending interaction while the latter showed a ductile response. Regarding the 1.1 m span beams, the interaction curves do not provide a definitive conclusion; however, L-1.1 series exceeded the dynamic interaction curves further than LT-1.1. It must be noted that the capacity curves shown in Figure 8 represent the envelope of the peak capacity of the beams. Thus, they are helpful to explain the development of shear cracks, but they do not provide information about the post-peak behavior. Consequently, further research in this field seems to be convenient.

6 CONCLUSIONS

This study investigated the behavior of RC beams with different shear-span to depth ratios ($2 \leq a/d \leq 5.3$) subjected to impact loads. An experimental campaign was carried out in 2.00 × 0.15 × 0.20 m prismatic longitudinally reinforced (ρ = 1.0%) concrete beams, six beams with shear reinforcement (ρ_w = 0.3%) and six without (ρ_w = 0%). Tests were measured with sensors and DIC, which combined allowed to derive the distribution of sectional forces in each stage of the impact. Experimental results were compared with a non-linear numerical beam model. The following conclusions can be drawn from the presented research:

1. The transversal reinforcement included prevented brittle failure for shear-span to depth ratios $a/d \geq 3.6$, allowing the formation of a plastic hinge. Beams tested with a/d = 2 were sensible to fail by the formation of a shear plug. This change of the failure mode might be attributed to the highly impulsive response of shorter span beams.
2. Non-linear numerical beam model presented has the potential to predict accurately the impact response of a structure, requiring low development and computational costs. These models are able to determine the impact forces and sectional forces distribution during the impact, essential to design structures resistant to collisions.
3. Introducing strain rate effects in existing shear-bending interaction models has allowed to discuss the formation of the shear failures cracks observed experimentally. However, further research is required in order to define improved dynamic *M-V* interaction formulations, including post-peak behavior.

ACKNOWLEDGEMENTS

The research presented in this paper was carried out with no particular funding. However, the experimental infrastructure is a result of previous projects funded by the Spanish Research Agency (Ref. BIA2012-30998 and BIA2016-74960-R AEI/FEDER, UE).

REFERENCES

[1] K.H. Kishi, H. Mikami, K.G. Matsuoka, T. Ando, “Impact behavior of shear-failure type RC beams without shear rebar”, *Int. J. of Impact Eng.*, vol. 27, pp. 955-968, 2002.

[2] S. Saatci, F.J. Vecchio, “Effects of shear resisting mechanisms on impact behavior of RC beams”, *ACI Struct. J.*, vol. 106, pp. 78-86, 2009.

[3] L.J. Malvar, J.E. Crawford, “Dynamic increase factors for concrete”. 28th DDESB Seminar, pp 1–1, 1998.

[4] L.J. Malvar, “Review of static and dynamic properties of steel reinforcing bars”, *ACI Mater J*, vol. 95(5), pp. 609–616, 1998.

[5] K. Fujikake, T. Senga, N. Ueda, T. Ohno, M. Katagiri, “Study on Impact Response of Reactive Powder Concrete Beam and Its Analytical Model”, *J Adv Concr Technol*, vol. 4(1), 99–108, 2006.

[6] J. Zhang, M. Maalej, S.T. Quek, “Performance of hybrid-fiber ECC blast/shelter panels

subjected to drop weight impact", *J. Mater. Civ. Eng.*, vol. 19(10), pp. 855–863, 2007.
[7] T. M. Pham, A. M. Asce, H. Hao, & F. Asce, "Impact Behavior of FRP-Strengthened RC Beams without Stirrups", *J. Compos. Constr.*, vol. 20(2), pp. 1–13, 2016.
[8] G.S.D. Ulzurrun, C. Zanuy, "Enhancement of impact performance of reinforced concrete beams without stirrups by adding steel fibers", *Constr. Build. Mater.*, vol. 145, pp.166–182, 2017.
[9] C. Zanuy, G.S.D. Ulzurrun, M. Curbach, "Experimental determination of sectional forces in impact tests: application to composite RC-HPFRCC beams", *Eng. Struct.*,vol. 256, pp. 114004, 2022.
[10] T.J. Ross, "Direct Shear Failure in Reinforced Concrete Beams under Impulsive Loading", U.S. Air Force Weapons Laboratory, New Mexico, 1983.
[11] Q.M. Li, S.R. Reid, H.M. Wen, A.R. Telford, "Local impact effects of hard missiles on concrete targets", Int. J. Impact Eng., vol. 32(1–4), pp. 224–284, 2005.
[12] K. Micallef, J. Sagaseta, M. Fernández Ruiz, A. Muttoni, "Assessing punching shear failure in reinforced concrete flat slabs subjected to localised impact loading." *Int. J. Impact Eng.*, vol. 71, pp. 17–33, 2014, doi:10.1016/J.IJIMPENG.2014.04.003
[13] K. Fujikake, A. Somraj, "Dynamic Shear Resistance of RC Beams Based on Modified Compression Field Theory", *Key Engineering Materials*, vol. 711, pp. 799–805, 2016.
[14] J. Sagaseta, P. Olmati, K. Micallef, D. Cormie, "Punching shear failure in blast-loaded RC slabs and panels", *Eng. Struct.*,vol. 147, pp. 177-194, 2017.
[15] J. Van Mier J, A.F. Pruijssers, H.W. Reinhardt, T. Monnier, "Load-time response of colliding concrete bodies", *J. Struct Eng*, vol. 117, pp. 354-374, 1991.
[16] D.M. Cotsovos, N.D. Stathopoulos, C.A. Zeris, "Behavior of RC beams subjected to high rates of concentrated loading", *J Struct Eng*, vol.134, pp. 1839–51, 2008.
[17] P. Isaac, A. Darby, T. Ibell, M. Evernden, "Experimental investigation into the force propagation velocity due to hard impacts on reinforced concrete members", *Int J Impact Eng*, vol.100, pp. 131–138, 2017.
[18] G.S.D. Ulzurrun, Capacidad resistente de elementos lineales de HA reforzado con fibras bajo cargas de impacto [Strength Capacity of FRC Beams Under Impact Loads], ETSI Caminos, Canales y Puertos (UPM), 2019, doi: 10.20868/UPM.thesis.58074.
[19] G.S.D. Ulzurrun, C. Zanuy, "Dynamic shear force-bending moment interaction diagrams in RC beams under impact", *Eng. Struct.*, vol. 308, pp. 118021, 2024.
[20] CEN (European Committee for Normalization). "EN 12390–3:2020 Testing hardened concrete - Part 3: Compressive strength of test specimens", Brussels, Belgium, 2020.
[21] CEN. "EN 12390–6:2010 Testing hardened concrete - Part 6: Tensile splitting strength of test specimens", Brussels, Belgium, 2010.
[22] CEN. "Eurocode 2. EN 1992-1-1:2012. 2012. Design of concrete structures - Part 1: General rules and rules for buildings", Brussels, Belgium, 2012.
[23] Spanish Ministry for Transportation, Mobility and Urban Planning, "Código Estructural. Vol. III. Dimensionamiento y comporbación de estructuras de hormigón" [Spanish code for structural concrete], Madrid, Spain, 2021.
[24] GOM. GOM Correlate 2018. Free version. 2018.
[25] ANSYS Inc., "ANSYS mechanical APDL. Release 2020 R2", 2020.
[26] CEB-FIP, "Model code for concrete structures 1990" Thomas Telford, 1993.
[27] FIB, "Model code for concrete structures 2010", Ernst & Sohn, 2013.
[28] G.S.D. Ulzurrun, C. Zanuy, "Time-variation of shear forces affecting the impact resistance of RC beams", *Hormigón y Acero*, vol. 75(302-303), pp. 65–78, 2024.
[29] W.J. Yi, D.B. Zhao, S.K. Kunnath, "Simplified approach for assessing shear resistance of RC beams under impact loads", *ACI Struct J*, vol. 113(4), pp. 747–756, 2016.
[30] E. Bentz, F. Vecchio, M. Collins, "Simplified modified compression field theory for calculating shear strength of RC elements", *ACI Struct J*, vol. 103(4), pp. 614-624, 2006.
[31] L.J. Malvar, C.A. Ross, "Review of strain rate effects for concrete in tension", *ACI Mat. J.*, vol. 95(6), pp. 735-739, 1998.

15th International Conference on
Shock & Impact Loads on Structures
12-13 June 2025, Gothenburg, Sweden

RESPONSE OF RC BEAMS SUBJECTED TO REPEATED DROP WEIGHT IMPACT AND RESIDUAL STATIC LOADING

Morgan Johansson[a,b], Joosef Leppänen[b], Sebastian Syversen[c], Christer Trinh[a]

[a]Norconsult Sverige AB, Sweden, email: morgan.johansson@norconsult.com, [b]Chalmers University of Technology, Sweden, [c]AFRY AB, Sweden

Keywords: reinforced concrete, impact loading, repeated impacts, residual response, energy absorption capacity, digital image correlation

Abstract

Reinforced concrete (RC) protective structures, designed to withstand impulsive loading such as blast and impact, may be subjected to both single and repeated loading. To effectively withstand such loads, the protective structure requires a large energy absorption capacity. This has been the focus of several studies, but research on repeated impulse loading is scarce, and its effect on the structure's dynamic response and total energy absorption capacity are not yet fully understood. Therefore, the aim of this study was to investigate the effect of repeated impulse loading, applied through impact, on the dynamic response and the total energy absorption capacity of RC beams.

Drop-weight impact tests of 12 beams were carried out and their residual capacity were tested statically after impact. In addition, six beams were statically tested as references. The beams (2.8 × 0.1 × 0.2 m) were simply supported with a span length of 2.6 m and provided with 2+2 reinforcement bars with a diameter of 6, 8 or 10 mm (reinforcement ratio 0.35-0.98%). The drop weight had a mass of 10, 20 or 40 kg and was released from a height of 5.0 m. The number of impacts varied with the mass of the drop weight: 10 kg, 4-6 impacts; 20 kg, 1-2 impacts; 40 kg, 1 impact. A high-speed camera (5000 fps) filmed the beams during the impact tests and digital image correlation (DIC) technique was used to measure deflections and crack propagation.

The influence of impact loading on the total energy absorption capacity varied between different beam configurations. In beams with ϕ6 bars, energy absorption increased by up to 50%, while in beams with ϕ8 or ϕ10 bars, it decreased significantly compared to the statically loaded reference beams. For the latter, only bending cracks occurred. However, for impact-loaded beams using 20 or 40 kg drop weights, distinctive diagonal shear cracks also formed below the impact zone. For a drop weight of 10 kg, though, such diagonal cracks did not appear until after 2-4 impacts. For this drop weight, the response was similar for the first 4 impacts, whereas for a 20 kg drop weight, the difference between the first and second impact was more distinct. Repeated impact loading caused increased local damage, even when the total impact energy applied was constant. This indicates that several small impulse loads may be more severe than a single large load of the same total magnitude.

1 INTRODUCTION

The high mass of reinforced concrete (RC) structures, combined with their capacity to withstand large plastic deformations while retaining load-bearing capacity, makes them highly suitable for resisting the effects of impulse loading caused by explosions or impact. Consequently, RC is commonly used in protective structures subjected to such loads. In the design of impulse-loaded structures, insights gained from static loading are often applied. However, the structural response under impulse loading can differ significantly from that under static loading [1], and hence it is not for sure that the observations made at static loading are also directly applicable to impulse loading.

The differences in structural response between impulse and static loading are attributed to a combination of various dynamic effects such as inertia, strain rate and wave propagation effects. Inertia resists changes in motion and thus provides additional resistance to the structure, while strain rate effects increase the stiffness and strength of the material [2], [3]. Furthermore, wave propagation can cause the structure to respond differently at both local and global levels [4], [5], [6]. Nevertheless, it is common practice to base the design of impulse-loaded structures on knowledge gained from static loading, such as bending moment capacity or plastic deformation capacity [7], [8], [9].

Impulse loading may be caused by events such as a blast wave from an explosion or the impact of an object. Although the loading characteristics of these events can vary significantly, the structural response of the affected structure is still similar in many respects. Therefore, when studying the dynamic response of a structure subjected to impulse loading, it is often feasible to use a simplified test set-up, in which the impulse loading is generated by a drop weight impact.

The design of impulse-loaded structures often relies on large plastic deformation capacities, where the structure's energy absorption capacity is provided by large deformations rather than high load-bearing capacity. Therefore, it is essential that the energy absorption capacity assumed in the design is applicable to the actual loading scenario. However, since the structural response under impulse loading may differ from that under static loading, the structure's plastic deformation capacity and failure modes may also change when subjected to impulse loading. Additionally, repeated impulse loading may further affect the structure's ability to withstand such loads. Consequently, it is important to ensure that observations made under static loading conditions, particularly regarding energy absorption capacity, remain valid for both single and repeated dynamic loading.

The aim of this paper is to examine how the energy absorption capacity of reinforced concrete beams is affected by single and repeated impulse loading. Drop weight impact tests were conducted to simulate the impulse loading. Similar studies have been carried out by several researchers (e.g., [10], [11], [12], [13]) to investigate the dynamic structural response of RC structures subjected to single impacts. To estimate the total energy absorption capacity, the effect of impact loading was combined with static loading, applied after the impact tests, in order to assess the residual capacity of the damaged beams.

2 TEST SERIES AND TEST SET-UP

The test series consisted of 18 beams, designated in accordance with Table 1. Each beam had a total length of 2800 mm and a span length of 2600 mm, with a cross-section measuring 100 × 200 mm (width × height). All beams were reinforced with 2+2 longitudinal ribbed steel bars of class K500C-T, with a nominal diameter ϕ = [6, 8, 10] mm, resulting in a reinforcement ratio ρ_s = [0.35, 0.63, 0.98]%.

The beams in Series I10, I20 and I40 were first subjected to n number of impact loads using a drop weight with a mass m_w = [10, 20, 40] kg[1], released from a height h_w = 5.0 m (resulting in an impact velocity $v_0 \approx 9.9$ m/s). Thereafter, the beams were loaded statically under deformation-controlled conditions until failure, and the results were compared with those from reference beams in Series S, which were subjected to static loading only. Impact tests were conducted on 12 beams, and static tests on six plus six beams with test set-ups shown in Figure 1. For the impact tests, the beams were supported on fixed, half-cylindrical supports with a diameter of 70 mm. The objective was to apply boundary conditions that were as well-defined as possible; therefore, no upper supports were used to restrict the upward movement of the beam. For safety reasons, a clamp was provided at each support, to prevent the beam from falling over during impact.

The beams in Series S3 and S4 were tested in three-point and four-point bending, respectively, while all other static tests were conducted using just four-point bending. Three-point bending best represents the equivalent static load condition of the impact loading applied here. However, due to extensive concrete damage suffered in the mid-region of most impact-loaded beams, this load set-up was not suitable, and four-point bending was employed instead. For further details of the tests, see [14].

Type of Loading	Series	Beam	ϕ [mm]	m_w [kg]	n [no.]	$n \cdot E_{k,0}$ 1) [J]	Static test set-up 2)
Static	S3	B-02	6	-	-	-	3p
		B-04	8				
		B-06	10				
	S4	B-01	6	-	-	-	4p
		B-03	8				
		B-05	10				
Impact + Static	I10	B-07	6	10	5	2453	-
		B-08	6		4	1962	4p
		B-09a	8		6	2943	-
		B-09b	8		6	2943	-
		B-10a	10		5	2453	-
		B-10b	10		4	1962	4p
	I20	B-11a	6	20	1	981	-
		B-11b	6		1	981	-
		B-12	8		2	1962	4p
		B-13	10		2	1962	4p
	I40	B-15	8	40	1	1962	4p
		B-16	10		1	1962	4p

1) Total impact energy: $E_{k,0}$ defined in Equation (4) in Section 3.3.
2) 3p = three-point bending test, 4p = four-point bending test, - = not tested.

Table 1. Test series.

[1] The drop weight was cylindrical in shape, with a length l_w = [112, 227, 458] mm, a diameter of 120 mm and a contact surface radius of 200 mm. A vertical hole was drilled through the drop weight to accommodate an accelerometer.

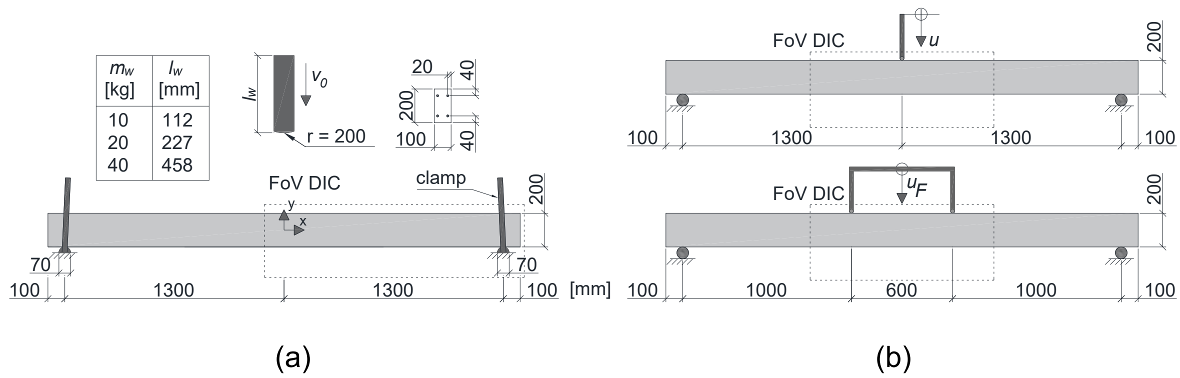

Figure 1. Test set-up for (a) drop weight impact tests, and (b) deformation-controlled static tests in three-point and four-point bending.

For the concrete, the compressive strength $f_{c,cube}$ and fracture energy G_F were determined using cubes and wedge splitting tests, respectively [15], [16]. The cylinder compressive strength was then calculated as $f_c = 0.8 \cdot f_{c,cube}$. For the steel reinforcement, coiled bars of class C were intended for use. However, for ϕ6 bars, a less ductile type (class A) was mistakenly delivered and used in the tests, which resulted in smaller deflections than anticipated. Coiled bars are transported in rolls and straightened before use, which often eliminates the distinct yield plateau. As a result, the mechanical property resembles that of a cold worked reinforcement, and hence, the proof stress $f_{0.2}$ was used to characterise the reinforcement together with the tensile strength f_t and the tensile strain ε_u corresponding to f_t. The average values of the concrete and reinforcement material properties are presented in Table 2. Further details of the material tests are provided in [14].

Concrete			
$f_{c,28d}$ [MPa]	$f_{c,57d}$ [MPa]	$f_{c,64d}$ [MPa]	$G_{F,57d}$ [N/m]
52.8	55.9	56.3	150

Steel reinforcement				
ϕ [mm]	$f_{0.2}$ [MPa]	f_t [MPa]	$f_t / f_{0.2}$ [-]	ε_u [‰]
6	547	588	1.07	29
8	588	688	1.17	98
10	569	699	1.23	116

Table 2. Material properties of concrete and steel reinforcement: mean values are based on three (six) tests for concrete (reinforcement), and the index for concrete denotes the age in days at the time of material testing.

The structural response of all beams was analysed using Digital Image Correlation (DIC); see e.g., [17] for detailed information. By analysing the deformation of a surface with a speckle pattern across a series of digital images acquired during loading, a deformation field is calculated. With the known frames per second (fps) rate during filming, velocities and accelerations can be determined as well. The impact tests of the beams were investigated using the 2D-DIC technique with a high-speed camera, which had a resolution of 1920 × 512 pixels and an image acquisition rate of 5000 fps. This camera configuration provided a field of view (FoV) of approximately 1.5 × 0.4 m, covering just over half of the beam, as shown in Figure 1. The images from the high-speed camera were analysed using GOM Correlate [18], where the dimensions of each subset were 15 × 15 pixels, and the subset step was 5 pixels. In the static tests, 3D-DIC measurements were conducted using a stereoscopic camera set-up with the ARAMIS 12M system [19]. The images were captured at a frequency of 0.5 fps, and the camera's FoV covered approximately the central 1.1 m of the beam, as shown in Figure 1.

3 RESULTS

3.1 Response at impact loading

A modified midpoint deflection over time $u(t)$ is used to represent the dynamic response under impact loading. It is here defined as

$$u(t) = u_{mid}(t) - u_{\sup}(t) \qquad (1)$$

in which $u_{mid}(t)$ is the midpoint deflection in the test and $u_{sup}(t)$ is the deformation at the support. In Figure 2a, $u(t)$ is illustrated for Beam B-07, and from this it can be observed that there is an initial uplift of the beam at the support (blue line), reaching a maximum of about 2 mm just prior to 5 ms, and regaining contact with the support at around 8 ms. This uplift occurred because no top support was used to restrain the beam's vertical movement. The midpoint deflection (black line) shows a smooth progression. However, when applying Equation (1), the curve of the modified midpoint deflection (red line) exhibits a sudden shift at approximately 7 ms. This shift is also evident in all subsequent deflection curves. The advantage of using $u(t)$ as defined by Equation (1) is that it highlights the plastic midpoint deflection u_{pl} is the graphs as the value around which the curves oscillate after reaching their maximum deflection ($u_{pl} \approx 5$ mm in Figure 2a).

In Figure 2b to d, the deflection-time curves for the first impact load on all tested beams are shown, illustrating the effects of drop weight mass and reinforcement amount. As expected, an increased reinforcement amount resulted in a decreased beam deflection while an increased drop weight mass led to increased deflection. Some load configurations were tested twice, and in Figure 2b, it can be seen that the scatter in the results was small when using a drop weight of m_w = 10 kg. Furthermore, in Figure 2c, the results of m_w = 20 kg and ϕ8 show a similar initial response. However, Beam B-11a failed due to reinforcement rupture, while Beam B-11b barely withstood the loading, reaching a substantial deflection.

Failure was not reached due to impact loading in any of the beams, except for one. In beam B-11a, failure occurred due to reinforcement rupture. Beam B-11b, which had the same reinforcement configuration and was subjected to impact loading from the same drop weight mass, was able to just withstand the applied impact loading[2]. However, in this case, the impact load condition was modified by placing a 10 mm thick rubber sheet between the impactor and the beam. This modification extended the duration of the impact and reduced the peak impact force, thereby creating a slightly less critical loading situation.

In Figure 3, the crack patterns at maximum deflection are presented for beams subjected to a single impact. One beam is shown for each load and reinforcement configuration. It can be observed that for m_w = 10 kg, the crack pattern is limited to vertical bending cracks, similar to those typically observed in beams subjected to three-point bending. However, in beam B-10a (ϕ10), a horizontal crack also appeared at midspan at the level of the bottom reinforcement. This horizontal crack is believed to be due to spalling and a partially failed bond between the reinforcement and concrete, caused by severe stresses during the initial response to impact. For beams subjected to impact from a drop weight with a mass of m_w = 20 kg, the crack patterns vary depending on the reinforcement amount. In beam B-11b (ϕ6), a very large and distinct vertical bending crack is visible at midspan. At the top of this crack, two nearly horizontal cracks converge, indicating concrete crushing at the top surface. In beam B-12 (ϕ8), in addition to vertical bending cracks, a diagonal shear crack originating from the top of the beam is clearly visible. This crack is attributed to severe local strains induced by the impact.

[2] Both bottom bars were torn off, but final failure was prevented due to the remaining residual capacity provided by the intact top reinforcement.

Beam B-13 (ϕ10) exhibits both vertical bending cracks and a diagonal shear crack, along with a horizontal crack similar to that observed in Beam B-10a. Finally, in beam B-15 (ϕ8) and beam B-16 (ϕ10), subjected to the impact from a drop weight with a mass of m_w = 40 kg, the resulting crack patterns were similar to those observed when m_w = 20 kg, but with more severe cracking.

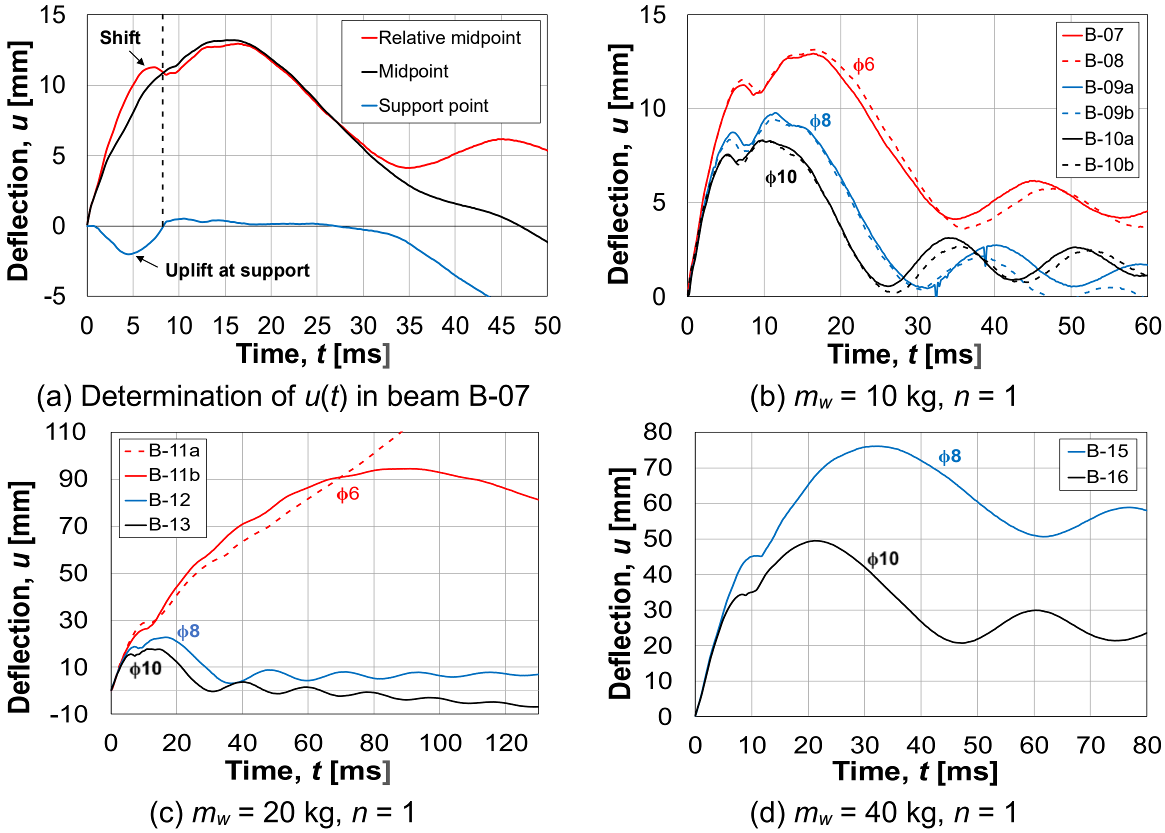

Figure 2. Deflection-time response of beams subjected to single impact loading: (a) Determination of the modified midpoint deflection $u(t)$, based on the midpoint deflection $u_{mid}(t)$ and support deformation $u_{sup}(t)$, (b) to (d) $u(t)$ for various drop weight m_w and reinforcement diameter ϕ.

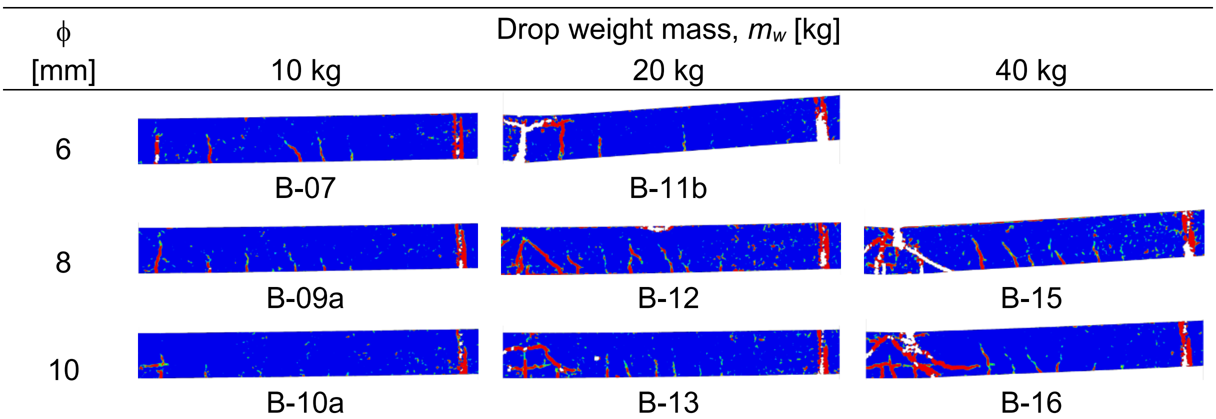

Figure 3. Crack pattern in the beam at maximum deflection due to a single impact. Only half of the beam is shown, and the red vertical line on the right-hand side of the beam indicates the presence of a clamp, not a crack (see Figure 1).

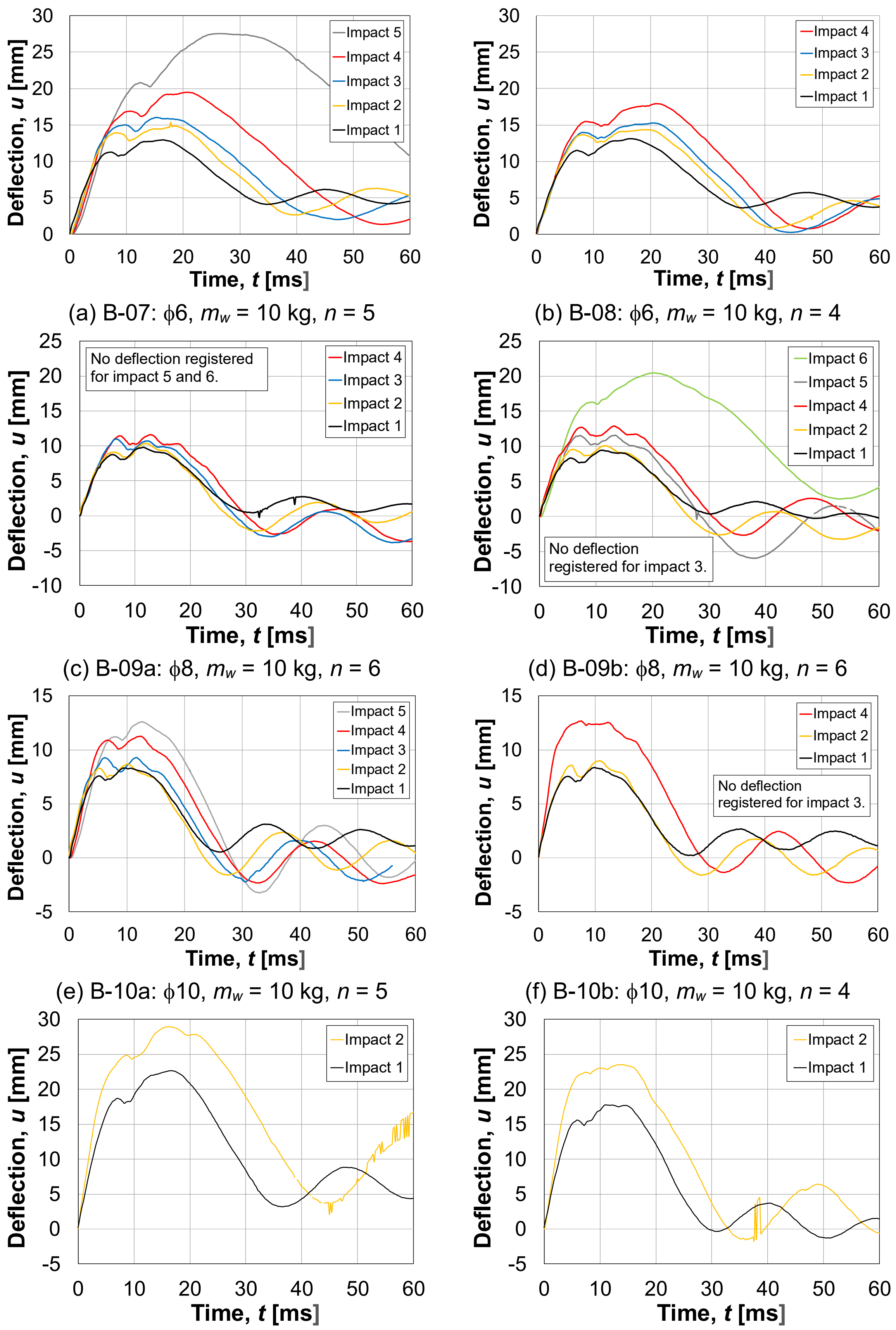

(a) B-07: $\phi 6$, m_w = 10 kg, n = 5

(b) B-08: $\phi 6$, m_w = 10 kg, n = 4

(c) B-09a: $\phi 8$, m_w = 10 kg, n = 6

(d) B-09b: $\phi 8$, m_w = 10 kg, n = 6

(e) B-10a: $\phi 10$, m_w = 10 kg, n = 5

(f) B-10b: $\phi 10$, m_w = 10 kg, n = 4

(g) B-12: $\phi 8$, m_w = 20 kg, n = 2

(h) B-13: $\phi 10$, m_w = 20 kg, n = 2

Figure 4. Deflection-time response of beams subjected to repeated impact loading.

In Figure 4, the deflection-time curves for all impact loads on beams subjected to repeated impacts are presented. It can be observed that the deflection gradually increases with each successive impact. When using a drop weight mass of m_w =10 kg, the increase in deflection was generally small for the first three impacts on beams with ϕ6 and ϕ10, and the first four impacts on beams with ϕ8. The associated damage obtained in the beam was also relatively limited during these stages. However, after a certain number of impacts (n = 5 for beam B-07 and n = 6 for beams B-09a and b), extensive damage was observed, and the additional deflection increased significantly compared to previous impacts. Figure 5 presents photographs showing the damage in beam B-07 after impacts two through five. Damage from the first impact was limited to minor cracking. After the second impact, spalling of the side concrete occurred, and diagonal shear cracks became visible after the fourth impact. By the fifth impact, the cracks had widened considerably, and local concrete crushing in the top region of the beam was evident. Notably, the top reinforcement was significantly deformed due to the fifth impact. For a higher drop weight mass, m_w =20 kg, the difference in maximum deflection between the first and second impact was more pronounced, with an increase of approximately 25-40%. In these beams, significant spalling of the side concrete was also observed.

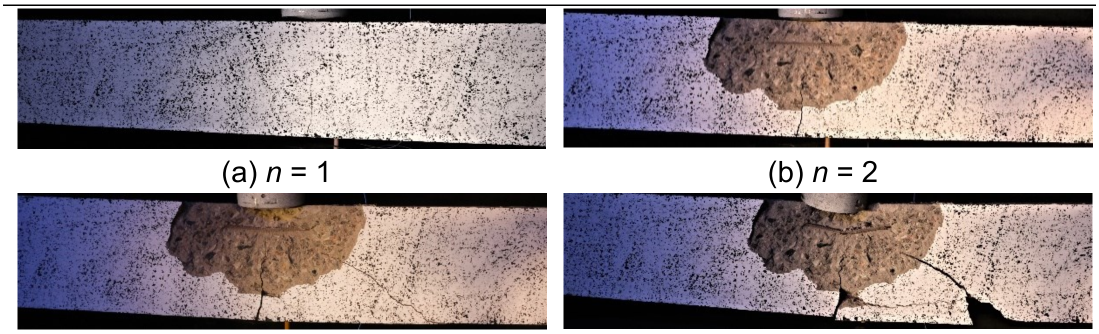

(a) n = 1 (b) n = 2

(c) n = 4 (d) n = 5

Figure 5. Photographs showing damage at the midspan of beam B-07 after *n* impacts.

From the impact-loaded tests, it was not possible to predict how close a given beam was to failure. To investigate this, static tests were conducted to determine the residual capacity of the previously impact loaded beams. However, the damage in beams subjected to more than four impacts was so extensive that subsequent static loading could not be performed. Therefore, in beams B-08 and B-10b, the number of impacts was limited to four to ensure that residual static testing could be carried out.

3.2 Response at static loading

Six out of twelve beams[3] subjected to impact loading were subsequently tested under static loading conditions to evaluate their residual response in terms of stiffness, load capacity, and energy absorption capacity. For comparison, three plus three undamaged reference beams were tested, and their responses are shown in Figure 6 as load-deflection curves, $F(u)$. The maximum load capacity F_{max} was limited by reinforcement rupture (RR) in beams with ϕ6, and by concrete crushing (CC) in beams with ϕ8 and ϕ10. In all cases except for beam B-06, the final failure was caused by reinforcement rupture at a final deflection $u_{F,W}$.

While three-point bending best represents the static load condition associated with the impact loading, extensive concrete damage at the midspan of most impact-loaded beams, necessitated the use of four-point bending for the residual static tests. In Figure 7, the residual static response $F(u)$ of the impact loaded beams is compared with the response of the

[3] Six beams were considered too severely damaged to undergo further testing.

corresponding reference beams in Series S3 and S4. Due to prior loading, an initial plastic deflection was already present, which is indicated in the graphs as an initial deflection at zero static load. To account for the measurement point being located at the position of the point load, this deflection was approximately determined as $u_{F,pl} = u_{pl} / \alpha$, where u_{pl} is the plastic midpoint deflection caused by impact loading and $\alpha = 1.3/1.0 = 1.3$ is the difference in distance between point load and support in three-point and four-point bending.

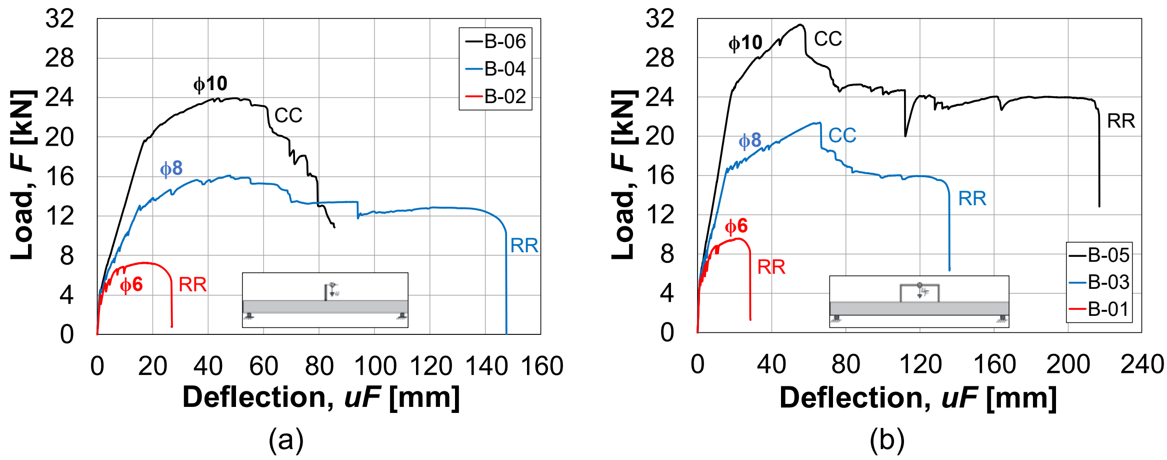

Figure 6. Load-deflection curves for statically loaded reference beams under (a) three-point bending and (b) four-point bending.

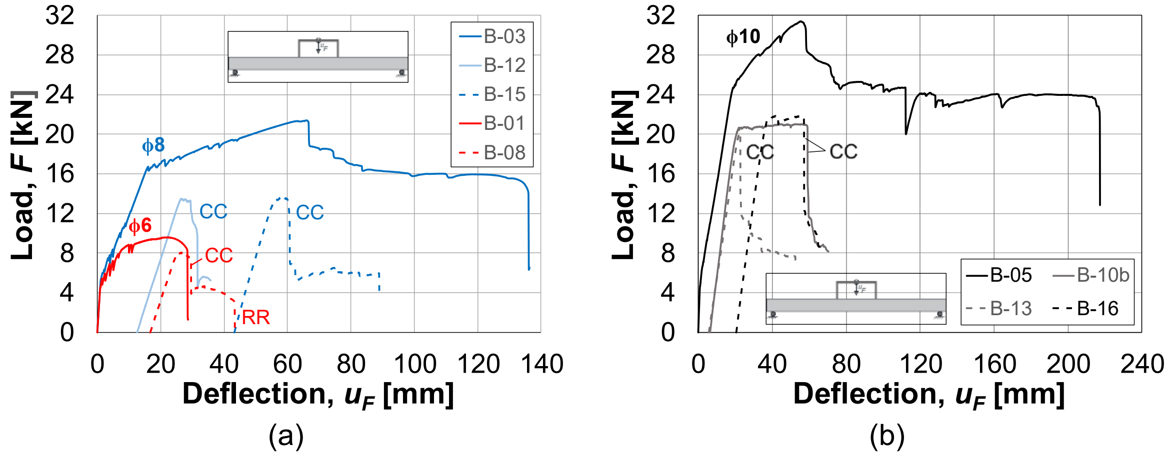

Figure 7. Comparison of load-deflection curves for reference beams and beams previously subjected to impact loading: (a) beams with ϕ6 and ϕ8 bars, and (b) beams with ϕ10 bars.

In all beams, the initial elastic stiffness of the residual response was similar to that obtained in the cracked reference beams. For beam B-08, with ϕ6 bars, a load capacity of 8 kN was reached at a total deflection of approximately 26 mm, thereby closely reaching the load-deflection curve of the reference beam B-01. Thereafter, the load capacity remained fairly constant until a deflection of 30 mm was reached, at which point a sudden drop, caused by concrete crushing, occurred. Thereafter, increased deflection was observed at a significantly reduced load capacity of around 4 kN, until final failure occurred at $u_{F,W} \approx 43$ mm due to reinforcement rupture. This response, characterised by delayed failure, indicates that the impact-loading had a positive effect on the total energy absorption capacity of the beam.

However, the response reached in the residual tests for beams with ϕ8 and ϕ10 bars did not exhibit the same positive effects due to impact loading. In these beams, the load capacity failed to reach the load-deflection curves of the reference beams, and final failure in all cases was governed by concrete crushing. This contrasts with the reference beams subjected to four-point bending, in which reinforcement rupture occurred at a substantially larger deflection. Although all except beam 13 (ϕ10) reached a load level with some stabilised plastic response, concrete crushing caused a sudden drop in load capacity at a deflection considerably smaller than that reached in the reference beams. As a result, both the load capacity and deflection at final failure were reduced, leading to a substantial decrease in the total energy absorption capacity.

3.3 Total energy absorption capacity

In Table 3, some key results from the impact and static tests are summarised. Apart from deflections u and the maximum static load F_{max}, the internal work W_i (energy absorption) is listed in the table. For the reference beams, the energy absorption $W_{i,sta}$[4] was defined as the sum of elastic ($W_{i,el}$) and plastic ($W_{i,pl}$) contributions, determined as the area under the $F(u)$ curves in Figure 6 and Figure 7. In several beams, the static test was interrupted before reaching total failure (F = 0 kN), meaning that the total energy absorption capacity could not be determined. However, including contributions from low load values was deemed questionable. As an approximation, the energy absorption contributions to $W_{i,pl}$ were only included up to a deflection $u_{F,W}$, corresponding to a post-peak load of $F = F_{max} / 2$, where F_{max} was the maximum static load for the corresponding reference beam.

In beams that were also subjected to impact loading, the same method could not be applied. Instead, a simplified approach based on energy equilibrium, the theory of plastic impact, and an equivalent single-degree-of-freedom system (SDOF), as described in for example [20], was used to estimate the internal work. The total energy absorption capacity $W_{i,tot}$ of these beams was defined as:

$$W_{i,tot} = W_{i,sta} + W_{i,imp,pl} \tag{2}$$

where $W_{i,imp,pl}$ represents the total plastic energy absorption due to impact loading. The contribution from the impact loading was limited to the plastic component, since the same elastic component $W_{i,el}$ is accounted for in both the response to impact loading and the subsequent static loading.

Due to energy equilibrium, the external energy applied due to a single impact loading is equal to the internal energy absorption in the loaded beam; that is, $W_{e,imp} = W_{i,imp}$. The plastic energy absorption due to n impacts may thereby be estimated as:

$$W_{i,imp,pl} = n \cdot \left(W_{e,imp} - W_{i,imp,el} \right) \tag{3}$$

where $W_{e,imp}$ is the external energy applied to the structure from a single impact, and $W_{i,imp,el}$ is the elastic internal energy absorbed by the structure during each impact.

[4] Results from three-point and four-point bending tests cannot be directly compared with each other; however, an approximate comparison is made here based on the following concept. It can be shown that, for the same simply supported beam, the forces F_{3p} and F_{4p} under three-point and four-point bending, respectively, produce the same maximum span moment M_{mid} if $F_{3p} = F_{4p} / \alpha$. Furthermore, if a plastic hinge forms at the beam midpoint under four-point bending, the relationship between the deflection $u_{4p,mid}$ and deflection $u_{4p,F}$ under the applied load can be approximated as $u_{4p,mid} \approx \alpha \cdot u_{4p,F}$. Hence, the plastic energy absorption $W_{i,pl}$, (the area under $F(u)$ at plastic response), would be approximately the same in three-point and four-point bending when comparing $F_{3p}(u_{3p,mid})$ and $F_{4p}(u_{4p,F})$. For the test set-ups shown in Figure 1, the factor is determined as α = 1.3 / 1.0 = 1.3.

Identification			Impact loading				Static loading					Total		
Series	Beam	ϕ [mm]	n [no.]	u_{tot} [mm]	$W_{i,imp,pl}$ [J]	$u_{F,pl}$ [mm]	$u_{F,W}$ [mm]	F_{max} [kN]	$W_{i,el}$ [J]	$W_{i,pl}$ [J]	$u_{F,W,tot}$ [mm]	$W_{i.tot}$ [J]	Type of failure
S3	B-02	6	-	-	-	-	27	7.3	34	135	27	169	RR
	B-04	8	-	-	-	-	147	16.1	129	1808	147	1937	RR
	B-06	10	-	-	-	-	83	24.0	198	1399	83	1597	CC
S4	B-01	6	-	-	-	-	28	9.6	60	176	28	236	RR
	B-03	8	-	-	-	-	136	21.4	164	2110	136	2274	RR
	B-05	10	-	-	-	-	217	31.4	272	4991	217	5263	RR
I10	B-07	6	5	51	324	-	-	-	-	-	-	351	-
	B-08	6	4	34	259	16	17	8.0	40	50	33	349	RR
	B-09a	8	6	14	389	-	-	-	-	-	-	416	-
	B-09b	8	6	-	389	-	-	-	-	-	-	416	-
	B-10a	10	5	15	324	-	-	-	-	-	-	351	-
	B-10b	10	4	17	259	7	68	21.0	232	1006	75	1497	CC
I20	B-11a	6	1	-	207	-	-	-	-	-	-	< 310	RR
	B-11b	6	1	95	207	-	-	-	-	-	-	310	RR
	B-12	8	2	36	413	12	24	13.5	123	78	36	614	CC
	B-13	10	2	26	413	6	22	20.2	231	9	28	653	CC
I40	B-15	8	1	76	783	43	23	13.6	115	85	66	983	CC
	B-16	10	1	49	783	20	48	21.8	248	561	68	1592	CC

n = number of impacts, u_{tot} = maximum midpoint deflection due to n impacts, $W_{i,imp,pl}$ = plastic energy absorption of the beam due to n impacts as defined in Equation (3), $u_{F,pl}$ = total plastic deflection beneath point load due to n impacts (start deflection when F = 0 kN), $u_{F,W}$ = deflection beneath point load at failure under static loading, F_{max} = maximum load under static loading, $W_{i,el}$ and $W_{i,pl}$ = elastic and plastic energy absorption of the beam during static loading, $u_{F,W,tot} = u_{F,pl} + u_{F,W}$ = total deflection beneath point load due to impact and static loading, $W_{i,tot}$ total energy absorption as defined in Equation (2) or $W_{i,tot} = W_{i,imp,el} + W_{i,imp,pl}$ if no static loading was conducted. Type of failure: CC = Concrete crushing, RR = Reinforcement rupture.

Table 3. Summary of impact and static test results.

The kinetic energy of the drop weight just prior to impact can be determined as

$$E_{k,0} = \frac{m_w \cdot {v_0}^2}{2} \tag{4}$$

where m_w = [10, 20, 40] kg is the mass of the drop weight in Series [I10, I20, I40] and $v_0 \approx 9.9$ m/s is the expected impact velocity for a drop height of h_w = 5.0 m. Assuming plastic impact and neglecting the effects of changed potential energy due to the beam's deflection, the external work on the beam may be estimated as

$$W_{e,imp} = \frac{m_w}{m_w + m_b} \cdot E_{k,0} \tag{5}$$

Here, $m_b = \kappa_{LM} \cdot m_{beam}$ is the effective mass of the beam, where κ_{LM} is a load-mass factor used to transform the beam into an equivalent SDOF system [21]. For the actual load case, a plastic response of the beam was observed, giving κ_{LM} = 0.333, which together with m_{beam} = 130 kg for the 2.6 m long beam segment between the supports, results in m_b = 43.3 kg. From this, the external energy applied in a single impact can be estimated as $W_{e,imp}$ = [92, 310, 942] J for Series [I10, I20, I40]. Here, the elastic internal energy $W_{i,imp,el}$ is based on the elastic energy $W_{i,el}$ obtained in the reference beams using three-point bending. However, to approximately account for the stiffer initial response of uncracked concrete, this energy is multiplied with a factor 0.8; that is, $W_{i,imp,el} = 0.8 \cdot W_{i,el}$ = [27, 103, 158] J for beams with bars ϕ = [6, 8, 10] mm.

From Table 3, it can be concluded that the energy absorption capacity was higher in beams subjected to four-point bending than in those subjected to three-point-bending. This result was expected, as a higher plastic rotational capacity typically develops in the former due to a more favourable moment distribution. A general trend observed for the reference beams is that an increased reinforcement amount leads to increased energy absorption capacity. However, this was not the case for beams B-04 and B-06. In both beams, the maximum force F_{max} was limited by concrete crushing, although the cause of final failure differed. The energy absorption in beam B-06 was lower, which may be attributed to its failure occurring due to concrete crushing at a deflection of $u_{F,W}$ = 83 mm, compared to reinforcement rupture in beam B-04 at a deflection of $u_{F,W}$ = 147 mm. This indicates that the cause of failure significantly influences the beam's energy absorption capacity.

When comparing the energy absorption capacities between the reference beams and those beams previously subjected to impact loading, it is observed that energy absorption increased with up to 50% in beams with ϕ6 bars but decreased significantly to a capacity of around 10-40% in beams with ϕ8 and ϕ10 bars. In the former case, reinforcement rupture was observed in both the reference beams and the beams subjected to both impact and static loading. In contrast, in the latter case, concrete crushing was the cause of final failure in all the beams subjected to impact loading.

The results for beams with ϕ8 and ϕ10 bars stand in stark contrast to the observations reported by e.g. [22], where it was concluded that beams previously subjected to a single impact exhibited the same or an increased energy absorption capacity. In that study, small-scale beams with a cross-section of 100 × 100 mm, a span length of 1300 mm, and a reinforcement ratio of 0.71% were subjected to a combination of impact and static loading. The impact was applied using drop weights of m_w = 10 or 20 kg released from a height h_w = 5.0 m, and final failure in those tests was primarily caused by reinforcement rupture. The increased energy absorption capacity was mainly attributed to beneficial effects associated with the formation of diagonal shear cracks near the impact zone. These cracks weakened the bond between the reinforcement and the surrounding concrete, allowing a larger portion of the reinforcement to yield prior to final failure by reinforcement rupture. As a result, the length of the plastic hinge increased, leading to greater plastic deflections and, consequently, enhanced energy absorption.

In the tests conducted in the present study, similar diagonal shear cracks and local weakening of the bond in the midspan region were observed. However, the main difference was the cause of final failure; here, it was due to concrete crushing occurring at relatively small deflections. A potential explanation for the differing results may be that the damage sustained by the concrete compressive zone was more severe and/or more sensitive in the present study. The latter can likely be attributed to size effects, which make the concrete compressive zone more brittle [23], [24] in beams with larger depths. Furthermore, the influence of repeated impacts and/or higher impact forces is another plausible explanation. Based on Table 3, the effect of repeated impacts seems to have a particularly large negative influence on the beams' energy absorption capacity. This may at least partly be due to the beams' narrow width; had a wider cross-section been used, the effects of side-surface spalling and local concrete crushing would probably have been less severe.

4 CONCLUSIONS

A test series of drop weight impact tests on reinforced concrete (RC) beams was conducted using a high-speed camera and digital image correlation (DIC) to study deflections and concrete crack patterns. The beams were first subjected to either single or repeated impacts using a drop weight of 10, 20 or 40 kg, released from a height of 5.0 m. Beams that did not sustain too severe damage were subsequently loaded statically until failure. The results were compared with reference beams that were only subjected to static loading. The aim of the study was to investigate the effect of different types of impact loading on the structure's total energy absorption capacity.

The following conclusions may be drawn:

- The influence of impact loading on the total energy absorption capacity varied between different beam configurations. In beams with a low reinforcement ratio (ϕ6 bars, 0.35%), the energy absorption increased by up to 50% compared to that of the statically loaded reference beam. However, in beams with higher reinforcement ratios (ϕ8 and ϕ10 bars, 0.63% and 0.98%), the energy absorption capacity decreased significantly, reaching only approximately 10-40% of the values observed in the statically loaded reference beams.
- The energy absorption capacity was higher when the final failure was governed by reinforcement rupture. The low values observed in beams with ϕ8 and ϕ10 bars were attributed to final failure being governed by concrete crushing. Damage caused by impact loading further increased the beams' sensitivity to concrete crushing.
- Repeated impact loading caused increased local damage, even when the total impact energy applied was constant. That is, if the total impact energy $n{\cdot}E_{k,0}$ remained unchanged, multiple impacts using a lighter drop weight proved more critical than fewer impacts with a heavier drop weight.
- The results of the present study contrast with findings from similar investigations on small-scale beams, where impact loading resulted in either comparable or increased energy absorption capacity. This discrepancy is believed to be due to size effects and the influence of multiple impacts. Accordingly, a follow-up study incorporating both experiments and nonlinear finite element analyses of beams with varying depths and reinforcement ratios, would be valuable.
- High-speed imaging combined with DIC analyses proved effective in studying the dynamic response of beams subjected to impact loading, enabling detailed monitoring of parameters such as deflections and crack propagation.

ACKNOWLEDGMENTS

This research has been carried out at Chalmers University of Technology and was financed by the Swedish Civil Contingencies Agency (MSB) and the Swedish Fortification Agency. The authors would like to thank the financiers, especially Lars Gråbergs (BSc) from MSB and Johan Magnusson (PhD) from the Swedish Fortification Agency. Additionally, research engineer Sebastian Almfeldt (MSc) at Chalmers, responsible for carrying out the experiments, and Leo Laine (PhD), are highly acknowledged for their support.

5 REFERENCES

[1] J. Magnusson, M. Hallgren, and A. Ansell, "Shear in concrete structures subjected to dynamic loads," *Structural Concrete*, vol. 15, no. 1, pp. 55–65, Mar. 2014, doi: 10.1002/suco.201300040.

[2] P. H. Bischoff and S. H. Perry, "Compressive behaviour of concrete at high strain rates," *Mater Struct*, vol. 24, no. 6, pp. 425–450, Nov. 1991, doi: 10.1007/BF02472016.

[3] L. J. Malvar and C. A. Ross, "Review of strain rate effects for concrete in tension," Nov. 01, 1998. doi: 10.14359/418.

[4] D. M. Cotsovos, N. D. Stathopoulos, and C. A. Zeris, "Behavior of RC Beams Subjected to High Rates of Concentrated Loading," *Journal of Structural Engineering*, vol. 134, no. 12, pp. 1839–1851, Dec. 2008, doi: 10.1061/(ASCE)0733-9445(2008)134:12(1839).

[5] P. Isaac, A. Darby, T. Ibell, and M. Evernden, "Experimental investigation into the force propagation velocity due to hard impacts on reinforced concrete members," *Int J Impact Eng*, vol. 100, pp. 131–138, 2017, doi: 10.1016/j.ijimpeng.2016.09.005.

[6] T. M. Pham and H. Hao, "Plastic hinges and inertia forces in RC beams under impact loads," *Int J Impact Eng*, vol. 103, 2017, doi: 10.1016/j.ijimpeng.2016.12.016.

[7] DOD, "Structures to Resist the Effects of Accidental Explosions. UFC 3-340-02, Department of Defence, USA," 2008.

[8] Swedish Fortifications Agency, "Building Regulations FKR 2011. Dnr. 4535/2011 (In Swedish). Eskilstuna, Sweden," 2011.

[9] R. R. Johansson Morgan, "Design of impulse loaded concrete structures: a comparison of FKR 2011 with various design regulations," Chalmers University of Technology, Report 2016-16, Gothenburg, Sweden, 2016.

[10] S. Saatci and F. J. Vecchio, "Effects of Shear Mechanisms on Impact Behavior of Reinforced Concrete Beams.," *ACI Struct J*, vol. 106(1), pp. 78–86, 2009, Accessed: Jun. 21, 2018. [Online]. Available: https://doi.org/10.14359/56286

[11] K. Fujikake, B. Li, and S. Soeun, "Impact Response of Reinforced Concrete Beam and Its Analytical Evaluation," *Journal of Structural Engineering*, vol. 135, no. 8, pp. 938–950, Aug. 2009, doi: 10.1061/(ASCE)ST.1943-541X.0000039.

[12] G. S. D. Ulzurrun and C. Zanuy, "Enhancement of impact performance of reinforced concrete beams without stirrups by adding steel fibers," *Constr Build Mater*, vol. 145, pp. 166–182, Aug. 2017, doi: 10.1016/J.CONBUILDMAT.2017.04.005.

[13] V. Peterson and A. Ansell, "Static and Dynamic Four-Point Flexural Tests of Concrete Beams with Variation in Concrete Quality, Reinforcement Properties and Impact Velocity," *Nordic Concrete Research*, vol. 65, no. 2, 2021, doi: 10.2478/ncr-2021-0007.

[14] M. Andersson and E. Pettersson, "Reinforced Concrete Beams Subjected - Experimental study of the influence of reinforcement properties on the structural," Master's Thesis, Chalmers University of Technology, 2019.

[15] CEN, "EN 12390-3: Testing hardened concrete - Part 3: Compressive strength of test specimens," 2009.

[16] I. Löfgren, J. F. Olesen, and M. Flansbjer, "Application of WST-method for fracture testing of fibre- reinforced concrete, Chalmers University of Technology, Department of Structural Engineering and Mechanics, Report 04:13," 2004.

[17] H. Schreier, J. J. Orteu, and M. A. Sutton, *Image correlation for shape, motion and deformation measurements: Basic concepts, theory and applications*. 2009. doi: 10.1007/978-0-387-78747-3.

[18] "GOM," GOM Correlate Professional, Hotfix 5. Accessed: Jun. 25, 2018. [Online]. Available: https://www.zeiss.com/metrology/en/software/metrology-software.html

[19] "Aramis," Aramis 12 M. [Online]. Available: https://www.zeiss.com/metrology/en/explore/topics/aramis-high-speed-dic-systems.html

[20] M. Johansson and L. Laine, "Bebyggelsens motståndsförmåga mot extrem dynamisk

belastning Del 3: Kapacitet hos byggnader, (The resistance of housing settlement subjected to extreme dynamic loading. Part 3: Building capacity. In Swedish)," Oct. 2012.

[21] J. M. Biggs, *Introduction to Structural Dynamics. McGraw-Hill, New-York, USA*. 1964.

[22] M. Johansson, J. Leppänen, M. Andersson, and E. Pettersson, "Residual capacity of RC beams subjected to impact loading: Influence of reinforcement ductility," *International Journal of Protective Structures*, vol. 16, no. 1, pp. 184–201, 2024, doi: 10.1177/20414196241277221.

[23] Bigaj A.J., "Structural Dependence of Rotational Capacity of Plastic Hinges in RC Beams and Slabs," PhD Dissertation, TU Delft, Civil Engineering and Geosciences, Delft, The Netherlands, 1999.

[24] A. Carpinteri, M. Corrado, G. Mancini, and M. Paggi, "Size-scale effects on plastic rotational capacity of reinforced concrete beams," *ACI Struct J*, vol. 106, no. 6, 2009, doi: 10.14359/51663190.

15th International Conference on
Shock & Impact Loads on Structures
12-13 June 2025, Gothenburg, Sweden

IMPACT RESPONSE ANALYSIS OF ROCKFALL PROTECTION FENCE INSTALLED ON CONCRETE FOUNDATION

Masato Komuro[a], Tomoki Kawarai[a], Fumio Yamasawa[b] and Norimitsu Kishi[a]

[a]Muroran Institute of Technology, Japan, email: komuro@muroran-it.ac.jp,
[b]Civil Engineering Research Institute for Cold Region, Japan

Keywords: rockfall protection fence, dynamic behavior, impact loading, finite element analysis, concrete foundation.

Abstract

In this paper, a 3D elasto-plastic impact response analysis of the rockfall protection fence placed on the concrete foundation blocks was conducted. The applicability of the proposed FE analysis model was investigated comparing with the proto-type impact loading test results. Here, the steel posts of the fence were anchored to the top surface of the concrete foundation with base plate. Findings from this study are as follows: 1) the time histories of the impact force and the tensile forces acting on the wire ropes can be accurately predicted by using the proposed analysis method; and 2) the axial strain distribution of the intermediate post and the local buckling behavior of the steel post near the base can also be better evaluated.

1 INTRODUCTION

In Japan, many rockfall protection structures constructed along the roads in mountainous areas and coastlines to protect transportation networks and human lives from natural disasters such as rockfalls. As one kind of these, there is a conventional rockfall protection fence (see, Figure 1) which is composed of H-shaped steel posts, wire ropes, diamond-shaped wire mesh, and clearance-keeping strips. Currently, the stability check of the foundation is carried out under the static loading following the Rockfall Prevention Handbook [1] in Japan. The dynamic effects due to falling rocks impacting have not been considered in the specifications. To establish a rational design specification, the authors conducted drop-weight impact loading tests for the fences placed on the foundation and investigated.

Figure 1. Conventional rockfall protection fence.

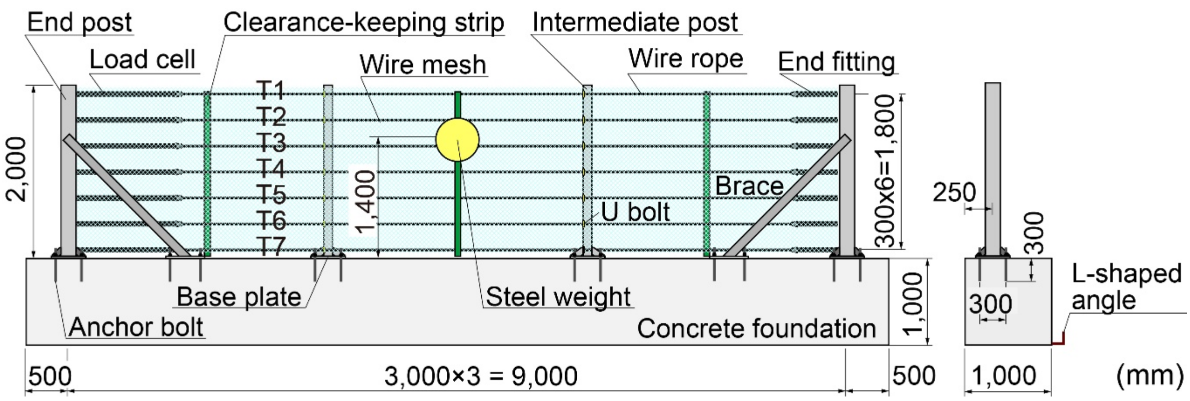

Figure 2. Dimensions of specimen.

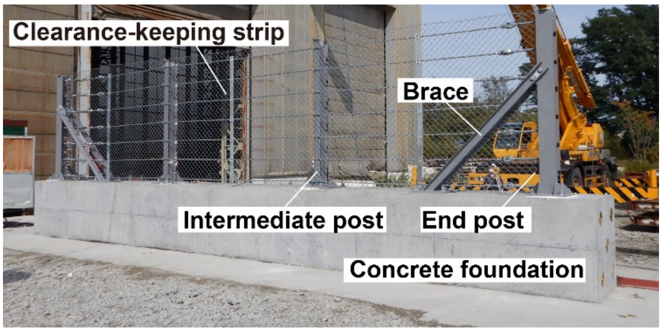

(a) General view

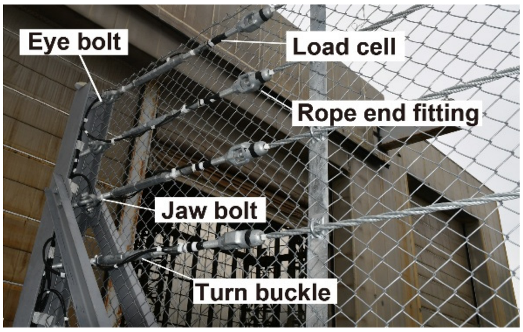

(b) Rope end

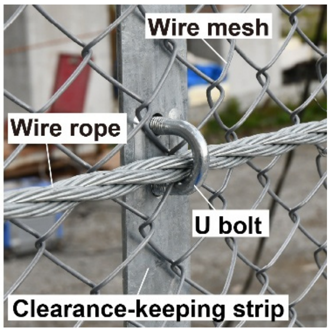

(c) Clearance-keeping strip

Figure 3. Overall view of specimen and close-up view of each component.

stability of the foundation [2]. However, these investigations should be efficiently conducted based on not only experimental study but also numerical simulations

From this point of view, in this study, in order to establish a numerical analysis method for adequately evaluating the impact-resistance behavior of the rockfall protection fences, a 3D elasto-plastic impact response analysis of the proto-type fence placed on the concrete foundation was conducted. The applicability of the proposed numerical analysis model was investigated comparing with experimental results [2]. The numerical analysis was conducted using a commercial finite element software, LS-DYNA [3].

2 OUTLINE OF EXPERIMENT

As illustrated in Figure 2, dimensions of the specimen used in this study are 2 m height and 9 m length having intervals of 3 m between the posts. Dimensions of the concrete foundation are 1 m width, 1 m height, and 10 m length. The steel posts and braces were anchored to the concrete foundation using base plates and bolts, and details and material properties for each component are listed in Table 1. A total of seven wire ropes (φ18) were placed at 300 mm intervals, and the diamond-shaped wire mesh was placed in front of the ropes to effectively capture the falling rocks.

Figure 3 shows an overall view of specimen and a close-up view of each component. One end of the wire rope was fixed to the end post using a socket-type rope end fitting. The other end was connected to the load cell through rope end fitting and turnbuckle, and was connected to the end post by using a jaw bolt and an eyebolt as shown in Figure 3(b), in which the load cell was used to measure the tensile force applied to the rope. To keep the falling rocks from pushing out from the space between two adjacent wire ropes, the clearance-keeping strip was placed at each mid-span point and was jointed to the wire rope with the wire mesh using U-bolts as shown in Figure 3(c). Before impacting, the tension force of approximately 5 kN was introduced into each wire rope to restrain from deflecting due to self-weight of the rope.

The impact loading test was carried out by lifting a steel weight suspended by a truck crane to a predetermined height and by subsequently releasing it as to collide with the center of the fence specimen through a pendulum motion as illustrated in Figure 4. Geometry and dimensions of the steel weight used in this test are shown in Figure 5. Mass of the weight was 1,181 kg and the impacted point was located at 1.4 m above the top surface of the concrete foundation. Measuring items were the time histories of the impact

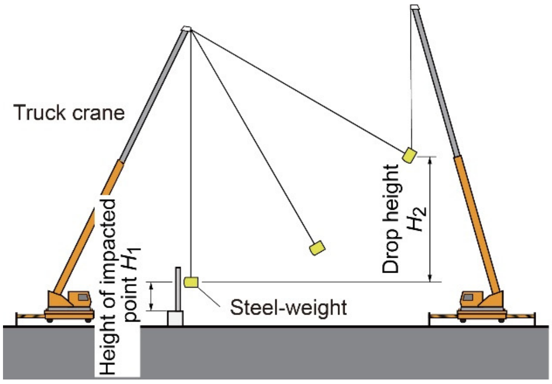

Figure 4. Setup for impact loading test.

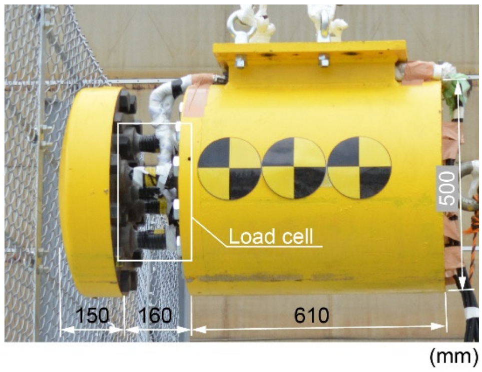

Figure 5. Steel weight.

Member	Dimensions	Yield stress f_y (MPa)	Tensile stress f_u (MPa)
End post	H175×175×7.5×11	320	435
Intermediate post	H200×100×5.5×8	374	479
Brace	[100×50×5×7.5	345	465
Clearance-keeping strip	PL-4.5×65	341	466
Rope end fitting	25φ×500	351	541
Wire rope	18φ (3×7 G/O)	118[#1]	202[#2]
Diamond-shaped wire mesh	3.2φ×50×50	-	429
Anchor bolt	D25(M24)×390	-	-

Note: [#1] Yield load (kN), [#2]Breaking load (kN)

Table 1. Details of components for specimen.

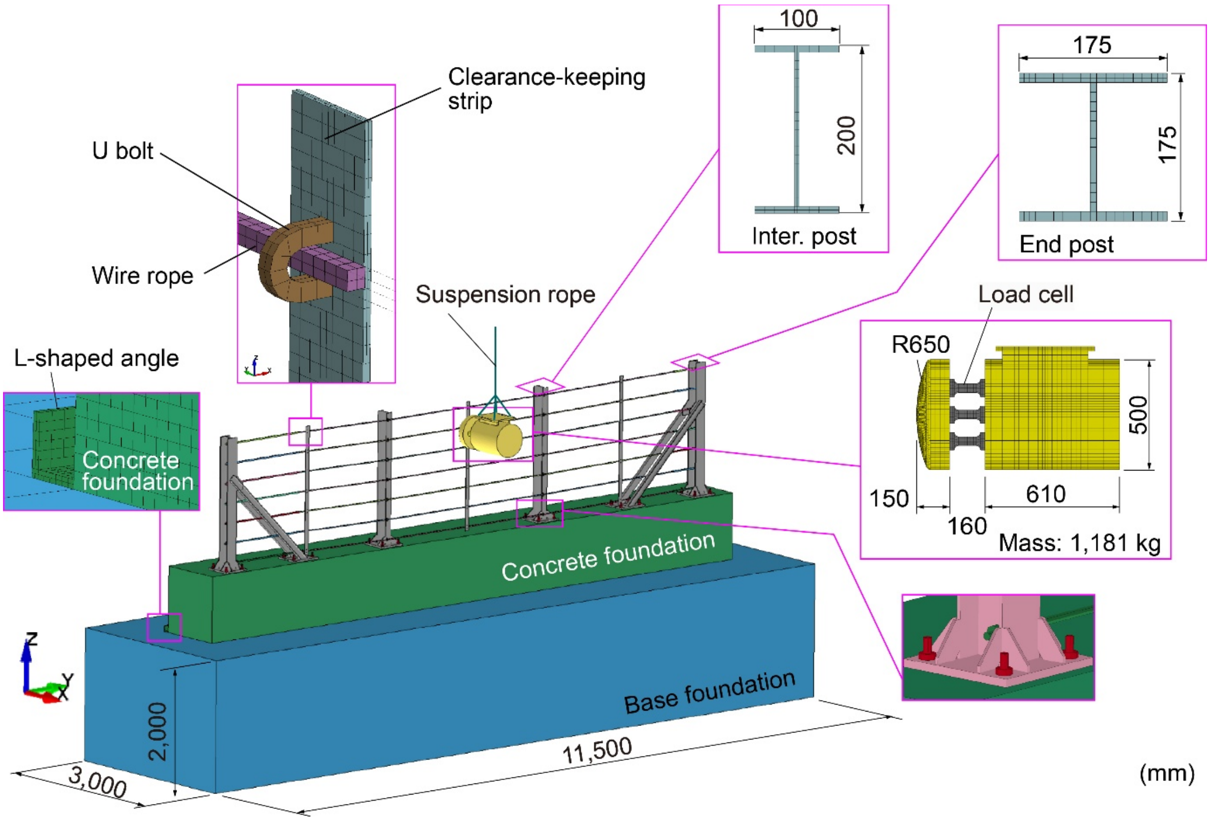

Figure 6. FE model.

force, the horizontal displacement of the weight, the tension forces applied to the wire ropes, and axial strains of the web of the intermediate post.

The input energy was determined as 52 kJ based on the design specifications [1] and then the drop height (H_2) of the weight was set to be 4.5 m. The actual collision velocity of the weight was estimated as 9.07 m/s by conducting image analysis of the photographs obtained from a 2,000 fps high speed camera and corresponding measured input energy was 49 kJ, which is approximately 94% of the absorbing energy for design.

3 NUMERICAL ANALYSIS

3.1 FE Model

Figure 6 shows the FE model used in this numerical analysis. In this study, 8-node solid elements were used to discretize the H-shaped steel posts, the braces, the clearance-keeping strips, and the steel weight. The wire ropes were also discretized by using 8-node solid element for the interaction between the wire rope and the weight as to be adequately evaluated. The wire mesh was not discretized in this study because the steel weight impacted directly the clearance-keeping strip and the influence of the mesh on the impact-resistance behavior of the fence may not be much. The L-shaped angles were placed at the bottom edge of the not impacted-side of the concrete foundation on the top surface of the base foundation following to the experimental conditions.

The boundary conditions for the FE model were defined as follows: the bottom surface of the base foundation was fully fixed whereas the normal components of displacement on the side surfaces were restrained and the upper end of the rope for hanging the steel weight was pinned. Contact surface model was applied to consider the interaction between the weight and the impacted clearance-keeping strip and between the weight and the wire ropes. The friction coefficient between the contact surfaces was assumed to be 0.4 based on the

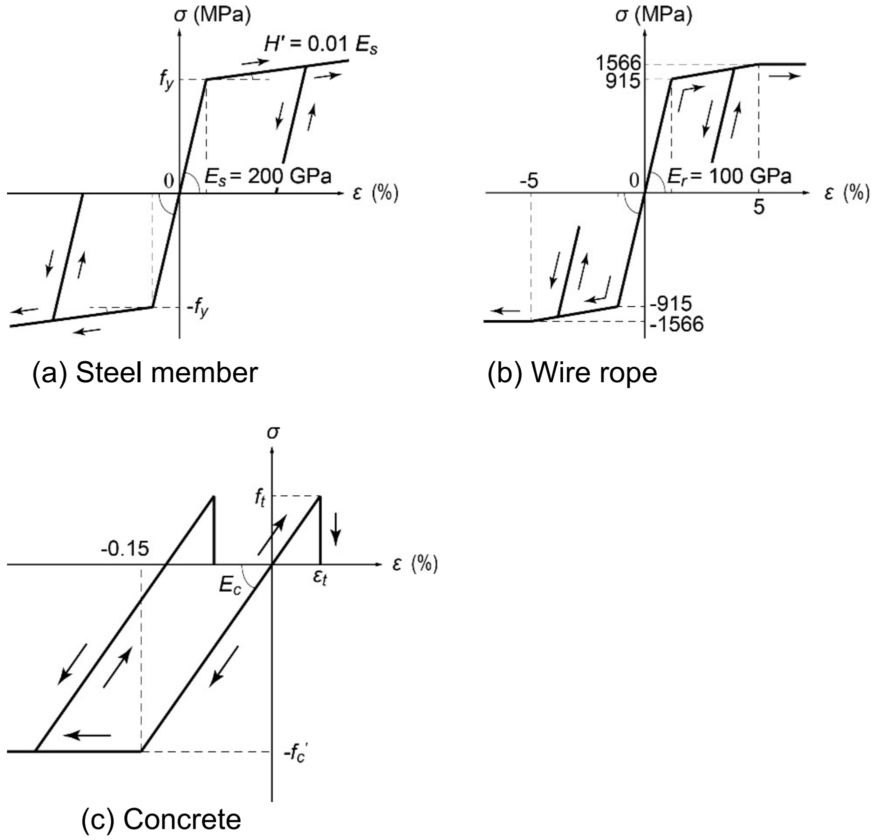

Figure 7. Stress-strain relationships of members.

preliminary analysis results and referring to the research report [4]. The penalty method was employed to better evaluate the contact surface. The mass damping, gravity, and the introduced tension force into the wire rope were not taken into account in this numerical analysis. The impact force was applied by inputting the initial velocity of 9.07 m/s for the whole elements of the steel weight according to the experiment.

3.2 Constitutive Model

Figure 7 shows the constitutive models for the steel members and the concrete used in this study. Figure 7(a) shows the stress-strain relationship used for the steel members; the posts, the braces, and the clearance-keeping strips. The relationship was modeled by using a tri-linear isotropic hardening model with the von Mises yield criterion, in which the plastic hardening modulus H' was assumed to be 1% of the elastic modulus E_s. Material properties of each steel member obtained from the mill test certificate, are listed in Table 1. Figure 7(b) shows the stress-strain relationship for the wire ropes by using a tri-linear model in which each stress was obtained from the static tensile loading test. Figure 7(c) shows the stress-strain relationship for the concrete foundation by using a bilinear model in the compression region. It is assumed for the concrete that: 1) the yield stress is equal to the compressive strength f_c' and 2) yielding causes at 0.15% strain and is evaluated based on the Drucker-Prager's yield criterion. The compressive strength f_c' was 28 MPa from the material test results. The tensile strength was set to be 1/10 of the compressive strength. The U bolts, the suspension rope, the steel weight, and the anchor bolts were assumed to be elastic body, and these Young's modulus and Poisson's ratio were assumed as E = 200 GPa and ν = 0.3, respectively. Density of the steel weight was estimated by dividing the measured mass by the volume from the FE model.

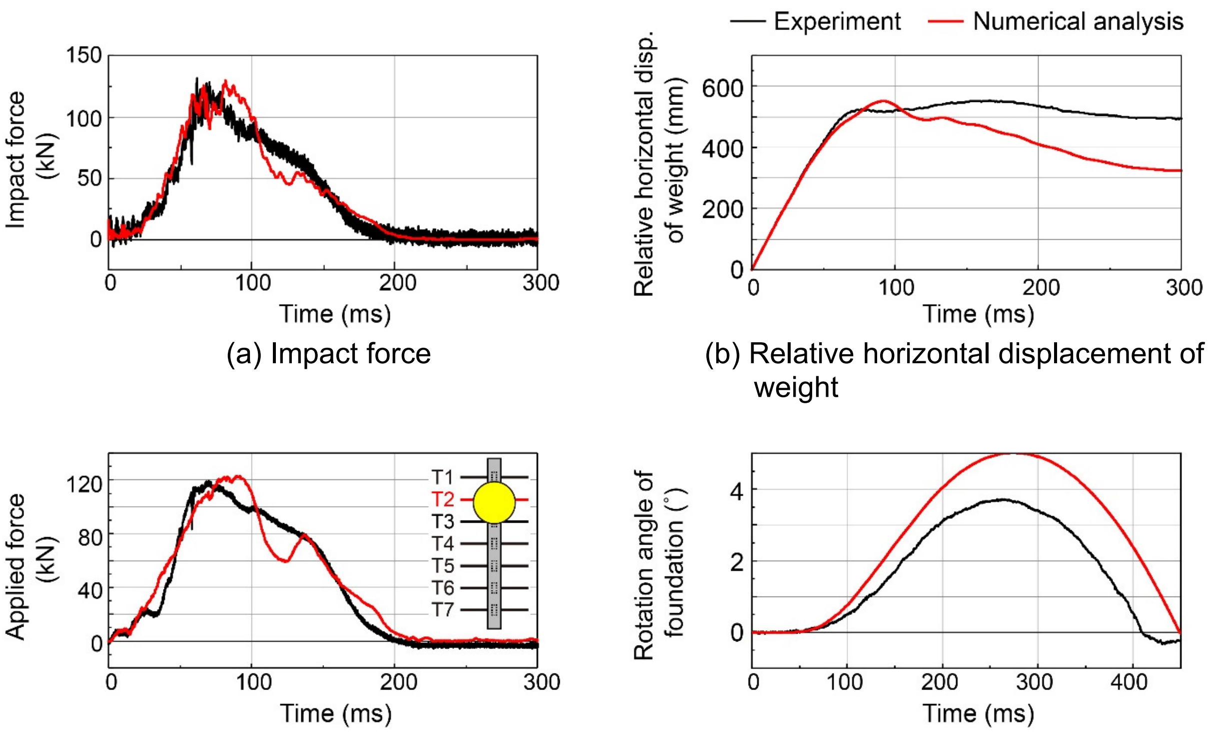

(a) Impact force

(b) Relative horizontal displacement of weight

(c) Applied force to wire rope

(d) Roration angle of foundation

Figure 8. Time histories of responses.

4 EXPERIMENTAL AND NUMERICAL RESULTS AND DISCUSSION

4.1 Time Histories of Responses

Figure 8 shows comparisons of the time histories of the impact force, the relative horizontal displacement of the steel weight, the tensile forces applied to the wire ropes near the loading point, and the rotation angle of concrete foundation between numerical and experimental results. The relative horizontal displacement obtained from the experimental results was evaluated through the image analysis due to tracking a target marker attached to the side surface of the weight and excluding the rotation component of the concrete foundation. In these figures, an origin of the abscissa was taken as the time when the weight impacts the fence.

From the impact force time histories shown in Figure 8(a), it is observed that the maximum amplitude obtained from the numerical results was slightly larger than that obtained from the experimental results, however the duration was in good agreement with the experimental results. Focusing on the relative horizontal displacement of the weight shown in Figure 8(b), the numerical results is better corresponded to the experimental results from the beginning of impact up to approximately t = 50 ms. However, afterwards, difference is gradually increased with passing of time.

From Figure 8(c), the numerical distribution configuration of the time history and duration of the tension force applied to the wire rope is corresponded well to that of the experimental results. In addition, since the tension force applied to the rope at the maximum impact force occurred was close to the yield load (118 kN), the rope might have yielded. From Figure 8(d), it is seen that even though the concrete foundation lost the stability if following the current design specifications, the foundation is actually and perfectly restored. It is also observed that the distribution configuration characteristics of the numerical rotation angle had similar to those of the experimental results. However, the maximum rotation angle was overestimated compared to the experimental results.

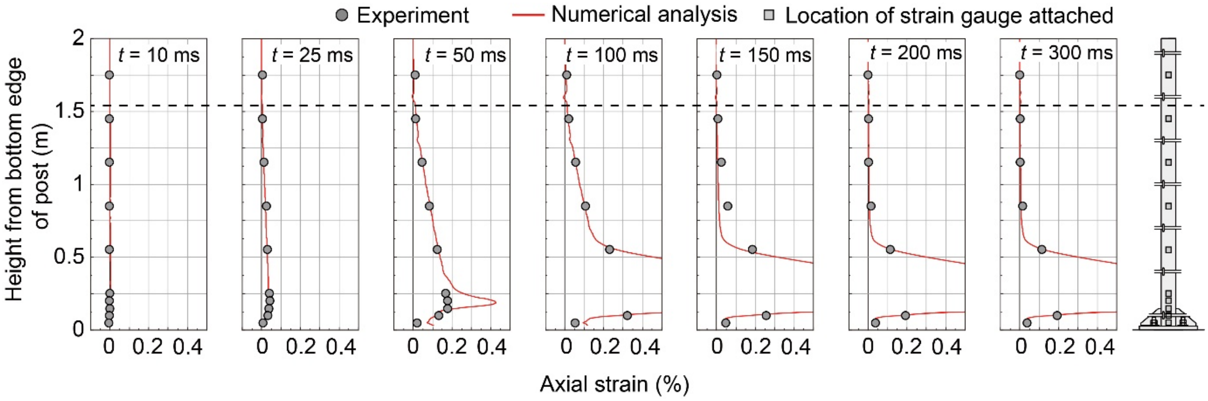

Figure 9. Temporal axial strain distribution of impacted-side fiber of flange of intermediate post.

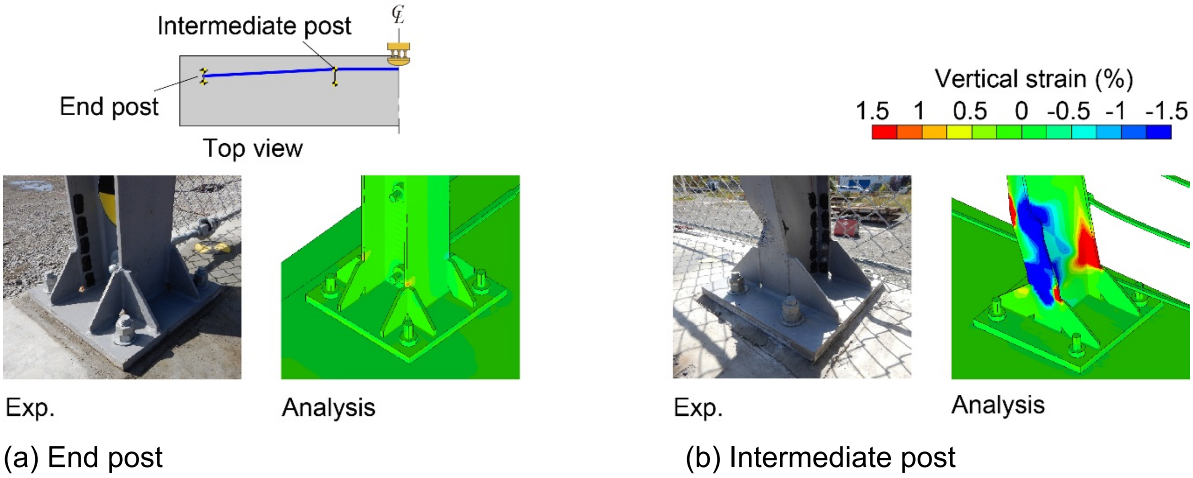

Figure 10. Comparisons of deformation of post near base plate after experiment with numerical analysis results.

4.2 Axial Strain Distribution

Figure 9 shows the temporal axial strain distributions at the impacted-side fiber of the flange of the intermediate post. The fiber strain was estimated by using measured two strains at the web based on the plane conservation concept for the cross section of the post. From this figure, it is observed that the numerical results are in good agreement with the experimental results for all time steps considered in this study. Since the axial strain of post near the base plate always distributed below 0.05%, the post near the base plate may be kept under the elastic state due to the strengthening effect of the rib plates.

4.3 Comparisons of Deformation near Bottom End of Post between Experimental and Numerical Analysis results

Figure 10 shows comparisons of the deformation near the bottom end of the post after impact loading between the experimental and numerical analysis results. From Figure 10(a), both experimental and numerical results exhibit that the end post was almost perfectly restored under the state before impact loading.

In the case of the intermediate post shown in Figure 10(b), it is observed that the local buckling clearly occurred at the post above the rib plates similarly to both experimental and numerical results. Therefore, the local buckling behavior of the post near the bottom end can be effectively simulated by using the proposed numerical analysis method.

5 CONCLUSIONS

1. The time histories of the impact force and tensile forces acting to the wire ropes, which may be key parameters for design procedure, can be more accurately predicted by using the proposed analysis method; and
2. The axial strain distribution of the intermediate post and the local buckling behavior of the steel post near the bottom end can also be effectively evaluated by using the method.

REFERENCES

[1] Japan Road Association, “Design guideline for anti-impact structures against falling rocks”, Maruzen, 2017.[in Japanese]

[2] F. Yamasawa, M. Komuro, T. Kawara, N. Kishi, T. Nakamura, and O. Hatakeyama, “Proto-type experiments on dynamic response behavior of foundation and rockfall protection fence when fence is subjected to impact load”, Journal of the Japan Society of Erosion Control Engineering, Vol. 72, No. 1, pp. 11-21, 2023, doi: 10.11475/sabo.76.1_11. [in Japanese]

[3] ANSYS, Inc., “LS-DYNA User’s Manual R13”, 2021.

[4] British Standards Institution, “BS 5975: Code of practice for falsework”, London, 1996.

15$^{\text{th}}$ International Conference on
Shock & Impact Loads on Structures
12-13 June 2025, Gothenburg, Sweden

DEVELOPMENT OF A DESIGN OPTIMIZATION FRAMEWORK FOR TPMS-BASED SANDWICH STRUCTURES UNDER BLAST LOADING

Niclas Strömberg

Department of Mechanical and Materials Engineering
Karlstad University
SE-651 88 Karlstad, Sweden
e-mail: niclas.stromberg@kau.se

Key words: Blast, Triply periodic minimal surfaces, Sandwich structures, Design optimization

Abstract. The demonstrated potential of energy absorption and impact resistance of triply periodic minimal surface (TPMS)-based lattice structures is the motivation of this project. The goal of the project is to develop an efficient framework for finding optimal designs of TPMS-based sandwich structures for blast protection. Optimal grading of the TPMS-based lattice structures is performed by numerical multi-fidelity experiments using Abaqus/Explicit and machine learning supported surrogate models. First, compactly supported radial basis function networks are trained for the low-fidelity data, and then ensembles of surrogate models are generated by minimizing the cross-validation error of the high-fidelity data obtained from the Abaqus/Explicit simulations. The optimization is then performed using these optimal ensembles of surrogate models. The blast pressure on the structure is applied using the empirical ConWep model which is implemented in Abaqus/Explicit. During the development of the framework 316L stainless steel is chosen as material for the sandwich structure, which is modelled using J2-plasticity with isotropic Johnson-Cook hardening. The constitutive Johnson-Cook parameters for the hardening are determined using the method of least squares applied to the Cauchy stress and the logarithmic strain. Additionally, a continuum damage model is activated when the logarithmic failure strain is reached. While strain rate and temperature dependencies will be included in future versions of the framework. Furthermore, the lattice structure is modelled using either shell elements with representative thicknesses, or solid elements with representative constitutive properties obtained from numerical homogenization. Finally, the optimal result is mapped back to the implicit surface geometry, which in turn is converted to a printable STL-file. The workflow of the framework and optimal designs will be presented at the conference.

1 INTRODUCTION

TPMS-based sandwich structures have emerged as a promising solution for lightweight, high-strength applications due to their superior mechanical properties, including high stiffness-to-weight ratio, energy absorption capabilities, and manufacturability using advanced additive manufacturing techniques. These properties make them particularly well-suited for applications where blast resistance is a critical design consideration, such as military armor, aerospace structures, and protective enclosures. However, the complex geometry of TPMS structures presents challenges in optimizing their performance under extreme loading conditions, including blast impacts [1, 2, 3, 4, 5].

To address these challenges, this study focuses on developing a design optimization framework tailored specifically for TPMS-based sandwich structures subjected to blast loading. The proposed multi-objective optimization framework integrates advanced finite element analysis (FEA), and multifidelity-based surrogate modeling using an ensemble of surrogates to efficiently explore the design space. By leveraging high- and low-fidelity FEA simulations alongside computationally efficient surrogate models, the framework enables a balance between accuracy and computational cost while optimizing blast resistance and structural efficiency. By systematically exploring different TPMS geometries, material distributions, and design parameters, the framework aims to provide an effective methodology for improving the protective performance of these advanced structures. The insights gained from this research contribute to the broader field of surrogate model-based design optimization and impact-resistant design, paving the way for innovative applications in defense, aerospace, and civil infrastructure.

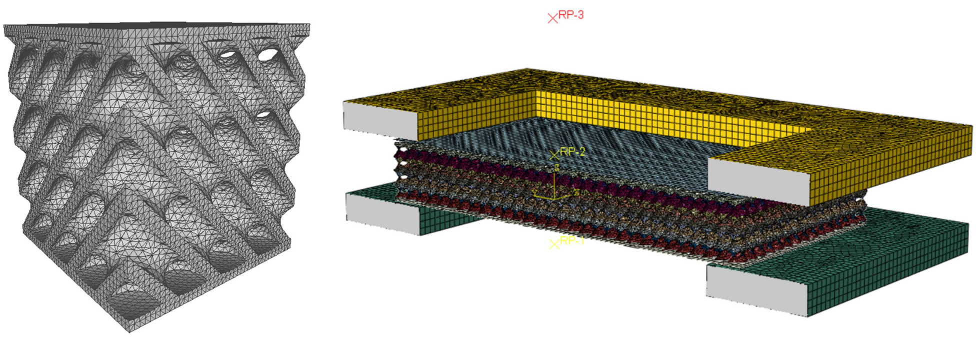

Figure 1: *The sandwich structure with Schwarz-D lattice core and the finite element model.*

2 FINITE ELEMENT ANALYSIS

In the development of the framework, we will start by optimizing a sandwich structure with a core of Schwarz-D lattice structures subjected to blast conditions. The Schwarz-D lattice structures is defined by the following implicit surface:

$$\begin{aligned} f = {} & \sin(\omega x)\sin(\omega y)\sin(\omega z) + \sin(\omega x)\cos(\omega y)cos(\omega z) + \\ & \cos(\omega x)\sin(\omega y)\cos(\omega z) + \cos(\omega x)\cos(\omega y)\sin(\omega z), \end{aligned} \tag{1}$$

where x, y, z are coordinates and ω is controlling the size of the period of the lattice. By letting $g = \min(f + \kappa, -f + \kappa)$, the shell-based lattice structures is obtained, where $g > 0$ represents the interior of the structure, $g < 0$ is the outside and $g = 0$ gives the boundary of the lattice structure. In this work, we will find an optimal distribution $\kappa = \kappa(x, y, z)$ for the core of lattice structure as well as optimal thicknesses of the upper and lower sheets of the sandwich structure by adopting surrogate model-based design optimization. Previously, we have studied topology optimization of Schwarz-D and other TPMS-based lattice structures [6, 7, 8].

A schematic illustration of the sandwich structure is presented in Figure 1. The figure also depicts the finite element model of the sandwich structure with the boundary conditions of the blast. Two rigid holders are clamping the sandwich structure, and the upper sheet of the sandwich structure is subjected to the blast load which is applied at a reference point (RP-3 in the figure).

Explicit FEA of the blast is performed using Abaqus/Explicit. The Schwarz-D core is modelled using triangular shell elements at the mid-surface of the lattice defined by $f = 0$ in (1) and square shell elements are used for the upper and lower sheets of the sandwich structure. The core and sheets are connected using tied constraints. Tied constraints are also utilized to represent the clamping between the rigid holders and the sandwich structure. The self contact conditions in the structures are in turn treated by using the general contact conditions with friction implemented in Abaqus/Explicit.

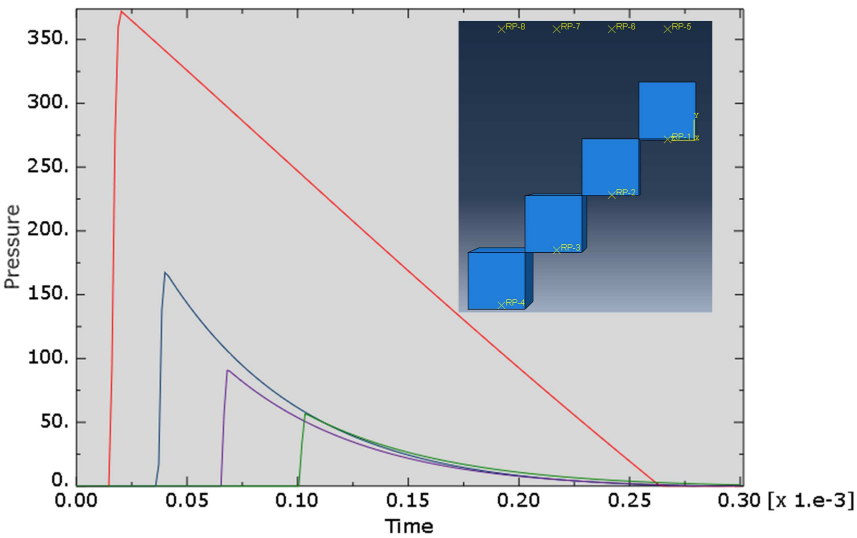

Figure 2: *Illustration of the pressure peak as function of time and distance for the ConWep model implemented in Abaqus/Explicit.*

The blast is modelled using the ConWep model that is implemented in Abaqus/Explicit. The ConWep model is an established empirical model developed by the U.S. Army and it predicts blast effects from conventional explosive detonations in free air [9]. The corresponding detonation pressure is applied on the exposed surface as a time history event depending on the amount of TNT, and the distance between the detonation center and the exposed surface. An illustration of the pressure peak as function of time from the ConWep model is illustrated in Figure 2, where the same amount of TNT is acting on surfaces with different distance from the center point of detonation.

The material of the sandwich structure is 3D-printed 316L stainless steel and this is modelled using J2-plasticity with isotropic Johnson-Cook hardening. In addition, a simple setting of the Johnson-Cook damage model is adopted to represent ductile failure of the material. The governing equations of these models are presented below as well as the corresponding constitutive parameters.

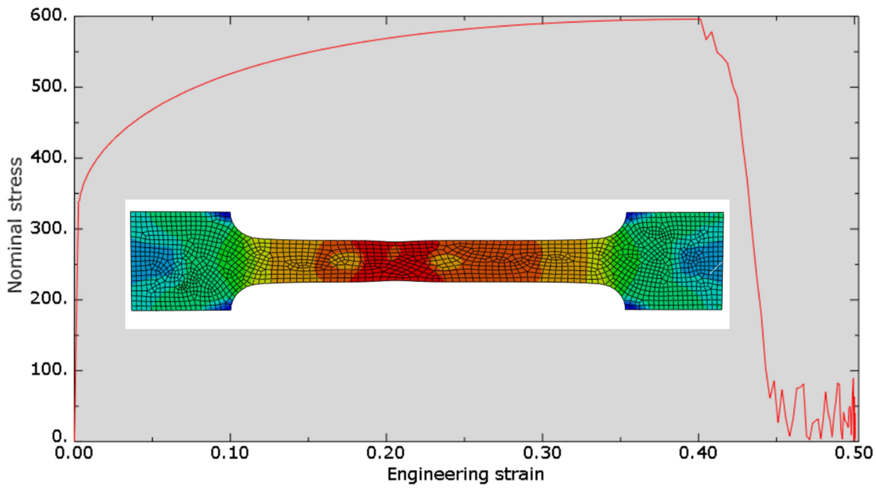

Figure 3: *The nominal stress versus the engineering strain.*

The yield surface of the material is given by

$$f(\sigma_{ij}, \bar{\epsilon}^p_{\text{eff}}) = J_2(\sigma_{ij}) - \sigma_y(\bar{\epsilon}^p_{\text{eff}}), \tag{2}$$

where $J_2 = J_2(\sigma_{ij})$ is the second invariant of the Cauchy stress σ_{ij},

$$\bar{\epsilon}^p_{\text{eff}} = \bar{\epsilon}^p_{\text{eff}}(t) = \int_0^t \dot{\epsilon}^p_{\text{eff}} \, \mathrm{d}t \tag{3}$$

is the total accumulated effective plastic strain at time t, and

$$\sigma_y = \sigma_y(\bar{\epsilon}^p_{\text{eff}}) = A + B(\bar{\epsilon}^p_{\text{eff}})^n, \tag{4}$$

where A, B and n are material parameters, see Table 1. Both strain rate and temperature dependency can be included in (4), but that is ignored in this study. In addition, we utilize a simple setting of the Johnson-Cook damage model, where damage evolution is initiated when $\bar{\epsilon}^p_{\text{eff}}$ reaches a critical value d_1, implying that all other parameters in the Johnson-Cook damage model are set to zero. After damage initiation, the material stiffness is degraded progressively with a simple linear law depending on the characteristic length of the elements used in the finite element model.

Table 1: *Johnson-Cook parameters.*

	A	B	n	d_1
This work.	326	951	0.5664	0.3365
Ref. [10]	312	1114	0.6	-

The following consistent unites are used: ton, s and mm. The density is $7.8e$-9, Young's modulus is 2.1e5 and Poisson's ratio is 0.3. The parameters for the Johnson-Cook isotropic hardening and damage laws are given in Table 1, and the hardening parameters are obtained by the method of least squares applied to Cauchy stress and logaritmic strain data. The parameters are in close resemble with the parameters derived in [10], where the split Hopkinson bar test was performed and evaluated. These parameters are also given in Table 1. In Figure 3 the stress-strain curve for this setting of the material parameters are plotted for a simulated tensile test in Abaqus/Explicit. The result is in good agrement with experimental data for the nominal stress $P = \sigma_{11}/(1+\epsilon_{11})$ and engineering strain $e = \exp(\epsilon_{11}) - 1$.

3 DESIGN OPTIMIZATION

For a given blast we would like to minimize the mass m of the sandwich structure that also minimize the maximum displacement $d_{\max}$ of the lower sheet of the sandwich structure. This is done by finding optimal thickness of the two outer sheets and optimal grading of the lattice core. In the finite element model the grading is treated by setting corresponding thicknesses of the shell elements using 13 sets of elements according to the colored element sets depicted in the finite element model in Figure 1. Four design variables $\boldsymbol{x} = \{x_1, x_2, x_3, x_4\}$ are used to define the thicknesses of the shell elements which are bounded by a lower limit of 1 mm and an upper limit of 4 mm. By first setting up 165 high-fidelity computer experiments using the finite element analysis procedure presented in the previous section, surrogate models for the mass $m = m(\boldsymbol{x})$ and the maximum displacement $d_{\max} = d_{\max}(\boldsymbol{x})$ are established. Secondly, multi-fidelity computer experiments are performed and the corresponding surrogate models and the trade-off curve are generated.

By using the surrogate models, the following multi-objective optimization problem is formulated:

$$
\begin{cases} \min\limits_{\boldsymbol{x}} \{m(\boldsymbol{x}), d_{\max}(\boldsymbol{x})\} \\ \text{s.t.} \begin{cases} 1 \leq x_i \leq 4, & i = 1, \ldots, 3, \\ 0 \leq x_4 \leq 1. \end{cases} \end{cases} \tag{5}
$$

A trade-off curve for this problem is generated by solving

$$
\begin{cases} \min\limits_{\boldsymbol{x}} d_{\max}(\boldsymbol{x}) \\ \text{s.t.} \begin{cases} m(\boldsymbol{x}) \leq \hat{m}, \\ 1 \leq x_i \leq 4, & i = 1, \ldots, 3, \\ 0 \leq x_4 \leq 1 \end{cases} \end{cases} \tag{6}
$$

for a range a values on $\hat{m}$ between the utopian solutions.

The thickness of the lower sheet is defined by x_1, the thickness of the upper sheet is defined by x_3, and the thickness at the center of the core is given by x_2. Two interpolations, $\hat{t}(z)$ and $\tilde{t}(z)$, of these three thickness variables are established according to the two first equations in (7). A thickness distribution $t(z)$ is then defined as convex combination by using x_4 as presented in the final equation of (7).

$$
\begin{gathered} \hat{t}(z) = \hat{\alpha}_1 + \hat{\alpha}_2 z + \hat{\alpha}_3 z^2, \\ \tilde{t}(z) = \tilde{\alpha}_1 + \tilde{\alpha}_2 z + \tilde{\alpha}_3 z^{16}, \\ t(z) = x_4 \min(\max(\hat{t}(z), 1), 4) + (1 - x_4) \min(\max(\tilde{t}(z), 1), 4). \end{gathered} \tag{7}
$$

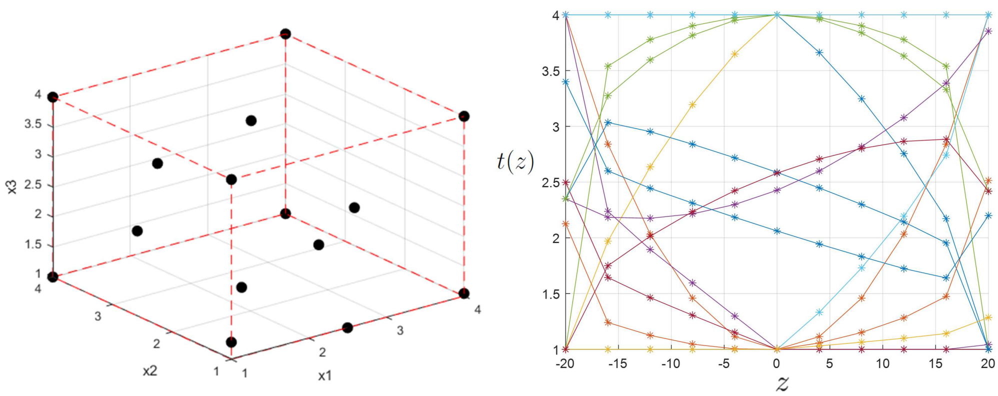

Figure 4: *Illustration of space optimal DoEs and the corresponding thickness distributions $t(z)$.*

By using (7) design of experiments of thickness distribution $t(z)$ are set up and for each distribution the corresponding blast simulation is performed. In the beginning of the development, a space optimal DoE of 165 data points is utilized. This is illustrated for 15 data points in Figure 4, where the space optimal DoE for x_1, x_2 and x_3 is plotted to the left in the figure and the corresponding thickness distributions $t(z)$ are plotted to the right in the figure.

A multifidelity-based surrogate model framework implemented in our toolbox MetaBox is adopted to establish $m(\boldsymbol{x})$ and $d_{\max}(\boldsymbol{x})$ in (5) for the DoE discussed above as well as multifidelity data presented in the next section. The computational time for a highfidelity (HF) non-linear finite element model is typically several hours or even days. Therefore, computer experiments using HF models only when establishing a surrogate model might be too time consuming. However, the trend of a finite element model response might be captured using lowfidelity (LF) finite element models using e.g. coarser meshes or simplified material models.

By combining LF and HF computer experiments, multifidelity (MF) based surrogate models can be developed within acceptable time, which both capture the trends of the responses and are sufficient accurate. Below, a hybrid MF surrogate model approach is presented that is built using LF and HF computer experiments. The approach follows the ideas presented in [11].

Let $\hat{\boldsymbol{x}}_{\mathrm{LF}} = \{\hat{\boldsymbol{x}}_{\mathrm{LF},1}, \ldots, \hat{\boldsymbol{x}}_{\mathrm{LF},N}\}$ and $\hat{\boldsymbol{f}}_{\mathrm{LF}} = \{\hat{f}_{\mathrm{LF},1}, \ldots, \hat{f}_{\mathrm{LF},N}\}$ denote the N sampling points and the responses of a LF model, respectively, and $\hat{\boldsymbol{x}}_{\mathrm{HF}} = \{\hat{\boldsymbol{x}}_{\mathrm{HF},1}, \ldots, \hat{\boldsymbol{x}}_{\mathrm{HF},M}\}$ and $\hat{\boldsymbol{f}}_{\mathrm{HF}} = \{\hat{f}_{\mathrm{HF},1}, \ldots, \hat{f}_{\mathrm{HF},M}\}$ be the M sampling points and responses of the corresponding HF model. An additive MF surrogate model $f^a_{\mathrm{MF}} = f^a_{\mathrm{MF}}(\boldsymbol{x})$ of this sampling data can be formulated as

$$f^a_{\mathrm{MF}}(\boldsymbol{x}) = f_{\mathrm{LF}}(\boldsymbol{x}) + f_{\Delta}(\boldsymbol{x}), \tag{8}$$

where $f_{\mathrm{LF}} = f_{\mathrm{LF}}(\boldsymbol{x})$ is a surrogate model of $\hat{\boldsymbol{x}}_{\mathrm{LF}}$ and $\hat{\boldsymbol{f}}_{\mathrm{LF}}$, respectively, and $f_{\Delta} = f_{\Delta}(\boldsymbol{x})$ is a surrogate model of the differences of the HF computer experiments $\hat{\boldsymbol{f}}_{\mathrm{HF}}$ and the LF surrogate model f_{LF} at $\hat{\boldsymbol{x}}_{\mathrm{HF}}$, i.e.

$$\hat{\boldsymbol{f}}_{\Delta} = \{\hat{f}_{\mathrm{HF},1} - f_{\mathrm{LF}}(\hat{\boldsymbol{x}}_{\mathrm{HF},1}), \ldots, \hat{f}_{\mathrm{HF},M} - f_{\mathrm{LF}}(\hat{\boldsymbol{x}}_{\mathrm{HF},M})\}. \tag{9}$$

Instead of applying an additive approach as presented above in (8), one can instead adopt a multiplicative scaling approach such that the MF surrogate model is formulated as

$$f^m_{\mathrm{MF}} = f^m_{\mathrm{MF}}(\boldsymbol{x}) = \beta_{\Delta}(\boldsymbol{x}) f_{\mathrm{LF}}(\boldsymbol{x}), \tag{10}$$

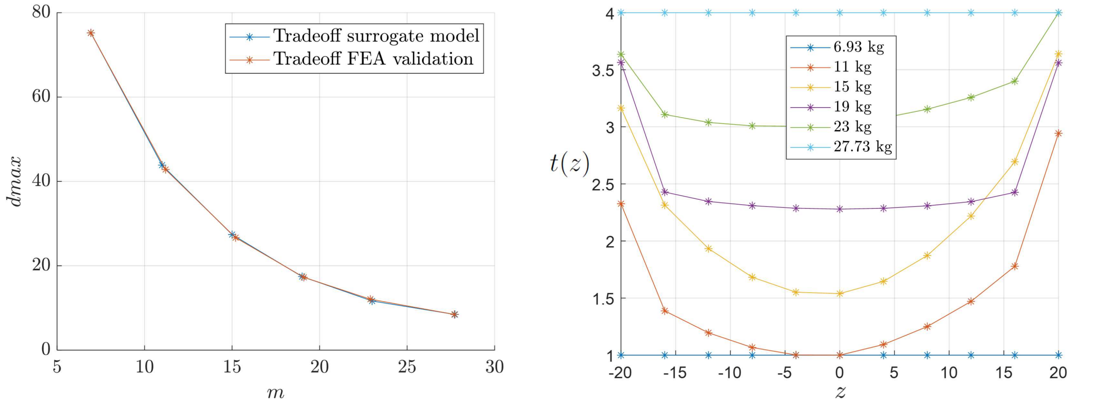

Figure 5: *Tradeoff curve and corresponding thickness distributions.*

where $\beta_\Delta = \beta_\Delta(\boldsymbol{x})$ is a surrogate model that scales the LF model in order to fit f^m_{MF} to $\hat{\boldsymbol{f}}_{\mathrm{HF}}$ at $\hat{\boldsymbol{x}}_{\mathrm{HF}}$. Thus, β_Δ is trained for

$$\hat{\boldsymbol{\beta}}_\Delta = \{\frac{\hat{f}_{\mathrm{HF},1}}{f_{\mathrm{LF}}(\hat{\boldsymbol{x}}_{\mathrm{HF},1})}, \ldots, \frac{\hat{f}_{\mathrm{HF},M}}{f_{\mathrm{LF}}(\hat{\boldsymbol{x}}_{\mathrm{HF},M})}\}. \tag{11}$$

In this work, the lowfidelity based surrogate model is a RBFN with Wendland's compactly supported radial basis functions. An investigation of different settings of RBFN can be found in [12]. The highfidelity surrogate models f^a_{MF} and f^m_{MF} are instead established using optimal ensembles of surrogate models following the approach presented by Strömberg [13].

The hybrid surrogate model of the two multifidelity surrogate models, f^a_{MF} and f^m_{MF}, presented above in (8) and (10) is formulated as

$$f_{\mathrm{MF}} = \alpha f^a_{\mathrm{MF}} + (1-\alpha) f^m_{\mathrm{MF}}, \tag{12}$$

where $0 \leq \alpha \leq 1$.

A most recent work on design optimization using the same developed multifidelity surrogate modeling approach is presented in [14].

4 PRELIMINARY RESULTS

First 165 high-fidelity computer experiments are executed using Abaqus/Explicit as outlined in Section 1 on 6 cores of AMD Ryzen Threadripper PRO 7945WX. The total CPU time is 30 hours. Surrogate models are trained for this data without any additional low-fidelity data, and a trade-off curve for the multi-objective problem in (5) is generated by solving (6). The result is presented to the left in Figure 5. To the right in this figure the corresponding optimal thickness distributions are plotted. The trade-off curve is also validated by performing FEA for the optimal thickness distributions, and the validated result is in close agreement with the result obtained by using the surrogate models. This is also depicted in the left plot of Figure 5. A stress-displacement plot of the FEA result for the 15 kg optimal solution is presented and compared to the utopian solution of 6.93 kg in Figure 6.

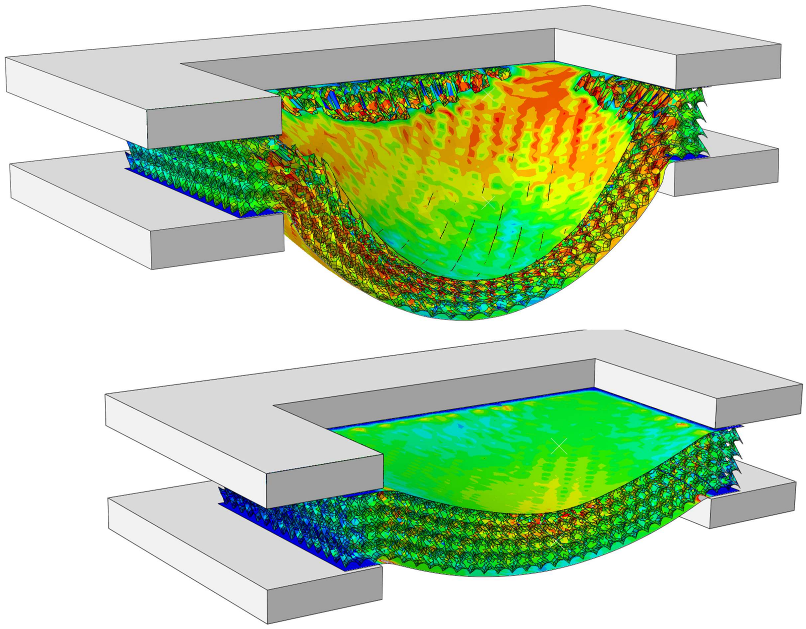

Figure 6: *FEA results: the utopian solution 6.93 kg and the optimal solution 15 kg.*

Secondly, 30 high-fidelity computer experiments as well as 165 low-fidelity computer experiments are generated. The low-fidelity model is simply obtained by selective mass-scaling of the high-fidelity model such that a speed-up factor of 5.5 is obtained (remember that the smallest element defines the critical time step). In total, the total CPU time of all 195 simulations is 10 hours compared to 30 hours for the 165 high-fidelity computer experiments used previously. The multi-fidelity surrogate model approach presented in the previous section is utilized to set up the multi-objective optimization problem in (5). The multi-fidelity trade-off is again generated by solving (6), and it is plotted to the left in Figure 7. The curve is compared in the same plot to the trade-off generated previously in Figure 5 and it is very similar. The corresponding multi-fidelity thickness distributions are plotted to the right in Figure 7. These are also similar to the previous distributions, although slight differences are appearing.

5 CONCLUDING REMARKS

In this paper a design optimization framework for blast of sandwich structures of cores with TPMS-based lattice structures is developed and presented. The framework is demonstrated for blast of a test rig example of a clamped square sandwich structure. A trade-off between maximum displacement and weight is generated by establishing optimal thickness distribution of the core of TPMS-based lattice as well as optimal thickness of the outer sheets of the sandwich structure using a multi-fidelity surrogate model approach. In a near future, the presented design optimization framework will be further developed by including strain rate and temperature dependency in the Johnson-Cook material model, and include additional objectives in the multiobjective optimization problem in (5). In addition, the multi-fidelity surrogate model approach will be further investigated and developed.

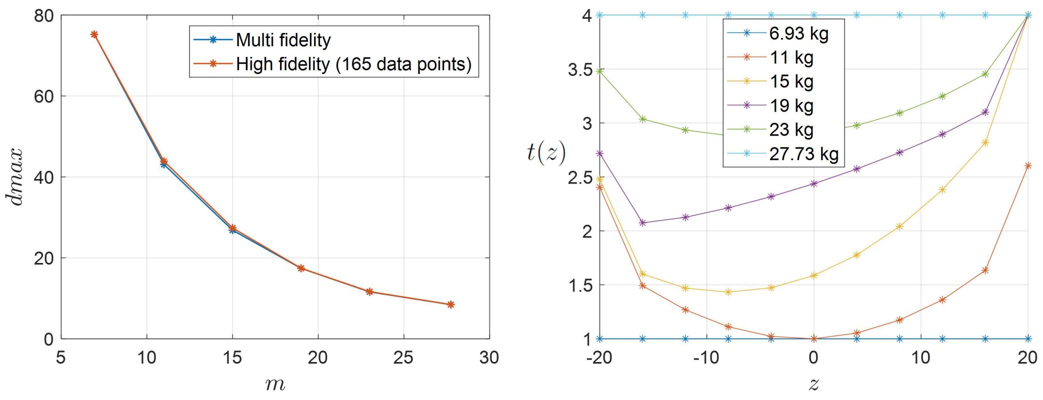

Figure 7: *Tradeoff curve and corresponding thickness distributions for the multi-fidelity approach.*

Acknowledgment: This work is supported by the by Vinnova in the project AutoLight4AM.

REFERENCES

[1] Almahri, S., R. Santiago, D-W. Lee, H. Lee, H. Ramos, H. Alabdouli, M. Alteneji, Z. Guan, W. Cantwell & M. Alves, Evaluation of the dynamic response of triply periodic minimal surfaces subjected to high strain rate compression, *Additive Manufacturing*, **46**, 102220, 2021.

[2] Novak, N., M. Borovinsek, O. Al-Ketan, Z. Ren & M. Vesenjak, Impact and blast resistance of uniform and graded sandwich panels with TPMS cellular structures, *Composites Structures*, **300**, 116174, 2022.

[3] Tran, P. & C. Peng, Triply periodic minimal surfaces sandwich structures subjected to shock impact, *Journal of Sandwich Structures & Materials*, **23:6**, 2146–2175, 2021.

[4] He, L., T. Li, D. Zhong, H. Tao, Y. Peng & S. Chen, Blast resistance in sandwich structures based on TPMS, *Buildings*, **13**, 2385, 2023.

[5] Peng, C. & P. Tran, Bioinspired functionally graded gyroid sandwich panel subjected to impulsive loading, *Composites Part B*, **188**, 107773, 2020.

[6] Strömberg, N., Optimal grading of TPMS-based lattice structures with transversely isotropic elastic properties, *Engineering Optimization*, **5 3:11**, 1871–1883, 2021.

[7] Strömberg, N., A new multi-scale topology optimization framework for optimal combinations of macro-layouts and local gradings of TMPS-based lattice structures, *Mechanics Based Design of Structures and Machines*, **52:1**, 257–274, 2024..

[8] Strömberg, N., A Two-Players Game for Multi-Scale Topology Optimization of Static and Dynamic Compliances of TPMS-based Lattice Structures, *Dynamics*, **4:4**, 757–772, 2024.

[9] Randers-Pehrson, G. & K. Bannister, *Airblast Loading Model for DYNA2D and DYNA3D*, Army Research Laboratory, ARL-TR-1310, March 1997.

[10] Chandrasekaran, H. & R. M'Saoubi, Modelling of material flow stress in chip formation process from orthogonal milling and split Hopkinson bar tests, *Machine Science and Technology*, **9**, 131–145, 2005.

[11] L. Zhang, Y.Wu, P. Jiang, S.-K. Choi & Q. Zhou, A multi-fidelity surrogate modeling approach for incorporating multiple non-hierarchical low-fidelity data, *Advanced Engineering Informatics*, **51**, 101430, 2022.

[12] K. Amouzgar & N. Strömberg, Radial basis functions as surrogate models with a priori bias in comparison with a posteriori bias, *Structural and Multidisciplinary Optimization*, **55**, 1453–1469, 2017.

[13] Strömberg, N., Comparison of Optimal Linear, Affine and Convex Combinations of Metamodels, *Engineering Optimization*, **53:4**, 702–718, 2020.

[14] Strömberg, N., Data-Driven Sizing and Shaping of Topology Optimization Concepts using Implicit Surfaces, Free Form Deformations and Multifidelity-Based Surrogate Models, in the proceedings of *ASME 2024 International Design Engineering Technical Conferences and Computers and Information in Engineering Conference, IDETC-CIE*, Washington, 25–28 August, 2024.

15th International Conference on
Shock & Impact Loads on Structures
12-13 June 2025, Gothenburg, Sweden

PRELIMINARY STUDY OF GRANITE SLABS EXPOSED TO CONTACT CHARGE

Jonas Rudshaug[a,b], Tormod Grue[a] and Benjamin Stavnar Elveli[a]

[a]Norwegian Defense Estates Agency, Norway, email: jonas.rudshaug@forsvarsbygg.no,
[b]Norwegian University of Science and Technology, Norway

Keywords: granite, concrete, contact charge, numerical simulation

Abstract

Norway's hilly landscape facilitates the extensive use of mountains for establishing shelters and other facilities requiring robust protection against military threats. A crucial aspect of ensuring the adequate design of these facilities is a deeper understanding of the rock's material properties under relevant load scenarios. The mountains in Norway comprise various rock types with differing properties. Typically, rocks exhibit high compressive strength and brittle fracture mechanisms, somewhat akin to the behavior of concrete. To ensure accurate material calibration, a variety of validation cases is needed, covering variations in strain rate, pressure, and more. In this study, we aim to supplement the existing validation cases for granite by designing an experimental setup to test granite slabs exposed to contact charge loading. Here, we focus on the preliminary numerical study of the experimental setup. To model the granite slabs, we use a relatively simple concrete model known as the modified Holmquist-Johnson-Cook model (MHJC).

1 INTRODUCTION

The study of rock materials for protective purposes has a long history, driven both by civil and military needs **[1, 2]**. With the advancements in precision-guided weapons and the current geopolitical situation, shelters and other facilities requiring robust protection against military threats are of high importance. The ability of earth-penetrating weapons to reach deeply buried targets has increased, posing new challenges for defense engineers. To provide robust guidelines for the development of new facilities and the maintenance of existing facilities, there is a need for greater understanding of the protective capabilities of rock materials. Modern computational tools like the finite element method provide a powerful foundation for the investigation of these types of problems.

An important detail to consider when working with rock materials and its mechanical behavior is the large variety of rock types and their different properties, such as varying stiffness and initial defects. Rock materials with high stiffness will exhibit different ground shock characteristics compared to those with a lower stiffness **[9]**. In this study, we focus on the high stiffness rock material granite. Several dynamic constitutive models for rock- and concrete-like materials have been developed over the years, including the Riedel–Hiermaier–Thoma (RHT) **[3, 4]**, the Karagozian–Case Concrete (K&C) **[5, 6]**, the Holmquist–Johnson–Cook (HJC) **[7]** and the modified Holmquist-Johnson-Cook model (MHJC) **[8]** model. These models have been widely used in research and showed promise for a wide range of applications. However, the research applications tend to be focused on one loading phenomenon at a time, making the material calibrations biased to the specific loading case.

Seah **[1]** conducted a comprehensive series of material and component tests on granite with a focus on ballistic resistance. In this study, we aim to supplement the existing validation cases for granite by designing an experimental rig to test granite slabs exposed to contact charge loading. Here, we focus on the preliminary numerical study used to design the experimental rig. To model the granite slabs, we use the relatively simple MHJC concrete model **[8]**.

2 EXPERIMENTAL RIG

To supplement the existing validation cases for granite we developed an experimental rig for contact charge loadings on slabs. Our aim is to establish an experimental facility that facilitates easy and reliable data extraction that is suitable for numerical modeling. The rig was developed in an iterative numerical process using the Impetus Afea Solver [10], where the structural response of the rig was monitored rigorously to ensure a robust setup without plastic deformations for the expected range of applications. Representative numerical concrete and rock slabs of varying strength were used to assess the expected loadings experienced by the experimental rig for multiple explosive contact charges.

An overview of the experimental rig is presented in **Figure 1**. The rig consists of a welded table structure of square hollow section (SHS) 150×10 mm steel profiles with a 1500×1500×40 mm steel top plate. **Figure 2** presents photos of the welded table structure, with the dimensions shown in **Figure 3**. The top plate has a 646 mm diameter hole opening in the center to facilitate filming with high-speed cameras for digital image correlation (DIC) applications. Mounting holes are placed around the plate opening to facilitate mounting of the test specimen. To ensure sufficient stiffness during loading, stiffeners were added underneath the steel plate, see **Figure 4**. A steel frame for the test specimen, presented in **Figure 5**, is bolted to the top plate using eight M24 bolts and is used to hold the test specimen and provide stable contact to four HBM C10/250 kN load cells, see **Figure 6**, mounted to the plate. The rig is bolted to the ground to minimize movement during testing.

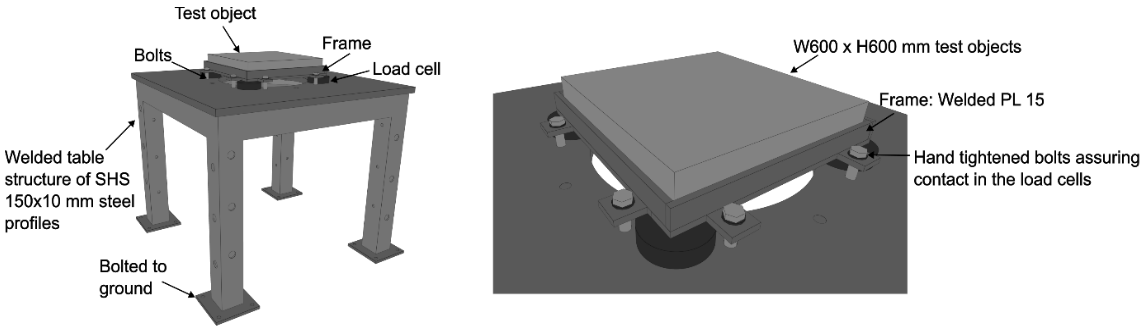

(a) (b)

Figure 1. Overview of the experimental rig (a) and a zoomed illustration of the top frame with the mounted test object (b).

(a) (b)

Figure 2. Photo of the welded table structure from the side (a) and top (b). The four small circles are threaded holes for mounting of the load cells.

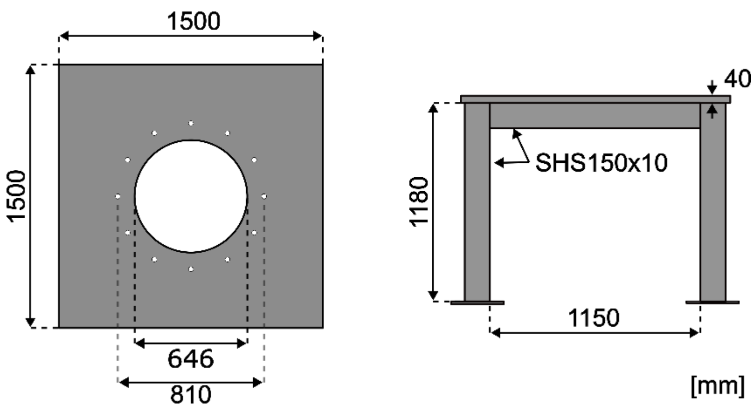

Figure 3. Dimensions of the welded table structure presented in **Figure 2**.

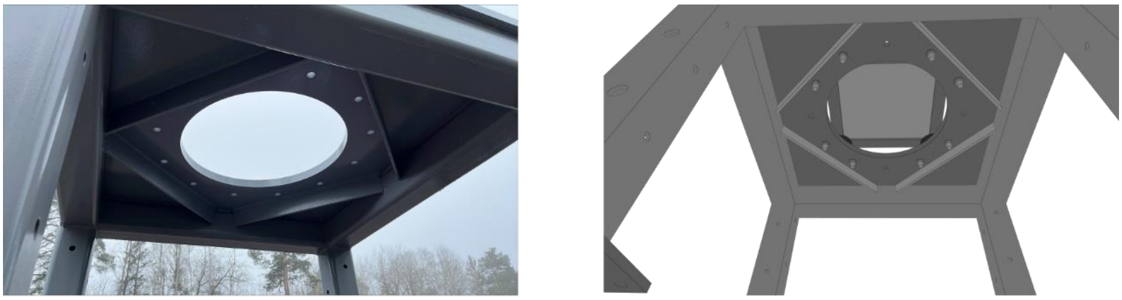

(a) (b)

Figure 4. Photo (a) and numerical model (b) seen from possible high-speed camera angle.

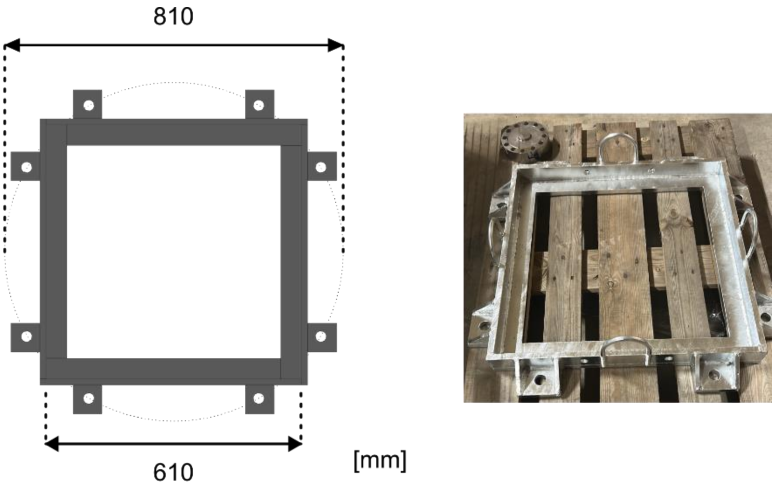

(a) (b)

Figure 5. Dimensions (a) and an image (b) of the test specimen frame.

Figure 6. HBM C10/250 kN load cell with a diameter of 154 mm and a thickness of 47.5 mm used between test specimen frame and top plate.

3 NUMERICAL VALIDATION AND DISCUSSION

The experimental rig was modeled using the Impetus Afea Solver. All the steel components in the rig were modeled using the Hershey high-exponent yield function combined with an associated flow rule and isotropic hardening [11]. The material parameters for the steel components were adopted from Gruben et al. [12]. Welded joints present in the welded steel table structure were modeled in a simplified manner by merging adjacent nodes of the different components. To model the load cells, we used the same steel material as for the other components and added a sensor that monitors the contact force experienced by the cell. The test specimen steel frame was placed on top of the load cells and fastened to the welded steel table structure using simplified steel bolts.

To model the representative slabs for the experimental rig, we use the MHJC material model with a similar strategy for the determination of the parameters as presented by Rudshaug et al. [13]. The MHJC material model is implemented using the user material interface of the Impetus Afea Solver. In short, the MHJC model divides the stress tensor into deviatoric and hydrostatic parts, each with its own yield surface and damage evolution. The damage evolution of both parts is combined into a total damage measure. In addition, the deviatoric yield surface is dependent on the total damage, linking the two parts indirectly. The model requires a total of 20 input parameters. **Table 1** presents an overview of the 18 parameters we fix or couple to the compressive strength, $\boldsymbol{f_c}$, in the simulations performed in this study. We apply element erosion in all simulations. To minimize the effects of the element erosion, we only erode elements when the volume of an integration point becomes negative or grows by a factor of five. At this point, we consider the concrete material to be dust.

The explosive in contact with the slab is modeled as a 100 g cylindrical C4 charge placed at the center of the slab. We use a 2 mm grid cell size in the CFD domain. The radius of the explosive is set equal to the explosive height with a value of ~27 mm, resulting in ~13.5 CFD grid cells over the C4 radius. We exploit the symmetry of the experimental rig and use a quarter model with symmetric boundary conditions. The slab is uniformly meshed with an element size of 2 mm. **Figure 7** presents the resulting predictions of the load cell force histories for the three compressive strengths. We note that the maximum force spans from ~25 kN to ~31 kN from the lowest to the highest compressive strength, well within the capacity of the load cells. Furthermore, the force histories demonstrate how the vibrations increase for increasing compressive strength. **Figure 8** compiles the predicted crack patterns for the different compressive strengths. We note the increasing number of cracks for decreasing compressive strength, implying more energy dissipation for the weaker compressive strength.

Table 1. Overview of the 18 material parameters used in the study, excluding the density, $\boldsymbol{\rho}$, and compressive strength, $\boldsymbol{f_c}$. The presented parameters are either given a fixed value or determined based on the stated relation. The reader is referred to [8] for details on the MHJC model.

Deviatoric response

Parameter	Description	Unit	Value
$\boldsymbol{E}$	Young's modulus	[MPa]	$33500\left(\frac{\rho}{\rho_{ref}}\right)^2\left(\frac{f_c}{f_{c_{ref}}}\right)^{1/3}$ [14]
$\boldsymbol{\nu}$	Poisson ratio	[-]	0.2 [15]
$\boldsymbol{B}$	Pressure hardening coefficient	[-]	2.0
$\boldsymbol{n}$	Pressure hardening exponent	[-]	0.8
$\boldsymbol{C}$	Strain rate sensitivity exponent	[-]	0.04 [15]
$\dot{\boldsymbol{\varepsilon}}_{\boldsymbol{0}}$	Reference strain rate	[1/s]	10^{-5} [15]
$\boldsymbol{S_{max}}$	Maximum normalized deviatoric strength	[-]	100
$\left(\boldsymbol{\varepsilon_f^p}\right)_{min}$	Minimum deviatoric plastic strain to failure	[-]	0

Hydrostatic response

Parameter	Description	Unit	Value/Equation
$\boldsymbol{T}$	Maximum hydrostatic tension	[MPa]	$f_c\left(B^{-\frac{1}{n}}-\frac{1}{3}\right)$
$\boldsymbol{P_{crush}}$	Crushing pressure	[MPa]	$\frac{f_c}{3}$
$\boldsymbol{\mu_{crush}}$	Volumetric strain at crushing	[-]	$\frac{f_c(1-2\nu)}{2G(1+\nu)}$
$\boldsymbol{P_{lock}}$	Locking pressure	[MPa]	800
$\boldsymbol{\mu_{lock}}$	Volumetric strain at locking	[-]	0.1
$\boldsymbol{K_1}$	Locking bulk modulus, constant 1	[MPa]	85000 [7]
$\boldsymbol{K_2}$	Locking bulk modulus, constant 2	[MPa]	0
$\boldsymbol{K_3}$	Locking bulk modulus, constant 3	[MPa]	0

Damage

Parameter	Description	Unit	Value
$\boldsymbol{\alpha}$	Deviatoric damage coefficient	[-]	0.5
$\boldsymbol{\beta}$	Deviatoric damage exponent	[-]	1.0

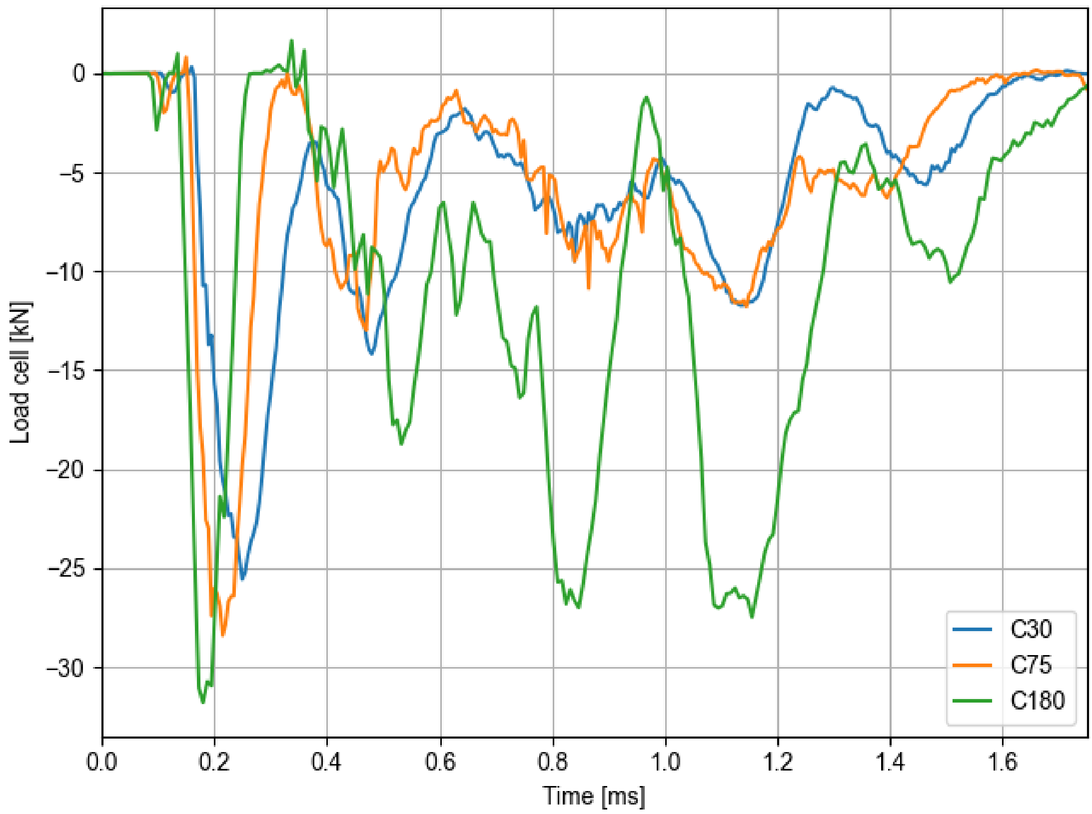

Figure 7. Predicted load cell measurements for the three simulated concrete strengths, C30, C75, and C180.

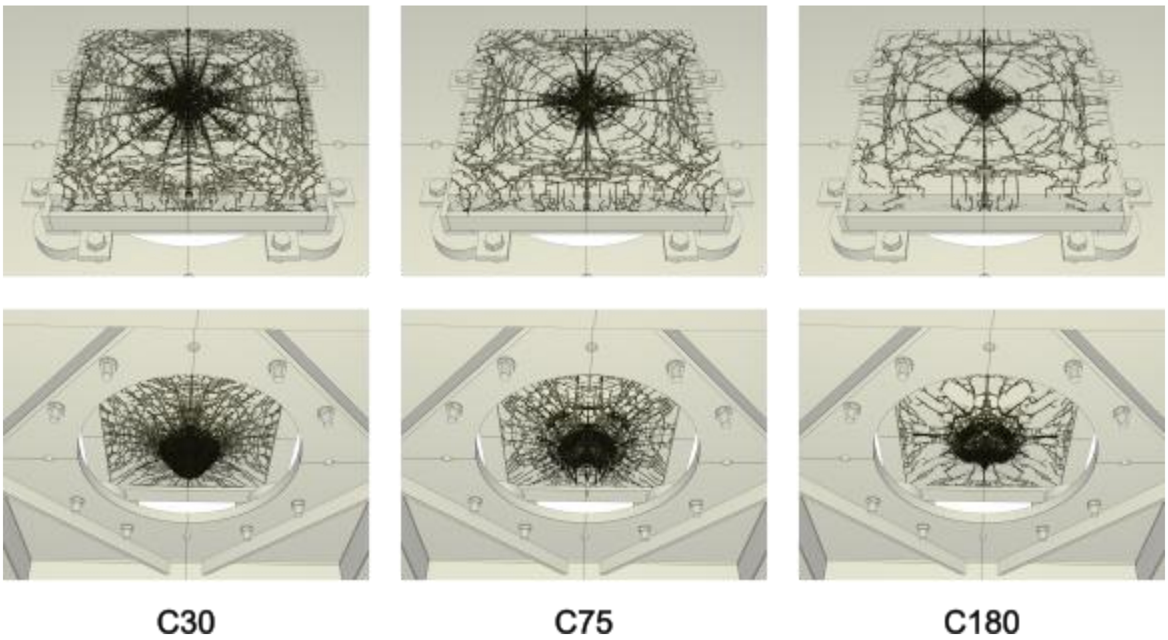

FIGURE 8. Damage patterns from the three simulated concrete strength, C30, C75, and C180.

4 SUMMARY

We designed an experimental rig for contact charge loadings with a focus on consistent data retrieval that is easy to model numerically. Four load cells are used to monitor the reaction forces from the granite slab specimens during contact charge loading. An iterative, numerical design process was performed using the Impetus Afea Solver where the steel materials of the rig are modeled with a Hershey high-exponent yield function combined with an associated flow rule and isotropic hardening and the concrete and rock-like slabs are modeled with a modified version of the Holquist-Johnson-Cook (MHJC) model implemented as a user material. Three simulations with concrete slabs of compressive strengths C30, C75, and C180 were performed to investigate the expected range of force levels experienced by the load cells for a 100 g C4 explosive charge.

REFERENCES

[1] C. C. Seah, Penetration and Perforation of Granite Targets by Hard Projectiles, Trondheim: NTNU, 2006.

[2] Y. Sun, L. Wang, J. Wang, C. Tan, Y. Ye and K. Lin, "A modified Holmquist–Johnson–Cook (HJC) constitutive model and its application to numerical simulations of explosions and impacts in rock materials," *Simulation Modelling Practice and Theory,* 2025.

[3] W. Riedel, K. Thoma, S. Hiermaier and E. Schmolinske, "Penetration of reinforced concrete by BETA-B-500 numerical analysis using a new macroscopic concrete model for hydrocodes.," in *Proceedings of the 9th International Symposium on the Effects of Munitions with Structures, vol. 315*, Berlin-Strausberg Germany, 1999.

[4] W. Riedel, N. Kawai and K. I. Kondo, "Numerical assessment for impact strength measurements in concrete materials," *International Journal of Impact Engineering,* 2009.

[5] L. J. Malvar, J. E. Crawford, J. W. Wesevich and D. Simons, "A plasticity concrete material model for DYNA3D," *International Journal of Impact Engineering,* 1997.

[6] J. M. Magallanes, Y. Wu, L. J. Malvar and J. E. Crawford, "Recent Improvements to Release III of the K&C Concrete Model," in *11th international LS-DYNA Users conference, Livermore Software Technology Corporation*, Livermore, CA, 2010.

[7] T. J. Holmquist, G. R. Johnson and W. H. Cook, "A Computational Constitutive Model for Concrete Subjected to Large Strains, High Strain Rates and High Pressures," in *14th International symposium, Vol 2; Warhead mechanisms, terminal ballistics*, Quebec, Canada, 1993.

[8] M. Polanco-Loria, O. S. Hopperstad, T. Børvik and T. Berstad, "Numerical predictions of ballistic limits for concrete slabs using a modified version of the HJC concrete model," *International Journal of Impact Engineering,* 2008.

[9] C. Wu and H. Hao, "Modeling of simultaneous ground shock and airblast pressure on nearby structures from surface explosions," *International Journal of Impact Engineering,* 2004.

[10] IMPETUS Afea, "IMPETUS Afea Solver," [Online]. Available: https://www.impetus.no/. [Accessed 22 2 2025].

[11] A. V. Hershey, "The Plasticity of an Isotropic Aggregate of Anisotropic Face-Centered Cubic Crystals," *Journal of Applied Mechanics,* 1954.

[12] G. Gruben, M. Langseth, E. Fagerholt and O. S. Hopperstad, "Low-velocity impact on

high-strength steel sheets: An experimental and numerical study," *International Journal of Impact Engineering,* 2016.

[13] J. Rudshaug, B. S. Elveli and T. Grue, "Modeling concrete in different load cases - projectile impact, contact detonation and far-field blast loading," in *19th International Symposium on Interaction of the Effects of Munitions with Structures,* Bonn, Germany, 2024.

[14] T. Noguchi and F. Tomosawa, "Relationship between compressive strength and modulus of elasticity of high strength concrete," *Journal of Structural and Construction Engineering (Transactions of AIJ),* 1995.

[15] Ø. E. K. Jacobsen, M. Kristoffersen, S. Dey and T. Børvik, "Projectile Impact on Plain and Reinforced Concrete Slabs," *Journal of Dynamic Behavior of Materials,* 13 6 2023.

15th International Conference on
Shock & Impact Loads on Structures
12-13 June 2025, Gothenburg, Sweden

EFFECT OF INTENSE DYNAMIC LOADS FOR REINFORCED CONCRETE ELEMENTS

Viktor Peterson[a]**,** Mikael Hallgren[a,b], Anders Ansell[a], Emma Ceberg[c], Elin Holm[d], Ellen Kolmodin[e], Klaudia Kubiak[f]

[a]KTH Royal Institute of Technology, Sweden, email: vpeterso@kth.se, [b]Tyréns AB, Sweden, [c]AFRY, [d]Kåver och Mellin AB,[e]Looström, Sweden, [f]WSP Sverige, Sweden

Keywords: blast load, impulse intensity, reinforced concrete, drop-weight impact

Abstract

Civilian or protective structures may during their lifetime be subjected to intense dynamic loads from explosions, ballistic impacts, fragment impacts or collisions. Under such extreme conditions, the resulting internal forces may differ substantially from those observed during static loading. In particular, large local shear forces can develop early, possibly leading to shear-type failures that differ from the more familiar failures of the flexural-shear type. These shear-dominated responses have been observed in tests with distributed air-blast loads, with abrupt failure near the supports, and during high-velocity impacts where local shear-plug failure at the impact zone occurred. Numerical simulations were carried out in two projects focusing on concentrated and distributed dynamic loads to investigate these local effects. The simulations with concentrated dynamic loads were modelled from previous drop-weight impact tests at KTH. Previous shock-tube tests were used to validate models subjected to distributed air-blast loads. Calibrated models for both load scenarios were then used to study higher loading intensities. Generally, the rate at which the impulse was applied had a major influence on the ultimate failure mode. The dominating shear-type failure transitioned closer to the load point for impact-loaded beams as the intensity of the load increased, and the shear-type failure moved closer to the support for the distributed air-blast load. The effect of the boundary conditions was also studied. The boundary conditions showed a low influence of the local failure mode for intense impact loads, while the influence was higher for air-blast loads.

1 INTRODUCTION

The design of impulse-loaded structural elements involves determining a configuration with a higher internal work capacity than the external work of the load. It is the energy absorption instead of the force capacity that is important. This design concept is reflected in the Swedish guidelines for impulse-loaded structures, FKR2011 [1], where reinforced concrete elements are configured to fail in a ductile flexural mode rather than in shear. This is done by limiting the flexural reinforcement to 0.5% and providing stirrups if the shear capacity is insufficient. The shear-type failures are avoided as their internal work capacity is significantly less than their flexural counterparts. While flexural damage involves the development of many cracks with large plastic deformation, shear-type failure involves opening one critical crack, which absorbs most of the energy before the structural element loses stability.

Despite more than a century of research on static shear, predicting shear capacity can vary by a factor of two when employing standard design provisions. By comparison, flexural capacity is generally accurately estimated, often within 10% [2]. The difficulty in determining the shear strength increases for intense dynamic loads. Experimental and numerical studies have indicated early shear-type failures before significant deformation has developed. This is due to local shear span-to-depth ratios smaller than the geometrical ratio used for static shear strength predictions, resulting in the need for new models that can predict this early shear strength.

An example of the local effects of high-intensity concentrated forces is shown in Figure 1 (a). Local deformations are shown to be limited to a relatively short segment of the beam at early times (t_1). Such a scenario may develop during collisions, dynamic loads due to falling masses, ballistic attacks or contact detonations. During this initial phase, the beam's inertia $i_b(x,t)$ provides the resistance, and external support reactions $R_R(t)$ and $R_L(t)$ are negligible. For this deformation mode to occur, mainly high-frequency components must be dominating, indicating that this occurs for times much shorter than the fundamental period of the beam. If the impulse transfer to the beam is significant during the initial phase shown in Figure 1 (a), only a small portion of the beam shows high velocity. In experimental studies, this has resulted in a unique shear-type failure for impact-loaded beams [4], denoted shear-plug failure. Shear-plug failure is characterized by diagonal cracks adjacent to the impact zones with inclinations of about 45 degrees. Figure 1 (b) shows how this differs from the typical static flexural-shear failure, which is inclined and initiates from vertical cracks. Previous experimental studies have indicated that the impact velocity is one of the governing factors increasing the risk for shear-plug failure, and at least 4 m/s is required for it to occur [3, 4, 5].

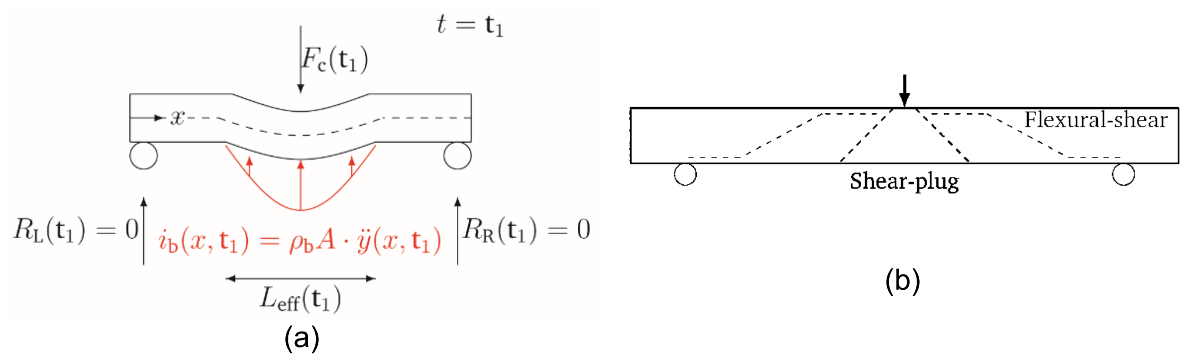

Figure 1. (a) Forces acting on the beam at t_1 shortly after impact and (b) the dominating shear-type failures; shear-plug and flexural-shear.

Similar local effects may occur for intense air-blast loads. Early deformation is governed by high-frequency components, as was shown in an analytical study by Magnusson et al. [6], at times much shorter than the fundamental period. This results in local deformation at the support over a small segment with length α_t as shown by Figure 2 (a), and the middle section moves like a rigid body without curvature. This early deformation was in experiments [7] and numerical studies [8] shown to possibly result in shear-type failure at the support, which in the literature is referred to as direct shear failure. The failure is initiated by crushing of a steep compressive strut at the support, shown by the damage from simulations [8] in Figure 2 (b). Magnusson [8] discussed that the early impulse density is important, as this leads to the large early velocity of the beam, resulting in direct shear-type failure. Simulations [8, 9] have indicated that scaled distances below 1.0 m/kg$^{1/3}$ are required for sufficient early impulse development to provoke direct shear-type failures.

Simulations of high-intensity concentrated and distributed dynamic forces were conducted in two projects at KTH during 2024. Simulations by Ceberg and Holm [10] were based on the drop-weight set-up presented in Figure 3 (a). A 70 kg mass was released from a height of 2.4 m onto reinforced concrete beams. A high-speed camera, load cells and accelerometers were used to monitor the response. The drop height resulted in measured impact velocities of approximately 6.3 m/s. Kolmodin and Kubiak [9] did simulations based on the shock-tube tests presented in Figure 3 (b). An explosive charge consisting of 2.5 kg explosives detonated 10 m from the face of the wall. This resulted in a peak reflected overpressure of about 1250 kPa with an impulse density of about 6.4 kPa s. In both test series, shear-type failure was dominating. A calibrated model was first developed for each project. This model was then used for parameter studies where load intensity and boundary conditions were varied. The results from these simulations are summarized in this paper.

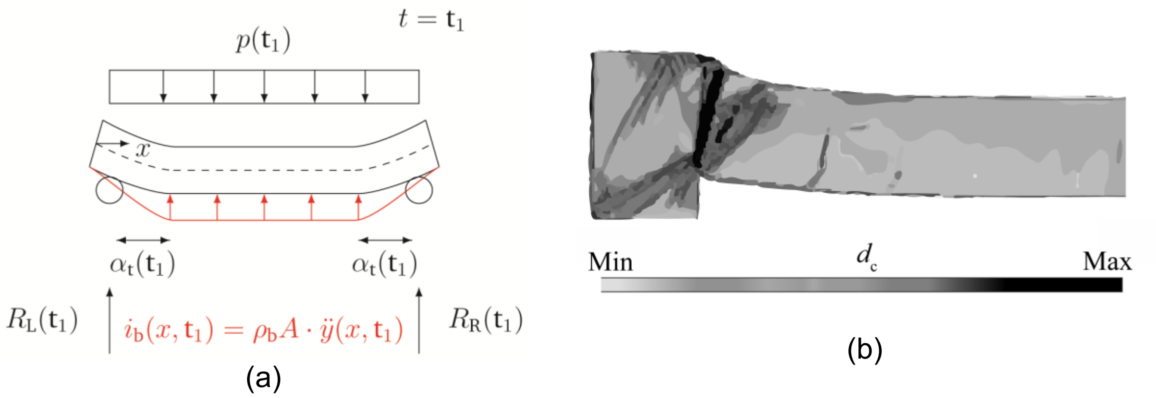

Figure 2. (a) Forces acting on a blast-loaded beam shortly after shock-wave arrival and (b) compressive damage in simulations, by Magnusson [8].

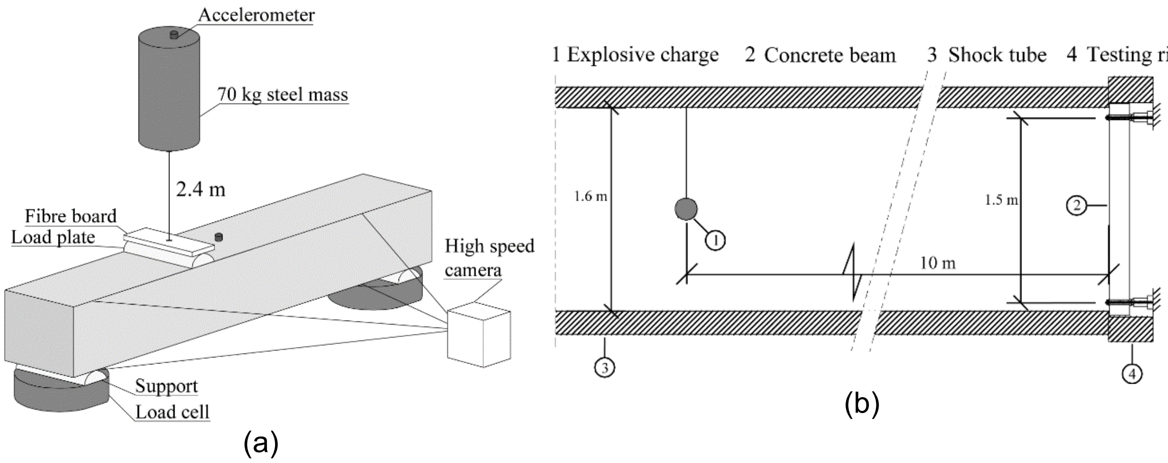

Figure 3. Experimental set-up for: (a) drop-weight testing at KTH (redrawn from [10]) and (b) shock-tube tests (redrawn from [11]).

2 NUMERICAL MODELS

2.1 Calibration against experiments

The calibrated model of the drop-weight tests by Ceberg and Holm [10] was simulated using the finite element analysis package Abaqus FEA [12]. The model was constructed in 2D using triangular linear plane stress elements with a 5.0 - 7.5 mm side length. The Concrete Damage Plasticity Model (CDPM) was used for the concrete. A bilinear tension softening law proposed by Grassl [13] was used for tension with fracture energy determined using the formulation in Model Code 2010 [14]. For compression, the non-linear formulation proposed by CEN [15] was used for the pre-peak response, and the post-peak response was determined using the regularization technique described by Červenka [16], where a crushing displacement is used and recalculated to strains. The reinforcement was modelled using an elastic-plastic model from measured stress-strain response applied to numerically integrated beam elements. The beam elements were on average 10 mm with a perfect bond to the concrete elements. Contact conditions were used for stress transfer between the beam, support, and load plate. For more information about the numerical model, see Ceberg and Holm's work [10].

The calibration results against the experiment are shown in Figure 4 (a) – (b). The tensile damage is plotted with the post-test crack pattern in Figure 4 (a). The model captures the diagonal cracks adjacent to the load-point well. The main discrepancy at the load point is the larger amount of flexural cracks in the model, where the experiment showed one main vertical crack right under the load. This is an effect of the assumption of a perfect bond, significantly influencing the crack spacing. In Figure 4 (b), the left R_L and right R_R support reactions are plotted for the experiment and simulation. For the left support reaction, the curves converge until unloading at around 6 ms, where discrepancies occur. The shape and amplitude for the right support reaction converge, but they are shifted in time by about 2 ms. With these discrepancies in mind, the model was deemed sufficient for parameter studies of the effect of higher load intensities.

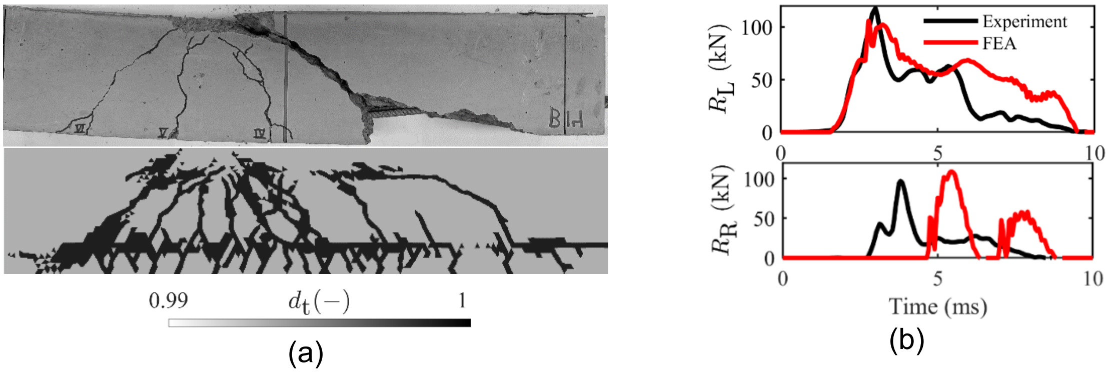

Figure 4. (a) Damage after experiment compared to simulated tension damage at maximum displacement and (b) comparison between measured and simulated support reactions.

The model of the blast-loaded beam simulated by Kolmodin and Kubiak [9] was based on the testing of beam B40-D4 using a shock tube, reported by Magnusson and Hallgren [11]. The finite element analysis package LS-Dyna [17] was used, and the model was created in 3D. Linear tetrahedral elements with an average side length of 10 mm were used for the concrete. Only half of the beam was modelled utilizing symmetry around the mid-point. A damage-plasticity model for concrete (MAT_273, CDPM2) was also utilized here, assuming a bilinear softening law in tension with parameters as recommended by Grassl et al. [18]. The reinforcement was modelled using linear beam elements with one integration point and a plastic kinematic material model. The average length of the beam elements was 10 mm, and the stress-strain response was assumed to be bilinear. The bond-slip was considered by a slip function following the expression in Model Code 2010 [14]. Contact conditions for stress transfer to the support were utilized with a static and dynamic friction coefficient of 0.15. For more information about the model, see the work by Kolmodin and Kubiak [9].

Figure 5 (a) – (b) shows the model calibration results. The tensile damage is plotted at the time of maximum displacement, and it agrees well with the damage pattern of the experimentally tested beam. The critical shear occurs at the position and follows the shape of the crack in the experiment. The curves indicating the support reaction and mid-point displacement in Figure 5 (b) also show convergence between experimental and numerical results. The main discrepancy is the unloading of the support reaction, which differs slightly, but the general shape and amplitude of both the support reaction and mid-point displacement converge. This model was afterwards used in studies to determine the effect of higher intensity of the dynamic load.

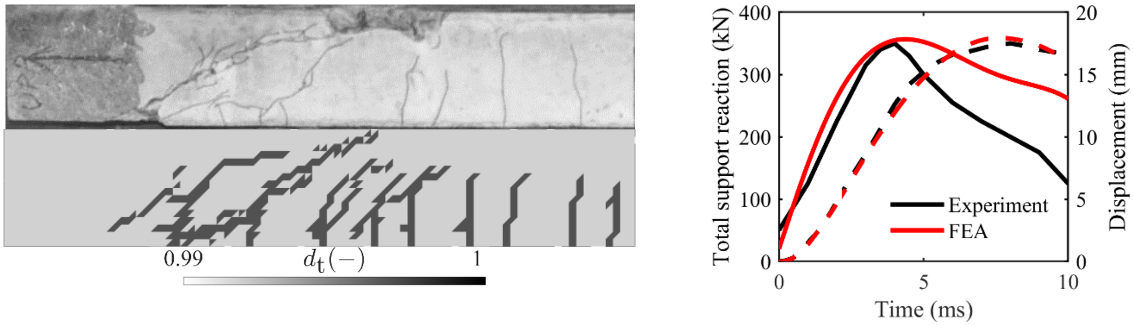

(a) (b)

Figure 5. (a) Damage after experiment compared to simulated tension damage at maximum displacement and (b) comparison between measured and simulated support reaction (solid lines) and mid-point displacement (dashed lines).

2.2 Load intensity studies

In order to study the effect of higher intensity of the dynamic concentrated force, experimentally measured impact forces were first parameterized. In Figure 6 (a), the solid black line shows an idealized curve based on an early triangular pulse, a following quasi-static phase with a rectangular shape and linear unloading. This curve was fit to three impact force curves from experiments denoted Beam 1 – 3. The idealized curve was determined by maintaining the impulse, as the dashed lines show. In Figure 6 (b), this idealized impact force curve, denoted IR1 for impulse rate 1, was successively increased in intensity. This was done by applying the same impulse over a shorter duration. The load intensity for IR2 – IR3 was chosen to provoke local shear-type failure at the load-point.

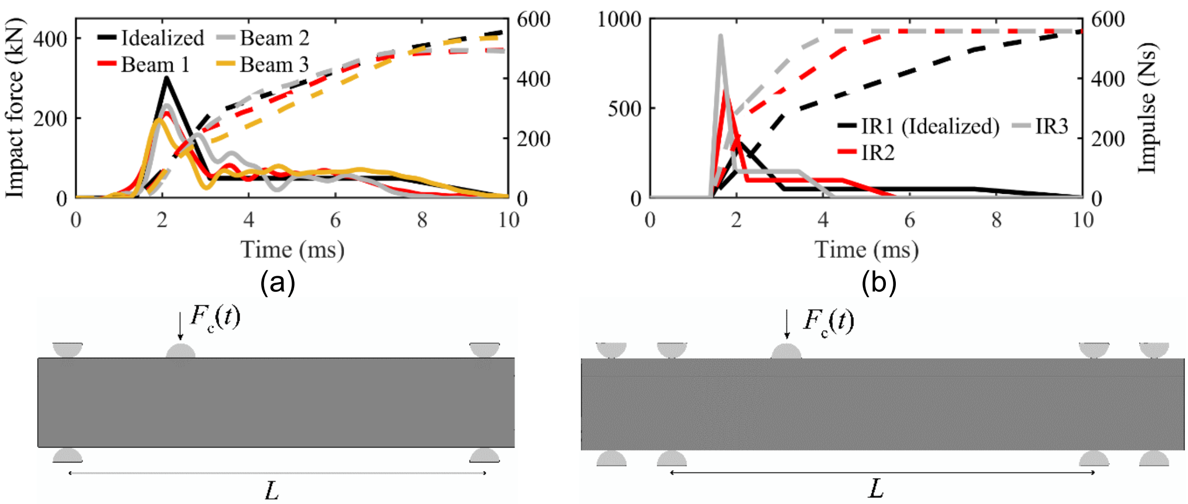

(c) Simply-supported (d) Fixed

Figure 6. (a) Idealized impact force from measured forces in experiments, (b) loads with increasing intensity and (c) – (d) boundary conditions (solid lines indicate the force and dashed line the corresponding impulse).

To study how the boundary conditions influence the local response, two support conditions were used for the study of concentrated dynamic forces, as shown in Figure 6 (c) – (d). The simply-supported conditions in Figure 6 (a) resemble those in the experiments conducted. The fixed conditions were modelled by extending the length of the beam and providing a second set of roller supports, as shown in Figure 6 (d). This second set of rollers provides rotation restraint at the support, resembling idealized fixed conditions.

A similar procedure was used for the study of intense distributed dynamic loads. The overpressure curve from a CFD simulation was idealized as a bilinear curve with the same peak overpressure in Figure 7 (a). The aim was to maintain the impulse density over time, as shown in the figure. The load intensity was then increased successively, as shown by IR2 - IR3 in Figure 7 (b). The total impulse density of the higher-intensity loads was maintained, but it was applied over a shorter time to provoke shear-type failures at the support. The study was conducted for two boundary configurations, as shown in Figure 7 (c) - (d). The simply-supported boundary conditions were predicted to result in low rotation restraint at the rollers, and a stiff plate was used to limit the rotation at the support for the fixed configuration. To provoke shear-type failure on both support conditions, the simply-supported beam contained five flexural reinforcement bars compared to the four for the fixed beam.

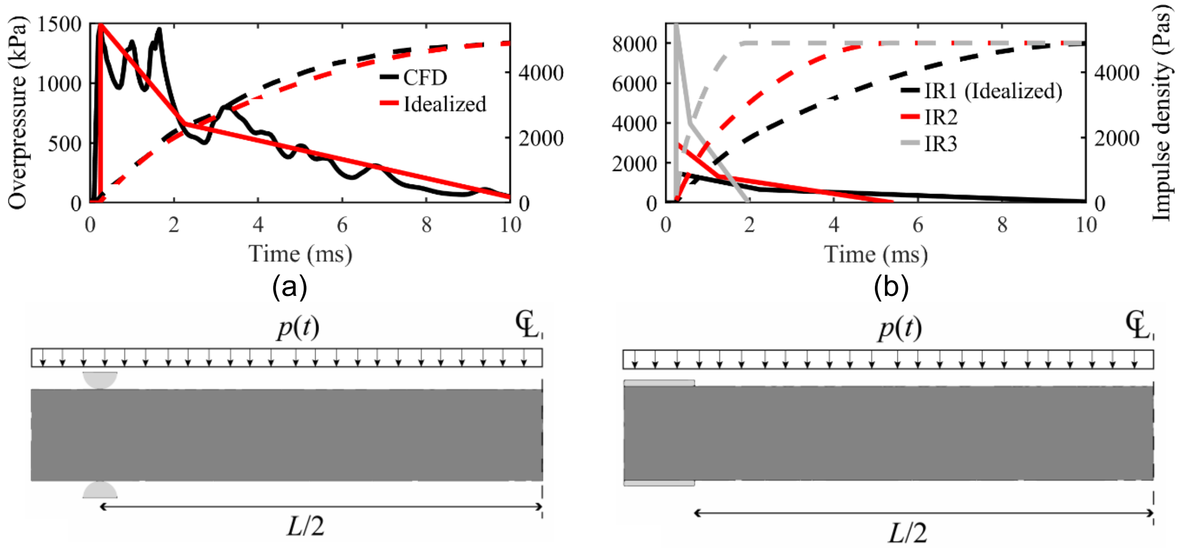

(a) (b)

(c) Simply-supported (d) Fixed

Figure 7. (a) Idealized impact force from measured forces in experiments, (b) loads with increasing intensity and (c) – (d) boundary conditions (solid lines indicate the force and dashed line the corresponding impulse).

3 RESULTS FROM LOAD INTENSITY STUDIES

3.1 Effect of intense concentrated loads

Results for the study of intense concentrated dynamic forces are first shown. Figure 8 shows the tensile damage at the point of maximum displacement for simply-supported and fixed beams as the load intensity increases from IR1 to IR3. The deflected shape, indicated by the vertical displacement extracted at mid-height at 10 ms, is also presented.

The simply-supported beams in Figure 8 (a) indicate that as the load intensity increases, inclined and diagonal cracks dominate over vertical flexural cracks at the load point. The flexural cracks for IR1 propagate over the mid-height, while they are below the mid-height for IR3. In the deflection curve, any severe discontinuities indicate significant shear damage. The position and shape of the dominating shear-type crack may be observed by extending lines from these severe discontinuities to the mid-height of the damage plot. For IR1, the dominating shear-type crack is located at approximately 460 mm from the left support. This crack initiates from a vertical crack, indicating a flexural-shear-type failure. For increased load intensities IR2 and IR3, the dominating shear-type crack shifts towards the load point at about 310 mm from the left support. Here, the dominating shear crack occurs early and does not initiate from any vertical flexural crack, instead indicating a shear-plug crack.

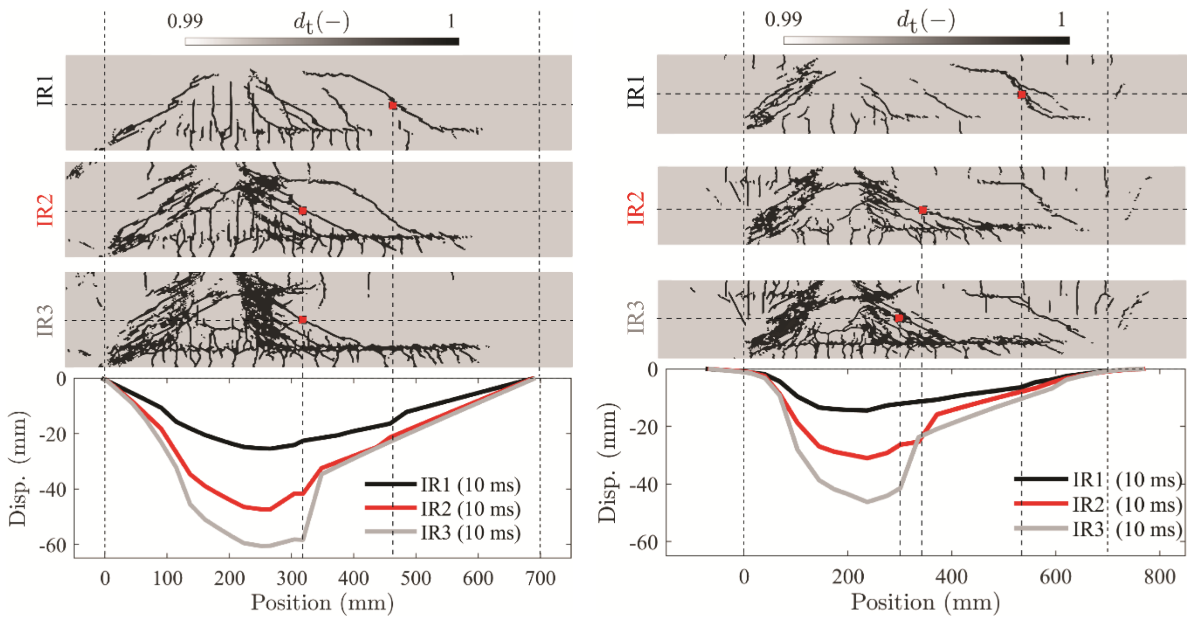

(a) Simply-supported (b) Fixed

Figure 8. (a) Tension damage and deflection curve for: (a) Simply-supported beams and (b) fixed beams.

Figure 8 (b) shows the results for the fixed beam. For IR1, the damage surrounding the load-point is highly asymmetrical due to the clamping supports. As the load intensity increases to IR2 and IR3, the damage surrounding the load point becomes more symmetrical and resembles the damage at the load point for each corresponding simply-supported beam. The deflected shapes for the fixed beams also show the same shape as the corresponding simply-supported beam, although the maximum deflection is decreased due to the reduced support slope from the clamping moment. This indicates that the dominating damage occurs early and locally at the load point, and at this point, the supports are not activated due to dominating local deformation. This means the failure may be independent of the support conditions for high-intensity dynamic concentrated forces.

To further study this reduced influence of the support conditions on the damage with increasing load intensity, the deflected shapes are compared at different points in time from 0.1 – 1.5 ms after load application in Figure 9. This comparison is conducted for the highest load intensity IR3 on both boundary conditions. The development of deflection in time is shown to the left, and the normalized deflected shapes are shown to the right. The curves for both boundary conditions converge well for all points in time. This indicates a low influence of the support reaction early for very high load rates.

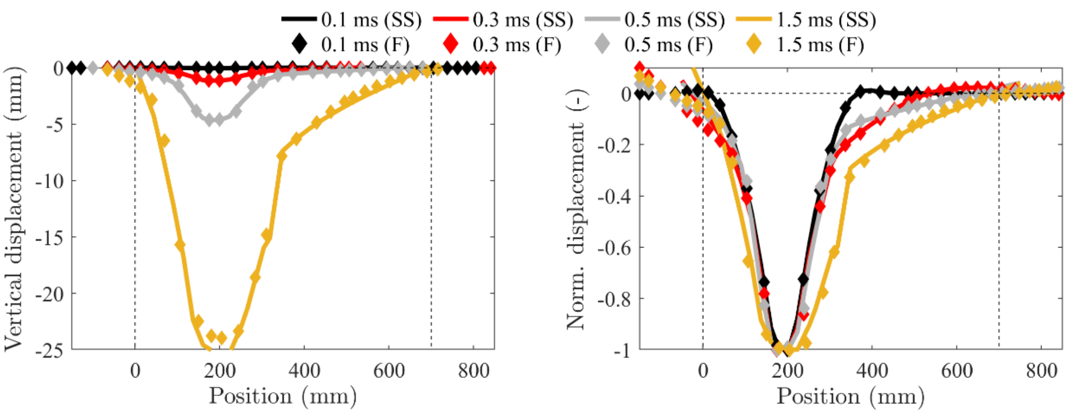

Figure 9. Left: Vertical displacement along the mid-height. Right: Normalized vertical displacement (for IR3, SS=Simply-Supported and F=Fixed).

The shear and moment distribution at early times (0.1 – 1.5 after load application) is shown in Figure 10 for the boundary conditions used. The results show similar shear and moment distributions for the boundary conditions. The main discrepancy is shown for IR1 in Figure 10 (a) and (c), where the simply-supported conditions show mainly positive moments at 1.5 ms. In contrast, the clamping conditions result in opposite sign moments at the supports. However, at earlier times with load IR1 and at all times with load IR3, the support conditions have a small influence on internal force distributions.

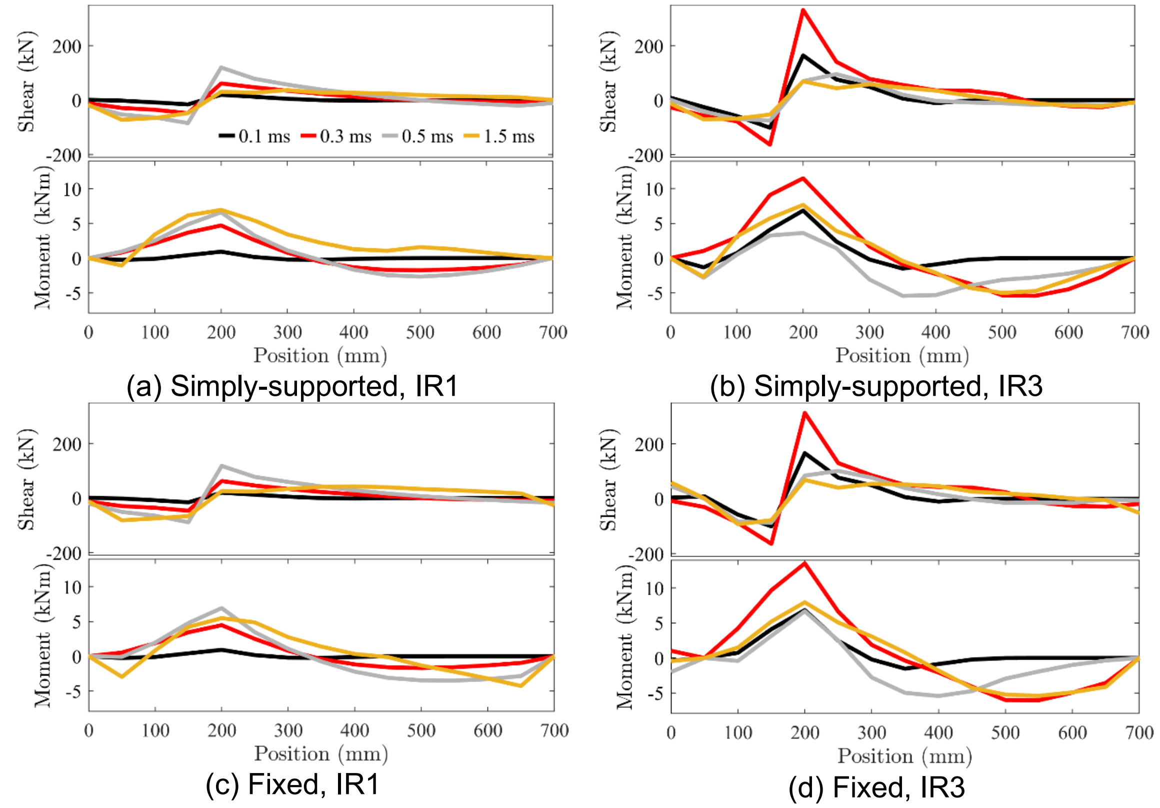

Figure 10. (a) – (d) Shear and moment distribution over the length at times 0.1 – 1.5 ms after load application for beams with simply-supported and fixed boundary conditions.

The maximum internal forces, load-point vertical deflection, and when they occur were extracted for the three load intensities and boundary conditions in Figure 11. With increasing load intensity, the shear force increases amplitude and occurs earlier. The maximum shear force occurs adjacent to the impact force position and follows the impact-force variation in time. The maximum internal moment follows the same trend: increasing amplitude with an occurrence earlier in time with increasing load intensity. The maximum moment also follows the time variation of the impact load in time. The maximum load-point vertical displacements occur later than the internal forces. Compared to the internal forces, the maximum displacement is thus governed by the load's impulse, not its amplitude and time variation.

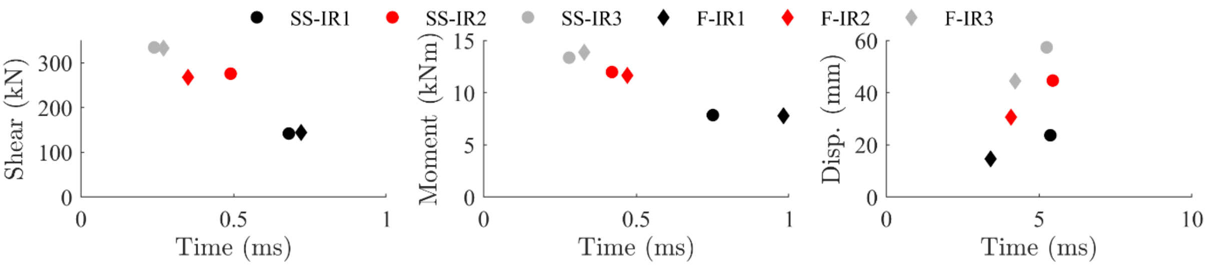

Figure 11. Scatter plot of maximum shear force (left), moment (middle) and load-point displacement (right) and when they occurred in time.

3.2 Effect of intense distributed loads

Similar analyses were conducted with distributed loads corresponding to air-blast loads. The deflection in Figure 12 presents the tensile damage for the simply-supported and fixed beams subjected to dynamic loading with varying intensity. The plots are extracted at the time determined as the point of failure, after which severe element distortion occurred. This is 6, 4 and 2 ms after load application for IR1, IR2 and IR3, respectively. Dashed lines from discontinuities are also drawn to their intersection with the beam mid-height to indicate the dominating shear crack.

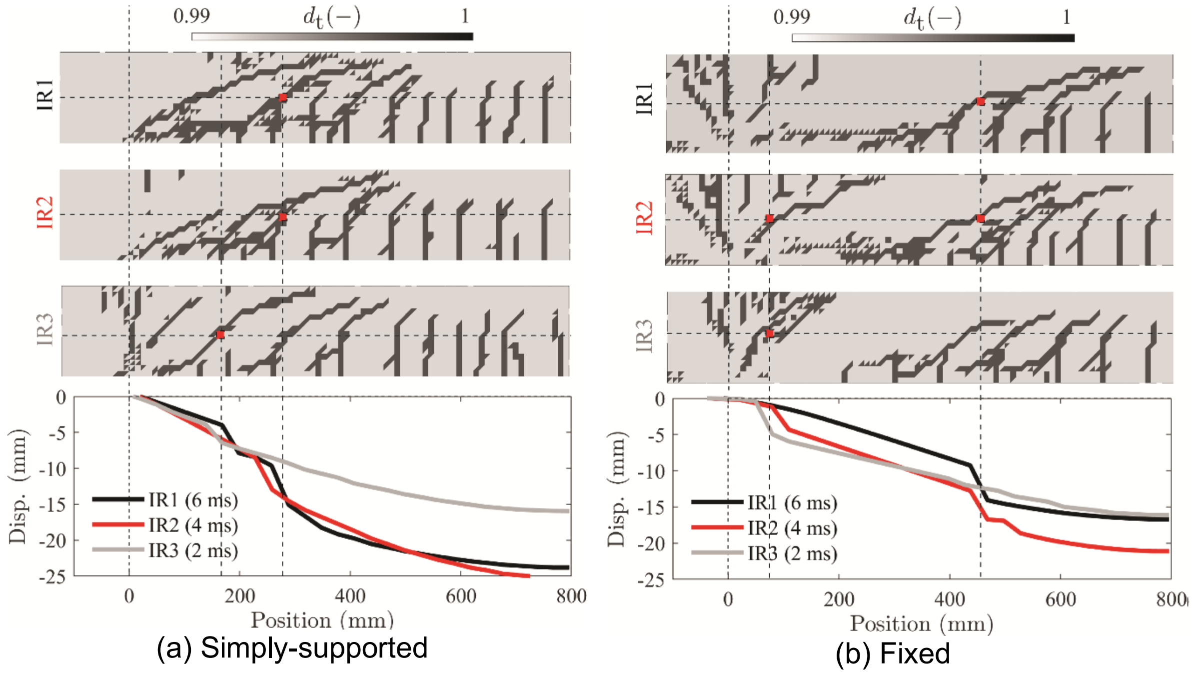

Figure 12. (a) Tension damage and deflection curve for: (a) Simply-supported beams and (b) fixed beams.

Results for the simply-supported beams are shown in Figure 12 (a). The position of the dominating shear crack is shifted towards the support as the load intensity increases. For IR1 and IR2, the position was approximately 290 mm from the left support, and it was shifted to approximately 170 mm for IR3. The dominating cracks, indicated by the discontinuities in deflection curves, generally originate from flexural cracks. The beam with the highest load intensity does, however, indicate some damage adjacent to the support, which resembles the direct shear type. For the fixed beams in Figure 12 (b), the dominating shear-type crack is for IR1 closer to the mid-point than the corresponding simply-supported beam. However, as the load intensity increases, the dominating shear crack moves adjacent to the support. The dominating shear-type cracks adjacent to the support for IR2 and IR3 resemble the direct-shear type crack. The results indicate a larger discrepancy between the support conditions, but for both conditions, the dominating cracks move closer to the support with increasing load intensity.

The early deflection for times 0.1 – 1.5 ms is shown for both boundary conditions subjected to the highest load intensity IR3 in Figure 13. The amplitudes of the curves are generally similar for all points in time. The main discrepancy is at 1.5 ms, where the two boundary conditions show their discontinuity at different positions. The discontinuity is closer to the support for the fixed beam, indicating larger differences in the support conditions for air blast-loaded beams, at least at a later point when shear-type failure is initiated. However, the early local deformation at the support, from 0.1 – 0.5 ms, is similar for both boundary conditions.

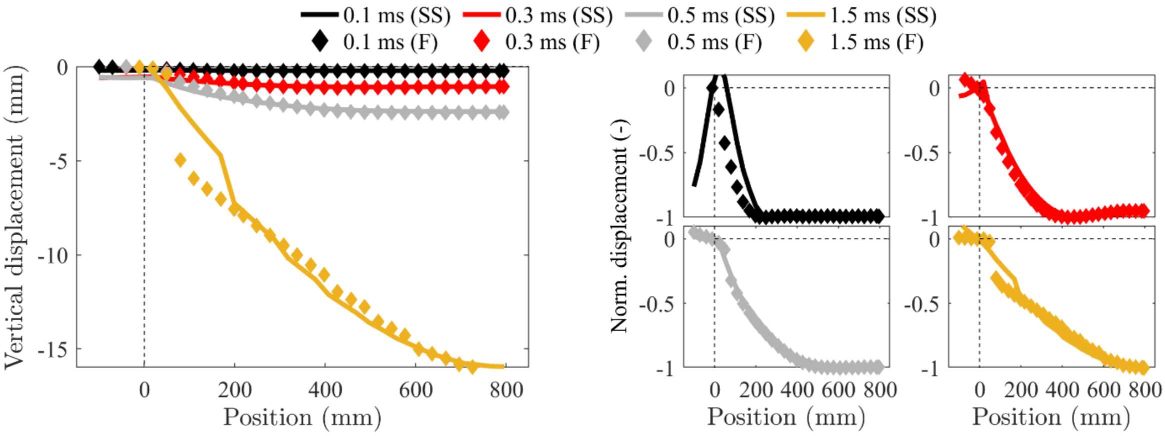

Figure 13. Left: Vertical displacement along the mid-height. Right: Normalized vertical displacement (for IR3, SS=Simply-Supported and F=Fixed).

The internal force distribution for beams with simply-supported and fixed boundary conditions at early points in time 0.1 – 1.5 ms after load application is shown in Figure 14. The support conditions were shown to have a higher influence for the distributed loading. Results with load IR1 in Figure 14 (a) and (c) indicate higher internal shear and moment for the fixed conditions. This also holds for IR3, where the shear force close to the support is already at its maximum 0.1 ms after load application in Figure 14 (d).

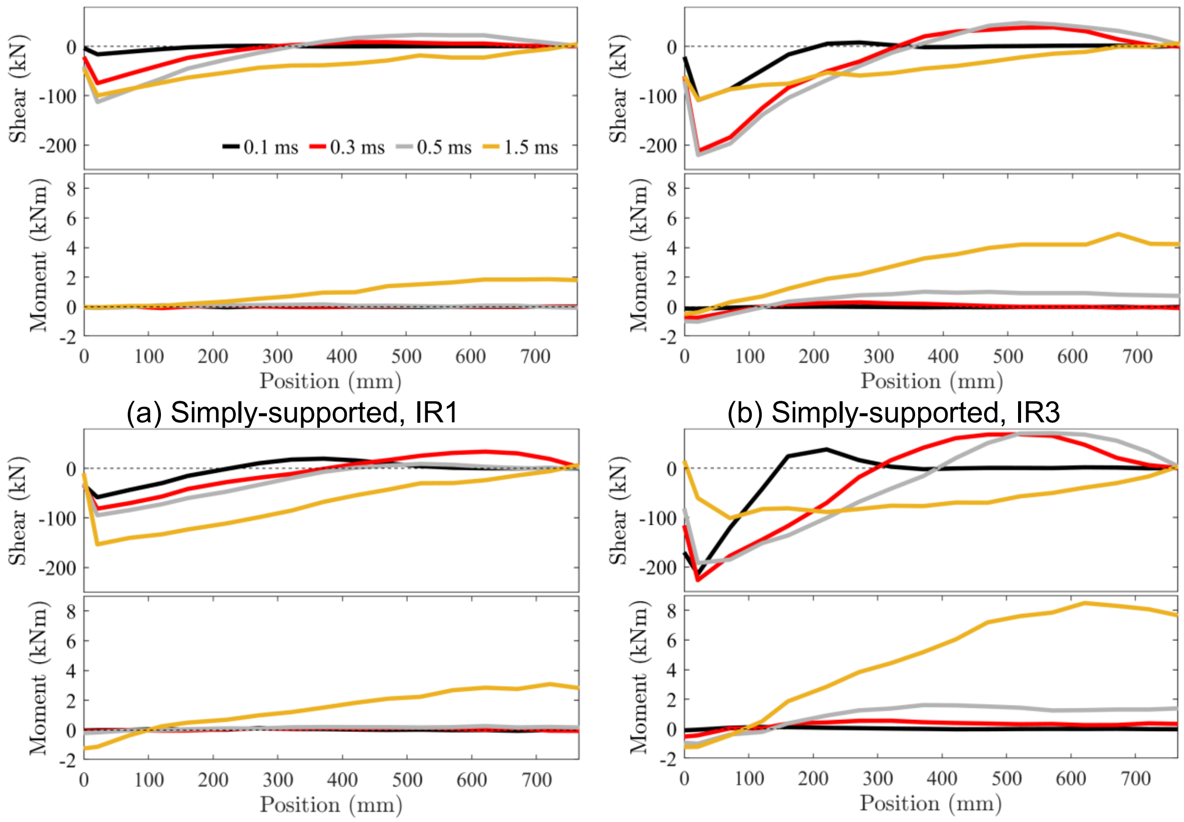

(a) Simply-supported, IR1 (b) Simply-supported, IR3

(c) Fixed, IR1 (d) Fixed, IR3

Figure 14. (a) – (d) Shear and moment distribution over the length at times 0.1 – 1.5 ms after load application for beams with simply-supported and fixed boundary conditions.

Similar conclusions are shown in Figure 15, where the maximum internal forces and when they occurred in time are plotted. The maximum amplitude for shear close to the support is generally larger and occurs earlier for the fixed boundary conditions. However, the maximum field moment at the symmetry section is larger for the simply-supported conditions and occurs later in time. This larger moment for the simply-supported beam is also an effect of the larger moment capacity, as this had one more flexural reinforcement bar.

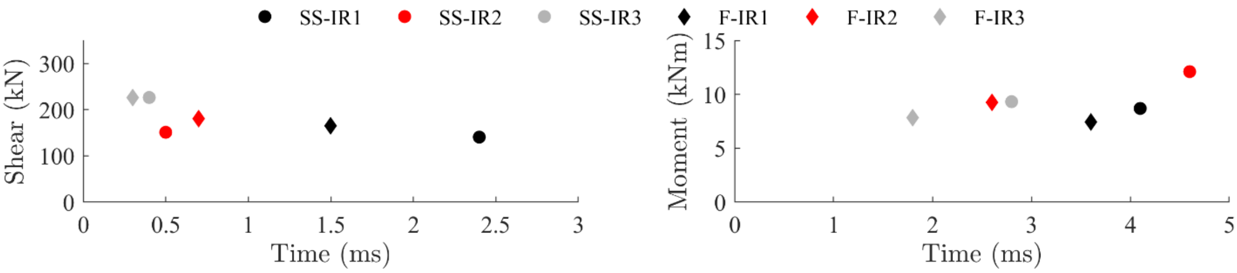

Figure 15. Scatter plot of maximum shear force (left) and moment (right), and when they occurred in time.

4 CONCLUSIONS

The results indicated a significant influence of the load intensity and boundary conditions for concentrated and distributed dynamic loads. For concentrated forces, the dominating shear-type crack transitioned towards the load-point with increasing load intensity. The boundary conditions showed a low influence on the response to high-intensity concentrated forces, as the damage mainly occurred before support reactions were activated. For the distributed load, the dominating shear-type crack transitioned towards the support with increasing load intensity. Here, the support conditions also showed a high influence for the high load rates. Generally, the shear forces were higher and occurred earlier for the fixed conditions, which resulted in a shear-type failure closer to the support for the highest load intensity.

ACKNOWLEDGEMENTS

Funding for the project was provided by the Swedish Transport Administration, the Swedish Fortifications Agency and the Civil Contingencies Agency (MSB).

REFERENCES

[1] Swedish Fortifications Agency, *Fortifikationsverkets konstruktionsregler FKR2011 (Design Manual for Protective Structures)*. Fortifikationsverket, Dnr 4535/2011 (in Swedish), Eskilstuna, Sweden, 2011.

[2] E. C. Bentz, F. J. Vecchio, and M. P. Collins, “Simplified Modified Compression Field Theory for Calculating Shear Strength of Reinforced Concrete Elements”, *ACI Structural Journal*, vol. 103, pp. 614-624, July-August 2006, doi: 10.14359/16438.

[3] S. Saatci and F. J. Vecchio, “Effects of shear mechanisms on impact behavior of reinforced concrete beams”, *ACI Structural Journal*, vol. 106, pp. 78-86 January-February 2009, doi: 10.14359/56286.

[4] N. Kishi, H. Mikami, K. G. Matsuoka and T. Ando, “Impact behavior of shear-failure-type RC beams without shear rebar”, *International Journal of Impact Engineering*, vol. 27, pp. 955-968 October 2002, doi: 10.1016/S0734.

[5] V. Peterson, M. Hallgren and A. Ansell, “On the Residual Static and Impact Capacity of Shear-Reinforced Concrete Beams Subjected to an Initial Impact”, *Applied Sciences*, vol. 12, pp. 1-19 November 2022, doi: 10.3390/app122211377.

[6] J. Magnusson, M. Hallgren and A. Ansell, “Shear in concrete structures subjected to dynamic loads”, *Structural Concrete*, vol. 15, pp. 55-65 March 2014, doi: /10.1002/suco.201300040.

[7] T. J. Ross, *Direct Shear Failure in Reinforced Concrete Beams under Impulsive.* Air Force Weapons Laboratory, AFWL-TR-83-84, Kirtland, USA, 1983.
[8] J. Magnusson, *Shear in Concrete Structural Elements Subjected to Dynamic Loads.* PhD Thesis, KTH Royal Institute of Technology, Div. Concrete Structures, Stockholm, Sweden, 2019, pp. 160.
[9] E. Kolmodin and K. Kubiak, *Effects of Impulse Intensity and Boundary Conditions for Blast-Loaded Reinforced Concrete Beams.* MSc Thesis, KTH Royal Institute of Technology, Div. Concrete Structures, Stockholm, Sweden, 2024, pp. 130.
[10] E. Ceberg and E. Holm, *Numerical Simulations of Impact-Loaded Reinforced Concrete Beams.* MSc Thesis, KTH Royal Institute of Technology, Div. Concrete Structures, Stockholm, Sweden, 2024, pp. 166.
[11] J. Magnusson and M. Hallgren, *High Performance Concrete Beams Subjected to Shock Waves from Air Blast.* Defence research establishment, FOA-R--00-01586-311--SE, Stockholm, Sweden, 2001.
[12] Dassault Systémes, *ABAQUS/Standard User's Manual, Version 6.14*, Dassault Systémes Simulia Corp, USA, 2014.
[13] P. Grassl, "Modelling the dynamic response of concrete with the damage plasticity model CDPM2", *10th International Conference on Fracture Mechanics of Concrete and Concrete Structures*, March 2023, France.
[14] fib, *fib Model Code for Concrete Structures 2010*, Wilhelm Ernst & Sohn, Germany, 2010.
[15] CEN, *Eurocode 2: Design of Concrete Structures – Part 1-1: General Rules and Rules for Buildings*, European Committee for Standardization, Belgium, 2005.
[16] V. Červenka, L. Jendele and J. Červenka, *ATENA Program Documentation – Part 1 Theory*, Cervenka Consulting, Prague, Czech, 2011.
[17]Ansys, *LS-dyna® keyword user's manual Bolume I-III*, Livermore software technology, California, USA, 2021.
[18] P. Grassl, D. Xenos, U. Nyström, K. Gylltoft, "CDPM2: A damage-plasticity approach to modelling the failure of concrete", *International Journal of Solids and Structures*, vol. 50, pp. 3805-3816 November 2013, doi: 10.1016/j.ijsolstr.2013.07.008.

DEVELOPMENT, TESTING AND COMPUTATIONAL SIMULATIONS OF AUXETIC CRASH PANEL

Nejc Novak[a], Hasan Al-Rifaie[b], Alessandro Airoldi[c], Matej Vesenjak[a], Zoran Ren[a]

[a] Faculty of Mechanical Engineering, University of Maribor, Maribor, Slovenia
[b] Faculty of Civil Engineering and Transport, Poznan University of Technology, Poznan, Poland
[c] Department of Aerospace Science and Technology, Politecnico di Milano, Milano, Italy

Keywords: cellular materials, auxetic panel, foam-filled, polyurethane foam, crash absorber, drop test, experimental testing, computational modelling

Abstract

The macro-scale auxetic crash absorbers with inverted honeycomb structures were fabricated by bending and glueing the aluminium sheets. The auxetic panels were fabricated using the relatively cheap and straightforward fabrication method, which was extended by adding the PU foam to obtain foam-filled samples. The samples were tested under compression loading at two different loading velocities using the universal testing machine (quasi-static) and drop tower (dynamic). Detailed quasi-static and dynamic drop tests were compared with a non-linear computational model. The stress-strain relationships, deformation patterns, specific energy absorption, crash force efficiency and Poisson's ratio were comprehensively evaluated. Foam-filled panels revealed higher specific energy absorption and more stable deformation than non-filled panels. The developed computational models successfully describe mechanical and deformation behaviour and can be used for future virtual testing of other configurations. The DIC and the FE models confirmed that the auxetic panel provides the auxetic response up to very large strains. The validated FE models enable the development of new foam-filled auxetic panels with a tailored response, where different geometries, sheet thicknesses, densities and distributions of the foams can be virtually tested before fabrication. This will hopefully lead to the application of modern crash absorption systems on newly built roads or blast protection elements in buildings.

1 INTRODUCTION

Cellular sandwich panels usually have two stiff plates and a crushable low-density core in between [1]. They have become widely used in engineering due to their excellent properties, in terms of lightweight, strength-to-weight ratios, and impact energy absorption, including high-rise buildings, aerospace engineering, automotive industry, defensive solutions, and other protective structures [2]. Sandwich panels with a cellular metallic core can dissipate significant dynamic energy through plastic deformation under impact or blast loading, especially when introducing the auxetic core [3]. The state-of-the-art review has shown that auxetic metamaterials provide improved energy dissipation compared to conventional cellular topologies [4]–[6]. The auxetic characteristic (negative Poisson's ratio) can be either naturally occurring (from the substance itself) or, in most cases, artificially created (changing the geometry of the metamaterial on the nano-, micro- or macro-level).

This paper aims to experimentally and computationally examine the behaviour of a novel re-entrant graded aluminium panel filled with PU foam in an auxetic pattern. The performance is assessed based on quasi-static and dynamic drop tower experiments supported by advanced non-linear finite element modelling and computer simulation.

2 MATERIALS AND METHODS

2.1 Geometry and fabrication of auxetic panels

Six different auxetic panels (APs) were considered in this research, three non-graded panels with different corrugated sheet thickness, and three graded panels, two of them filled with PU foam. All the panels have the same basic geometry with six re-entrant auxetic layers, built by corrugating and glueing twelve aluminium sheets. Figure 1 shows the geometry of the fabricated auxetic panels, where the unit cells have a width of 40 mm and a height of 30 mm. The overall dimensions of the auxetic panel are 315 x 180 mm.

Corrugated sheets made of aluminium alloy (AW-5754, T111, Impol, Slovenska Bistrica, Slovenia) were used to create the auxetic cores. The corrugated sheets were then assembled to auxetic panels with epoxy adhesive LOCTITE® EA 9466 (Düsseldorf, Germany), as shown in Figure 1. At room temperature, the glue hardens, forming a solid bond with good peel resistance and shear strength.

The three non-graded auxetic panels have a uniform corrugated sheet thickness throughout the whole panel of 0.8 mm, 1.0 mm and 1.2 mm, respectively. The graded auxetic panels were fabricated with varying sheet thicknesses. The two auxetic layers at the bottom have a sheet thickness of 0.8 mm, the two auxetic layers in the middle have a sheet thickness of 1 mm, and the two auxetic layers at the top have a sheet thickness of 1.2 mm. Two graded panels were filled with commercially available PU foam (Tekapur low expansion, TKK d.o.o., Slovenia) as a full-filled graded panel (FFG) and auxetic-filled graded panel (AFG), shown in Figures 1b-c. The foam was applied to the empty cells directly from the spray and was left to harden at room temperature for 24 hours.

The AFG configuration was chosen to introduce the multi-scale auxetic behaviour of the panels, where the filling itself introduces the auxetic effect. At least two samples from each group were tested to determine the representative response of each experimental testing type.

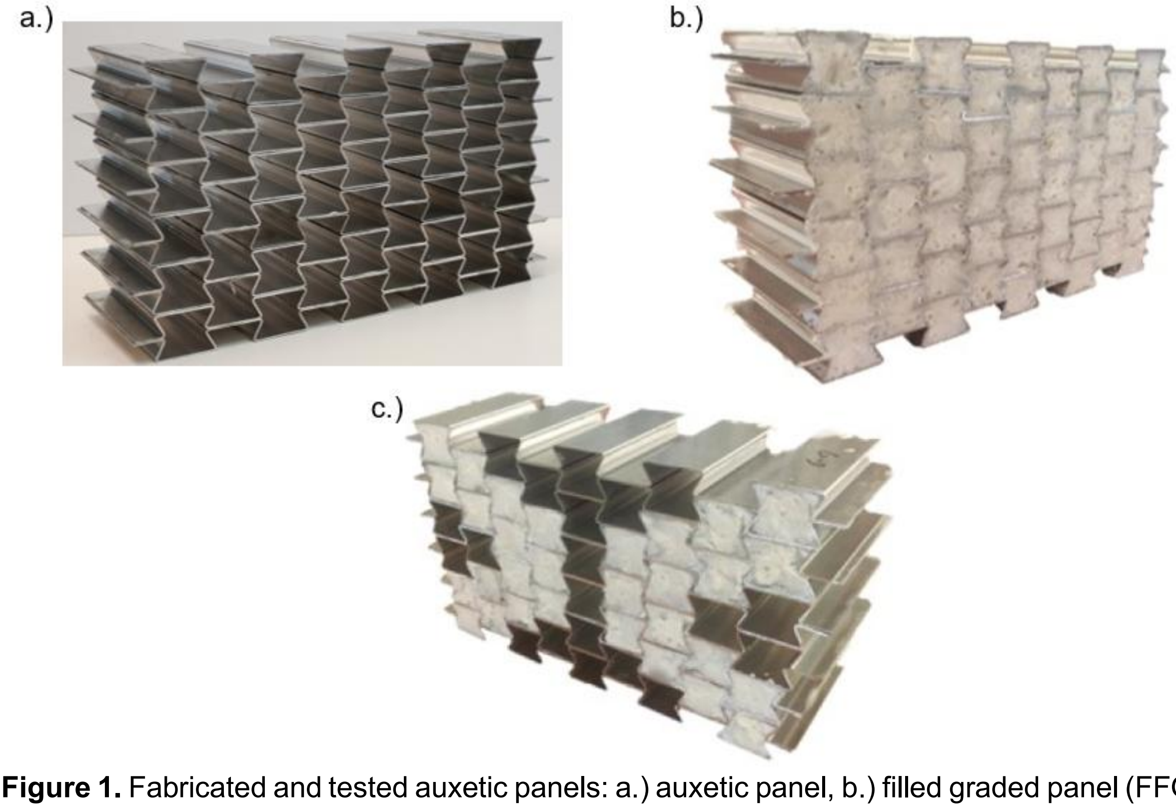

Figure 1. Fabricated and tested auxetic panels: a.) auxetic panel, b.) filled graded panel (FFG) and c.) auxetic-filled graded panel (AFG)

2.2 Experimental testing

The quasi-static testing of auxetic panels was performed using the universal testing machine Instron INSTRON 8801 with a position-controlled crosshead rate of 0.5 mm/s. The nominal stress-strain responses were calculated using the initial dimensions of the samples. Furthermore, the drop tower testing was carried out, consisting of a drop sledge with variable masses guided by two 6 m tall columns. A steel plate was fixed to the sledge to serve as the impacting surface to the top of the auxetic panel specimens. The specimens were positioned on a steel base. The total weight of the impacting mass was 99.5 kg at 10 m/s.

2.3 Computer simulations

The computational simulations were performed using the LS-DYNA software. The finite element (FE) model is shown in Figure 2. The model was discretised with 5 mm fully integrated shell finite elements with 5 through-thickness integration points, determined by a convergence study. The glue between the panels was not considered in the model since the adhesive joints did not fail during the experimental tests. The tie condition was assumed by using a single layer of shell elementsin the area of glue connections, which resulted in the different thicknesses of shell FE in these areas, as shown in Figure 2a.

The loading conditions were modelled with two steel plates modelled with shell FE with 1 mm thickness and the following material properties: Young's modulus 210000 MPa, Poisson's ratio 0.3. In the case of quasi-static testing, the upper loading plate has a prescribed constant velocity of 2000 mm/s toward the sample. The increase of the loading velocity in the FE model compared to the QS experimental tests was determined based on the parametric study to ensure the homogenous and quasi-static mechanical response without any inertia effect leading to the formation of the shock response. In the case of drop tower testing, the loading plate weighing 99.5 kg, and the initial velocity were prescribed the same as achieved in the experiments. The initial velocity in the case of the drop test was determined by the free fall equation and confirmed with the DIC from a high-speed video camera. The bottom support plate had fixed all degrees of freedom.

The *CONTACT_AUTOMATIC_NODES_TO_SURFACE contact was used between the plates and the auxetic panel and the auxetic panel and PU foam inserts, while the *CONTACT_AUTOMATIC_GENERAL was used for the contact between the shell FEs in the auxetic panel.

The elasto-plastic material model with strain hardening and rate dependence (MAT_024) based on the data from experimental testing (Figure 3a) was used to model the metal sheet material behaviour. The volume FEs of PU foam inserts were modelled with a crushable foam material model (MAT_063). The hardening behaviour (yield stress vs. volumetric strain) of the crushable foam material model was determined by the experimental tests, where the approximation curve with 50 data points was used to describe the simplified experimental curve. Additionally, the strain rate dependence of AW 5754 was considered using the Cowper-Symonds model with material parameters c = 6500 s-1 and p = 4.

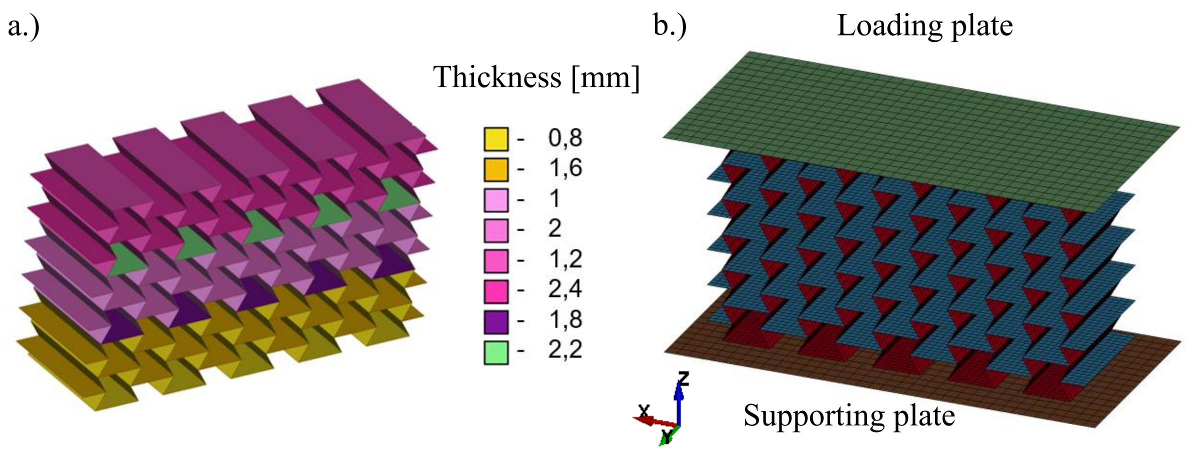

Figure 2. Computational model of auxetic panel: a.) the thickness definition, b.) boundary conditions

3 RESULTS AND DISCUSSION

Uniform panels deformed predictably at shear planes, while in graded panels deformation initiated in thinner layers, distributing forces progressively to other layers, as shown in Figure 3. Adhesive bonds withstood significant strain without failure.

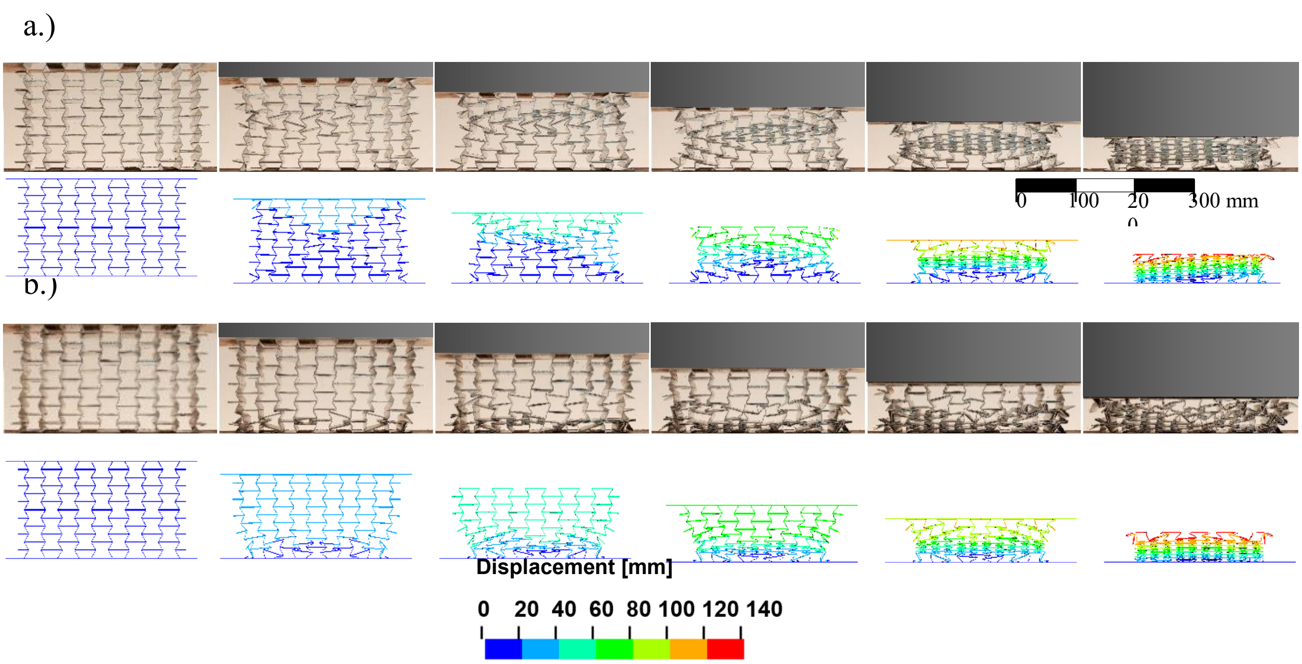

Figure 3. Experimental and computational QS deformation behaviour of a) uniform AP 1.0 mm and b.) graded auxetic panel (displacement increment: 25 mm)

The comparison between the experimental and computational quasi-static stress-strain results is shown in Figure 4. Good agreement can be observed for all analysed geometries up to the densification. The largest discrepancy between the computational and experimental responses can be observed in the initial stiffness of the panels with thicker sheets. This can be a consequence of the precise modelling of the panels in the FE model, where the geometry is perfectly aligned together, and starts to deform in a predicted (auxetic) way at lower stress levels.

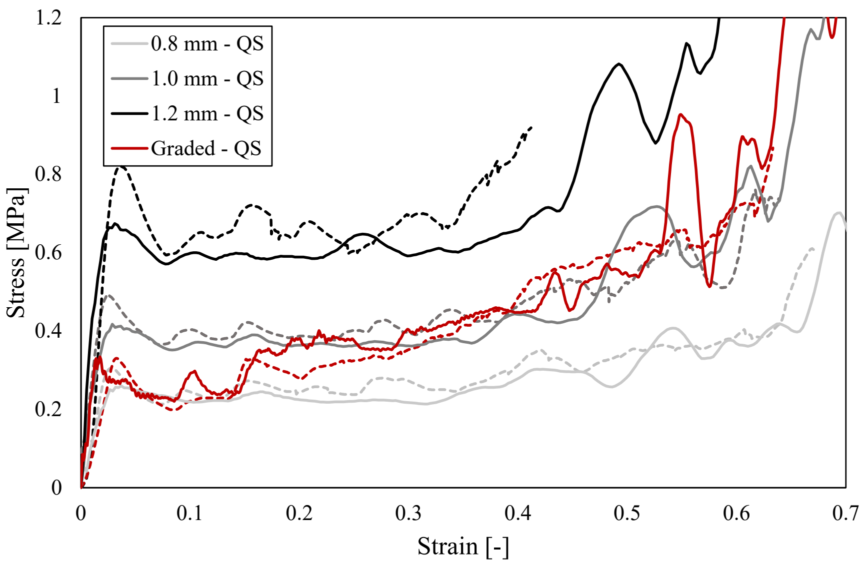

Figure 4. Comparison of experimental (dashed lines) and computational (solid lines) results under quasi-static loading conditions

As can be seen from Figure 5, SEA values increased with sheet thickness and foam filling. Foam-filled panels displayed superior SEA, with the FFG panel achieving a 23% increase over non-filled graded panels. The progressive densification of foam layers contributed to smoother energy absorption, enhancing crash force efficiency. CFE values were higher at 30% strain, particularly for foam-filled panels, which exhibited a more uniform load distribution during compression.

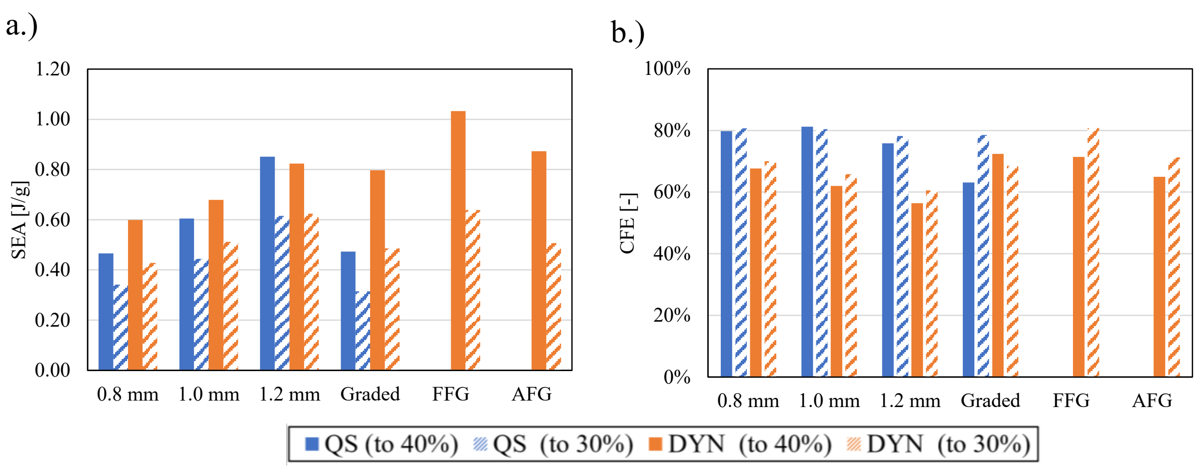

Figure 5. Comparison of different auxetic panel results, a) specific energy absorption (SEA) and b) crash force efficiency (CFE) of the considered auxetic panels evaluated up to 30 % and 40 % strain

4 CONCLUSION

The auxetic panels were fabricated using the relatively cheap and straightforward fabrication method. Stiffness of some panels was upgraded by adding the PU foam to obtain foam-filled samples. The samples were tested under compression loading at two different loading velocities using the universal testing machine (quasi-static) and drop tower (dynamic). The mechanical properties of aluminium material and PU foam were also determined.

Mechanical testing reveals that an increase in the sheet thickness from 0.8 mm to 1.2 mm increases the SEA capabilities almost by 50 % in the case of quasi-static and dynamic testing. The foam-filled auxetic panels increase the SEA capabilities even further and provide superior energy absorption capabilities compared to empty auxetic panels. The CFE of uniform auxetic panels decreases when dynamically loaded if compared to quasi-static loading. The opposite was observed for a graded auxetic panel and the foam-filled samples, where the CFE does not change significantly.

The developed FE models successfully describe the deformation behaviour of auxetic panels. The DIC and the FE models confirmed that the auxetic panel provides the auxetic response up to very large strains. The validated FE models enable the development of new foam-filled auxetic panels with a tailored response, where different geometries, sheet thicknesses, densities and distributions of the foams can be virtually tested before fabrication. This will hopefully lead to the application of modern crash absorption systems on newly built roads or blast protection elements in buildings.

ACKNOWLEDGEMENTS

This research was funded by the Slovenian Research Agency postdoctoral research project (No. Z2-2648) and national research programme funding (No. P2-0063).

REFERENCES

[1] X. Jin, Z. Wang, J. Ning, G. Xiao, E. Liu, and X. Shu, “Dynamic response of sandwich structures with graded auxetic honeycomb cores under blast loading,” *Compos. Part B Eng.*, vol. 106, pp. 206–217, 2016, doi: 10.1016/j.compositesb.2016.09.037.

[2] H. Al-Rifaie, R. Studziński, T. Gajewski, M. Malendowski, W. Sumelka, and P. W. Sielicki, “A New Blast Absorbing Sandwich Panel with Unconnected Corrugated Layers—Numerical Study,” *Energies*, vol. 14, no. 1, p. 214, Jan. 2021, doi: 10.3390/en14010214.

[3] N. Novak, M. Vesenjak, and Z. Ren, “Auxetic cellular materials - a Review,” *Strojniški Vestn. - J. Mech. Eng.*, vol. 62, no. 9, pp. 485–493, 2016, doi: 10.5545/sv-jme.2016.3656.

[4] G. Imbalzano, S. Linforth, T. D. Ngo, P. V. S. Lee, and P. Tran, “Blast Resistance of Auxetic and Honeycomb Sandwich Panels: Comparisons and Parametric Designs,” *Compos. Struct.*, vol. 183, pp. 242–261, 2017, doi: 10.1016/j.compstruct.2017.03.018.

[5] N. Novak, L. Starčevič, M. Vesenjak, and Z. Ren, “Blast response study of the sandwich composite panels with 3D chiral auxetic core,” *Compos. Struct.*, vol. 210, no. November 2018, pp. 167–178, 2019, doi: https://doi.org/10.1016/j.compstruct.2018.11.050.

[6] H. Al-Rifaie, N. Novak, M. Vesenjak, Z. Ren, and W. Sumelka, “Fabrication and Mechanical Testing of the Uniaxial Graded Auxetic Damper,” *Materials (Basel).*, vol. 15, no. 1, p. 387, Jan. 2022, doi: 10.3390/ma15010387.

15th International Conference on
Shock & Impact Loads on Structures
12-13 June 2025, Gothenburg, Sweden

SHEAR IN CONCRETE ELEMENTS SUBJECTED TO BLAST LOADS

Johan Magnusson[a], Mikael Hallgren[b], Richard Malm[c] and Anders Ansell[d]

[a]Swedish Fortifications Agency, Sweden,
email: johan.magnusson@fortifikationsverket.se,
[b]Tyréns AB, Sweden, [c]FOI Swedish Defence Research Agency, Sweden, [d]KTH Royal Institute of Technology, Sweden

Keywords: blast load, concrete element, initial response, flexural shear, direct shear, shear span, support reactions, numerical simulations.

Abstract

Concrete elements subjected to intense dynamic loads have been reported to fail in shear, even if they are designed to fail in a flexural mode under static loads. A flexural response with yielding of the reinforcement is always preferrable over a shear damage response with a limited deformation capacity. This is the case for conditions with static loading and is certainly also the case under dynamic loads such as blast loads. Previous experiments and analyses have provided a greater insight and understanding of shear failures of concrete elements subjected to blast loads. The purpose of this paper is to present the findings of a few selected experimental campaigns and also to discuss the results from the corresponding analyses. The distribution of the deformations, the bending moments and shear are initially significantly different from those in static events and show large variations both in time and space. Analyses of these initial variations provide a better insight into where cracking and failure due to flexure and due to shear may appear. Such analyses are discussed in the paper along with the evolution of shear failures. For static loads, it is well known that the shear slenderness has an influence on shear in concrete elements. Depending on the shear slenderness, different shear failure modes for sufficiently large loads may occur. The issues of the shear slenderness variations throughout a dynamic response are also discussed in the paper.

1 BACKGROUND

Concrete elements subjected to intense dynamic loads have been reported to fail in shear, even if they are designed to fail in a flexural mode under static loads. A flexural response with yielding of the reinforcement is always preferrable over a shear damage response with a limited deformation capacity. This is the case for conditions with static loading and is certainly also the case under dynamic loads. Shear failures in concrete beams have been experimentally reported in several investigations involving different levels of blast and impact loads, e.g. [1]–[5]. In several cases, these tests also confirm that even if a concrete element obtains a flexural failure under a static load, a shear failure may occur as a result of extreme dynamic loads. In a few particular test series [6]–[7], concrete slabs were shown to fail in direct shear with limited or without any noticeable deformations in the slab.

In this paper, dynamic loads refer to blast loads with an almost instantaneous increase in pressure with a subsequent pressure relief over time. Such an intense load may cause a structural element to vibrate in several bending modes above the fundamental mode of vibration, which imposes a higher degree of shear demand in the element.

Previous experiments and analyses have provided a greater insight and understanding of shear failures in concrete elements subjected to blast loads. The purpose of this paper is to present the findings of a few selected experimental campaigns and also to discuss the results from the corresponding analyses.

2 SHEAR IN CONCRETE ELEMENTS

2.1 Static Shear

Concrete elements subjected to different types of loading and support conditions need to resist shear forces, which usually act in combination with bending moments. Shear cracks in concrete elements can generally be related to the tensile strength of concrete. Due to the distribution of principal tensile stresses in a beam subjected to an external load, shear cracks are inclined with respect to the longitudinal axis of the element. A concrete element resists shear through beam and arch action [8]. Beam action requires perfect bond between the reinforcement and the concrete, while arch action transfers shear through inclined compression struts in the element from the load to the supports. Since perfect bond can not develop due to slip of the reinforcing bars and cracking of the concrete, the beam and arch mechanisms will provide a combined resistance against shear. As shear cracks develop, a gradual transition from beam action to arch action will occur. The element will eventually fail when the capacity of the combined beam and arch actions are exceeded.

In the investigations [9]–[10] on reinforced concrete beams without transverse reinforcement subjected to concentrated loads, it was found that the shear strength depend on the reinforcement content and the shear slenderness, i.e. the shear span to depth ration *a/d*. According to these findings, a beam mechanism governs for *a/d* values above 2.5–3.0, while an arch mechanism governs for values below these values. Such failures are controlled by the area in the vicinity of the arch or by failure of the arch itself. In the case of an element subjected to a distributed load, the shear slenderness is instead referred to as the full span to depth ratio (*L/d*). Experimental investigations on reinforced concrete beams by [11] also show that the shear slenderness plays an important role in different shear mechanisms. The corresponding *L/d* values for a beam mechanism are 10–11.

Depending on the shear slenderness, the behaviour of reinforced concrete elements in shear may be divided into four categories with distinct differences in the shear transfer mechanism as discussed in [8], [11], [12], [13]. Thus, shear failures may generally be classified into (1) flexural shear, (2) shear compression (initiated by web shear), (3) splitting or crushing of the compressive strut and (4) direct shear, see Figure 1 for point loaded beams. Figure 2 illustrates the shear capacity for beams subjected to uniformly distributed loads [11].

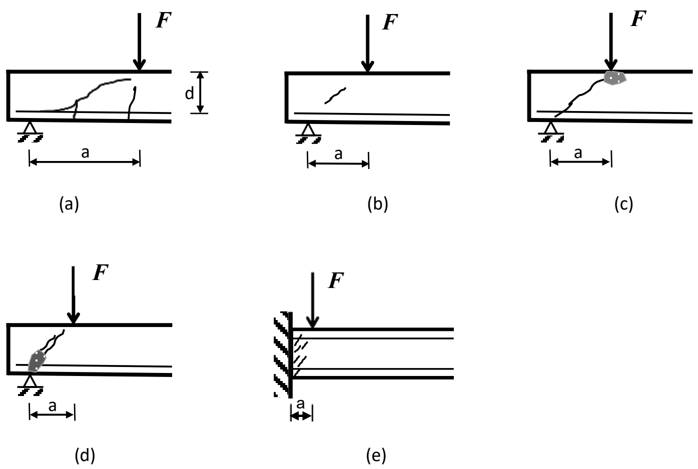

Figure 1. Schematic view of (a) flexural shear, (b) diagonal tension by web shear, (c) shear compression, (d) crushing/splitting of the concrete strut and (e) direct shear [14].

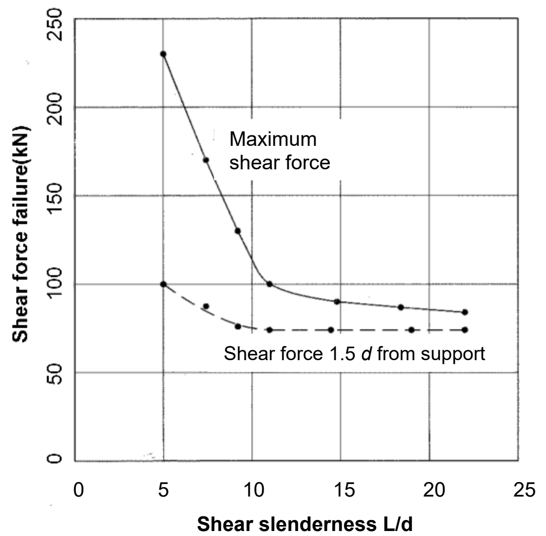

Figure 2. Shear capacity at varying shear slenderness for beams subjected to uniformly distributed loads according to [11], from [13].

2.2 Dynamic Shear

A structure subjected to dynamic loads may exhibit a significantly different behaviour compared to the same structure subjected to static loads, especially if the applied load is impulsive in nature. Both flexural shear and direct shear have been reported to occur due to dynamic loads. In a static case, it is not likely that a distributed static load can cause a direct shear failure due to the necessary concentration of a load close to the support. However, tests have shown that uncracked concrete elements can fail in direct shear under the action of a distributed blast load with high intensity [7] and [15]. In this context, direct shear refers to the vertical or near vertical failure surface that occurred in the intense blast tests.

Under dynamic loading conditions, local high stresses and strains can develop and their location may change before an initiated crack has time to propagate. An example is a case with a mass impacting a simply supported beam where cracks may initiate on the top surface at a distance from the load and propagate to a certain limit. Due to such conditions, wave propagation effects become increasingly important in the analyses. Shear failures may occur at an early stage, and it is therefore of interest to analyse the initial structural response soon after the load has been applied. In such conditions, a concrete element exhibits distributions of deflections, bending moments and shear forces that significantly deviate from the distributions of the same element subjected to a static load. For the purpose of investigating the initial response, theoretical analyses have previously been conducted on reinforced concrete beams with the Euler-Bernoulli and Timoshenko beam theories, e.g. [1], [15], [16], [17], and with the use of finite element analyses [14] and [18].

2.3 Modelling of Dynamic Shear

A series of simulations of reference tests were performed in order to analyse different shear failures in Abaqus 2011 with the use of the Concrete Damage Plasticity (CDP) model. Thus, the tested beams B40-D3 and B40-D4 reported in [4] and further analysed in [19] were used as verifications of a flexural shear failure. For verification of direct shear failures, tests DS1 and DS4 of a concrete box structure reported in [7] were used. Strain rate effects of the concrete and the reinforcement were included in all simulations. The reference simulations were used as a basis for the subsequent parametric studies.

2.3.1 Simulations of Reference Tests

The beam used as reference for flexural shear failures, has a cross-section of 300×160 mm (width×depth) and a span of 1500 mm [4]. The concrete and the rebars with interface (allowing for slip) were modelled using solid elements (4×4×4 mm for the concrete). The beams were simply supported and subjected to a uniformly distributed blast load across the surface with a peak pressure of 1.2 MPa and impulse density 6.4 kPas [4], [14]. Due to symmetry, half the beam span was modelled, with a symmetry plane at midspan.

Simulations for verification of direct shear failures were performed on tests on a concrete box structure, see Figure 3. The roof slab thickness measured 140 mm with a clear span of 1220 mm and the reinforcement consisted of bars in both directions and vertical stirrups. The boundary conditions of the bottom surfaces of the walls were modelled as fixed in all directions. The concrete was modelled with 4×4×4 mm solid elements and all reinforcement with beam elements without interface between concrete and bars. The applied blast load was modelled across the entire top surface using a piecewise linear approximation of the average values of the registered pressure-time curves from gauges IF-2 and IF-3 in [7]. These gauges registered impulsive loads with approximate peak pressures and duration of 22–25 MPa and 0.6 ms, respectively.

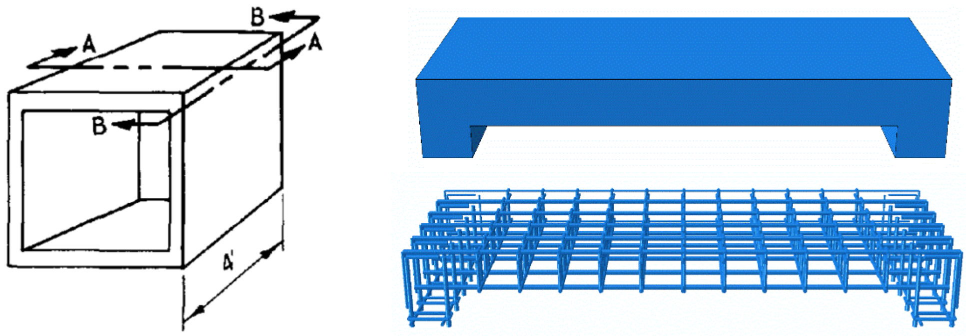

Figure 3. Concrete box structure (left) [7] and modelled roof slab and reinforcement [14].

2.3.2 Parametric Study of Shear Failures

Simulations of the simply supported beams (using symmetry at midspan) with a width and span of 300 mm and 1500 mm and with three different depths were performed, see Figure 4 and Table 1. Also, the amount of tensile reinforcement (K500C-T) was varied such that each beam section had a reinforcement content of approximately 0.6 % and 1.5 %, respectively. No transverse reinforcement was included in the models. The beam depth and, thereby, the value of *L/d* was particularly chosen to resemble beams subjected to uniformly loads and typically responding in a beam and an arch mechanism as discussed in Section 2.1. Both the concrete and the rebars with interface (allowing for slip) were modelled using solid elements (4×4×4 mm for the concrete). A compressive concrete strength and yield strength of the reinforcement of 45 MPa and 500 MPa was employed, and strain rate effects of these materials were included. The blast load was idealised as a triangular pressure pulse with an almost instant rise to peak pressure, immediately followed by a linear decay to zero, and uniformly distributed across the beam surface. For analyses of a flexural shear response, peak pressures of 0.5–4 MPa and durations of 2 ms or 10 ms were used. For direct shear the corresponding values were 5–20 MPa with durations of 0.5 ms and 4 ms, respectively.

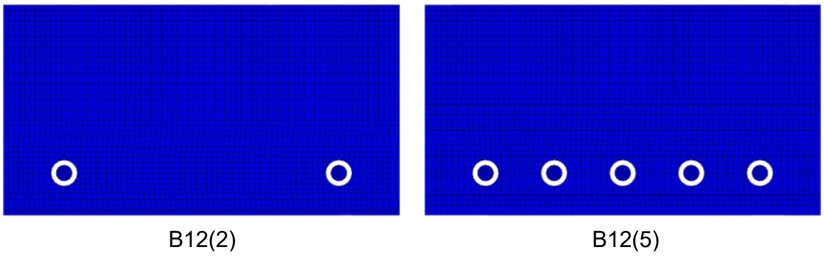

Figure 4. Modelled cross sections of beam type B12 with two amounts of reinforcement and interface around each bar [14].

Table 1. Geometry and reinforcement of the modelled beams.

Beam type	h (m)	d (m)	L/d	Reinforcement	ρ (%)
B7(2)	0.260	0.228	6.6	2ϕ16	0.59
B7(5)				5ϕ16	1.47
B12(2)	0.160	0.128	11.7	2ϕ12	0.59
B12(5)				5ϕ12	1.47
B27(2)	0.084	0.056	26.8	2ϕ8	0.60
B27(5)				5ϕ8	1.50

3 ANALYSES OF RESULTS

3.1 Initial Response

Figure 5 presents the calculated deflections, bending moments and shear forces for a simply supported beam subjected to an evenly distributed impulsive load at two points in time using Euler-Bernoulli beam theory. The values of the vertical axes are normalized to the corresponding static quantities in a static loading condition. The bending moment and shear distributions close to each support in Figure 5 show similarities to the distributions of smaller beams. Thus, at this stage, the entire beam may initially be regarded as divided into two smaller beams, each responding with an apparently low shear slenderness *L/d*. Structural wave motions will over time change the moment and shear distributions to eventually become similar to that of the entire beam being loaded statically. One interpretation of the initially low *L/d* values is that the beam shear strength could be relatively high initially while it reduces to the flexural shear strength over time, as the response resembles that of a statically loaded beam.

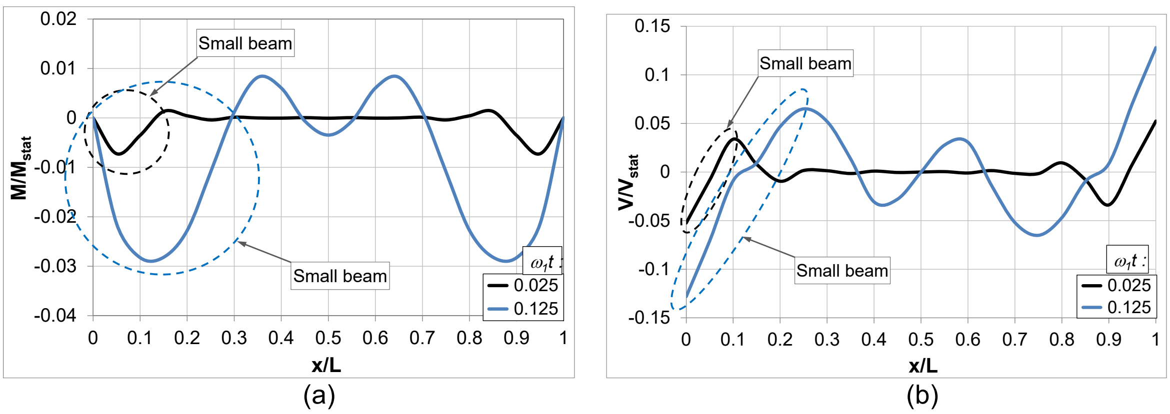

Figure 5. Normalized (a) bending moments and (b) shear forces for a simply supported beam subjected to a uniformly distributed dynamic load according to Euler-Bernoulli theory [14].

3.2 Dynamic Shear Span

Figure 5 shows that a structural element subjected to a distributed dynamic load may, in its initial response, be regarded as divided into two smaller beams, each responding with its own apparent shear slenderness *L'/d*, which over time will grow and become the static shear slenderness. In the simulations using the three beam cross sections as presented in Table 1, the growth of *L'/d* over time was evaluated by considering the von Mises stress distribution. The compressive zone and the inclined compressive struts at the supports at two points in time are clearly visible in Figure 6. The distance from the face of the support to the centre of the compressive zone resembles half of the temporary beam span, which resembles half the apparent shear slenderness *L'/(2d)* at that point in time. The estimation of the average *L'/d* growth over time is presented as linear curves for the three beam types in Figure 7. Thus, the growth of *L'/d* at a certain velocity is apparent in this figure. With the curves in Figure 7 as a basis, the bending wave velocity of each beam type when subjected to uniform blast loads were estimated and compared with the theoretical value of structual wave propagation which is calculated as:

$$c_f = \frac{n\pi}{L} \cdot \sqrt{\frac{EI}{\rho A}} \qquad [\mathrm{m/s}] \tag{1}$$

where L is the span, EI the flexural stiffness of uncracked concrete section, ρA the mass per unit length and n the bending mode. The same parameter values were used as in the simulations with the exception that the static value for E was used. Also, the moment of inertia for an elastic cross section was used, which is a reasonable assumption considering cracking is minimal at these early times. Considering the change in *L'/d* over time for the three beam types enabled estimations of the structural bending wave velocity. These values together with the calculated bending wave velocities are summarised in Table 2, which show that the FEA-based estimations are within approximately 10 % of the theoretical values for the third bending mode. Thus, this is an indication that the third mode is driving the structural wave motions.

Table 2. Calculated values of the bending wave velocitis based on FEA results and wave theory.

Beam type	c_{FEA} (m/s)	c_{mode3} (m/s)	c_{FEA}/c_{th}
B7	1908	1739	1.10
B12	960	1070	0.90
B27	525	562	0.93

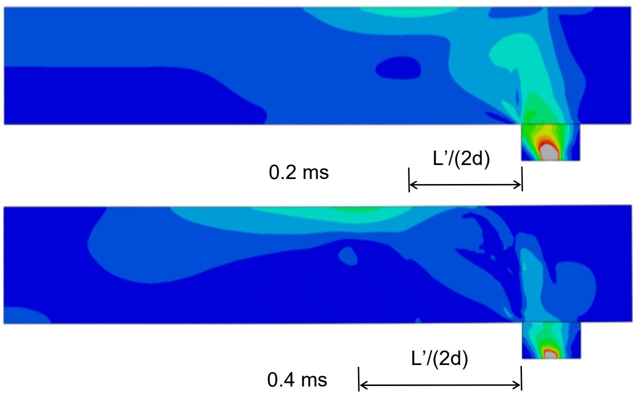

Figure 6. Evaluation of the shear span using the von Mises stress distributions. The simulations are shown at 0.2 ms and 0.4 ms after the load was applied.

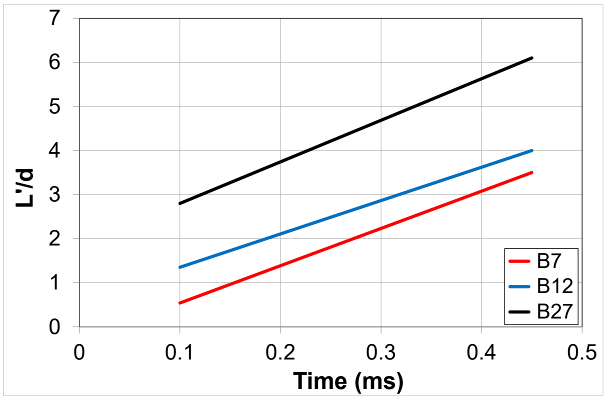

Figure 7. Evaluation of the apparent shear slenderness *L'/d* for the three beam cross sections.

3.3 Dynamic Failure Modes

In the simulations of the reference tests with flexural shear failures, it was noted that these shear failures follow the same sequence as in a static loading case, see Figure 8. A similar result was obtained with another software as presented in [17]. Thus, the blast load did not have the high level of intensity for a direct shear failure to occur.

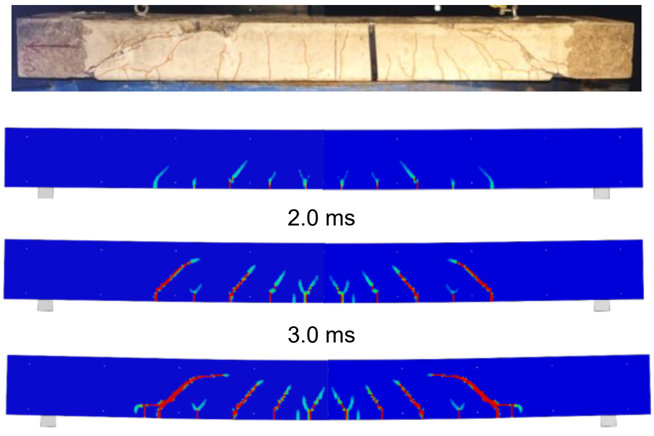

Figure 8. Simulation sequence of the propagation of cracks at different times after the load was applied, with reference test on top [14].

A test reported by [11] shows that a simply supported beam subjected to a uniformly distributed static load failed in flexural shear where the shear crack appeared at approximately 1*d* (1 effective depth) from the support. In several tests of beams subjected to blast loads, the flexural shear crack appeared at an average of approximately 1.6*d* from the support [4], [19]. Simulations of the same tests show that the shear cracks appeared at a distance of appoximately 1.6*d*–2.5*d*, see also Figure 8. A cause for the shear crack position at a greater distance from a support could possibly be found in the rather large variations in shear forces shown in Figure 9. These are the results of the calculated shear forces up to 3 ms after the load was applied using Euler-Bernoulli theory for the same beam as in Figure 8. The moment of inertia used in these calculations was chosen as half the value of that of an uncracked concrete section to account for the cracking. This is an approximation of the average moment of inertia for an uncracked and cracked cross section [20]. Figure 9 shows that large shear forces develop at a relatively long distance from the support during the first 3 ms, which may be the cause for the shifted position of the shear crack in the dynamic loading cases.

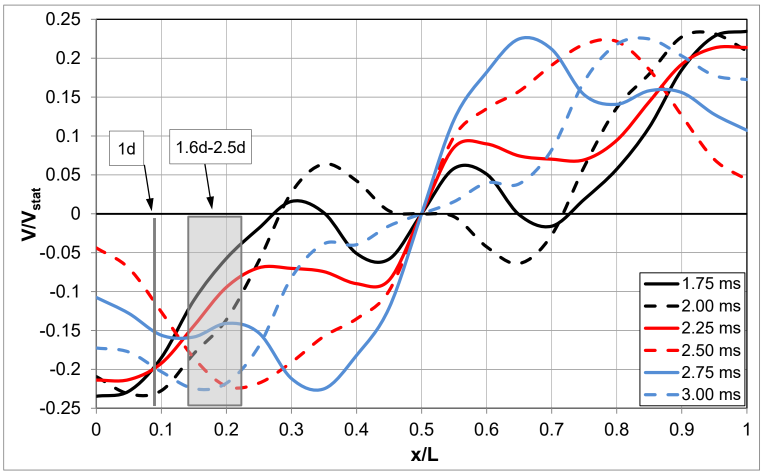

Figur 9. Normalized shear forces for a simply supported beam subjected to a uniformly distributed load according to Euler-Bernoulli theory for the first 3 ms after the load was applied.

In the DS1 test [7], the roof slab was completely separated from the supports. A large portion of the slab was observed to remain relatively flat, which indicates that the main deformations occurred in a narrow region around the supports. In the corresponding simulations, the slabs exhibit severe concrete crushing throughout the entire depth at each support and with most of the remaining slab flat, see Figure 10. Simulations of both tests (DS1 and DS4) show that the failure planes at the supports are inclined with respect to the vertical, which deviates from that observed in the DS1 test but is in agreement with the observations from test DS4. Note that the slab at 0.5 ms is still moving in a downward motion, and due to the crushed concrete at the supports, the slab will eventually separate completely from the supports and fall down.

The observation that a large portion of the slab remains flat is in agreement with the calculated moment and shear distributions in Figure 5. The crushed compressive struts were quite developed already at 0.3 ms and fully developed at approximately 0.5 ms after the load was applied, which can be considered as during the initial response of the slab. Thus, both the Euler-Bernoulli calculations and simulations show results that resemble the test.

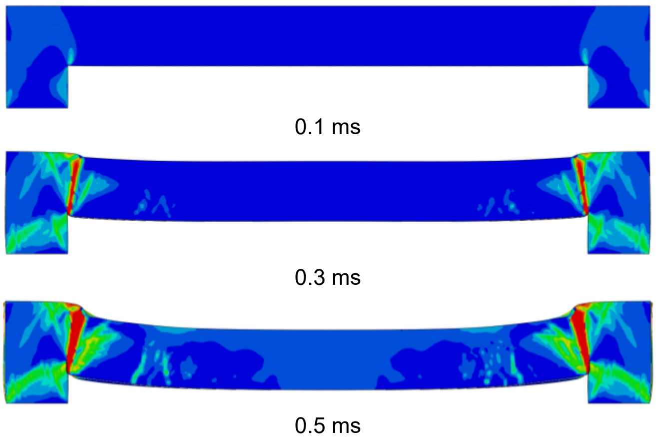

Figure 10. Simulation sequence of the propagation of compressive damage (of DS1 test) at different times after the load was applied [14]. The deformations are enhanced 10 times.

3.3 Support Reactions

The simulations of the simply supported beams, using different combinations of loads and durations, indicate that flexural shear depends on both these load parameters. A comparison of support reactions in Figure 11 shows that a beam subjected to a relatively high pressure but short duration (2 ms) or a lower pressure but longer duration (10 ms) resulted in flexural shear failure. Thus, it is apparent that the load duration is also a driving parameter that influences the failure mode. The reason for this may be found when comparing the impulses of the reactions as shown in Figure 11(b). This figure reveals that the impulses for the reactions in Figure 11(a) are higher compared to the simulations with lower pressures at the same durations where the beams did not fail in shear. Thus, the results indicate that the beam needs to be exposed to a certain level of impulse at an early stage of the structural response in order to develop a shear failure.

The results of the simulations causing direct shear failures show that the support reactions also depend on, other than the load amplitude, the duration of the applied load, see Figure 12. Furthermore, the figure also illustrates that the reactions depend on beam depth, where the deepest beam exhibits the greatest reactions. However, at a duration of approximately 4 ms the reactions level off.

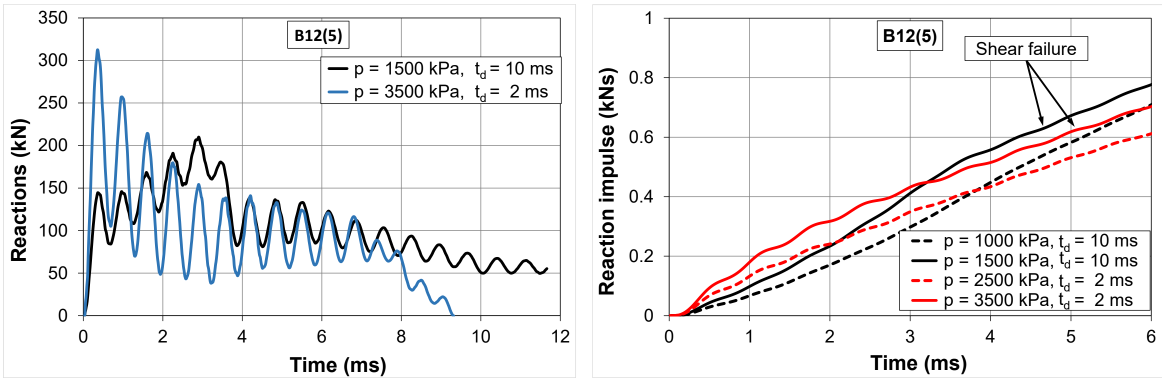

(a) (b)

Figure 11. (a) Support reactions for beam type B12(5) subjected to blast loads of 2.0 and 10 ms durations that failed in flexural shear. (b) Calculated reaction impulses.

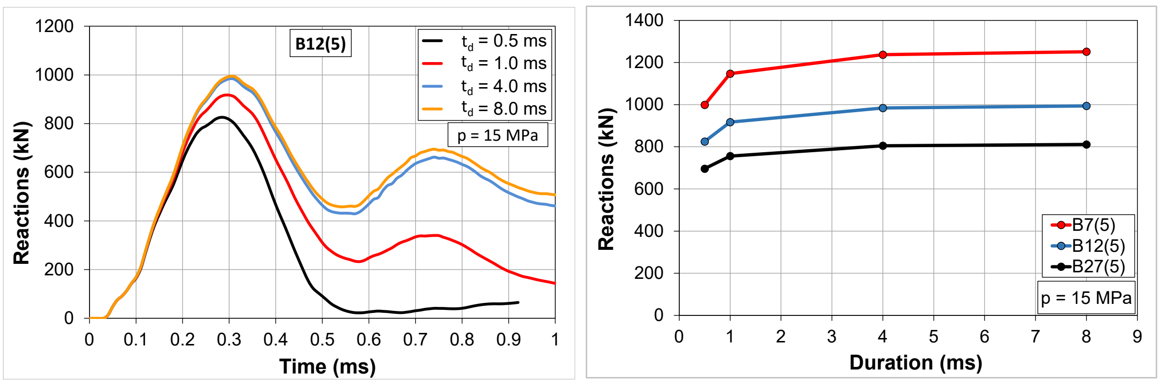

(a) (b)

Figure 12. Support reactions from simulations of (a) beam type B12(5) with a peak pressure of 15 MPa and varying durations, and (b) peak reaction forces for all three beam types.

4 DISCUSSION

The initial bending moment and shear distributions shown in Figure 5 is a simplification since the initial wave propagation effects through the element depth are ignored. This wave propagation is, however, neglected because the structural wave propagation is of much more importance. It is also regonised that the Euler-Bernoulli theory does not account for rotary inertia and shear displacements, which become increasingly significant for deep beams and higher bending modes. Nevertheless, the results in Figure 5 could be verfied in simulations where an apparent shear slenderness *L'/d* was identified to start at low values and grow over time. This initial behaviour shows that the element initially trensfers the applied loads to the supports in a similar manner as in a deep beam response, temporarily providing for a higher shear strength in relation to that of the same element subjected to static loading.

The dynamic analyses show that the evolution of flexural shear follows the same sequence of events as in a static loading case. This motivates using the same design models for shear as in static design and distributing stirrups where large shear forces appear. However, the results from both tests and simulations indicate that the flexural shear crack may be initiated and develop further away from the supports compared to cracking due to static loads. Figure 9 illustrates the significant variations in shear force distributions at times up to at least 3 ms after the load was applied. The figure indicates that shear forces with similar amplitudes as the reactions at the supports can develop at distances 2–3 times the effective depth (*d*) of the element. Thus, it is recommended to account for the maximum support reactions without reducing the shear force at 1*d* from the supports. If found necessary, it is also advisable to place vertical stirrups along a greater length compared to in a static design situation.

The analyses of flexural shear indicate that not only the amplitude of the load but also the duration is an important factor in development of flexural shear failures. It is shown that the element needs to be exposed to a certain level of impulse at an early stage of the structural response in order to develop a shear failure. Thus, this may be of importance to consider for certain loading conditions.

The simulations of the roof slab of a concrete box structure show that the failure planes at the roof supports are inclined due to the compressive struts that develop at each support. Such inclined failure planes were observed in three tests, while four other tests were reported in [7] to exhibit vertical failure planes. Furthermore, the roof slab was still attached to the supporting walls in at least two tests although severe damage zones of crushed and/or cracked concrete at the supports had appeared. The simulations reveal that the inclined compressive struts at the supports can be crushed during the initial response for a sufficiently intense impulsive load. Thus, dynamic direct shear appears to follow the same sequence of events as in a static case of shear in a deep beam with concrete crushing and possibly splitting of the compressive struts at the supports. The dynamic direct shear mechanism is therefore different from the static direct shear mode.

The Swedish design manual for protective structures [20] incorporates a model that accounts for the initial direct shear response of a concrete element. The model includes criteria for determining the design shear slenderness for a certain blast load, and an equation for calculation of the shear strength of the cross section. This model is based on the static behaviour of a deep beam response and that way applies the initially higher shear strength. Further analyses of the existing shear model is of interest to investigate possible improvements if found necessary. Such work could also include analysing models for calculating the dynamic strength of flexural shear.

Further analyses in [14] inicate that direct shear can occur in elements with fixed as well as with simple support conditions. Those are reasonable results considering the damage propagation at very early times. Vertical stirrups will not be effective to prevent such failures, but it may be possible to use a combination of vertical and horisontal, rather dense, reinforcement in the regions near the supports. Stirrups installed with an inclination with respect to the longitudinal beam axis may also be more effective.

4 CONCLUSIONS

The conclusions and suggestions for future work are as follows:

- The evolution of flexural shear follows the same sequence of events as in a static loading case. This motivates using the same design models for flexural shear as in static design. The stirrups needs to be placed where large shear forces appear, which can have a significantly different distribution compared that in a static loading case.
- The development of flexural shear failures appear to depend on both the amplitude as well as on the duration of the blast load.
- The analyses show that the dynamic direct shear mode appears to be a combination of bending moment and shear in a deep beam response and is therefore different from the static direct shear mode. There is an indication that the direct shear mode can occur in elements with both simple and fixed support conditions.
- Further analyses of the existing shear model in the Swedish design manual for protective structures is of interest to investigate possible improvements if found necessary. Such work could also include analysing models for calculating the dynamic strength of flexural shear.

ACKNOWLEDGEMENTS

The work on this paper was carried out at the Swedish Fortifications Agency. Their support is gratefully acknowledged by the authors.

REFERENCES

[1] G. Hughes and A.W. Beeby, "Investigation of the effect of impact loading on concrete beams", *The Structural Engineer*, vol. 60B, No. 3, 45-52, 1982.

[2] G. Niklasson, *Skjuvbrott i armerade betongbalkar: utvärdering av försöksserie* (*Shear Failure in Reinforced Concrete Beams: An experimental investigation*). Report D 20241-2.6., Swedish Defence Research Establishment (FOA), Sundbyberg, Sweden, 1994. (in Swedish)

[3] N. Kishi, H. Mikami, K.G. Matsuoka, and T. Ando, "Impact behaviour of shear-failure type RC beams without shear rebar", *Int. Journal of Impact Engineering*. 27, pp. 955-968, 2002.

[4] J. Magnusson, M. Hallgren and A. Ansell, "Air-blast-loaded, high-strength concrete beams. Part I: Experimental investigation", *Magazine of Concrete Research*, 62(2), pp. 127-136, 2010.

[5] J. Abdalnour and M. Saliba, *Drop-weight impact tests on reinforced concrete beams*. Master Thesis, KTH Royal Institute of Technology, Stockholm, Sweden, 2023.

[6] SA. Kiger and JV. Getchell, *Vulnerability of shallow-buried flat-roof structures*. Report SL-80-7, U.S. Army Engineer Waterways Experiment Station, Vicksburg, USA, 1980-1982.

[7] T.R. Slawson, *Dynamic Shear Failure of Shallow-Buried Flat-Roofed Reinforced Concrete Structures Subjected to Blast Loading*. Technical Report SL-84-7, U.S. Army Engineer Waterways Experiment Station, Vicksburg, USA, 1984.

[8] R. Park and T. Paulay, *Reinforced Concrete Structures*. John Wiley & Sons, New York, USA, 1974.

[9] G.N.J. Kani, "Basic facts concerning shear failure", J. ACI;63, pp. 675-692, 1966.

[10] G.N.J. Kani, "How safe are our large reinforced concrete beams", J. ACI;64(3), pp. 128-141, 1967.

[11] F. Leonhardt and R. Walther, "Schubversuche an einfeldrigen Stahlbetonbalken mit und ohne Schubbervehrung", *Deutscher Ausschuss für Stahlbeton*, Heft 151, Berlin, Germany, 1962.

[12] A.H. Mattock and N.M. Hawkins, "Shear Transfer in Reinforced Concrete – Recent Research", *Journal of the Prestressed Concrete Institute*, 17 (2), pp. 55-75, 1972.

[13] A. Ansell, H. Hallgren, J. Holmgren, B. Lagerblad and B. Westerberg, *Concrete Structures.* Report 143, KTH Royal Institute of Technology, Stockholm, Sweden, 2012.

[14] J. Magnusson, *Shear in Concrete Structural Elements Subjected to Dynamic Loads*. Doctoral Thesis, KTH Royal Institute of Technology, Stockholm, Sweden, 2019.
[15] T.J. Ross, *Direct Shear Failure in Reinforced Concrete Beams under Impulsive Loading*. AFWL-TR-83-84, Air Force Weapons Laboratory, Kirtland, USA, 1983.
[16] G. Svedbjörk, *Elastic beam subjected to transient load: Moment and shear distributions in time and space*. Publ. 42, Swedish Fortifications Agency, Eskilstuna, Sweden, 1975. (in Swedish)
[17] J. Magnusson, M. Hallgren and A. Ansell, "Shear in concrete structures subjected to dynamic loads", *Structural Concrete*, 15(1), pp. 55-65, 2014.
[18] S. Andersson and H. Karlsson, *Structural Response of Reinforced Concrete Beams Subjected to Explosions. Time Dependent Transformation factors, Support Reactions and Distribution of Section Forces*. Master Thesis 2012:103, Chalmers University of Technology, Gothenburg, Sweden, 2012.
[19] J. Magnusson, A. Ansell and H. Hansson, "Air-blast-loaded, high-strength concrete beams. Part II: Numerical non-linear analysis.", *Magazine of Concrete Research*, 62(4), pp. 235-242, 2010.
[20] Swedish Fortifications Agency, *Fortifikationsverkets konstruktionsregler FKR 2011* (*Design Manual for Protective Structures*), Dnr 4535/2011, Eskilstuna, Sweden, 2011. (in Swedish)

FEM MESO-SCALE MODELLING OF BRICK WALLS SUBJECTED TO IMPACTS AND BLASTS

FORMULATION AND LABORATORY TEST VALIDATION

Michele Godio [a], Mathias Flansbjer [b]

[a] RISE Research Institutes of Sweden, Sweden, email: michele.godio@ri.se
[b] RISE Research Institutes of Sweden, Sweden

Keywords: FEM, Contact, Brick masonry, Drop-weight impact, Blast, DIC

Abstract

Outer walls are a crucial component of the building envelope, providing insulation and structural support. While they are originally designed to support axial loads, these walls can be subjected to extreme loads, like the ones generated by impacts and blasts. Unreinforced brick masonry walls are particularly vulnerable to these actions and pose significant risks when damaged, including flying debris and progressive collapse. Careful engineering judgment is required to evaluate their resistance and design their strengthening in order to address this problem.

A 3D FEM-based meso-scale modelling strategy is developed to simulate the response of masonry walls to blasts and impacts. The models were created in a general-purpose proprietary FEA software package, by making use of material models available in it. Bricks were modelled as nonlinear solid elements, while mortar joints were modelled by contact interfaces with cohesive-damage frictional behaviour. The models were built and verified upon the findings of impact pendulum and quasi-static four-point bending tests, both conducted at RISE Research Institutes of Sweden under various wall configurations. Once validated, the ability of this modelling strategy to conduct blast simulations was demonstrated for one of the tested wall configurations.

This numerical work complements the experimental work previously conducted at RISE to characterize the response of brick masonry walls under impulsive loads. The modelling strategy presented here can assist the analyst evaluate the resistance of brick facades to these loads, allowing for a more precise assessment of urban areas at risk of damage.

1 INTRODUCTION

Up to the middle of the 20th century, brick masonry was a crucial construction material, representing more than 50 % of the outer walls in the Swedish built environment [1]. Interest in this material has waned over the past 70 years, but the deteriorated international security situation has sparked renewed attention over the last 10 [2]. Masonry is vulnerable to out-of-plane actions, especially when unreinforced. When impulsive loads like blasts and impacts act on the wall surface, extensive damage is generated. This damage can lead to flying debris and, in the case of load-bearing members, compromise the building stability [3,4].

A series of actions are undertaken by RISE Research Institutes of Sweden and the Swedish Fortification Agency to characterize the out-of-plane response of brick masonry walls to blasts and impacts. Experimental and numerical methods were reviewed [5] and new were developed. A series quasi-static four-point bending tests on 11 clay brick masonry walls with different thicknesses, axial load ratios, and boundary conditions was initially conducted [6]. Two series of impact pendulum tests followed. In the first series, 3 brick walls were subjected to point-load impacts run at relatively low impact velocity (3÷4.5 m/s) to study the role of arching in increasing the wall resistance to repeated impacts [7]. In the second, point- and line-load impacts were applied on 4 walls under larger, and more destructive, impact velocities (7÷8.5 m/s) [8].

The goal of this study is to develop a reliable modelling strategy that can represent with fidelity the out-of-plane response of brick walls under both quasi-static static and impulsive loads, namely, impacts and blasts. The goal is achieved through the implementation of a 3D FEM-based meso-scale modelling strategy, a typology of numerical model that is common for masonry structures [9]. For this strategy, the literature leverages the use of dedicated simulation tools [10,11], or ad-hoc user-defined materials developed for commercial tools [12,13], which can be difficult to access and utilize by the common practitioner. In this study, the model is deliberately created in a well-known, general-purpose FEA software package (Abaqus 2022 [14]), making use of the material models available in it, and run within the offered computational framework.

Meso-scale models stand out for their capability of replicating the brickwork and accessing directly the mechanical parameters of the masonry components, i.e. bricks and mortar, while remaining computational feasible as compared to, e.g., models where the mortar joints thickness is also reproduced [12]. Meso-scale models can still capture the crack propagation along the mortar joints, leading to orthotropic response and failure. However, since they can only model failures inside the mortar and at the brick-mortar interface in an equivalent manner, the approach requires careful calibration of the model parameters.

In what follows, the steps undertaken to build and verify the meso-scale models are reported. The modelling strategy is first described (section 2). Models for brick walls are then developed to reproduce their static behaviour under in-plane shear-compression [15] and four-point bending [6] (section 3). The models are next extended to reproduce impact pendulum tests [7,8] (section 4). Once these models are verified, they are used to simulate blast scenarios on one of the tested wall configurations (section 5), broadening the scope of applications of the experimental studies previously performed.

2 MODELLING STRATEGY

The meso-scale modelling strategy, also referred to as “simplified micro” modelling [9], consists in modelling the bricks as distinct bodies and the mortar joints as zero-thickness interfaces (**Figure 1**).

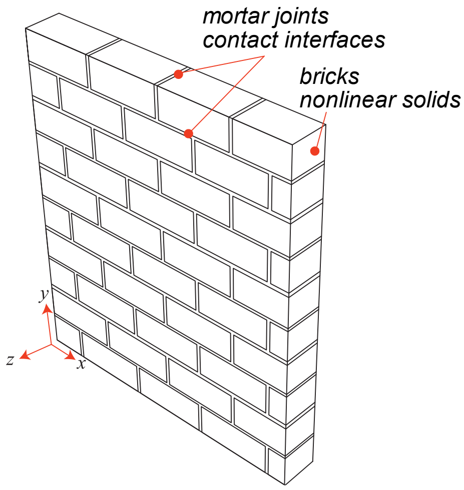

Figure 1. Meso-scale modelling strategy employed for brick masonry.

Discrete (DEM), finite (FEM), and hybrid DEM/FEM formulations can be used interchangeably for this purpose. Here, the models are developed in an explicit 3D FEM computational framework using Abaqus/Explicit. Explicit solution procedures are usually preferred to implicit ones when solving transient response calculations, and quasi-static simulations where complex nonlinear phenomena occur [14].

2.1 Modelling of the bricks

Bricks are modelled as nonlinear solid elements with expanded geometry to cover the mortar joints. The concrete damage plasticity (CDP) material model is used [14]. This is a very common material model for bricks, especially when using Abaqus, see [16,17].

2.1 Modelling of the mortar joints

Mortar joints are modelled by cohesive-damage frictional contact interfaces [14]. In tension, the cohesive damage model corresponds to an elastic-plastic linear-softening stress-displacement relationship. In compression, a linear elastic behaviour is implemented since Abaqus does not offer compression cap models. The tangential behaviour is characterized by a cohesive-damage frictional model, with the maximum shear strength being not affected by the frictional contribution and friction being activated in the damaged contact points only [18], i.e., when the cohesive part is lost. The tangential behaviour is verified against shear-compression tests conducted on masonry couplets under different compression stresses σ [19], showing good performance (**Figure *2***).

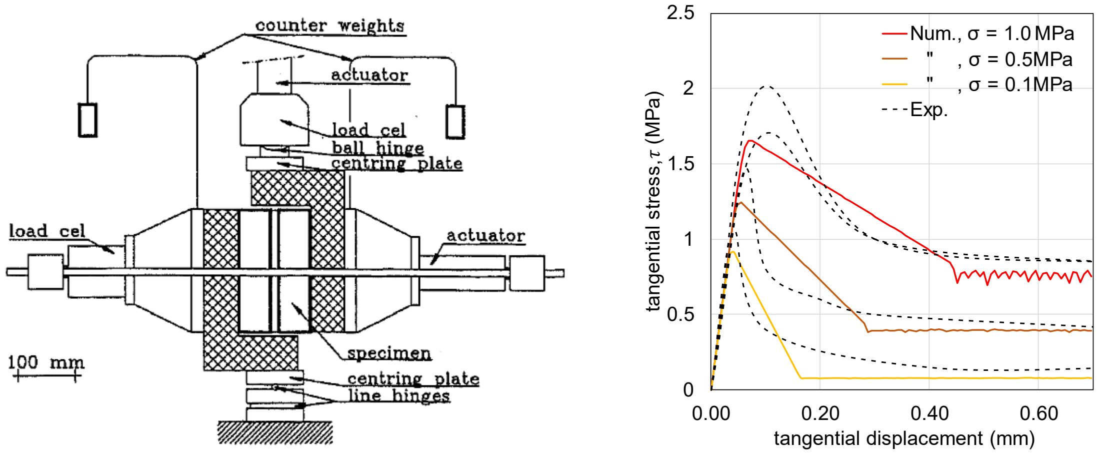

Figure 2. Modelling of shear-compression tests on masonry couplets [19]. The model parameters used in this benchmark are taken from the literature.

3 QUASI-STATIC TEST SIMULATIONS

3.1 Measures taken for quasi-static simulations

A series of measures is taken to simulate quasi-static loading conditions within the framework of an explicit solution procedure:

● Mass-scaling is operated on the whole model. The value for the mass-scale factor is found by trial-and-error until large changes in the solution are observed.

● Damping is introduced both for the mortar joints and the bricks. This limit unwanted oscillations in the response, allowing a quasi-static behaviour to be modelled. Damping coefficients usually are adjusted to keep kinetic energy below 10% of internal energy [20].

● Loads are smoothly applied using input time-velocity histories, with the final input velocity kept low throughout the analysis.

3.2 Modelling of in-plane loaded masonry panels

The modelling strategy is first tried out on shear-compression tests conducted on masonry panels [15]. The comparison comprehends meso-scale models from the literature, making use of an implicit solution procedure [17]. Fair precision simulations are run in about 10 minutes on a common single-core laptop computer (**Figure 3**).

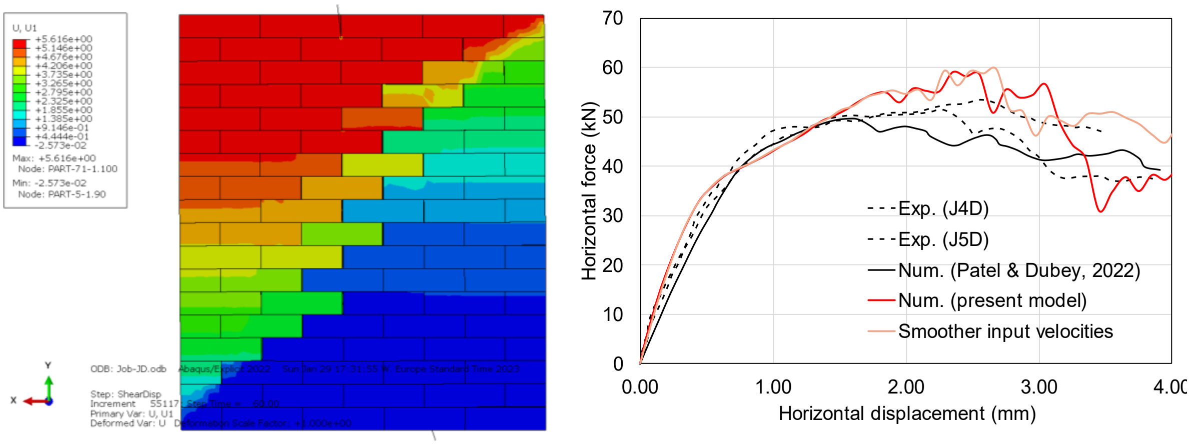

Figure 3. Modelling of shear-compression tests on masonry panels [15]. The model parameters used in this benchmark are taken from the literature.

3.3 Modelling of out-of-plane loaded masonry walls

Meso-scale models representing quasi-static four-point bending tests on brick masonry walls [6] are built (**Figure 4**). The test specimens consisted of single- and double-wythe spanning vertically between two RC slabs. The walls were initially subjected to vertical compression and subsequently to displacement-controlled four-point bending.

The models are calibrated and validated by considering wall configurations of increasing complexity. The focus is initially on single-wythe walls displaying vertical bending mechanisms, to end with complex double-wythe walls displaying combined bending-punching shear mechanisms. This allows for the calibration of dedicated sets of model parameters governing only certain mechanisms. For each parameter, properties from material tests are used when available; when not, best-fit parameters are determined thought trial-and-error, using educated guesses from the literature. The models are validated on different specimens than those used for calibration.

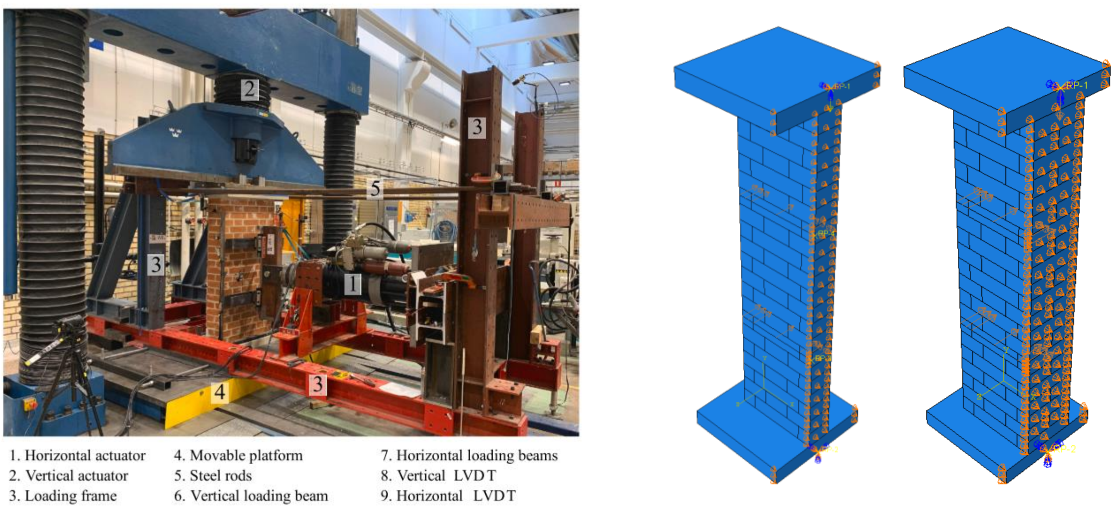

Figure 4. Four-point bending test setup [6] and the corresponding FEM meso-scale models.

The walls governed by combined bending-punching shear mechanisms are the most challenging to capture. **Figure 5** shows how the meso-scale models capture not only the overall behaviour for one of these walls – see diagrams – but also its failure observed throughout the test – see comparison with DIC data.

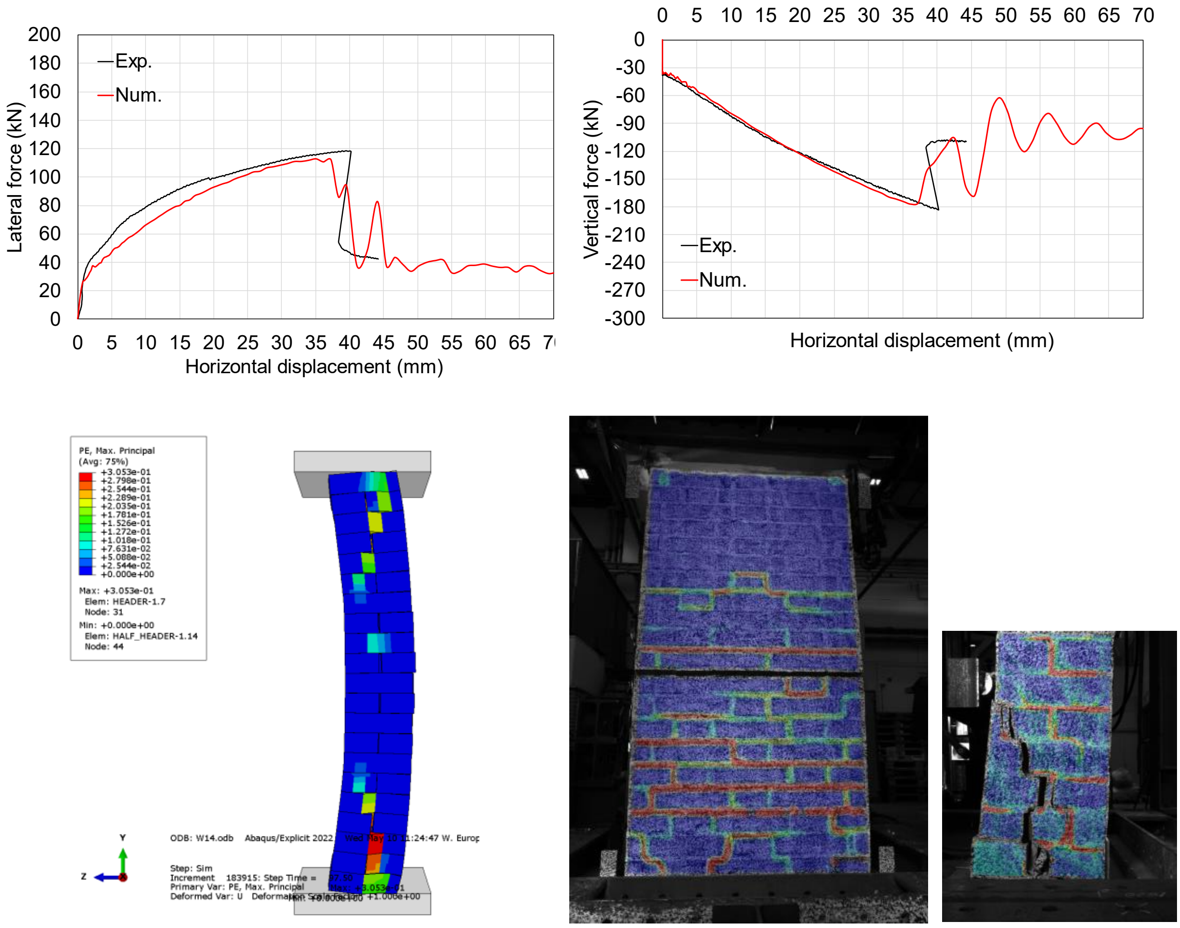

Figure 5. Meso-scale modelling of four-point bending tests [6]. Specimen W14.

4 IMPACT PENDULUM TESTS SIMULATIONS

The FEM meso-scale modelling strategy developed for quasi-static simulations is expanded to reproduce the transient response of brick masonry walls subjected to low- and moderate-velocity impacts [7,8]. The test specimens that are intended to be modelled have same geometry and properties than those tested under four-point bending [6]. The walls were initially subjected to vertical compression and subsequently to impacts. The impactor, of 116 kg, consisted of two steel beams assembled with a hemispherical head. The impact occurred at wall mid-height, directly on the wall surface (point-load impacts) or for the intermediary of a steel profile distributing the load across the wall width (line-load impact), see **Figure 6**.

4.1 Measures taken for impact simulations

The measures taken in developing the FEM meso-scale models for quasi-static simulations are lifted in view of their extension to impulsive loads:

● Mass-scaling is turned off. This allows proper mass densities to be inputted, allowing for realistic inertial and impact force distributions. In addition, this decreases the allowable stable timestep, increasing the accuracy of the numerical solution.

● Damping is relaxed for the mortar joints. It is common practice in impact and blast simulations to make use of zero damping, partly because of the expected fast dynamic structural response, partly because the oscillations that occur first are often the most dominant ones [5]. Here, damping is not set to zero but kept to a minimum to avoid numerical issue related to, e.g., element penetrability across the contact interfaces [14]. The damping models are kept unchanged for the bricks, in order to control sudden energy releases due to brick failures, which may affect the model stability.
In addition, new actions are taken to increase the efficacy of the modelling strategy:
● Although it is common to model impulsive loads by means of load-time histories [5], here it is preferred to include the impactor in the model. This results in a more realistic simulation of the wall-impactor interaction, capturing momentum transfer and contact conditions, without adding complexity to the model.
● While a regular mesh was used for quasi-static simulations, here the central region of the wall – where impact occurs – is finely discretized. This increases the accuracy in modelling the impact forces, resulting in a better representation of the structural response.

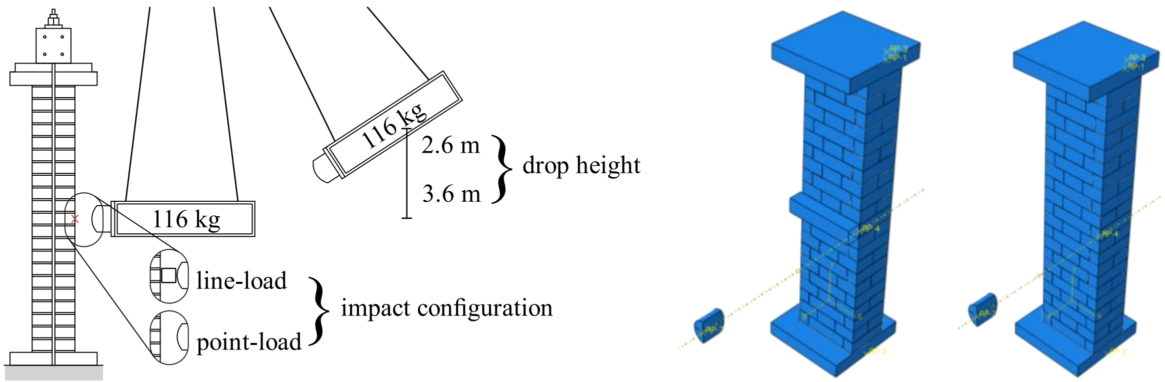

Figure 6. Impact pendulum test setups [7,8] and the corresponding FEM meso-scale models.

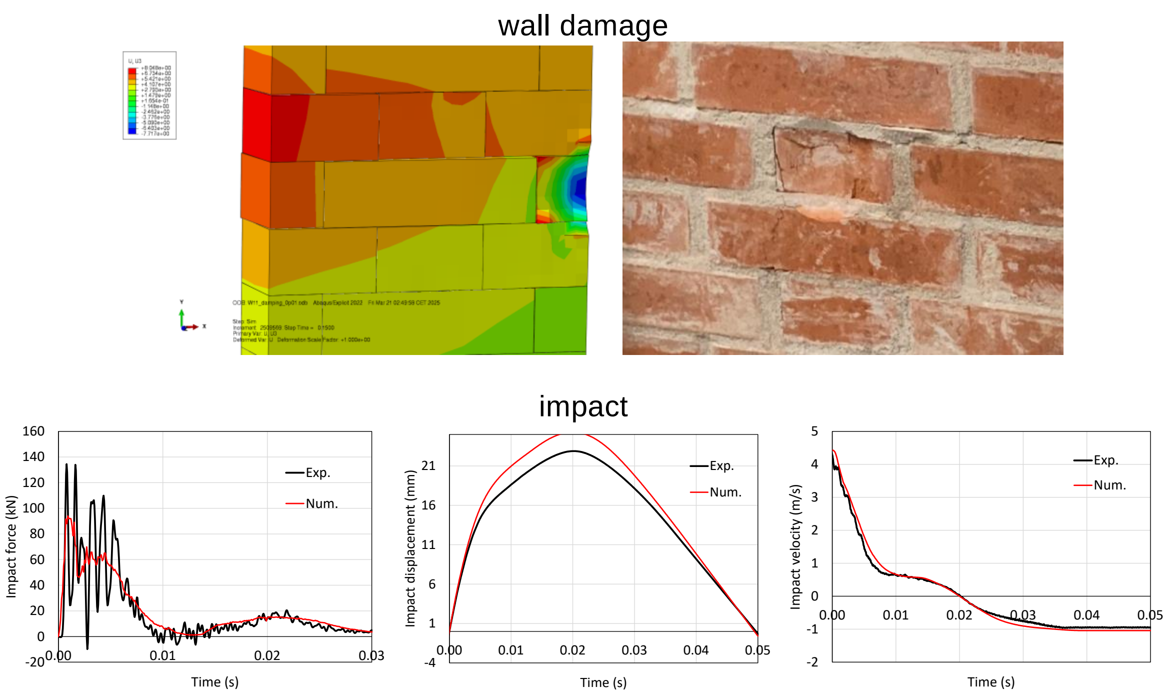

Figure 7. Meso-scale modelling of low-velocity point-load impact tests [7]. Specimen W11-1.

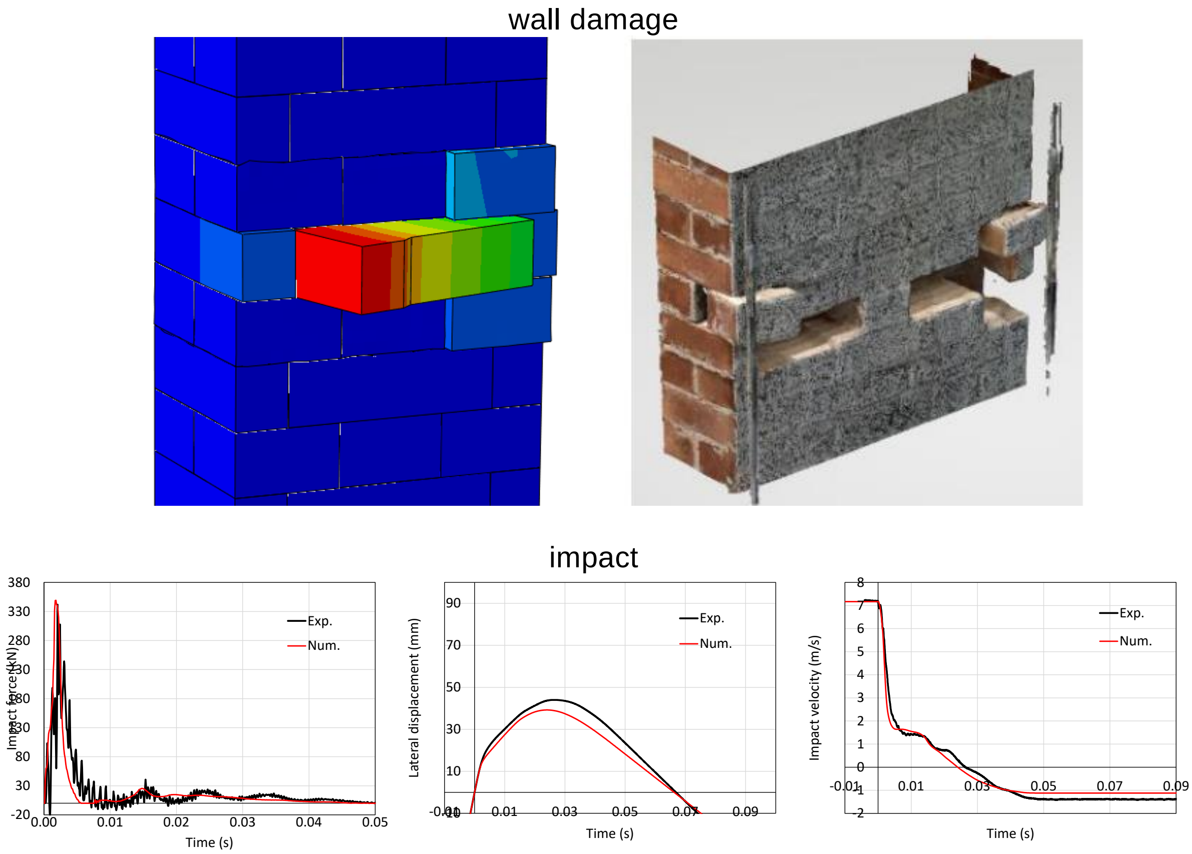

Figure 8. Meso-scale modelling of moderated-velocity line-load impact tests [8]. Spec. W18.

4.2 Modelling of low-velocity impacts

The models, once validated against four-point bending tests, are used for the simulation of the impacts without further calibration of the model parameters.
When tested on the low-velocity impact tests [7], the FEM meso-scale model shows able performance in capturing the impact displacement, velocity, and force (**Figure 7**). The model appears to seize correctly also the damage created by the impact on the wall face.

4.3 Modelling of moderate-velocity impacts

When benchmarked against moderate-velocity impacts [8], the FEM meso-scale model shows the good performance in capturing both the impact response and damage generated on the wall (**Figure 8**).

5 BLAST SIMULATIONS

The ability of the FEM meso-scale modelling strategy to conduct blast simulations is demonstrated on one of the tested wall configurations (specimen W18 [8]). The blast load consists of a triangular load history uniformly distributed onto the wall surface. The load is characterized by a peak overpressure of 35 kPa and an impulse of 1000 kPa·ms, with the peak occurring at 1/10 of the load duration. The wall can sustain this blast (**Figure 9**).
The peak overpressure is then amplified by factors of 10 and 100, with the impact duration remaining constant, resulting in impulse amplification. The wall fails at an amplification factor of 10 and above. For the amplification factor 10, a bending mechanism is observed (**Figure 9**). For the amplification factor 100, the wall is propelled away due to the blast.

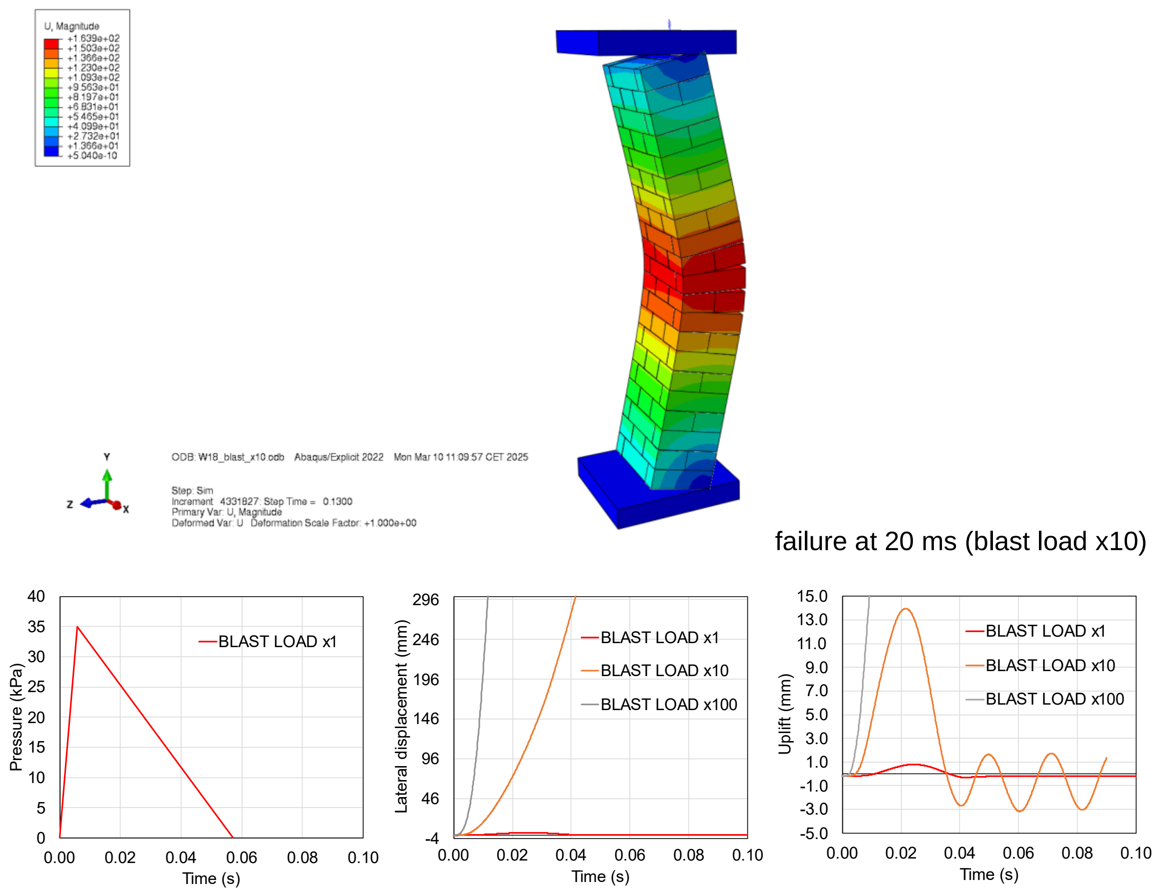

Figure 9. Meso-scale modelling of blast simulations of increasing intensity. Specimen W18.

6 CONCLUSIONS

The study builds on the knowledge built upon a state-of-the-art review on numerical and experimental tools for brick masonry walls [5], along with the findings of four-point bending [6] and impact pendulum test [7,8], to create reliable numerical models for unreinforced masonry subjected to extreme actions.

A 3D FEM-based meso-scale modelling strategy is successfully developed. The models, created using a general-purpose FEA software package and validated against accurate experimental data, show great capability in capturing both global responses and local failures for all tested wall configurations, under static and impulsive loadings.

When used in blast simulations, the modelling strategy appears to offer a reliable and affordable tool for practitioners needing to assess the resistance of brick facades to impulsive loads. The flexibility and viability of this numerical approach make it appealing for real-world applications, allowing for effective planning and design of strengthening solutions for masonry structures in urban environments.

Future work should focus on investigating the model sensitivity to model parameters and exploring additional wall configurations to enhance the robustness and applicability of the modelling strategy, especially in blasts simulations. In relation to this, dedicated studies examining the occurrence of strain-rate effects should be conducted.

ACKNOWLEDGEMENTS

Dr Johan Magnusson (FortV) is acknowledged for his support throughout the study.

REFERENCES

[1] C. Björk, P. Kallstenius, L. Reppen, Så byggdes husen 1880-2000: arkitektur, konstruktion och material i våra flerbostadshus under 120 år, Formas, Stockholm, 2003.

[2] G. Michaloudis, N. Gebbeken, Modeling masonry walls under far-field and contact detonations, Int J Impact Eng 123 (2019) 84–97. https://doi.org/10.1016/j.ijimpeng.2018.09.019.

[3] B. Gabrielsen, C. Wilton, K. Kaplan, Response of arching walls and debris from interior walls caused by blast loading, Redwood City, California, 1975.

[4] R.A. Keys, S.K. Clubley, Experimental analysis of debris distribution of masonry panels subjected to long duration blast loading, Eng Struct 130 (2017) 229–241. https://doi.org/10.1016/j.engstruct.2016.10.054.

[5] M. Godio, N. Williams Portal, M. Flansbjer, J. Magnusson, M. Byggnevi, Experimental and numerical approaches to investigate the out-of-plane response of unreinforced masonry walls subjected to free far-field blasts, Eng Struct 239 (2021) 112328. https://doi.org/10.1016/j.engstruct.2021.112328.

[6] M. Godio, M. Flansbjer, N. Williams Portal, Single- and double-wythe brick masonry walls subjected to four-point bending tests under different support conditions: Simply supported, rigid, non-rigid, Constr Build Mater 404 (2023) 132544. https://doi.org/10.1016/j.conbuildmat.2023.132544.

[7] M. Godio, M. Flansbjer, N. Williams Portal, Low-velocity out-of-plane impact tests on double-wythe unreinforced brick masonry walls instrumented with optical measurements, Int J Impact Eng 178 (2023) 104597. https://doi.org/10.1016/j.ijimpeng.2023.104597.

[8] M. Godio, M. Flansbjer, Experimental response of unreinforced brick masonry walls to moderate-velocity point-load and line-load impacts, Under Review (2025).

[9] P.B. Lourenço, Computational strategies for masonry structures, Delft University of Technology, 1996.

[10] A. Ferrante, D. Loverdos, F. Clementi, G. Milani, A. Formisano, S. Lenci, V. Sarhosis, Discontinuous approaches for nonlinear dynamic analyses of an ancient masonry tower, Eng Struct 230 (2021) 111626. https://doi.org/10.1016/j.engstruct.2020.111626.

[11] J. V. Lemos, V. Sarhosis, Dynamic analysis of masonry arches using Maxwell damping, Structures 49 (2023) 583–592. https://doi.org/10.1016/j.istruc.2023.01.139.

[12] A.M. D'Altri, S. de Miranda, G. Castellazzi, V. Sarhosis, A 3D detailed micro-model for the in-plane and out-of-plane numerical analysis of masonry panels, Comput Struct 206 (2018) 18–30. https://doi.org/10.1016/j.compstruc.2018.06.007.

[13] A.J. Aref, K.M. Dolatshahi, A three-dimensional cyclic meso-scale numerical procedure for simulation of unreinforced masonry structures, Comput Struct 120 (2013) 9–23. https://doi.org/10.1016/j.compstruc.2013.01.012.

[14] Simulia, Abaqus 2022, (2022).

[15] P.B. Lourenço, J. Rots, J. Blaauwendraad, Two approaches for the analysis of masonry structures: Micro and macro-modeling, 40 (1995) 313–340. http://www.narcis.nl/publication/RecordID/oai:tudelft.nl:uuid:c39b29ab-3c75-47db-9cb5-bf2b1c678f1f (accessed November 8, 2013).

[16] B.V. Wilding, K.M. Dolatshahi, K. Beyer, Shear-compression tests of URM walls: Various setups and their influence on experimental results, Eng Struct 156 (2018) 472–479. https://doi.org/10.1016/j.engstruct.2017.11.057.

[17] K.P. Patel, R.N. Dubey, Effect of flanges on the in-plane behavior of the masonry walls, Eng Struct 273 (2022). https://doi.org/10.1016/j.engstruct.2022.115059.

[18] Z. Zou, M. Hameed, Combining interface damage and friction in cohesive interface models using an energy based approach, Compos Part A Appl Sci Manuf 112 (2018) 290–298. https://doi.org/10.1016/j.compositesa.2018.06.017.

[19] R. van der Pluijm, SHEAR BEHAVIOUR OF BED JOINTS, in: The Sixth North American Masonry Conference, Philadephia, Pennsylvania, Philadelphia, 1993: pp. 125–136.

[20] L. Macorini, B.A. Izzuddin, A non-linear interface element for 3D mesoscale analysis of brick-masonry structures, Int J Numer Methods Eng 85 (2011) 1584–1608. https://doi.org/10.1002/nme.3046.

15th International Conference on
Shock & Impact Loads on Structures
12-13 June 2025, Gothenburg, Sweden

A STUDY ON THE CLASSIFICATION AND EVALUATION OF LOADS ACTING ON DRIFTWOOD CATCHMENT BASED ON THE FLOW PROCESS OF DRIFTWOOD GROUPS

Taishi Tatsukawa[a], Toshiyuki Horiguchi[b], Taro Uchida[c], Masuhiro Beppu[d]

[a] National Defense Academy, Japan email: 63025@nda.ac.jp
[b] National Defense Academy, Japan
[c] University of Tsukuba, Japan
[d] National Defense Academy, Japan

Keywords: driftwood groups, debris flow mixed with driftwood, driftwood catchment, impact load

Abstract

In Japan, driftwood-related disasters are increasing annually, and the amount of driftwood reaching downstream areas is increasing. Due to buoyant effects, driftwood is transported by shallow currents, allowing it to easily travel to downstream regions where residential areas and infrastructure are located, resulting in bridge blockages and loss of life. Furthermore, groups of driftwood collide with driftwood catchments such as steel protective barriers causing damage to their crests and side sections. Currently, driftwood catchment countermeasures are being constructed to prevent driftwood from flowing downstream, and large amounts of driftwood are trapped. However, in current designs of driftwood catchment, only the static water pressure load is considered, and the impact loads produced by driftwood groups have not been considered. This study evaluates the impact loads exerted by driftwood groups on driftwood catchment. First, an evaluation of loads with and without the formation of driftwood groups was conducted, demonstrating that driftwood groups can influence impact loads. Subsequently, the experimental results were organized to clarify how changes in the number and length of driftwood affect the acting loads. The time-dependent characteristics of these loads are examined, and their defining features are clarified. In addition, because driftwood catching countermeasures are installed in the downstream area, experiments were conducted to examine the effects on the acting load by changing the gradient and flow rate, and parameters of the downstream environment, and the results were compiled. The results demonstrated that the loads exerted by driftwood groups on driftwood catchment can be divided into three categories (impact zone, transition zone, and deposition zone) based on their temporal progression. Additionally, the maximum impact load depends strongly on the total mass, flow velocity, and deposition *height of the driftwood group. Furthermore, the maximum impact load clearly exceeds the static water pressure load, suggesting the necessity of accounting for dynamic impact forces in the design of driftwood catchment.*

1 INTRODUCTION

Driftwood disasters caused by record-breaking torrential rains are increasing annually. Statistical data on driftwood over the past 30 years have indicated an increasing trend in the amount of driftwood flowing downstream [1,2]. Consequently, debris flows increasingly incorporate driftwood, exacerbating their destructive potential.

Driftwood is transported by buoyancy forces in shallow, fast-moving currents and often reaches downstream areas where residential zones and critical infrastructure are

Figure 1. Driftwood catchment

concentrated, posing significant risks to human lives. Moreover, when driftwood flows out into the sea, it creates additional challenges by accumulating in fishing ports and damaging coastal facilities. Additionally, driftwood groups can cause severe damage to Sabo dams, affecting their tops, sleeves, and forebay structures [3]. There is a growing concern that future large-scale debris flows could transport unprecedented amounts of driftwood downstream, potentially overwhelming Sabo dams and causing damage on an unprecedented scale. For instance, during the Niigata Prefecture disaster in August 2022, the increased volume of driftwood may have reduced the effectiveness of the Sabo dams, leading to greater downstream damage.

The current design standards for driftwood catchments, as shown to **Figure 1,** in debris flow sections are outlined in the Technical Guidelines for Measures against Debris Flow and Driftwood [4]. These guidelines also describe the basic concepts for countermeasures against driftwood during sediment and flood inundation [5],[6]. One such countermeasure is the construction of driftwood catchment facilities. These facilities were designed to trap driftwood in the traction section, with the spacing-to-length ratio (w/l_{max}) between the facility spacing (w) and the maximum length of driftwood (l_{max}) set to less than 1/2. The load-bearing capacity is typically evaluated based on the hydrostatic pressure under design load conditions. However, the impact load caused by driftwood has not been thoroughly investigated.

Previous studies explored various aspects of driftwood catchments. Ishikawa et al. [7] proposed an equation to estimate the driftwood catchment rate of Sabo dams and driftwood trapping screens installed on sub-banks. Shibuya et al. [8] investigated the effects of spacing, slope, and flow rate on the performance of driftwood catchment facilities and developed an estimation equation for catchment structures. Kuniyori et al. [9] experimentally examined the loads acting on driftwood catchment structures. They found that the impact load was smaller than the hydrostatic pressure, whereas the load during the blockage of the permeable section was close to the hydrostatic pressure. Yamada et al. [10] analyzed the load characteristics when trapping groups of driftwood and demonstrated that the load exerted by a group of driftwood was significantly greater than that of a single piece. Watanabe et al. [11] found that the load was instantaneously higher when driftwood groups appeared higher than the water surface and struck the weir in a highly concentrated mixture of only a large amount of driftwood. Matsutomi [12] and Ikeno et al. [13] proposed estimation equations for load effects based on the impact phenomenon of a single piece of driftwood, incorporating contact theory [14]. However, the loads acting on driftwood catchment structures owing to groups of flowing driftwood remain insufficiently studied. Furthermore, current design methods do not consider the addition of impact loads to the design loads.

This study examined the applicability of hydrodynamic force evaluation by analyzing the factors that influence applied loads. This was achieved by varying the key parameters of the flowing environment, such as the slope and flow rate.

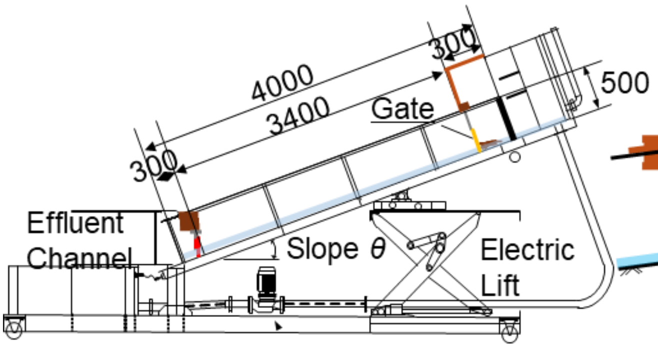

Figure 2. Experiment device

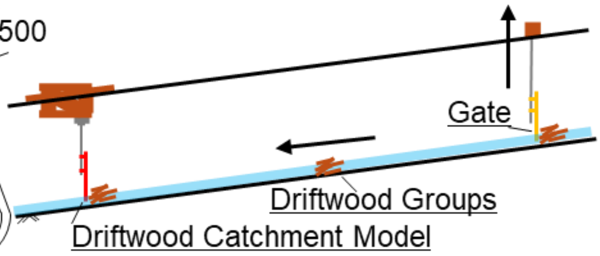

Figure 3. Driftwood grouping type

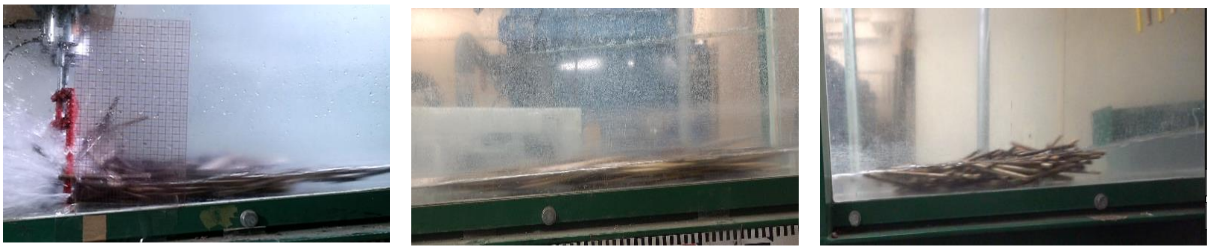

(a) Lower **(b)** Midstream **(c)** Upstream

Figure 4. Situation of flow downstream

2 MATERIALS AND METHODS

2.1 Experiment summary

Figure 2 shows an overview of the experimental device. The channel flume is length L = 4.0 m, width B = 0.3 m, depth H = 0.5 m, and channel slope (θ = 0° to 20°). The flow rate was controlled manually. The flow rate in this experiment was determined by calculating the flow rate from the water depth using the Manning equation. The driftwood input location in this experiment was 3.4 m upstream of the driftwood catchment model. **Figure 3** shows the method by which driftwood is fed by a conveyor belt at a constant rate. This method is known as driftwood grouping. The gate was placed 3.4 m upstream of the channel. Initially, a constant flow was maintained in the channel, and driftwood was randomly thrown into the gate to be captured. After the waveforms settled, the gate was opened and the captured driftwood flowed downstream, forming a driftwood swarm and impacting the driftwood catchment model. **Figure 4** shows the actual situation of the driftwood swarming model. Driftwood flows from the upstream section to the downstream section as a driftwood group.

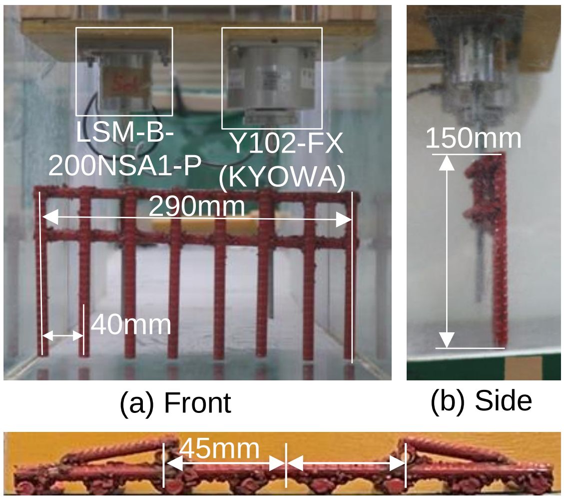

(a) Front (b) Side

(c) Top

Figure 5. Driftwood catchment model

2.2 Driftwood catchment model

Figure 5 illustrates the driftwood catchment model and installation of the measurement device. The driftwood catchment had a height of h_c =150 mm, width b_c = 290 mm, catch spacing w_c = 40 mm, and pipe diameter D = 10 mm as shown to **Figure 5(a),(b)**. Deformed steel bars with sufficient rigidity to withstand the applied load were used for the members because they were thought to capture the driftwood more adequately than the increased contact area with the driftwood groups and the suppression of slippage. To measure all

Table 1. Experimental condition

Item	Similarity	Channel		Driftwood catchment			Driftwood	
		Length L (m)	Width B (m)	Height h_c (mm)	Width b_c (mm)	Interval w_c (mm)	Length l (mm)	Diameter d (mm)
Model	1/20	3.4	0.3	150	290	40	120	5.5
Real	1	68	6	3000	5800	800	2400	110

Table 2. Experimental case

Slope θ (°)	Rate of flow Q (L/s)	Number of driftwoods	Repetition
1.0	2.3	100	5
2.0	4.7	200	5
3.0	6.9	300	5

the loads acting on the driftwood catchment model, the model was secured using two force meters (LSMB-200NSA1-P, Y102-FX, KYOWA) and hung such that the bottom of the model did not touch the channel bottom. The total force of the force meters was measured up to a maximum of 200 N. As shown in **Figure 5(c)**, force gauges were placed 45 mm from the center of the driftwood catchment model to measure the applied load. The force meter was connected to a threaded rod extending from the force meter through a 6-mm inner diameter hollow cylinder welder to the driftwood catchment, and the hollow cylinder was connected from above and below by a steel rod secured with nuts. The sampling frequency was set to 200 Hz. A 100 Hz low-pass filter was used to remove high-frequency noise.

2.3 Driftwood model

The driftwood model is based on an actual driftwood survey by Shibuya et al. [15]. The diameter and length of the driftwood were set to d = 5.5 mm and l = 120 mm, respectively, because the relationship between the channel width and length of the driftwood would limit the movement of the driftwood if a model with long driftwood was used. The material used was Ramin, soaked thoroughly in water. The specific gravity of each driftwood model was 0.76 when dry and 1.11 when wet.

2.4 Test case

The experimental conditions are listed in **Table 1**. The experiment was set up at a scale of 1/20 by applying the fluid similarity rule. The scale of the experiment was close to that used for driftwood control and catching in rivers when converted to a real scale. **Table 2** shows the experimental cases of the driftwood grouping type, in which three cases of flow rate and three cases of driftwood were combined for three instances of gradient, and each case was conducted five times, for a total of 135 times.

2.5 Method of measuring the impact load

To confirm the measurement accuracy of the applied load, a preliminary experiment was conducted to measure hydrostatic pressure. At this stage, water leaked between the film and the waterway. Therefore, a constant flow rate was maintained while adjusting the water depth by operating a lever that controlled the flow rate. After the waves disappeared and the water depth stabilized, the load acting on the driftwood catchment model was measured. The theoretical values of the hydrostatic pressure loads are shown in **Figure 5**. The theoretical and measured values were almost identical, confirming that the measuring device can measure static loads.

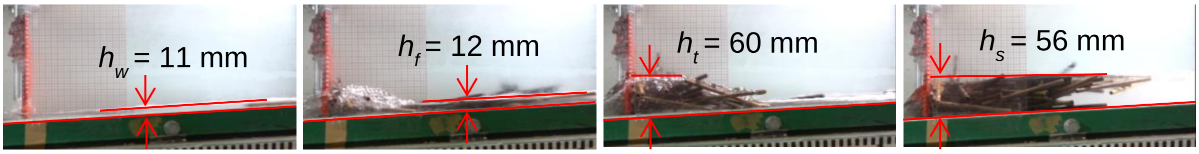

(a) $t = t_0$ [s] (b) $t = t_0 + 1.12$ [s] (c) $t = t_0 + 1.36$ [s] (d) $t = t_0 + 10.0$ [s]

Figure 6. $\theta = 3$ °, $Q = 2.3$ L/s , $n = 200$

(a) $t = t_0$ [s] (b) $t = t_0 + 0.32$ [s] (c) $t = t_0 + 0.64$ [s] (d) $t = t_0 + 10.0$ [s]

Figure 7. $\theta = 3$ °, $Q = 6.9$ L/s, $n = 200$

3 EXPERIMENTAL RESULTS

3.1 Driftwood groups flow

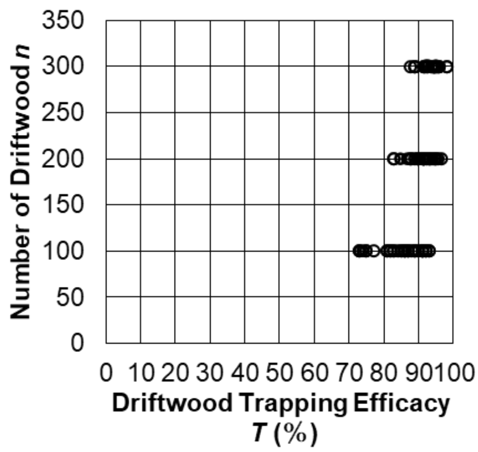

Figure 8. Driftwood trapping efficacy

The flow state was considered when the flow rate was varied. Similar trends were observed even when the number of driftwood and the gradient were changed; thus, in this chapter, the flow state is shown under the following conditions: number of driftwood n = 200, gradient $\theta = 3°$, flow rate Q = 2.3 L/s, 6.9 L/s. **Figures 6** and **7** show the situation just before the driftwood hit the catchment model. By setting the initial time as $t = t_0$ s, all images were compared in the same time series. The height at which the driftwood reached its highest point was the dam-rise height, h_t. Various heights were measured using image analysis software k-Software (Kato Kogyo Kenkyusha). **Figures 6** shows the situation in which is Q = 2.3 L/s. **Figures 6(a)** shows the initial state ($t = t_0$ s). In **Figures 6(b)** ($t = t_0 + 1.12$ s), the driftwood group reached the driftwood catchment model just before colliding with it, and the flow depth was h_f = 12 mm. In **Figures 6(c)** ($t = t_0 + 1.36$ s), after the driftwood group collided, the subsequent driftwood accumulated, and the driftwood climbed up the dam, reaching the highest point (h_t = 60 mm). The dam rise height and hydraulic jump were smaller at low flow rates than under other experimental conditions. In **Figures 6(d)** ($t = t_0 + 10$ s), the driftwood was captured, and water accumulated behind it, generating hydrostatic pressure, and the deposition height was h_s = 56 mm. Photo 4 presents the situation in which is Q = 6.9 L/s. **Figure 7(a)** illustrates the initial state ($t = t_0$ s). In **Figure 7(b)** ($t = t_0 + 0.32$ s), the driftwood group reached the driftwood catchment model just before colliding with it, and the flow depth was h_f = 24 mm. In **Figure 7(c)** ($t = t_0 + 0.64$ s), after the driftwood group collided, the subsequent driftwood piled up and the driftwood went up the dam, reaching the highest point (h_t = 112 mm). The driftwood collided with the driftwood capture model, and the subsequent driftwood pushed up the accumulated driftwood, reaching its highest point (h_t = 112 mm). As the flow rate increases, the dam rise height and hydraulic jump also increase; therefore, if the flow rate increases beyond this value, the dam height may be exceeded. In addition, because driftwood catchment is aimed at preventing overflow, experiments with flow rates higher than this were not conducted. In **Figure 7(d)** ($t = t_0 + 10$ s), the driftwood is trapped, generating hydrostatic pressure, with the deposition height h_s = 112 mm. It was found that driftwood flows downstream in a driftwood clump and collides with driftwood catchments. It was also found that the shape of the driftwood clumps flowing downstream changed depending on the flow velocity and that there were differences in the flow conditions from the impact of the driftwood clumps to their deposition.

3.2 Driftwood trapping efficacy

Considering that the effect of the applied load is related to the trapping efficacy. The driftwood trapping efficacy is calculated as *T* (%). **Figure 8** plots the driftwood trapping rates for all the cases. The driftwood trapping efficacy was greater than 70 % in all cases.

3.3 Maximum impact Load

The experimental results showed that after five runs, the behaviour in each case was almost identical. Similar behaviour was observed under other conditions; therefore, **Figure 9** plots the relationship between load and time as a representative example. The load reaches the maximum value immediately after generation, which then gradually converges and settles at a certain load. Such load transitions can be divided into three sections on the time axis, the section from when the driftwood collides to when it reaches the maximum collision load, called the “impact zone”, the maximum impact load transitions to hydrostatic pressure, and the transition zone wherein the load transforms into hydrostatic pressure is called the “deposition zone.” **Figures 9(a)** and **(b)** show the relationship between load and time when is θ = 5 °, Q = 2.3 L/s, 6.9 L/s. The maximum impact load increased with the flow rate, and the impact zone was shortened. This was because the flow rate increased, and the driftwood collided faster. Moreover, the deposition zone was lengthened, because the amount of water stored in the driftwood changed depending on the flow rate. **Figure 9(c)** plots the relationship between load and time when is θ = 1 ° and Q = 6.9 L/s. The maximum load increased with the gradient. Based on these observations, we classified the relationship between the driftwood load and time into three zones: impact, transition, and deposition zones. Moreover, the three factors of the number of driftwood pieces, flow rate, and gradient significantly affect the response of the driftwood load.

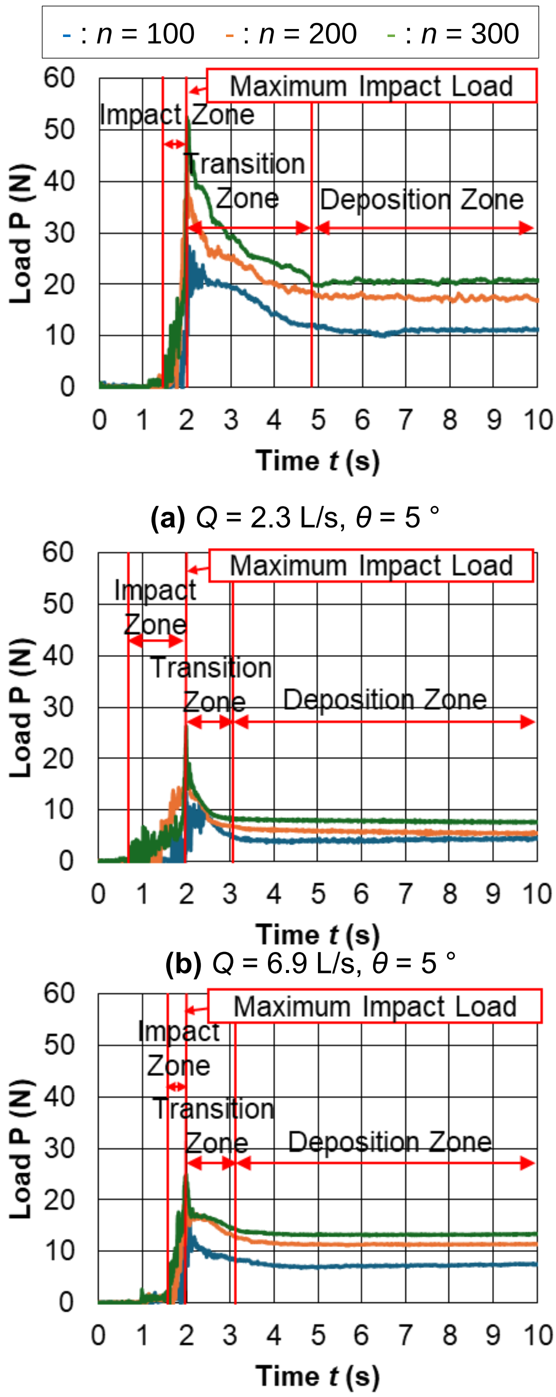

(a) Q = 2.3 L/s, θ = 5 °

(b) Q = 6.9 L/s, θ = 5 °

(c) Q = 6.9 L/s, θ = 1 °

Figure 9. Load–Time Relationship

3.4 The effect of driftwood groups on maximum impact loads

Figure 10 shows the relationship between maximum impact load and driftwood group velocity

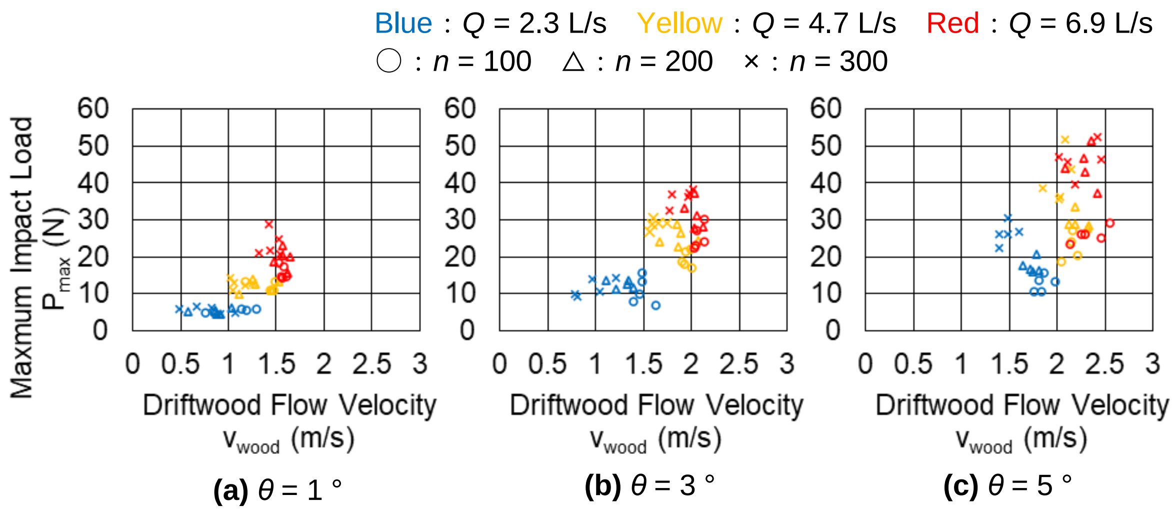

Figure 10. Maximum impact load - Driftwood flow Velocity

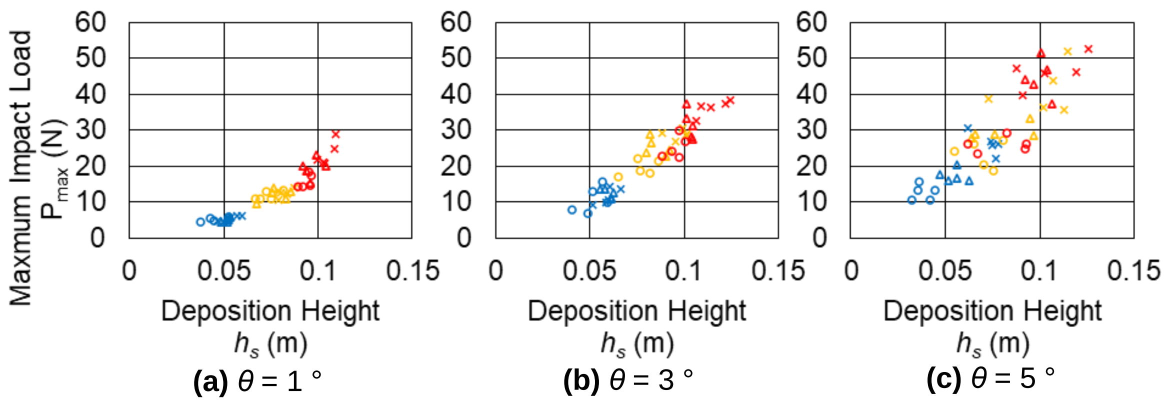

Figure 11. Maximum impact load - Deposition Height

for each gradient, with maximum impact load - driftwood group velocity for gradients θ = 1 °, 3 °, and 5 °, respectively. When the flow rate was held constant and the number of driftwoods was focused on, it was confirmed that the driftwood group velocity tended to decrease as the number of driftwoods increased. However, the maximum impact load increased with the number of driftwoods despite the decrease in the driftwood velocity. The results showed that the velocity and maximum impact load tended to increase when the number of driftwoods was kept constant and the flow rate increased. When the number of driftwoods and flow rate were kept constant and the slope was varied, the driftwood velocity and maximum impact load showed an increasing trend. These results suggest that driftwood group velocity, a key factor, causes the maximum impact load. When the number of driftwoods was large, the velocity of the driftwood group decreased but the maximum impact load increased, indicating that the mass of the driftwood group affected the velocity and maximum impact load.

Figure 11 indicates the relationship maximum impact between the load–deposition height for slopes θ = 1 °, 3 °, and 5 °, respectively. **Figure 11(a)** shows that the deposition height tends to increase with the number of driftwood pieces under low-flow conditions. However, no significant changes were observed in the maximum impact loads. However, as the flow rate increased, the deposition height increased with the number of driftwood pieces, and the maximum impact load tended to increase proportionally with the increase in the number of driftwood pieces. **Figure 11(b)** shows that under low-flow conditions, the relationship between the maximum impinging load and deposition height did not change significantly regardless of the number of driftwood pieces. However, as the flow rate increased, both the maximum impingement load and deposition height tended to increase as the number of driftwood pieces increased. **Figure 11(c)** exhibits a clear tendency for the deposition height and maximum

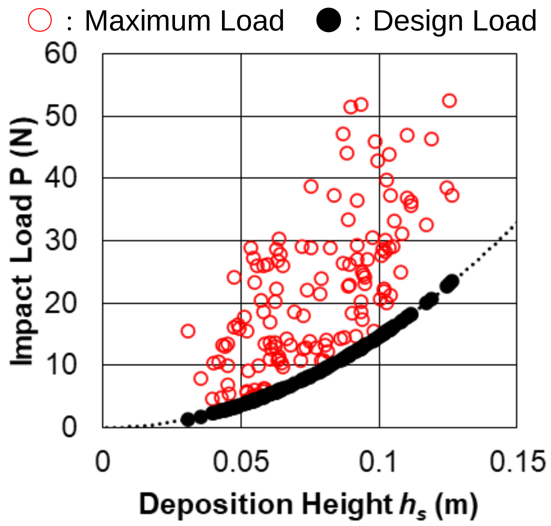

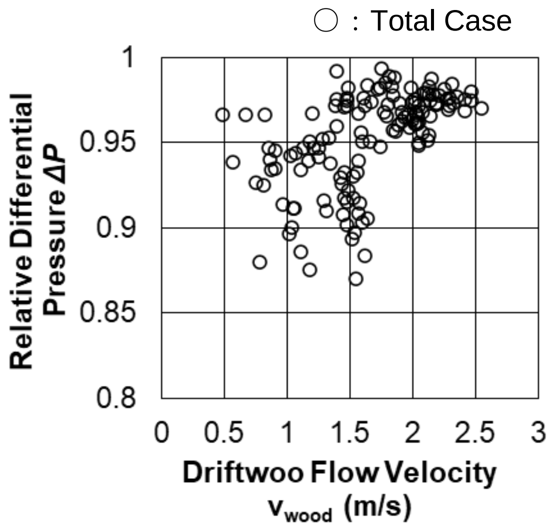

Figure 12. Design load and Experimental load **Figure 13.** Relative difference pressure

impact load to increase with the number of driftwood pieces and flow rate under all conditions. This result suggests that the relationship between deposition height and maximum impact load is most pronounced under high flow conditions.

3.5 Comparison between design load and maximum load of experiment

In the design of the driftwood catchment, a design that applies only a hydrostatic load is adopted, and the design formula is given by the following equation:

$$P_h = \frac{1}{2} \cdot \gamma_w \cdot \{(H + D_h) \cdot K_{hw}\}^2 \tag{1}$$

where, P_h: hydrostatic load (N), γ_w: unit weight of water (N/m^3), H: dam height (m), D_h: overflow depth (m), K_{hw}: hydrostatic coefficient (= 1.0).
In design, the unit weight of water was set at γ_w = 11.17 kN/m^3. Conversely, as water was used in this experiment, the water density was calculated as ρ = 1000 kg/m^3. In addition, the combined value of dam height and overflow depth represents the water depth. However, the pileup height h_s obtained from the experimental results were used in this experiment. **Figure 12** shows the maximum impact load P_{max} obtained from this experiment and the hydrostatic load P_h calculated using the design formula. The maximum impact loads were clearly larger. This shows the need to consider impact loads in relation to hydrostatic loads.

4 EXAMINATION OF DRIFTWOOD GROUPS LOAD

4.1 Relative differential pressure

Figure 13 shows the relationship between the relative pressure difference ΔP and the wood flow velocity v_{wood}. The relative pressure difference was calculated by subtracting the hydrostatic load P_h calculated from the design formula from the maximum collision load P_{max} and dividing the result by the maximum collision load P_{max}. This value is a dimensionless index that indicates the extent to which a purely dynamic collision load, excluding the hydrostatic load, accounts for the maximum collision load. As the wood flow velocity increased, the relative pressure difference approached 1.0. As the relative pressure difference is 0.86 or higher in all cases, it is believed that the maximum collision load is caused by fluid forces.

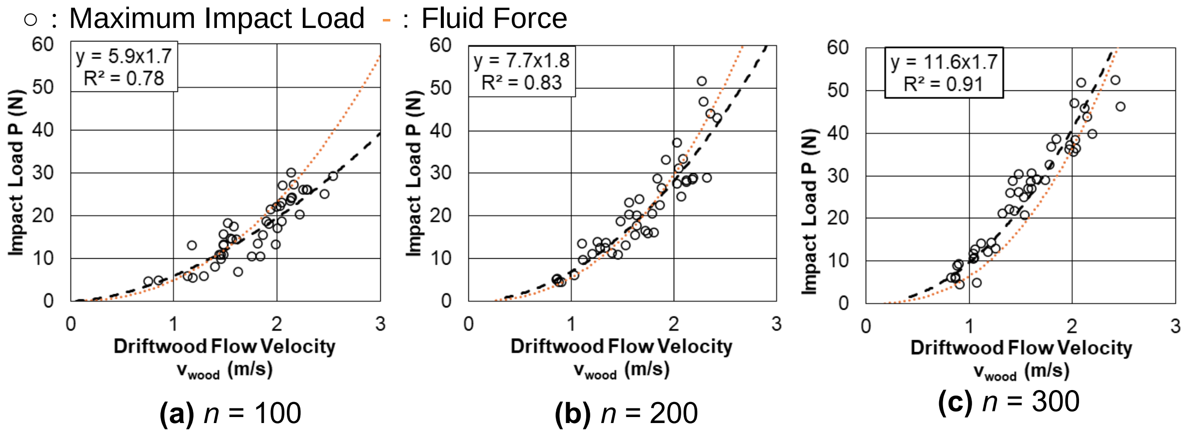

Figure 14. Maximum impact load - fluid force

4.2 Evaluation of fluid forces

Figure 14 shows the relationship between the maximum impact load and the flow velocity of the driftwood group. The data were organized according to the number of driftwood pieces. The results were obtained by applying a power approximation to each of the three datasets. These results show that there is a correlation between collision load and flow velocity. The exponent shown in **Figure 12** is close to the square of the flow velocity, suggesting that the fluid force may be the main cause of the collision load.
Compared the load of the driftwood group with the fluid force of the debris flow. The equation for the fluid force of the debris flow is as follows:

$$F_{flow} = \frac{\gamma_d}{g} \cdot W \cdot D_d \cdot U_d^2 \tag{2}$$

Where, F_{flow} : debris flow fluid force (N), γ_d : unit weight of debris flow (N/m³), g : gravitational acceleration (m/s²), W : riverbed width (m), D_d : debris flow depth (m), U_d : average flow velocity of debris flow (m/s).
Figure 14 plots the relationship between the value calculated from Eq.(2) and the flow velocity of the driftwood group. When calculating the value from Eq.(2), the flow depth hf and flow velocity of the driftwood group v_{wood} obtained from this experiment were used for the debris flow depth D_d and the average velocity U_d of the debris flow. In this experiment, the density of water was used for the debris flow density γ_d/g. Many of the experimental values were approximately the same as the load of the debris flow fluid force. Although further consideration is needed regarding the evaluation of the detailed specific gravity and maximum impact load of driftwood groups based solely on debris flow fluid forces, it was confirmed that the evaluation of the acting load on driftwood groups based on the debris flow fluid force equation has a certain degree of validity. These results demonstrate that the design accuracy of driftwood catchments can be improved further by incorporating impact forces into the load acting on the driftwood groups.

5 CONCLUSIONS

This study characterized the impact loads acting on driftwood catchments by analysing the impact load factors of a driftwood group. The experimental results were compared based on the hydrostatic loads and forces of debris flow.
1) When the driftwood flows as a group, it produces an impact load on the driftwood catchment. The load exerted by driftwood groups on driftwood catchments can be divided into three categories: impact, transition, and depositional zones.

2) The maximum impact load due to the driftwood group was found to be affected by the number of driftwoods, the velocity of the group, and the height of the pile. The maximum impact load was clearly larger than the hydrostatic load.
3) The maximum impact load was correlated with the velocity of the driftwood groups. This exponential relationship is like that of the debris flow fluid force, suggesting that hydrodynamic forces may be the main cause of the impact load.

This study suggests that the impact load characteristics of driftwood groups may be caused by fluid forces. However, there are still many unresolved issues regarding the density of driftwood groups, the effect of driftwood shape, and fluid density, including scoured sand, which need to be investigated through experiments and analysis.

REFERENCES

[1] Ministry of Land, Infrastructure, Transport and Tourism, "*Regarding the heavy rains of July2020*", Water Management and Disaster Management Bureau of the Ministry of Land, Infrastructure, Transport and Tourism Meeting Materials, 2021.

[2] S. Uchiyama,and T. Danjo, "*Characteristics of the flood disaster in Hitoyoshi City and the Wataeri district id Kumamura, Kumamoto Prefecture, caused by the heavy rains of July 2020*" Survey report 1st edition, July 9, 2020, National Research Institute for Faith Science and Disaster Resilience Survey Report, 2020.

[3] F. Akazawa, E. Takezawa, Y. Ishii, "*A study on the cause of the collapse of the sleeve of the Dukawa no.1 Sabo Dam during the heavy rains in northern Kyushu in July 2017*", Journal of the Erosion control Society, Vol.72, No.5, pp.15-36, 2020.

[4] Ministry of Land, Infrastructure, Transport and Tourism, National Institute for Land and Infrastructure Management, "*Guidelines for formulating basic erosion control plans (debris flow and driftwood countermeasures) and their explanations, Technical guidelines for designing debris flow and driftwood countermeasures and their explanations*" ,2018.

[5] Ministry of Land, Infrastructure, Transport and Tourism. Erosion Control Department "*Basic concept of countermeasure plan for driftwood washed away during landslides and floods (trial proposal)*", 2024.

[6] Ministry of Land, Infrastructure, Transport and Tourism, Water Management and Land Conservation Bureau, Sabo Department, "*Design Guidelines for Erosion Control Facilities Part 5: Design of Erosion Control Facilities in the Bed-flow Area*", March 2020.

[7] Y. Ishikawa, T. Mizuyama, M. Fukuzawa, "*Effect of sabo dams and driftwood screens on trapping driftwood*", Civil engineering data, Vol.31, No.9, pp.41-47, 2019.

[8] H. Shibuya, S. Katsuki, H. Osumi, N. Ishikawa, T. Mizuyama,"*Experimental study on woody debris trap performance of drift wood capturing structure*", Journal of the Japan Society of Erosion Control Engineering, Vol.63, No.3, pp.34-41, 2010.

[9] H. Kokuryou, H. Shibuya, S. Katsuki, N. Ishikawa, T. Mizuyama,"*Experimental study on load acting on driftwood catchers*", Abstracts of the Japan Society of Erosion Control Engineering Research Presentation, pp.308-309, 2011.

[10] T. Yamada, H. Nakatani, R. Inoue, M. Isimaru, T. Ishigaki, S. Katsuki, T. Horiguthi, "*A study on the load characteristics when capturing driftwood in driftwood capture works*", Abstracts of the FY2024 Society of Erosion Control Engineering Research Presentations, pp.91-92, 2024.

[11] T.Watanabe, T. Horiguchi, "*Load measurement experiment of a hangover-type driftwood catchment on an existing Sabo dam*", Journal of structure engineering, Vol.68A, pp.887-895, 2022.

[12] H. Matsutomi, "*Practical evaluation formula for driftwood impact force and its change characteristics*", Proceedings of the Japan Society of Civil Engineers, No.621/2-47, pp.111-127, 1999.

[13] M. Ikeno, H. Tanaka, "*Experimental study on the collision force between run-up*

tsunami and drifting debris", Journal of Coastal Engineering, Vol. 50, pp. 721-725, 2003.

[14] K. Mizuhara, A. Takei, T. Minami, "*Fundamental research on preventing drifting trees (II) - Impact force and retention rate of driftwood on fence-like structures -*", Journal of the Japan Society Erosion Control Society, No. 114, 1980.

[15] H. Shibuya, S. Katsuki, H. Osumi, H. Kokuryou, "*Investigation of driftwood caused by heavy rain at Shobara, Hiroshima on July 16, 2010*" Journal of the Japan Society Erosion Control Society, Vol.64, No.1, pp.34-39, 2011.

15th International Conference on
Shock & Impact Loads on Structures
12-13 June 2025, Gothenburg, Sweden

INVESTIGATING KEY PARAMETERS FOR OPTIMISING BLAST DOOR PERFORMANCE

Sherlene Ng*, Paolo Del Linz*, and Le Shen*

*Cluster of Engineering, Singapore Institute of Technology, 138683, Singapore

Emails: Sherlene.Ng@singaporetech.edu.sg; Paolo.DelLinz@singaporetech.edu.sg

Keywords: OpenRadioss; blast protection; door optimisation; ironmongery

Abstract. *Blast protection is critical for the safety and security of critical infrastructures, such as data centres and government facilities. One of the key components in blast-resistant structures is the blast door, which serves as a protective barrier against shock waves and debris. Traditionally, blast doors are typically designed with high safety margins, making them excessively heavy and costly due to increased material usage. To address this challenge, this study aims to optimize blast door designs by examining the effects of three key parameters: the number of stiffeners, panel thickness and the presence of ironmongery, on overall structural behaviour. Typically, blast doors are constructed using two steel plates reinforced with stiffeners, such as C-sections or I-beams, to withstand blast loads. To evaluate the structural behaviour of various design configurations under a bare charge blast, finite element analysis (FEA) simulations were conducted using OpenRadioss. Key performance metrics, including central deflection, deflection angle, and internal energy, were analysed to assess the blast performance. The findings from this study provide significant insights into the structural behaviour of blast doors, allowing us to identify an optimal configuration of stiffener count and panel thickness. This optimised configuration minimises material usage and overall weight while still maintaining structural integrity and compliance with safety standards.*

1 INTRODUCTION

With an increase in war and terrorist attack occurrences all over the world, many critical infrastructures such as data centres and government facilities have become vulnerable targets [1]. Blast protection has become a crucial for these infrastructures to maintain their operations and minimise economic losses in the event of an attack. The blast door is a key component in blast-resistant structures as it acts as a shield against shock waves and debris. Many numerical studies have been conducted to investigate the effectiveness of various blast door designs, which generally fall into three categories. The first category consists of traditional designs which employ steel panels reinforced with stiffeners [2], [3], [4], [5]. In these designs, the stiffeners are typically C-sections or I-beams which enhance the structural strength of the door by distributing blast loads over a larger area. The second category comprises of reinforced concrete doors [6], [7] which rely on the mass of concrete to withstand blast impacts. The third category consists of novel designs incorporating a sandwich core [8], [9], [10], [11] which absorbs and dissipates blast wave energy, thereby protecting the structure from deformation. These cores can be made from materials such as honeycomb, auxetics, metal foams, rubber or damping mechanisms.

Existing numerical studies have primarily focused on modelling of the door panels and core, often neglecting other crucial components such as the ironmongery, which includes hinges and locking mechanisms. The role of ironmongery in blast performance remains largely unexplored, despite its potential impact on blast performance. Additionally, traditional blast door designs adopt high safety margins which often exceed the required safety standards and performance criteria. While this approach ensures the robustness of the door, it also results in an excessively heavy and costly design due to increased material usage [12], [13]. These limitations underline the need for a more comprehensive blast door model that incorporates ironmongery while optimizing material efficiency.

To address these limitations, this study aims to develop a more comprehensive blast door model which incorporates ironmongery to evaluate its impact on blast performance. This study also aims to optimize blast door designs by examining the effects of two key parameters: number of stiffeners and panel thickness, on overall structural behaviour.

2 BLAST DOOR CONFIGURATIONS AND NUMERICAL MODELLING

2.1 Blast Door Configurations

Two initial standard designs were examined in this study. The first design features C-sections spanning horizontally between two panels. Each C-section has a depth of 50 mm and width of 100 mm, while each panel measures 2152 mm in height and 1052 mm in width. The configurations of the C-section model are labelled C0-C3 (Figure 1), where C0 represents the initial design. As shown in Table 1, the number of C-sections varies from 5 to 8, while the thickness of the panel varies from 9 mm to 6 mm. All the configurations include ironmongery, with an additional configuration excluding ironmongery denoted as C0-a (Figure 2).

The second design features I-beams spanning vertically between two panels. Each I-beam has a depth of 222.2 mm and a width of 209 mm, while each panel measures 5940 mm in height and 2740 mm in width. The configurations of the I-beam model are labelled I0-I3 (Figure 1), where I0 represents the initial design. As shown in Table 1, the number of I-beams varies from 6 to 3, while the panel thickness varies from 10 mm to 13 mm. All the I-beam models include ironmongery, with an additional configuration excluding ironmongery denoted as I0-a (Figure 2).

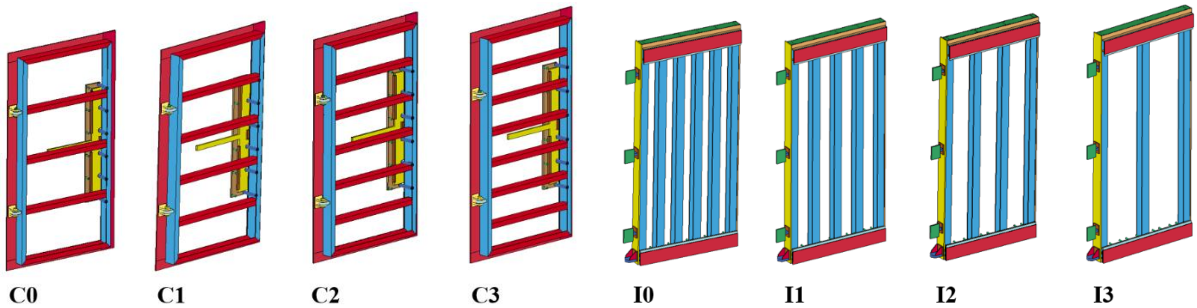

Figure 1. Various configurations of the C-section and I-beam model

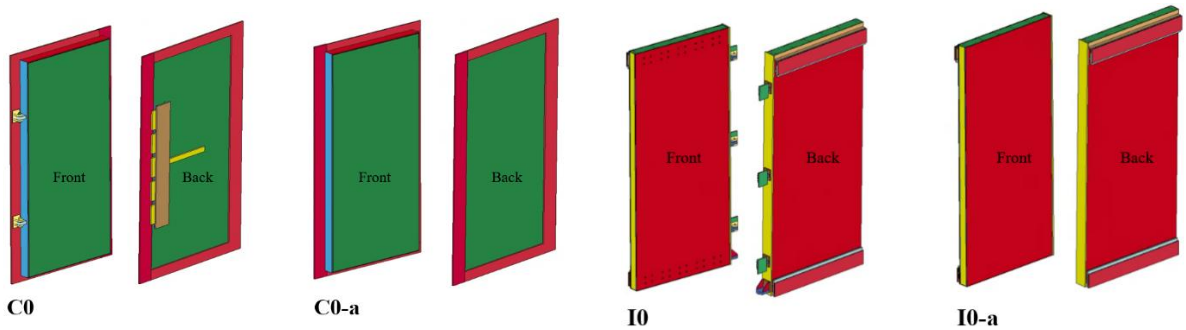

Figure 2. Initial designs with and without ironmongery

Table 1. Number of stiffeners and panel thickness for each configuration

Model	Number of stiffeners	Panel thickness (mm)	Ironmongery included
C0	5	9	Yes
C1	6	8	Yes
C2	7	7	Yes
C3	8	6	Yes
C0-a	5	9	No
I0	6	10	Yes
I1	5	11	Yes
I2	4	12	Yes
I3	3	13	Yes
I0-a	6	10	No

2.2 Numerical Modelling

OpenRadioss [14] was used to simulate the response of various door configurations under a bare charge load. The doors are constructed of structural-grade steel S355, known for its good impact resistance and toughness. The strain rate effects were taken into consideration using the Johnson-Cook material model [15], with the governing equation (1) as follows:

$$\sigma = [A + B\varepsilon^n][1 + C\ ln\dot{\varepsilon}^*][1 - T^{*m}] \tag{1}$$

ε is the equivalent plastic strain, $\dot{\varepsilon}^* = \frac{\dot{\varepsilon}}{\dot{\varepsilon}_0}$ is the dimensionless plastic strain rate for $\dot{\varepsilon}_0 = 1.0s^{-1}$, T^* is the homologous temperature, and the material constants are represented by A, B, n, C, m. Table 2 lists the material's mechanical properties and Johnson-Cook parameters.

Table 2. Mechanical properties and Johnson-Cook parameters [16]

$\rho\ (kg/m^3)$	$E\ (MPa)$	v	$A\ (MPa)$	$B(MPa)$	n	C
7850	210,000	0.3	350	234	0.643	0.076

All door components, including the panels, stiffeners, supports, ironmongery, were modelled using a standard eight-node solid element with a single Gauss integration point. A minimum of 3 elements was used to represent the thickness, with an element size not exceeding 10mm to ensure that the element thickness remains at least one-fifth of its in-plane dimension. Blast loading was modelled using /PLOAD which functions similarly to CONWEP [17] as both are intended to simulate the maximum blast pressure load on structures. /PLOAD applied a uniformly distributed pressure of 2 MPa on the target panel over a 3 ms duration, based on a realistic design scenario.

For boundary conditions, the door supports and hinge bolts were constrained to prevent translational movement, aligning with the case of a simply supported beam under a uniformly distributed load. General contacts between components were modelled using /INTER/TYPE24, while tied contacts were modelled using /INTER/TYPE2. Spot welds with a diameter of 26.6 mm, were placed at 200 mm intervals along the length of the stiffeners. The total duration of the simulation was 50 ms.

To evaluate the blast performance, three evaluation metrics were considered: central deflection, deflection angle and internal energy. The deflection angle corresponds to the ratio of the maximum central deflection at the centre of the door to its height (Figure 3). For structural steel doors, the deflection angle should not exceed 2 degrees as per the United Facilities Guide Specifications (UFGS 08 39 54) [18] to ensure the door remains functional after blast.

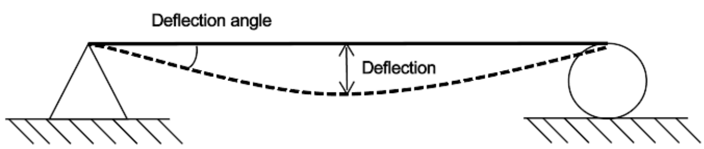

Figure 3. Deflection angle

3 RESULTS & DISCUSSION

3.1 Overall Structural Behaviour

Analysis of Figure 4 revealed a common observation across the C-section configurations, where majority of the deflection occurs at the centre of the panel. Areas of the panel not in direct contact with the stiffeners displayed greater deflections compared to areas in direct contact. This observation was evident in both the front and back panels. Amongst the various configurations, C2 displayed the largest deflection across the panel while C3 displayed the smallest. In Figure 5, the I-beam configurations revealed a similar pattern, with majority of the deflection occurring at the centre of the panel and greater deflections observed in areas not in direct contact with the stiffeners. Amongst the various configurations, I3 displayed the largest deflection across the panel while I0 displayed the smallest.

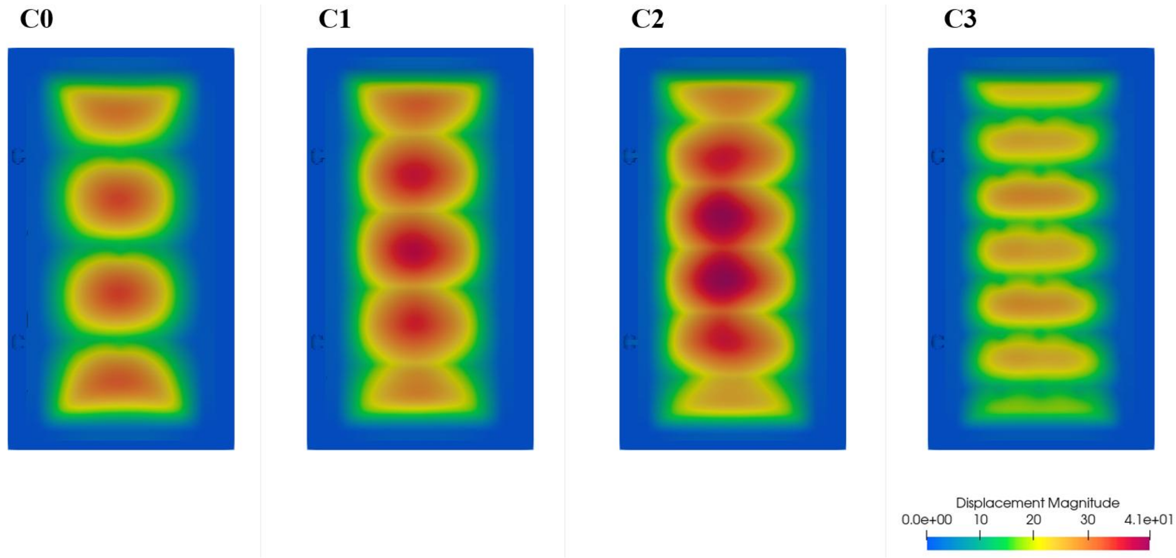

Figure 4. Deflection of the front panel for C-section configurations C0-C3 at 10ms

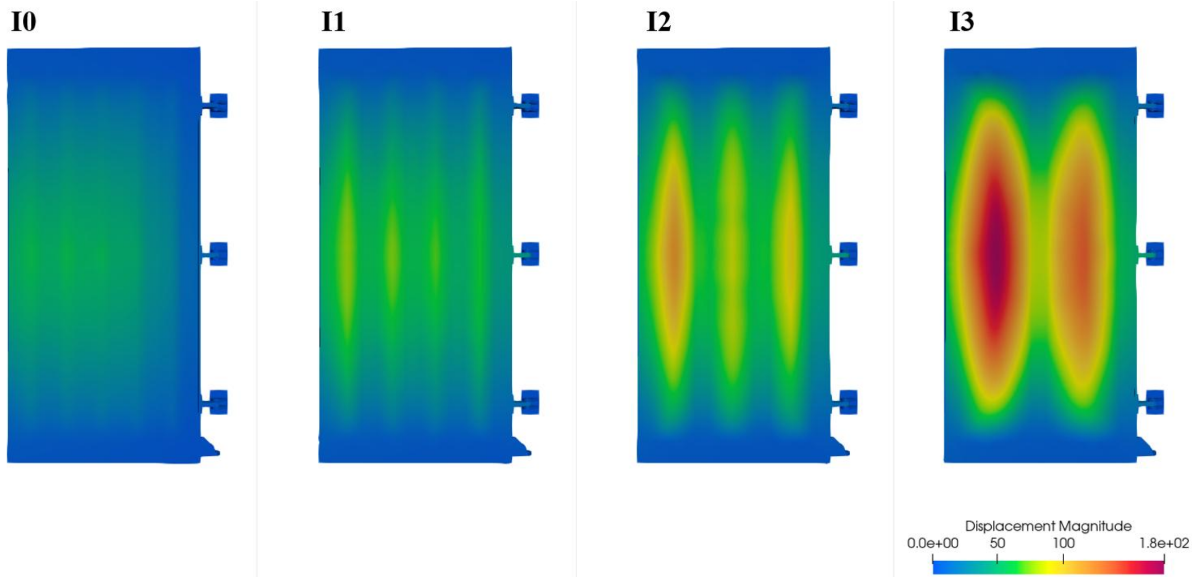

Figure 5. Deflection of the front panel for I-section configurations I0-I3 at 10ms

Figures 6 and 7 illustrate the deflections of both C-section and I-beam models in the absence of ironmongery. In both cases, the deflection across the entire panel increased slightly when ironmongery was excluded. In Figures 8 & 9, the maximum plastic strain remained relatively unchanged when ironmongery was excluded. To determine the material's yield strain, the yield strength is divided by the Young's modulus, as obtained from Table 2. Since the maximum plastic strain did not exceed the material's yield strain of 0.167%, the deformation remained fully reversible, and no permanent damage occurred.

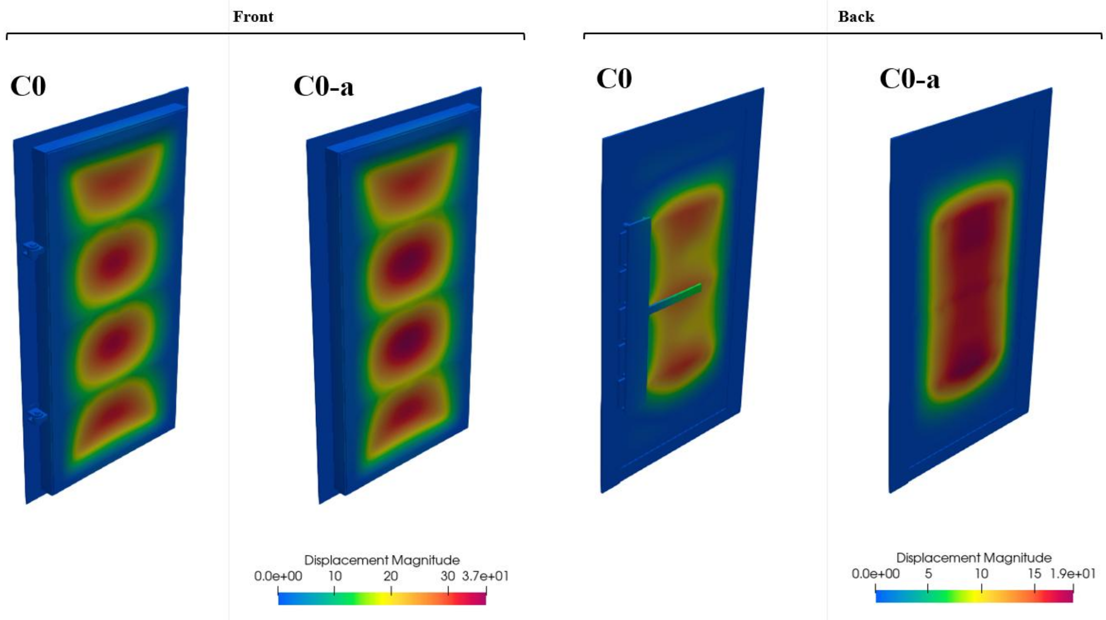

Figure 6. Deflection of C-section model with (C0) and without ironmongery (C0-a) at 10ms

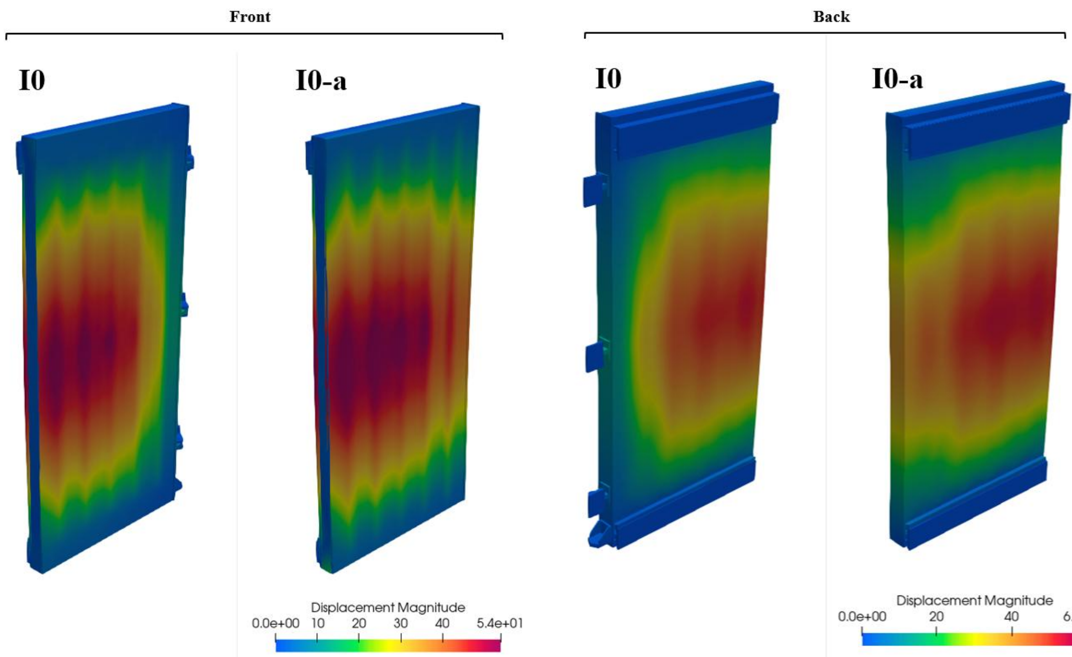

Figure 7. Deflection of I-beam model with (I0) and without ironmongery (I0-a) at 10ms

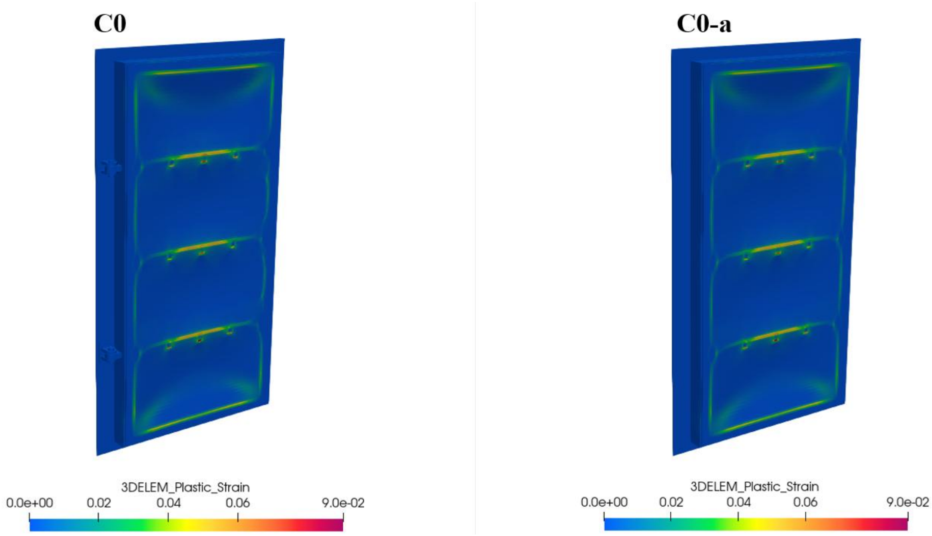

Figure 8. Plastic strain of C-section model with (C0) and without ironmongery (C0-a) at 50ms

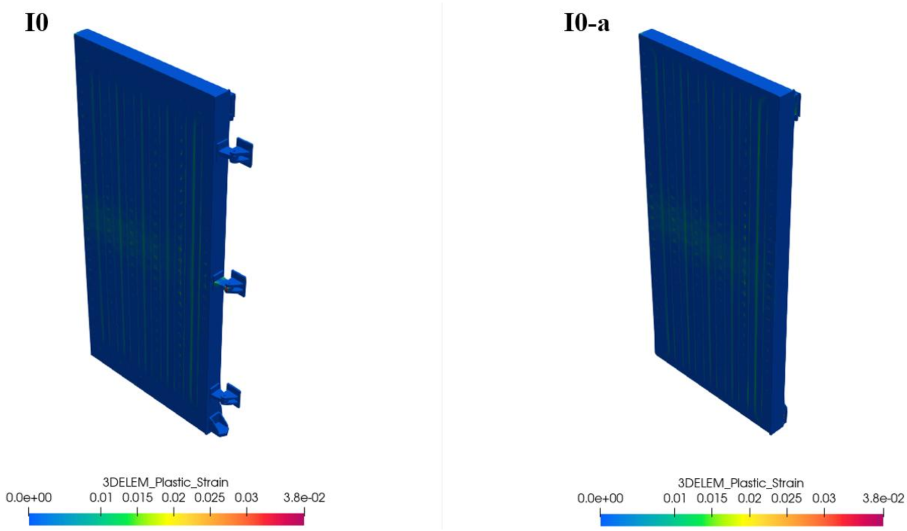

Figure 9. Plastic strain of I-beam model with (C0) and without ironmongery (C0-a) at 50ms

3.2 Deflection and Energy Response

In the C-section model, the maximum central deflection, deflection angle and internal energy increased gradually from C0 to C2, before decreasing at C3 (Table 3). This can be explained by the fact that the results only considered the deflection at the centre node of the panel. Since the placement of the stiffeners vary across configurations, the deflection at this node would naturally be smaller if it aligns directly with the stiffener, as this provides additional structural support. Across all configurations, the deflection angles were below 2 degrees. The smallest maximum central deflection and internal energy recorded were 22.50 mm and 43.70 kJ respectively (Figure 10), noted in configuration C3 consisting of eight stiffeners and a 6 mm panel thickness. A similar trend was observed in the I-beam model. As shown in Table 3, the maximum central deflection and deflection angle increased from I0 to I2, with a notable spike between I1 to I2, before decreasing at I3. Across all configurations, the deflection angles were below 2 degrees. The smallest maximum central deflection and internal energy recorded were

55.70 mm and 188.00 kJ respectively (Figure 11), noted in configuration I0 which consists of six stiffeners and a 10 mm panel thickness.

When ironmongery was excluded from both models, slight differences in results were observed (Figures 10 & 11). In the C-section model, maximum central deflection and maximum internal energy increased by 4.28% and 2.75% respectively, while in the I-beam model, these values increased by 4.48% and 8.51%. This observation could be attributed to a reduction in the overall structural stiffness, as hinges and locking mechanisms contribute to the rigidity of the door. Additionally, ironmongery might have enhanced the damping within the door system, thereby reducing deflection. These observations suggest that incorporating ironmongery in numerical modelling has a small but measurable impact on blast performance.

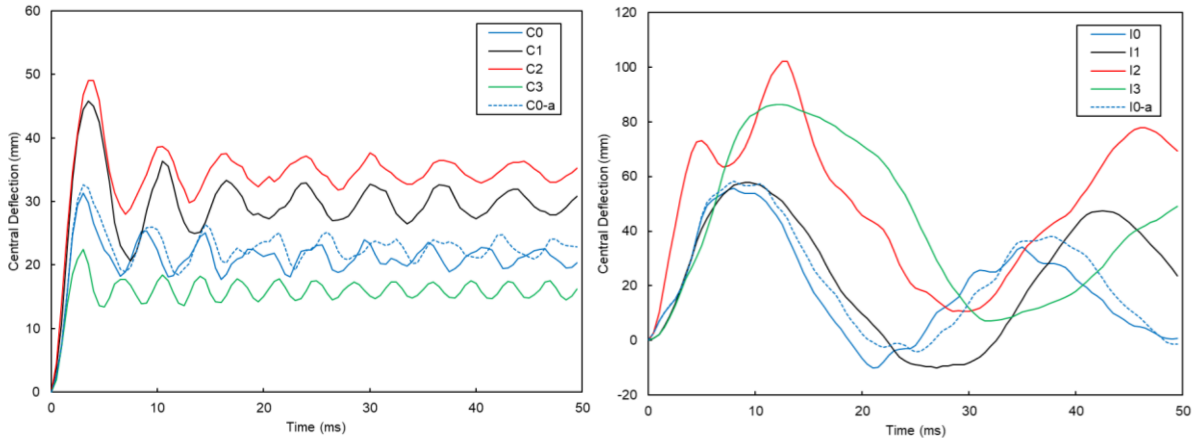

Figure 10. Central deflection of the C-section (left) and I-beam (right) configurations

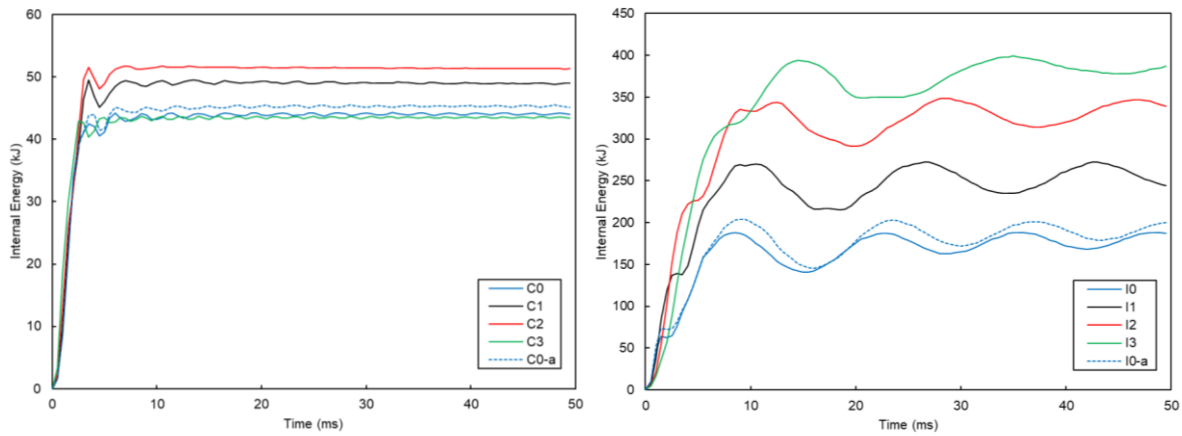

Figure 11. Internal energy of the C-section (left) and I-beam (right) configurations

Table 3. Maximum central deflection, deflection angle and maximum internal energy of various configurations

Model	Maximum Central Deflection (mm)	Deflection Angle (°)	Maximum Internal Energy (kJ)
C0	31.30	1.67	44.30
C1	45.80	2.44	49.50
C2	49.00	2.61	51.80
C3	22.50	1.20	43.70
C0-a	32.64	1.74	45.52
I0	55.70	1.07	188.00
I1	57.70	1.11	272.00
I2	102.00	1.97	348.00
I3	86.20	1.66	399.00
I0-a	58.20	1.12	204.00

3.3 Optimal Door Configuration

With reference to Figure 12, the total weight of each door was calculated to determine the optimal configuration. The weight comprises of the door panels, core and supports. For the C-section model, configuration C3 consisting of eight stiffeners and a 6 mm panel thickness was identified as the most optimal design. It demonstrated the smallest maximum central deflection, deflection angle and maximum internal energy, while also weighing the least.

For the I-beam model, configuration I3 consisting of three stiffeners and a 13 mm panel thickness, was identified as the most optimal design. Although it did not demonstrate the smallest maximum central deflection, deflection angle or maximum internal energy, it was the lightest configuration. Its deflection angle was also within the acceptable 2-degree threshold as specified by the UFGS design guide for blast resistant doors. Thus, this configuration would remain functional post-blast and represented as a viable design.

By adopting these optimised configurations, the weight of the C-section and I-beam doors could potentially be reduced by 21.53% and 12.57% respectively. This contributes to reduced material usage and cost while complying with safety standards and performance requirements.

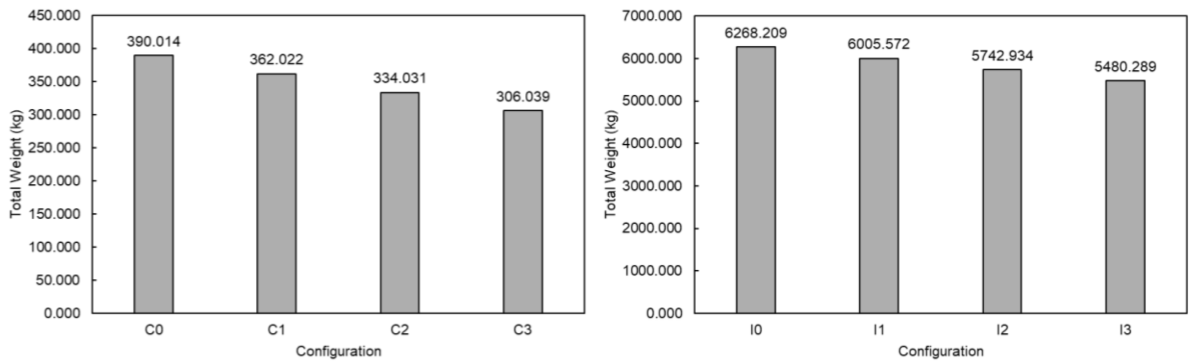

Figure 12. Total weight of each C-section (left) and I-beam (right) configuration

4 CONCLUSION

In this study, a comprehensive blast door model was developed by incorporating ironmongery, a component often overlooked in numerical simulations. Additionally, by examining the influence of stiffener count and panel thickness on overall structural behaviour, this study offered insights into the optimal design configuration of a blast door for balancing structural integrity and material efficiency. The key findings are as such:

1. Incorporating ironmongery in numerical modelling has a small but measurable impact on blast performance. The results showed a minor reduction in maximum central deflection, deflection angle and maximum internal energy in the presence of ironmongery.
2. In the C-section model, increasing stiffener count while decreasing panel thickness reduced maximum central deflection and deflection angle. The optimal configuration was identified as eight stiffeners and a panel thickness of 6 mm, bringing about a potential weight reduction of 21.53%.
3. In the I-beam model, decreasing stiffener count while increasing panel thickness increased maximum central deflection and deflection angle. However, as the deflection angle was within an acceptable 2-degree threshold, the design remained viable. The optimal configuration was identified as three stiffeners and a panel thickness of 13 mm, bringing about a potential weight reduction of 12.57%.

It is important to acknowledge that this study modelled only the positive phase of the blast loading. As the negative phase was not considered, the influence of ironmongery on the overall blast performance of the door may not be fully captured. Furthermore, since these findings are derived from numerical simulations, future research should incorporate experimental testing to validate the reliability of these optimised design configurations.

ACKNOWLEDGEMENT

This work is supported by Construction Technology Innovation Laboratory (CTIL) in SIT, Woh Hup Pte. Ltd., TTJ DE Pte. Ltd, National Research Foundation, Singapore, and Building and Construction Authority (BCA) under its Built Environment Technology Alliance (BETA) Catalyst Funding Grant (Award No: BETA-20230224004).

DISCLAIMER

This work is partly funded by National Research Foundation, Singapore and Building and Construction Authority (BCA) Singapore under its Built Environment Technology Alliance (BETA) Catalyst Funding Grant (Award No: BETA-20230224004). Any opinions, findings and conclusions or recommendations expressed in this material are those of the authors and do not reflect the views of the National Research Foundation, Singapore and the Building and Construction Authority (BCA) Singapore.

REFERENCES

[1] United Nations Security Council Counter-Terrorism Committee, 'Compendium of good practices on the protection of critical infrastructure against terrorist attacks', 2021. [Online]. Available:

https://www.un.org/securitycouncil/ctc/sites/www.un.org.securitycouncil.ctc/files/files/documents/2021/Jan/compendium_of_good_practices_eng.pdf
[2] V. A. Salomoni, G. Mazzucco, G. Xotta, R. Fincato, C. E. Majorana, and M. Schiavon, 'Nonlinear modelling, design, and test of steel blast-resistant doors', *Advances in Mechanical Engineering*, vol. 5, p. 908373, Jan. 2013, doi: 10.1155/2013/908373.
[3] L. S. B. Veeredhi and N. V. Ramana Rao, 'Studies on the impact of explosion on blast resistant stiffened door structures', *J. Inst. Eng. India Ser. A*, vol. 96, no. 1, pp. 11–20, Mar. 2015, doi: 10.1007/s40030-014-0103-x.
[4] Y. Choi, J. Lee, Y.-H. Yoo, and K.-J. Yun, 'A study on the behavior of blast proof door under blast load', *Int. J. Precis. Eng. Manuf.*, vol. 17, no. 1, pp. 119–124, Jan. 2016, doi: 10.1007/s12541-016-0015-y.
[5] B. Zhang, H. Chen, Z. Zhao, H. Fan, and F. Jin, 'Blast response of hierarchical anisogrid stiffened composite panel: Considering the damping effect', *International Journal of Mechanical Sciences*, vol. 140, pp. 250–259, May 2018, doi: 10.1016/j.ijmecsci.2018.03.007.
[6] S. Lan, T.-S. Lok, and L. Heng, 'Composite structural panels subjected to explosive loading', *Construction and Building Materials*, vol. 19, no. 5, pp. 387–395, Jun. 2005, doi: 10.1016/j.conbuildmat.2004.07.021.
[7] H.-S. Shin, S.-W. Kim, J.-H. Moon, and W.-W. Kim, 'FE analysis on the structural behavior of a double-leaf blast-resistant door according to the support conditions', *jcoseik*, vol. 33, no. 5, pp. 339–349, Oct. 2020, doi: 10.7734/COSEIK.2020.33.5.339.
[8] X. Li, C. Miao, Q. Wang, and Z. Geng, 'Antiknock performance of interlayered high-damping-rubber blast door under thermobaric shock wave', *Shock and Vibration*, vol. 2016, pp. 1–9, 2016, doi: 10.1155/2016/2420893.
[9] K. Ganorkar, M. D. Goel, and T. Chakraborty, 'Numerical analysis of double-leaf composite stiffened door subjected to blast loading', *J. Perform. Constr. Facil.*, vol. 37, no. 1, p. 04022067, Feb. 2023, doi: 10.1061/(ASCE)CF.1943-5509.0001783.
[10] N.-R. Yun, D.-H. Shin, S.-W. Ji, and C.-S. Shim, 'Experiments on blast protective systems using aluminum foam panels', *KSCE J Civ Eng*, vol. 18, no. 7, pp. 2153–2161, Nov. 2014, doi: 10.1007/s12205-014-0092-3.
[11] H. Al-Rifaie, W. Sumelka, and P. W. Sielicki, 'Application of passive damping systems in blast resistant gates: doctoral thesis', Wydawnictwo Politechniki Poznańskiej, Poznań, 2019.
[12] F. Meng, B. Zhang, Z. Zhao, Y. Xu, H. Fan, and F. Jin, 'A novel all-composite blast-resistant door structure with hierarchical stiffeners', *Composite Structures*, vol. 148, pp. 113–126, Jul. 2016, doi: 10.1016/j.compstruct.2016.03.066.
[13] Meng Fan Mao, Xu Ying, Gong Hua Dong, Ma Shu Na, and Wu Xiao Yan, 'Review on design and research of protective door', *Sichuan Ordnance Journal*, no. 10, pp. 161–164, 2015.
[14] Altair Radioss, *OpenRadioss*. (2025). Altair Engineering. [Online]. Available: https://www.openradioss.org.
[15] Gordon R. Johnson and William H. Cook, 'A constitutive model and data for metals subjected to large strains, high strain rates, and high temperatures', in *Proceedings of the 7th International Symposium on Ballistics*, Apr. 1983, pp. 541–547.
[16] M. M. Rana, A. Khan, P. Del Linz, C. K. Lee, and T. C. Fung, 'Effect of cased charges on plain steel and steel-concrete sandwich targets', *Thin-Walled Structures*, vol. 136, pp. 302–314, Mar. 2019, doi: 10.1016/j.tws.2018.12.022.
[17] D. W. Hyde, 'User's guide for microcomputer programs ConWep and FunPro, applications of TM 5-855-1: Fundamentals of protective design for conventional weapons', U.S. Army Engineer Waterways Experiment Station, 1988.
[18] U.S. Department of Defense, 'United Facilities Guide Specifications (UFGS) 08 39 54: Blast resistant doors', Aug. 2009. [Online]. Available: https://www.wbdg.org/FFC/DOD/UFGS/UFGS%2008%2039%2054.pdf

15th International Conference on
Shock & Impact Loads on Structures
12-13 June 2025, Gothenburg, Sweden

EFFECT OF PARTIAL CONFINEMENT ON VAPOUR CLOUD EXPLOSIONS ON A ROAD: A NUMERICAL STUDY

Fabio Lozano[a], Morgan Johansson[a, b], Joosef Leppänen[a], Mario Plos[c]

[a]Chalmers University of Technology, Sweden, email: fabio.lozano@chalmers.se
[b] Norconsult Sverige AB, Sweden,
[c] Swedish Transport Administration, Sweden

Keywords: vapour cloud explosions, traffic environment, computational fluid dynamics, overpressure

Abstract

An accidental release of flammable gas during transport may enable the formation of a premixed cloud of fuel gas and air on the road. In a confined or obstructed environment, combustion of such a gas cloud may result in a powerful vapour cloud explosion (VCE). On an open road, partial confinement or obstruction may occur due to the presence of vehicles. Indeed, the region between the vehicles and the ground, where the flow is largely two-dimensional, is a likely source of strong blast. Fixtures on the road, such as noise barriers, may also enhance the strength of the resulting explosion. While VCEs in industrial settings have been extensively researched, little research work has been devoted to gas explosions in open traffic environments. Therefore, more research efforts in this type of environment are needed to complement the current knowledge. This article presents a numerical investigation of different geometrical parameters that influence the degree of confinement of gas clouds in a traffic environment. Several scenarios consisting of a stoichiometric mixture of propane and air engulfing a group of vehicles were studied. The parameters of interest were the uncertainty in the location of the vehicles, the influence of noise barriers, and the ground clearance. The investigation was conducted using Computational Fluid Dynamics. A considerable influence on the resulting explosion due to the variation of the three studied parameters was observed. Infinitely rigid noise barriers were shown to enhance the explosion strength by up to 30 %. Even barriers that failed at a low overpressure (5 kPa) enabled up to 20 % increase in overpressure. Likewise, varying the location of the vehicles (with regard to an ideal structured configuration) resulted in increased peak overpressure and impulse by approximately 30 % in the critical regions. Finally, in scenarios with a single vehicle, the maximum overpressure was found to decrease as the ground clearance increased. However, in cases with multiple vehicles, the overpressure increased with increasing ground clearance. Overall, the study highlighted the usefulness of Computational Fluid Dynamics methods for evaluating VCEs in traffic-related settings.

1. INTRODUCTION

In many countries, flammable gases, such as liquified petroleum gas (LPG) and liquified natural gas (LNG), are transported by road with high frequency and at large volumes. An accidental release of such a gas during transport may result in a catastrophic vapour cloud explosion (VCE). A VCE is defined as the violent combustion of a premixed cloud of a fuel gas and air that produces high values of overpressure and temperature. Furthermore, VCEs generate a blast wave that propagates away from the centre of the explosion, potentially extending the affected zone.

A premixed cloud (also known simply as a gas cloud) is formed in conjunction with delayed ignition, which allows for the leaking fuel gas to mix with the surrounding air. Given the right conditions, the cloud will disperse and engulf vehicles and other objects on the road and adjacent areas. The expansion of the cloud may enable the formation of pockets of flammable mixture in regions with a significant degree of confinement and congestion. These two factors play a vital role in the strength (i.e. the overpressure generated by the explosion) and overall characteristics of the resulting explosion. Confinement limits the free expansion of the flow, which boosts flame acceleration. The interaction of the flow with obstacles ahead of the flame produces turbulent vortices, which also contribute to flame acceleration. Hence, since the overpressure increases with flame acceleration, both confinement and congestion contribute to pressure buildup.

In a traffic environment, regions with partial confinement or congestion may appear due to the presence of vehicles. In this article, a traffic environment is defined as a location on or near a road where a group of vehicles is likely to be present in the event of an unintended spill of a flammable gas. In this type of environment, the vehicles are the main or only source of confinement or obstruction, which makes them the likely centre of strong blast should the gas cloud be ignited. Indeed, in the region underneath tightly parked vehicles, the flow is confined by two parallel surfaces. Moreover, the interaction of the flow with the wheels and other components under the vehicles may enhance flame acceleration. Other road fixtures of significant size, such as noise barriers, may also provide partial confinement and thus have an impact on the resulting explosion.

Structures near routes in which transport of flammable gasses is allowed may be affected either directly by the explosion or the ensuing blast wave. For the design of these structures, it is often necessary to estimate the characteristics of the resulting blast wave, which involves estimating blast wave parameters such as peak overpressure and peak impulse. A critical step in estimating the blast wave is the reliable prediction of the strength of the VCE. Because conducting experimental research is not possible in most situations, the best tools available for determining the strength of the VCE are codes based on Computational Fluid Dynamics (CFD). Indeed, several examples of evaluation of gas explosions using CFD are available in the literature. However, most of these studies are concerned with gas explosions in industrial settings, and only a few focus on gas explosions in traffic-related settings. Among the latter, two particular settings are the focus of most studies: vehicular tunnels, e.g. [1–3], and refuelling stations, e.g. [4–6]. In contrast, very few research efforts have been focused on accidental explosions in open traffic environments in which vehicles are the only or main source of confinement and congestion [5,7].

The work by Lozano [7] is a recent example of an investigation of the blast strength of gas explosions in an open road environment using CFD analysis. Several scenarios with a group of vehicles with different configurations and surrounded by a propane-air cloud with stoichiometric concentration were studied. However, due to the large amount of variables and scenarios studied, it was necessary to impose some limitations on the scenarios, such as regular traffic layouts and constant distance between the vehicles and the ground (ground clearance). Hence, it is necessary to explore the effects of such assumptions to complement the knowledge generated in [7].

This work evaluated gas explosions in traffic environments with a focus on different geometrical parameters that influence the degree of confinement of the gas cloud. Several scenarios in an open area consisting of a group of vehicles engulfed by a stoichiometric mixture of propane and air were studied. The parameters of interest included partial confinement caused by noise barriers along the road, variation of the spacing in a group of vehicles, and variation of the ground clearance under the vehicles. The goal was to quantify their influence on the resulting explosion in comparison to an ideal reference case and to characterize to what degree they are relevant. The study was conducted with CFD calculations using FLACS-CFD [8].

2. METHODOLOGY

2.1. Overview

This work evaluated the effect of different geometrical parameters on the resulting gas explosion in a traffic environment. The hypothetical background is an unintended release of LPG during transport of the fuel by road. LPG was chosen as this is the most often transported fuel gas in Sweden and it is commonly adopted as the reference fuel for risk analysis related to transport of flammable gases in the country [9]. An illustrative example of the target scenario is given in Figure 1. In the figure, the flammable gas leaking from a road tanker mixes with the surrounding air to form a flammable mixture, which surrounds stationary vehicles on the road.

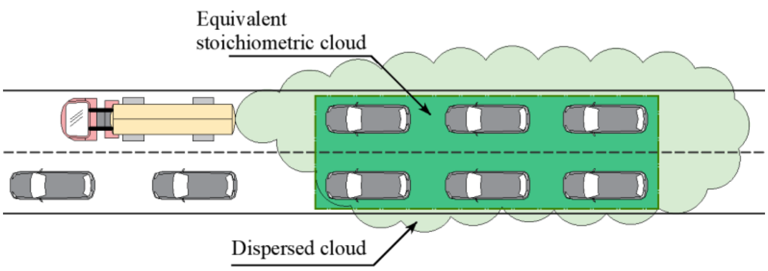

Figure 1. Schematic example of a scenario of gas dispersion in a road environment relevant for the work in this article. The light green region is the dispersed cloud. The dark green region is the equivalent stoichiometric cloud assumed in the CFD model.

The study was conducted using CFD calculations. This allows for evaluation of several more scenarios than what would be feasible with experimental testing. Furthermore, CFD calculations facilitate sampling of results across a greater number of points.

The research was divided into three numerical campaigns, as described in Table 1. Further details about each campaign are provided in Section 3.

Campaign	No. scenarios	Focus
I	6	Effect of noise barriers along the road
II	4	Uncertainty in the location of the vehicles
III	10	Variable ground clearance

Table 1. Summary of the different numerical campaigns in this work.

Several simplifications were made to facilitate the modelling and evaluation of the studied scenarios. Firstly, the released LPG was assumed to consist of 100 % propane. This assumption was considered reasonable as LPG mixtures sold in Sweden are composed of at least 95 % propane. Secondly, the real dispersed gas cloud, which in reality has an arbitrary shape and non-uniform concentration, was modelled as an equivalent stoichiometric cloud with a rectangular shape, see Figure 1. Next, all vehicles were assumed to have equal shape and size, roughly representing a typical personal car. All dimensions were rounded to a multiple of 50 mm to facilitate a perfect match between the geometry of the vehicles and the calculation grid. Figure 2 shows the geometry of the mock-up vehicle. The ground clearance, h, was set to 0.30 m in Campaigns I and II. The effect of varying h was studied in Campaign III. Finally, the ignition point was placed at the edge of the group of vehicles, which produces the greatest overpressure in this type of scenario, according to [7].

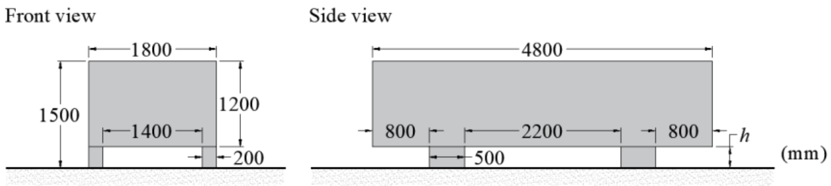

Figure 2. Adopted geometry of the mock-up vehicle.

2.2. CFD modelling

The CFD calculations were performed using the finite volume code FLACS-CFD, v.22.1 [8]. The scenarios in FLACS-CFD can only be solved on a structured cartesian grid. To compensate for this limitation, the software uses the Porosity Distributed Resistance approach to account for the effects of sub-grid objects on turbulence generation and flame wrinkling. However, in this study care was taken to align the calculation grid to the geometry of the vehicles, which means that the porosity values in the studied scenarios were either 0 (i.e. completely blocked cell) or 1 (i.e. completely open cell).

The calculation domain was divided into a *core domain* and a *stretched domain*, which surrounds the core domain on all sides. Only results within the core domain are considered reliable. The purpose of the stretched domain is to decrease the impact of the boundary conditions on the results within the core domain. The vehicles and undisturbed gas cloud were placed completely inside the core domain. A cell size of 50 mm was used within the core domain. Outside this domain, the cell size was gradually increased up to a maximum size of 1.0 m. The ground and vehicles were modelled as perfectly rigid objects. Boundary conditions of type PLANE WAVE (non-reflecting) were used on all outlets. The Courant-Friedrich-Levy numbers were kept to their default values (CFLC = 5 and CFLV = 0.05). The initial fluctuating velocity was set to 1.0 m/s, according to the recommendations in [7]. The turbulence length scale was set to 50 % of the cell size. Calculations were carried out in parallel with 16 CPUs. The maximum overpressure was stored at all cells. All other outputs were stored at monitor points located at 0.18 m above ground and arranged in a structured pattern with a spacing of 1.0 m in the horizontal plane.

3. RESULTS AND DISCUSSION

3.1. Campaign I: Effect of side noise barriers

This campaign focused on the effect of noise barriers located along the road on the resulting explosion. The vehicles were arranged in a 2×3 layout (2 lanes × 3 vehicles/lane) with a regular spacing of 1.5 m. The cloud size for all scenarios was set to 25.4×13.1×3.6 m. The barriers were modelled with a length equal to the length of the calculation domain. That is, the barriers were assumed to be much longer than the line of vehicles. Most scenarios had one barrier placed at two meters from the nearest vehicles. However, one scenario had two parallel barriers with a distance of 14.0 m in between. In most scenarios, the height of the barrier, H_{bar}, was set to 3.0 m, which is a standard height for noise barriers in Swedish roads. However, H_{bar} was set to 4.0 m in one of the scenarios to investigate the influence of this parameter.

Figure 3 summarises the scenarios in this campaign. The figure also presents the maximum value of peak overpressure (hereinafter also referred to simply as *maximum overpressure*) and the mean value of peak overpressure (hereinafter also referred to simply as *mean overpressure*) for each scenario. The maximum overpressure was calculated as the average peak overpressure over a volume of 1.0 m^3 around the greatest value. This was done to smoothen out the pressure peak. The mean value of peak overpressure is defined as the average value of the peak overpressure inside a rectangular cuboid engulfing the group of vehicles. This cuboid extended 0.5 m from the edges of the group of vehicles in all directions. While the maximum overpressure is a measure of the strength of the localised external explosions, the mean overpressure is an indication of the strength of the global explosion.

Scenario	Description
I-01	No Barrier
I-02	One barrier, $H_{bar} = 3$ m
I-03	One barrier, $H_{bar} = 4$ m
I-04	One barrier, $H_{bar} = 3$ m, $P_{bar,fail} = 5$ kPa
I-05	Two barriers, $H_{bar} = 3$ m,
I-06	One barrier, $H_{bar} = 3$ m, opposite ignition

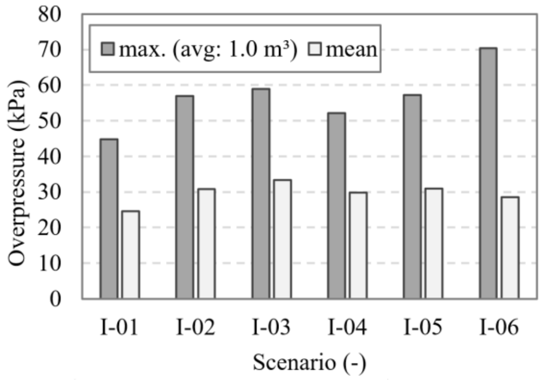

Figure 3. Scenarios in Campaign I: Overview and maximum and mean peak overpressure.

As given in Figure 3, the reference scenario without barrier (scenario I-01) produced a maximum overpressure of 45 kPa and a mean overpressure of 25 kPa. Figure 4 shows the contour plot of peak overpressure for all scenarios in the campaign. The plot gives the peak overpressure at each point (x, y). It should be noted that the plotted values did not necessarily occur at the same time or at the same distance above ground. That is, the plot was "flattened" in time and space. The contour plots are similar in the sense that localised zones with high overpressure were obtained on the side opposite to the position of the ignition point. However, these areas with high overpressure were expanded by the presence of the side barriers, as evidenced by comparing scenario I-01 with scenarios I-02 and I-03. In scenario I-02, which has an infinitely rigid barrier with H_{bar} = 3.0 m, the maximum and mean overpressure were 57 kPa and 31 kPa, which represents an enhancement of 27 % and 24 % compared to the reference case. Increasing the height of the barrier from 3.0 to 4.0 m (scenario I-03) introduced further enhancement up to 31 % and 32 % compared to the reference case.

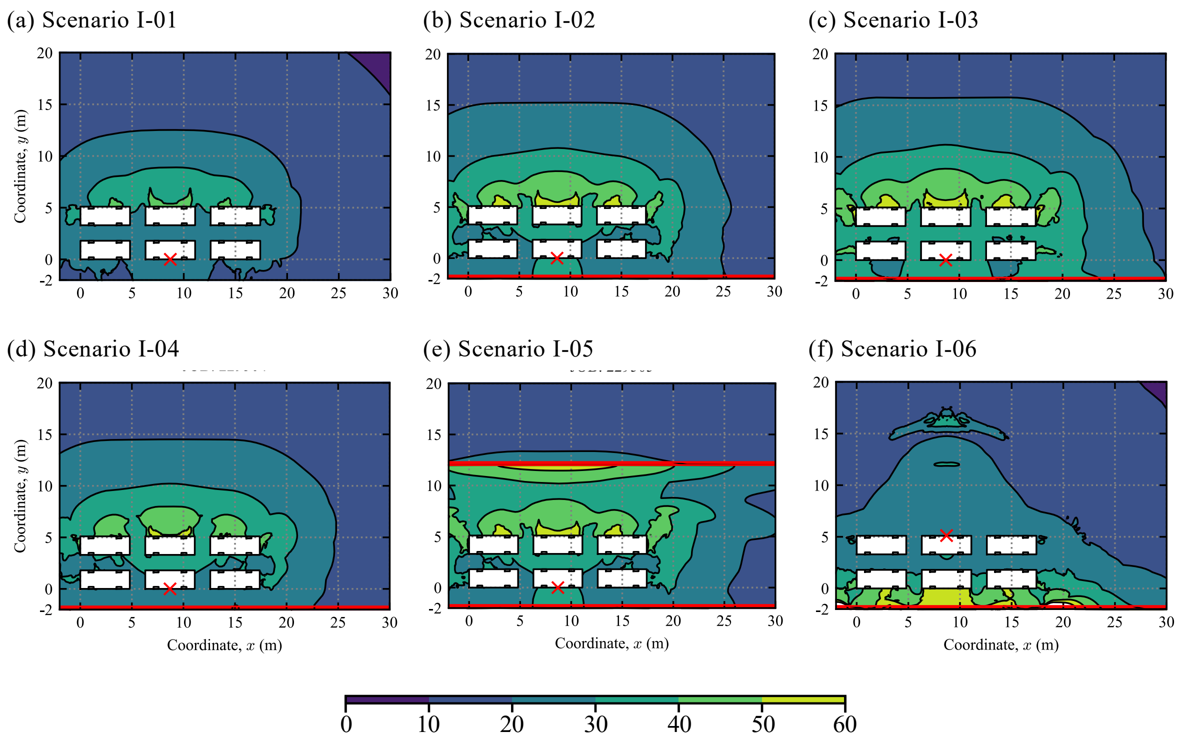

Figure 4. Contour plot of peak overpressure for the scenarios in Campaign I. The thick horizontal red lines give the position of the barriers. The red cross represents the ignition point.

In scenario I-04 the barrier was set to fail at 5 kPa. Numerically, this was implemented by allowing sections of the barrier with length of 5 m to be removed from the calculations when the pressure on the section exceeded the specified failure pressure. Even though the barrier failed relatively early, it still had a marked effect on the resulting explosion, although not as much as the cases with infinitely rigid barriers. The maximum overpressure increased by 16 %, while the mean value increased by 20 %. The enhancement on the overpressure, despite the early failure of the barrier, was probably due to amplified turbulence in the flow ahead of the flame due to interaction of the flow with the barrier, which occurred before the pressure rose above the capacity of the barrier.

The influence of a second barrier, placed on the opposite side of the road at seven meters from the nearest vehicle, was studied in scenario I-05. The results show that in the immediate vicinity of the group of vehicles the contour plot of peak overpressure is almost identical to that of scenario I-02. That is, the second barrier does not appear to have a significant influence on the explosion in the proximity to the group of vehicles. However, the overpressure increased closer to the second barrier, reaching values in the same order of magnitude as the maximum overpressure near the group of vehicles. This was likely due to the combined effect of interaction of the flow with the barrier (which magnifies turbulence) and reflection against the barrier.

Figure 5 gives the peak overpressure and peak impulse at several monitor points located along a path in the y-direction at x = 8.7 m (same x-coordinate as the ignition point). Only minor difference can be discerned between the profiles of peak overpressure for scenarios I-02 and I-05 up to y = 9.0 m. From that point onwards, the second barrier in scenario I-05 clearly caused an increase in overpressure. That is, the influence of the barrier is noticeable within 3.0 m from the barrier. In contrast, the peak impulse in scenario I-05 is greater at all plotted positions, although initially only about 5 % greater. This is mainly due to the additional impulse content in the wave reflecting off the barrier. Behind the second barrier, both the overpressure and impulse decreased drastically, below the levels reported for the reference case. Moreover, the results behind the barrier show minor variation until they approach the curve from the reference case at about y = 18.0 m.

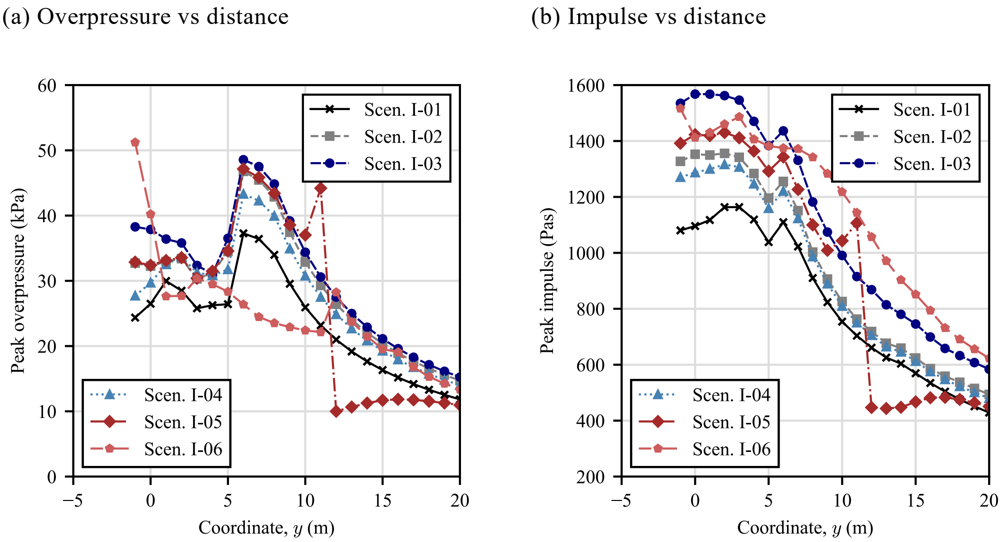

Figure 5. Peak overpressure and peak impulse at selected monitor points for the scenarios in Campaign I. The points are located along a path at x = 8.7 m and z = 0.18 m.

The greatest value of maximum overpressure was obtained in scenario I-06, in which the ignition point was placed on the opposite side, while maintaining the barrier at two meters from the closest vehicles. This means that the barrier was located in the zone where the greatest overpressure would have been nonetheless generated solely due to combustion across the group of vehicles. That is, this scenario gives the greatest overpressure overall because several enhancing factors acted simultaneously in the critical zones: flame acceleration through congested region, turbulent flow near the barrier region, and reflection off the barrier. The maximum overpressure in this scenario was enhanced by 56 % compared to the case without barrier. However, it is interesting to notice that the mean value increased only by 16 %. This was because the overpressure behind the ignition point in scenario I-06 was low compared to the pressure behind the ignition point in scenario I-02. However, the overpressure behind the ignition point in scenario I-06 was still greater than in the reference case with no barrier.

An interesting observation from the results presented in Figure 5 is that the height or failure pressure of the barrier in the scenarios with one barrier appear to have less relevance on the peak overpressure farther away from the explosion, which is evidenced by comparing the curves for scenarios I-02, I-03, and I-04, which come close together with increasing distance. Similarly, the failure pressure seems to lose relevance for the peak impulse far away, as discerned by comparing the results from scenarios I-02 and I-04. However, the impulse values for the case with H_{bar} = 4.0 m remained greater than that for I-02 at all plotted distances.

The greatest peak impulse in the positive y-direction outside the vehicle cluster was obtained in scenario I-06. This was mainly due to the reflected wave traveling from the barrier. This reflected wave is present in the other scenarios, but it is most significant in I-06. While the reflected peak is smaller than the main peak overpressure (hence, not visible on Figure 5(a)), its impulse content is relatively large compared to the impulse content in the main peak.

3.2. Campaign II: Effect of spacing of vehicles

In studies concerning explosion risk in traffic conditions, it is common practice to assume regular spacing of vehicles. In [7], for instance, even though the effects of the spacing between vehicles across different scenarios were investigated, the spacing was kept regular and constant in both directions within a given scenario. The advantage of this assumption is that it reduces the amount of variables considered. However, in any real traffic situation, the clear distance between cars in fact behaves similarly to a random variable, constrained mainly by the characteristics of the road, traffic conditions, and the size of the vehicles.

This campaign evaluated the effect of the uncertainty of the location of the vehicles compared to an ideal arrangement of 3×3 vehicles with regular spacing of 1.5 m in both directions. The cloud dimensions were set to 25.4×16.4×3.6 m in all scenarios. In two scenarios, the spacing was multiplied by a random factor α characterised by a normal distribution with mean μ_α = 1.0 and standard deviation σ_α = 0.2. This gives a distribution of the spacing with mean 1.5 m, 5th percentile of 1.0 m, and 95th percentile of 2.0 m. Finally, in one scenario, the spacing was kept constant (1.5 m), but the lanes of vehicles were staggered.

Figure 6 summarizes the key overpressure values for the scenarios. The maximum peak overpressure appears to be particularly sensitive to the layout of the configuration. Hence, this value is reported in two ways: as an average over a volume of 0.1 m^3 around the peak value, and as an average over a volume of 1.0 m^3 around the greatest value. It can be seen that both randomised scenarios produced greater values of maximum overpressure than the reference case (scenario II-01). Scenario II-02 gives the greatest maximum overpressure overall, with an enhancement of around 26 % over the reference case. The case with staggered lanes produced a maximum overpressure (when averaged over 1.0 m^3) which is slightly less than the refence case, although the maximum value when averaged over 0.1 m^3 is still 15 % greater. In general, the values of maximum overpressure averaged over 0.1 m^3 showed greater deviation from the reference case than when averaging was done over 1.0 m^3. This shows that the main effect of the uncertainty of the location of the vehicles lies on the localised zones of high pressure. In contrast, the mean value of peak overpressure remained virtually constant regardless of the spacing or location of the vehicles. This indicates that for points located in the far-field, the exact spacing may not be relevant, as long as an appropriate representative value is used in the evaluation of the explosion.

Figure 7 gives the contour plot of peak overpressure. For all cases, it holds that the greatest overpressure occurs in the zone opposite to the position of the ignition point. However, the shape and magnitude of this area is influenced by the location of the vehicles. While the contour plot of peak overpressure for the reference scenario in Figure 7(a) is symmetric around the y-axis, the other scenarios produced asymmetric contours, with some zones with greater overpressure and others with lower overpressure than the reference case.

In scenario II-02 in Figure 7(b), the external explosion outside the rightmost column of vehicles is weaker than the corresponding location in Figure 7(a). This was likely caused by the first vehicle (bottom right vehicle) standing far apart from the others. Scenario II-03 in Figure 7(c) also shows weaker explosion in this area. In this case, the decrease in pressure was possibly due to the shorter length of the congested region in this part of the configuration. Conversely, the external explosion outside the middle column of vehicle is stronger for the two randomised configurations. In scenario II-02, this seems to be caused by the additional layer of wheels between ignition point and the external explosion (even though the length of the congested region was reduced in this case). In scenario II-03, it appears that an optimal arrangement of wheels between ignition point and the area with the greatest overpressure was achieved.

Scenario	Description
II-01	Regular spacing
II-02	Randomised scenario A
II-03	Randomised scenario B
II-04	Staggered arrangement

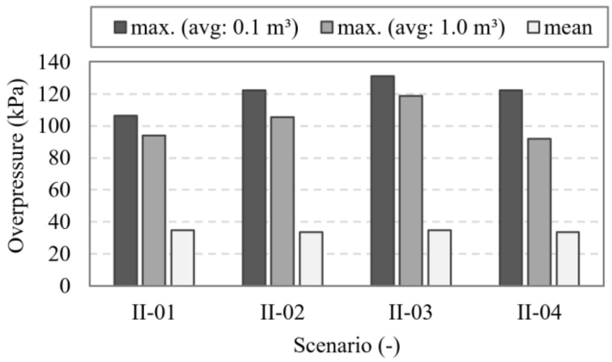

Figure 6. Scenarios in Campaign II: Overview and maximum and mean peak overpressure.

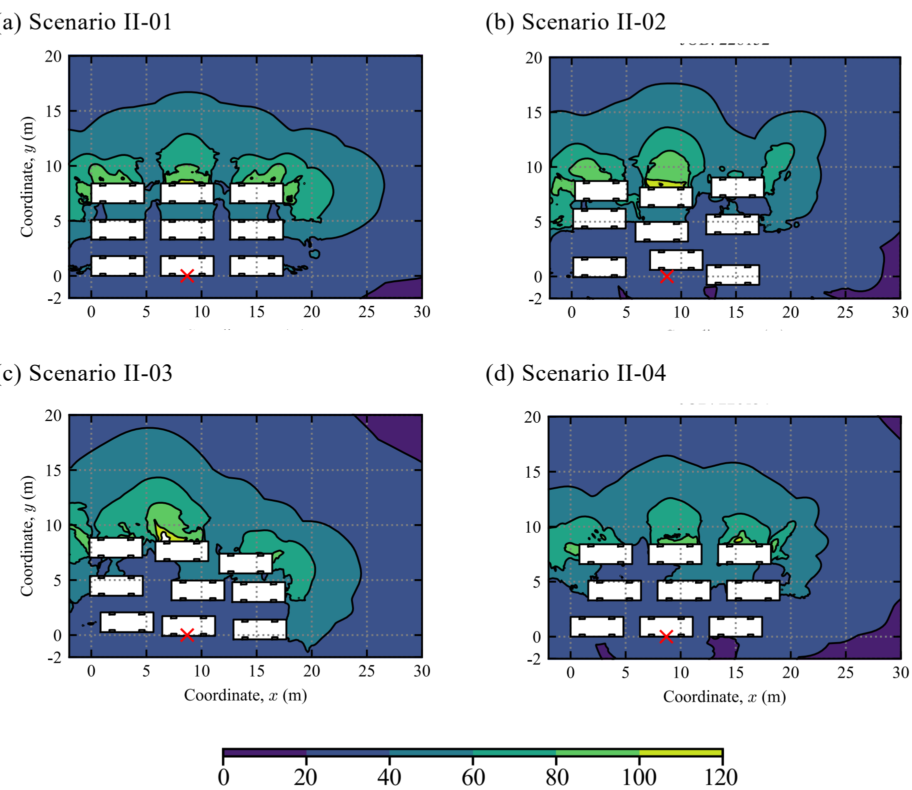

Figure 7. Contour plot of peak overpressure for scenarios in Campaign II. The red cross represents the ignition point.

Figure 8 gives the peak overpressure and peak impulse along a path in the y-direction at x = 8.7 m. The profile of peak overpressure from the two randomised scenarios are similar. However, the peak impulse from scenario II-02 is greater than that of scenario II-03 along the same path. The staggered scenario gives comparable results to the reference case. That is, it appears that the variation of the spacing is more important than shifting the lanes. Furthermore, the trend of the profile of peak overpressure and impulse remains similar for all cases. The uncertainty on the prediction of overpressure and impulse with regard to the ideal case seems to be in the order of -5 % to +15 %. This holds for most regions in the calculation domain, apart from the very localised zones with the greatest overpressure peaks.

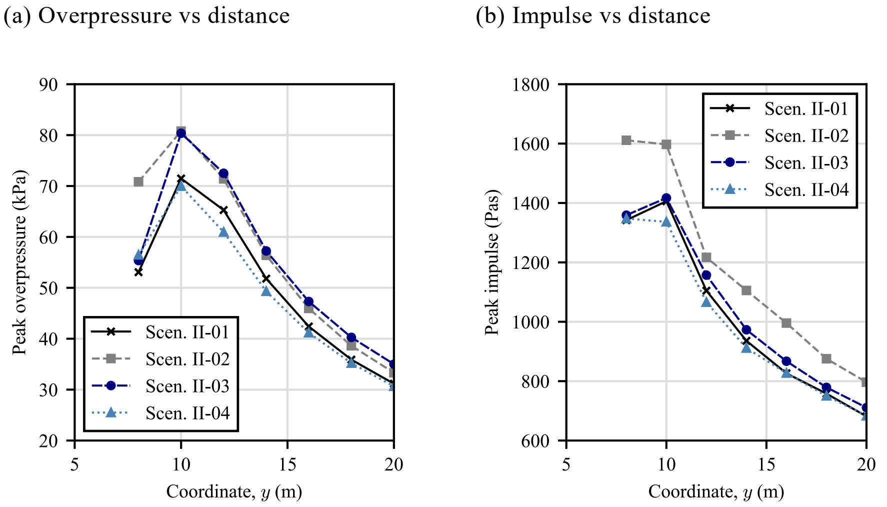

Figure 8. Peak overpressure and peak impulse at selected monitor points for the scenarios in Campaign II. The points are located along a line at x = 8.7 m and z = 0.18 m.

3.3. Campaign III: Effect of ground clearance

In the parametric study carried out by Lozano [7], the ground clearance, h, was set to 0.30 m and kept constant throughout the study. The same ground clearance was used in the research carried out by Makarov et al [5]. Hence, this value of ground clearance has been previously considered a good representative value. However, the ground clearance is likely to vary within any group of vehicles. This campaign investigated the effect of varying this parameter. Five values of the ground clearance were evaluated: 0.15, 0.20, 0.30, 0.40, and 0.50 m. It is worth noting that, even though personal vehicles do not have a ground clearance as large as the greater values assessed here, these values do occur among larger types of vehicles, such as busses and trucks.

Two settings were studied. A setting with one (1×1) vehicle and a gas cloud with dimensions 8.8×5.8×3.6 m. The other setting consisted of three vehicles arranged side-by-side (3×1) and engulfed by a cloud with dimensions 8.8×10.4×1.8 m. The spacing between cars was set to 0.5 m. The cloud dimensions were defined by assuming that the cloud extended two meters outside the group of vehicles in x- and y-direction.

Figure 9 gives the maximum and mean value of peak overpressure for the studied scenarios. The maximum peak overpressure was averaged over a volume of 1.0 m^3 around the peak value. The overpressure values were normalised with regard to the maximum overpressure of the reference unconfined case. The reference unconfined case had the same cloud and ignition location, but no vehicle was present. It is worth noting that the reference overpressure used for the scenarios with 3×1 vehicles is lower. This was due to the smaller height of the cloud in this case (1.8 m), compared to the height of the cloud used in the scenarios with 1×1 vehicle (3.6 m). Figure 10 shows the contour plot of peak overpressure for some selected scenarios.

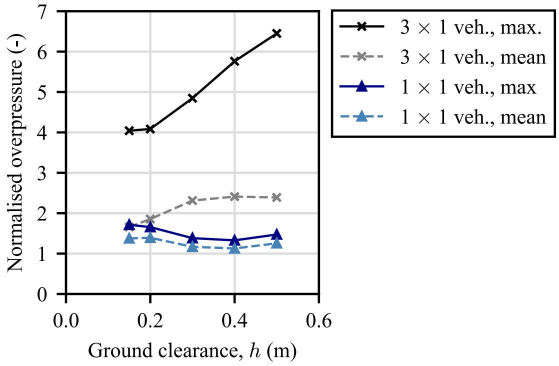

Figure 9. Overpressure as a function of the ground clearance in Campaign III. The overpressure was normalised with regard to the reference unconfined overpressure: 3.8 kPa for scenarios with 3×1 vehicles, and 6.2 kPa for scenarios with 1×1 vehicle.

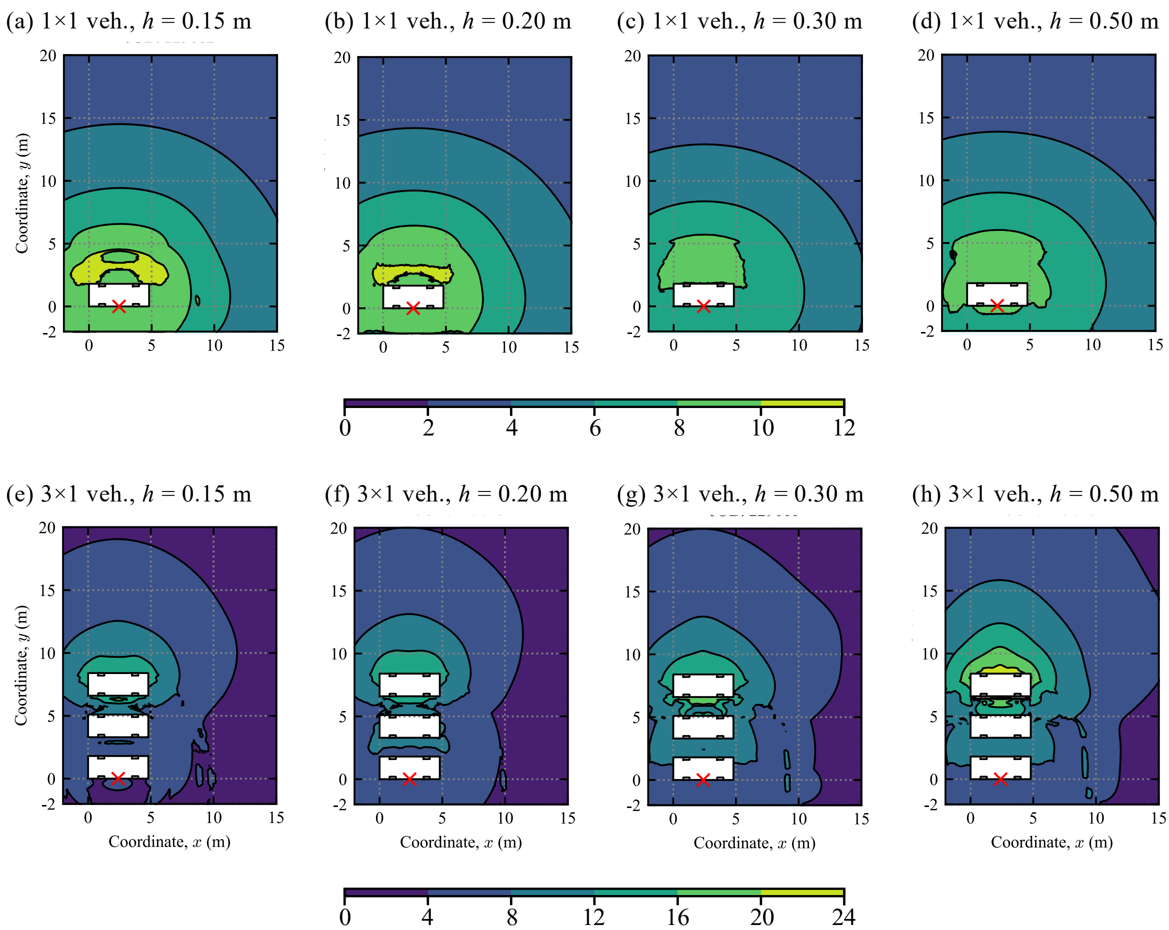

Figure 10. Contour plot of peak overpressure for scenarios in Campaign III. The red cross represents the ignition point.

In the scenarios with 1×1 vehicle, both the maximum and mean peak overpressure appear to follow the same trend. The greatest values were obtained for the case with the smallest clearance (h = 0.15 m). These values are greater than the reference unconfined overpressure by 56 % and 25 %, respectively. In general, the pressure decreased as the ground clearance increased. For all cases, the maximum overpressure was at least 21 % greater than in the reference unconfined explosion. However, the mean overpressure was almost equal to the reference unconfined overpressure for the greater values of h. This may indicate that the influence of the confinement provided by the vehicle is not significant far away from the explosion. In Figure 10, it can be seen that the maximum overpressure was obtained in a localised zone just beyond the vehicle. Indeed, the greatest difference between cases occurred in this region. However, farther away (y > 10 m) the profile of peak overpressure shows minor difference, which indicates that the ground clearance losses relevance in the far-field.

Interestingly, the opposite trend was obtained for the scenarios with 3×1 vehicles. The lowest value of overpressure was obtained for h = 0.15 m, and it increased with greater h. However, the mean overpressure levelled off at h = 0.30 m, and no further increase was noticed for greater h. These results conflict with the commonly accepted understanding of confined explosions, in that a higher degree of confinement is expected to result in increased maximum overpressure.

A potential explanation for this behaviour is that combustion under the vehicle does not develop in a pure two-dimensional environment. Furthermore, there are two main mechanisms contributing to pressure buildup: confinement and turbulence around the wheels and in the space between layers of vehicles. In scenarios with 3×1 vehicles, turbulence may have a greater weight on the resulting overpressure. Hence, a larger gas volume (due to a greater value of h) burning under turbulent conditions results in enhanced overpressure. On the other hand, in the scenarios with one vehicle, combustion under the vehicle is dominated by confinement, as there is a single layer of obstacles which the flame flows around, which explains the decrease in pressure for a decrease in confinement level.

Considering that the greater overpressure was obtained around and beyond the third vehicle (furthest from the ignition point), another explanation could be related to the amount of unburned gas pushed out from the region underneath the vehicles. The expelled unburned gas subsequently explodes in a highly turbulent region outside. A greater ground clearance allows for a larger volume to explode outside and therefore leads to greater overpressure values.

In general terms, the results indicate that h = 0.30 m is a suitable representative value for this type of explosion scenarios. In cases with several personal vehicles, this value would produce conservative results compared to smaller (and more likely) values of ground clearance. In contrast, this value would underestimate the overpressure if the real ground clearance were greater. However, personal cars with greater ground clearance are not likely to be found on urban roads. Furthermore, the effect on the mean peak overpressure was seen to remain neatly constant for h > 0.30 m. In scenarios with one vehicle, using h = 0.30 m may underestimate the overpressure. However, the overpressure values are relatively low for these scenarios, and they might not become the decisive loading conditions.

4. CONCLUSION

This article employed Computational Fluid Dynamics (CFD) to conduct a numerical investigation of different parameters contributing to or affecting confinement and congestion in the event of a gas explosion on a road. The studied parameters included: noise barriers along the road, uncertainty in the location of the vehicles, and ground clearance. Each parameter was evaluated in a separate numerical campaign consisting of several scenarios with a group of vehicles engulfed by a stoichiometric mixture of propane and air. All three studied parameters had a clear effect on the resulting explosion and may enhance the explosion strength given the right conditions.

An infinitely rigid noise barrier on one side of the road was shown to enhance the explosion strength by up to 30 %. A higher barrier was found to produce greater overpressure. Even if the barrier failed at a low overpressure (5 kPa), a clear increase of the explosion strength was observed, although less so than for an infinitely rigid barrier. For the adopted geometrical conditions, the influence of the barrier was the most significant within three meters from the barrier. Furthermore, compounding of the effects of the barrier (i.e. turbulence enhancement and reflection) and other enhancing factors was found to increase the pressure further.

Randomised location of the vehicles with regard to an ideal structured arrangement was found to have the potential to increase the maximum values of overpressure and impulse by up to 30 % in critical localised regions. This effect was most significant along paths in which the number and relatively location of the obstacles interacting with the flame front were optimised for flame acceleration. In general, it appears that the uncertainty in prediction from the ideal case lay in the range from -5 % to +15 %.

Finally, in scenarios with a single vehicle, the maximum overpressure was found to decrease as the ground clearance increased. This agrees with commonly accepted consensus on confined gas explosions. However, in cases with three vehicles, the overpressure increased with increasing ground clearance. This is attributed to the interplay between confinement and congestion. In cases with three vehicles, the interaction of the flow with obstacles, which enhances turbulence, may be the dominant effect. In this case, greater volume in the region under the car allow for grater gas volume to burn in a highly turbulent regime. Altogether, a ground clearance of 0.30 m was found to be a good representative value of this parameter for evaluation of gas explosions on a road.

In general, the study showcased how CFD methods could be used to investigate vapour cloud explosions in non-traditional settings as a substitute to experimental research.

ACKNOWLEDGEMENTS

This work was supported by the Swedish Transport Administration; the Swedish Fortifications Agency; and the Swedish Civil Contingencies Agency.

The calculations were performed on the high-performance computing (HPC) cluster *Vera*, which is managed by Chalmers e-Commons at Chalmers.

REFERENCES

[1] D. Baraldi, A. Kotchourko, A. Lelyakin, J. Yanez, P. Middha, O.R. Hansen, A. Gavrikov, A. Efimenko, F. Verbecke, D. Makarov, V. Molkov, An inter-comparison exercise on CFD model capabilities to simulate hydrogen deflagrations in a tunnel, International Journal of Hydrogen Energy 34 (2009) 7862–7872. https://doi.org/10.1016/j.ijhydene.2009.06.055.

[2] Y.Z. Li, Study of fire and explosion hazards of alternative fuel vehicles in tunnels, Fire Safety Journal 110 (2019) 102871. https://doi.org/10.1016/j.firesaf.2019.102871.

[3] P. Middha, O.R. Hansen, CFD simulation study to investigate the risk from hydrogen vehicles in tunnels, International Journal of Hydrogen Energy 34 (2009) 5875–5886. https://doi.org/10.1016/j.ijhydene.2009.02.004.

[4] W. Li, X. Shen, Z. Huang, T. Mao, Q. Hu, C. Ma, Study of Leakage and Explosion Hazard Characteristics of a Compressed Natural Gas at a Gas Station, J Eng Phys Thermophy 97 (2024) 387–396. https://doi.org/10.1007/s10891-024-02904-3.

[5] D. Makarov, F. Verbecke, V. Molkov, O. Roe, M. Skotenne, A. Kotchourko, A. Lelyakin, J. Yanez, O. Hansen, P. Middha, S. Ledin, D. Baraldi, M. Heitsch, A. Efimenko, A. Gavrikov, An inter-comparison exercise on CFD model capabilities to predict a hydrogen explosion in a simulated vehicle refuelling environment, International Journal of Hydrogen Energy 34 (2009) 2800–2814. https://doi.org/10.1016/j.ijhydene.2008.12.067.

[6] C. Zhou, Z. Yang, G. Chen, X. Li, Optimizing hydrogen refueling station layout based on consequences of leakage and explosion accidents, International Journal of Hydrogen Energy 54 (2024) 817–836. https://doi.org/10.1016/j.ijhydene.2023.09.210.

[7] F. Lozano, Explosions in urban environments: Modelling of gas explosions and risk of premature shear failure in reinforced concrete structures, Lic. Thesis, Chalmers University of Technology, 2023.

[8] Gexcon AS, FLACS-CFD v22.1 User's Manual, (2022).

[9] E. Dahlén, Inventory of knowledge needs, with regard to explosion loading, in a densified urban environment., M.Sc. thesis, Chalmers University of Technology, 2019.

15th International Conference on
Shock & Impact Loads on Structures
12-13 June 2025, Gothenburg, Sweden

SECURITY BARRIER PERFORMANCE ASSESSMENT WITH NUMERICAL SIMULATIONS USING GENERIC VEHICLE MODELS

Damijan Markovic[a], Alessandro Scattina[b] and Martin Larcher[a]

[a]European Commission, Joint Research Centre at Ispra, Italy,

email: damijan.markovic@ec.europa.eu

[b]Politecnico di Torino, Department of Mechanical and Aerospace Engineering, Italy

Keywords: vehicle impacts, hostile vehicle mitigation, security barriers, crashworthiness

Abstract

Vehicle security barriers preventing the entry of vehicles into pedestrian zones can effectively mitigate terrorist attacks by vehicle-ramming. The performance of barriers against vehicle impact can be certified through physical tests using real vehicles of given UNECE categories following ISO 22343 (2023). Due to a high cost, the number of performed crash-tests is very limited and cannot cover all impact scenarios of interest for the assessment of a barrier performance.

The use of numerical simulations seems to be the most appropriate way to enhance the physical testing approach, since they are more accurate than simple analytical methods and more cost efficient than experiments. Over the last decades, the automotive industry and associated research communities have developed efficient numerical simulations tools to analyse the vehicle impact, related to the passenger's and vulnerable road users' safety. With some adjustments, these simulations methods and tools can be directly transposed to the analyses of vehicle impacts on security barriers.

The numerical vehicle models used for passengers' safety are far too detailed and too specific than needed for vehicle ramming applications. Namely, in our domain of interest, the objective of the simulation is to assess the performance of a barrier not a passenger safety. In addition, a barrier's performance needs to be assessed for an entire category of vehicles, not for one specific vehicle.

Therefore, for simulating vehicle impacts on security barriers several generic vehicle models have been developed to represent vehicles of a broad range of categories (from 3.5t to 30t trucks). These models are generic in the sense that they do not represent a specific vehicle brand, but are representative of one specific category among those defined by the standard ISO 22343. In addition, they are adjustable through a set of parameters, so that their properties could fit to various vehicle configurations. In particular, the mass of the vehicle, including its distribution, the main vehicle dimensions (length, width, etc.) and mechanical characteristics related to the crash behaviour can be varied.

In this communication, several numerical simulations using the generic vehicle models are presented. Model validation with experimental results and sensitivity analyses of vehicle characteristics and impact configurations are discussed. It is shown that there are several

crucial vehicle properties, which can significantly influence the crash behaviour and therefore the load on a security barrier subjected to an impact.

1 INTRODUCTION

For vehicle barriers to serve as an effective mitigation solution, they must be designed, produced, and installed to protect against specific levels of threats related to vehicle category and impact velocity, general methodology for protecting public spaces being provided by [1] and [2]. Commonly, the performance of security barriers can be certified through physical tests, following the ISO standard [3]. However, the crash experiments are relatively expensive and are not suitable for testing many different impact scenarios. Therefore, numerical simulations can provide a cost-efficient assessment of barrier performance, complementary to physical testing.

For the crash-test certified barriers, numerical simulations could be used to assess a barrier performance for a larger spectrum of possible impact scenarios (e.g. impact speed, angle, specific site conditions, etc.), for physical tests would be economically inefficient.

While the ISO standard [4] recognises the usefulness of the Finite Element Analysis (FEA) during the design process, it considers at the same time that: "*the current level of sophistication of such models is low with limited validation against full-scale impact tests and poor understanding of the limitations of using mathematical formulae in a dynamic impact where many of the variables are still to be ascertained or understood"* (citation from [4]). Therefore, the standard allows the use of numerical models only for a certification of a barrier, which underwent only minor changes from the design already crash-tested before. With other words, according to the ISO standard [4], the FEA is not considered as mature enough in order to play a significant role in a barrier certification process. Hence, more effort is needed from the research community to make the numerical tools more reliable.

In addition, it is important to stress that in some cases, the authorities cannot afford to protect all the sites by using certified solutions. For these cases, numerical simulations could be used to assess the protection performance of the existing urban furniture (e.g. benches, planters, etc.), which cannot be certified as security barriers, but could still provide a certain level of protection through deterrence.

For performing a complete full-scale simulation, it is necessary to develop adequate models of the three main subsystems: the impacting vehicle, the barrier system and the surrounding environment. From the modelling perspective, the most challenging subsystem is by far the vehicle model. This is because of the complexity of vehicles' crash behaviour, where there are many components interacting with each other and undergoing very large deformations.

Moreover, a correct modelling of the vehicle crashing is crucial for the determination of the load imposed to a barrier. Even if the barrier itself is usually a much simpler structure compared to a vehicle, the modelling of the interaction with the surrounding soil or other structures in the vicinity is not simple. The general methodology on modelling of the coupled system is presented in [11].

Since vehicle-ramming threats are most usually defined in terms of a vehicle category, not in terms of a specific vehicle brand and model, it is convenient to use “generic vehicle models” to perform numerical crash simulations. These models are not brand specific and are adjustable to represent a wide range of vehicle configurations. Recently, three different generic vehicle models have been developed by the European Commission [13], corresponding to the following categories:

i) N1 (≤3.5t trucks, [8]),
ii) N2A, N3C and N3D (7t to 12t trucks, [9]) and
iii) N3G (≤30t trucks, [10]).

Two main approaches are considered: a full simulation approach, which requires detailed information about the barrier and its foundation [11], and a simpler uncoupled approach, according to which the barrier is considered undeformed during the impact [12]. The assumption of undeformability is rather realistic for barriers designed and certified for a given impact scenario, for which they undergo very little deformation. For these configurations, the numerical simulation models can be simplified by considering barriers as rigid.

The vehicle impact load is characterized by using generic vehicle finite element models used for calculating impact forces subjected to the barrier. The impact force is a function of time, but can also be analysed with a response spectrum to estimate the "dynamic load factor" (DLF). The DLF can be used to estimate an equivalent static load, allowing for a rough and fast assessment of the barrier performance.

2 METHODOLOGY FOR FULL-SCALE IMPACT SIMULATIONS

The methodology is summarized in the **Figure 1**. In the following subsections, the main steps of the methodology are briefly presented.

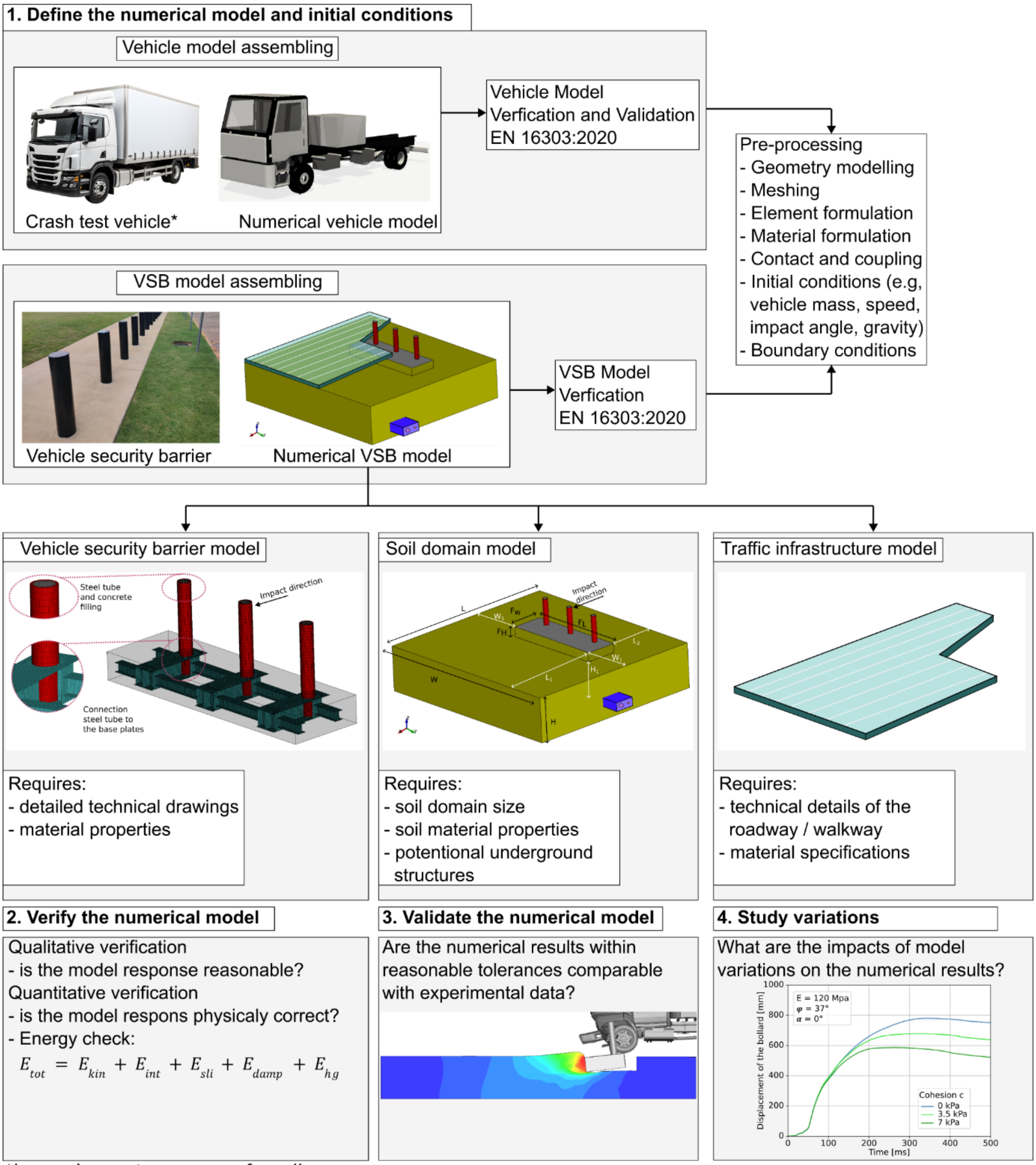

*image by vector_corp on freepik.com

Figure 1. Schematic presentation of the general methodology [11] for assessing the performance of security barriers subjected to vehicle impacts.

2.1 Development of numerical models

The first step in the process involves defining the numerical models for each subsystem. A modular modelling approach is recommended, which involves dividing the full model into several sub-models: vehicle, barrier system and surrounding soil.

Numerical vehicle model:
The numerical vehicle model should preferentially be a "generic vehicle model" (see the next Section), adapted to represent an entire category not only a specific brand and model.

Numerical model of the vehicle security barrier:
The vehicle security barrier (VSB) itself often needs to be modelled individually based on the technical details of the barrier. The numerical model shall reproduce the shape, mass and the mechanical behaviour by representing the connections and interactions between the components, e.g., fixation/anchoring, joints and possible contacts between barrier, vehicle, soil and road infrastructure. Appropriate material formulations are needed to represent the material behaviour (e.g., non-linearity and failure).

Numerical model of the soil domain:
An appropriate setup of the soil domain is needed selecting appropriate material properties. Testing of the site soil conditions might be necessary for accurate characterisation of the material properties. If site-specific information is not available, literature-based assumptions can be made, accompanied with sensitivity analysis covering potential soil properties' effects. The geometrical shape of the soil domain can be quite simple in topology, e.g., rectangular. However, special care shall be taken to select appropriate edge distances between the foundation and the outer limit of the soil domain. Together with the size of the soil elements, sensitivity studies should be used to determine a suitable soil setup.

2.2 Model verifications

The vehicle model can be verified according to the standard EN 16303:2020, for simple conditions (e.g. idle, linear track or curb test). Regarding the impact behaviour, the verifications should be qualitative, controlling the consistency of the overall behaviour and quantitative, based on energy balance analysis for each sub-model (i.e. vehicle, barrier and soil). Model verifications can help to detect eventual modelling errors and they should be applied to all types of configurations of interest.

2.3 Model validation

The main difficulty of the model validation concerns the limited access to experimental data. As mentioned before, crash tests are relatively expensive and are never performed in a large quantity. In addition, the tests are most commonly instrumented in order to assess the performance of the barrier under impact and very little information is available on the vehicle's deformation.

Nevertheless, when a crash-test video is available, it is always possible to compare the overall behaviour of a vehicle and to estimate the deceleration at various points (e.g. [9]).

2.4 Sensitivity analyses

Since it is difficult to use extensive validation data, sensitivity analyses are strongly recommended in order to characterize better the properties of the model.

Sensitivity analyses can have various objectives, such as:

- studying the influence of the impact scenarios on the barrier performance, e.g., vehicle velocities, vehicle mass, impact angle, vehicle type
- studying the influence of the barrier setups and boundary conditions, e.g., other possible soil types, interaction with different traffic infrastructures,
- strengthening the verification and validation by assessing quantitatively the effects of different parameters
- assisting the design of impact tests.

2 GENERIC VEHICLE MODELS

The aim of generic vehicle models is to represent a group of vehicles of a given category as defined in the standard [3] and not only one specific vehicle. For this reason, only the features of the vehicle structure, which are brand and model independent and it is present (in some form) on any vehicle in its category are included in the model. Another aspect, which governs the decision, which parts of the vehicle should be included and which should be omitted, is the requirement for the computational efficiency of a simulation.

The vehicle models considered here are designed specifically for virtual barrier testing. Unlike typical vehicle models used for passive safety assessment, they do not need to represent components that have negligible impact on crash behaviour. As a result, the model includes only the components that are crucial for crash stiffness and vehicle mass distribution, ensuring the vehicle model can accurately simulate the impact on the barrier. In addition, the crash effects of parts, which do not (or very little) contribute to the overall behaviour of the vehicle impact behaviour, like interior trims and components (e.g. dashboard, seats), are unimportant for these analyses and do not need to be represented in the model. However, in the used models the total mass is preserved by increasing the mass of other modelled components.

According to these guidelines, three different generic vehicle models have been developed by the European Commission, corresponding to the following categories: a) N1, b) N2A, N3C and N3D and c) N3G, see **Figure *2***.

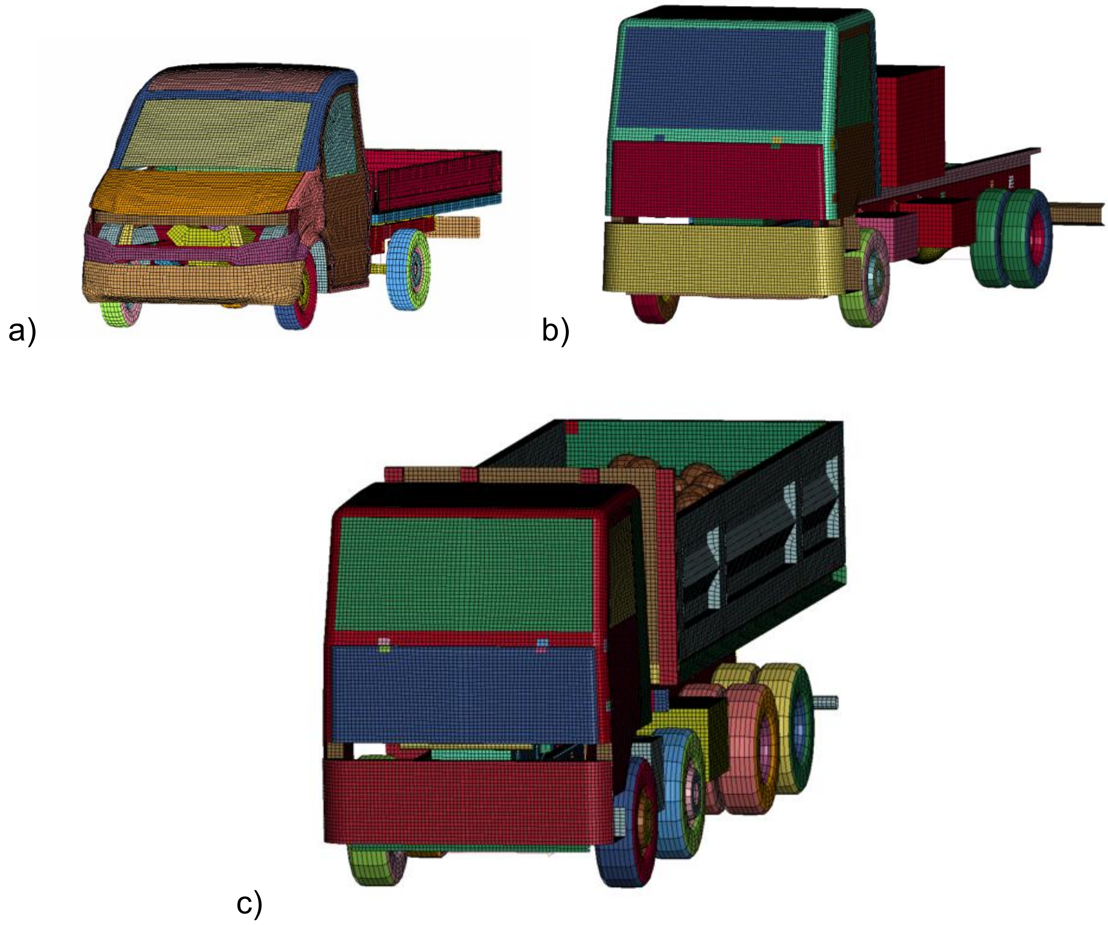

Figure 2. Three different generic vehicle models for the following categories as defined by the ISO standard [3]: a) N1 (≤3.5t trucks), by) N2A, N3C and N3D (7t to 12t trucks) and c) N3G (≤30t trucks).

The parametric nature of these models allows manipulating key vehicle attributes such as mass distribution, dimensions, suspension properties and crash-related stiffness to accurately represent a vast range of real vehicles within a specific category. This flexibility is achieved by defining parameters for these attributes, which can be easily adjusted to simulate different vehicle configurations, conditions and impact scenarios, thus broadening the scope of barrier performance assessments beyond the limitations of physical crash tests. The parametric approach also enables the models to account for the inherent variability in vehicles' age and condition, which can significantly influence their behaviour in a crash scenario.
One of the significant advantages of parametric generic vehicle models is the potential for conducting sensitivity analyses, which can enable a comprehensive understanding of barrier performance under different conditions.

All the three presented models are tested through crash-test simulations ([8], [9], [10]). The performance of the models to replicate correctly an impact on a bollard is assessed by comparisons to experimental data extracted from crash-test videos. It is important to stress that the experimental data available is very scarce, so the model must be thoroughly checked, because certain errors could be hidden if the simulations were compared only to the test data.

3 IMPACT LOAD CHARACTERIZATION

3.1 Vehicle crashing behaviour

A vehicle ramming threat is usually defined only by the vehicle category, its total mass and the impact velocity. However, the actual load on a barrier (e.g. a bollard) also depends on the mass distribution, the stiffness of different vehicle components, and the connections between these components. The most important component for the crash behaviour is the frame (i.e. the chassis), composed of two longitudinal beams, connected with several cross-members and to which all other components are connected directly or indirectly (**Figure 3**). During an impact on a rigid barrier, the frame absorbs the largest part of the total energy. Its overall crushing mechanism and strength directly determine the impact duration and, consequently, the average impact force. The stiffer the frame, the shorter will be the impact duration and the higher the average force for the same initial vehicle velocity.

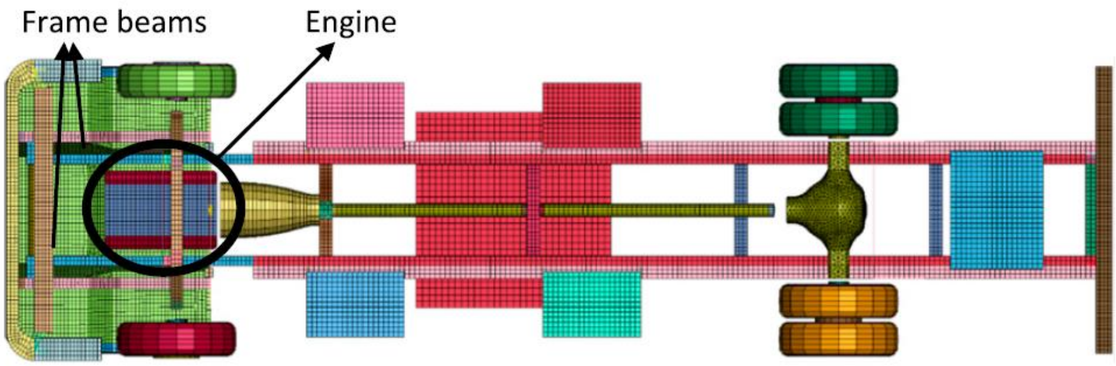

Figure 3. Bottom view of the generic vehicle model for categories N2/N3. Two main components in terms of the crash behaviour, the frame and the engine, are highlighted.

The impact forces also depend a lot on the engine (**Figure 3**), which is a relatively big, heavy and rigid component, and it is very different from all other components in terms of energy absorption. In typical configurations (e.g. [5], [7], [12]), the engine is responsible for the highest force peak acting to the barrier. At the same time, the stiffness of the engine cannot be assessed with accuracy, which means that the computed peak forces in a simulation might not be realistic.

3.2 Barrier response

The barrier dynamic response depends not only on its design (dimensions, materials, etc.), but also on its interaction with the environment through its foundation, which can be of very different types (shallow, deep, etc.). Simulating the entire system barrier-foundation-environment is feasible, but requires a lot of input information, in addition to being computationally costly [11].

In order to obtain a conservative estimation of a vehicle impact load, it is convenient to assume that the barrier undergoes a very small deformation, not affecting the crashing behaviour of the vehicle. Under this assumption, the impact force-time load is independent from the barrier's dynamic response and can be computed by a simulation assuming a completely rigid barrier.

The assessment of the barrier response to the impact can be done by the so-called "equivalent static force" approach, according to which a static force is determined to induce the same maximum deformation of the barrier as the direct dynamic analysis approach [12].

Although the "equivalent static force" approach is much less accurate than the fully coupled simulation approach, especially for barrier systems expected to undergo multimodal dynamic responses or non-linear deformations, it is more practical for rapid assessment and can help in selecting the most critical vehicle impact scenarios for a given barrier.

Additionally, it is important to note that using the perfect rigidity assumption to determine the force history for flexible barriers overestimates the force amplitude, ensuring the conservatism of the approach (e.g. see [6]).

4 RESULTS AND DISCUSSION

The objective of the presented numerical simulations is to assess the sensitivity of the impact load on a rigid barrier of different crash configurations. A N2A vehicle configuration is studied, using the model developed in [9] and assuming the impact velocity of 48 km/h.

As it is shown further on, the relative vehicle-bollard position changes significantly the crashing stiffness of the vehicle reflected by significantly different force-time functions, even if the initial vehicle velocity and mass are kept the same.

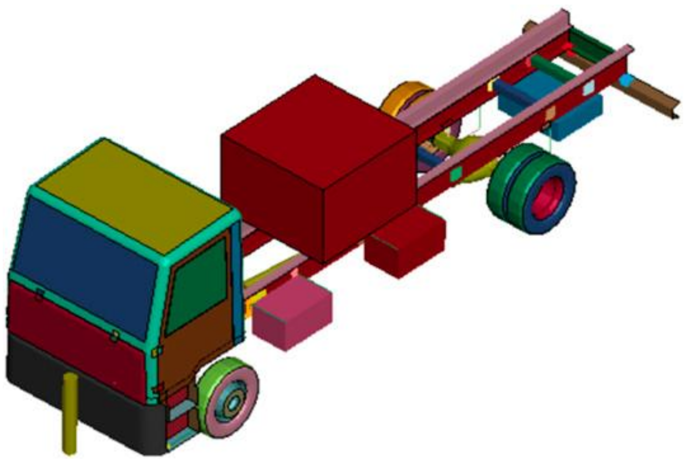

Figure 4. Numerical model for the vehicle categories N2A, N3C and N3D, together with a bollard, considered undeformable in this study.

The N2A category corresponds to a family of medium heavy trucks, with maximum mass of 7.2t ISO 22343 (2023). The basic characteristics of the model used are the following:

- Wheelbase (horizontal distance between the front and rear wheels): 5090 mm
- Vehicle length: 8500 mm
- Total mass (vehicle, including cargo): 7200 kg

All the details on the used generic vehicle model (**Figure 4**) are available in [9].

Several relative bollard-vehicle positions were analysed. In addition to the baseline "centred" scenario, the positions where the bollard-to-vehicle centre distance is equal to: *150mm,* *400mm and 750mm* (**Figure 5**) were also considered. The distance of *400mm* corresponds to a position of the bollard aligned with one of the frame longitudinal beams (i.e. “beam-centred”), the distance of *150mm* corresponds to a “non-centred” scenario and the distance of *750mm* corresponds to a situation where the vehicle hits a bollard with the part external to the frame longitudinal beams.

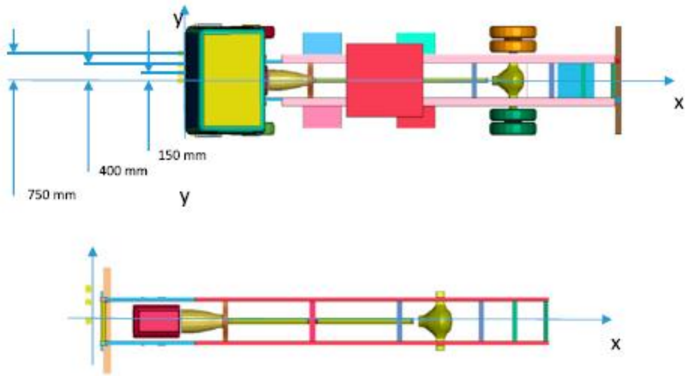

Figure 5. Four impact scenarios analysed with the N2A model. The considered bollard distances from the vehicle symmetric axis are: 0mm (“centred”), 150mm, 400mm (“beam-centred”) and 750mm (“outlying”). On the top, the whole model and in the bottom, the vehicle without the cabin are shown in a top view.

The **Figure 6** shows the deformed states of the vehicle after the impact for the various scenarios. As expected, the more the bollard is distanced from the symmetric axis of the vehicle the more the vehicle exhibits rotation around the vertical axis. In the *0mm* (“centred”) and *150mm* (“non-centred”) scenarios, the engine hits the bollard directly, whereas in the scenarios *400mm* (“beam-centred”) and *750mm* (“outlying”) it rather slides along.
The direct shock of the engine to the bollard creates the highest force peaks for the configurations 0mm (“centred”) and 150mm (“non-centred”). Nevertheless, for the 400mm “beam-centred” scenario, the force peak is even higher, due to the stiffness of the frame beams.
It is important to stress that the vehicles heavier than 3.5t usually do not have shock absorbers like passenger vehicles or N1 vehicles, since from the road safety perspective they are more considered like “threats” than “victims”. As a consequence, the frame beams exhibit a very stiff shock behaviour. For the *750mm* (“outlying”) scenario, the force peak is due to the bollard interacting with the first wheel axle, which leads to lower peak values. Due to the rotation around the vertical axis of the vehicle during impact, the friction interaction with the ground becomes significant for the *750mm* (“outlying”) scenario, leading to a reduced load on the barrier.

The “equivalent static load” is also presented in the **Figure 6**. The results show that the “equivalent static load” is strongly dependent on the barrier’s natural frequencies. However, the natural frequencies of a barrier are not easy to be determined because they can be significantly influenced by the barrier’s foundation design and the surrounding soil conditions. If the bollard considered in this study was perfectly anchored in the ground, its first natural frequency is expected to be between *80Hz* and *120Hz*, depending also on the material used (usually a bollard is a steel shell filled with concrete). Due to the foundation flexibility, the first natural frequency of the bollard system could be much lower. On the other hand, the natural frequencies could be also higher for different bollard geometries (e.g. a bigger diameter).

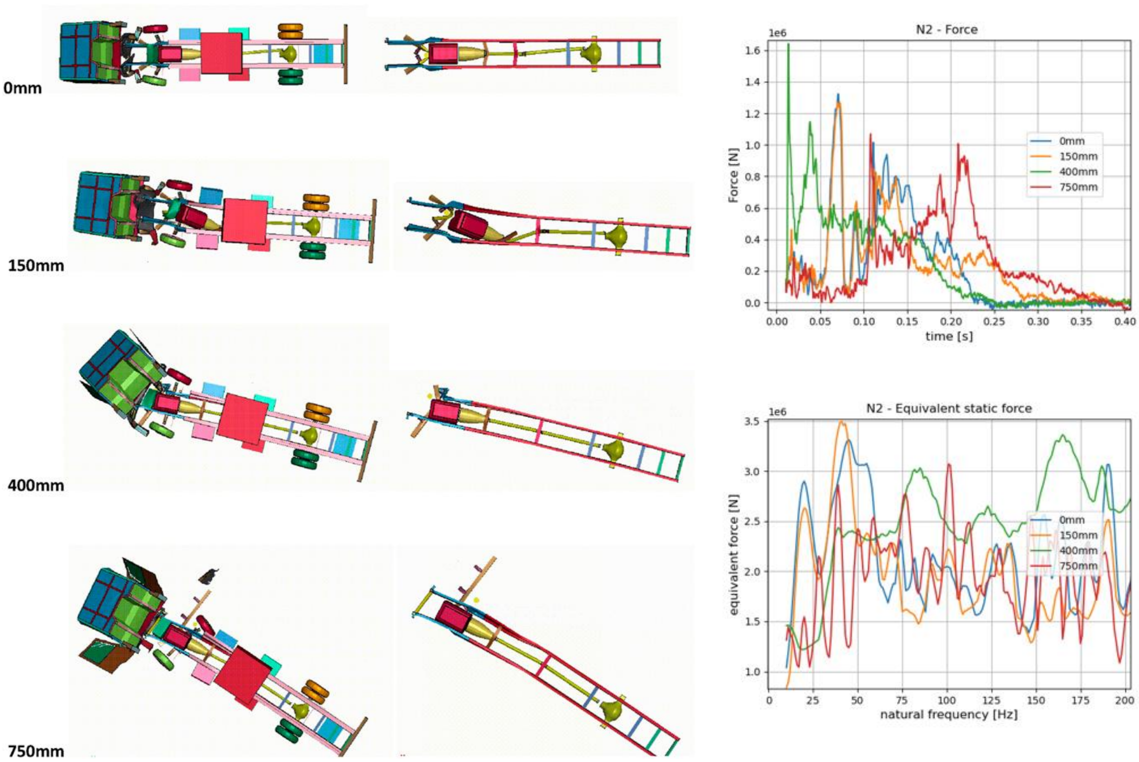

Figure 6. Vehicle deformed state (left columns) during the impact for four studied scenarios shown in **Figure 5**: 0mm ("centred"), 150mm ("non-centred"), 400mm ("beam-centred") and 750mm ("outlying"). On the left, the whole vehicle is shown and, in the middle, the full frame and the engine with the driveline are visible. The force-time plot (top right) and the "equivalent static force" are also shown on the right.

4 CONCLUSION

The generic vehicle models have been developed for simulating impacts on security barriers. They are a key ingredient in a general methodology, according to which the performance of a security barrier can be assessed by a full-scale simulation based on three distinct subsystems: the vehicle, the barrier and the surrounding soil.

In a first approximation, the barrier can be considered as rigid in comparison to the vehicle, which allows performing vehicle impact simulations without modelling explicitly the barrier and its surrounding soil. In this framework, the impact load can be characterized in terms of force-time functions or an "equivalent static force", a further simplification.

The conducted sensitivity studies lead to the conclusion that the impact load on a security barrier depends a lot on the vehicle crash-stiffness, not only on the impact velocity and on the total mass of the vehicle. In particular, the study shows that only a slight shift of a vehicle-bollard impact from the vehicle centre leads to a significant change in the vehicle response and thus in the load on the barrier.

Further and extensive sensitivity studies are necessary for a full understanding of loads on security barriers in case of vehicle impacts.

REFERENCES

[1] Security by design (2022) “*Security by Design: Protection of public spaces from terrorist attacks*”, Joint Research Centre of the European Commission.

[2] Karlos, V., Larcher, M., Solomos, G. (2018), “*Guideline: Selecting proper security barrier solutions for public space protection*”, EUR 113778, Joint Research Centre of the European Commission.

[3] ISO 22343 (2023), “*Security and resilience — Vehicle security barriers — Part 1: Performance requirement, vehicle impact test method and performance rating*”, standard ISO 22343-1:2023.

[4] ISO 22343 (2023), “*Security and resilience — Vehicle security barriers — Part 2: Application*”, standard ISO 22343-2:2023.

[5] Chen, L., Xiao, Y., Xiao G., Liu C.L. (2015), Agrawal, A.K., ”*Test and numerical simulation of truck collision with anti-ram bollards*”, International Journal of Impact Engineering (75). p.30-39.

[6] Valsamos, G., Larcher, M., Casadei, F., Karlos, V. (2020), “*A numerical framework to support the certification of barrier testing*”, EUR 30165 European Commission, Ispra, Italy.

[7] Chen, L., Wu, H., Fang, Q., Zhang, T. (2018), ”*Numerical analysis of collision between a tractor- railer and bridge pier*”, International Journal of Protective Structures, Vol. 9(4), p. 484–503.

[8] Sebik, M., Popovic, M., and Kleteckova, K. (2022), “*Generic vehicle model N1*”, JRC130165, Joint Research Centre of the European Commission.

[9] Sebik, M., Kodajkova, Z. (2023), “*Generic vehicle model N2A & N3D*”, JRC135531, Joint Research Centre of the European Commission.

[10] Sebik, M., Kodajkova, Z. (2024), “*Generic vehicle model N3G*”, JRC139954, Joint Research Centre of the European Commission.

[11] Andrae, M., Markovic, D., Schumacher, R., Karlos, V., Larcher(2024), M, “*Methodology for numerical simulations of vehicle impact on security barriers considering soil-barrier interaction*”, EUR 31844, Joint Research Centre of the European Commission.

[12] Markovic, D., Scattina, A., Larcher, M., (2025), ”*Impact load characterization for security barrier performance assessment through simulations using generic vehicle models*”, International Journal of Protective Structures, Vol. 16(1), p. 266–290.

[13] JRC web page (2025), “*Data and Tools to Counter Terrorism - Hostile Vehicle Mitigation - Generic Vehicle Models*”, Joint Research Centre of the European Commission, website: https://counterterrorism.ec.europa.eu/hvm/generic-vehicle-models.php.

15th International Conference on
Shock & Impact Loads on Structures
12-13 June 2025, Gothenburg, Sweden

CABLE FENCE AS AN EFFECTIVE VEHICLE SECURITY BARRIER

Tat-Seng LOK[a], Danny Chin-Teck ONG[b] and Robert STEPHENS[c]

[a]PHM Technologies Pte Ltd, Singapore, email: ctslok@ntu.edu.sg
[b]B P (Systems) Engineering Pte Ltd, Singapore, [c]8o65 Ltd, UK.

Keywords: Cable Fence System, Design Construction & Testing, Full-Scale Testing, Vehicle Security Barrier, International Test Standard, Compliance

Abstract

This paper considers the design, construction and testing of a cable fence system as a vehicle security barrier (VSB) to resist the impact of a vehicle to comply with existing international test standards. However, the cable fence barrier is not referenced in current standards even though the principles of vehicle intrusion and vehicle penetration are important parameters in risk assessment methodology. The cable fence system differs in configuration from conventional "hard target" designs outlined in existing test standards. In spite of the system being ignored in current VSB test standards, the use of a cable fence system has gained traction due to increasing demand for alternative VSB systems in different threat scenarios, for sustainable and low carbon footprint construction, construction-maintenance-cost pressures in the built environment, security of industrial facilities and in rejuvenation projects where planners prefer the "green" agenda to improve security protection of public spaces.

The authors outline a cable fence barrier, its design, construction and testing to sustain a vehicle impact in accordance with existing international test standards. The system being tested allows project specifiers to select an appropriate standard in their jurisdictions where the current standard may overlap with the most recent test standard for VSB performance. The preliminary design is based on an idealised energy conservation principle to determine vehicle penetration. Acceleration-time history obtained from past tests conducted by the authors on hard RC targets provided appropriate load duration data of the process. This enables estimation of cable force and subsequent vehicle penetration, albeit conservatively. Compliance with two test standards was made possible by using an appropriate vehicle of a certain age. Details of the design, construction and testing are outlined. Video footage of the vehicle impact test showed the efficiency of the designed system.

1 INTRODUCTION

Vehicle security barriers are essential to prevent the risk of a breach by vehicles driven at high speed, intentionally or accidentally, into crowded spaces or critical infrastructure. In view of recent cases of weaponised vehicles around the world, there has never been a more urgent time to implement effective, rapidly deployable and user-friendly vehicle security barriers as part of a hostile vehicle mitigation scheme. The purpose of the VSB is clearly to mitigate and to protect public/facilities from the hazards caused by a fast-moving vehicle. Reports on advice and guidance on hostile vehicle mitigation philosophies, potential hazards and the use of vehicle mitigation engineered VSBs are available in the public domain [1 – 4], including recent changes to hostile vehicle mitigation (HVM) methodology and adoption of modern test standards.

Traditional barriers are normally hard targets constructed either as a series of bollards, individual engineered mass street furniture or simply a length of reinforced concrete wall. A check on the *Catalogue of Security Equipment* website of the UK NPSA (public access) indicates a handful of cable/rope fence system as a VSB compared to hard targets. Perhaps, the risk profile excludes the cable fencing system, and even fewer are categorised as an effective VSB complying with the latest test standards. It is unsurprising that hard targets dominate the range of VSBs because the effectiveness of such barriers is the stiffness of the system to prevent vehicle penetration. A further risk of breach by the perpetrator following a preventable vehicle access is outside the scope of this paper and will not be addressed here.

This paper presents a preliminary design to include approximate sizing of structural members, possible tilting of foundations/cable posts due to poor ground conditions, number of cables to restrain vehicle penetration, vertical spacing of cables to avoid vehicle vaulting the barrier, and compliance with existing international test standards. The designed barrier was constructed and tested in accordance with international test standards by using a designated vehicle to impact perpendicular to the cables and at the most vulnerable location of the barrier.

2 REVIEW OF CURRENT VSB TEST STANDARDS AND PAST TESTS

The current accepted crash barrier standard tests in UK, European and other jurisdictions are the International Workshop Agreement, IWA 14-1 [5], the International Organisation for Standardization, ISO 22343-1 [6], and the American Society for Testing and Materials, ASTM F2656M-20 [7]. However, the cable fence system is neither illustrated nor mentioned as a vehicle security barrier. A number of examples of “wire rope fence or vehicle restraint system” may be seen in The *Catalogue of Security Equipment (NPSA)* for security practitioners, but none of the designated systems complied with current test standards [5, 6]. A related but comprehensive document [8] on highway safety structures contains a wealth of information and recommendations on the safety performance assessment of “highway features”. The document outlines a range of impact conditions and penetration performance levels to establish performance of highway structures in the same way as other test standards [5–7]. MASH [8] further recognises that duplication of site and safety layout conditions as impossible. Nevertheless, test compliance requirement with [5, 6] was an issue for the authors.

Project specifiers are advised to exercise caution when using test standards alone as a precondition to safeguard facilities and the public in open spaces. For example, each standard has its own approach in defining vehicle type and procedure for determining penetration. Nevertheless, all international standards have a long tri-partite history of engagement between the standards organisation, professional security engineers and approved testing houses to establish vehicle crash tests to consistently assess the performance of VSBs. Where standards differ, users should specify the test standard that aligns with the risk assessment to minimise harm/hazards. The differences depend on the risk appetite of security authorities and building owners in the environment that the risk assessment is designed to protect taking account of the significance of the open space, importance of the building or the designated critical national infrastructure.

The principles of protection and a comparison of test standards were previously outlined by the authors [9]. While the use of a cable fence as a protective anti-crash highway structure is not new, the cable system is rarely discussed as a VSB despite its extensive use in important industrial and high-value manufacturing facilities. Used in combination with an anti-climb fencing system, the cable fence barrier can be an effective deterrent against hostile vehicles. The authors have previously conducted several tests on “hard targets” VSBs, and the cable fence system is one of several configurations presently being examined. One of the hard targets investigated by the authors is shown in Figure 1. Clearly, the use of a flexible cable fence represents a departure from the “usual” barrier designs, especially for engineers who are familiar with [5–7].

1(a) Before vehicle crash

1(b) After vehicle crash

Figure 1. Previous test on a reinforced concrete surface mounted low-wall VSB

For cable fence assessment, Reference [10] provides a useful guide to estimate the cable strain, vehicle displacement and cable tension to prevent users from over-manoeuvring their vehicle during parking in multi-storey car parks or open spaces. The guidance is applicable to light vehicles, with the mass well below that of larger commercial vehicles. Further, vehicle impact on the cable fence is quasi-static due to the low impact speed and the vehicle displacement being based on static consideration.

In this paper, the authors approached the design with little or no information on cable fencing systems as VSBs. Thus, this approach is preliminary to estimate the penetration of a proposed cable fence barrier shown in Figure 2, and to derive the number of cables needed to sustain the dynamic impact load. Using energy conservation principles, similar to impacting billiard balls, the dynamic penetration is derived. As the cables are stretched, the vehicle will pull the foundations/columns B and C inwards. Thus, soil conditions need to be considered. Using data from previous tests, a preliminary outline of the cable fence was determined. The vertical cable arrangement was designed to match the vehicle characteristics and the calculated dynamic penetration is compared with static displacement [10].

3 PRELIMINARY APPROACH TO THE PROPOSED DESIGN

For hard target design, the authors adopted the principle of linear momentum to determine the force on impact so that the rate of change of momentum, R_m, may be expressed (assuming no energy losses, energy dissipation during impact, etc.) as:

$$R_m = (M_f - M_i)/\ (t_f - t_i) \tag{1}$$

where M_f and M_i are the final and initial linear momentum of the vehicle, and where the subscripts of the impact time duration ($t_f - t_i$) represent the final and initial time of the vehicle respectively. If the final time is taken as zero, Equation 1 may be re-written as:

$$R_m = (m_f.v_f - m_i.v_i)/t \tag{2}$$

where m is the vehicle mass and v *is* the velocity on impact, t is the duration of impact loading characterised by a sudden rise of the load on impact and attenuating to 0 at time t_f. If the vehicle remains completely intact (with no loss of vehicle parts) at impact, $m_f = m_i$. Since $v_f =$ 0, Equation 2 is reduced to:

$$R_m = (m.v_i)/t \tag{3}$$

Thus, the rate of change of momentum (R_m) represents the dynamic applied force (F) on the hard wall at the end of the impact process. In a test using the DAF vehicle shown in Figure 1, the duration of loading from the recorded time history is of the order of 150-250 milliseconds. The duration is specific and needs to be assessed for different vehicles since different vehicles behave differently on impact onto hard targets. Clearly, the duration depends on the rigidity of the target and the vehicle. A flexible cable system may have durations longer while a more rigid cable system may have a shorter duration during the restraining process. Estimates of the duration for a cable fence system vary from 200-400 milliseconds. Nevertheless, a longer duration implies a lower impact force. However, this does not imply a lower penetration.

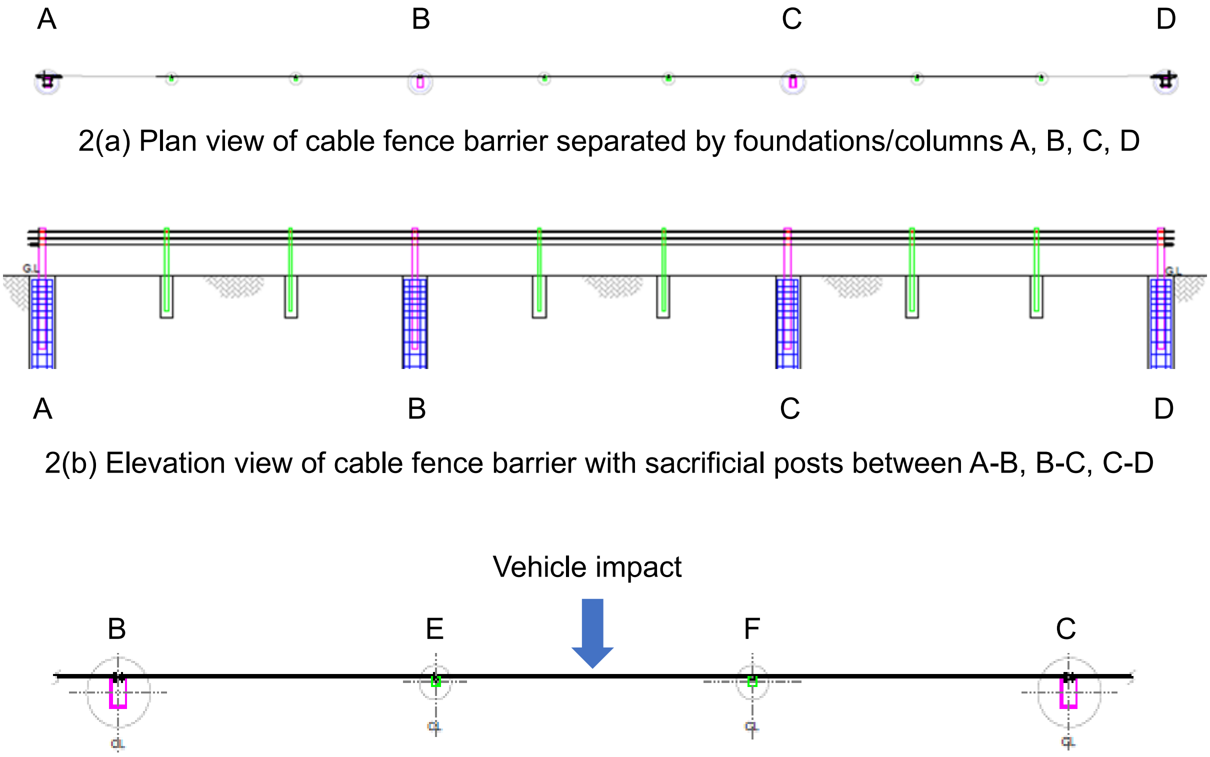

2(a) Plan view of cable fence barrier separated by foundations/columns A, B, C, D

2(b) Elevation view of cable fence barrier with sacrificial posts between A-B, B-C, C-D

2(c) Enlarged plan view of centre portion B-C, separated by sacrificial posts, E and F

Figure 2. Test layout of proposed cable fence barrier design

Figures 3(a) and 3(b) show the central section of the cable fence system with the vehicle just before and after impact respectively. The cables are not pre-tensioned so that the kinetic energy of the vehicle just before the cable is impacted is given by:

$$KE = ½\, m.v_i^2 \quad (4)$$

The two sacrificially posts, E and F, are merely cosmetic and are provided to support the cables and to prevent excessive sagging of the cables over the 9-metre length (see Figure 2). They are also designed to restrain the critical parts of the vehicle on impact. Since E and F play no part in resisting the vehicle force as the cables are stretched during impact, the distance traversed by the vehicle beyond the cable is obtained by equating the kinetic energy to potential energy of the vehicle. Thus, the preliminary idealised vehicle penetration is:

$$\delta = (½\, v_i).t \quad (5)$$

where the penetration of the vehicle, δ, is in metres, v_i is the impact speed in m/sec and t is the duration of impact used to calculate the rate of change of momentum, in seconds.

Equation 5 is independent of vehicle mass because the same vehicle is used in developing their respective energy. From this simplified assessment, vehicle penetration may initially be predicted beyond the barrier. Experience shows that on impact, the vehicle loses some of its body components, which can be clearly seen in Figure 1. Some of the impact force may be absorbed by flexure of the concrete wall. Lateral translation of the whole wall will absorb some energy since the base sits on a layer of lean concrete below the surface, and where the top face is levelled with the ground surface.

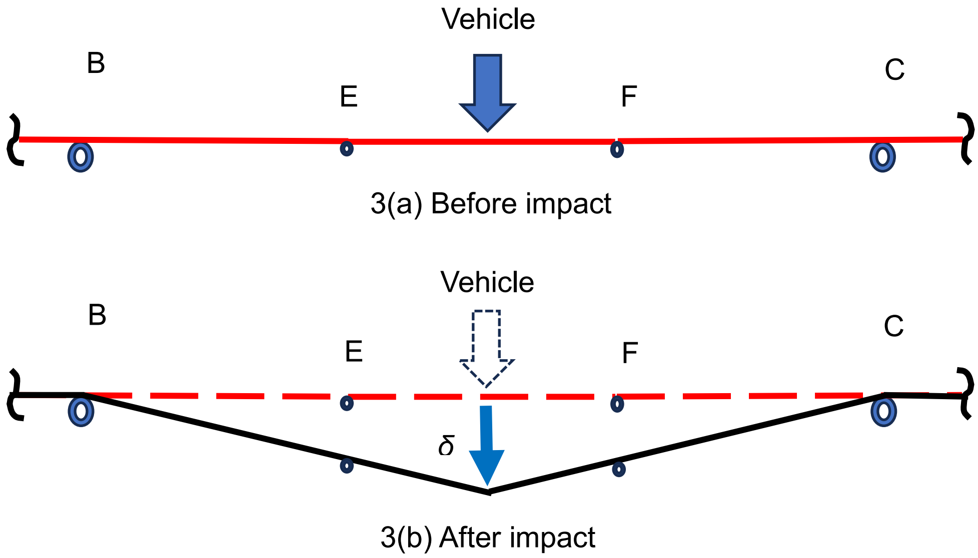

Figure 3. Preliminary analysis of cable response

Effects such as the development of inertia forces and strain-rate effect of cables are not considered. Further, the load imparted during the event depends on the kinetic energy of the collision of the vehicle and the cable. This interaction is dependent on their stiffness, mass, material properties and non-linear behaviour. So, the energy assessment is applicable to an ideal case. Nevertheless, it provides a conservative design basis to initiate assessment of the cable fence barrier without the aid of computational software and dedicated manpower.

If the main columns, B and C, shown in Figure 3(b), are pulled inwards by the cables on impact, additional penetration of the vehicle is imminent. To consider this additional displacement, it is assumed that the below-ground column rotates by an angle, θ, at peak penetration. Figure 4 depicts the possible rotation of the foundation or the above-ground flexure of columns B and C.

The rotation of the main columns (A, B, C, D in Figure 2) is governed by the ground condition on which these posts are set. The soil condition determines whether increased rotation should be considered. To comply with [6], a ground investigation was conducted separately by a geological team engaged by the testing house. Borehole records were obtained adjacent to the test site and the soil characteristic profile was determined.

The soil characteristics in the vicinity is not uncommon in the test area. The borehole records display mainly firm but friable gravelly-sandy-clay up to and over 2.5 metres in depth, and surrounded by stiff mudstone. This information was adequate to convince the authors that the two columns, B and C, are unlikely to tilt on impact. However, in sandy soil or filled sites, the possibility of column rotation should be considered. The design of the reinforced concrete base prevents them from being pulled out of the ground completely. The far posts, A and D, are assumed to remain completely unmoved. To minimise strain and sag of the cables, a spring-loaded cable-end connector was fitted. An examination of the water table poses no issues to the proposed design. The water table level was confirmed during the auguring process in the construction of the foundation.

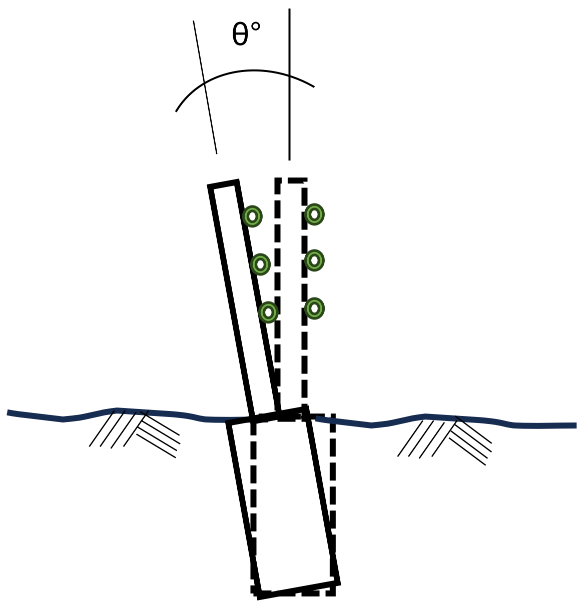

Figure 4. Tilting of foundation/columns B and C by angle, θ (and/or flexure of the column)

4 PENETRATION PREDICTION AND OTHER DESIGN CONSIDERATIONS

An N2A class vehicle was specified for the test as this is the same vehicle used in previous hard target tests. Such vehicles are commonly used in industrial settings and are also employed extensively in commercial business environments. The dimension from the front bumper to the vehicle datum measuring point is crucial to judge vehicle penetration. However, the vehicle comes in several different masses, ranging from 6,800 kg to 7,500 kg. The gross mass of the vehicle was chosen as 7,200 kg in the analysis and the vehicle was specified as less than 10 years old. In this way, the selected test vehicle achieves compliance with Reference [6], which is the test standard in the UK and other jurisdictions, while [5] continues to be used as an overlap until it is superseded in future. With continuous updates on risk assessment, [5] or [7] may no longer be applicable to satisfy new risk analysis methodology that [6] was designed to unify. Indeed, [5] and [7] are being updated continuously.

Using the aforementioned data, the authors were able to consider a preliminary design using the vehicle mass and an impact speed of 48 kph. Equation 5 gives the calculated vehicle displacement as 1.33 metres. An average impact duration of 200 milliseconds (derived from records of previous hard target tests) was used to obtain the dynamic force of the vehicle. As discussed earlier, the duration is the key to the estimation but data for the cable fence system was unavailable at the time of design. Note that the impact duration is only applicable for this vehicle. As a comparison, the static displacement calculated from [10] is 0.59 metres.

The number of cables was determined from a static force equilibrium of the configuration shown in Figure 3(b). Three cables were adopted (from a selected static capacity of 40 tonnes per cable) to sustain the dynamic load. The calculation assumes that the main columns, B and C, remain unmoved.

If the exposed main column with a length of 1.15 metres were to rotate/bend with a rigid-body rotation (θ) of 15°, then the additional penetration is 0.31 metres. Thus, the total calculated vehicle penetration is 1.64 metres. This value may cause consternation amongst risk analysts or hostile vehicle mitigation engineers but [5, 6] will rate the proposed cable system as "zero penetration" because the dimension between the front bumper to the vehicle penetration datum point exceeds the calculated total penetration. Based on these initial estimates, the proposed cable fencing system was prepared for construction and testing.

5 CONSTRUCTION AND TESTING

All the parts of the cable fence barrier system were fabricated in Singapore using locally-sourced and available materials to demonstrate constructability. The fabrication process of, for example, the foundation reinforcement cage and cable-end connectors, were completed by a local workforce. The assembled fabricated parts, together with a full set of technical drawings and construction sequence instructions, were quantified and shipped to the UK testing house to be constructed and assembled by a UK workforce. The construction instructions list the process of setting up, with key dimensions highlighting the proposed cable fence system.

Once the position was identified, the ground was augured with 600mm and 300mm diameter borers for the main columns and sacrificial posts respectively. Ready-made reinforcement cages and above-ground steel posts were lowered into the excavation, adjusted and aligned before concrete was poured. The concrete was cast in January 2025. Details of the foundation construction sequence which took 2 days, are shown in Figure 5. The specified characteristic concrete strength was 35.0 N/mm^2. The average compressive cube strength at 7 and 14 days was 32.6 N/mm^2 and 40.9 N/mm^2 respectively. The average compressive cube strength at 28 days, which coincided with the vehicle impact test, was 46.7 N/mm^2. The cables were installed 14 days after the concrete pour. If rapid hardening concrete had been used for the foundations, the entire set-up of the cable fence barrier system could have been completed and functional within 4 days. Details of the installed cable are shown in Figure 6.

If a security fence were installed on a project site, the security practitioner may demand that the same fencing is also installed exactly as constructed in the test arrangement. In this case, the fencing, or parts thereof, will form part of the test report. Post-test debris include fencing parts (mullions, nuts/bolts, etc), cables and posts or any part(s) of the vehicle weighing 2 kg or more shall be noted and located within the 25m perimeter of the test barrier [6]. This requirement is a risk-intended safety net should the VSB be constructed adjacent to facilities in a compact built environment or where vehicle penetration and debris may pose hazards to delicate equipment, infrastructure or to the public.

On the day of the test, the designated vehicle was positioned at the impact location of the cable fence as shown in Figure 7(a). This procedure allows final checks on vehicle alignment and the positioning of gantries with attached hi-speed photography equipment. Various sensors were attached to the main columns and the cable-end springs. Thereafter, the vehicle was retracted to a position for final checks of on-board instrumentation. Structural monitoring equipment were armed as the vehicle was launched. The final post-impact position of the vehicle is shown in Figure 7(b).

6 POST-TEST OBSERVATION AND FUTURE DEVELOPMENT

The cable fence system restrained the vehicle from further penetration, drawing similarity between Figures 1(b) and 7(b). From the video recording, the maximum dynamic penetration was measured as 0.90 metres [5, 6]. The static (at rest) penetration was -0.10 metres, and the tested cable fence system is rated zero penetration (static) in accordance with [5] and [6]. All the foundations/columns A, B, C and D remained vertical. The estimated penetration from the idealised energy conservation principle overestimated the penetration by a factor of 1.48, which accounts for all unquantified resistance to the impact force. The static displacement [10] underestimated the dynamic penetration. The results showed that the proposed design is safe based on the assumptions made, and the system may be viewed as an effective VSB.

The final outcome of the test was as predicted. Vertical measurements and slow-motion observation of all the main steel columns showed slight elastic displacement. The sacrificial posts were not sheared off but flattened while all the cables slid horizontally by about 20mm, confirming that the correct torque had been applied to the C-clip cable bolts. Both the outer columns deflected elastically and all the cable end-springs were activated. The end-assuage connectors that bind the cable ends within showed no cable pull-out. Examination of the slow-motion footage of the test showed the performance at various points of the cable fence barrier system as a safe and effective VSB when used as constructed and tested. If rapid-hardening concrete, coupled with an additional one or two cables (below the existing three cables), had been used, the system may be regarded as a "*rapid-deployable vehicle cable catcher system*".

Various electronic and end cable spring compression data was recorded but this data will not be discussed here. Instead, the authors shall continue with the test programme and incorporate all gathered information as part of a process to develop a non-linear numerical computational model of the cable fence system.

5(a) Augur into ground (note water table)

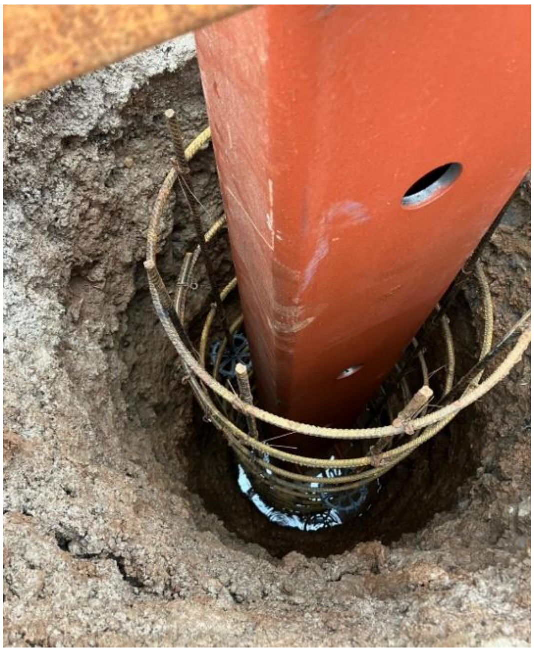

5(b) insert and set reinforcement/post

5(c) Cable columns/posts alignment

5(d) Concreting operation

Figure 5. Construction sequence

6(a) Un-tensioned cables

6(b) Eliminated slack/sag of cables

Figure 6. Installation of cables

7(a) Positioning/alignment of test vehicle

7(b) Final position of vehicle (post-impact)

Figure 7. Vehicle impact test sequence

7 CONCLUSIONS

(a) Cable fence barrier system differs in configuration and behaviour from conventional hard targets designed as vehicle security barriers.
(b) Existing International test standards used in Europe/UK/USA do not reference the cable fence system as a vehicle security barrier.
(c) The tested cable fence barrier system could supplement existing HVM mitigation risk methodology. However, the cable fence barrier needs to be included in vehicle test standards to be accepted as a VSB.
(d) Cable fence systems have been used extensively as part of perimeter security eco-system in industrial environments and in major highways. They may gain further traction as a temporary or permanent security barrier in view of increasing demand for protection of open spaces, in sustainable and low carbon footprint construction, and rapid construction-maintenance-cost pressures.
(e) Preliminary analysis using idealised energy conservation principle suggests a good and safe starting point to formulate a cable fence barrier system design. However, a more detailed analysis, including the use of non-linear computational tools, is essential to improve understanding. The impact duration is key to establishing robustness and integrity of the system, and providing better estimates of the penetration.
(f) A vehicle impact test was conducted on a designed cable fence system and the outcome confirmed the effectiveness of the cable fence as a safe vehicle security barrier.

(g) By using an appropriate ballasted age-limit vehicle, the test process complied with two international test standards in current use.
(h) The test provided valuable data to enable re-assessment of the design approach, allows closer examination of strong/weak joints and support the design to improve robustness, resilience, safety, and with the possibility of including additional cables to use as a rapid deployable vehicle cable catcher security barrier to fully comply with test standards.

ACKNOWLEDGEMENT

The support of staff from Highway Safety and Protection of Infrastructure, HORIBA-MIRA, UK, is gratefully acknowledged. Their conversation over many years of engagement is appreciated. To other individuals who provided valuable feedback on HVM/VAW methodology, we thank them for their generous sharing of views. Finally, we are grateful to B P (Systems) Engineering, Singapore, for funding this continuous R&D programme.

REFERENCES

[1] Hostile Vehicle Mitigation, Guidance to help practitioners determine the vehicle-borne threat, assess site strengths and vulnerabilities, and identify suitable options for hostile vehicle mitigation, *NPSA, Crown Copyright.* Dec 2024.

[2] Hostile Vehicle Guidelines for Crowded Places, A Guide for Owners, Operators and Designers, *Australia-New Zealand National Counter-Terrorism Committee (ANZCTC)*, Commonwealth of Australia 2017.

[3] FEMA 426, Reference Manual to Mitigate Potential Terrorist Attacks against Buildings, *Federal Emergency Management Agency, US Dept of Homeland Security*, Dec 2003.

[4] J. Coaffee, C. Moore, D. Fletcher and L. Bosher, "Resilient design for community safety and terror-resistant cities", *Proceedings of the Institution of Civil Engineers*, Municipal Engineer 161, Paper 700057, Jun 2008, Issue ME2, pp 103–110

[5] IWA14-1:2013 – Vehicle Security Barrier: Part 1: Performance requirement, vehicle impact test method and performance rating, *International Worksop Agreement*, 2013.

[6] ISO 22343-1:2023, Security and resilience. Vehicle security barriers Part 1: Performance requirement, vehicle impact test method and performance rating, *International Organization for Standardization*, Switzerland, 30 Sept 2023. (corresponding *British Standard BS ISO 22343-1:2023*, 31 Jan 2024).

[7] Standard Test Method for Vehicle Crash Testing of Vehicle Security Barriers, *ASTM International, ASTM Designation: F2656M-20*, West Conshohocken, PA 19428-2959, 2020.

[8] Manual for Assessing Safety Hardware (MASH), *American Association of State Highway and Transport Officials*, 2nd Edi, 2016 (replacement of *NCHRP Report 350, Transport Research Board, National Research Council, Nat Acad Press, 1993*).

[9] T.S. Lok, C.T. Ong and A. Crooks. "Vehicle security barrier as a countermeasure facility against deliberate and accidental vehicle impact", *Proceedings of PROTECT-2024: 9th International Colloquium on Performance, Protection and Strengthening of Structures under Extreme Loading & Events*, Singapore, Paper SMP-13, pp58-68, 13-16 Aug 2024. https://www.protect2024.org/conference-proceedings

[10] James D. Rogers, "Design of prestressed barrier cable systems", Technical notes, Issue 14, Dec 2004, pp 1-8, *Post-Tensioning Institute*, Phoenix, Arizona 85021, USA.

DISCLAIMER

Views and opinions of the Authors are based on available publications in the public domain, and the combined experience of the Authors in protective security and full-scale testing. The contents of this paper should not be regarded as expert advice since the failure of a single test could occur even if the VSB had been adequately designed with a high factor of safety. Thus, we accept no responsibility of anyone using our approach to design the cable fence as a vehicle security barrier.